



Evolving Attention

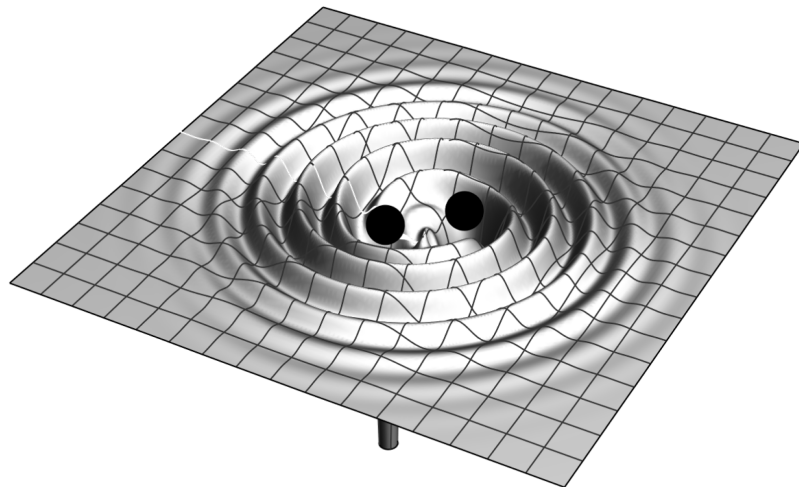
Exploring the Use of Genetic Algorithms and Attention for
Gravitational Wave Data Science

Michael R K Norman

Submitted for the degree of Doctor of Philosophy
School of Physics and Astronomy
Cardiff University
2023-12-30

Evolving Attention

Exploring the Use of Genetic Algorithms and Attention for
Gravitational Wave Data Science



Michael R K Norman

I Summary

This thesis investigates the application of machine learning to gravitational-wave data analysis. Primarily, it focuses on artificial neural networks, but it also presents work to optimize the design and application of these networks with genetic algorithms, another machine learning method. This method of hyperparameter optimisation was utilised to design models for a low-latency burst search pipeline, MLy. Along with the use of genetic algorithms for hyperparameter optimisation, work is also performed to test the performance of attention-based networks on two gravitational wave data analysis tasks, compact binary coalescence detection, and the estimation of the parameters of overlapping pairs of compact binary coalescences.

Section 2 introduces gravitational wave science, in order to contextualize the data analysis problems examined throughout.

Section 3 examines the underlying principles of artificial neural networks and presents a simple example which demonstrates the effectiveness of artificial neural networks as a data analysis method.

Section 4 then explores the intersection between the two introduced fields. It presents the methodology used for training dataset generation throughout the thesis and introduces the custom software developed in order to enable rapid dataset generation and iteration. This section also contains a review of previous work that has been done to use artificial neural networks for gravitation wave data analysis, as well as a series of experiments to demonstrate the ineffectiveness of unspecialized artificial neural networks for the task. This section concludes with recreations of some important results from the literature which act as a comparative baseline for the rest of the thesis.

Section 5 presents Dragonn, a genetic algorithm that can act as a general optimisation method for neural networks in gravitational wave data science. Dragonn can optimize the network architecture, the training dataset, and the training procedure simultaneously, and easily allows for the inclusion of new hyperparameters.

Section 6 presents experiments to test the effectiveness of attention-based networks for gravitational-wave analysis, more specifically, compact binary coalescence detection. It demonstrates a marginal improvement over recreated convolutional neural networks from the literature presented in Section 4.

Finally, Section 7 expands the exploration of attention-based models to investigate cross-attention between multiple gravitational-wave detector outputs. We use this novel approach to examine the problem of parameter estimation on overlapping signals. We find that a standard convolutional neural network adapted from the literature is sufficient to distinguish between single gravitational wave signals and pairs of overlapping signals. The larger cross-attention architecture demonstrates the ability to extract parameters from multiple signals simultaneously, providing results that, in the future, may be used to aid more developed parameter estimation techniques.

II Contents

I Summary	i
III List of Figures	v
IV List of Tables	xxxi
V List of Listings	xxxiv
VI Collaborative Work	xxxvi
VII Acknowledgments	xxxvii
1 Introduction	1
2 Gravitational Waves	3
2.1 Gravity	3
2.1.1 Ye Old Times	3
2.1.2 Special Relativity	6
2.1.3 General Relativity and Spacetime	9
2.2 Orbits are Not Forever	12
2.2.1 Orbits	12
2.2.2 Gravitational Radiation	13
2.3 Gravitational Wave Detection	16
2.3.1 Interferometry	16
2.3.2 The Global Detector Network	18
2.3.3 Interferometer Noise	19
3 Machine Learning	21
3.1 The Artificial Neural Network	22
3.1.1 The Artificial Neuron	23
3.1.2 Training Artificial Neurons	25
3.1.3 Testing the Model	33
3.1.4 Neurons Together Strong	36
3.1.5 Activation Functions	39
3.1.6 Loss Functions	44
3.1.7 Network Design	47
3.2 The Gradients Must Flow	47
3.2.1 Momentum	49
3.2.2 AdaGrad (Adaptive Gradient Algorithm)	50
3.2.3 RMSProp (Root Mean Square Propagation)	51
3.2.4 Adam (Adaptive Moment Estimation)	51
3.2.5 Backpropagation	52
3.3 Overfitting and Regularisation	54
3.3.1 Dropout	55
3.3.2 Batch normalisation	56
3.3.3 Early Stopping	56
3.4 Infrastructure Layers	57
4 The Application of Machine Learning to Gravitational-Wave Data Analysis	58
4.1 Gravitational-Wave Classifiers	59
4.2 Dataset Design and Preparation	62
4.2.1 The Power Spectral Density (PSD)	62
4.2.2 Noise Generation and Acquisition	65
4.2.3 Waveform Generation	68
4.2.4 Waveform Projection	74
4.2.5 Waveform Scaling	76

4.2.6 Data Dimensionality and Layout	83
4.2.7 Feature Engineering and Data Conditioning	85
4.2.8 Transient Glitch Simulation	95
4.3 Perceptron Results	96
4.3.2 CBC Detection Dense Results	100
4.3.3 Burst Detection Dense Results	107
4.4 Introducing Convolutional Neural Networks (CNNs)	111
4.4.1 Convolutional Layers	112
4.4.2 Stride, Dilation, and Padding	119
4.4.3 Pooling	121
4.5 Results from the Literature	122
4.5.1 Convolutional Neural Networks (CNNs) for the detection of Compact Binary Coalescences (CBCs)	122
4.5.2 Convolutional Neural Networks (CNNs) for the detection of Gravitational-Wave Bursts	
127	
4.5.3 CBC Detection Recreation	128
5 Dragonn: Exploring Deep Gravitational-Wave Classifier Hyperparameter Space with Genetic Algorithms	139
5.1 The Problem with Parameters	139
5.1.1 Human-guided trial and error	141
5.1.2 Grid Search	141
5.1.3 Random Search	142
5.1.4 Bayesian Optimisation	143
5.1.5 Gradient-Based Optimisation	144
5.1.6 Population-Based Methods	144
5.2 Dragon Method	146
5.2.1 Why Genetic Algorithms?	146
5.2.2 Selection of Mutable Hyperparameters	148
5.2.3 Genetic Algorithms in Detail	150
5.2.4 Choice of Mutation Method	151
5.2.5 Datasets	152
5.3 Dragonn Results	152
5.4 Dragonn Training	152
5.5 Discussion	159
5.6 Deployment in MLy	159
6 Skywarp: An Attention-Based model for the Detection of Gravitational-Wave Compact Binary Coalescences	161
6.1 Attend Closely	162
6.1.1 Tokenisation and Embedding	162
6.1.2 Positional Encoding	165
6.1.3 Attention!	167
6.1.4 Multi-Head Attention	174
6.1.5 Attention Blocks	175
6.1.6 Transformers	175
6.2 Transient Detection beyond CNNs	177
6.3 Skywarp Method	179
6.3.1 Skywarp Architectures	179
6.3.2 Skywarp Training, Testing, and Validation Data	181
6.3.3 Training Procedure	182

6.4 Skywarp Results	183
6.5 Discussion	190
7 CrossWave: Cross-detector Attention for the Detection and Parameterisation of Overlapping Gravitational-Wave Compact Binary Coalescences	191
7.1 Frequency of Overlapping Compact Binary Coalescences (CBCs)	191
7.2 Detection and Parameter Estimation (PE) of Overlapping Compact Binary Coalescences (CBCs) .	
192	
7.3 CrossWave Method	193
7.3.1 Crosswave Training, Testing, and Validation Data	194
7.4 Overlapnet Results	197
7.4.1 Classification	197
7.4.2 Regression	204
7.5 Aditional Structural Elements	205
7.5.1 Cross-Attention	205
7.5.2 Autoencoders and Denoising	206
7.6 CrossWave Architecture	208
7.7 CrossWave Dataset	214
7.8 CrossWave Results	215
7.8.1 Merger Time Parameter Estimation Results	215
7.8.2 Other Parameter Estimation Results	220
7.9 Discussion and Limitations	226
Bibliography	0

III List of Figures

Figure 2.1 | An illustration of Newton's law of universal gravitation, as described by Equation 2.1. Two particles, here distinguished by their unique masses, m_1 and m_2 , are separated by a distance, r . According to Newton's law, they are pulled toward each other by the force of gravity acting on each object F [1], each being pulled directly toward the other by a force that is equal and opposite to its partner's.

Figure 2.2 | An illustration of two competing historical views on the nature of space and time [2]. *Upper:* Newton's vision of absolute universal time and absolute space, wherein time moves forward at a constant and uniform rate across the universe and space is immobile and uniform. In this model, both time and space can exist independently of objects within, even in an entirely empty universe. *Lower:* Leibniz's view wherein time and space did not and could not exist independently of the objects used to measure them. Within this model, space is simply a measure of the relative distances between objects, and time is a measure of the relative motion of objects as their relative positions change. In this model, it makes little sense to talk of a universe without objects since time and space do not exist without objects with relative positions and velocities.

Figure 2.3 | An illustration of the light clock thought experiment. The light clock thought experiment is a scenario that can be imagined in order to illustrate the apparent contradiction that arises from a universally constant speed of light. In order to rectify this contradiction, the concepts of time dilation and length contraction are introduced, fundamentally changing our understanding of the nature of time and space. Two observers stand in inertial reference frames. From special relativity, we know all inertial reference frames are equal, and the laws of physics, including the speed of light, should look identical [3,4]. *Upper:* The observer on the train measures the time it takes a single photon of light to bounce from a mirror at the bottom of the train, to a mirror at the top, and back again. The distance travelled by the light beam is two times the height of the train, H , which gives $2H$. The time it takes a particle to transit a given distance, D , is given by $\Delta t = \frac{D}{v}$. Since light always travels at c , we know the measured photon transit time in this reference frame will be $\Delta t = 2\frac{H}{c}$. *Lower:* A second observer, standing on a platform, watches as the train passes at a constant velocity, v . Through a large window in the carriage, they observe the first observer performing their experiment. However, from the second observer's reference frame, the light now has to move on a diagonal path created by the motion of the train, we can calculate its new transit length $2D$, using Pythagoras's theorem. Each of the two transit, will, by definition take half of the total transit time measured by the platform observer, $\frac{1}{2}\Delta t'$, and in this time the train will have moved, $\frac{1}{2}\Delta t'v$, this gives us $D = \sqrt{H^2 + (\frac{1}{2}\Delta t'v)^2}$. If we substitute this new distance into the original equation to calculate the duration of the transit $\Delta t' = \frac{D}{v}$, we get $\Delta t' = \frac{\sqrt{H^2 + (\frac{1}{2}\Delta t'v)^2}}{v}$. This means that the platform observer measures a longer transit duration. Since the bouncing light beam is a type of clock, a light clock, and all functioning clocks in a given inertial reference will tick at a consistent rate, we can conclude that time is passing more slowly for the observer on the train when observed from the platform's reference frame. In reality, these effects would only become noticeable to a human if the velocities involved were significant fractions of the speed of light. In everyday life, the effects of special relativity are negligible, which was probably why it took so long for anyone to notice.

Figure 2.4 | Two depictions of Einstein's spacetime. For illustrative purposes, since we are not 4D beings and the paper on which this will be printed very much isn't, the four dimensions of our universe have been compacted down into two. It should also be noted that these illustrations were not generated with correct physical mathematics but only to give an impression of the concepts being described. *Left:* Minkowski space — in the absence of any mass, spacetime will not experience any curvature [5]. This is the special case that Einstein's special relativity describes. If we were to place a particle into this environment, it would not experience any acceleration due to gravity. If the

particle were massive, it would distort the spacetime, and the spacetime would no longer be considered Minkowski space even though, alone, the particle would not experience any acceleration. Often, when dealing with particles of low mass, their effects on the distortion of spacetime are ignored, and we can still accurately describe the scenario with special relativity [4]. *Right:* Spacetime distorted by a massive object, shown in blue. Curved space is described by Einstein's more general theory, general relativity [5]. In this scenario, we can see how the presence of mass imprints a distortion into the shape of spacetime. Any particles also present in the same universe as the blue object, assuming it has existed indefinitely, will experience an apparent acceleration in the direction of the blue sphere. A beam of light, for example, comprised of photons and entirely massless, would be deflected when moving past the sphere. Even though light will always travel along its geodesic through the vacuum of space, the space itself is distorted; therefore, a geodesic path will manifest itself as an apparent attraction toward the sphere. Notice that the mass of the photon is zero; therefore, using Newton's universal law of gravitation Equation 2.1, it should not experience any gravitational attraction, and indeed, gravitational lensing of the passage of starlight, as it moved past the Sun, was one of the first confirmations of Einstein's theory of general relativity [6]. Even if we assume the photon has some infinitesimal mass, Newtonian mechanics predicts a deflection angle that is only half as large as General Relativity predicts, and half as large as what is observed. Were this sphere several thousand kilometres in diameter, any lifeforms living on its surface, which would appear essentially flat at small scales, would experience a pervasive and everpresent downward force. Note that the mass of the object is distributed throughout its volume, so in regions near the centre of the sphere, the spacetime can appear quite flat, as equal amounts of mass surround it from all directions.

Figure 2.5 | Two further depictions of spacetime. Again, these images are a 2D representation of 4D spacetime, and they were generated without correct physical descriptions but for illustrative purposes alone. *Left:* Two objects, one in blue with a lesser mass and one in yellow with a greater mass. Objects with a larger mass distort spacetime to a greater extent. Objects close to either sphere will experience acceleration as the space curves and the objects continue to move in a straight line. In this scenario, if stationary, the yellow and blue objects will accelerate and move toward each other and, without outside interference, inevitably collide. However, if either the blue or yellow ball is given an initial velocity perpendicular to the direction of the other sphere so that its straight-line path orbits the other sphere, they can remain equidistant from each other in a stable orbit for potentially very long periods of time. As we will see, this orbit will eventually lose energy and decay, but depending on the masses of the two objects, this could take an extremely long time. *Right:* A black hole. The three red lines represent the geodesic paths of three light beams as they move past the black hole at different distances. Thus far, we have assumed that the mass of the yellow and blue objects are evenly distributed through their volume, so the spacetime at the very centre of the object is, at its limit, entirely flat. In many scenarios, this is a physically possible arrangement of matter, as although gravity pulls on every particle within the object, pulling it toward the centre, it is a very weak pull compared to the other forces of nature, which push back out and stop the particles continuing on their naturally preferred trajectory. This prevents a complete collapse of the object. Gravity, however, has one advantage on its side, and that is that there is no negative mass, only positive, so whereas large bodies tend to be electrically neutral as positive and negative charges cancel each other out, gravity always grows stronger. If enough mass congregates in the same place, or if the forces pushing matter away from the centre stop, there's nothing to stop gravity from pulling every particle in that object right to the centre, right into a singular point of mass with infinite density known as the singularity. As this collapse occurs, the curvature of spacetime surrounding the object gets stronger and stronger, eventually reaching the point where within a region around the singularity, known as the event horizon, all straight-line paths point toward the singularity. Meaning that no matter your speed, no matter your acceleration, you cannot escape,

even if you are light itself. Consequently, no information can ever leave the event horizon, and anything within is forever censored from the rest of the universe.

Figure 2.6 | Two illustrations of scenarios involving simple orbital mechanics. *Left:* In this thought experiment we imagine a cannon atop a large mountain on an unphysically small spherical planet with mass, m . As is described in both Newtonian mechanics and general relativity, objects are attracted toward the centre of mass of the planet. Left to their own devices they will fall until they meet some force resisting their motion, most likely, the surface of the planet. The cannon operator can control the velocity of the projected cannon balls. They note that the more velocity they impart, the longer it takes for the ball to impact the surface of the planet. The balls can travel further before impacting the ground when their velocity is greater, even if the time to impact remains the same. However, with this increased distance travelled along the surface of the sphere, the distance between the ball and the ground increases as the surface of the planet curves away from the ball. Eventually, the ball's trajectory will circularise around the planet, and, if not impeded by any other forces, the ball would remain on this circular trajectory indefinitely. *Right:* Two identical massive objects, such as planets, in a circular orbit with a shared centre, called a barycentre (note that the objects do not have to have equal mass or be in a circular orbit, to have a shared barycentre, in fact, this will always be the case). Any massive objects can orbit each other, including black holes.

Figure 2.7 | A depiction of the region of spacetime surrounding two inspiraling black holes. The spacetime grid visible is a 2D representation of the true 4D nature of our universe as described by general relativity [5]. This depiction was not produced by an accurate simulation but was constructed as a visual aid alone. Two massive objects can orbit each other if they have sufficient perpendicular velocity; this is a natural state for objects to find themselves trapped in because the chances of direct collisions between objects are low, and any objects that find themselves gravitationally bound together and do not experience a direct collision will eventuate in an orbit. The same is true for black holes; whether they form from pairs of massive stars that both evolve into black holes after the end of their main sequence lives or whether they form separately and through dynamical interaction, end up adjoined and inseparable, the occurrence of two black holes orbiting is not inconceivable [7]. Over time, small amounts of energy will leak from these binaries; ripples are sent out through the cosmos, carrying energy away from the system and gradually reducing the separation between the companions. As they get closer, the curvature of the spacetime they occupy increases, and thus, their acceleration toward each other grows. They speed up, and the amount of energy that is lost through gravitational radiation increases, further increasing the speed of their inspiral in an ever-accelerating dance. If they started just close enough, this process would be enough to merge them within the lifetime of the universe; they will inevitably collide with an incredible release of energy out through spacetime as powerful gravitational waves. It is these waves, these disturbances in the nature of length and time itself, that we can measure here on Earth using gravitational wave observatories.

Figure 2.8 | The effect of two polarisation states of gravitational waves as they oscillate whilst passing through a region of spacetime. Each of the black dots represents freely falling particles unrestricted by any other forces. The plus and cross polarisations shown are arbitrary names, and the polarisation can be at any angle, but plus and cross are a convention to distinguish the two orthogonal states.

Figure 2.9 | A very simplified interferometer diagram. Real gravitational wave detection apparatus have considerably more optics than what is shown. The power recycling and signal recycling mirrors help maintain a high laser power within the cavities. Higher laser powers are preferable as they help reduce quantum shot noise, the limiting source of noise at high frequencies.

Figure 2.10 | Location of currently operation LIGO detectors: LIGO Livingston (L1), LIGO Hanford (H1), Virgo (V1), Kagra (K1), and GEO600 (G1) [8]. Arm angles are accurate, the arm lengths were generated with a relative scale with the real detectors: 4 km for the two LIGO detectors, 3 km for

Virgo and Kagra, and 600 m for GEO600.

Figure 2.11 | Full noise budget of the LIGO Hanford Observatory (LHO) during the 3rd joint observing run. This image was sourced from [9].

Figure 3.1 | The loose hierarchical relationship between different umbrella terms used in artificial intelligence [10].

Figure 3.2 | *Upper*: The Artificial Neuron. This figure illustrates the operations that compose the archetypical artificial neuron, where \vec{x} is the input vector, f is the activation function, \vec{w} is the weights vector, and b is the neuron bias. An artificial neuron takes an input vector, \vec{x} , and performs some useful calculations (hopefully). Both the weights vector, \vec{w} , and bias value, b , comprise the neuron's adjustable parameters, $\vec{\theta}$, that must be tuned for the neuron to perform any useful operations [11]. *Note*: During computation, the bias, b , is not normally added in a separate operation; instead, it is added as an extra x_0 term included in the same calculation as the summation of the product of the weights, \vec{w} , and input values, \vec{x} . *Lower*: An abstraction of the more complicated interior structure of the artificial neuron. Abstraction is common and necessary when describing artificial neural networks as networks are often comprised of thousands if not millions of artificial neurons.

Figure 3.3 | Example MNIST data [12]. A single example of each of the ten classes within the MNIST example dataset. As can be seen, the classes range from zero to nine inclusive. Each example consists of a grid of 28 by 28 pixels containing one float value between 0.0 and 1.0. In the above image, values near one are represented as nearly white, and values near 0.0 as black. When ingested by our single-layer perception, they will be flattened into a 1D vector; see Section 3.4.

Figure 3.4 | Various representations of a Single-Layer Perceptron or Single-Layer Artificial Neural Network. *Upper*: Diagram illustrating the structure and operation of a single-layer perceptron. In the example shown, a handwritten zero is fed into the single-layer perceptron. The 2D image is first flattened into a 1D vector, see Section 3.4; then, the entire vector is fed into each neuron. If the training process has worked correctly, each neuron will have learned to identify one of the possible classes, in this case, digits. As can be seen from the output values, $\vec{\hat{y}} = [\hat{y}_0, \dots \rightarrow \hat{y}_9]$, which are taken from a real trained model, this model can correctly identify this input as a zero with high confidence. *Middle*: An abridged version of the upper diagram demonstrating the operation of feeding a handwritten one into the perceptron. This shows how future network diagrams will be abstracted for simplicity and that the perceptron outputs a different, correct value when it ingests a one rather than a zero. *Lower*: A further abstraction of the network. This type of abstraction will be used commonly throughout this thesis when dealing with networks consisting of multiple layers. A dense layer, wherein all neurons are attached to all previous neurons, will be shown as a filled black rectangle, and the icon next to it represents that the activation function applied is a softmax activation function [13]; see Section 3.1.5.4.

Figure 3.5 | An illustration of gradient descent, where $\vec{\nabla}L_{M\vec{x}\vec{y}}(\vec{\theta})$ is the loss at a fixed model architecture, M , input vector \vec{x} , and data label \vec{y} . This simplified example of the shape of a 1D parameter space shows how the gradient of the loss function with respect to the model parameters can be used to move toward the minimum of the loss function. The shape of the loss function in this example is given by $L_{M\vec{x}\vec{y}}(\vec{\theta}) = \theta^2$. In almost all cases, the parameter space will be much more complex than the one depicted in both dimensionality and shape complexity. Usually, the shape of the loss function will be an N-dimensional surface, where N is the number of parameters, $\vec{\theta}$, in the model, but the principle is still the same. For a 2D example of a gradient space; see Figure 3.12. This plot can be recreated with the code found here: <https://tinyurl.com/3ufb5my3>.

Figure 3.6 | *Upper*: The performance of the single layer perceptron model described in Section 3.1.2 over 15 epochs, where one epoch consists of training the model on all training examples in the MNIST dataset of handwritten Arabic numerals [12]. The model loss is defined as the categorical

cross-entropy of the model’s output vector, $\vec{\hat{y}}$ and the ground-truth label, \vec{y} , whereas the accuracy metric is defined as the number of examples in the test dataset that are correctly classified, where a correct classification is any output with 50 per cent or more probability in the correct class. *Lower*: Two examples of less successful classifications. The left example would still be measured as a successful classification by our accuracy metric, whereas the right example would be marked as an unsuccessful classification.

Figure 3.7 | Learned model parameters. Each artificial neuron in our single-layer perception is represented by a labelled parameter map shaped into the same dimensions as the input images. These maps show the learned weight values that correspond to each pixel of the input images. Very little structure can be made out by the human eye. Perhaps in the weight maps for the zero-classifier neuron, we can see an area toward the centre of the map that is negatively weighted. This might be expected as there are rarely high-value pixels at the centre of the circular zero. A similar but opposite effect might also be attributed to the one-classifier, where the centre of the image often contains high-value pixels. In general, unless you squint very hard, it is difficult to make out patterns in the parameters. This “black-box” effect means that after even one more layer is added to the network, it becomes very difficult to determine the action of dense layer neurons intuitively.

Figure 3.8 | *Upper*: Diagram of a multi-layer network with one output layer and one hidden layer. The non-linear computation introduced by the ReLU activation function applied to the hidden layer allows this network to solve considerably more complex problems than the previously described single-layer perceptron model. See Section 3.1.5.3 . As can be seen, by the displayed output, which again is taken from a real instance of a trained model, this network has no problem classifying the previously difficult image of a five. *Lower*: An abstraction of the same model.

Figure 3.9 | The performance of the multi-layer perceptron model described in Section 3.1.4 over 15 epochs. As can be seen in comparison to Figure 3.6, the training is both faster and with a better final result.

Figure 3.10 | *Left*: The generalised dense feed-forward artificial neural network. Where T is the number of hidden layers in your network, H is the number of neurons at that layer, N , is the number of elements in the input vector, \vec{x} , and O is the number of elements in the output vector $\vec{\hat{y}}$. As can be seen in the diagram, the number of hidden layers in your network is unconstrained, as is the number of neurons in each of those layers, which should be noted does not have to be the same. This is opposed to the output layer, which must have the same number of neurons as is expected by your loss function. *Right* A very simple illustration of a recurrent neural network. This network illustrates the retroactive data flow that is possible in a recurrent neural network. In this example, the output of the network from one inference operation is added to the input of the next inference operation. It should be noted that this is a very naive implementation of a recurrent neural network. In actuality, the networks usually have a much more complex structure, such as LSTMs (Long Short Term Memory) networks.

Figure 3.11 | Four of the most common activation functions. *Upper Left*: A linear activation function. In this case, the slope, k , is 1, meaning that the shape of the output is unchanged vs the input. *Upper Right*: Sigmoid activation function, a special case of the logistic activation function, which limits the output value between 0 and 1. *Lower Left*: ReLU (Rectified Linear Unit) activation function and its variants, an easy way to provide non-linearity to multi-layer networks. *Lower Right*: SoftMax activation function. In the case of multi-neuron outputs, when using softmax, the output of each neuron depends on the value of each other neuron. For this reason, the simplest non-trivial case, where the length of the output vector, N , is 2, has been chosen, and the outputs are represented on a 3D plot. This figure can be recreated with the notebook found at: <https://tinyurl.com/muppechr>.

Figure 3.12 | *Left*: An idealised gradient descent path. This gradient descent process quickly reaches the true function minimum where, in this case, the loss is close to zero. However, this is a constructed example by first finding a point near the function minimum and performing a gradient

ascent operation. *Right:* A more realistic gradient descent path. This example shows a simple but real gradient descent function running on the cost function. As can be seen, it takes many more steps and has not yet converged on the true minimum; in fact, the process might be at risk of getting stuck in a local minimum. Both examples were generated using this notebook: <https://tinyurl.com/3ufb5my3>.

Figure 3.13 | A flattening layer. This layer takes a 2D input matrix $X = \begin{pmatrix} x_1^1 & x_2^1 \\ x_1^2 & x_2^2 \end{pmatrix}$ and converts it into a 1D vector, $\vec{y} = [y_1, y_2, y_3, y_4]$, without using any learned parameters or altering the values of the data. It simply rearranges the indexes and removes all but one dimension. Reshaping layers are a more general version of a flattening layer, where an input vector or matrix can be transformed into any equivalently sized output vector or matrix.

Figure 4.1 | A non-exhaustive hierarchical depiction of some of the features, and proposed features, of gravitational-wave interferometer data. The first fork splits the features into two branches, representing the duration of the features. Here, **continuous** features are defined as features for which it is extremely unlikely for us to witness their start or end within the lifespan of the current gravitational-wave interferometer network and probably the current scientific community [14]. These features have durations anywhere from thousands to billions of years. **Transient** features have comparatively short durations [15], from fractions of seconds in the case of stellar-mass Binary Black Hole (BBH) mergers [15] to years in the case of supermassive BBH mergers [16]. It should be noted that the detectable period of supermassive binaries could be much longer; although the mergers themselves are transient events, there is no hard cut-off between the long inspiral and the merger event. Nevertheless, the mergers are probably frequent enough that some will end within the lifetime of the proposed LISA space constellation, so in some cases, they can be considered transients [16]. The next fork splits features by origin. Features of **astrophysical** origin originate from beyond Earth. This distinction is practically synonymous with the distinction between gravitational waves and signals from other sources since no other astrophysical phenomena are known to have a similar effect in interferometers [15]. Features of **terrestrial** origin, unsurprisingly, originate from Earth. These primarily consist of detector glitches caused by seismic activity or experimental artifacts [17]. Astrophysical transients have a further practical division into CBCs and bursts. The category of **bursts** contains all astrophysical transients that are not CBCs [18]. The primary reason for this distinction is that CBCs have been detected and have confirmed waveform morphologies [15,19]. As of the writing of this thesis, no gravitational-wave burst events have been detected [18,20,21]. Bursts often require different detection techniques [22,23]; of the proposed sources, many are theorised to have waveforms with a much larger number of free parameters than CBCs, as well as being harder to simulate as the physics are less well-understood [24,25]. These two facts compound to make generating large template banks for such signals extremely difficult. This means that coherence detection techniques that look for coherent patterns across multiple detectors are often used over matched filtering [23,26,22,27,28]. The astrophysical leaves of the diagram represent possible and detected gravitational-wave sources; the text's colourings represent their current status. Green items have been detected using gravitational-wave interferometers, namely the merger of pairs of Binary Black Holes (BBHs) [15], Binary Neutron Stars (BNSs) [19], or one of each (BHNSs) [29]; see [30–32] for full catalogues of detections. Yellow items have been detected via gravitational waves but using Pulsar Timing Arrays (PTAs) rather than interferometers [33]. Blue items represent objects and systems that are theorised to generate gravitational waves and have been detected by electromagnetic observatories but not yet with any form of gravitational wave detection. This includes white dwarf binaries [34,35], the cosmological background [36,37], starquakes [38,39], and core-collapse supernovae CCSN [40,41]. This is because they are too weak and/or too uncommon for our current gravitational-wave detector network to have had a chance to detect them. Finally, red items are possible, theorised sources of gravitational waves that have not

yet been detected by any means. These are, evidently, the most contentious items presented, and it is very possible that none of these items will ever be detected or exist at all. It should be noted that the number of proposed sources in this final category is extensive, and this is far from an exhaustive list. The presented proposed continuous sources are neutron star asymmetries [42], and the presented transient sources are extraterrestrial intelligence [43], cosmic string kinks and cusps [44], accretion disk instabilities [45], domain walls [46], and nonlinear memory effects [47].

Figure 4.2 | Examples of Power Spectral Density (PSD) transforms. *Left:* Two time domain series. The red series is a 20 Hz wave with a duration of 0.7 s, and the blue series is this same time series concatenated with a 40 Hz wave from $t = 0.7$ s onwards. *Right:* The two PSDs of the time series are displayed in the left panel. The red PSD was performed across only the 0.7 s of the red wave's duration, whereas the blue PSD was taken over the full 2.0 s duration. As can be seen, the blue PSD has two peaks, representing the two frequencies of the two waves combined to make the blue time series — each peak is lower than the red peak, as they are averaged across the full duration, and their respective heights are proportional to their durations as both waves have the same amplitude and vary only in duration.

Figure 4.3 | One-second examples of the four possible types of simulated and real noise considered by this thesis. Where real noise is used, it is taken from the LIGO Livingston detector during the third observing run at the GPS times listed. In order, from top to bottom, these are examples of white Gaussian noise, coloured Gaussian noise, pseudo-real noise, and real noise. A description of these noise types and their generation can be found in Section 4.2.2. The left column shows the unaltered values of the noise. Note that the noise has been scaled in all cases except for the pure white noise, which is generated at the correct scale initially. This scaling is used to reduce precision errors and integrate more effectively with the machine learning pipeline, as most loss and activation functions are designed around signal values near unity; see Section 3.1.6 and Section 3.1.5. The right column shows the same noise realisations after they have been run through a whitening filter. In each case, the PSD of a 16.0 s off-source noise segment not displayed is used to generate a Finite Impulse Response (FIR) filter, which is then convolved with the on-source data; see Section 4.2.7. For the simulated and pseudo-real noise cases, the off-source data is generated using the same method as the on-source data but with a longer duration. In the real noise case, the off-source data consists of real interferometer data drawn from 16.5 s before the start of the on-source segment to 0.5 s before the start of the on-source segment. This 0.5 s gap is introduced because 0.5 s must be cropped from the data following the whitening procedure in order to remove edge effects induced via windowing, as well as acting as a buffer to reduce contamination of the off-source data with any features present in the on-source data. Note that the whitened noise plots look very similar for the three simulated noise cases — a close examination of the data reveals that there is some small variation between the exact values. This similarity occurs because the off-source and on-source noise segments for these examples are generated with identical random seeds and thus have identical underlying noise realisations (which can be seen exactly in the unwhitened white noise plot). Since the PSDs of the on-source and off-source data are nearly identical for the simulated cases, the whitening procedure is almost perfect and reverts it nearly perfectly to its white state. If anything, this similarity boosts confidence that our custom whitening procedure is operating as expected.

Figure 4.4 | Eight simulated waveforms that could be used for injection into noise to form an obfuscated training, testing, or validation example for an artificial neural network. Note that only the plus polarisation component of the strain, h_+ , has been plotted in order to increase visual clarity. The leftmost four injections are IMRPhenomD waveforms generated using cuPhenom [48], with parameters (shown in the adjacent grey information boxes) drawn from uniform distributions between $5.0 M_\odot$ and $95.0 M_\odot$ for the mass of both companions and between -0.5 and 0.5 for the dimensionless spin component. Note that during injection generation, the two companions are always reordered so that the mass of companion one is greater and that the IMRPhenomD waveform

ignores the x and y spin components. They are included just for code completion. The rightmost four injections consist of WNB waveforms generated via the method described in Section 4.2.3. Their parameters are again drawn from uniform distributions and are shown in the grey box to their right. The durations are limited between 0.1 s and 1.0 s, and the frequencies are limited to between 20.0 Hz and 500.0 Hz, with the minimum and maximum frequencies automatically swapped.

Figure 4.5 | The plus polarisation component of the gravitational-wave strain of a simulated core-collapse supernova at a distance of 10 kpc, this data was taken from [49]. Although some structures can clearly be observed, it is possible to imagine that a method trained to detect WNB signals, such as those presented in Figure 3.4, might be able to detect the presence of such a signal.

Figure 4.6 | Example projection of two artificial gravitational-wave waveforms. The blue waveforms have been projected into the LIGO Livingston interferometer, the red waveforms have been projected into the Ligo Hanford interferometer, and the green waveforms have been projected into the VIRGO interferometer. The left column displays different projections of an IMRPhenomD waveform generated with the cuPhenom GPU library [48]. The right column displays different projections of a WNB waveform generated with the method described in Section 4.2.3. The projections are performed using a GPU adaptation of the PyCBC Python library's [50] `project_wave` function. Both waveforms are projected from different source locations; the projection and time displacement are different in each case.

Figure 4.7 | Eight examples of artificial injections scaled to a particular scaling metric and added to a real noise background to show variance between different scaling methods. The blue line demonstrates the whitened background noise plus injection; the red line represents the injection after being run through the same whitening transform as the noise plus injection, and the green line represents the injection after scaling to the desired metric. The leftmost column contains an IMRPhenomD waveform, generated using [48], injected into a selection of various background noise segments and scaled using SNR; see Section 4.2.5.2. From upper to lower, the SNR values are 4, 8, 12, and 16, respectively. The rightmost column displays a WNB injected into various noise distributions, this time scaled using h_{rss} ; see Section 4.2.5.1. From upper to lower, the h_{rss} values are as follows: 8.52×10^{-22} , 1.70×10^{-21} , 2.55×10^{-21} , and 3.41×10^{-21} . As can be seen, though both sequences are increasing in linear steps with a uniform spacing of their respective metrics, they do not keep in step with each other, meaning that if we double the optimal SNR of a signal, the h_{rss} does not necessarily also double.

Figure 4.8 | Possible data layouts for multi-detector examples. Here, d is the number of included detectors, and N is the number of input elements per time series. There are three possible ways to align interferometer time-series data from multiple detectors. These layouts are discussed in more detail in Section 4.2.6.

Figure 4.9 | An example of a segment of interferometer data before and after whitening. The two leftmost plots in blue show the PSD, *upper*, and raw data, *lower*, output from the LIGO Hanford detector before any whitening procedure was performed. The two rightmost plots show the same data after the whitening procedure described in Section 4.2.7.2 has been implemented. The data was whitened using the ASD of a 16.0 s off-source window from 16.5 s before the start of the on-source window to 0.5 s before. The 0.5 s gap is introduced as some data must be cropped after whitening due to edge effects caused by windowing. This also acts to ensure that it is less likely that any features in the on-source data contaminate the off-source data, which helps reduce the chance that we inadvertently whiten any interesting features out of the data.

Figure 4.10 | Demonstration of the on-source and off-source regions used to calculate the ASD used during the whitening operations throughout this thesis wherever real noise is utilised. Where artificial noise is used, the off-source and on-source segments are generated independently but with durations equivalent to what is displayed above. The blue region shows the 16.0 s off-source period, the green region shows the 1.0 s on-source period, and the two red regions represent the 0.5 s crop

periods, which are removed after whitening. During an online search, the on-source region would advance in second-long steps, or if some overlap was implemented, less than second-long steps, meaning all data would eventually be searched. The leading 0.5 s crop region will introduce an extra 0.5 s of latency to any search pipeline. It may be possible to avoid this latency with alternate whitening methods, but that has not been discussed here.

Figure 4.11 | Example whitened on-source and correlation plots of real interferometer noise from a pair of detectors, in this case, LIGO Livingston and LIGO Hanford, with either coherent, incoherent, or no injections added. The leftmost plots adjacent to the info panels are grouped into pairs. In each case, LIGO Livingston is at the top, and LIGO Hanford is underneath. Identical on-source and off-source noise segments are used for each example of the same detector, and noise for each detector was gathered with a time difference of no more than 2048.0 s. In the leftmost plots, the green series is the unwhitened but projected waveform to be injected into the real noise from that detector. The red series is that same injection but subject to the same whitening procedure that will also be applied to the on-source plus injections, and the blue series is the whitened on-source plus injections. The rightmost plots each correspond to a pair of detectors and display the rolling Pearson correlation values between those two whitened on-source plus injection series. Since there is approximately a max arrival time difference of 0.01 s between LIGO Livingston and LIGO Hanford, the number of correlation calculations performed corresponds to the rounded number of samples required to represent 0.02 s of data at 2048.0 Hz. This number is two times the maximum arrival time difference because the difference could be positive or negative. In this case, that difference comes to 40 samples. All injections have been scaled to an optimal network SNR of 30 using the method described in Section 4.2.5.2. The upper pair of detectors has no injection. As would be expected, the correlation is low regardless of the assumed arrival time difference. The second pair from the top has been injected with a coherent white noise burst (WNB), see Section 4.2.3, which has been projected onto the two detectors using a physically realistic mechanism previously described in Section 4.2.4. Here, the correlation is much stronger. We can see it rise and fall as the waveforms come in and out of coherence. The third from the top, the central plot, shows an injection of two incoherent WNBs. They are processed identically to the coherent case, but the initial waveforms are generated independently, including their durations. The Pearson correlation looks very similar to the pure noise case in the uppermost plot, as might be expected. The second from the lowest pair has been injected with a coherent IMRPhenomD waveform, which again has been correctly projected. We can observe that a small correlation is observed at an arrival time difference of around 0.005 s, suggesting that the two waveforms arrived at the detectors 0.005 s apart. Finally, the lowest plot depicts two incoherent IMRPhenomD waveforms projected into the noise. Though these are generated with different parameters, the shared similarities in morphology between all CBC waveforms cause correlation to be registered. By maximum amplitude alone, it may even appear as though there is more correlation happening here than in the correlated case. This highlights one potential weakness of using the Pearson correlation, which can sometimes show some degree of correlation even if the two waveforms are not produced using the same physically simulated mechanism.

Figure 4.12 | Six example noise segments and their corresponding spectrograms. In all cases, the noise is real interferometer data acquired from the LIGO Hanford detector during the 3rd observing run. It is whitened using the procedure described in Section 4.2.7.2. For the time series plots, the green series represents the original, unwhitened waveform before injection, the red series is the waveform with the same whitening transform applied to it as was applied to the on-source background plus injection, and the blue series is the whitened on-source background plus injection, except for the first two time series plots which contain no injection. The spectrograms are generated using the STFT described by Equation 4.29, converted into power with Equation 4.30, and finally transformed into a decibel logarithmic scale for plotting using Equation 4.32. The two uppermost plots and their respective spectrograms have no injections. The two middle plots and their respective

spectrograms have IMRPhenomD [51] approximants created with cuPhenom injected into the noise [48], and the two lower plots and their respective spectrograms, have White Noise Burst (WNB) waveforms generated using the method described in Section 4.2.3, injected into the noise. In all cases, the injections are scaled to an optimal SNR randomly selected between 15 and 30; these are quite high values chosen to emphasize the features in the spectrograms. As can be seen, the whitened noise that contains injected features has spectrograms with highlighted frequency bins that have a magnitude much larger than the surrounding background noise; the different signal morphologies also create very different shapes in the spectrograms. This allows us to see the frequency components of the signal more easily, observe the presence of interesting features, and differentiate between the WNB and the CBC case.

Figure 4.13 | Perceptron diagrams. The four different architectures used to test the use of purely dense models for both the single-detector CBC detection case and the multi-detector burst detection problem. The only differences are that the input vector sizes are different between the cases: (NUM_EXAMPLES_PER_BATCH, NUM_SAMPLES) in the case of the single detector CBC search and (NUM_EXAMPLES_PER_BATCH, NUM_DETECTORS, NUM_SAMPLES) in the multi-detector coherent burst search. All models take in two input vectors into a custom-designed GWFlow whitening layer, the off-source and the on-source vectors; see Section 4.2.7.2 for more information about the whitening procedure, and all models are capped with a dense layer with a single output neuron that is used to feed the binary loss function, with a sigmoid activation function. Each hidden layer has been tested with 64, 128, and 256 neurons, and one hidden layer was tested with 512 as a sample with higher neuron counts: *Top*: Zero-hidden layer model. *Second to top*: Two-hidden layer model. *Second to bottom*: Three-hidden layer model. *Bottom*: One hidden layer model.

Figure 4.14 | The accuracy history of perceptron models training to detect IMRPhenomD waveforms generated using cuPhenom [48] that have been obfuscated by real interferometer noise sampled from the LIGO Livingston detector during the 3rd observing run. Visit <https://tinyurl.com/ypu3d97m> for interactive plots, whilst they’re still working. The optimal SNR of waveforms injected into the training and validation sets was uniformly distributed between 8 and 15. Input was from a single detector only. A rough search was performed over a relatively arbitrary selection of model architectures, which varied the number of layers and the number of perceptrons in each layer. The architectures of each model can be seen in the figure legends as a list of numbers where each digit is the number of artificial neurons in that layer. All are trained with the same training hyperparameters, details of which can be found in Table 3.3. Each epoch consisted of 10^5 training examples, and it should be noted that, unlike the regular training pipelines, each training epoch consisted of newly generated waveforms injected into unseen noise segments, though the validation examples are consistent. Training of each model was halted after ten consecutive epochs with no improvement to validation loss, the values of which are shown in Figure 3.15. Validation noise was drawn from a separate pool of data segments inaccessible to the training data loader. We can see that the maximum accuracy achieved by any perceptron model only approaches 75%. Although these validations are performed with a pool containing mixed waveform SNRs and at an unrestrained False Alarm Rate (FAR) (this accuracy uses a score threshold of 0.5 regardless of FAR), it is clear that this is insufficient to be useful. *Upper*: Plot of model accuracies when measured with training data (10^5 epoch-unique examples). *Lower*: Plot of model accuracies when measured with validation data (10^4 epoch-consistent examples).

Figure 4.15 | Training loss history of perceptron models training to detect IMRPhenomD waveforms generated using cuPhenom [48], obfuscated by real interferometer noise from the LIGO Livingston detector from the 3rd observing run. The loss is computed using binary cross entropy loss function and is used by the gradient descent algorithm, in this case, the Adam optimizer, as a minimization target. It also acts as the monitor by which the pipeline knows to stop the training process early. If the pipeline detects that the validation model loss has not decreased in more than 10 epochs,

training is halted. Visit <https://tinyurl.com/ypu3d97m> for interactive plots. See Figure 3.14 for a more detailed description of the training data. *Upper:* Plot of model loss when measured with training data (10^5 epoch-unique examples). *Lower:* Plot of model loss when measured with validation data (10^4 epoch-consistent examples).

Figure 4.16 | Perceptron False Alarm Rate (FAR) curves. This plot was created by running each of our 14 models over a pure noise validation dataset of 10^5 noise examples. A relatively small number of noise examples are used due to the observed inaccuracy of the models during training which suggested that they would not be able to reach low FAR scores and thus would not necessitate a larger validation dataset. The output scores of the model from each inference over the pure noise validation dataset are sorted and plotted on this graph. The x-axis is the output score of the model inference on that example of noise. The y-axis is calculated by using Equation 4.33 and provides the estimated number of false alarms that the model would output per second of pure noise data given the threshold score displayed on the x-axis. We can use this graph to calculate positive result thresholds for our classifier, at different false alarm rates. Once again, the models are listed with the number of artificial neurons in each hidden layer. Visit <https://tinyurl.com/2wkaarkh> to view an interactive plot.

Figure 4.17 | Perceptron efficiency curves. For each of the 14 perceptron models trained, 31 efficiency tests are performed at evenly spaced optimal SNR values between 0 and 15. For each test, 8192 examples with signals of the relevant SNR are examined by the model, and the percentage of those that scored above the threshold was plotted, see Equation 4.34, for three different False Alarm Rate (FAR) thresholds: 0.1 Hz, 0.01 Hz, and 0.001 Hz. The efficiency curve for each FAR threshold is presented on a unique plot. Some models have been excluded, they are shaded grey on the legends, because they are incapable of performing any classification at the chosen FAR thresholds. Visit <https://tinyurl.com/2wkaarkh> to view an interactive plot. . *Upper:* Efficiency curves at a FAR of 0.1 Hz. *Middle:* Efficiency curves at a FAR of 0.01 Hz. *Lower:* Efficiency curves at a FAR of 0.001 Hz.

Figure 4.18 | Receiver Operator Curve (ROC) Curve at $\rho_{\text{opt}} = 8$. To create this plot a validation dataset containing waveforms all of an SNR of eight was generated. The ability of the model to detect these waveforms was then measured at different FARs. All models show very similar, poor performance. Visit <https://tinyurl.com/2wkaarkh> to view an interactive plot.

Figure 4.19 | The accuracy history of perceptron models training to detect multi-detector WNBs generated using GWFlow and obfuscated by real interferometer noise sampled from the LIGO Livingston and LIGO Hanford detectors during the 3rd observing run. Visit ADD_LINK for interactive plots. The optimal SNR of waveforms injected into the training and validation sets was uniformly distributed between 12 and 30. The input was generated using real noise from LIGO Hanford and LIGO Livingston. The training procedure was identical to the single detector case, except for the SNR range increase and the multiple detector data supply. We can see in these training plots, that despite the increased SNR range, training and validation accuracy barely creep above 50% (which can be achieved by random selection). This indicates that dense networks are even less suited for the more complex coherence detection problem. Further validation will be performed for completion. Visit <https://tinyurl.com/4jj3t5fj> to view an interactive plot. *Upper:* Plot of model accuracies when measured with training data (10^5 epoch-unique examples). *Lower:* Plot of model accuracies when tested with validation data (10^4 epoch-consistent examples).

Figure 4.20 | The loss history of perceptron models training to detect multi-detector WNBs generated using GWFlow and obfuscated by real interferometer noise sampled from the LIGO Livingston and LIGO Hanford detectors during the 3rd observing run. Visit ADD_LINK for interactive plots. The optimal SNR of waveforms injected into the training and validation sets was uniformly distributed between 12 and 30. The input was generated using real noise from LIGO Hanford and LIGO Livingston. The losses show a similar picture to the accuracy plots, and although we see a gradual decline it is very shallow and triggers the patience early stopping before it has had

any chance to gain significant performance, assuming that is even possible. Patience could be increased, but as we will see in later architectures, this is not competitive. *Upper*: Plot of model losses when measured with training data (10^5 epoch-unique examples). *Lower*: Plot of model losses when tested with validation data (10^4 epoch-consistent examples). Visit <https://tinyurl.com/4jj3t5fj> to view an interactive plot.

Figure 4.21 | Perceptron False Alarm Rate (FAR) curves. This plot was created by running each of our 14 models over a pure noise validation dataset of 10^5 noise examples. Performance is low across the board demonstrating that dense layer perceptrons are unsuitable for this kind of WNB detection, at least within the hyperparameter range tested. Visit <https://tinyurl.com/bdz9axpf> to view an interactive plot.

Figure 4.22 | Perceptron efficiency curves for the multi-detector WNB detection model. For each of the 14 perceptron models trained, 31 efficiency tests are performed at evenly spaced optimal SNR values between 0 and 30. For each test, 8192 examples with signals of the relevant SNR are examined by the model. The percentage of those that scored above the threshold is plotted, see Equation 4.34, for two different False Alarm Rate (FAR) thresholds: 0.1 Hz and 0.01 Hz, lower FARs are excluded due to small accuracies. *Upper*: Efficiency curves at a FAR of 0.1 Hz. *Lower*: Efficiency curves at a FAR of 0.01 Hz. Visit <https://tinyurl.com/bdz9axpf> to view an interactive plot.

Figure 4.23 | Reciever Operator Curve (ROC) Curve at an optimal SNR of eight. To create this plot a validation dataset containing waveforms all of an SNR of eight was generated. The ability of the model to detect these waveforms was then measured at different FARs. Again, all models show very similar, poor performance. Visit <https://tinyurl.com/bdz9axpf> to view an interactive plot.

Figure 4.24 | Diagram of a single kernel, $\frac{1}{1}k$, in a single convolutional layer. In this example, a 1D vector is being input; therefore, the single kernel's output is also 1D. This kernel has a kernel size of three, meaning that each neuron receives three input values from the layer's input vector, \vec{x} , which in this case is length five. This means there is room for three repeats of the kernel. Its parameters are identical for each iteration of $\frac{1}{1}k$ at a different position. This means that if a pattern of inputs recognised by the kernel at position 1, $\frac{1}{1}k_1$ is translated two elements down the input vector, it will be recognised similarly by the kernel at $\frac{1}{1}k_3$. Although this translational invariance is only strict if the translation is a whole pixel multiple and no subsampling (pooling, stride, or dilation) is used in the network, this pseudo-translational invariance can be useful, as often, in images and time series data, similar features can appear at different spatial or temporal locations within the data. For example, in a speech classification model, a word said at the start of the time series can be recognised just as easily by the same pattern of parameters if that word is said at the end of the time series (supposing it lies on the sample pixel multiple). Thus, the same kernel parameters and the same filter can be repeated across the time series, reducing the number of parameters needed to train the model. This particular kernel would have $3 + 1 = 4$ total parameters, as it applied to a 1D input vector, and has a kernel size of three, with an additional parameter for the neuron bias. With only a single kernel, only one feature can be learned, which would not be useful in all but the most simple cases. Thus, multiple kernels are often used, each of which can learn its own filter.

Figure 4.25 | Illustration of how different values of kernel size would be laid out on a 4×4 input image. In each case, unused input image values are shown as empty black squares on the grid, and input values read by the kernel are filled in red. The grids show the input combinations that a single kernel would ingest if it has a given size, assuming a stride value of one and zero dilation. The kernel sizes are as follows: *Upper left*: 2×2 . *Upper right*: 3×2 . *Lower left*: 2×3 . *Lower right*: 3×3 . One pixel in the output map is produced for each kernel position. As can be seen, the size of the output map produced by the kernel depends both on the input size and the kernel size; smaller kernels produce a larger output vector.

Figure 4.26 | *Upper*: Diagram of three convolutional kernels, $[\frac{1}{1}k, \frac{1}{2}k, \frac{1}{3}k]$, in a single convolutional

layer. Each kernel is coloured differently, in red, green, and blue. Artificial neurons of the same colour will share the same learned parameters. Again, a 1D vector is being input; therefore, the output of each of the kernels is 1D, and the output of the kernels stack to form a 2D output vector, with one spatial dimension retained from the input vector and an extra discrete depth dimension representing the different features learned by each of the kernels. Again, each kernel has a kernel size of three. Multiple kernels allow the layer to learn multiple features, each of which can be translated across the input vector, as with the single kernel. Using Equation 4.36, this layer would have $3 \times ((1 \times 3) + 1) = 12$ trainable parameters. It should be noted that this is a very small example simplified for visual clarity; real convolutional networks can have inputs many hundreds or thousands of elements long and thus will have many more iterations of each kernel, as well as many more kernels sometimes of a much larger size. *Lower:* Abstracted diagram of the same layer with included hyperparameter information.

Figure 4.27 | Upper: Diagram of two convolutional layers, each with independent kernels. The first layer has three kernels, each with a size of three. The second layer has two kernels, both with a size of two. Again, this is a much-simplified example that would probably not have much practical use. Different kernels are coloured differently, in red, green, and blue. Although it should be noted that similar colours across layers should not be taken as any relationship between kernels in different layers, they are each tuned independently and subject to the whims of the gradient descent process. This example shows how the kernels in the second layer take inputs across the entire depth of the first layer but behave similarly along the original dimension of the input vector. In theory, the deeper layer can learn to recognise composite features made from combinations of features previously recognised by the layers below and visible in the output feature maps of the different kernels. This multi-layer network slice would have $(3 \times ((1 \times 3) + 1)) + (2 \times ((3 \times 2) + 1)) = 26$ total trainable parameters. This was calculated by applying Equation 4.36 to each layer. *Lower:* Abstracted diagram of the same layers with included hyperparameter information.

Figure 4.28 | Upper: Diagram of a very simple convolutional neural network binary classifier consisting of four layers with tunable parameters plus one infrastructure layer without parameters. Two consecutive convolutional layers ingest the five-element input vector, \vec{x} . The 2D output of the latter of the two layers is flattened into a 1D vector by a flattening layer. This flattened vector is then ingested by two dense layers, the latter of which outputs the final classification score. The first convolutional layer has three convolutional kernels, each with a size of three, and the second convolutional layer has two kernels, both with a size of two. The first dense layer has three artificial neurons, and the final output dense layer has a number of neurons dictated by the required size of the output vector. In the case of binary classification, this is either one or two. Different kernels within a layer are differentiated by colour, in this case, red, green, or blue, but a similar colour between layers does not indicate any relationship. Dimensionless neurons are shown in black; it should be noted that after flattening, dimensional information is no longer necessarily maintained by the network structure. Of course, no information is necessarily lost either, as the neuron index itself contains information about where it originated, so, during training, this information can still be used by the dense layers; it is just not necessarily maintained as it is in convolutional layers. This network will have in total $26 + (3 \times 4 + 4) + (2 \times 3 + 2) = 50$ trainable parameters. This network is very simple and would probably not have much practical use in real-world problems other than straightforward tasks that would probably not necessitate using neural networks. *Lower:* Abstracted diagram of the same model with included hyperparameter information.

Figure 4.29 | Illustration of how different values of kernel stride would be laid out on a 4×4 input image. In each case, unused input image values are shown as empty black squares on the grid, and input values read by the kernel are filled in red. Similar to kernel size, different values of stride result in a different output vector size. The strides shown are as follows: *Upper left:* 1, 1. *Upper right:* 2, 1. *Lower left:* 1, 2. *Lower right:* 2, 2.

Figure 4.30 | Diagram illustrating how different values of kernel dilation affect the arrangement of the kernel input pixels. In this example, the receptive field of a single 3×3 kernel at three different dilation levels is displayed; differing colours represent the input elements at each dilation level. The shaded red kernel illustrates dilation level zero; the shaded blue region is a kernel with dilation of one, and the green kernel has a kernel dilation of two.

Figure 4.31 | Diagram illustrating how padding can be added to the edge of an input vector in order to allow for otherwise impossible combinations of kernel, stride, size, and dilation. In each case, unused input image values are shown as empty black squares on the grid, input values read by the kernel are shaded red, and empty blue squares are unused values added to the original input vector, containing either zeros or repeats of the closest data values. In this example, the kernel size is 3×3 , and the kernel stride is 2, 2.

Figure 4.32 | The two CNN architectures presented in George *et al.* [52]. *Upper*: Smaller model.

Lower: Larger model.

Figure 4.33 | CNN architecture from Gabbard *et al.* [53].

Figure 4.34 | The accuracy history of attempts to retrain Convolutional Neural Networks (CNNs) with architectures adapted from the literature using the GWFlow pipeline. A custom GWFlow whitening layer has been added to the start of each model in order to reproduce the whitening data conditioning step applied in the original studies. The structure of the models is otherwise identical. Differences in the training and validation procedures, however, may lead to slightly different results than in the original studies. Rather than exactly attempting to mimic the datasets and training process used in each of these studies, it has been kept consistent with the other results throughout the thesis, in order to facilitate comparison. The models presented are the two models from George *et al.* [52], labeled “George Small”, and “George Large”, to differentiate them in terms of parameter count, and the single model from Gabbard *et al.* [53]. The network structure of these models can be seen in Figure 3.32 and Figure 3.33, respectively. The training and validation datasets were maintained from the perceptron single-detector training experiment. The dataset contains IMRPhenomD waveforms generated using cuPhenom [48] injected into real interferometer noise sampled from the LIGO Livingston detector during the 3rd joint observing run [54]. The optimal SNR of waveforms injected into the training and validation sets was uniformly distributed between 8 and 15. Input was from a single detector only. Each epoch consisted of 10^5 training examples, and it should be noted that, unlike regular training pipelines, each training epoch consisted of newly generated waveforms injected into unseen noise segments, though the validation examples are consistent. Training of each model was halted after ten consecutive epochs with no improvement to validation loss, the values of which are shown in Figure 3.35. Validation noise was drawn from a separate pool of data segments inaccessible to the training data loader. It is immediately clear that this is a huge improvement over the perceptron models, and it makes it evident why we abandon the idea of perceptrons so quickly. Both the training and validation accuracies jump to above 90% almost immediately, and in the case of the model from Gabbard *et al.*, and the largest of the models from George *et al.*, they plateau at approximately 98% accuracy, with only marginal improvements from there. The smaller model from George *et al.* plateaus closer to 96% accuracy. Considering approximants from both the training and validation datasets are generated with CBCs drawn uniformly between an optimal SNR of 8 and 15, this demonstrates good performance. Because two of the models plateau at statistically similar accuracies with quite different architectures, it suggests that they are approaching the detectability limit in both cases. An interesting examination will be to compare their performance with FAR-calibrated detection thresholds. *Upper*: Plot of model accuracies when measured with training data (10^5 epoch-unique examples). Visit <https://tinyurl.com/mwxfvp33> for interactive plots. *Lower*: Plot of model accuracies when measured with validation data (10^4 epoch-consistent examples).

Figure 4.35 | The loss history of attempts to retrain Convolutional Neural Networks (CNNs) from

the literature using the GWFlow pipeline. These loss values correspond to the accuracies displayed in Figure 3.34. The models presented are the two models from George *et al.* [52], labeled “George Small”, and “George Large”, to differentiate them in terms of parameter count, and the single model from Gabbard *et al.* [53]. The network structure of these models can be seen in Figure 3.32 and Figure 3.33, respectively. The training and validation datasets were maintained from the perceptron single-detector training experiment. The dataset contains IMRPhenomD waveforms generated using cuPhenom [48] and real interferometer noise sampled from the LIGO Livingston detector during the 3rd joint observing run [54]. The optimal SNR of waveforms injected into the training and validation sets was uniformly distributed between 8 and 15. Input was from a single detector only. Each epoch consisted of 10^5 training examples, and it should be noted that, unlike regular training pipelines, each training epoch consisted of newly generated waveforms injected into unseen noise segments, though the validation examples are consistent. The loss is the metric used to determine when training is halted; this is done after ten epochs have passed with no improvement. Again we can see that this is a vast improvement over the perceptron case, see Figure 3.15, at least in the time frame that is monitored, with loss values quickly falling to a region with a much smaller reduction gradient and then gradually improving from there with diminishing returns. It is these diminishing returns that can have a great impact on the ability of the model to sustain high accuracies with low FAR thresholds. Visit <https://tinyurl.com/mwxfvp33> for interactive plots. *Upper:* Plot of model losses when measured with training data (10^5 epoch-unique examples). *Lower:* Plot of model accuracies when measured with validation data (10^4 epoch-consistent examples).

Figure 4.36 | False Alarm Rate (FAR) plotted against the score threshold required to achieve that FAR, for three recreations of models from the literature. Two models are adapted from George *et al.* [52], labeled “George Small”, and “George Large”, to differentiate them in terms of model parameter count, and the single model from Gabbard *et al.* was also adapted. The network structure of these models can be seen in Figure 3.32 and Figure 3.33, respectively. The presented FAR curves are significantly lower than those achieved by the perceptrons in the single detector case, see Figure 3.16. This means that we will be able to achieve lower FARs with lower score thresholds, which typically, though not necessarily, leads to higher efficiencies at those FARs. We explore the efficiency results in Figure 3.37. Visit <https://tinyurl.com/2s3dtd8a> for interactive plots.

Figure 4.37 | Model efficiency curves for three models adapted from the literature. Two models are adapted from George *et al.* [52], labelled “George Small”, and “George Large”, to differentiate them in terms of model parameter count, and the single model from Gabbard *et al.* [53] was also adapted. The network structure of these models can be seen in Figure 3.32 and Figure 3.33, respectively. These models verify that CNNs can achieve much higher accuracies within the training regime utilized, even when using threshold scores that are calibrated to specific False Alarm Rates (FARs). The perceptron efficiency curves for the single detector CBC detection case can be seen in Figure 3.17. They achieve higher accuracies almost across the board at the highest FARs depicted, 0.1 Hz and 0.01 Hz, except at SNRs where detection becomes virtually impossible (< 2) in which case they perform similarly. They are also able to achieve results at lower FARs 0.001 Hz and 0.0001 Hz at these FARs, the perceptron models had negligible performance and were not depicted, so this is a significant improvement. Visit <https://tinyurl.com/2s3dtd8a> for interactive plots. *First:* Efficiency curves at a FAR of 0.1 Hz. *Second:* Efficiency curves at a FAR of 0.01 Hz. *Third:* Efficiency curves at a FAR of 0.001 Hz. *Fourth:* Efficiency curves at a FAR of 0.0001 Hz.

Figure 4.38 | Reciever Operator Characteristic (ROC) curves, for three models adapted from the literature. Two models are adapted from George *et al.* [52], labelled “George Small”, and “George Large”, to differentiate them in terms of model parameter count, and the single model from Gabbard *et al.* [53] was also adapted. The network structure of these models can be seen in Figure 3.32 and Figure 3.33, respectively. In comparison with the ROC curves achieved by the perception models, see Figure 3.18, which at an optimal SNR of 8 looks to be almost randomly guessing, this is a significant

improvement. The curves shown illustrate the model operating on a pool of injected signals at an optimal SNR of 8. Visit <https://tinyurl.com/2s3dtd8a> for interactive plots.

Figure 5.1 | An example arbitrary hyperparameter space generated from a random mixture of Gaussians. The space presented here is 2D. In actuality, the space is likely to have a much larger dimensionality. Unlike in gradient descent where we are trying to minimize our loss, here we are trying to maximize our objective function, whatever we have determined that to be.

Figure 5.2 | An example of the samples a grid search might use to find an optimal hyperparameter solution.

Figure 5.3 | An example of the samples a random search might use to find an optimal hyperparameter solution.

Figure 5.4 | An example of the samples a Bayesian optimization might use to find an optimal hyperparameter solution. The descent method shown here has used a Gaussian Process to attempt to find the objective function maximum but has not done so particularly successfully. The method was not tuned to try and increase performance, as it was just for illustratory purposes.

Figure 5.5 | Dragonn model training histories from each of the four generations. All models were trained with identical training datasets and validated with epoch-consistent validation data. After each epoch, a new population was generated by applying the genetic algorithms mechanism to select performant genes in previous generations. In all generations many models lack any classification ability, this is anticipated because, because of the scope of the hyperparameter search, many of the models generated will be nonsensical, with extremely small data channels or near complete dropout layers. However, we also see that our population size was enough for a considerable number of performance models. With increasing generations, we see increasing numbers of performant models, demonstrating that our genetic optimiser is operating as intended.

Figure 5.6 | Dragonn average metrics from each of the four generations. The blue line is the average best model accuracy across its training run, The red line is the average model loss, the purple line is the average number of epochs in a model's training history, and the green line is the average model fitness. These results are mostly as all average metrics improve with increasing generation count, the drop in loss is particularly impressive, but this probably corresponds to the shedding of extremely poorly designed models after the first epoch. Accuracy is slowly improving, as the number of performant models increases, and with it the average number of epochs in a model's training history. Within increasing numbers of performant models comes increasing numbers of models that can perform better than their last epoch after further training.

Figure 5.7 | Efficiency curves of the top performing model from the population of Dragonn trials. The curves maintain high accuracy at low FARs, though their performance at high SNRs above 10 is worse, never reaching a 100% accuracy, their performance at an SNR of 6 is considerably greater. It is hypothesized that this is due to an inoculation effect generated by the erroneous injection of WNB glitches into the dataset during the first generation. *Top*: Efficiency curve using a threshold calibrated to a FAR of 0.1 Hz. *Middle*: Efficiency curve generated using a threshold calibrated to a FAR of 0.01 Hz. *Bottom*: Efficiency curve generated using a threshold calibrated to a FAR of 0.001 Hz.

Figure 5.8 | MLy Coincidence Model developed with Dragonn [28].

Figure 5.9 | MLy Coherence Model developed with Dragonn [28].

Figure 6.1 | The process of conditioning text data for input into a deep learning model. Text data is not intrinsically digestible by artificial neural network models, as artificial neurons can only process numerical inputs. Therefore, in order to apply deep learning models to text data, we must have some method of converting the data into a numerical format [55]. Transformers expect a sequence of same-length vectors forming an input matrix, X . This diagram shows the process of converting text data into an input matrix. Typically, this conversion is completed in three steps, tokenization, vectorisation, and embedding. However, often, and in the case of the first described transformer model, vectorisation and embedding occur simultaneously and are often labelled simply embedding

[56]. This is the method depicted in the diagram. In the example, we see the sentence “The quick brown fox jumped over the lazy dog.” as it is prepared for ingestion by an NLP model. **Tokenisation** is the process of splitting one contiguous sequence of characters into a number of unique discrete tokens, N . This can be done at multiple levels but is usually done at the scale of words. Sometimes, especially with longer words, words can be split into multiple tokens, as is seen in this example where the word “jumped” is split into “jump” and “ed” [55]. There are numerous algorithms to achieve this, which will not be discussed in detail. Every word, or word subset, within the training dataset, should have a unique token ID. Before running inference on new text data, that data must be tokenized, and each word in the new data will be mapped onto an existing token ID that was generated during the initial tokenisation process. Often some information-low words, known as “stop words”, and punctuation are removed during the tokenisation process [55]. In the example shown, the words “The”, and full stops are removed from the input string. During **vectorisation**, each token is assigned a numerical vector, and **embedding** ensures that this vector is transformed into a meaningful vector space to allow for easier interpretation by the model. There are a number of methods to achieve both of these steps, some of which are simultaneous. In the example shown, each token ID is associated with a vector of tunable weights, as was the case in the first transformer paper. These vectors are randomised at the start of training, but as the process continues, they become tuned to values that represent the information contained by the tokens. In this manner, the vectorisation and embedding steps occur at the same time.

Figure 6.2 | Different embedding possibilities to discretise and embed gravitational-wave time-series data. *Upper*: “Chunking” method of discretisation, where the input time-series is split into N equal-length segments which can be fed into an attention-based model. This method would seem to have the disadvantage that it could split the waveform at any point, leading to chunks with very different waveform content depending on the waveform offset; it also assumes that the innate interferometer output vector is a good embedding for the attention mechanism, which is not necessarily true. *Middle*: Embedding with dense layers, this setup is similar to the chunking method, but it applies one or more dense layers to each chunk so that the model can learn an embedding that will be better adapted to the attention mechanism in subsequent layers. Since the parameters of the dense layers are repeated for each chunk, this method is equivalent to a convolutional layer with N filters and no overlap, where N is the size of your embedded vector output. *Lower*: Embedding with convolutional layers. This type of embedding involves creating feature maps of the input vector using a combination of convolutional and/or pooling layers. It is the equivalent of attaching a CNN head at the front of your model. The output of a 1D CNN would be a 2D matrix where one dimension, the depth, is different features, and the other is time. This can then be split into discrete vectors by splitting it along the time dimension to create vectors of features with length equivalent to the number of features.

Figure 6.3 | A “Bag of words”. Without ordinality, the meaning represented by this sentence becomes significantly harder, if not impossible, to parse. If we had not already seen this sentence then we would not know if the fox was lazy or quick, or rather if it were the dog that was lazy or quick, and just who is jumping over whom? There are NLP models that are designed to use a bag of words as inputs, but it is easy to see that much information is lost when word order is discarded, thus we can infer that the order and position of the words contain a significant amount of information. The same can be true for time series, a CBC signal that contains a merger, an inspiral, and a ringdown, in that order, can probably be discounted as a glitch, but if we feed it in as a bag of words model, there could be no distinction between this and the expected arrangement.

Figure 6.4 | Generation of query, key, and value vectors for each element in the input sequence of length, N . Before attention scores are calculated, each input vector, \vec{x}_i is dotted with the learned query, W_q , key, W_k , and value, W_v , weights projection matrices to produce a query, \vec{q}_i , key, \vec{k}_i , and value \vec{v}_i vector for the input element, \vec{x}_i . This operation is equivalent to the multiplication of the

projection matrices and the input matrix, X , to produce the query, Q , key K , and value V matrices. The key takeaway is that the only tunable parameters are contained in the weights matrices, which act as projection functions to convert the input vector into functional vectors.

Figure 6.5 | Illustration of example query, key, and value vectors generated for the sentence “The quick brown fox jumped over the lazy dog.”. After tokenisation and embedding, each vector in the embedded input sequence generates its own query, key, and value vector. Which together form query, key, and value matrices.

Figure 6.6 | Illustration of the operation of how the alignment function utilizes the query and key vectors to produce alignment scores for each sequence element. In dot-product attention [57], this is achieved using Equation 6.6. Note that the numbers used here are for illustratory purposes only and not extracted from a real model.

Figure 6.7 | Illustration of how the alignment scores are used to scale the respective value vectors for each sequence element, and are then summed to produce a new vector that contains global information embedded contextually. Each value vector is multiplied by the respective score, and then these scaled elements are summed together to produce the new vector.

Figure 6.8 | Illustration of the operation of a single attention head. Here a very small three-element sequence is examined. Each element of the original input sequence is coloured differently, in red, green, and blue. All vectors and scalars associated with an input element are coloured similarly. The output sequence vectors are coloured with a mix of the input colours to show their new information content which consists of distilled global information. More detailed descriptions of the processes shown can be found in Figure 3.4, Figure 3.6, and Figure 3.7.

Figure 6.9 | *Upper*: Alternate method of visualizing attention mechanism as a network diagram. Although this is more similar to how networks have been displayed elsewhere in the thesis, it might obfuscate some aspects of the reasoning behind the attention layer operation. As in the Figure 3.8, this illustrates the operation of the attention mechanism on a sequence of length three, with each input vector coloured differently, in red, green, and blue. In this representation, the projection matrices, W_q , W_k , and W_v , are represented as dense layers, which are applied to each of the column vectors that comprise the input matrix in turn. It should be noted that although the dense layers are coloured differently as they are applied to each input element, this is just to show the different data flows, the weights are maintained by each application of each dense layer. The key, query, and value-dense layers, however, have different weights, and notably, no activation function, as they are just supplying a linear mapping rather than any more complex behaviour. *Lower*: Abstraction of a single attention head layer, that will be used in future diagrams of models which contain attention layers, in order to limit diagram complexity.

Figure 6.10 | *Upper*: Network diagram of multi-attention head. Similar to how multiple convolutional kernels work in tandem in convolutional layers, multiple attention heads work together in multi-attention heads to focus on different information aspects of the input vector. These are then concatenated along the feature axis before finally being multiplied by a further weights matrix, here shown as a dense layer, which serves to mix the output of the different heads and to reshape the output to a desired size. *Lower*: Abstraction of a multi-head attention layer, that will be used in future diagrams of models which contain attention layers.

Figure 6.11 | Typical attention block comprising multiple layers. Residual attention blocks vary in design between architectures but usually maintain the consistent elements shown. The skip connection is here represented by the encircling arrow, which shows that the input of the block is fed to the output before it is returned. There are also several regularisation methods present, batch normalisation, and dropout which help to reduce overfitting and ensure that values within the network remain bounded. Finally, the addition of dense layers and activation functions ensures that non-linear computation can be performed. Sometimes, if a reduction in total model parameter count and inference time is required, convolutional layers can be used in place of dense layers. The

question marks indicate user-selectable hyperparameters.

Figure 6.12 | The transformer model described by Vaswani *et al.* [56]. This encoder-decoder architecture can be used to generate predictions of the next token in a sequence. In the case of [56], this sequence was natural language.

Figure 6.13 | Skywarp pure attention model with dense embedding. This model architecture was used to test the purest application of attention layers to the detection problem by removing any convolutional layers within the model. The single convolutional layer was employed to increase the input dimensionality of the sequence elements from 16 to 128; this was necessary in order to add positional encoding of the appropriate size. Without positional encoding, models were almost impossible to train. The other hyperparameters were obtained using a rough trial-and-error search of the parameter space. Using a more sophisticated hyperparameters search, though a desired goal, proved difficult due to the increased computational requirements of attention-based models over CNNs. (Attention layer's memory usage scales approximately quadratically with input dimensionality, $N: O(N^2)$ [58] similar to dense layers, as opposed to CNNs, which scale linearly with input dimensionality, N , and the number of filters, F , in the layers: $O(N \times F)$ [59], so we encountered so difficulty fitting attention models in memory compared to CNNs.)

Figure 6.14 | Skywarp convolutional attention with convolutional embedding. This model architecture was employed to test if a convolutional embedding scheme, using the proven CNN architecture of Gabbard *et al.* [53] embeds the input into feature maps which could then be input into attention layers. We have the greatest success with this model variety, again hyperparameters were manually tuned, so it is expected that with a more thorough hyperparameter investigation, a superior model could be found.

Figure 6.15 | Model False Alarm Rate (FAR) vs score threshold required to achieve that false alarm rate for the three Skywarp models and the recreated CNN model from Gabbard *et al.* [53] The four models display notably different FAR curve profiles, though it is important to note that a lower curve on this plot will not necessarily translate to model performance as it says nothing about the True Positive Rate, a classifier that labels everything as noise, for example, would be entirely flat on this plot, but would remain useless. Still, there is a notable difference between the curves, the pure attention model, consistently requires a much higher score threshold than the other three models, which will be seen in its poor efficiency performance.

Figure 6.16 | Efficiency curves of the Skywarp models and the recreated model from Gabbard *et al.* at different False Alarm Rates. For each of the 4 models trained, 61 efficiency tests are performed at evenly spaced optimal SNR values between 0 and 15. For each test, 16384 examples with signals of the relevant SNR are examined by the model. The most evident distinction is between the pure attention model utilizing dense embedding, and the other models, which are either purely convolutional or have a convolutional head. There is considerably less distinction between the other three models, which appear statistically indistinguishable at FARs of 10^{-1} Hz and 10^{-2} Hz. A slight advantage may arise between the combined attention-convolution model and the other two competitive models at the 10^{-3} Hz, which is perhaps the strongest evidence of an advantage, but this small difference is still too small to draw any definite conclusions of improved efficacy. At 10^{-4} Hz, the difference is much more apparent, but we are approaching 32-bit precision limits, so it is unclear exactly how seriously we should view these results. The efficiencies at this low FAR are also considerably reduced, reducing the appeal of the use of these models at this FAR. *First:* Efficiency curves at a FAR of 10^{-1} Hz. *Second:* Efficiency curves at a FAR of 10^{-2} Hz. *Third:* Efficiency curves at a FAR of 10^{-3} Hz. *Fourth:* Efficiency curves at a FAR of 10^{-4} Hz.

Figure 6.17 | Receiver Operator Curves (ROCs) generated for each of the four Skywarp models for a variety of different SNR pools. The story demonstrated by these plots is very similar to what is shown by the efficiency curves, Figure 3.16, albeit with less granularity. The pure attention model performs considerably worse than the other three models, which are nearly indistinguishable. The

pure convolution model has a slightly higher area under the ROC curve, primarily boosted by higher efficiencies at higher false alarm rates and the combined convolutional-attention network achieves higher accuracies at the lower FAR ranges, with the single-layer convolutional-attention network somewhere between the two. *First*: ROC generated with a pool of signals with optimal SNRs drawn uniformly between 8 to 20. *Second*: ROC generated with a pool of signals with optimal SNRs of 12. *Third*: ROC generated with a pool of signals with optimal SNRs of 10. *Fourth*: ROC generated with a pool of signals with optimal SNRs of 8. *Fifth*: ROC generated with a pool of signals optimal SNRs of 6.

Figure 7.1 | Two illustrative examples of the example used to train CrossWave, the upper demonstrates the single signal case, the lower the multiple signal case. Since the real data used to train CrossWave was unwhitened, it is not easy to parse by eye. Thus, as an illustrative example, these two examples are shown in whitened data generated using cuPhenom and GWFlow. The example duration has also been cropped from 16 s to 5 s, since the merger times never have a separation greater than 2 s this is ample as an example. Both examples show time series from both detectors, simulating LIGO Livingstone and LIGO Hanford. *Upper*: Single waveform injected into noise drawn from the two LIGO detectors. *Lower*: A pair of waveforms injected into noise drawn from the two LIGO detectors. The waveforms are always injected with merger times less than 2 s distant.

Figure 7.2 | Classification error of Overlapnet output when fed validation examples, plotted with signal A optimal network SNR and signal B optimal network SNR. A total of 4×10^4 validation examples were used to produce this plot. All examples consist of two-channel synthetic detector noise generated by colouring Gaussian white noise with the LIGO Hanford and LIGO Livingston aLIGO design specifications. Half the validation examples were injected with one each of 2×10^4 IMRPhenomTPHM waveforms with no repetitions, these are the single injection examples, which only contain Signal A. In these cases the SNR of signal B is always zero, these signals are seen arranged along the bottom of the plot. The other half of the examples consist of two each of the same 2×10^4 IMRPhenomTPHM waveforms with two repeats of the same pairs of signals injected into different noise realizations. A model score near one indicates the model has determined that the example has two hidden signals and a score near zero indicates that the model thinks the example has only one hidden signal. The classification score error shows the difference between the ground truth value and the predicted model output. Therefore an error nearer zero indicates good model performance, and an error nearer one indicates poor model performance. Assuming a classification threshold of 0.5 we can see that the model can successfully classify almost all single examples, and can successfully classify most pairs of signals when the Network SNR of both signals is above an optimal SNR of ten. We note that although classification is achieved in most cases, there is still substantial error in many cases, though mostly below the threshold required for an inaccurate classification, 0.5. It is theorised that this is because the model is trained with many examples of pairs of detectors with one low SNR that are hard to distinguish from single detectors with one signal. This confusion could add considerable uncertainty to the model predictions, and it is recommended that if this project were to be repeated the minimum SNR threshold for both of the signals should be increased. When either of the optimal network SNRs of one of the signals falls below 10, the rate of classification error increases in a curve that is consistently shaped with the detection efficiency curves discussed in previous sections. This is anticipated – in the case that one of the SNRs becomes low, the signal will appear to look like a single signal as the other signal becomes hard to distinguish. In the case where both signals have a low SNR, both signals are hard to distinguish and it becomes difficult to differentiate between a single hard to identify signal and multiple hard to identify signals. In this latter case, where both signals have a low SNR, the model appears to favour classification as a single signal rather than double. It is hypothesized that this may be because the pairs and single examples were not normalized to have consistent excess power,

meaning that the total excess power contained in the set of all two signal examples will be double that of the total excess power in all single signal examples. This might bias the network to associate low excess power with single signal examples. *Left:* Full validation results. *Right:* Zoomed result for increased detail below optimal network SNRs of 50.

Figure 7.3 | Overlapnet pair efficiency plots created from the combined overlapnet validation data pool using rolling averages with a window of 1000 and plotting every 100th average value. This plot gives an approximate comparison to the efficiency plots generated in the detection cases; although generation was done with a rolling average over a pool of logarithmically distributed SNRs rather than with pools of discrete SNRs at specific test SNR values that have been used previously in the detection cases. Also note that this plots the model output score, rather than the percentage of cases which fall above a calibrated SNR threshold. These efficiency plots show the relationship between the SNR values of one of the signals and the model prediction. One of the five lines gives the rolling average model score when the validation results pool is sorted by minimum SNR value. This is perhaps the most useful of the four lines as it is the bottleneck in classification ability. It reaches a classification score of 1.0 at a minimum optimal network SNR of around 37. It remains above 0.9 for SNRs above 19 and increases slowly until 37. This separates it from the detection case and is presumably because there are extra factors not accounted for on this plot, primarily the SNR of the second signal, but also things like the parameter space difference of the two waveforms and the merger time separation of the two waveforms, which could both add increased difficulty without being visible on the efficiency plot. Two of the lines plot the rolling average model score when plotted with the SNR of one of the two signals, signal A and signal B. Signal B always arrives before signal A. The similarity between these lines shows that it is unlikely there is any bias between whether signal A has the lower SNR or signal B. The maximum scores achieved by these lines are less than the minimum, as there are always low SNR signals in the average used to calculate this. The last of the four pair example lines shows the moving average when the validation pool is sorted by the maximum SNR of the two injected signals. This is the lowest still, as it is more likely that the uncounted-for signals have low SNR. Lastly, we show the single signal SNR scores. Unlike the other signals, a lower score is better in this case, as a model prediction of zero indicates the lack of a second signal. We see that at low SNRs this score is lowest; this is expected as there are considerably more low SNR single signals in the dataset than pairs of signals, and this supports our hypothesis that the network is using excess power as a differentiation method. Above an optimal network SNR of 18 the classification score plateaus at an average of 0.2, as stated previously it is believed this is induced through confusing examples in the training dataset where it is almost impossible for the network to determine between a pair of signals where one signal has a low SNR and a single signal, teaching the network to guess with some uncertainty in all apparent single signal cases. We also see a slight decrease in prediction accuracy as SNR increases, again this probably results from the excess power bias. From this plot we can conclude that as expected the lowest SNR signal in the pair is the largest factor in model efficiency, but that other factors are probably also relevant.

Figure 7.4 | Overlapnet classification results plotted against the time elapsed in seconds between the arrival of the merger of signal B and signal A. The coloured circles represent individual validation classification results colour-coded for visual clarity. The red line is the moving average model prediction error at the stated time separation with a window of 500 validation examples. Only pairs are plotted, as single examples have no time separation. We see that for time differences above 0.8 s the separation has little effect on the average prediction error. Between 0.2 s and 0.8 s there is a slight but notable increase in error, and below a merger time difference of 0.2 s there is a more notable uptick in error. It appears that this uptick at lower time separations is mostly caused by signals that have very low separation (< 0.1 s) – this seems to be the only significant predictor of model performance, other than this, and the small decrease in performance below 0.8 s the classifier seems to work with equal efficiency across time separations. This is perhaps less of a correlation than

might be expected, but it demonstrates that only very close signals are problematic if at detectable SNRs. This is a good sign for the chances of developing a useful classifier.

Figure 7.5 | Overlapnet classification results compared with the mass parameters of the constituent waveforms. *Left:* Overlapnet classification scores plotted with source chirp masses for signal A and signal B. There appears to be some correlation between lower chirp masses and poor model performance, however, because there are highly performing examples even in cases where both chirp masses are low we can conclude that this does not explain the entire picture. It is hypothesized, that this correlation is primarily caused by the fact that lower chirp masses are more likely to produce a low SNR signal. If two sources were at the same luminosity distance but one had a higher chirp mass, the higher chirp mass would have a louder SNR (assuming identical detector noise conditions, sky localization, and signal polarisation). This hypothesis is supported by the lower model performance of single signals at higher chirp masses, as we have seen that single signal classification is slightly worse at higher SNRs. *Right:* Overlapnet classification scores plotted with source mass ratio for signal A and signal B. This plot shows that there is very little, if any correlation between the mass ratio of the two signals, and model performance. This continues to show that signal morphology does not make a decisive difference in classification ability, which is primarily determined by the minimum SNR of a signal in the pairs, and secondarily weakened if the signals have a very small time separation.

Figure 7.6 | Illustration of the action of a single cross-attention head. In contrast to a self-attention head, a cross-attention head takes two sequences as input: a querier sequence, and a queried sequence. The queryer sequence is converted into query vectors with a learned weights matrix, and the queried sequence is converted into key and value vectors. The rest of the attention mechanism functions identically to self-attention but uses query, key, and value vectors that originate from different sources. For more details on the self-attention mechanism see the description in Section 6.1.3.

Figure 7.7 | Illustration of two trivial autoencoder architectures, one using only dense layers, the other using convolutional layers. Both networks have very few neurons and would likely not see use in any real practical application but are presented for illustration only. Autoencoders consist of an encoder that performs dimensional reduction on an input vector to reduce its dimensionality to a smaller latent space and produce a latent vector, this latent vector is then processed by the decoder which attempts to perform the inverse operation and reconstruct the original input image, or a slightly altered version of the input, for example a denoised version of the original input. Often the decoder is simply an inverted version of the encoder, which introduces the concept of transposed convolutional layers which perform the inverted operation of convolutional layers. *Upper:* Illustrative dense layer autoencoder with a two-layer encoder and a two-layer decoder. The latent space of this autoencoder has two dimensions meaning the dimensionality of the input vector has been reduced from five down to two. *Lower:* Illustrative convolutional autoencoder with a two-layer encoder consisting of convolutional layers and a two-layer decoder consisting of transposed convolutional layers. The latent vector of this autoencoder has four elements, which means there has only been a reduction of one element between the input vector and the latent space.

Figure 7.8 | Diagram of the network structure of the smaller of the two trialled CrossWave models. Both the CrossWave models have a novel structure with denoising heads, and feature extraction layers adapted from Gabbard *et al.* [53], as well as utilization of cross-attention layers. The denoising heads are composed of an autoencoder structure, with one for each input detector. In this case, we have used simulated inputs from the LIGO Hanford and LIGO Livingston detectors so there are two autoencoding heads. Each autoencoder has independently trained weights. It is envisioned that during network training these will adapt individually to the peculiarities of the noise in its given detector, and, due to the shared weights utilized by the feature extractor, learn to output a standardized denoised version of the input from each detector, although it is expected this will not

be a perfect correlated to a denoised detector stream since the autoencoders were not independently pre-trained before training of the larger model. After the autoencoding heads, several feature-extracting layers also adapted from Gabbard *et al.* [53] are used to embed the autoencoder outputs into two sequences that can be ingested by the attention layers. It is imagined, that because these feature-extracting layers share weights between detectors, they will map the output of the denoising layers into a shared latent space that can be interpreted similarly by the attention layers, and is therefore useful for cross-attention between detectors.

The core of the small CrossWave model utilizes a repeating block of self-attention layers applied repeatedly to each detector data stream, much like in the Skywarp transformer. These blocks are repeated three times. This repeating self-attention layer should help the model understand the global context of the data within each detector. After completion, these data streams are combined in a cross-attention block, and then processed by two dense layers to give the final regression output scores. This model was trialled and was somewhat performant, but the application of the cross-attention in this method was causing a lot of information to be lost, so the model was abandoned in favour of the larger variant shown in Figure 3.9.

Figure 7.9 | Diagram of the network structure of the larger of the two trialled Crosswave models. Both the CrossWave models have a novel structure with denoising heads, and feature extraction layers adapted from Gabbard *et al.* [53], as well as utilization of cross-attention layers. The denoising heads are composed of an autoencoder structure, with one for each input detector. In this case, we have used simulated inputs from the LIGO Hanford and LIGO Livingston detectors so there are two autoencoding heads. Each autoencoder has independently trained weights. It is envisioned that during network training these will adapt individually to the peculiarities of the noise in its given detector, and, due to the shared weights utilized by the feature extractor, learn to output a standardized denoised version of the input from each detector, although it is expected this will not be a perfect correlated to a denoised detector stream since the autoencoders were not independently pre-trained before training of the larger model. After the autoencoding heads, several feature-extracting layers also adapted from Gabbard *et al.* [53] are used to embed the autoencoder outputs into two sequences that can be ingested by the attention layers. It is imagined, that because these feature-extracting layers share weights between detectors, they will map the output of the denoising layers into a shared latent space that can be interpreted similarly by the attention layers, and is therefore useful for cross-attention between detectors.

The core of the larger CrossWave block contains both self-attention blocks and cross-attention blocks in each iteration, this means that the model can compare data streams from both detectors multiple times, each time adding extra relevant information from the other detector into that detector's branch. Also, since the cross-attention is being performed in both directions, no information is lost as it was in the small model. Again, these blocks are repeated three times. After the repeating blocks, rather than using a cross-attention block to combine the branches, the outputs from each branch were concatenated before being fed into the dense tail, which then produced the final regression outputs.

Figure 7.10 | CrossWave merger time prediction error of Signal A, *upper left*, and Signal B, *upper right*. Compared to the classification results, the merger time errors look more consistent. This is primarily because the model output is not restricted between one and zero like it is in classification, so a few outliers with very high errors saturate the colour map. Given this, we have also plotted the same results with all examples that have errors greater than 0.25 s removed, for a more granular view of the bulk of the regression prediction errors. These are the lower two plots. In these focused plots, we can see that a significant number of results have a regression error of less than 0.1 s, which could be helpful to aid a secondary parameter estimation method. On these lower plots, there is also a notable difference between the average error on signal A merger time predictions, and the average

error on signal B merger time predictions, with a higher average error on signal B. It is unclear exactly why this is the case, but we speculate that this is because signal B arrives first in the detector, meaning that the inspiral of signal A can interfere significantly with signal B, whereas the opposite is only the case when the merger separation is very small. It is also possible that sometimes, signal A can be misclassified as signal B. We would expect this latter confusion to have some correlation to SNR, but this does not seem to be the case. It could also be due to the aforementioned normalisation error reducing model training efficacy for signal B merger time predictions. Interestingly, the relationship between signal SNR and regression error appears low. This suggests that the substantive cause of regression error lies elsewhere, we plot additional comparisons to further investigate.

Figure 7.11 | CrossWave rolling average merger time prediction error plotted when ranked by different SNR combinations. Since the model now has two outputs, one for each merger time in the input example, a plot was generated for each merger time prediction. A plot showing signal A merger time prediction on the left, and a plot showing signal B merger time prediction on the right. At low SNR, the error is dominated by the SNR in the given signal, which is anticipated — a low SNR in a given signal would, evidently, make it difficult for the model to detect, and hence, estimate the merger time, of that signal. We can also see the notable difference in average prediction error between the upper signal A plot and the lower signal B plot. Interestingly, we see that the error on the signal B merger time increases when the SNR of signal A is higher. This seems to be the case regardless of the SNR of signal B. Since signal B always arrives first in the detector, this could be because a loud signal A inspiral obfuscates the presence of signal B, rendering the signal B merger time hard to identify.

Figure 7.12 | CrossWave merger arrival time prediction errors compared with the time separation between signal A and signal B merger arrival times in the LIGO Hanford detector. *Left:* Error on signal A merger time prediction compared with the time separation between the two mergers. *Right:* Error on signal B merger time prediction compared with the time separation between the two mergers. The colour of the plotted examples depicts the absolute error between the model prediction and the ground truth value, and the red line shows the rolling average absolute prediction error. For both merger times, we can see a spike in erroneous merger time predictions when the time separation is near zero. This is similar behaviour to what is seen in the classification examples. It is also expected here, since if the mergers are hard to distinguish from each other it will be difficult to determine the specific merger times. An asymmetry arises in which way the model will incorrectly predict the merger, in signal A, defined as the second to arrive in the detector, the model often predicts the signal will arrive later than it does, and for signal B, the model often thinks it will arrive earlier than it does. Since B always arrives first, these are logical assumptions for the model to make in both cases. In both cases, we also see lines of erroneous predictions where the model error equals the time separation. These are believed to be cases where the model believes signal A to be signal B and vice versa. This line is more pronounced for signal B errors, suggesting that signal B's are more commonly mistaken for signal A's than the other way around.

Figure 7.13 | CrossWave signal merger time parameter estimation results. Each pair of plots shows the merger time estimate of signal A (*left*) and signal B (*right*). For each validation example, the ground truth value is represented on the x-axis, and the model prediction is on the y-axis. Each represents the signal merger time in seconds. The colour of each circle depicts the absolute difference between the ground truth value and the model prediction, which will be zero if the point falls on the line of $x = y$, which is also shown on the plot as a dashed grey line. Due to an error in label normalisation, some ground truth values for signal B were less than zero. Unfortunately, due to the choice of loss function used for the regression (ReLU), the model could not output predictions below zero, this meant that it was unable to predict these values correctly. This error may have interfered slightly with the rest of the training process, however other than its inability to classify

these examples, there does not seem to be a significant reduction in the performance of classification of signal B merger times. Validation examples with round truth values below zero, and their associated predictions have been omitted from signal B plots for visual clarity. If training were to be repeated this error could be easily rectified, either by correcting the normalization or by altering the choice of activation function. *Upper Left*: Predicted against actual signal A merger time in the simulated LIGO Hanford output. *Upper Right*: Predicted against actual signal B merger time in the simulated LIGO Hanford output. *Lower Left*: Predicted against actual signal A merger time in the simulated LIGO Livingston output. *Lower Right*: Predicted against actual signal B merger time in the simulated LIGO Livingston output.

Figure 7.14 | CrossWave companion mass parameter estimation results. Each pair of plots shows the companion mass estimates of signal A (*left*) and signal B (*right*). For each validation example, the ground truth value is represented on the x-axis, and the model prediction is on the y-axis. Each represents the companion mass in solar masses. The colour of each circle depicts the difference between the ground truth value and the model prediction, which will be zero if the point falls on the line of $x = y$, which is also shown on the plot as a dashed grey line. After the merger time predictions, the mass plots show the greatest promise, able to predict component masses with a moderate degree of accuracy. Without a comparison to another parameter estimation method, it is unclear exactly how much use these results can be. *Upper Left*: Predicted against actual signal A companion 1 mass. *Upper Right*: Predicted against actual signal B companion 1 mass. *Lower Left*: Predicted against actual signal A companion 2 mass. *Lower Right*: Predicted against actual signal B companion 2 mass.

Figure 7.15 | CrossWave regression results for the dimensionless spin components of the two companions in each binary merger, A and B. The left plots show the parameter extracted from merger A, whereas the right results show the same parameter extracted by CrossWave from merger B. The plots show the ground truth value of the dimensionless spin component plotted against the predicted value of the dimensionless spin component. The colour of each validation example indicates the difference between the ground truth and the predicted value, in this case, equivalent to the distance the point is from the line of $x = y$. The results are in the following order from upper to lower:

1. Mass 1 Spin Component X [*Left*: Signal A, *Right*: Signal B]
2. Mass 1 Spin Component Y [*Left*: Signal A, *Right*: Signal B]
3. Mass 1 Spin Component Z [*Left*: Signal A, *Right*: Signal B]
4. Mass 2 Spin Component X [*Left*: Signal A, *Right*: Signal B]
5. Mass 2 Spin Component Y [*Left*: Signal A, *Right*: Signal B]
6. Mass 2 Spin Component Z [*Left*: Signal A, *Right*: Signal B]

There appears to be little difference in classification ability between signal A and signal B. The X and Y components show no classification ability, with the model finding an approximate output value to omit for all validation examples. It was known that extracting the spin parameters from the injected signals would be a challenging task, so this is anticipated. The model appears to show limited classification ability for the Z components, with the Z component for the more massive companion extracted with a stronger correlation than the lower mass companion, for which CrossWave shows only very slight predictive ability.

Figure 7.16 | CrossWave model predicted luminosity distance vs ground truth luminosity distance of simulated BBH waveforms. *Left*: Predicted signal A luminosity distance. *Right*: Predicted signal B luminosity distance. The colour of each example point indicates the difference between the predicted and the ground truth value for that example. These plots indicate that there is almost no correlation between the predicted luminosity distance and the ground truth value. The model outputs a very similar value independent of luminosity distance, it is unclear whether this inability arises from a

problem with model training and/or data processing, or whether luminosity distance is too difficult for the model to determine because of degeneracy with other parameters such as inclination.

IV List of Tables

Table 3.1 | Problems often solvable by artificial neural networks and their associated activation and loss functions. This table demonstrates the most commonly used activation and loss functions for several common problem types that machine learning attempts to solve. The activation functions listed are described in Section 3.1.5, whereas the loss functions were described in this section Section 3.1.6. MSE is an abbreviation of Mean Squared Error, and MAE is an abbreviation of Mean Absolute Error.

Table 4.1 | The frame, channel, and state flags used when obtaining data from the respective detectors during the 3rd observing run (O3). This data was used as obfuscating noise when generating artificial examples to train and validate artificial neural network models throughout this thesis. It should be noted that although the clean channels were produced offline in previous observing runs, the current observing run, O4, produces cleaned channels in its online run, so using the cleaned channels during model development ensures that the training, testing, and validation data is closer to what would be the normal operating mode for future detection methods.

Table 4.2 | A non-exhaustive table of possible data conditioning modes. Feature engineering is often used in order to simplify a problem before it is presented to a machine learning model. There are many ways we could do this with gravitational-wave data. Presented are some of the most common. Each is described in more detail in Section 4.2.7.

Table 4.3 | The common training and dataset hyperparameters shared by the CBC and Burst perceptron experiments. Note that the scale factor here refers to the factor used during the upscaling of the CBC waveforms and real interferometer noise from their extremely small natural dimensions to make them artificial neuron-friendly. This is done both to ensure that the input values work well with the network activation functions and learning rates, which are tuned around values near one, and to reduce precision errors in areas of the code that use 32-bit precision, employed to reduce memory overhead, computational cost and duration. Data acquisition batch duration is a parameter of the GWFlow data acquisition module [60]. For speed, the GWFlow data acquisition system downloads data in larger segments than is required for each training batch, then randomly samples examples from this larger segment to assemble each training batch. The data acquisition batch duration determines how long this larger batch is. Smaller values will result in a more evenly mixed training data set and a lower overall GPU memory overhead but will be more time-consuming during the training process.

Table 4.4 | A comparison of results from the literature, red values indicate the significant feature of the study. Note: Some accuracy values are extracted from plots by eye, so substantive error will have been introduced. Some results were not included as they did not state comparable performance metrics.

Table 5.1 | Possible Dataset Hyperparameters. These are parameters that alter the structure and composition of the dataset used to train or model. None of these parameters were selected for inclusion in our hyperparameter optimization test, in order to decrease convergence time.

Parameters with a superscript symbol become active or inactive depending on the value of another parameter in which that symbol is contained within brackets. Range entries are left black for Hyperparameters not included in optimisation, as no ranges were selected for these values.

Table 5.2 | Possible Training hyperparameters. These are parameters that alter the training procedure of the model. None of these parameters were selected for inclusion in our hyperparameter optimization test, in order to decrease convergence time. Parameters with a superscript symbol become active or inactive depending on the value of another parameter in which that symbol is contained within brackets. There are different optimiser parameters that could also be optimized depending on your choice of optimiser, for example, values for momentum and decay. It is not typical to optimise your choice of loss function for most tasks, but some are possible with a range of

loss functions, such as regression, which could benefit from optimisation of this parameter. Range entries are left black for Hyperparameters not included in optimisation, as no ranges were selected for these values.

Table 5.3 | Possible architecture hyperparameters. These are parameters that alter the architectural structure of the model, or the internal structure of a given layer. All these parameters were selected for optimisation. Parameters with a superscript symbol become active or inactive depending on the value of another parameter in which that symbol is contained within brackets. For each of the N layers, where N is the value of the number of hidden layers genome, a layer type gene determines the type of that layer, and other hyperparameters determine the internal structure of that layer.

Table 5.4 | The top ten models in any of the populations throughout the genetic optimisation process, out of a total of 800 trial solutions, 200 at each epoch. Unexpectedly, the three top-scoring models when ranked by fitness, the very metric our optimization method is attempting to optimise are in the first generation. The first generation of a genetic optimisation search will alone act as a random search, so it is perhaps not unsurprising that it has some ability to find good solutions, however, we would expect better solutions to arise out of on average better-performing populations. This could perhaps be a result of our very low epoch count, or a statistical fluke. If it were the latter, however, it would seem very unlikely that the top three spots were taken by a first-generation model. The other option is that there was some asymmetry between the generations.

Table 6.1 | The training and dataset hyperparameters used in Skywarp experiments. This is very similar to the data used for the burst and perceptron experiments seen in Section 4.3. Note that the scale factor here refers to the factor used during the upscaling of the CBC waveforms and real interferometer noise from their extremely small natural dimensions to make them artificial neuron-friendly. This is done both to ensure that the input values work well with the network activation functions and learning rates, which are tuned around values near one, and to reduce precision errors in areas of the code that use 32-bit precision, employed to reduce memory overhead, computational cost, and duration. Data acquisition batch duration is a parameter of the GWFlow data acquisition module. For speed, the GWFlow [60] data acquisition system downloads data in larger segments than is required for each training batch, then randomly samples examples from this larger segment to assemble each training batch. The data acquisition batch duration determines how long this larger batch is. Smaller values will result in a more evenly mixed training data set and a lower overall GPU memory overhead but will be more time-consuming during the training process.

Table 6.2 | Accuracy results at different optimal SNRs from the four models tested at different FAR thresholds. Scores in red are the highest results for that SNR threshold at that FAR, in the one case where there is a tie, both scores are highlighted. With a very marginal lead, the single-layer attention-convolution hybrid appears to be the best model at a FAR of 10^{-1} Hz, only losing out to the CNN and deeper hybrid model by 0.1 percentage points at the highest SNR of 10. This is not a particularly useful FAR range, however, and as we decrease the FAR, the deeper attention layer seems to be victorious, but again the lead is quite small. This appears to show that the convolutional-attention model may have a slight advantage at lower FARs. At the lowest FAR presented, 10^{-4} Hz, the required score threshold for both convolutional-attention hybrid with the single attention layer, and the pure attention model, have reached one, and therefore lack any classification ability. For the remaining models, the required model score threshold is greater than 0.999, and although at this FAR the deep attention hybrid appears to be the clear winner, it is unclear whether victory at such a high score threshold is meaningful, or simply due to statistical variance in model training and the validation dataset. Although it should be noted that the lead is similar in all SNR bins, which were created independently, so if it is statistical variance, it is suggested that it probably originates in the training procedure.

Table 7.1 | Estimated overlap rates of BBH signals in current and future detectors, sourced from Relton [61] and Relton and Raymond [62]. Presented error values are 90% credible intervals. Note

that these results, including past observing runs are estimates rather than real values, and are meant only as an illustration of the probable difference in overlap rates between current and future detector configurations. The number of overlapping signals, N_{overlap} , anticipated within one year is determined by the number of detections, N_{events} , and the visible duration of those detections, which are, in turn, affected by the detection range and lower frequency cut off the detector configuration in question. We can see that although with the current and previous detector configurations an overlapping event is extremely unlikely, it will increase with LIGO-Voyager to the point where we would expect $6.3^{+7.7}_{-3.4}$ overlapping signals per year of observing time, and further increase with the Einstein Telescope to the point where we would not expect any event to be detected without components of other signals also present in the detector. Similar overlaps are expected for LISA and Cosmic Explorer.

Table 7.2 | The training and dataset hyperparameters used in CrossWave and Overlapnet experiments.

Table 7.3 | Results of the CrossWave parameter estimation model. For each of the model's outputted parameters, a Mean Absolute Error (MAE) along with an R^2 score is presented. The MAE indicates the average magnitude of the errors between the model's predictions on the validation dataset and the corresponding ground truth values. It is a measure of average prediction accuracy, though it doesn't distinguish between overestimation and underestimation. The R^2 score quantifies how well the model's predictions explain the variance of the ground truth values in the validation dataset. An R^2 score of one signifies perfect prediction accuracy in the validation examples used. In contrast, a score of zero suggests the model's predictive capability is no better than simply using the mean value of the validation examples. Negative R^2 values indicate that the model performs worse than a model that would always predict the mean, possibly signalling errors in the training process or model selection.

V List of Listings

Listing 3.1 | Python [63]. Required imports to run subsequent code listings in this section. NumPy [64] is used for its fast numerical CPU operations. TensorFlow [65] is used for fast numerical GPU operations, machine learning functionality, and loading the Modified National Institute of Standards and Technology (MNIST) dataset [12]. Bokeh [66] is used to plot figures.

Listing 3.2 | Python [63]. Function to load and prepare the MNIST dataset [12]. The MNIST dataset [12] consists of many examples of handwritten Arabic numerals from one to nine. The images, x , are reshaped, and the labels, y , are one-hot encoded [67].

Listing 3.3 | Python [63]. Function to initialise TensorFlow [65] tensors to store the artificial neuron's parameters, $\vec{\theta}$. In the case of MNIST [12] digit recognition, ten neurons are being trained, so we have ten bias values, \vec{b} , and the input images are of dimension $28 \times 28 = 784$. Therefore, our weights matrix, W , is shaped [784, 10].

Listing 3.4 | Python [63]. Function to perform the computation of artificial neurons in our single-layer perceptron. Since TensorFlow [65] is natively vectorised, this function will calculate the output of all our tensors simultaneously. This function performs the same operation described in Equation 3.1, with a softmax function as the activation function, f . Softmax activation functions are described in Section 3.1.5.4.

Listing 3.5 | Python [63]. Function to compute the loss of the model. The loss function utilised in this case is categorical cross-entropy loss, a loss function commonly used for multi-class, single-label datasets. A more detailed description of the function of this loss function can be found in Section 3.1.6.2.

Listing 3.6 | Python [63]. Function to execute a single training step. This function runs an example, $x = \vec{x}_t$, through the model (usually multiple examples at once as explained in Section 3.2) and computes the loss, $\text{loss} = L_{M\vec{x}_t\vec{y}_t}(\vec{\theta}_t)$ of the output of that model, $y_{\text{pred}} = \hat{y}_t$ compared with the ground truth label of that example, $y = \vec{y}_t$. The gradients, $\text{gradients} = \vec{\nabla}L_{M\vec{x}_t\vec{y}_t}(\vec{\theta}_t)$, are automatically computed for each parameter by `tf.GradientTape()`, which produces a list of gradients for the weights, $w = W$, and biases, $b = \vec{b}$, which are then used multiplied by the learning rate $\eta = \eta$ and used to update the parameters, $\vec{\theta}$, for the next training step; see Equation 3.5.

Listing 3.7 | Python [63]. Function to execute multiple training steps across multiple epochs. This function runs the function defined in Listing 5.6 for each example in the training_dataset, x_{train} , and repeats this process for each requested epoch, num_epochs , updating the model parameters each time. It returns the model parameters, W , b , and some metrics measuring the model's performance; see Equation 3.5.

Listing 4.1 | Python [63]. TensorFlow [65] graph function used by GWFlow [60] to calculate the PSD of a signal. `signal` is the input time series as a TensorFlow tensor, `nperseg` is the number of samples per segment, L , and `noverlap` is the number of overlapping samples, D . TensorFlow has been used in order to utilise GPU parallelisation, which offers a significant performance boost over a similar function written in NumPy [64].

Listing 4.2 | Python [63]. TensorFlow [65] graph function to generate the plus and cross polarisations of WNB waveforms; see Section 4.2.3 for a description of the generation method. `num_waveforms` takes an integer value of the number of WNBs we wish to generate.

`sample_rate_hertz` defines the sample rate of the data we are working with. `max_duration_seconds` defines the maximum possible duration of any signals within our output data. `duration_seconds`, `min_frequency_hertz`, and `max_frequency_hertz` all accept arrays or in this case TensorFlow tensors, of values with a number of elements equal to `num_waveforms`, each duration. Both polarisations of the WNB are generated with parameters determined by the value of these three arrays at the equivalent index. This method is implemented by the GWFlow pipeline [60].

Listing 4.3 | Python [63]. The GWFlow TensorFlow [65] graph function to calculate the optimal SNR, ρ_{opt} , of a signal. `injection` is the input signal as a TensorFlow tensor, `background` is the noise into which the waveform is being injected, `sample_rate_hertz` is the sample rate of both the signal and the background, `fft_duration_seconds` is the duration of the FFT window used in the PSD calculation, `overlap_duration_seconds` is the duration of the overlap of the FFT window in the PSD calculation, and `lower_frequency_cutoff` is the frequency of the lowpass filter, below which the frequency elements are silenced.

VI Collaborative Work

A small amount of the work presented in this thesis was performed in collaboration with others. Here is a list of the sections that contain collaborative work:

- Several of the figures presented in Section 2 were produced by Meryl Kinnear using her impressive knowledge of Mathematica. Specifically, these were: Figure 6.4, Figure 6.5, and Figure 6.7 which is also the image on the half-cover page. This was done as a favour to me and is greatly appreciated. All other figures, aside from Figure 6.11, were created by the author for this thesis.
- Although the work done to train the MLy models using the genetic-algorithm-based hyperparameter optimisation method presented in this thesis was not strictly collaborative, it is described in Section 5.6 as a use case of the method and software that was developed. Work to optimise and train these models was performed solely by Vasileios Skliris, with whom I have collaborated in the past on development work for the MLy pipeline, but not for any of the work presented in this thesis other than what is mentioned in Section 5.6.
- The work presented in Section 7 was collaborative. The problem was presented, and the training and testing datasets were generated by Philip J. Relton. I performed all the work to create and train the models, although some guidance on the nature of the problem and the importance of different aspects was provided by Phil. Our collaboration extended only to the first of the models presented, Overlapnet, after which Phil left the project. The parameter estimation model, CrossWave, was a continuation of the concept, and the same training and validation datasets generated by Phil were used, however, there was no further input from Phil in the training of CrossWave. All data analysis was performed independently, although again, the importance of certain aspects of the problem had previously been highlighted by Phil.

VII Acknowledgments

A great number of people, fortuitous events, and cups of coffee were required to create the conditions necessary for the production of this thesis. It would be a hopeless task to try and name them all (although perhaps I could train a neural network to do it). Nonetheless, I will attempt to highlight and express my overwhelming gratitude toward the most crucial contributors.

Firstly, I would like to thank my supervisor Patrick Sutton. He has helped improve my skills as a scientist in innumerable ways and managed to direct me toward my goal whilst still providing me with the freedom to explore my ideas. I imagine achieving this balance must be one of the most difficult parts of being a Ph.D. supervisor, but he has excelled at the task.

Of course, I need to cover the basics, although thankfully in my case it is not only down to a sense of obligation. I have the most supportive family anyone could ever wish for. I am fortunate enough that they have never shown a single moment of doubt or uttered a single question as to whether this was a thing I could do and whether was a thing I should do. They have always been there, in the background, to support me and let me know that even if things didn't work out it would be okay in the end. I give special thanks to my father, Mark, who has always shown an interest in my work and even attempted to read this thesis, my mother Caroline, who sends me an advent calendar every year, and my siblings, Vanessa, Chris, and Adam.

Speaking of support, I would be remiss not to mention my source of funding, AIMLAC (it's a terrible acronym that I won't do the dignity of expanding), and the wonderful people who run it. I have made many hopefully enduring connections through the myriad of conferences and events they have put on for us, both academically and socially. Through AIMLAC, I have met many people whom I now consider friends, including Tom, Hattie, Ben, Cory, Maciek, Sophie, Robbie, and Tonichia.

Perhaps the largest contribution to the ideas behind this thesis, and the intersection between gravitational waves and machine learning research at Cardiff, comes from Vasileios Skliris. He was Patrick's student prior to me and paved much of the path that this work follows. Despite having to deal with me and my constant stream of new ideas, he continues to push for real applications of machine learning methods with his development of the MLy pipeline.

Next, we come to those who have supported me beyond an academic sense, but whose roles have been of equal importance. Without them, the thought of four years of Ph.D. work is almost incomprehensible (although maybe I could have got it done in two if I didn't have anyone in the office that I could distract). There are a great many people who fit into this category and I will certainly forget some of them (the thesis is long enough as it is). Firstly, Phil, Zoltan, and Sander, you kept me sane with many opportunities for terrible coffees, shots of gin, and rants about AI destroying the world. I already miss you all. I'd also be remiss not to mention all those who came before me, including Ali, Johnathan, and Virginia, who are hopefully enjoying the sunshine in California; and all those who will remain here after I'm gone (I swear I'm perfectly healthy), including Abhinav, Debatri, Jordan, Alex, Wasim, and of course Sama, who promised to read my thesis when it's done (I'm sorry it's so long. Good luck). I hope that she will continue to work on our joint unstarted project, Crocodile. I will also mention friends I have somehow managed to retain from the world outside gravitational waves, all of whom are very dear to me: Harvey, Luke, Patrick, and Elliot. With special thanks to Elliot, who has been my agony aunt through many situations. Oh, and I should probably thank some astronomers too, including Jacob, who helped develop the best game that can be played on the surface of a table; Andy, who continues the noble tradition of gin shots; and a myriad of others who are too numerous to mention.

Lastly, (I put these three in a separate paragraph because I think it'll be funny if they think I've missed them) thank you to Meryl, Terri, and Eva. Thank you for encouraging me to write an acknowledgments section, for supplying me with a good proportion of my current wardrobe, and for your unsuccessful attempts to help me get over my fear of sauce. You've made this last year a lot less stressful than it could have been.

1 Introduction

We live in an exciting time. Now dawns an age of remarkable confluence and innovation; machine learning and artificial intelligence stand poised to remake almost every aspect of science, technology, and everyday life. At the same time, our understanding of the world is increasing with ever more fervour. The era of gravitational-wave astronomy has well and truly begun, and bountiful volumes of new data will soon be at our fingertips. The machine learning community is unlocking novel new tools every month, and it would be an odious missed opportunity not to turn some of these powerful techniques onto the data hidden beneath interferometer noise.

This thesis is an exploration of the use of artificial neural networks to solve problems within gravitational-wave data analysis. Certainly, it is not the first work to attempt such a task, and indeed the intersection between the two fields has attracted much interest in recent years, perhaps that is unsurprising – both fields are new and exciting; it is only natural to try and merge the two. Despite this busy environment, we find that there is some room for innovation. Crucially, we try and work upward from first principles, and present our results in a manner that is easily comparable with other studies. The entirety of the codebase used in the creation of this thesis and all associated work is available online through this URL: https://github.com/mrknorman/evolving_attention, although, unfortunately, some of the data acquisition methods are gated behind LIGO collaboration membership.

Section 2 and Section 3, are introductory chapters that present background information in the areas of gravitational waves and machine learning respectively. They aim to both contextualize the data analysis methods presented throughout the rest of the thesis and in the case of the machine learning chapter introduce many of the analysis methods and nomenclature used throughout. Section 2 gives a brief introduction to gravitational wave science, but it is considered less necessary for the understanding of this thesis than the following chapter. Section 3 in a more rigorous examination of the basics of artificial neural networks, which form the backbone of this work.

Section 4 acts as a general methodology for the data analysis techniques used in later chapters and introduces the custom software that was generated to facilitate the faster iteration of machine learning model training: cuPhenom [48] a GPU implementation of IMRPhenomD, and GWFlow, a custom data acquisition and model training pipeline designed for machine learning in gravitational wave science. In Section 4 we also review the relevant literature, to explore the work others have contributed to the field, before performing a series of experiments to evaluate the performance of unspecialized artificial neural networks to show the necessity of experimentation. We conclude this chapter by recreating some prominent results from the literature, which then act as a baseline for comparison in further chapters.

When designing artificial neural network models, there are a large number of free parameters that are not optimised during model training, these parameters are known as hyperparameters. They pose a significant barrier when attempting to find optimal deep-learning solutions for data analysis tasks. Often, hyperparameter optimization is performed by human-guided trial and error. This increases the already difficult task of comparisons between the performance of models presented in the literature. It is never clear how optimal the hyperparameter optimisation process has been. Section 5 presents Dragonn, a hyperparameter optimisation method that utilises genetic algorithms to find optimal network solutions. It is hoped that by exploring methods for automatic hyperparameter selection we might move a little toward a more robust and repeatable method for optimizing and comparing the performance of different model architectures. This work was used in the early development of the models that form the core of the MLy rapid burst detection pipeline [28].

Section 6 explores the use of a more contemporary neural network architecture, the transformer [56], which has found the most prominent use in natural language processing applications such as ChatGPT

[68]. More precisely, we explore the use of the core innovations presented by the initial transformer paper [56], the attention mechanism. We apply attention-based models to the CBC detection problem and find a marginal improvement over more widely used convolutional neural networks.

In Section 7 we focus on a more specific problem that is currently not an issue but will become a major component of search pipelines when next-generation gravitational wave detectors come online. We explore the possibility that artificial neural networks can aid in the differentiation between single gravitational wave signals and pairs of overlapping gravitational wave signals. We also build a large network utilizing cross-attention layers in order to attempt to extract the parameters from both signals in an overlapping pair. We do this both to provide an established parameter estimation method with more information to improve its operation and as an exercise in its own right, potentially as a prelude to an entire machine-learning-based method to perform parameter estimation on overlapping signals.

2 Gravitational Waves

Since time immemorial, humanity has gazed at the stars. With wonder rooted deep in their minds, they imagined strange and divine mechanisms in order to try and make sense of what they saw. Over the millennia, the vast skies have revealed much about their workings, and with ever-improving tools we have come much closer to understanding their mysteries, but there is still much to be uncovered. It is unclear how deep the truth lies. Perhaps we have but only scratched at the surface. The depths are so vast we simply do not know.

Almost all of that knowledge, all of that understanding and academia, has been built upon the observation of just a single type of particle. Until very recently, the only information we had about the world above us came from light, and although the humble photon has taught us a great deal about the scope of our universe, the discovery of new messengers promises pristine, untapped wells of science. It has only been in the last century that we have achieved the technological prowess to detect any other extraterrestrial sources of data except that which fell to us as meteors. We have brought rocks home from the moon [69]. We study data sent back from probes shot out across the solar system and even ones that have peaked just beyond the Sun's mighty sphere of influence [70]. We have seen neutrinos, tiny, almost massless particles that pass through entire planets more easily than birds through the air [71], and single particles with the energy of a Wimbledon serve [72]. Most recently of all, we have seen the skin of space itself quiver — gravitational waves, the newest frontier in astronomy [15].

Practical gravitational-wave astronomy is still in its infancy; compared to the other fields of astrophysics, it has barely left the cradle, with the first confirmed gravitational-wave detection occurring in 2015 [15]. Although the field has progressed remarkably quickly since its inception, there is still a lot of work to be done — a lot of groundwork to be performed whilst we uncover the best ways to deal with the influx of new data that we are presented with. It seems likely, assuming both funding and human civilization prevail, that work undertaken now will be but the first bricks in a great wall of discovery. New gravitational-wave observatories that are even today being planned will increase our sensitive range by orders of magnitude [73–75]. With any luck, they will open our ears further to previously undiscovered wonders.

This chapter will introduce a small part of the science of gravitational waves; it will not be an extensive review as many of the particularities are not especially relevant to the majority of the content of this thesis. Instead, this section aims to act as a brief overview to give context to the purpose behind the data-analysis methods presented throughout. We will cover the theoretical underpinning of gravitational waves, and perform a glancing tour through the experiments used to detect them.

2.1 Gravity

Gravity is one of the four fundamental forces of nature, the other three being the electromagnetic force and the strong and weak nuclear forces [76]. It is, in some ways, the black sheep of the interactions, as it is the only one not explained by the standard model of particle physics, which is, by some measures, the most accurate theory of physics ever described [77]. Luckily, gravity has its own extremely accurate descriptive theory [78]. It has a storied history, which, if you are unfamiliar, is worth skimming for context.

2.1.1 Ye Old Times

In the beginning, men threw rocks at each other and were entirely unsurprised when they hit the floor. Over time, people became more and more confused as to why this was the case. Many philosophers proposed many reasons why one direction should be preferred over all others when it came to the unrestrained motion of an object. For a long time, there was much confusion about the relationship between mass, density, buoyancy, and the nature and position of various celestial objects. Sometime after we had decided that the Earth was not, in fact, at the centre of the universe and that objects fell

at the same speed irrespective of their densities, came the time of Sir Issac Newton, and along with him arrived what many would argue was one of the most influential theories in the history of physics.

The idea of gravity as a concept had been around for many thousands of years by this point [79], but what Newton did was formalise the rules by which objects behaved under the action of gravity. Newton's universal law of gravitation states that all massive objects in the universe attract all others [1], acting upon each other, much to Newton's displeasure, whether surrounded by a medium or not. Gravity appeared to ignore all boundaries and was described in a simple formula that seemed to correctly predict everything from the motion of the planets (mostly) to the fall of an apple

$$F = \frac{Gm_1m_2}{r^2}. \quad 2.1$$

where F is the force along the direction between the two masses, G is the gravitational constant equal to $6.67430(15) \times 10^{-11} \text{ m}^3\text{kg}^{-1}\text{s}^{-2}$ [80], m_1 is the mass of the first object, m_2 is the mass of the second object, and r is the distance between the two objects. Newton's law of universal gravitation describes the force every massive object in the universe experiences because of every other – an equal and opposite attraction proportional to the product of their two masses [1]; see Figure 2.1. Though we now know this equation to be an imperfect description of reality, it still holds accurate enough for many applications to this day.

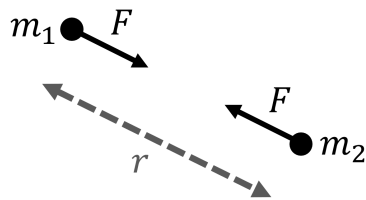
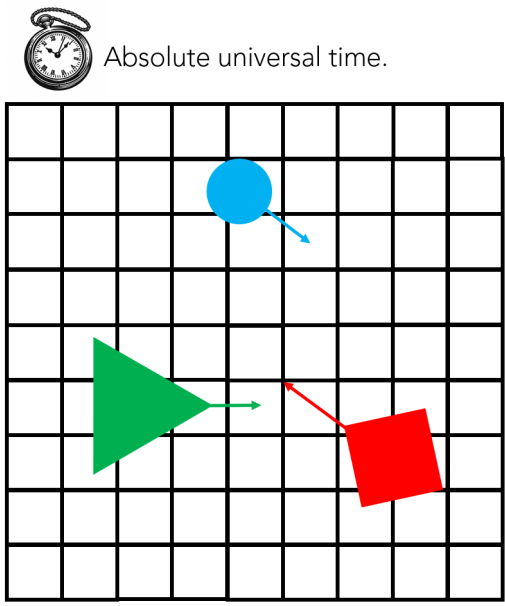


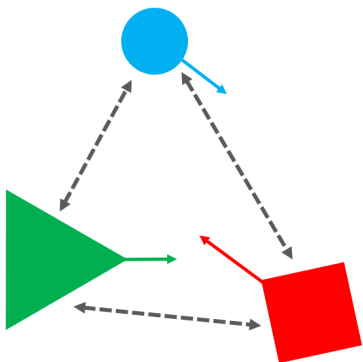
Figure 2.1 | An illustration of Newton's law of universal gravitation, as described by Equation 2.1. Two particles, here distinguished by their unique masses, m_1 and m_2 , are separated by a distance, r . According to Newton's law, they are pulled toward each other by the force of gravity acting on each object F [1], each being pulled directly toward the other by a force that is equal and opposite to its partner's.

It was also at this time that a fierce debate raged over the nature of time and space. Newton proposed a universal time that ticked whether in the presence of a clock or not, and a static, ever-present grid of space that never wavered nor wandered. Both space and time would continue to exist whether the rest of the universe was there or not [2]. Leibniz, on the other hand, argued that space and time were little more than the relations between the positions of objects and their velocities. By his reasoning, if there were no objects, there would be nothing to measure, and there would be no space. If there were no events, there would be nothing to time, and there would be no time; see Figure 2.2. At the time, they did not come to a resolution, and to this day we do not have a definite answer to this question [81], but as we will see, each saw some aspect of the truth.

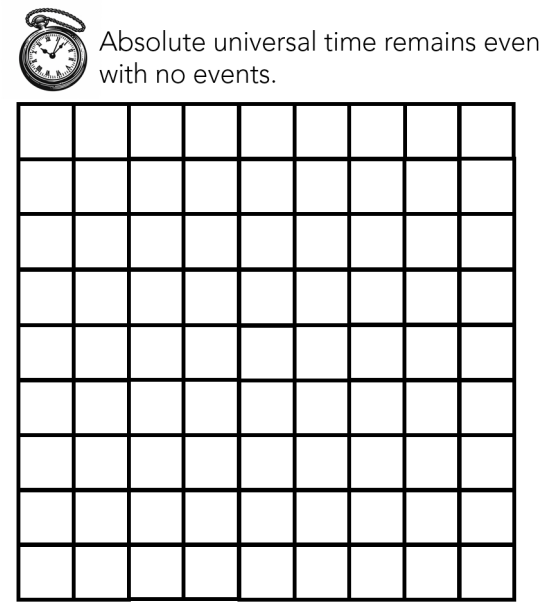


Absolute space.

 Relative time is the relative motion of objects.



Relative space is the relative position of objects.



Absolute space remains even with no objects.

With no events, there is no relative time.

With no objects, there is no relative space.

Figure 2.2 | An illustration of two competing historical views on the nature of space and time [2]. *Upper:* Newton's vision of absolute universal time and absolute space, wherein time moves forward at a constant and uniform rate across the universe and space is immobile and uniform. In this model, both time and space can exist independently of objects within, even in an entirely empty universe. *Lower:* Leibniz's view wherein time and space did not and could not exist independently of the objects used to measure them. Within this model, space is simply a measure of the relative distances between objects, and time is a measure of the relative motion of objects as their relative positions change. In this model, it makes little sense to talk of a universe without objects since time and space do not exist without objects with relative positions and velocities.

For a good few centuries, Newton's law of universal gravitation stood as our fundamental understanding of gravity, with its impressive descriptive and predictive power [82]. As our measurements of the

solar system became more precise, however, a major discrepancy was noted, one that Newton's law failed to describe. The planet Mercury, so close to the sun and so heavily influenced by its gravity, was found to be behaving ever so slightly strangely [83]. Under Newton's laws, the orbits of the planets were described precisely — ellipses plotted through space. The influence of other gravitational bodies, such as the other planets, would cause these ellipses to precess, their perihelion increasing with time. The vast majority of the precession of Mercury was accounted for by applying Newton's laws to the solar system as a whole. However, a small amount, only the barest fractions of a degree per century, remained a mystery. For a long time, it was thought there was an extra hidden planet in the inner solar system, but none was ever found. If this extra precession was an accurate measurement, the difference was enough to state with confidence that Newton's universal law of gravitation was not a complete description of gravity.

2.1.2 Special Relativity

By the start of the 20th century, two more thorns in Newton's side had been revealed. Experiments failed to detect a change in the speed of light irrespective of the Earth's motion through space [84] — if light behaved as we might expect from ordinary matter, then its measured speed should change depending on whether we are moving toward its source, and hence in opposition to its own direction of motion, or against and in unison with its direction of motion. That is not what was observed. Light appeared to move at the same speed no matter how fast you were going when you measured it, whether you measured your velocity relative to its source or any other point in the universe. There was no explanation for this behaviour under Newtonian mechanics. The second tantalising contradiction arrived when attempting to apply Maxwell's hugely successful equations describing electromagnetism, which proved incompatible with Newtonian mechanics, again in large part because of the requirement for a constant speed of light at all reference frames [85]. This failing of Newtonian mechanics was noted by Hendrik Lorentz and Henri Poincaré, the former of which developed many of the ideas and mathematics later used by Einstein [86].

In 1905, Einstein built upon Lorentz's work [86] and proposed his theory of special relativity as an extension beyond standard Newtonian mechanics in a successful attempt to rectify the previously mentioned shortcomings [4]. The initial presentation of special relativity was built upon two revolutionary principles. Firstly, the speed of light was the same in all reference frames, meaning that no matter how fast you were travelling relative to another body, the speed of light would, to you (and to all observers), appear the same as it always has — light would move away from you as it always had done, unaffected by your apparent velocity. Secondly, and closely related to the first principle, special relativity states that the laws of physics will act identically in all inertial reference frames. If you are isolated from the outside world by some impenetrable shell, there is no experiment you can perform to determine that you are moving relative to another body — the only situations between which you could tell the difference were between different non-inertial reference frames (and between a non-inertial reference frame and an inertial one), wherein the shell surrounding you was accelerating at different rates. By introducing these postulates, Einstein explained the observations of light-speed measurements and allowed for the consistent application of Maxwell's laws.

What special relativity implied was that there was no one true “stationary” reference frame upon which the universe was built [4], seemingly disproving Newton's ideal of an absolute universe. All inertial frames were created equal. This seemingly innocent fact had strange consequences for our understanding of the nature of space and time. In order for the speed of light to be absolute, space and time must necessarily be relative — were they not, then the cause-and-effect nature of the universe would break down.

We can visualize the problem in a thought experiment, as Einstein often liked to do [3]. Imagine an observer standing in the carriage of a train moving at a constant velocity relative to a nearby platform.

The observer watches as a light beam bounces back and forth between two mirrors, one on the ceiling, and the other on the floor. From the perspective of the observer, the time taken for light to transit this fixed vertical distance is also fixed, and determined by the speed of light and the distance between the mirrors.

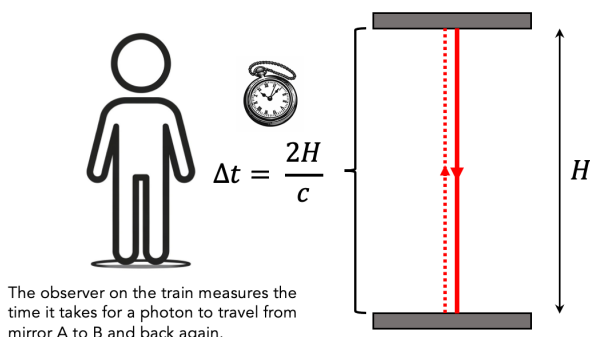
A second observer stands on a nearby platform and looks into the moving train as it passes (it has big windows) [3]. As they watch the light beam bounce between the two mirrors, they see that, from their reference frame, the beam must take a diagonal path between the mirrors as the train moves forward. This diagonal path is longer than the vertical path observed in the carriage's reference frame. If we take special relativity to be true, the speed of light must be constant for both observers. However, in one reference frame, the light must travel a greater distance than in the other. It cannot be the case that the time taken for the photon to travel between the mirrors is the same for the observer on the carriage and the observer on the platform — their measurements of time must differ in order to preserve the supremacy of the speed of light. The observer on the platform would indeed see time passing on the train more slowly than time on the apparently “stationary” platform around them — this effect is known as **time dilation**, and it has since been experimentally verified [87]. We can quantify this effect using

$$\Delta t' = \frac{\Delta t}{\sqrt{1 - \frac{v^2}{c^2}}} = \gamma(v)\Delta t, \quad 2.2$$

where $\Delta t'$ is the measured duration of an event (the time it takes light to move between the two mirrors) in a secondary inertial reference frame (the train carriage) which has a relative velocity, v , compared with the inertial reference frame of the current observer (the platform), Δt is the measured duration of the same event when measured in the secondary inertial reference frame (the train carriage), c is the speed of light in a vacuum, $299,792,458\text{ ms}^{-1}$, and γ is the Lorentz factor given by

$$\gamma(v) = \frac{1}{\sqrt{1 - \frac{v^2}{c^2}}}. \quad 2.3$$

An illustration of this effect can be seen in Figure 2.3.



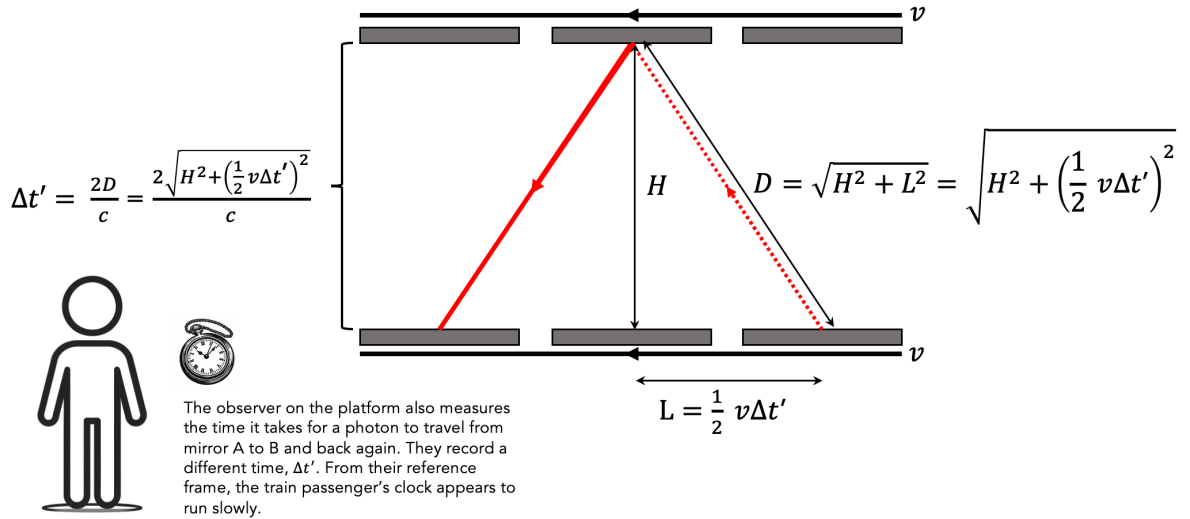


Figure 2.3 | An illustration of the light clock thought experiment. The light clock thought experiment is a scenario that can be imagined in order to illustrate the apparent contradiction that arises from a universally constant speed of light. In order to rectify this contradiction, the concepts of time dilation and length contraction are introduced, fundamentally changing our understanding of the nature of time and space. Two observers stand in inertial reference frames. From special relativity, we know all inertial reference frames are equal, and the laws of physics, including the speed of light, should look identical [3,4]. *Upper:* The observer on the train measures the time it takes a single photon of light to bounce from a mirror at the bottom of the train, to a mirror at the top, and back again. The distance travelled by the light beam is two times the height of the train, H , which gives $2H$. The time it takes a particle to transit a given distance, D , is given by $\Delta t = \frac{D}{v}$. Since light always travels at c , we know the measured photon transit time in this reference frame will be $\Delta t = 2\frac{H}{c}$. *Lower:* A second observer, standing on a platform, watches as the train passes at a constant velocity, v . Through a large window in the carriage, they observe the first observer performing their experiment. However, from the second observer's reference frame, the light now has to move on a diagonal path created by the motion of the train, we can calculate its new transit length $2D$, using Pythagoras's theorem. Each of the two transits, will, by definition take half of the total transit time measured by the platform observer, $\frac{1}{2}\Delta t'$, and in this time the train will have moved, $\frac{1}{2}\Delta t'v$, this gives us $D = \sqrt{H^2 + (\frac{1}{2}\Delta t'v)^2}$. If we substitute this new distance into the original equation to calculate the duration of the transit $\Delta t' = \frac{D}{v}$, we get $\Delta t' = \frac{\sqrt{H^2 + (\frac{1}{2}\Delta t'v)^2}}{v}$. This means that the platform observer measures a longer transit duration. Since the bouncing light beam is a type of clock, a light clock, and all functioning clocks in a given inertial reference will tick at a consistent rate, we can conclude that time is passing more slowly for the observer on the train when observed from the platform's reference frame. In reality, these effects would only become noticeable to a human if the velocities involved were significant fractions of the speed of light. In everyday life, the effects of special relativity are negligible, which was probably why it took so long for anyone to notice.

Similarly, if we orient the mirrors horizontally, so that the light travels along the length of the carriage, a different relativistic effect becomes apparent [3]. The observer on the platform, observing the light's path as longer due to the train's motion, must reconcile this with the constant speed of light. This reconciliation leads to the conclusion that the train, and the distance between the mirrors, are shorter in the direction of motion from the platform observer's perspective. This phenomenon, where objects

in motion are contracted in the direction of their movement, is known as **length contraction** and is described by

$$L' = L \sqrt{1 - \frac{v^2}{c^2}} = \frac{L}{\gamma(v)}, \quad 2.4$$

where L' is the length of an object when measured from an inertial reference frame that has a velocity, v , relative to the inertial frame of the measured object, L is the “proper length” of the object when its length is measured in the object’s inertial frame, c is the speed of light in a vacuum, $299,792,458\text{ ms}^{-1}$, and γ is the Lorentz factor given by Equation 2.3.

Together, length contraction and time dilation shatter Newton’s notions of absolute time and space [4]. It should be remembered, however, that neither the carriage observer nor the platform observer can be said to be in the true stationary reference frame. The observer standing in the station is in the same inertial reference frame as the rest of the Earth, but that doesn’t make it any more valid than any other. If the observer at the station had a similar setup of mirrors and light beams, and the train occupant looked out at them, the train occupant would observe the same phenomenon. To the passenger, time outside the train appears slowed, and the station shorter than it ought to be. This seems to be a paradox, often known as the twin paradox. What happens if the train later stopped and the two observers were to meet? Who would have experienced more time? It is a common misconception that acceleration must be introduced in order to reconcile the two clocks, however, even staying within the regime of special relativity, we can observe an asymmetry between the two observers [88]. In order for the two observers to meet in a shared reference frame, one of the observers, in this case, the train passenger, must change between reference frames, even if that change is instantaneous. This asymmetry allows us to solve the paradox, but the explanation is a little complex so will not be discussed here.

As alluded to, special relativity only deals with inertial reference frames, hence it is a “special” case of a larger, cohesive theory — that theory, developed by Einstein in the following years, is general relativity [5].

2.1.3 General Relativity and Spacetime

Although the notions of independent and absolute time and space were dislodged, it is still possible to describe the new universe illuminated by special relativity as an all-pervasive 4D geometry inside which the universe sits. Unlike Newton’s world, however, space and time are inseparably linked into one joint four-dimensional continuum wherein motion can affect the relative measurements of time and space. We call this geometry **spacetime**. Time intervals between events are not fixed, and observers don’t necessarily agree on their order. Distances must be described by a combination of temporal and spatial coordinates, and because all reference frames are equal, all coordinate systems (ways of assigning reference values to points in spacetime) are also equally valid.

Special relativity deals with flat spacetime. This type of spacetime is known as **Minkowski space** [5]; see Figure 2.4 for an illustration. Although it is non-Euclidian, and its geometry can sometimes be counterintuitive to people used to travelling at pedestrian velocities, it is still isotropic and homogeneous.

Einstein realized that by introducing deformations to the otherwise flat Minkowski spacetime described by special relativity you could induce accelerations in particles within this spacetime without imparting any forces on the particles [5]. Rather than being attracted by some gravitational “force”, the particles continue to behave as they always had, following their natural paths or **geodesics**. A geodesic is the shortest path between two points in a given geometry; in Euclidian geometry, all geodesics are straight lines, in other geometries however, this is not necessarily the case. Thus, depending on the shape of the spacetime they exist within, these particles can accelerate with respect to each

other whilst remaining within inertial frames. This is the reason that it is often stated that gravity is “not a force” — gravitational attraction is a result of the geometry of the spacetime in which objects exist, rather than because of any fundamental force in the traditional understanding of a force.

It should be noted that although under general relativity gravity is not described in the same way as the other fundamental forces, it is still often useful and valid to describe it as such. We don’t have a unifying theory of all of the forces, so they may end up being more similar than current theories describe.

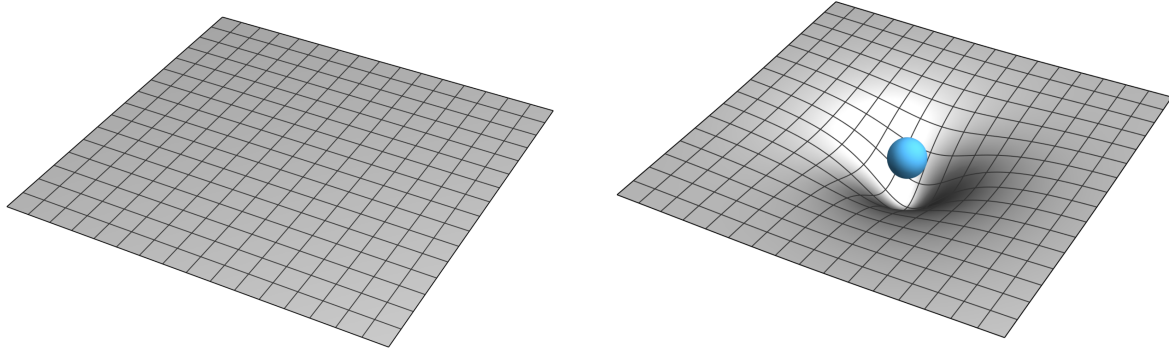


Figure 2.4 | Two depictions of Einstein's spacetime. For illustrative purposes, since we are not 4D beings and the paper on which this will be printed very much isn't, the four dimensions of our universe have been compacted down into two. It should also be noted that these illustrations were not generated with correct physical mathematics but only to give an impression of the concepts being described. *Left:* Minkowski space — in the absence of any mass, spacetime will not experience any curvature [5]. This is the special case that Einstein's special relativity describes. If we were to place a particle into this environment, it would not experience any acceleration due to gravity. If the particle were massive, it would distort the spacetime, and the spacetime would no longer be considered Minkowski space even though, alone, the particle would not experience any acceleration. Often, when dealing with particles of low mass, their effects on the distortion of spacetime are ignored, and we can still accurately describe the scenario with special relativity [4]. *Right:* Spacetime distorted by a massive object, shown in blue. Curved space is described by Einstein's more general theory, general relativity [5]. In this scenario, we can see how the presence of mass imprints a distortion into the shape of spacetime. Any particles also present in the same universe as the blue object, assuming it has existed indefinitely, will experience an apparent acceleration in the direction of the blue sphere. A beam of light, for example, comprised of photons and entirely massless, would be deflected when moving past the sphere. Even though light will always travel along its geodesic through the vacuum of space, the space itself is distorted; therefore, a geodesic path will manifest itself as an apparent attraction toward the sphere. Notice that the mass of the photon is zero; therefore, using Newton's universal law of gravitation Equation 2.1, it should not experience any gravitational attraction, and indeed, gravitational lensing of the passage of starlight, as it moved past the Sun, was one of the first confirmations of Einstein's theory of general relativity [6]. Even if we assume the photon has some infinitesimal mass, Newtonian mechanics predicts a deflection angle that is only half as large as General Relativity predicts, and half as large as what is observed. Were this sphere several thousand kilometres in diameter, any lifeforms living on its surface, which would appear essentially flat at small scales, would experience a pervasive and everpresent downward force. Note that the mass of the object is distributed throughout its volume, so in regions near the centre of the sphere, the spacetime can appear quite flat, as equal amounts of mass surround it from all directions.

After observing that deformations in spacetime would cause apparent accelerations akin to a force of gravity, the natural jump to make is that massive objects that have gravity deform spacetime [5]. The more massive the object, the larger the gravitational well and the more negative the gravitational potential energy of an object within that valley. The more dense the object, the steeper the gravitational well, and the stronger the gravitational attraction. See Figure 2.5 for an illustration.

What we experience as the force of gravity when standing on the surface of a massive body like Earth, is an upward acceleration caused by the electromagnetic force of the bonds between atoms within the Earth. These atoms exert upward pressure on the soles of our feet. We know we are accelerating upward because we are not in freefall, which would be the case if gravity was a force that was balanced against the force of the planet below. Our bodies, and all particles, simply wish to continue on their geodesics, and in the absence of any other forces, that path would be straight down toward the centre of the Earth.

Perhaps not the first question to arise, but certainly one that would come up eventually, would be, what happens if we keep increasing the density of a massive object? Is there a physical limit to the density of an object? Would gravity keep getting steeper and steeper? The mathematical solution to this question was inadvertently answered by Karl Schwarzschild, who found the first non-flat solutions to Einstein's equations [5]. The solution described the exterior of a spherical mass [5]. This metric introduces multiple singularities, some introduced at a particular radius, known as the Schwarzschild radius, which can be shown to be coordinate singularities alone that can be removed via choice of coordinate system. However, the other singularity that is introduced, at the centre of the mass, known simply as the singularity, cannot be removed by such a trick. There was at first much confusion about the nature of this singularity, it was assumed by some that the solution was theoretical alone and such an object could not exist in nature.

It was later discovered that there were indeed physical scenarios in which matter could become so compressed there was nothing to stop it from collapsing into what can mathematically be described as a single point [5]. No known repulsive forces exist which are strong enough to prevent this kind of gravitational collapse. Such objects would create a gravitational well so steep that light itself would not be able to escape, and since light travels at the fastest possible velocity, nothing else could either. It was from this complete state of darkness that these objects received their name – black holes. See Figure 2.5 for a depiction of a black hole.

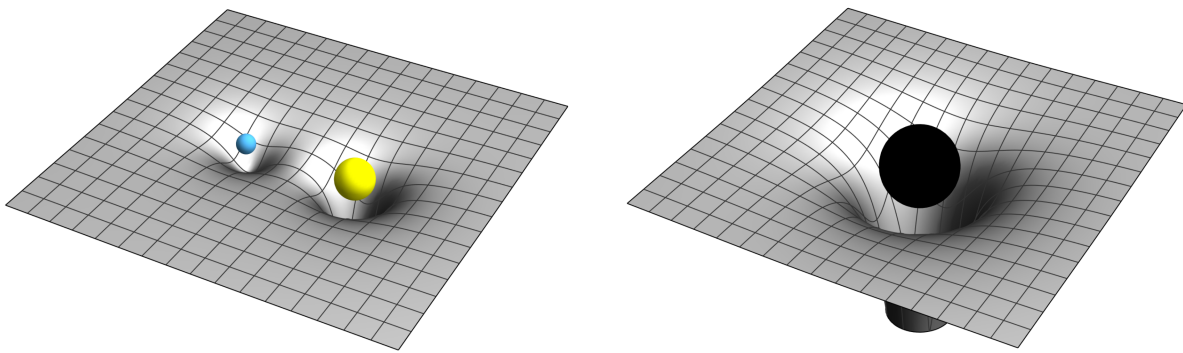


Figure 2.5 | Two further depictions of spacetime. Again, these images are a 2D representation of 4D spacetime, and they were generated without correct physical descriptions but for illustrative purposes alone. *Left:* Two objects, one in blue with a lesser mass and one in yellow with a greater mass. Objects with a larger mass distort spacetime to a greater extent. Objects close to either sphere will experience acceleration as the space curves and the objects continue to move in a straight line. In this scenario, if stationary, the yellow and blue objects will accelerate and move toward each other and, without out-

side interference, inevitably collide. However, if either the blue or yellow ball is given an initial velocity perpendicular to the direction of the other sphere so that its straight-line path orbits the other sphere, they can remain equidistant from each other in a stable orbit for potentially very long periods of time. As we will see, this orbit will eventually lose energy and decay, but depending on the masses of the two objects, this could take an extremely long time. *Right:* A black hole. The three red lines represent the geodesic paths of three light beams as they move past the black hole at different distances. Thus far, we have assumed that the mass of the yellow and blue objects are evenly distributed through their volume, so the spacetime at the very centre of the object is, at its limit, entirely flat. In many scenarios, this is a physically possible arrangement of matter, as although gravity pulls on every particle within the object, pulling it toward the centre, it is a very weak pull compared to the other forces of nature, which push back out and stop the particles continuing on their naturally preferred trajectory. This prevents a complete collapse of the object. Gravity, however, has one advantage on its side, and that is that there is no negative mass, only positive, so whereas large bodies tend to be electrically neutral as positive and negative charges cancel each other out, gravity always grows stronger. If enough mass congregates in the same place, or if the forces pushing matter away from the centre stop, there's nothing to stop gravity from pulling every particle in that object right to the centre, right into a singular point of mass with infinite density known as the singularity. As this collapse occurs, the curvature of spacetime surrounding the object gets stronger and stronger, eventually reaching the point where within a region around the singularity, known as the event horizon, all straight-line paths point toward the singularity. Meaning that no matter your speed, no matter your acceleration, you cannot escape, even if you are light itself. Consequently, no information can ever leave the event horizon, and anything within is forever censored from the rest of the universe.

2.2 Orbits are Not Forever

2.2.1 Orbits

In both Newtonian mechanics and general relativity it is possible to describe two objects that are in an excited state of constant motion, each object gravitationally bound to the other but never directly touching, similar to an electron caught in an atomic orbital. As expected, both theories are correctly describing existent phenomena. When in this state, the objects are said to be **orbiting** each other. If one object is significantly smaller than the other, then the smaller is usually referred to as the orbiter, and the larger the orbited, although in reality, they both exert equal force on each other and the centre of their orbit, known as the barycentre, will never quite align with the centre of the more massive object, even if it is negligibly close.

It is also quite easy to arrive at the notion of an orbit starting from everyday intuition. We can imagine that we live on the surface of a massive spherical object, such as a planet. Hopefully, this is not a particularly hard thing to imagine. We feel an apparent gravitational attraction toward the planet's centre, but the planet's crust prevents us from following our natural geodesic. If we drop something it will fall to the ground until it hits something stopping its motion, the ground. If we throw something, it will still fall, but it will also move a distance across the surface of the sphere since we have imparted some velocity onto the object. Now if we imagine this planet, for some reason, has an incredibly tall mountain and no atmosphere, and we go to the top of that mountain with a suitably sized cannon, we can throw objects (cannon balls in this case), much further. As we increase the amount of gunpowder we use to propel our cannonball, we impart more and more initial velocity onto the balls. We start to notice that as the velocity increases the ball takes longer and longer to reach the ground as the surface of the planet below curves away from it as it falls toward it. Eventually, if we increase the initial velocity enough, we reach a point where the curvature of the planet below exactly matches the rate at which the ball falls toward the centre of the planet. Assuming no external forces, and that the

ball doesn't crash into the back of your head as it completes its first full orbit, this ball could circle the planet forever; see Figure 2.6. Whilst in orbit the ball would be moving along its natural geodesic and would experience no net forces and hence no acceleration, it would be in freefall. This is the microgravity experienced by astronauts aboard the international space station, their distance from Earth's centre is not massively larger than on the surface of the planet and things would still quite happily fall down if left at that altitude with no velocity with respect to the planet's surface.

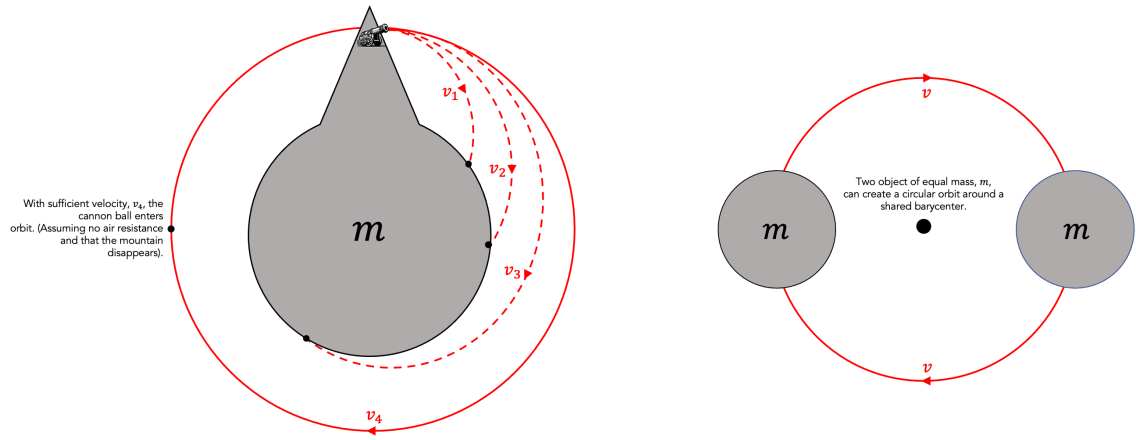


Figure 2.6 | Two illustrations of scenarios involving simple orbital mechanics. *Left:* In this thought experiment we imagine a cannon atop a large mountain on an unphysically small spherical planet with mass, m . As is described in both Newtonian mechanics and general relativity, objects are attracted toward the centre of mass of the planet. Left to their own devices they will fall until they meet some force resisting their motion, most likely, the surface of the planet. The cannon operator can control the velocity of the projected cannon balls. They note that the more velocity they impart, the longer it takes for the ball to impact the surface of the planet. The balls can travel further before impacting the ground when their velocity is greater, even if the time to impact remains the same. However, with this increased distance travelled along the surface of the sphere, the distance between the ball and the ground increases as the surface of the planet curves away from the ball. Eventually, the ball's trajectory will circularise around the planet, and, if not impeded by any other forces, the ball would remain on this circular trajectory indefinitely. *Right:* Two identical massive objects, such as planets, in a circular orbit with a shared centre, called a barycentre (note that the objects do not have to have equal mass or be in a circular orbit, to have a shared barycentre, in fact, this will always be the case). Any massive objects can orbit each other, including black holes.

2.2.2 Gravitational Radiation

In Newtonian mechanics, assuming no other gravitational interactions, and no energy losses through tidal heating or other means (so not in reality), orbits are eternal and will never decay. This is not the case under general relativity, however, where orbiting bodies will release energy through gravitational radiation otherwise known as gravitational waves [5]. Two objects in orbit will continuously emit gravitational waves which will carry energy away from the system and gradually decay the orbit until eventually, the two objects merge. For most objects in the universe, the energy released through gravitational radiation will be almost negligible, and orbital decay from other factors will usually be vastly more significant. However, when we look again at the densest objects in the universe, black holes, and their slightly less dense cousins, neutron stars, their gravitational wells are so extreme that the energy lost through the emission of gravitational waves becomes significant enough for them to merge within timeframes less than the lifespan of the universe, outputting a colossal amount of energy in a frenzy of ripples in the moments before their collision. These huge amounts of energy propagate

out through the universe at the speed of light, causing imperceptible distortions in the geometry of spacetime as they go. They pass through planets, stars, and galaxies with almost no interaction at all.

Like many things, the existence of gravitational waves was predicted by Einstein [89] (although there had been earlier proposals based on different physical theories), as a consequence of the mathematics of general relativity. General relativity predicts that any non-axisymmetric acceleration of mass, linear or circular, will generate gravitational waves. This is because these motions induce changes in the system's quadrupole moment. A perfect rotating sphere will not produce any gravitational waves, no matter how fast it is spinning, because there is no change in the quadrupole moment. A sphere with an asymmetric lump however, like a mountain, will produce gravitational radiation [42], as will two spheres connected by a bar spinning around their centre, or a massive alien starship accelerating forward using immense thrusters. However, as Einstein quite rightly calculated, for most densities and velocities, the energy released in such a manner is minuscule.

Under general relativity, gravitational waves travel at the speed of light [5]. They are not predicted by Newtonian mechanics, as in Newtonian mechanics the propagation of gravitational effects is instant. Special and general relativity, do not allow any information to travel faster than the speed of light, gravitational information is no different [4,5]. All current observations suggest gravitational waves appear to travel at, or very close to, the speed of light, however, this is still some limited debate on the matter [90]. As a perfectly spherical body rotates, the gravitational field remains constant in all directions. Due to the lack of a quadrupole moment, its rotation has no effect on the surrounding spacetime, thus no waves are created that can propagate, and no energy is lost from the spinning sphere.

Aside from detections of the stochastic gravitational wave background [33], we have, thus far, only detected, gravitational waves from extremely dense binary systems consisting of pairs of black holes [15], neutron stars [19], and their combination [29]. These systems, known as Compact Binary Coalescences (CBCs), have a clear quadrupole moment that produces strong gravitational waves that propagate out through the universe, removing energy from the system which will eventually result in the merger of the companions into one body. See Figure 2.7 for an illustration. Gravitational waves from many events of this type pass through the Earth regularly, at the moment, it is only the loudest of these that we can detect. The fact that we can detect them all, however, remains an impressive feat only possible due to the nature of gravitational waves themselves. The amplitude of gravitational waves scales inversely with distance from their source, rather than by the inverse square law as might naively be expected. If this were not the case, detection would be all but impossible. The energy contained within the waves still decreases with the inverse square law, so the conservation of energy is maintained [5].

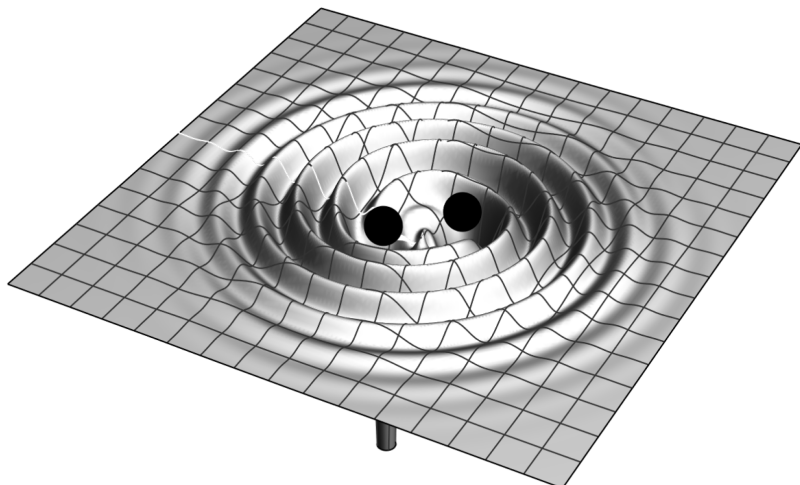


Figure 2.7 | A depiction of the region of spacetime surrounding two inspiraling black holes. The spacetime grid visible is a 2D representation of the true 4D nature of our universe as described by general relativity [5]. This depiction was not produced by an accurate simulation but was constructed as a visual aid alone. Two massive objects can orbit each other if they have sufficient perpendicular velocity; this is a natural state for objects to find themselves trapped in because the chances of direct collisions between objects are low, and any objects that find themselves gravitationally bound together and do not experience a direct collision will eventuate in an orbit. The same is true for black holes; whether they form from pairs of massive stars that both evolve into black holes after the end of their main sequence lives or whether they form separately and through dynamical interaction, end up adjoined and inseparable, the occurrence of two black holes orbiting is not inconceivable [7]. Over time, small amounts of energy will leak from these binaries; ripples are sent out through the cosmos, carrying energy away from the system and gradually reducing the separation between the companions. As they get closer, the curvature of the spacetime they occupy increases, and thus, their acceleration toward each other grows. They speed up, and the amount of energy that is lost through gravitational radiation increases, further increasing the speed of their inspiral in an ever-accelerating dance. If they started just close enough, this process would be enough to merge them within the lifetime of the universe; they will inevitably collide with an incredible release of energy out through spacetime as powerful gravitational waves. It is these waves, these disturbances in the nature of length and time itself, that we can measure here on Earth using gravitational wave observatories.

Gravitational waves have two polarization states, typically named plus, +, and cross, \times . They are named as such due to the effect the different polarisations have on spacetime as they propagate through it. In both cases, the two polarisations cause distortions in the local geometry of spacetime along two axes at once, this is a result of their quadrupole nature. Gravitational waves are transverse waves, meaning they oscillate in a direction that is perpendicular to their direction of propagation. They alternate between stretching spacetime along one of the two axes of oscillation and squeezing along the other, to the inverse, as the wave oscillates. See Figure 2.8 for an illustration of the effect of the passage of a gravitational wave through a region of spacetime. It is this stretching and squeezing effect that we have been able to detect in gravitational wave detectors on Earth. It is worth noting that because they are quadrupole waves and oscillate in two directions simultaneously, the polarisation states are 45 deg apart rather than the 90 deg separation of states seen in electromagnetic waves. This means that any two points on a line that is at a 45 deg angle to the polarisation of an incoming wave, will not see any effect due to the passing wave.

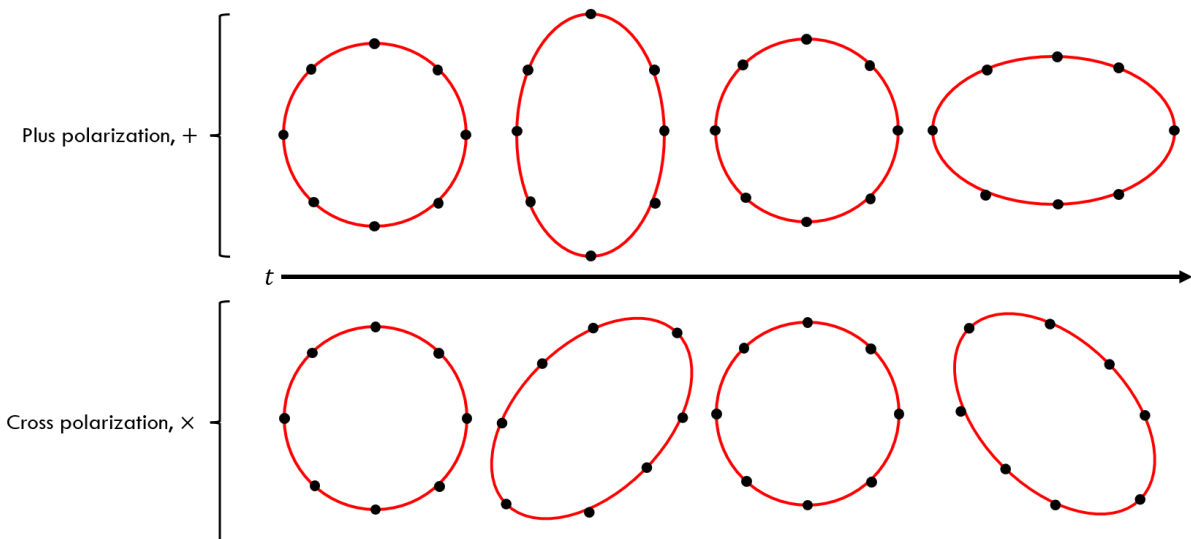


Figure 2.8 | The effect of two polarisation states of gravitational waves as they oscillate whilst passing through a region of spacetime. Each of the black dots represents freely falling particles unrestricted by any other forces. The plus and cross polarisations shown are arbitrary names, and the polarisation can be at any angle, but plus and cross are a convention to distinguish the two orthogonal states.

2.3 Gravitational Wave Detection

Detecting gravity is quite easy, just let go of whatever you’re holding. Detecting gravitational waves, however, requires the use of some of the most precise measurement instruments humanity has ever constructed. This subsection will cover the basics of how we detect gravitational waves and the challenges that our detection methods embed into the data.

2.3.1 Interferometry

After the notion of detectable gravitational waves became more widespread, a few methods were put forward as possible avenues of investigation, the most notable alternative to current methods was the resonant bar antenna [91]. In the end, interferometers have been proven as viable gravitational wave detectors [15], along with, more recently, pulsar timing arrays [33]. These two detection methods operate in very different frequency regimes and so can detect very distinct gravitational wave phenomena — the former able to detect gravitational waves from individual CBC events, and the latter able to detect the pervasive stochastic gravitational wave background, generated by the overlapping and interfering signals of many supermassive black hole mergers.

We will focus our discussion on laser interferometry, as that is the most relevant to work in this thesis. As illustrated by Figure 2.8, gravitational waves have a periodic effect on the distance between pairs of freely falling particles (assuming their displacement doesn’t lie at 45 deg to the polarisation of the wave). We can use this effect to create a detection method if we can measure a precise distance between two freely floating masses [92]. In the absence of all other interactions (hence freely falling), the distance between two particles should remain constant. If there is a change in this distance we can deduce that this arises from a passing gravitational wave.

Masses suspended by a pendulum are effectively in a state of free fall in the direction perpendicular to the suspension fibers, this allows us to build test masses that are responsive to gravitational wave oscillations in one direction, provided they have significant isolation from other forces — which is no small task; a considerable amount of engineering goes into ensuring these test masses are as isolated as possible from the outside world [92].

Once we have our test masses we must be able to measure the distance between them with incredible accuracy. The LIGO interferometers can measure a change in the length of their four-kilometer arms of only 10^{-18} m, a distance equivalent to $\frac{1}{200}^{\text{th}}$ of the diameter of a proton [92], a truly remarkable feat. In order to achieve this degree of accuracy they use laser interferometers.

Interferometers use lasers to accurately measure a change in the length of two arms — in the case of all current interferometers these arms are perpendicular to each other, but there are designs for future gravitational wave interferometers that use different angles but combine multiple overlapping interferometers [73]. In the case of single interferometer designs, right-angled arms capture the largest possible amount of information about one polarisation state, so they are preferred.

What follows is a very rudimentary description of the optics of a gravitational wave detecting interferometer [93]. The real detectors have a complex setup with many additional optics that will not be discussed here. A single laser beam produced by a coherent laser source is split between the two arms by a beam-splitting optic. Each of the beams travels down the length of its respective arm before being reflected off of a mirror suspended by multiple pendulums — the test masses. These beams are reflected

back and forth along the arms thousands of times, before leaving the cavity and being recombined with the beam from the other detector and directed into a photodetector. The path lengths of the two beams are very slightly different, calibrated so that under normal operation the two beams will destructively interfere with each other, resulting in a very low photodetector output. This is the output expected from the interferometer if there are no gravitational waves within the sensitive amplitude range and frequency band passing through the detector. When a detectable gravitational wave passes through the interferometer, it will generate an effective difference in the arm lengths that will cause the distance between the freely falling mirrors to slightly oscillate. This oscillation will create a difference in the beam path lengths, and the two beams will no longer exactly cancel each other causing the photodetector to detect incoming laser light. If the detector is working correctly the amount of light detected will be proportional to the amplitude of the incoming gravitational wave at that moment. See Figure 2.9.

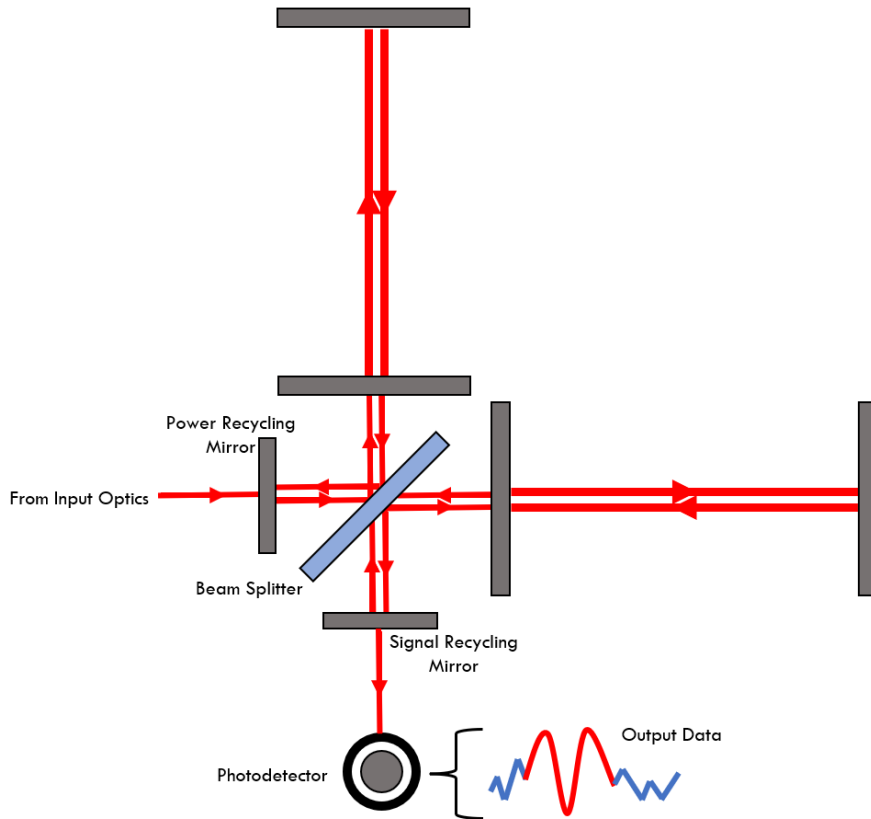


Figure 2.9 | A very simplified interferometer diagram. Real gravitational wave detection apparatus have considerably more optics than what is shown. The power recycling and signal recycling mirrors help maintain a high laser power within the cavities. Higher laser powers are preferable as they help reduce quantum shot noise, the limiting source of noise at high frequencies.

A detector of this kind can only detect elements of incoming gravitational wave signals that align with its polarisation [94]. An incoming signal that was completely antialigned to the detector arms would be entirely undetectable. Fortunately, this is a rare occurrence as most signals are at least partially aligned with a given detector. Interferometers are also sensitive to the angle between their tangent and the source direction, known as the orientation. Interferometers are most sensitive to signals that lie directly above or below the plane of the detector arms, and least sensitive to signals whose propaga-

tion direction is parallel to the plane of the arms. These two factors combine to generate the antenna pattern of the detector, which dictates which regions of the sky the detector is most sensitive to.

2.3.2 The Global Detector Network

There are currently five operational gravitational wave detectors worldwide: LIGO Livingston (L1), LIGO Hanford (H1), Virgo (V1), Kagra (K1), and GEO600 (G1) [8]. See Figure 2.10. Several further future detectors are planned, including LIGO India [95], and three future next-generation detectors: the Einstein Telescope [73], Cosmic Explorer [74], and LISA [75], a space-based detector constellation.

Having multiple geographically separated detectors has multiple advantages.

- **Verification:** Separation provides verification that detected signals are from gravitational wave sources, and are not local experimental glitches or terrestrial phenomena that appear to be signals [96]. Since there are no other known phenomena that can cause a similar effect in such spatially separated detectors, if we see a similar signal in multiple detectors we can say that either they were caused by gravitational wave signals or a statistical fluke. The chances for the latter to occur decrease with the number of detectors.
- **Sky Localisation:** Gravitational-Wave detectors cannot be targeted in a particular area of the sky. Other than their antenna pattern, which is fixed and moves with the Earth, they can sense detections from many directions [96]. This means we don't have to worry about choosing where to point our detectors, but it also means that we have very little information about the source location of an incoming signal, other than a probabilistic analysis using the antenna pattern. Because gravitational waves travel at the speed of light, they won't usually arrive in multiple detectors simultaneously. We can use the arrival time difference between detectors to localize the gravitational wave sources with a much higher constraint than using the antenna pattern alone. With two detectors we can localize to a ring in the sky, and with three we can localize further to two degenerate regions of the sky, narrowing it down to one with four detectors. Adding this triangulation method with the antenna patterns of each of the detectors in the network can provide good localization if all detectors are functioning as expected.

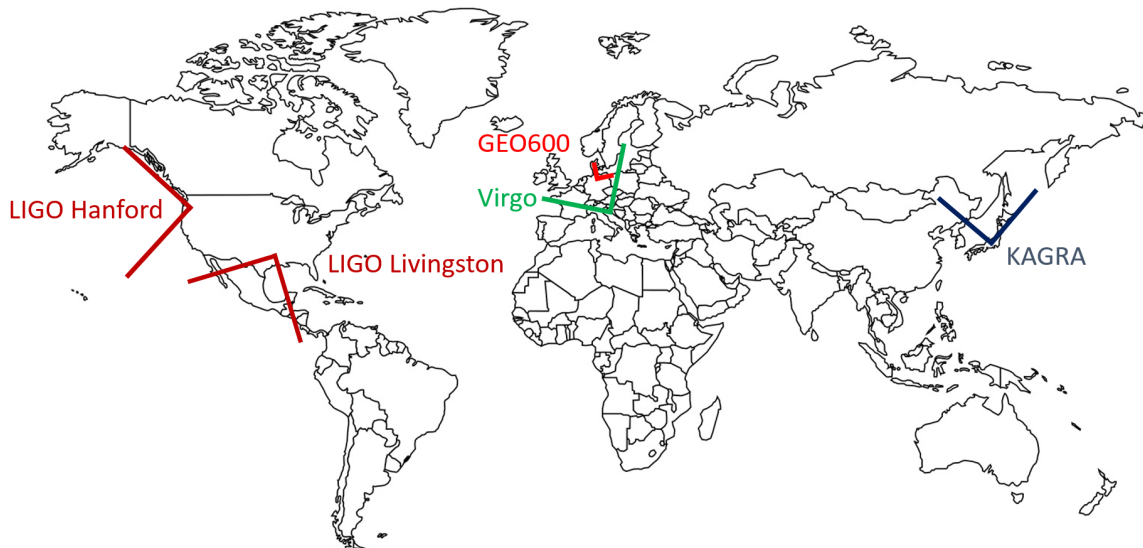


Figure 2.10 | Location of currently operation LIGO detectors: LIGO Livingston (L1), LIGO Hanford (H1), Virgo (V1), Kagra (K1), and GEO600 (G1) [8]. Arm angles are accurate, the arm lengths were generated with a relative scale with the real detectors: 4 km for the two LIGO detectors, 3 km for Virgo and Kagra, and 600 m for GEO600.

2.3.3 Interferometer Noise

Perhaps the area of experimental gravitational wave science that is most relevant to gravitational wave data analysis is interferometer noise. Data scientists must examine the interferometer photodetector outputs, and determine whether a gravitational wave signal is present in the data (signal detection), then make statements about the properties of any detected signals, and how they relate to the gravitational wave source and its relation to us (parameter estimation).

Because it is not possible to reduce noise in all areas of frequency space at once, gravitational wave interferometers are designed to be sensitive in a particular region of frequency space [9] — this region of frequency space is chosen to reveal a particular type of gravitational wave feature that is of interest to us. It makes sense then, that the current generation of detectors were designed with a sensitivity range overlapping the area in which it was correctly predicted that CBCs would lie. The design specification of LIGO Livingston can be seen in Figure 2.11, it shows the main sources of noise in the detector, which we will cover very briefly.

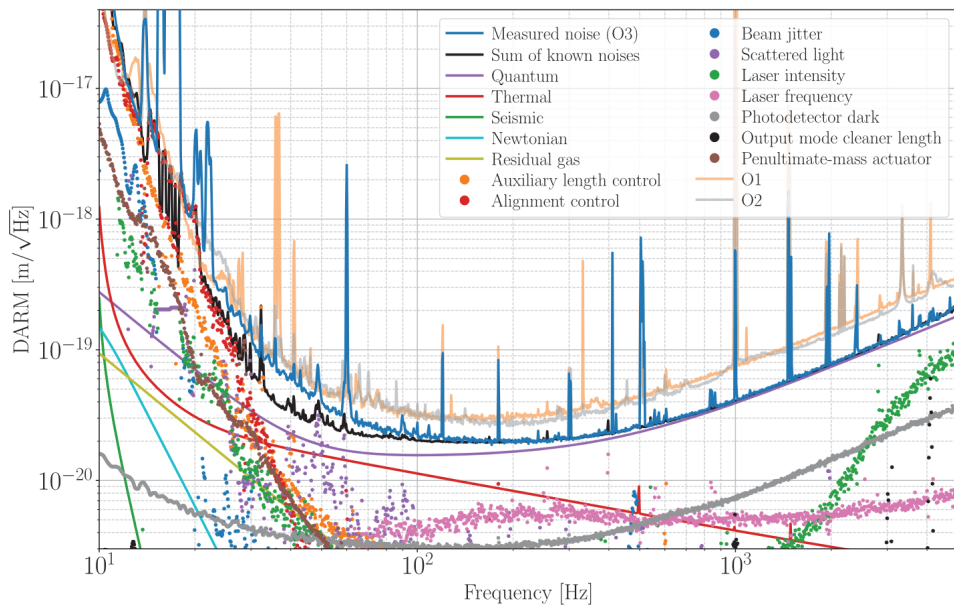


Figure 2.11 | Full noise budget of the LIGO Hanford Observatory (LHO) during the 3rd joint observing run. This image was sourced from [9].

1. **Quantum** noise is the limiting noise at high frequencies [9]. This is primarily in the form of quantum shot noise and quantum radiation pressure noise. It is caused by stochastic quantum fluctuations in the vacuum electric field. Quantum shot noise is the noise generated by the uncertainty in photon arrival time at the photodetector, this can be mitigated by using higher laser power. Quantum radiation pressure noise is caused by variations of the pressure on the optics caused by quantum fluctuation; this kind of noise increases with laser power, but it has a much smaller overall contribution to the noise budget so reducing shot noise is usually preferable.
2. **Thermal** noise is caused by the motion of the particles that comprise the test mass, coating, and suspensions. This is the noise caused by the random motion of particles present in all materials not cooled to absolute zero (all materials). Thermal noise dominates at lower frequencies. Reductions in thermal noise are primarily achieved through the design of the optics and suspension systems.
3. **Seismic** noise is noise generated from ground motion. One of the purposes of the test mass suspensions is to try and reduce this noise. It performs this job admirably. Seismic noise is not a dominant noise source at any frequency range.

These types of noise, plus several other accounted-for sources and small amounts of unaccounted-for noise sum to make a coloured Gaussian background. Some elements of the noise can vary depending on the time of day, year, and status of the equipment because they are sensitive to changes in the weather, local geography, and human activity. This means the noise is also non-stationary and can fluctuate quite dramatically even on an hourly basis [17]. There are also a number of known and unknown sources of transient non-linear glitches that can cause features to appear in the noise. These are some of the most difficult noise sources to deal with and are discussed in more detail in Section 4.2.8. The non-stationary nature of the noise, in addition to the presence of non-linear glitches, makes for an intriguing backdrop in which to perform data analysis. Most of these problems already have working solutions, but there are certainly potential areas for improvement.

Gravitational wave interferometers are not perfect detectors. Their sensitivity is limited by noise present in their output. Despite best efforts, it is not, and will never be, possible to eliminate all sources of noise. When such precise measurements are taken, the number of factors that can induce noise in the output is considerable. It is remarkable that the detectors are as sensitive as they are. Nonetheless, a challenge remains to uncover the most effective techniques for extracting information from signals obfuscated by detector data. The deeper and more effectively we can peer through the noise the more information will be available to us to advance our knowledge and understanding of the universe.

This thesis focuses on a very small part of that problem. We attempt to apply the latest big thing in data science, machine learning, to both detection and parameter estimation problems in the hopes that we can make a small contribution to the ongoing effort.

3 Machine Learning

Machine learning techniques can be applied to almost any area of gravitational-wave data science; therefore, an exhaustive list would be difficult to compile and quickly outdated. However, here are some current areas of investigation: transient detection [52,53,97] and parameterisation [52,98,99], including compact binary coalesces [52,53,97], bursts [100,101,28,102], and detector glitches [103,104]; continuous waveform detection [105–107] and parameterisation [108]; stochastic background detection and parameterisation [109]; detector noise characterisation [110] and cleaning [111]; detector control and calibration [112,113]; and approximant generation [114]. This thesis will focus on the application of machine learning to transients, including compact binary coalesces and burst events. To contextualise this research, this chapter will serve as a brief introduction to machine learning.

Many ambiguous, sometimes contradictory definitions exist within machine learning and artificial intelligence. The definitions used throughout this thesis will be discussed here, attempting to use the most technically correct, or failing that, most commonly used definitions available.

Artificial Intelligence is perhaps the broadest of the terms associated with machine learning and perhaps also the vaguest. It has various, sometimes conflicting, definitions but is often defined as a property of human-designed intelligent agents — systems that take, as input, information about the world and process that data, along with any internal state, to produce an output that maximises the chance of achieving a specific goal [115]. This broad definition can be applied to an extensive range of artificial devices, from a toaster, which takes as an input the twist of a dial and tries to maximise its goal of applying heat for an amount of time relating to the position of the dial, to a chess engine with the all-consuming goal of checkmating its opponent. Most people would probably not consider a toaster artificially intelligent, and indeed, in the years since DeepBlue first defeated Garry Kasparov [116], many have come to consider chess engines in much the same light. This phenomenon is known as the ‘A.I. effect’, wherein a task is only considered something requiring intelligence until it has been successfully demonstrated by a machine [117]. At that point, it is pushed out of the realm of intellectual endeavour and into the mundane, therefore preserving human supremacy over their cognitive dominion. I fear that with the rise of large language models, a few years is all that separates the act of writing a thesis such as this from the same relegation [118]. This transience can make artificial intelligence a tricky definition to use in a technical sense, so the term will, where possible, be avoided.

Machine Learning is somewhat easier to define. Depending on your definition of artificial intelligence, it could be considered either a subset of that field or merely at an intersection with it [119]. It is loosely defined as the study of agents who can gain competency at a task without explicit human instruction [120]. This is achieved through the use of specialised algorithms and statistical methods [120]. Since, for the context of this thesis, it is probably more helpful to think of these agents as statistical techniques rather than actors that react to the world, the rest of this thesis will use the term **model** to refer to these agents, as they often model the relationship between a specific distribution of input data and a specific distribution of output data.

Machine learning can be subdivided in multiple ways, but one of the most common distinctions separates it into three basic paradigms: supervised learning, unsupervised learning, and reinforcement learning [121].

Supervised Learning refers to any machine learning task wherein the model attempts to match its outputs with preexisting values labelled by humans or another technique [121]. Training a model through supervised learning requires datasets of labelled training data from which the model learns. After which, if successful, the model should be able to approximate the desired output given new unseen input data.

Unsupervised learning, on the other hand, does not provide the model with any preexisting values to attempt to match its outputs with [121]. This can include techniques that use the input data as the desired output data, such as in autoencoders [122], or techniques that attempt to divine patterns within the dataset previously unknown to the model and, often, the model user. For example, clustering tasks look for similar latent features between groups of training examples [123].

Semi-supervised learning lies, perhaps unsurprisingly, in the lacuna between supervised and unsupervised learning [124]. Whilst training under this paradigm, some of the training data is labelled and some unlabeled. This can be used when the labels are too computationally expensive to compute for the entirety of the training dataset or when some of the labels are intractable by other techniques or simply unknown.

Reinforcement Learning is a paradigm based on slightly different principles. Instead of using extensive data sets to train an agent, reinforcement learning utilises algorithms that try to maximise themselves against an externally defined reward function [121]. While training a model using reinforcement learning, the model can take actions that affect the state of the environment in which the model is allowed to act. The state of its environment will then be mapped to a score; this score is used to update the model. Through an iterative process, the model is updated to improve its ability to maximise the score of its environment.

Reinforcement learning is commonly used in scenarios where huge training datasets are not available, and the model is primarily designed to interact with an environment (virtual or real), such as training a robot to walk [125] or training a virtual car to drive around a virtual track [126]. Though this has proved a powerful technique for many machine learning applications, it has not been investigated in this thesis and thus will not be discussed in detail.

3.1 The Artificial Neural Network

The Artificial Neural Network is a machine-learning technique that has seen rapid innovation, development, and adoption over the last decade [127]. They've shown the ability to solve many long-standing problems in artificial intelligence, including image, audio, and text classification, captioning, and generation, [128–136], as well as producing game-playing algorithms that have attained superhuman performance in previously human-superior games like Go [137]. They can teach themselves the rules from scratch in a matter of hours [138] – compared to the many years of development required for previous game-playing engines. They can compete in complex, highly-dimensional computer games like Starcraft 2 [139] and League of Legends [140] and they have achieved large-scale adoption across many industrial sectors, managing power grids [141], performing quality control [142], and paving the way, albeit slowly, toward fully autonomous self-driving cars [143]. Artificial neural networks have also been applied to many scientific problems, such as AlphaFold [144], a method that, to some extent, solved the protein folding problem.

With their rampant and rapid success across many domains previously thought intractable or at least many decades away from a solution, it is easy to ascribe to artificial neural networks more than what they are, but it is also easy to underestimate their potential to solve previously unthinkable problems. Artificial neural networks are little more than simple statistical structures compiled into complex architectures, which allow them to perform intricate tasks [11,10,145].

They are loosely inspired by the structures of biological neurons inside animal brains [146,145]. Although they indeed show a greater likeness to the workings of biological systems than most computers, this analogy should not be taken too literally. Biological brains are far more complex than current artificial neural networks, and there is much about them we do not yet understand. There may still be something missing from state-of-the-art models that prevents them from the full range of computation available to a biological brain [147]. Having said that, there are still ample further developments that

can be made with artificial neural networks, even considering their possible limits. We do not yet seem close to unlocking their full potential [148].

There is no universally agreed-upon definition of **deep learning**, but one of the most widely accepted definitions is that it must have a Credit Assignment Path (CAP) depth greater than two. This means that there must be more than two data transformations from input to output [149]. This equates to a dense artificial neural network with more than two layers, or in other words, one or more hidden layers. This enables **representation learning**, where a network can learn to identify hierarchical features in the model [150]. It is proven that models with a CAP of two can act as universal function approximators [151], so adding more layers beyond this act only improves convergence on a parameter solution by reducing training difficulty. In practice, almost all contemporary applications of artificial neural networks are more than two layers deep. The hierarchical relationship between A.I. and machine learning is illustrated by Figure 3.1.

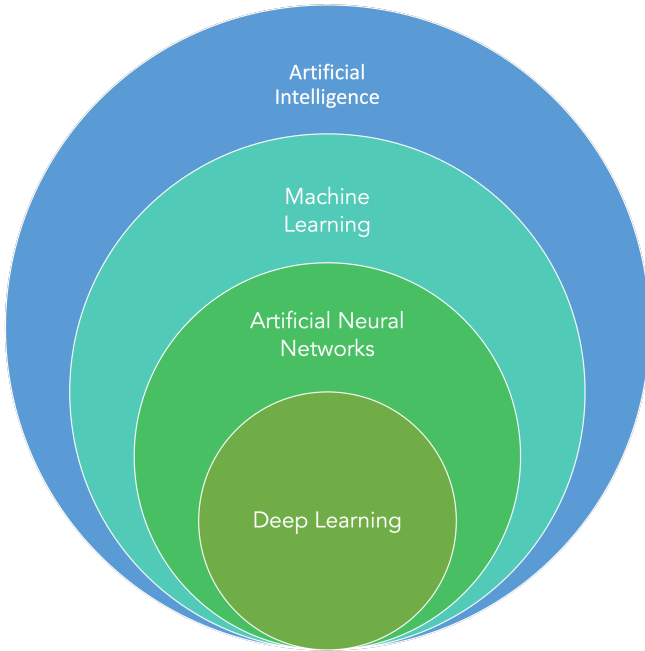


Figure 3.1 | The loose hierarchical relationship between different umbrella terms used in artificial intelligence [10].

There are a plethora of different types and arrangements of artificial neural networks, often known as architectures [10]. The following sections will introduce the main concepts surrounding artificial neural networks.

3.1.1 The Artificial Neuron

As mentioned previously, artificial neural networks are loosely inspired by biological neural networks [146,145], and as one might expect, their base unit is analogous to the biological base unit, the neuron [11]. Artificial neurons form the basic building block of all artificial neural networks, though their form and design can vary between architectures [11].

The artificial neuron takes a number, N , of continuous numerical inputs $\vec{x} = [x_1, \dots, x_i, \dots, x_N]$ and outputs a single numerical output $A(\vec{x})$ [11]. Each neuron has a number of tunable parameters associated with it, $\vec{\theta}$. A single neuron has many weight values $\vec{w} = [w_1, \dots, w_i, \dots, w_N]$ and a single bias value b . Suppose these parameters, $\vec{\theta}$, are selected correctly. In that case, the artificial neuron can, in some simple cases, act as a binary classifier that can correctly sort input vectors, \vec{x} , drawn from a limited

distribution into two classes [145,11]. This kind of single-neuron classifier is often known as a perceptron, the original name given to this kind of classifier [152].

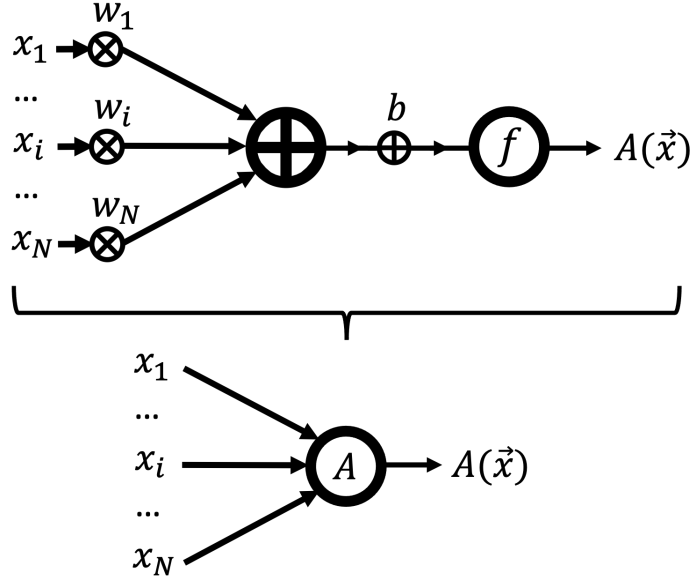


Figure 3.2 | Upper: The Artificial Neuron. This figure illustrates the operations that compose the archetypical artificial neuron, where \vec{x} is the input vector, f is the activation function, \vec{w} is the weights vector, and b is the neuron bias. An artificial neuron takes an input vector, \vec{x} , and performs some useful calculations (hopefully). Both the weights vector, \vec{w} , and bias value, b , comprise the neuron's adjustable parameters, $\vec{\theta}$, that must be tuned for the neuron to perform any useful operations [11]. *Note:* During computation, the bias, b , is not normally added in a separate operation; instead, it is added as an extra x_0 term included in the same calculation as the summation of the product of the weights, \vec{w} , and input values, \vec{x} . **Lower:** An abstraction of the more complicated interior structure of the artificial neuron. Abstraction is common and necessary when describing artificial neural networks as networks are often comprised of thousands if not millions of artificial neurons.

As can be seen in Figure 3.2, the standard artificial neuron is comprised of several consecutive mathematical operations. First, the input vector, \vec{x} , is multiplied by the weights vector, \vec{w} , and then the result of this operation is summed along with the bias value, b [11,145]. Finally, the output is then fed into an activation function f ; see Section 3.1.5. This sequence of operations is given by:

$$A(\vec{x}) = f \left(\sum_{i=1}^N w_i x_i + b \right) = f(\vec{x} \cdot \vec{w} + b), \quad 3.1$$

where N is the number of elements in the input vector. In the case of the single-layer perceptron, the output of the neuron, $A(\vec{x})$, is equivalent to the output of the perceptron, \hat{y} , where our desired ground-truth output value is y . Since each element of the weights vector, \vec{w} , is multiplied by each component of the input vector, \vec{x} , the weights can be thought of as representing the significance of their corresponding input value, x_i , to the desired output value, y . The bias, b , acts as a linear shift to the activation function, and tuning this value can make it more or less difficult for the neuron to activate. Having well-tuned parameters, $\vec{\theta}$, is crucial for the performance of the artificial neuron.

The purpose of the activation function, f , is to coerce the distribution of the output value, $A(\vec{x})$, into a particular shape [153]. The intricacies of why you might want to do this will not become apparent

until the model training is understood. Therefore a more detailed discussion of activation functions follows in Section 3.1.5.

3.1.2 Training Artificial Neurons

Now that the structure of the artificial neuron has been described, the question becomes, how does one go about ascertaining useful values for the neuron's tunable parameters, $\vec{\theta}$, namely the weights vector, \vec{w} , and the bias, b . It would, in theory, be possible to approach this problem by manually discovering values for each parameter, θ_i , using human-guided trial and error. Whilst this would be unwise, we can use this thought experiment to arrive at the automated solution to the problem. This section will describe the step-by-step process of training an artificial neuron, or in this case, multiple neurons, and for each step, illustrate how the manual approach can be automated, displaying a Python [63] function demonstrating this. Listing 3.1 shows the required library imports to run all subsequent code listings in this section. An iPython notebook containing the described code can be found here: <https://tinyurl.com/4m4n3m7n>.

```
# Importing necessary libraries
import numpy as np
import tensorflow as tf
from tensorflow.keras.datasets import mnist
from bokeh.plotting import figure, show
from bokeh.io import output_notebook
```

Listing 3.1 | Python [63] . Required imports to run subsequent code listings in this section. NumPy [64] is used for its fast numerical CPU operations. TensorFlow [65] is used for fast numerical GPU operations, machine learning functionality, and loading the Modified National Institute of Standards and Technology (MNIST) dataset [12]. Bokeh [66] is used to plot figures.

We will attempt to train an ensemble of ten artificial neurons to classify the Modified National Institute of Standards and Technology (MNIST) example dataset [12] correctly. The MNIST dataset consists of 70,000 black-and-white images of handwritten numbers with a resolution of 28 by 28. Pixel values range from 0 for black pixels to 255 for white pixels, with the integer values representing 253 shades of grey. 10,000 images are reserved for testing, with the remaining 60,000 used for training. See Figure 3.3 for examples of the images contained within the dataset.

Though slightly confusing, this ensemble of multiple neurons is often known as a single-layer perceptron [145], as it consists of many neurons acting (almost) independently in a single layer; see Figure 3.4. The only collaboration between neurons is the normalisation that is applied to each neuron by the softmax activation function Equation 3.12, which ensures the produced output vector sums to one and can act as a probability; see Section 3.1.5.4. Because we are moving from a single neuron with one bias value b , and a vector of weights values \vec{w} , to multiple neurons, the bias value becomes a vector \vec{b} , and the weights vector becomes a matrix W .

$$W = \begin{pmatrix} w_{1,1} & \dots & w_{1,j} & \dots & w_{1,P} \\ \vdots & \ddots & \vdots & \ddots & \vdots \\ w_{i,1} & \dots & w_{i,j} & \dots & w_{i,P} \\ \vdots & \ddots & \vdots & \ddots & \vdots \\ w_{N,1} & \dots & w_{N,j} & \dots & w_{N,P} \end{pmatrix}, \quad 3.2$$

where N is the number of neurons in the layer, and P is the number of weights per neuron, typically determined by the number of neurons in the previous layer or the number of elements in the input vector if the layer is the input layer.

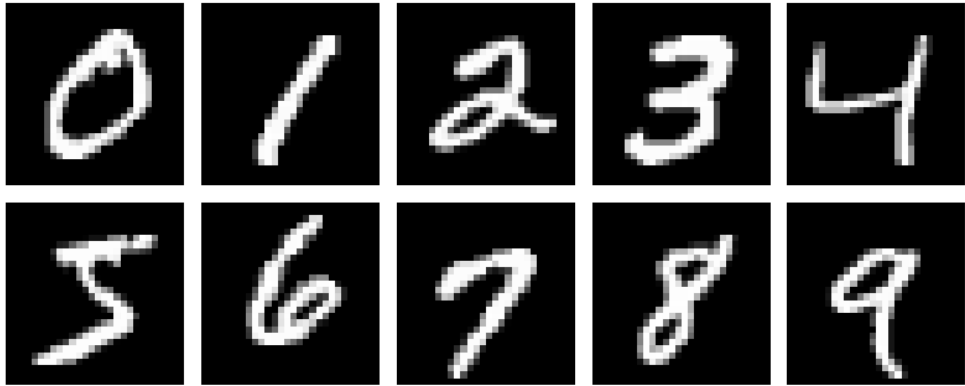
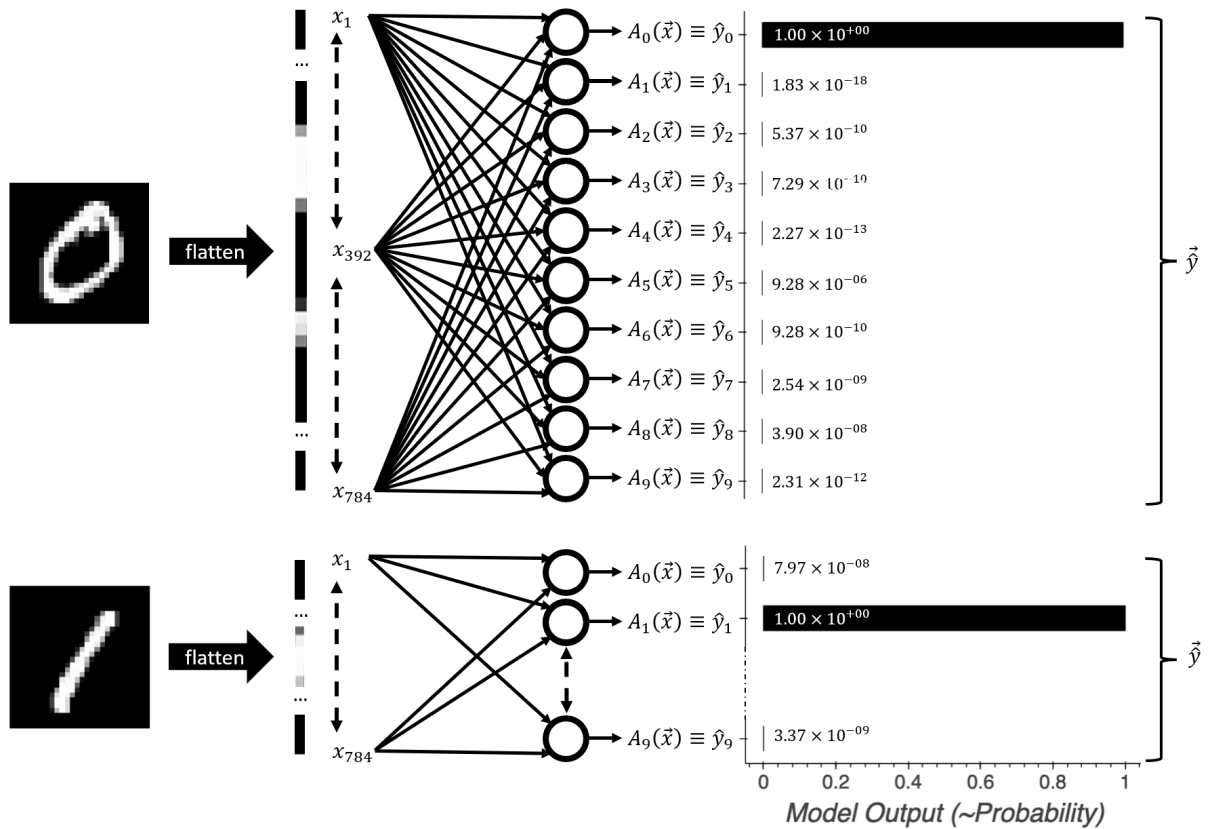


Figure 3.3 | Example MNIST data [12]. A single example of each of the ten classes within the MNIST example dataset. As can be seen, the classes range from zero to nine inclusive. Each example consists of a grid of 28 by 28 pixels containing one float value between 0.0 and 1.0. In the above image, values near one are represented as nearly white, and values near 0.0 as black. When ingested by our single-layer perception, they will be flattened into a 1D vector; see Section 3.4.



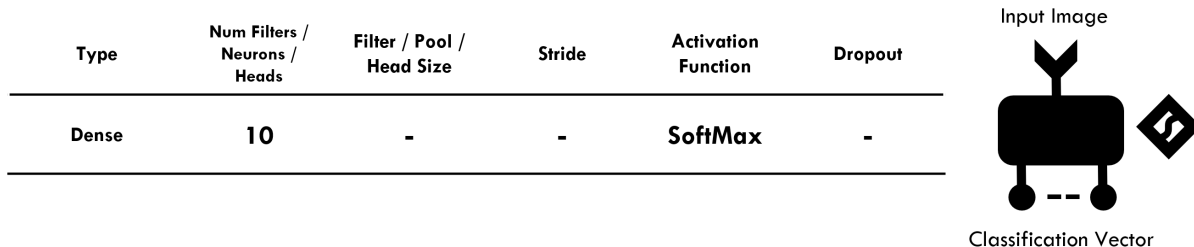


Figure 3.4 | Various representations of a Single-Layer Perceptron or Single-Layer Artificial Neural Network. *Upper:* Diagram illustrating the structure and operation of a single-layer perceptron. In the example shown, a handwritten zero is fed into the single-layer perceptron. The 2D image is first flattened into a 1D vector, see Section 3.4; then, the entire vector is fed into each neuron. If the training process has worked correctly, each neuron will have learned to identify one of the possible classes, in this case, digits. As can be seen from the output values, $\hat{y} = [\hat{y}_0, \dots \rightarrow \hat{y}_9]$, which are taken from a real trained model, this model can correctly identify this input as a zero with high confidence. *Middle:* An abridged version of the upper diagram demonstrating the operation of feeding a handwritten one into the perceptron. This shows how future network diagrams will be abstracted for simplicity and that the perceptron outputs a different, correct value when it ingests a one rather than a zero. *Lower:* A further abstraction of the network. This type of abstraction will be used commonly throughout this thesis when dealing with networks consisting of multiple layers. A dense layer, wherein all neurons are attached to all previous neurons, will be shown as a filled black rectangle, and the icon next to it represents that the activation function applied is a softmax activation function [13]; see Section 3.1.5.4.

Step 1: Dataset Acquisition: When we train a machine learning model, we are attempting to model the relationship between an input and an output distribution. In some ways, the model can be considered a compressed version of the matched input and output distributions. After training, when you feed in a single data point from the input distribution, the model will, hopefully, be able to map that input value to the correct value in the output distribution. This makes the training data a fundamental part of the training process [154]. Whether naively attempting a manual solution or optimising through more efficient means, we must acquire a suitable training dataset.

In many cases, the input distribution will be very large or even continuous, so an exhaustive training dataset covering every possible value in the distribution will be either technically or literally impossible. For this reason, we have to ascertain or generate a training dataset that will appropriately sample the entire input distribution. There are many preexisting example training sets; as stated, we will use the MNIST dataset [12] for illustrative purposes.

Automating the process of acquiring a dataset is simple. TensorFlow [65] has built-in functions to allow us to acquire the MNIST dataset [12] easily. Listing 3.2 below shows us how this process can be performed. The listed function also prepares the data for ingestion by the ensemble of artificial neurons. **One hot encoding** changes a single numerical class label, i.e. 0, 1, ..., 9 into a Boolean vector where each index of the vector represents a different class; for example, 0 becomes [1, 0, 0, 0, 0, 0, 0, 0, 0, 0], whereas 1 becomes [0, 1, 0, 0, 0, 0, 0, 0, 0, 0] [67]. This is because each neuron will learn to distinguish a single class by returning a float value closer to 0.0 if the input falls outside its learned distribution or closer to 1.0 if the input falls within its learned distribution. Therefore to perform the vector operations necessary for training, one hot encoding must be performed [67].

```
# Step 1: Load and prepare the MNIST dataset.
def load_and_prepare_data():
```

```

# This data is already split into train and test datasets.
(x_train, y_train), (x_test, y_test) = mnist.load_data()

# Reshape and normalize the images to feed into the neural network.

x_train, x_test = x_train.reshape(-1, 784)/255.0, x_test.reshape(-1, 784)/255.0

# Convert labels to one-hot vectors. This is necessary as our output layer will
have 10 neurons,
# one for each digit from 0 to 9.
y_train, y_test = tf.one_hot(y_train, depth=10), tf.one_hot(y_test, depth=10)

return x_train, y_train, x_test, y_test

```

Listing 3.2 | Python [63] . Function to load and prepare the MNIST dataset [12]. The MNIST dataset [12] consists of many examples of handwritten Arabic numerals from one to nine. The images, `x`, are reshaped, and the labels, `y`, are one-hotted [67].

Step 2: Parameter Initialization: For an artificial neuron to produce a result when it consumes an input vector, all parameters, $\vec{\theta}$, must be initialised to some value. One could imagine choosing these initial parameters, $\vec{\theta}_0$, in a few distinct ways. Perhaps most intuitively, you could decide on the parameters based on some prior knowledge about the dataset, aiming to get as close as possible to the optimal tunings in order to minimise the number of steps required during training. However, this option is impossible if the human tuner lacks such intuition or if the input size is too large for any human to form such an intuition. That leaves choosing a uniform value for all parameters or randomly initialising all parameters.

In any automated process, a uniform initialisation is a bad choice. If one sets all initial parameters, $\vec{\theta}_0$, to the same value, this creates symmetry [155]. Suppose we subsequently try to use a mathematical method to adjust these parameters. In that case, the method will have no way to choose one parameter over another, meaning all parameters will be tuned identically. We will need the parameters to be adjusted independently in order to model complex relationships. For this reason, we will initiate the weights matrix, W , randomly by sampling values from a normal distribution. This choice of random distribution will not be discussed here, but note that there is an open area of research hoping to speed up and/or improve the training process by selecting more optimal distributions for parameter initialisation [155]. The bias values, \vec{b} , will be initialised to zero. Since there is only one bias value per neuron, we don't have to worry about creating asymmetry, as that is provided automatically by values passed through the neuron's weights.

Listing 3.3 demonstrates the initialisation of two variable tensors to hold the weights and biases of our artificial neurons. Because there are ten classes of numbers in the training dataset, we will initialise ten artificial neurons – one to recognise each class of digit. There will be a single bias value for each neuron. Hence there are C bias elements in the bias tensor, `biases`, where $C = \text{num_classes} = 10$, and the input size is $N = 28 \times 28 = 784$, so there are $N \times C = 784 \times 10 = 7840$ elements in our weights tensor, now a matrix, $W = \text{weights}$, arranged in the shape `[784, 10]`. This means the total number of tunable parameters in our set of ten neurons is $7840 + 10 = 7850$.

```

# Step 2: Define the model
# We are using a simple single-layer perceptron model

```

```

# This is essentially a single fully-connected layer

def define_model():
    # Define weights and biases. We initialise the weights with a random normal
    # distribution.
    # There are 784 input neurons (one for each pixel in the 28x28 image) and ten
    output
    # neurons. We initialise biases to zero.

    weights = tf.Variable(tf.random.normal([784, 10]), name="weights")
    biases = tf.Variable(tf.zeros([10]), name="biases")
    return weights, biases

```

Listing 3.3 | Python [63]. Function to initialise TensorFlow [65] tensors to store the artificial neuron's parameters, $\vec{\theta}$. In the case of MNIST [12] digit recognition, ten neurons are being trained, so we have ten bias values, \vec{b} , and the input images are of dimension $28 \times 28 = 784$. Therefore, our weights matrix, W , is shaped `[784, 10]`.

Step 3: Define the model's action: To perform any optimisation method, there must be a way to test the model. Thus we must define the action of the model, $M(\vec{x})$. We have already shown what form this must take in Section 3.1.1 and Equation 3.1. This is very easily defined by a Python [63] function, as seen in Listing 3.4.

```

# Step 3: Define the model's computations:
def model(x, W, b):
    return tf.nn.softmax(tf.matmul(x, W) + b)

```

Listing 3.4 | Python [63]. Function to perform the computation of artificial neurons in our single-layer perceptron. Since TensorFlow [65] is natively vectorised, this function will calculate the output of all our tensors simultaneously. This function performs the same operation described in Equation 3.1, with a softmax function as the activation function, f . Softmax activation functions are described in Section 3.1.5.4.

Step 4: Define the loss function: Now that we have set up a procedure to run the model with a set of randomised parameters, $\vec{\theta}$, we must define a measure of success so that we can see how well the model is performing whilst we perform our parameter tuning operation. If we have no performance metric, then we have no indication of how to tune the model to improve its performance. To do this, we define a loss function, L , a function which takes in some information about the state of the model after it has ingested data, usually including the model's output, and returns a numerical output value: the loss of the model with a given set of parameters, $L(M_{\vec{\theta}}(\vec{x}), \vec{y})$, where \vec{x} is a particular instance, or batch, of input vectors, and \vec{y} is, in the case of classification, the data label [10]. Note that in unsupervised learning, the loss function does not ingest a label, \vec{y} , as the data is not labelled [10].

By convention, a high loss value indicates that the model performance is worse than that which would be indicated by a lower loss value [10]. Our optimisation process, therefore, should attempt to minimise the average of this loss value across all potential input vectors.

There are many possible metrics for measuring the performance of a model, a large number of which can be used as the loss function [10]. The loss function is an important aspect of the training process, which can alter the efficiency of the training significantly. They can be highly specialised to particular

scenarios, to the point where using an inappropriate loss function can completely remove any possibility of training [10]. A more detailed description of loss functions is available in Section 3.1.6.

For this model, we elect to use the categorical cross-entropy loss function [10] as described in Section 3.1.6. An implementation of that loss function is shown by Listing 3.5.

```
# Step 4: Define the loss function
def compute_loss(y_true, y_pred):
    return tf.reduce_mean(-tf.reduce_sum(y_true * tf.math.log(y_pred), axis=[1]))
```

Listing 3.5 | Python [63]. Function to compute the loss of the model. The loss function utilised in this case is categorical cross-entropy loss, a loss function commonly used for multi-class, single-label datasets. A more detailed description of the function of this loss function can be found in Section 3.1.6.2.

Step 5: Train the model: Finally, after we have assembled all the pieces, we can start to tune the parameters, $\vec{\theta}$, so that our perceptron can output useful values when fed input. As we have previously stated, we will initialise our weight parameters, W , randomly; this means that no matter what images we feed into the untrained model, we will get non-sensical classification values with no correlation to the ground truth labels unless by extremely unlikely fluke. Using some process, we want to move the model toward successful categorisation.

If we again move back to our analogy of attempting to perform this operation manually, what we might imagine is that we would start by feeding it an image from our training dataset. We could then examine the model's output and see which parameters we would need to tune in order to move our network, for that particular image, toward the correct answer. We could achieve this by determining how much each parameter moves the current model's output, \vec{y} , toward or away from the ground truth value, \vec{y} , and then adjusting each parameter accordingly.

If we tuned the parameters by a large amount, then the model could easily become overtuned to a particular image, so we might instead choose to move it a little bit toward the correct input value and then repeat this process over hundreds, if not thousands, of examples, moving the network slowly toward a useful configuration.

Gradient descent is an algorithmic implementation of this thought experiment [10]. In its most simple case, the loss that is given by the loss function, $L(M_{\vec{\theta}}(\vec{x}), \vec{y})$, measures the distance between the model output, \vec{y} , and the ground truth, \vec{y} . Since the model is largely defined by its parameters, $\vec{\theta}$, the loss function can be thought of as a function that takes in an input vector, \vec{x} , the model parameters $\vec{\theta}$, and the ground truth label, \vec{y} . So the output of the loss function for a particular input vector and set of parameters becomes

$$L(M_{\vec{\theta}}(\vec{x}), \vec{y}) = L(M(\vec{\theta}, \vec{x}), \vec{y}) = L_M(\vec{\theta}, \vec{x}, \vec{y}), \quad 3.3$$

where L is the model-architecture-agnostic loss function, L_M is the loss function for a particular model architecture, $M_{\vec{\theta}}$, is a model with a fixed set of parameters, $\vec{\theta}$, M is a model with a set of parameters as a functional input, \vec{x} , is a particular input vector to the model, and, \vec{y} , is the label vector corresponding to the model input vector.

The gradient of the model is defined as the vector of partial derivatives of the model's loss function with respect to its parameters [156]. If $L_{M\vec{x}\vec{y}}(\vec{\theta})$ is the loss function with a fixed model architecture, input vector, and ground-truth label, then the gradient of the model is

$$\vec{\nabla} L_{M\vec{x}\vec{y}}(\vec{\theta}) = \left[\frac{\partial L_{M\vec{x}\vec{y}}}{\partial \theta_1}, \dots, \frac{\partial L_{M\vec{x}\vec{y}}}{\partial \theta_i}, \dots, \frac{\partial L_{M\vec{x}\vec{y}}}{\partial \theta_N} \right] \quad 3.4$$

where N is the total number of tunable parameters.

Equation 3.4 describes a vector, $\vec{\nabla} L_{M\vec{x}\vec{y}}(\vec{\theta})$. Each element of the vector, $\frac{\partial L_{M\vec{x}\vec{y}}}{\partial \theta_i}$, is a gradient that describes the effect of changing the value of the corresponding parameter, θ_i , on the model loss. If the gradient is positive, then increasing the value of the parameter will increase the value of the loss, whereas if it's negative, increasing the value of that parameter will decrease the model loss. The magnitude of the gradient is proportional to the magnitude of that parameter's effect on the loss [156].

Since we want to reduce the model loss, we want to move down the gradient. Therefore, for each parameter, we subtract an amount proportional to the calculated gradient [156]. [10].

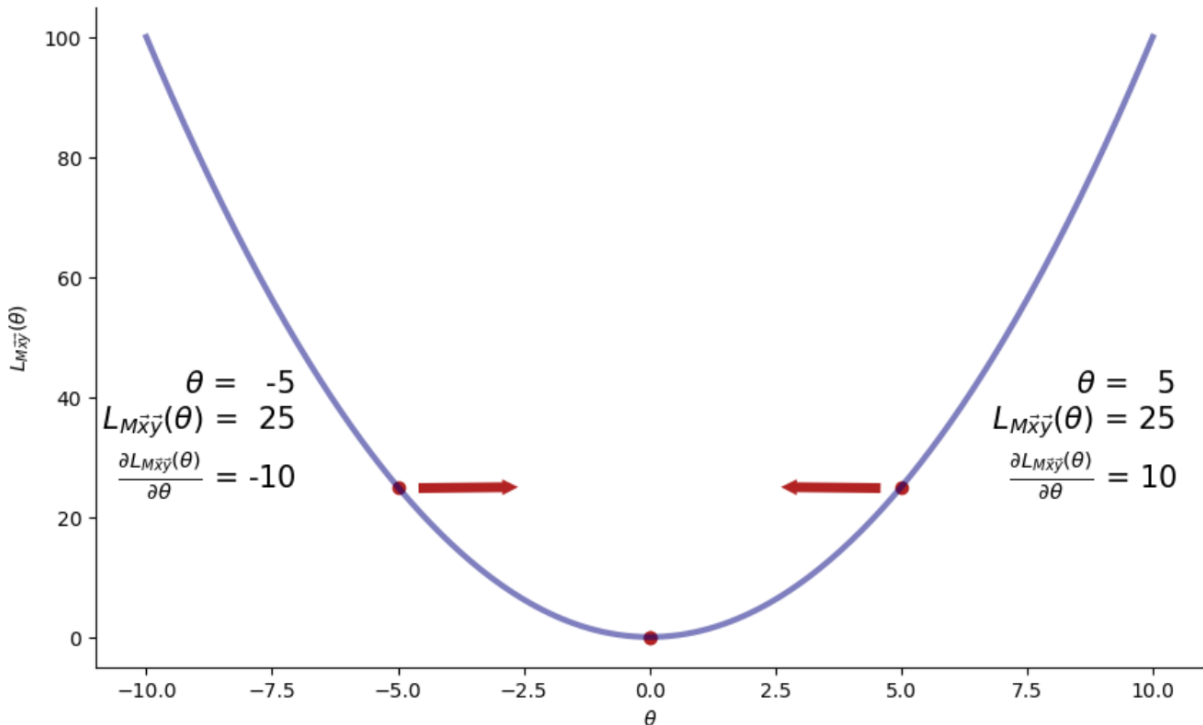


Figure 3.5 | An illustration of gradient descent, where $\vec{\nabla} L_{M\vec{x}\vec{y}}(\vec{\theta})$ is the loss at a fixed model architecture, M , input vector \vec{x} , and data label \vec{y} . This simplified example of the shape of a 1D parameter space shows how the gradient of the loss function with respect to the model parameters can be used to move toward the minimum of the loss function. The shape of the loss function in this example is given by $L_{M\vec{x}\vec{y}}(\vec{\theta}) = \theta^2$. In almost all cases, the parameter space will be much more complex than the one depicted in both dimensionality and shape complexity. Usually, the shape of the loss function will be an N-dimensional surface, where N is the number of parameters, $\vec{\theta}$, in the model, but the principle is still the same. For a 2D example of a gradient space; see Figure 3.12. This plot can be recreated with the code found here: <https://tinyurl.com/3ufb5my3>.

We need to be able to control the magnitude of the parameter adjustment because the gradient is only measured for the current parameter values, $\vec{\theta}$. Therefore we are unsure of the shape of the loss function. It's possible for the tuning process to overshoot the loss function minimum. In order to apply this control, we introduce a constant coefficient to scale the gradient, known as the learning rate, η [156,10].

Therefore, if we want to find the new adjusted parameters after one optimisation step, we can use

$$\vec{\theta}_{t+1} = \vec{\theta}_t - \eta \vec{\nabla} L_{M\vec{x}_t\vec{y}_t}(\vec{\theta}_t) \quad 3.5$$

where t is the step index, we can see this process in a Python [63] form in Listing 3.6. In this function, the gradients are captured using the `tf.GradientTape` scope, which automatically captures the gradients of all “watched” tensors within its scope. This automatic differentiation utilises a process called back-propagation [156,10], which will be discussed in more detail in Section 3.2.5.

```
# Step 5: Define the training step
@tf.function
def train_step(x, y, W, b, η):
    with tf.GradientTape() as tape:
        y_pred = model(x, W, b)
        current_loss = compute_loss(y, y_pred)
    gradients = tape.gradient(current_loss, [W, b])
    W.assign_sub(η * gradients[0]) # update weights
    b.assign_sub(η * gradients[1]) # update biases
    return current_loss
```

Listing 3.6 | Python [63]. Function to execute a single training step. This function runs an example, $x = \vec{x}_t$, through the model (usually multiple examples at once as explained in Section 3.2) and computes the loss, $\text{loss} = L_{M\vec{x}_t\vec{y}_t}(\vec{\theta}_t)$ of the output of that model, $y_{\text{pred}} = \hat{y}_t$ compared with the ground truth label of that example, $y = \vec{y}_t$. The gradients, $\text{gradients} = \vec{\nabla} L_{M\vec{x}_t\vec{y}_t}(\vec{\theta}_t)$, are automatically computed for each parameter by `tf.GradientTape()`, which produces a list of gradients for the weights, $w = W$, and biases, $b = \vec{b}$, which are then used multiplied by the learning rate $\eta = \eta$ and used to update the parameters, $\vec{\theta}$, for the next training step; see Equation 3.5.

If we repeat this process over T steps, where T is the number of training examples in our dataset, then the model will hopefully begin to gain aptitude at the classification task. The process of tuning the model parameters once with all examples in the training dataset is called a training epoch [145]. Oftentimes, if our training dataset is not large enough, we can improve the model performance by running for multiple epochs, hence training the model with the same examples multiple times. Between epochs, the training dataset is usually shuffled in order to explore new areas of parameter space and avoid repeating exactly the same pathway [145].

Pulling all the functions we have defined together; we can now implement our main training loop, Listing 3.7.

```
def train_model(epochs, batch_size, η, x_train, y_train):
    # Define model
    W, b = define_model()

    # Store loss and accuracy for each epoch
    loss_per_epoch = []
    accuracy_per_epoch = []

    # Training loop
    for epoch in range(epochs):
        i = 0
        while i < len(x_train):
```

```

        start = i
        end = i + batch_size
        x_batch = x_train[start:end]
        y_batch = y_train[start:end]
        current_loss = strategy.run(train_step, args=(x_batch, y_batch, W, b,
    ))
        i += batch_size

        # Compute loss and accuracy for each epoch
        y_pred = strategy.run(compute_model, args=(x_test, W, b))
        loss_per_epoch.append(current_loss)
        accuracy_per_epoch.append(compute_accuracy(y_test, y_pred))
        print(f'Epoch {epoch+1} completed')

    return loss_per_epoch, accuracy_per_epoch, W, b

```

Listing 3.7 | Python [63]. Function to execute multiple training steps across multiple epochs. This function runs the function defined in Listing 3.6 for each example in the `x_train`, and repeats this process for each requested epoch, `num_epochs`, updating the model parameters each time. It returns the model parameters, `W`, `b`, and some metrics measuring the model’s performance; see Equation 3.5.

3.1.3 Testing the Model

Once we have trained our model using the aforementioned procedure, we can evaluate its performance. Often the first step toward this is to look at the model’s performance at each step during training; see Figure 3.6.

The model training progresses quickly at first but soon reaches a point of diminishing returns at about 85 per cent accuracy. Although we may be able to squeeze out a little more performance by running the training for more epochs, this can lead to overfitting, where a model becomes tailored too specifically to its training dataset and cannot generalise well, or at all, to other points in the training distribution [145]. In most cases, we will want our model to classify new unseen data drawn from a similar distribution as the training dataset but not overlapping with any existing points, so we try to avoid this.

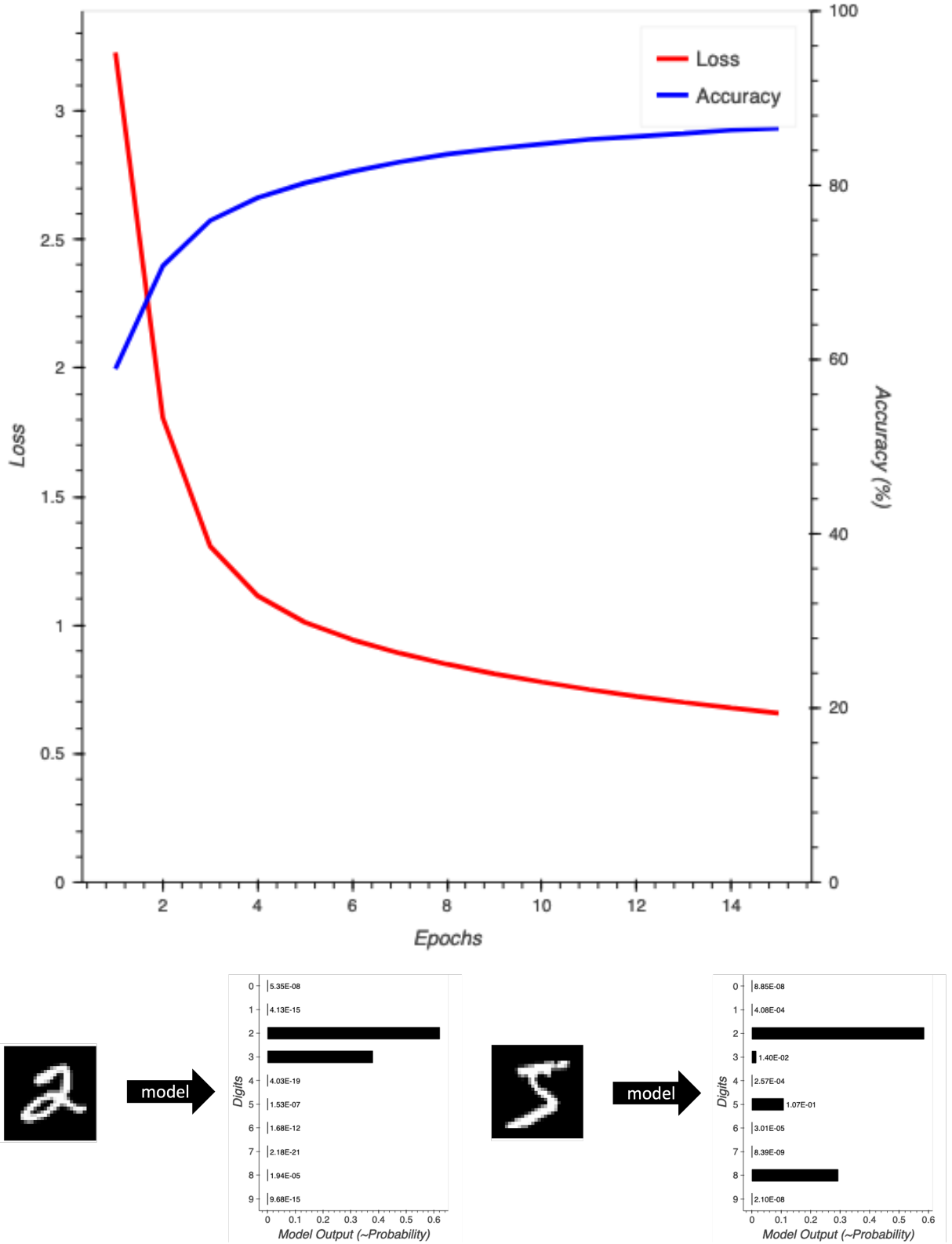


Figure 3.6 | Upper: The performance of the single layer perceptron model described in Section 3.1.2 over 15 epochs, where one epoch consists of training the model on all training examples in the MNIST dataset of handwritten Arabic numerals [12]. The model loss is defined as the categorical cross-entropy of the model's output vector, \vec{y} and the ground-truth label, \vec{y} , whereas the accuracy metric is defined as the number of examples in the test dataset that are correctly classified, where a correct classification is any output with 50 per cent or more probability in the correct class. **Lower:** Two examples of less

successful classifications. The left example would still be measured as a successful classification by our accuracy metric, whereas the right example would be marked as an unsuccessful classification.

We can also investigate what parameters the neurons have actually learned over this process; see Figure 3.7. It is often very difficult to come to much of a conclusion about the true inner workings of artificial neural networks, especially dense layers, which are the most general but also the most non-intuitive [157,10]. Network interpretability is a large and ongoing area of machine learning research for many obvious reasons. Being able to see why a model has given you the answer that it has can massively boost confidence in that answer [157,10]. However, this thesis will not focus heavily on interpretability, as that could be a whole other thesis on its own.

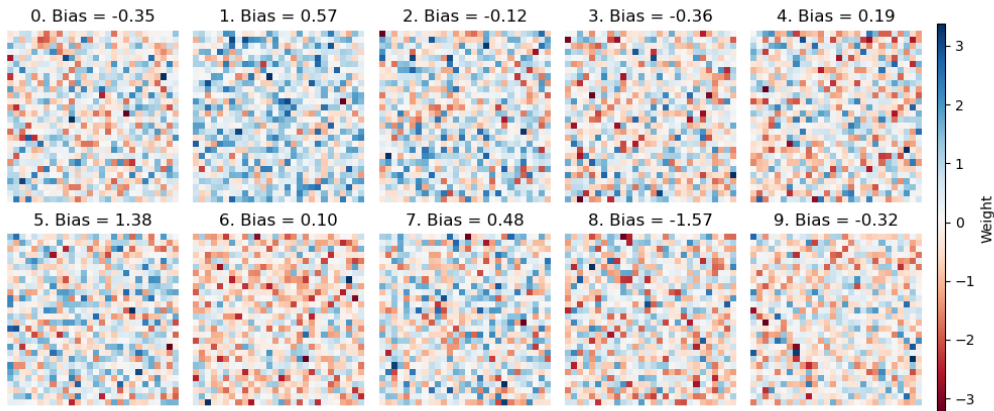


Figure 3.7 | Learned model parameters. Each artificial neuron in our single-layer perception is represented by a labelled parameter map shaped into the same dimensions as the input images. These maps show the learned weight values that correspond to each pixel of the input images. Very little structure can be made out by the human eye. Perhaps in the weight maps for the zero-classifier neuron, we can see an area toward the centre of the map that is negatively weighted. This might be expected as there are rarely high-value pixels at the centre of the circular zero. A similar but opposite effect might also be attributed to the one-classifier, where the centre of the image often contains high-value pixels. In general, unless you squint very hard, it is difficult to make out patterns in the parameters. This “black-box” effect means that after even one more layer is added to the network, it becomes very difficult to determine the action of dense layer neurons intuitively.

Whilst it is difficult to make specific claims on how artificial neural networks are doing what they are doing, we can often speculate on general methods of operation. In the case of the single-layer perceptron, like the one we have built here, the only kinds of operations that can be learned are linear ones. The only path each neuron has available to it is to learn which pixels are often highly valued in its class of digit and which pixels are very rarely highly valued in its class which are more likely to be highly valued in another class. Then it can adjust the bias value so that the neuron only activates when a certain criterion is met. If we were distinguishing between ones and zeros, for example, which have, in general, very different highlighted pixels, then this might be enough for a high degree of classification efficiency. However, there are a multitude of digits which can share many common pixel values, which makes this problem more difficult.

In order to solve the problem with more accuracy, we must add a non-linear element to the computation and the ability for the model neurons to work collaboratively on the problem [10,153]. This

allows the model to extract more complex “features” from the input vector. We, therefore, introduce the concept of multi-layered neural networks and deep learning.

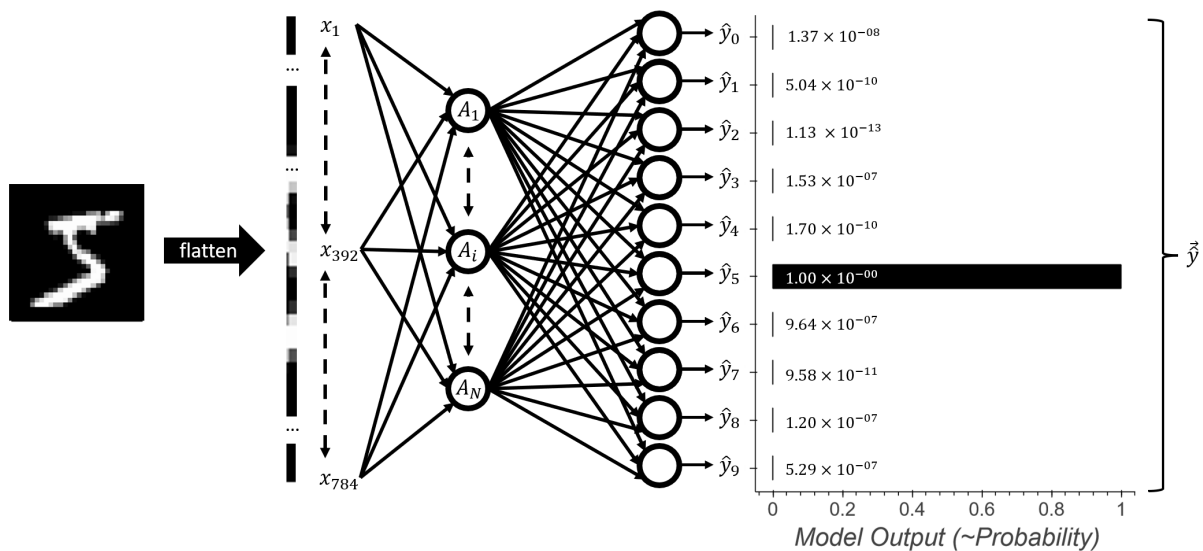
3.1.4 Neurons Together Strong

As we have seen, a single layer of artificial neurons can be trained to perform a small amount of computation, which is often enough for many simple problems. There are, however, a great many problems which require more complex solutions. In order to do this, we can add what is known as “hidden layers” to our network [10,145]. They are called hidden layers because the exact computation that is performed by these additional layers is much more difficult to divine than in output layers, layers that directly output solution vectors, as we have seen in our single-layer perceptron [145].

For simplicity of design, artificial neural networks are usually organised into layers of neurons, which are usually ordered, and interactions are usually limited to between adjacent layers in the network [145]. Layer one will usually only pass information to layer two, and layer two will receive information from layer one and pass information to layer three if there are three layers; see Figure 3.8. This is not always the case, and there are exceptions to all the rules mentioned in this paragraph, including skip connections [158,159], recurrent neural networks [160,10], and Boltzmann machines [161].

Artificial neural network layers come in many varieties, the most simple of which are feed-forward dense (or sometimes linear) layers [10]. Dense layers consist of N neurons, where every neuron takes as an input vector the output of every neuron on the previous layer unless the dense layer is acting as the input layer, in which case every neuron takes in as input every element of the input vector [145]. If the dense layer is acting as the output layer, as was the case for our single-layer perceptron where one layer was both the input and output layer, then N must equal the required size of our output vector, \vec{y} . In the case of a classification problem, this is equal to the number of classes, C . In hidden layers, the number of neurons, N , can be any number and is, therefore, a customisable non-trainable parameter known as a hyper-parameter that must be chosen before network training by some other method; see Section 5.1.

As can be imagined, finding the gradient for networks with one or more hidden layers is a more complex problem than for a single layer. Backpropagation allows us to do this [145,10,156] and, in fact, is the tool that unlocked the true power of artificial neural networks; see Section 3.2.5.



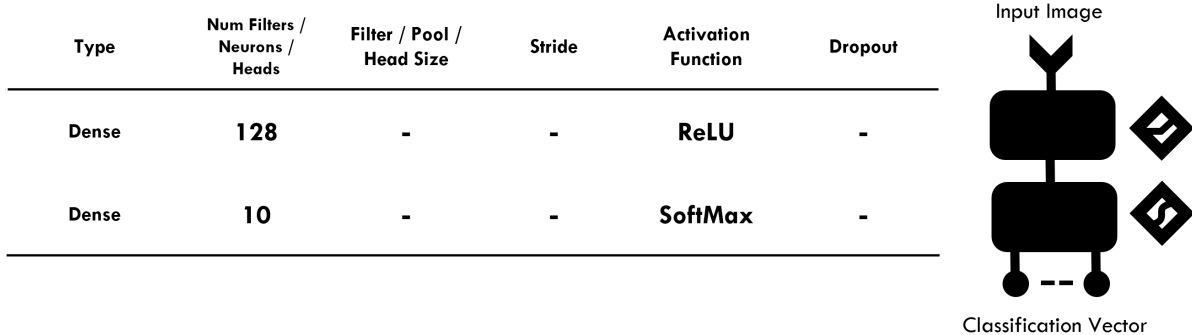


Figure 3.8 | Upper: Diagram of a multi-layer network with one output layer and one hidden layer. The non-linear computation introduced by the ReLU activation function applied to the hidden layer allows this network to solve considerably more complex problems than the previously described single-layer perceptron model. *See Section 3.1.5.3*. As can be seen, by the displayed output, which again is taken from a real instance of a trained model, this network has no problem classifying the previously difficult image of a five. **Lower:** An abstraction of the same model.

This model performs considerably better than the previous model; see Figure 3.8; and seems to be complex enough to more or less solve the problem; see Figure 3.9. We might, in fact, even try reducing the number of neurons in the hidden layer. It is often beneficial to find the simplest possible network, by the number of parameters, that is able to achieve the desired computation, as more complex networks are more computationally expensive and time-consuming to train, require more training data, have an increased inference time (inference meaning to run the model on new unseen data), and crucially are more prone to overfitting to the training dataset [10]. This model reaches a high accuracy within just a few epochs, and unless we are very concerned about false alarm rates, then there is no need to add extra complexity to our model. The notebook used to train this model can be found here: <https://tinyurl.com/yrbwuw4e>.

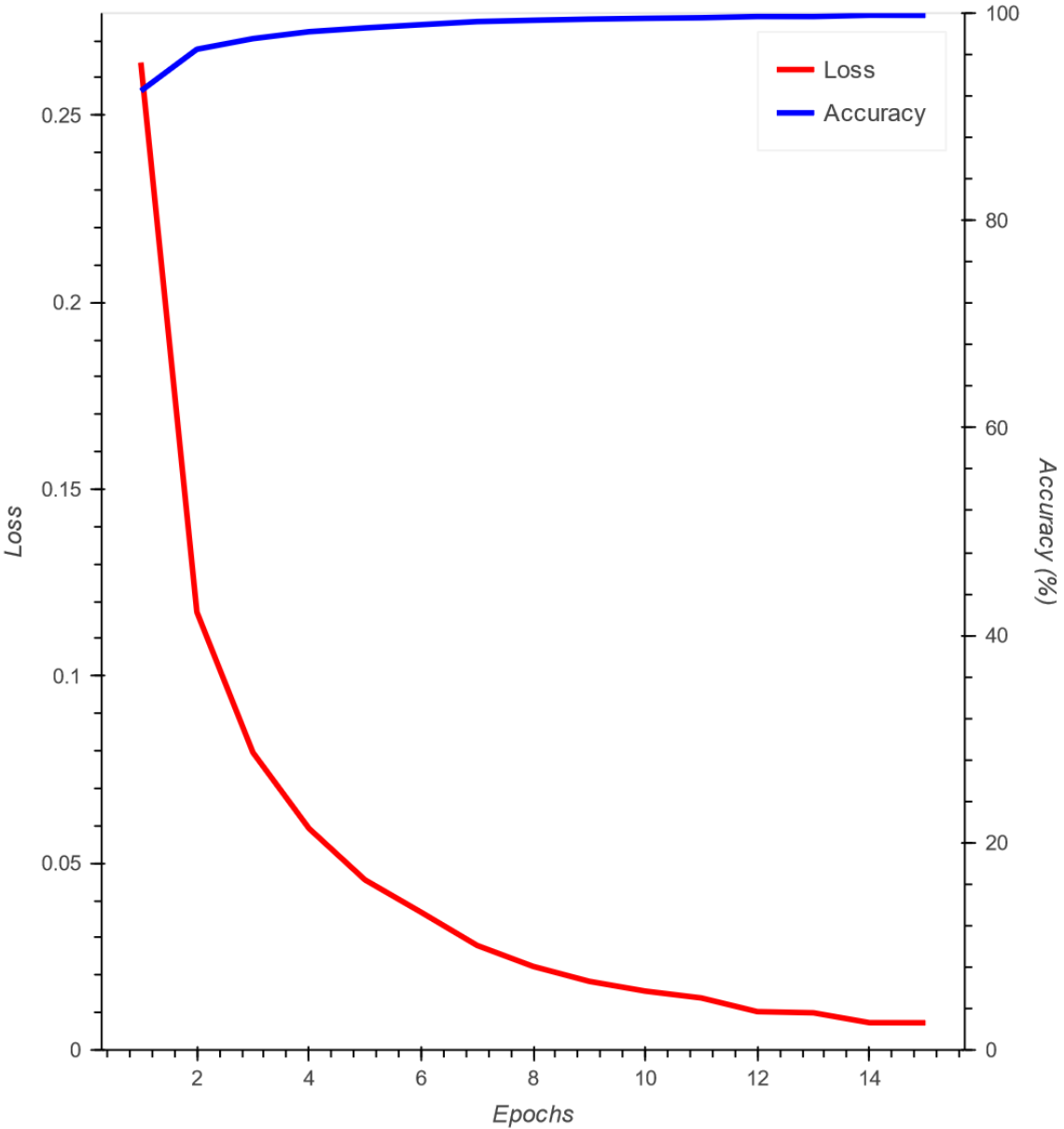


Figure 3.9 | The performance of the multi-layer perceptron model described in Section 3.1.4 over 15 epochs. As can be seen in comparison to Figure 3.6, the training is both faster and with a better final result.

The addition of hidden layers to our network architectures introduces the possibility of all kinds of structural variations. For more complex problems than the recognition of simple handwritten digits, we have many tools in our arsenal to increase performance. The first thing you might do is try the addition of more than one hidden layer; in fact, there is no inherent theoretical limit to the number of hidden layers that can be added to a network. Of course, at some point, you would run into computational limits, and although the gradient can be calculated, there are problems when attempting to run gradient descent algorithms on very deep networks that are designed without careful consideration. Gradients that vanish over many layers can lead network training to become an almost impossible task [162,10].

These problems with increasing complexity lead researchers to explore types of layers beyond the dense layer. Although the dense layer alone can be thought of as a universal function approximator, there exists no perfect training algorithm to find the ideal set of parameters to achieve every possible

function, and this statement is technically only true for all possible arbitrarily complex functions as the number of layers approaches infinity. For this reason, different layer designs and network architectures can create easier environments for training [10], saving computational resources and allowing feasible routes to massively increase network ability. Most often, these non-dense layers are designed with some insight into the structure of the input vectors. An example of this would be the convolutional neural network, see Section 4.4, which uses the spatial information of the input, as well as the notion that there will be transform-invariant features within the image, to create layers that can perform a similar or better job than dense layers with far fewer parameters [162].

One could also experiment by moving away from the paradigm of feed-forward networks, although this can increase solution complexity significantly. Within feed-forward neural networks, neuron connections only ever move toward neurons that have not yet causally influenced the emitting neurons. Within recurrent networks, however, signal paths can loop, taking either previous inferences as inputs or looping within the calculation itself [163,10]. This can allow the network memory of previous inferences, something feed-forward networks do not possess.

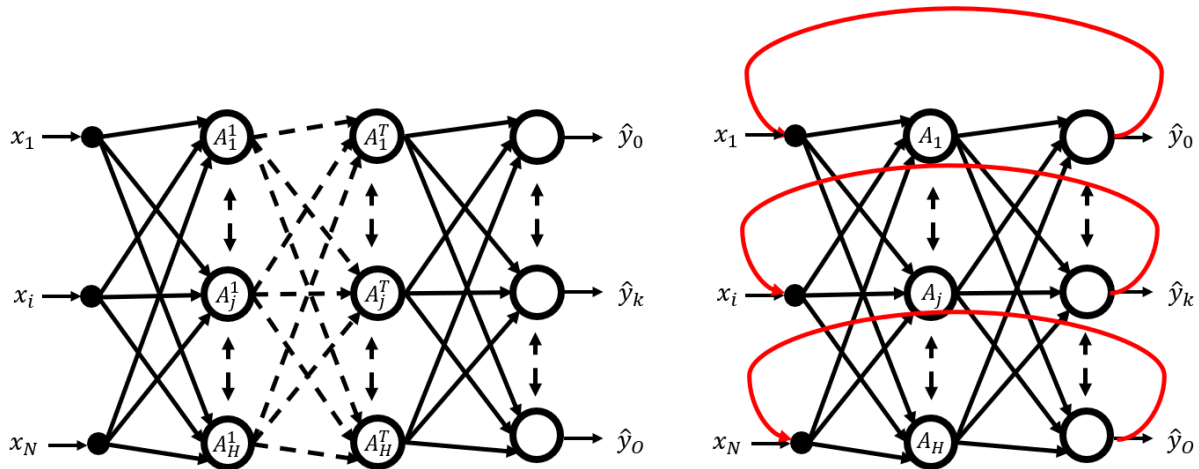


Figure 3.10 | Left: The generalised dense feed-forward artificial neural network. Where T is the number of hidden layers in your network, H is the number of neurons at that layer, N , is the number of elements in the input vector, \vec{x} , and O is the number of elements in the output vector $\vec{\hat{y}}$. As can be seen in the diagram, the number of hidden layers in your network is unconstrained, as is the number of neurons in each of those layers, which should be noted does not have to be the same. This is opposed to the output layer, which must have the same number of neurons as is expected by your loss function. **Right** A very simple illustration of a recurrent neural network. This network illustrates the retroactive data flow that is possible in a recurrent neural network. In this example, the output of the network from one inference operation is added to the input of the next inference operation. It should be noted that this is a very naive implementation of a recurrent neural network. In actuality, the networks usually have a much more complex structure, such as LSTMs (Long Short Term Memory) networks.

There will be a more detailed discussion of many of these different network layers and architectures further on in the thesis; the following few sections will explore the concepts outlined in the last two sections in more detail.

3.1.5 Activation Functions

There are many different activation functions; as with most things in machine learning, they are an active area of research [10,153]. As such, this small section will only give a brief introduction plus a few examples. Since the activation function normally acts on the weighted sum of the inputs plus the

bias, in this section, we will define $z = \sum \vec{x} \cdot W + \vec{b}$ to avoid confusion with the raw input values previously denoted x . It should be considered that z could also be other values in some cases. We will define the vector of all z values in a single network layer of N neurons, i.e. $\vec{z} = [z_1, \dots, z_N]$.

As noted in Section 3.1.1, the activation function aims to coerce an artificial neuron's output into a particular shape [10,153,145]. This has several purposes. Firstly, it can act as a thresholding function, which along with a specific value of bias, b , can activate or deactivate the neuron depending on the weighted sum of the input vector, z . The activation function also limits the output values to a specific range, ensuring that values within the network do not grow without bounds along favoured pathways and destabilise the network. These values can be considered in some way analogous to the maximum firing rate of a biological neuron. Without activation functions, instability can cause values to explode to infinity or vanish to zero. Finally, activation functions provide a non-linear component to the neuron. Without non-linear activation functions, neuron output, hence network outputs, could only be linear combinations of the input values and so would need to be, in general, much more complex to solve non-trivial problems.

There are some limits to the type of function we can use within a neural network, primarily since we must be able to flow gradients through the function during backpropagation; the function must be differentiable at all points [153]. For example, if we tried to use a step function as an activation function, the derivative would be 0 at all points, except for at the step where it would be undefined. This would make backpropagating through this function very difficult, as it would fail to update the weights and bias of its corresponding neuron. In other non-continuously differentiable functions, like the ReLU function, we can use a trick to avoid the undefined derivative by defining the value of the derivative at that point, $z = 0$ in this case, to 0 or 1.

As well as the distinction between linear and non-linear activation functions, a few further distinctions can be made. Outside of the linear function, we can split activation functions into three types: ridge [164], radial basis [121], and fold [13].

Ridge functions are standard activation functions that change an input's shape based on directionality around a specific point or ridge [164]. The most common example is the ReLU function [165,153] and its variants described below. Ridge functions are computationally efficient and introduce non-linearity without requiring exponentiation or other computationally expensive operations.

Radial basis functions [121,166], on the other hand, are less commonly used. They are symmetric around a specific point rather than just directional. Their value, therefore, depends entirely on the magnitude of the distance to this point rather than in ridge functions where the sign is also vital. Radial basis functions can create complex surfaces which can localise to a specific region, which can be helpful if you believe your data structure to be localised in such a manner. A typical example of a radial basis function would be the Gaussian function, which can localise a neuron's activation to a particular region. However, they can be computationally expensive and lead to overfitting due to their ability to form complex surfaces.

Fold functions are complex activation functions that aggregate over multiple neuron z values, such as mean or max functions in pooling layers, or even over the entirety of \vec{z} , such as in softmax layers described below [13]. Calculating these can be computationally expensive, so they are used in moderation.

3.1.5.1 Linear

The most straightforward activation function is the linear activation, represented simply by Equation 3.6 below. The linear activation function will not change the shape of the data and is crucial for many applications where this is a desired feature:

$$\text{linear}(z) = kz. \quad 3.6$$

Evidently, in the case where $k = 1$, this is equivalent to not applying any activation function and thus, all the previously stated problems resulting from no activation function will apply. The derivative of the linear activation function is always a constant irrespective of the input values, so it is straightforward to compute. This simplicity brings a significant drawback when dealing with complex data. If it is the only activation function used, the entire network, regardless of complexity or number of layers, will behave as a single-layer model because of the lack of non-linearity between layers. As we have seen, single-layer perceptrons are insufficient for many tasks we wish to tackle with artificial neural networks.

One of the primary uses of linear activation functions is as the output layer of regression problems, where the output is expected to be a continuous float value not constrained within a particular distribution [10]. The drawbacks are alleviated if the rest of the network before the output layer involves non-linear activation, leaving the output layer to combine inputs into a final output value linearly. They can also sometimes be used in straightforward networks where non-linearity is not required and computational efficiency is highly prized. Therefore, while the linear activation function has its uses, it is not commonly applied in hidden layers of deep learning models, wherein non-linear layers, such as ReLU and its variants, are more valuable; see Figure 3.11 for a graphical depiction.

3.1.5.2 Logistic

The logistic activation function [167] is a ridge function defined

$$f(z) = \frac{L}{1 + e^{-k(z-z_0)}}, \quad 3.7$$

where $z_{\{0\}}$ represents the z-coordinate of the function's midpoint, L signifies the maximum value that the function can reach, often referred to as the function's supremum and k is a parameter that controls the steepness of the function's curve, determining the logistic growth rate. The particular case where $L = 1$, $k = 1$, and $x_0 = 0$ is known as the sigmoid function

$$\sigma(z) = \frac{1}{1 + e^{-kz}}. \quad 3.8$$

See Figure 3.11 for a graphical depiction.

Since this smoothly limits the output of the neuron to between 0 and 1, it is often used on output neurons in a network designed for classification since, in this case, the ground truth vector would consist of entirely Boolean values, meaning an activation function that tends to 0 and 1 in the extreme is very useful [167]. The sigmoid activation function is used in multi-class, multi-label classification problems, where each class variable is independent, and an example can be in multiple classes and single-class single-label problems, where there is only one output neuron. Since each output is calculated independently, it is unsuitable for cases where an example can be in only one class and there are multiple classes; in that case, a Softmax layer, as described in Section 3.1.5.4, is more appropriate.

The sigmoid function's derivative is at maximum at the midpoint $z = 0$ and falls off as z moves in either direction $z \rightarrow \infty \vee z \rightarrow -\infty$; this is a suitable environment for backpropagation as the derivative is always defined and never 0. There are, however, some limitations since the gradient, although never quite 0, can become very small, leading to the “vanishing gradients” problem wherein the model's parameter updates can become negligible, and hence learning is very slow. Secondly, the sigmoid function is not centred at 0. This can lead to zig-zagging during gradient descent, also slowing down convergence. Finally, the sigmoid function involves the computation of exponentials, which can be computationally expensive, especially for large-scale networks.

Despite these limitations, the sigmoid function is widely used, particularly in the output layer, for multi-class, multi-label classification problems. However, for hidden layers, modern practices prefer other functions like ReLU or its variants to mitigate some of the issues related to the sigmoid function.

3.1.5.3 ReLU (Rectified Linear Unit)

One of the most common activation functions used very widely in neural network hidden layers is the ReLU (Rectified Linear Unit) function [167,153], defined by

$$\text{ReLU}(z) = \begin{cases} z & \text{if } z > 0 \\ 0 & \text{if } z \leq 0 \end{cases} \quad 3.9$$

ReLU is another example of a ridge function. This function is 0 for $z \leq 0$, and z for $z > 0$, meaning it is equivalent to the linear function above 0. It is a very simple function but still provides the neuron with the ability to threshold values and adds a non-linear component to the neuron.

Because of its simplicity, ReLU is very computationally efficient compared to other activation functions that require expensive operations such as exponentiation or division, an essential factor when deciding on activation functions to use, especially in very large networks [150]. The derivative is also very simple, either 1 above z or 0 below z ; hence it lacks the possibility of becoming very small. This means that the use of ReLU functions can be efficient for training. Having a large section of the domain with a derivative of 0 does, however, also lead to problems. During the training process, some neurons can “die”, only able to emit 0s, and since the gradient is also 0, they can become stuck in this state, unable to reactivate [168]. Evidently, this can reduce the capacity of the network for practical computation since these dead neurons can no longer contribute valuable operations.

To ameliorate some of the downsides, there are a plethora of possible ReLU variants, most of which have a non-zero gradient below $z = 0$. These include but are not limited to Leaky ReLU (LReLU) [169], Randomized Leaky ReLU (RReLU) [170], Parametric ReLU (PReLU) [171], Exponential Linear Unit (ELU) [171], and Scaled Exponential Linear Unit (SELU) [171]. The first three variants, LReLU, RReLU, and PReLU, are defined by

$$\text{LeakyReLU}(z) = \begin{cases} z & \text{if } z > 0 \\ \alpha z & \text{if } z \leq 0 \end{cases} \quad 3.10$$

where α depends on the variant in question; in standard LeakyReLU, α is a small, predefined value such as 0.05, meaning the slope is much shallower before 0 than after it; this prevents dying neurons whilst still allowing the function to threshold the input value. In the case of Randomised Leaky ReLU, α is randomly sampled from a specified distribution during training but fixed during model inference [170]. This solves the dying neuron problem and adds robustness to the training process. Finally, in Parametric ReLU, α is treated as a trainable parameter that the model can adjust during backpropagation, allowing it to hopefully self-optimise to a good value [171].

ELU and SELU are also both based on a similar definition

$$\text{SELU}(z) = \begin{cases} sz & \text{if } z > 0 \\ s\alpha(\exp(z) - 1) & \text{if } z \leq 0 \end{cases} \quad 3.11$$

For any α value if $s = 1$, the equation defines ELU. ELU has all the death-defying properties of the previously mentioned ReLU variants whilst also introducing differentiability at $z = 0$, meaning that the redefinition trick is not required. Unlike other ReLU variants, it saturates as $z \rightarrow \inf$, increasing robustness to errors. These extra benefits come at the cost of the computational simplicity of the previous ReLU variants, as the calculation of exponentials is a significant computational expense.

If $\alpha = 1.673263\dots \wedge s = 1.05070\dots$, the equation defines SELU, a self-normalising activation function. These very specific values of α and s are designed to work in conjunction with LeCun initialization, a method that initializes neuron parameters with values drawn from distributions with mean zero and variance $\frac{1}{N}$, where N is the number of neurons in that layer. These values of α and s massage the neurons toward outputs with a distribution centred on zero and with a variance of one. Which can help smooth the training process by avoiding vanishing or exploding gradients.

In practice, ReLU and its variants are the most commonly used activation functions in the hidden layers of deep neural networks due to their efficiency and performance. See Figure 3.11 for a graphical depiction.

3.1.5.4 Softmax

Softmax is a more complicated fold distribution and is of interest due to its use in multi-class, single-label classification problems [121,13]. It is an extension of the Sigmoid function described above in Section 3.1.5.2, which aims to convert a vector of continuous unconstrained output values, in our case \vec{z} , into a vector representing probabilities, with outputs limited between 0 and 1 and a vector sum equal to exactly 1. It does this by finding the exponential of each z value, then normalising by the sum of the exponential of all elements in \vec{z}

$$\text{softmax}(\vec{z})_i = \frac{e^{z_i}}{\sum_{j=1}^N e^{z_j}}, \quad 3.12$$

where N is the number of elements in \vec{z} , equivalent to the number of neurons in the layer and the number of classes in the dataset, and i is the index of the neuron/class whose output value is calculated. See Figure 3.11 for a graphical depiction.

The softmax function represents a way of mapping the non-normalized output of the network to a probability distribution over predicted output classes, making it invaluable for multi-class, single-label classification problems. It is also differentiable so that it can be used in gradient-decent methods.

Softmax can be computationally expensive, particularly in the case of a large number of classes, as each output classification requires the use of multiple expensive operations such as exponentiation and division; it can also suffer from numerical instability when the scores in the input vector are very large or small which may result in numerical overflow or underflow problems. This is not typically too much of an issue as it is usually only used in the output layer of a network.

The Softmax function remains the standard choice for multi-class classification problems due to its ability to provide a probabilistic interpretation of the outputs, handle multiple classes, and its differentiability.

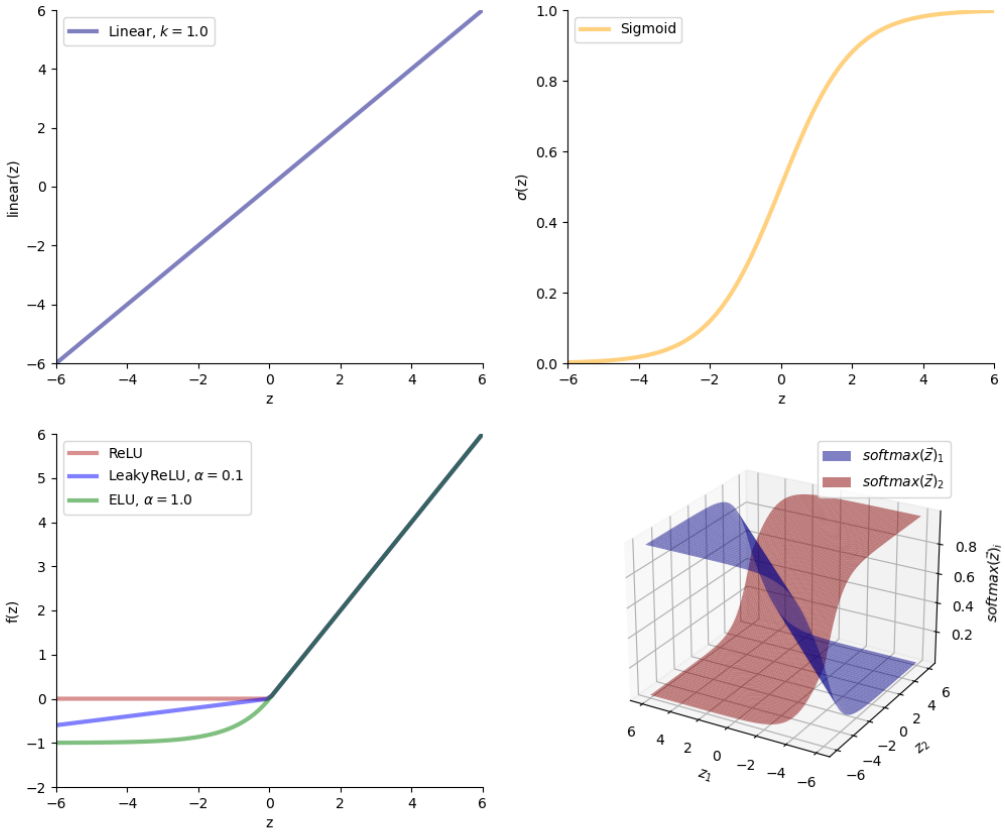


Figure 3.11 | Four of the most common activation functions. *Upper Left:* A linear activation function. In this case, the slope, k , is 1, meaning that the shape of the output is unchanged vs the input. *Upper Right:* Sigmoid activation function, a special case of the logistic activation function, which limits the output value between 0 and 1. *Lower Left:* ReLU (Rectified Linear Unit) activation function and its variants, an easy way to provide non-linearity to multi-layer networks. *Lower Right:* SoftMax activation function. In the case of multi-neuron outputs, when using softmax, the output of each neuron depends on the value of each other neuron. For this reason, the simplest non-trivial case, where the length of the output vector, N , is 2, has been chosen, and the outputs are represented on a 3D plot. This figure can be recreated with the notebook found at: <https://tinyurl.com/muppechr>.

3.1.6 Loss Functions

The loss function (sometimes cost or objective function) is an important part of the model training process [10]. The purpose of the loss function is to act as a measure of the effectiveness of the model when acting on a particular batch of examples. In doing this, the loss function gives us a metric to evaluate the performance of the model, compare it against other models, and act as a guide during the training process. In specific cases, it can also act to regularise the model to prevent overfitting or to balance multiple objectives.

In supervised learning, this loss function is some measure of the distance between the model's output and the ground truth labels of the examples fed into the model. These are one of the more common types of loss functions, but it should be noted that as long as it is differentiable, a great many terms

can be included as part of the loss function, and indeed some of the more complex architectures have complex loss functions.

In unsupervised learning, Autoencoders [122] are a formulation of a regression problem where the model input is equal to the model output, and thus, they follow the same principles as the typical regression problem, only the difference between their output, $\vec{\hat{y}}$, and their input, \vec{x} in the loss, rather than an external label, \vec{y} . Clustering, on the other hand, attempts to split a data distribution into groups by minimising the distance between elements in a given group while maintaining some balance with the number of groups generated – there are a variety of different ways to do this depending on your desired outcome.

3.1.6.1 Binary Cross Entropy

The Binary Cross Entropy loss is used primarily for binary classification problems wherein each class label is independent [172]. This can be the case either for single-class single-label tasks (binary classification tasks) or multi-class multi-label tasks. It is defined by Equation 3.13.

$$L(\vec{y}, \vec{\hat{y}}) = - \sum_{i=1}^N y_i \log(\hat{y}_i) - (1 - y_i) \log(1 - \hat{y}_i) \quad 3.13$$

where $L(\vec{y}, \vec{\hat{y}})$ is the loss function applied to the model output and ground truth vectors, N , is the number of elements in the output vector, y_i is the i^{th} element of the ground truth vector, and \hat{y}_i is the i^{th} element of the ground truth vector.

In the single-class single-label case where $N = 1$, Equation 3.13 becomes

$$L(y, \hat{y}) = -y \log(\hat{y}) - (1 - y) \log(1 - \hat{y}). \quad 3.14$$

Some confusion can arise in the case of binary classification problems [172], wherein the examples can either be in a class or not in that class since this is the same as the situation where there are two distinct classes. As such, these problems can be treated in two ways, either with a single output neuron and an output vector, \vec{y} of length one, (an output value i.e. $\vec{y} = y$), where a high value indicates inclusion in the one class and a low-value exclusion, or with two output neurons where each neuron represents a “class”, one being inside the class and the other being outside the class.

In the first case, we would use a sigmoid activation function and a binary cross-entropy loss, and in the second case, you would use a softmax activation function and categorical cross-entropy loss. These produce very similar outcomes, with the first method being slightly more straightforward, giving a directly interpretable output and reducing the number of parameters, whereas the second case, whilst increasing the model parameter count, can sometimes be more numerically stable.

3.1.6.2 Categorical Cross Entropy

Categorical Cross Entropy loss is very similar to binary cross-entropy loss but is used primarily in multi-class single-label problems, such as the problem we presented in the MNIST [12] classification task [10]. It is a highly effective loss function, and it is often much easier to classify data into one class using this method than it would be to find multiple labels in a multi-class multi-label problem. So this kind of task is often a desirable framing of your problem. The loss is given by

$$L(\vec{y}, \vec{\hat{y}}) = - \sum_{i=1}^N y_i \log(\hat{y}_i), \quad 3.15$$

where $L(\vec{y}, \vec{\hat{y}})$ is the loss function applied to the model output and ground truth vectors, N is the number of elements in the output vector, y_i is the i^{th} element of the ground truth vector, and \hat{y}_i is the i^{th} element of the ground truth vector.

Both binary cross entropy and categorical cross entropy are loss functions that attempt to measure the difference between probability distributions. In the case of binary cross-entropy, it treats each output element as a separate probability distribution, whereas for categorical cross-entropy, the entire output vector is treated as one probability distribution.

They are derived from the concept of entropy in information theory, which quantifies the expected amount of information from a source. Lower information states will have numbers that are closer to one or zero — in that way minimising the function forces the output to values of one or zero, i.e., toward definite yes/no classifications.

3.1.6.3 Mean Square Error

For regression tasks, wherein the output vectors are not limited to boolean values, we must have more flexible activation and loss functions [173]. In these cases, we still want to compare our desired output to our actual output, but we don't want to encourage the output to values near zero and one. There are a number of options to achieve this goal, the choice of which will depend on the specifics of your problem.

One option is mean square error loss, the sum of the squares of the error, $\vec{y} - \hat{\vec{y}}$, normalised by the number of elements in the output vector [173]. It is defined by

$$L_{\text{MSE}}(\vec{y}, \hat{\vec{y}}) = \frac{1}{N} \sum_{i=1}^N (y_i - \hat{y}_i)^2, \quad 3.16$$

where $L_{\text{MSE}}(\vec{y}, \hat{\vec{y}})$ is the loss function applied to the model output and ground truth vectors, N is the number of elements in the output vector, y_i is the i^{th} element of the ground truth vector, and \hat{y}_i is the i^{th} element of the ground truth vector.

Mean square error is a good choice for regression problems; it is fully differentiable, unlike mean absolute error; however, unlike mean absolute error, it heavily emphasises outliers which can be beneficial or detrimental depending on your scenario.

3.1.6.4 Mean Absolute Error

The mean absolute error can be used in the same problems that the mean square error is used for [173]. Again it is normalised by the total sum of the output vector. It is given by

$$L_{\text{MAE}}(\vec{y}, \hat{\vec{y}}) = \frac{1}{N} \sum_{i=1}^N |y_i - \hat{y}_i|, \quad 3.17$$

where $L_{\text{MAE}}(\vec{y}, \hat{\vec{y}})$ is the loss function applied to the model output and ground truth vectors, N is the number of elements in the output vector, y_i is the i^{th} element of the ground truth vector, and \hat{y}_i is the i^{th} element of the ground truth vector.

Unlike mean squared error, it has a non-differentiable point at zero where the gradient must be artificially replaced, which is not a particularly elegant solution. Mean absolute error punishes small errors more than mean squared error, but large errors less, which can be a desired trait in a model training procedure.

3.1.6.5 Huber

Huber loss is an attempt to combine the benefits of both mean square error and mean absolute error and remove some of their respective disadvantages [174]. It uses a combination of both methods to achieve differentiability at all points whilst removing mean squared error's large penalty to outliers. It does, however, introduce a new user-tuned hyperparameter δ , which, as has been discussed, is never ideal. It is defined by

$$L_\delta(\vec{y}, \vec{\hat{y}}) = \frac{1}{N} \sum_{i=1}^N \begin{cases} 0.5(y_i - \hat{y}_i)^2 & \text{if } |y_i - \hat{y}_i| \leq \delta \\ \delta |y_i - \hat{y}_i| - 0.5\delta^2 & \text{if } |y_i - \hat{y}_i| > \delta \end{cases}, \quad 3.18$$

where $L_\delta(\vec{y}, \vec{\hat{y}})$ is the loss function applied to the model output and ground truth vectors, N is the number of elements in the output vector, δ is a user-tuned hyperparameter which controls how much of the loss function obeys mean squared error and how much obeys mean absolute error, y_i is the i^{th} element of the ground truth vector, and \hat{y}_i is the i^{th} element of the ground truth vector.

The choice of loss function for regression problems is very much problem-dependent and discoverable only through intuition about the dataset or failing that through investigation.

3.1.7 Network Design

The choice of loss function is largely down to the problem being attempted and, as such, is often correlated with an associated output layer activation function; see Table 3.1.

Problem	Example Label	Activation Function	Loss Function
Single-class Single-label Classification	[1] or [0, 1]	Sigmoid or Softmax	Binary or Categorical Cross Entropy
Multi-class Single-label Classification	[0, 1, 0, 0]	Softmax	Categorical Cross Entropy
Multi-class Multi-label Classification	[0, 1, 0, 1]	Sigmoid	Binary Cross Entropy
Regression including Autoencoders	[0.12, -1.34]	Often ReLU or Linear	Often MSE, MAE, or Huber

Table 3.1 | Problems often solvable by artificial neural networks and their associated activation and loss functions. This table demonstrates the most commonly used activation and loss functions for several common problem types that machine learning attempts to solve. The activation functions listed are described in Section 3.1.5, whereas the loss functions were described in this section Section 3.1.6. MSE is an abbreviation of Mean Squared Error, and MAE is an abbreviation of Mean Absolute Error.

3.2 The Gradients Must Flow

Without a method to find useful parameters, artificial neural networks are useful for little more than hopelessly scrambling input data. As mentioned previously, this method is gradient descent [10,175], using the local gradient of model parameters to find a path toward the minimum loss.

It is useful to imagine the entirety of all possible model parameters forming a surface defined by the model's loss function. Every combination of parameters is a coordinate on this highly dimensional landscape, where the corresponding loss function tells us the height of the land. We can abstract away all this high dimensionality and reduce the problem to a two-dimensional mountain range, as long as we keep in mind that, in actuality, the number of dimensions of our surface equals the number of parameters we are fitting to.

Imagine we are lost in these Parameter Peaks. Our goal is to find the lowest point in this mountain range, for that will be the location of our helicopter rescue. In the same way that we can only calculate the gradient for one set of parameters at a time, we can only see the ground right beneath our feet; it is a very foggy day on the peaks. If we were to try to get to the lowest point, naturally, what we would do is look at the ground, examine the slope, and walk downhill; the same is true for gradient descent.

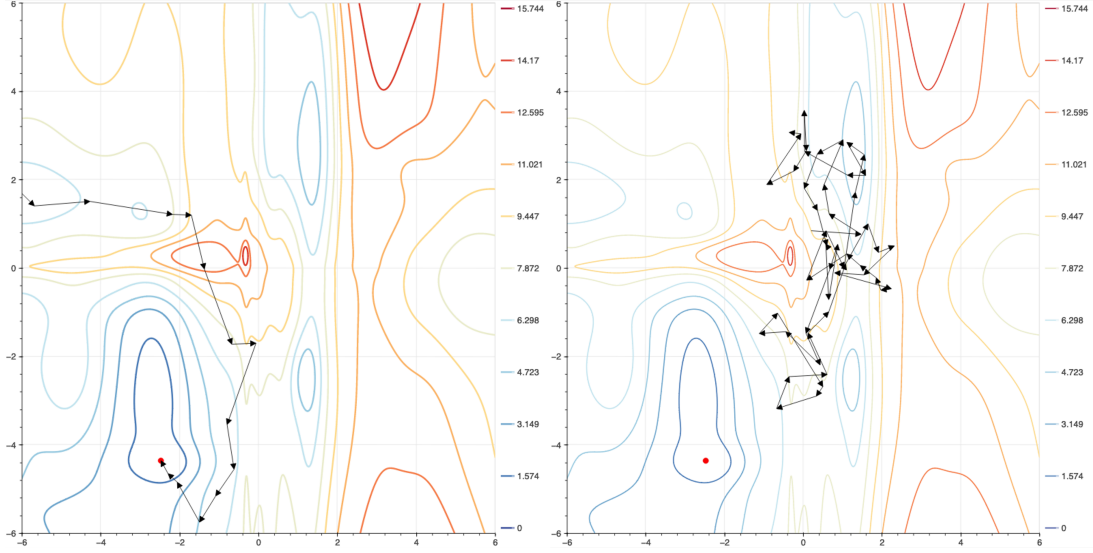


Figure 3.12 | Left: An idealised gradient descent path. This gradient descent process quickly reaches the true function minimum where, in this case, the loss is close to zero. However, this is a constructed example by first finding a point near the function minimum and performing a gradient ascent operation. **Right:** A more realistic gradient descent path. This example shows a simple but real gradient descent function running on the cost function. As can be seen, it takes many more steps and has not yet converged on the true minimum; in fact, the process might be at risk of getting stuck in a local minimum. Both examples were generated using this notebook: <https://tinyurl.com/3ufb5my3>.

This works perfectly if all gradients point toward the bottom, what is called a convex parameter space with one global minimum and no local minima. Parameter peaks, however, can often have some nasty tricks in store. Just like real-life mountain ranges, there can be local minima. Divits and valleys look like they might be the bottom of the mountain, but without some global information, it is impossible to tell. The parameter space is non-convex. Thus, we must explore before we settle on our final choice, moving up and down smaller hills, generally moving toward lower regions, but always searching for better outcomes — that is, until our time runs out, model training ends, and we must make a final decision about where to await the helicopter. Although perhaps if our training lasts multiple epochs, we'll have multiple days to figure it out, taking new paths each time.

There are, perhaps unsurprisingly, a number of different algorithms to achieve this purpose beyond the naive descent suggested by Equation 3.5, which could leave you stuck blindly in a divot on the top of a mountain whilst wide chasms stretch unseen before you. The first misconception to correct beyond what has been previously discussed is that usually when performing gradient descent, it is not performed one example at a time but rather in batches of N_{batch} examples, the gradient of which is calculated simultaneously. This N_{batch} adds a further user-adjustable hyperparameter, batch size, N_{batch} , to our growing collection of hyperparameters. It also creates a distinction between three distinct gradient descent modes.

Stochastic gradient descent is the method that was illustrated in Section 3.1.2. This involves updating the model parameters based on the gradient of a single example at a time, looping through every example in the dataset one at a time, $N_{\text{batch}} = 1$ [175].

Stochastic gradient descent can converge faster than other methods as it updates the parameters as frequently as possible. This is more useful with larger datasets that cannot fit into memory, as it can make progress long before it has seen all the data, and ample data will help it converge on a correct solution. Stochastic gradient descent does introduce a lot of noise into the dataset as the smoothing effects from averaging across examples are not present. This has advantages and disadvantages. The noise can help prevent the descent from getting stuck in the local minima, but by the same process, it can struggle to settle in even the true minimum, and convergence can take a long time. It can also be slow, as gradients need to be calculated for each example sequentially.

Mini-batch descent is perhaps the most commonly used of the gradient descent paradigms [176]. In contrast to stochastic gradient descent, the gradient is calculated for multiple examples simultaneously. Unlike batch descent, however, it does not calculate the gradient for the entire dataset at once. The only restraint, therefore, is that the batch size, N_{batch} , must be larger than one and smaller than the number of elements in your training dataset, $N_{\text{batch}} > 1 \wedge N_{\text{batch}} < N_{\text{dataset}}$. This number is usually a lot smaller than the size of the entire dataset, however, with power of two values around 32 being commonplace.

This method can produce a more stable convergence than stochastic descent. Because it averages the gradient over many examples at once, there is less noise. It is a compromise between batch and stochastic descent, and its strengths and weaknesses depend largely on the batch size you select. This is also one of its largest downsides; any additional hyperparameter is one more factor that has to be tuned by some other external method.

Batch descent occurs when the gradient is calculated for all examples in our training dataset simultaneously, $N_{\text{batch}} = N_{\text{dataset}}$; it is, therefore, in some ways, the purest form of gradient descent, as the gradient has been calculated with all available data included [177]. In theory, it will have the most stable and direct convergence of all the methods, although in practice this is not often the case, [177]. However, whilst sometimes producing good results, this can suffer from problems getting stuck in local minima, as there is no ability for exploration. It also has the considerable downside of being very computationally expensive. For very large training datasets, this could quickly become time and computationally impossible. This method is rarely used in modern machine learning due to infeasibly large training datasets.

What follows is a brief explanation of various optimisation algorithms that can be used during the training process. The choice of optimiser can again be considered another hyperparameter that must be externally selected.

3.2.1 Momentum

In order to avoid local minima and introduce more exploration to our training process, many optimisers introduce the concept of “momentum” to the descent process [178–180]. This cannot be applied to batch gradient descent since there is only one step in the process.

Adding momentum to a descent algorithm is quite literally what it sounds like; if we consider the descent process to be a ball rolling down a hill, momentum is a property that changes more slowly than the gradient of the terrain beneath it. In that way, it acts to smooth the inherent noise generated from gradient descent by adding a proportion of the previous gradient to the determination of the next parameter space step. This can help improve convergence and prevent progress from getting stuck in a local minimum.

In order to describe this process mathematically, we introduce the concept of a parameter space velocity, $v_\theta(t)$, which is recorded independently of parameter space position, i.e. the parameter values themselves, $\vec{\theta}$. The two equations that fully describe the descent are

$$v_\theta(t) = \alpha v_\theta(t-1) + \eta \vec{\nabla} L_{M\vec{x}_t \vec{y}_t} \quad 3.19$$

and

$$\vec{\theta}_{t+1} = \vec{\theta}_t - v_\theta(t), \quad 3.20$$

where t is the current batch index, $v_{\theta(t)}$ is the parameter velocity at the current batch, $v_{\theta(t-1)}$, is the parameter velocity at the previous batch (initialized to 0 at $t-1$), α is the momentum parameter, η is the learning rate, $\vec{\nabla} L_{M\vec{x}_t \vec{y}_t}$, is the gradient of the model parameters with respect to the loss function, $\vec{\theta}_{t+1}$, are the updated model parameters, and $\vec{\theta}_t$ are the model parameters at the current step. As with the previous training steps, this process can be used for either stochastic or mini-batch descent and will be repeated across all training examples or batches of training examples in the training data set. The momentum parameter is a newly introduced hyperparameter which must be set before the initiation of training. The momentum value indicates what fraction of the previous parameter velocity is added to the current velocity; for any valid descent algorithm, this must be below one, $\alpha < 1$, as otherwise, the velocity will grow unbounded with each step. Common choices for momentum values hover around 0.9.

Momentum can be combined with stochastic or mini-batch descent and is an important aspect of other gradient techniques, including RMSProp and Adam [179,180].

3.2.2 AdaGrad (Adaptive Gradient Algorithm)

In standard gradient descent, every parameter, θ_i , within your parameter vector, $\vec{\theta}$, is treated equally by the descent algorithm. We can, however, imagine scenarios where treating all parameters equally is not the ideal method. A given training dataset may not contain an equal representation of all features present in that dataset. Indeed, even individual examples may have some features that are much more common than others. Often, these rarer features can be crucial to the efficient tuning of the network. However, the parameters that represent these features might see far fewer updates than other parameters, leading to long and inefficient convergence.

To combat this problem, AdaGrad, or the adaptive gradient algorithm, was introduced [181,179,180]. This method independently modifies the learning rate for each parameter depending on how often it is updated, allowing space parameters more opportunity to train. It achieves this by keeping a record of the previous sum of gradients squared and then adjusting the learning rate independently by using the value of this record. This is equivalent to normalising the learning rate by the L2 norm of the previous gradients. This approach is defined by

$$\vec{g}_t = \vec{g}_{t-1} + \left(\vec{\nabla} L_{M\vec{x}_t \vec{y}_t} \right)^{\circ 2} \quad 3.21$$

and

$$\vec{\theta}_{t+1} = \vec{\theta}_t - \left(\frac{\eta}{(\vec{g}_t + \varepsilon)^{\circ \frac{1}{2}}} \right) \circ \vec{\nabla} L_{M\vec{x}_t \vec{y}_t} \quad 3.22$$

where t is the current batch index, \vec{g}_t is a vector containing the sum of the square of all parameter gradients up to the training iteration, t , \vec{g}_{t-1} is the sum of the square of all parameter gradients except the current gradient squares, $\vec{\nabla} L_{M\vec{x}_t \vec{y}_t}$ is a vector containing the gradients for each parameter at the

current iteration, $\vec{\theta}_{t+1}$ are the parameters at the next iteration, $\vec{\theta}_t$ are the parameters at the current iteration, and ε is a very small value to prevent division by zero errors in the calculation.

This method has the advantage of self-tuning the learning rate for individual parameters, removing the need for manual per-parameter tuning, and it helps the model update sparse parameters more quickly by increasing the learning rate for parameters which learn more rarely seen features [181,179,180]. These small features are often very important for whatever operation is being optimised for.

AdaGrad still leaves the global learning rate, η , as an open hyperparameter which must be user-defined. It can also lead to problems when training deep networks with many layers. Similarly, the vanishing gradient problem can lead to tiny parameter updates when calculating the gradient of the network through very deep networks [181,179,180]. The vanishing learning rate problem can arise when training using AdaGrad with very large training datasets. In models with large amounts of parameters, it is crucial that the parameters continue to be updated throughout the training process to ensure that all of the many parameters meet optimally tuned values. However, if the normalisation factor, \vec{g} for some parameters, grows too big over the training process, the gradient updates can become very small, and training can slow to a crawl. Root Mean Square Propagation is a proposed solution to this problem.

3.2.3 RMSProp (Root Mean Square Propagation)

RMSProp, or root mean square propagation, is an alternative method to solve the adaptive learning rate issue, which attempts to alleviate the vanishing learning rate problem by less aggressively normalising the learning rate [182]. Instead of using the L2 Norm of all previous gradients to normalise each parameter learning rate, like AdaGrad, it uses a moving average of the squared gradients. This also deals with non-convex scenarios better, as it allows the gradient descent to escape without the learning rate falling to tiny values. This process is described by

$$\vec{E}_{g^2}(t) = \beta \vec{E}_{g^2}(t-1) + (1 - \beta) \left(\vec{\nabla} L_{M\vec{x}_t\vec{y}_t} \right)^2 \quad 3.23$$

and

$$\vec{\theta}_{t+1} = \vec{\theta}_t - \left(\frac{\eta}{(\vec{E}_{g^2}(t) + \varepsilon)^{\frac{1}{2}}} \right) \circ \vec{\nabla} L_{M\vec{x}_t\vec{y}_t}, \quad 3.24$$

where t is the current batch index, $\vec{E}_{g^2}(t)$ is the moving average of parameter gradients squared with respect to the loss function, β is the decay rate for the moving average, which controls how quickly the effect of previous gradients on the current learning rate falls off, $\vec{\nabla} L_{M\vec{x}_t\vec{y}_t}$ is a vector containing the gradients for each parameter at the current iteration, $\vec{\theta}_{t+1}$ are the parameters at the next iteration, $\vec{\theta}_t$ are the parameters at the current iteration, and ε is a very small value to prevent division by zero errors in the calculation.

This is a similar method to AdaGrad, so it has many of the same strengths and weaknesses but alleviates the vanishing gradient problem [179,180]. It also introduces one new hyperparameter, the decay rate, β , which must be decided, and it does not necessarily completely eradicate the vanishing gradient problem in all situations.

3.2.4 Adam (Adaptive Moment Estimation)

Adam (Adaptive Moment Estimation) combines the advantages of AdaGrad and RMSProp [183]. Instead of normalising by the L2 loss alone, like AdaGrad, or the moving squared average alone, like RMSProp, it uses an exponential of the moving average of both the gradient, $E_g(t)$ and the squared gradient, $E_{g^2}(t)$ and uses the parameters, β_1 and β_2 to control the decay rates of these averages respectively. The moving average of the gradient and the moving average of the squared gradient are

$$\vec{E}_g(t) = \beta_1 \vec{E}_{g(t-1)} + (1 - \beta_1) \vec{\nabla} L_{M\vec{x}_t \vec{y}_t} \quad 3.25$$

and

$$\vec{E}_{g^2}(t) = \beta_2 \vec{E}_{g^2}(t-1) + (1 - \beta_2) \left(\vec{\nabla} L_{M\vec{x}_t \vec{y}_t} \right)^{\circ 2}. \quad 3.26$$

As with previous methods, both moving average values are initialised to vectors of zeros at the start of the descent [183]. This poses an issue as early steps would be weighted toward zero. In order to solve this, the algorithm introduces two new terms, $\hat{E}_g(t)$, and $\hat{E}_{g^2}(t)$, to correct this issue:

$$\hat{E}_g(t) = \vec{E}_g \frac{t}{1 - (\beta_1)^t} \quad 3.27$$

and

$$\hat{E}_{g^2}(t) = \vec{E}_{g^2} \frac{t}{1 - (\beta_2)^t}. \quad 3.28$$

These terms are then collected in Equation 3.29.

$$\vec{\theta}_{t+1} = \vec{\theta}_t - \eta \hat{E}_g \circ \frac{t}{\left(\hat{E}_{g^2}(t) + \varepsilon \right)^{\circ \frac{1}{2}}} \quad 3.29$$

where t is the current batch index, $E_g(t)$ is the moving average of parameter gradients with respect to the loss function, $E_{g^2}(t)$ is the moving average of parameter gradients squared with respect to the loss function, β_1 and β_2 are the decay rate for the moving average and the moving squared averages respectively, which controls how quickly the effect of previous gradients on the current learning rate falls off, $\vec{\nabla} L_{M\vec{x}_t \vec{y}_t}$ is a vector containing the gradients for each parameter at the current iteration, $\vec{\theta}_{t+1}$ are the parameters at the next iteration, $\vec{\theta}_t$ are the parameters at the current iteration, and ε is a very small value to prevent division by zero errors in the calculation.

The Adam optimiser can intuitively be thought of as combining the adaptive learning rate methods with a form of momentum [183]. $E_g(t)$ carries the first moment, the momentum of the past gradients, which, like momentum, will keep you moving in the general direction that you have been travelling, moderated by the β_1 parameter. E_{g^2} carries information about the second moment, which remembers the magnitude of the gradients. This will make the algorithm move more cautiously if it has been encountering steep gradients, which can normally cause large learning rates and make the optimiser overshoot. This can act as a break to the momentum built up in the first moment. The β_2 parameter moderates this aspect.

The Adam optimiser is perhaps the most widely known and widely used in modern artificial neural network training due in large part to its efficacy [179,180]. Although there have been many adaptations and variants of the Adam optimiser which have tried to improve its operation, none have been so successful as to overthrow its position as the standard choice for gradient descent algorithms.

3.2.5 Backpropagation

So far, we have been using the parameter gradient vector, $\vec{\nabla} L_{M\vec{x}_t \vec{y}_t}$, without considering how we might calculate this value.

In the case of a single-layer perceptron, this process is not particularly difficult. As discussed before, first, we must pass an example (or batch of examples) through a randomly initiated network. This network, though untuned, will still produce an output vector, \hat{y} , albeit a useless one. We can then work

backwards from the model output, \hat{y} , and, in the case of supervised learning, compare it to our desired output, y , by using the loss function, L . We can do this by applying the chain rule for the weights [184].

Let's work through an example of how we might do this for a simple single-layer perceptron, with parameters, $\vec{\theta}$, split into a weights matrix, W , and bias vector, \vec{b} .

The action of the model is defined by:

$$M(\vec{x}) = f(\vec{z}) \quad 3.30$$

where $\vec{z} = W\vec{x} + \vec{b}$ is the raw input to the activation function, and f is the activation function. The i^{th} element of the output is given by the softmax function of the raw input, \vec{z} :

$$\hat{y}_i = \frac{e^{z_i}}{\sum_{j=1}^N e^{z_j}} \quad 3.31$$

and the loss function is given by

$$L = - \sum_{i=1}^N y_i \log(\hat{y}_i), \quad 3.32$$

where L is the loss function, N is the number of elements in the output vector and \hat{y}_i is the i^{th} element of the output vector. We want to find the gradients of the model parameters with respect to the loss function. In this case, $\frac{\partial L}{\partial W}$ and $\frac{\partial L}{\partial b}$. We can start by using the chain rule to compute $\frac{\partial L}{\partial z_i}$, the derivative of the loss with respect to the i^{th} component of z :

$$\frac{\partial L}{\partial z_i} = \sum_{j=1}^N \frac{\partial L}{\partial y_j} \frac{\partial y_j}{\partial z_i} \quad 3.33$$

Here, $\frac{\partial L}{\partial y_j}$ is the derivative of the loss with respect to the j^{th} output, and $\frac{\partial y_j}{\partial z_i}$ is the derivative of the j^{th} output with respect to the i^{th} input before activation. In our case, because we are using categorical cross-entropy loss:

$$\frac{\partial L}{\partial y_j} = \frac{\hat{y}_j}{y_j} \quad 3.34$$

And, due to the softmax activation function, in which the value of all output neurons affects the gradient of all others,

$$\frac{\partial \hat{y}_j}{\partial z_i} = \begin{cases} \hat{y}_j(1 - \hat{y}_j) & \text{if } i = j \\ -\hat{y}_j\hat{y}_i & \text{if } i \neq j \end{cases} \quad 3.35$$

Substitution of Equation 3.34 and Equation 3.35 into Equation 3.33 gives

$$\frac{\partial L}{\partial z_i} = -\frac{y_i}{\hat{y}_i} \hat{y}_i(1 - \hat{y}_i) + \sum_{j \neq i} \frac{y_j}{\hat{y}_j} (-\hat{y}_j\hat{y}_i). \quad 3.36$$

Simplifying gives:

$$\frac{\partial L}{\partial z_i} = -y_i(1 - \hat{y}_i) + \sum_{j \neq i} -y_j\hat{y}_i. \quad 3.37$$

We can simplify this further because $\sum_j y_j = 1$, as the input label is a one-hot vector and will always sum to one:

$$\frac{\partial L}{\partial z_i} = y_i - \hat{y}_i. \quad 3.38$$

This shows that the derivative of the softmax function with respect to the sum of the weighted inputs and bias values, $\frac{\partial L}{\partial z_i}$, is equal to the difference between the ground truth label value and the model output value. This provides us with another insight into the design of the softmax function and its use of exponentials.

We can then again use the chain rule to find the gradient of the weights and biases

$$\frac{\partial L}{\partial W} = \frac{\partial L}{\partial \vec{z}} \frac{\partial \vec{z}}{\partial W} = (\vec{y} - \hat{\vec{y}}) \circ \vec{x} \quad 3.39$$

and

$$\frac{\partial L}{\partial b} = \frac{\partial L}{\partial \vec{z}} \frac{\partial \vec{z}}{\partial b} = y - \hat{y}. \quad 3.40$$

Both of the gradients, Equation 3.39, and Equation 3.40, are quite intuitively what you might expect from a single-layer network. There is no non-linear behaviour, and as we previously speculated, the network is just training to find pixels that are most often activated by certain classes.

We can use a similar method for artificial neural networks of all complexities and depths. For a feed-forward dense network with N layers, let us denote the weighted sums of the inputs plus the biases of a layer with index i , as \vec{z}_i , the output of the activation function, f of layer i as $a_i = f(z_i)$, the weights matrix and biases vector of layer i as W_i and b_i , and the loss function again as L .

First, we compute the forward propagation by running an input vector, \vec{x} , or batch of input vectors, through the network to produce an output vector $\hat{\vec{y}}$. Then follow the following procedure.

1. Compute the derivative of the loss function with respect to the final output values: $\frac{\partial L}{\partial a_N} = \frac{\partial L}{\partial \hat{y}}$.
2. Compute $\frac{\partial L}{\partial z_N} = \frac{\partial L}{\partial a_N} \frac{\partial a_N}{\partial z_N}$, where $\frac{\partial a_N}{\partial z_N}$ is the derivative of the activation function in the final layer. This gives the gradient of the loss function with respect to the final raw outputs, \vec{z}_N .
3. Compute $\frac{\partial L}{\partial W_N} = \frac{\partial L}{\partial z_N} \frac{\partial z_N}{\partial W_N}$ and $\frac{\partial L}{\partial b_N} = \frac{\partial L}{\partial z_N} \frac{\partial z_N}{\partial b_N}$. This gives the gradients with respect to the final layer's weights and biases.
4. To propagate the error back to the previous layer, compute $\frac{\partial L}{\partial a_{N-1}} = \frac{\partial z_N}{\partial a_{N-1}} \frac{\partial L}{\partial z_N} = W_N^T \frac{\partial L}{\partial z_N}$.
5. Recursively repeat steps 1 to 4 until you reach the input layer and you have gradients for all parameters.

This method is known as backpropagation because you work backward from the output of the model toward the input vector [184].

3.3 Overfitting and Regularisation

Thus far, we have been partaking in perhaps one of the most heinous sins when developing a machine learning method — we have not made a distinction between the dataset we use to train our model, our **training** dataset, and the dataset we use to test our model, our **testing** dataset. It is vital that whenever possible we produce these datasets independently, and keep them entirely separate so that a model never has the chance to use any information present in the testing dataset to adjust its weights, ensuring that the first time a model sees any of the testing examples, is when it is being validated with them.

This hard segregation acts as a test to see if our model has **overfit** [185]. If the model learns the features of each of our training examples to the point where it can remember each specific example and match that example to a label, then our model may just associate each training example individually to an example rather than learning the general features of the dataset which will allow for classification of new unseen examples. If this is the case, when presented with new examples, such as examples from our testing dataset, the classifier will fail because it does not know what class this example belongs to. Thus keeping a separate dataset for testing is crucial to accurately assess model performance. Without such a distinct dataset, we cannot make any claims about the efficacy of our model. Whether, and to what degree, it is possible for a model to overfit to a particular dataset depends on the size and complexity of the training dataset and the size and complexity of the model. The larger the training dataset the more unlikely it is for overfitting to occur; however, a larger model ensures that a model can “remember” more data, which gives it an increased possibility to overfit to its training dataset.

Often, a further distinction is made between testing, training, and validation datasets. Although the nomenclature is often mixed up between these three datasets. The purpose of introducing a third **validation** dataset is to act as a final check of generality. Since the training procedure and model architecture are often altered throughout the development of the model, it is important to make sure that these alterations are not also accidentally tailored to our testing dataset. This third, validation dataset is set aside, ideally until the finalization of the data analysis method, to act as a final test of performance. Ideally, this dataset would have been created prior to the commencement of the project, to ensure that there is no possibility that the validation dataset is generated with the designed method in mind.

There may also be a need for more than three datasets, for example, you might want to have a test dataset that a training model is compared against every epoch, then another test dataset after a full training procedure has completed, but before the final method has been selected, which would necessitate a fourth dataset in this case. The term validation dataset will be used throughout this thesis for any dataset that is not the training dataset.

Overfitting is one of the most prominent and difficult problems in artificial neural network development, and thus there has been a large body of methods to try and ameliorate the issues it causes [185]. These methods are known as regularisations, the following few sections will briefly describe some of these methods.

3.3.1 Dropout

One of the most powerful ways to deal with overfitting is to employ dropout layers with your network [186]. Dropout layers can prevent overfitting by ensuring that the model does not rely on any one given neuron (or any given set of neurons), in order to produce its final output. Dropout layers do this by randomly setting a certain percentage of the previous layer’s outputs to zero, ensuring that information from that neuron cannot be used to produce the model’s output during this inference. The choice of neurons that are zeroed is randomised between each training instance, this teaches the model to explore different feature recognition pathways in each training batch.

The percentage of outputs dropped is a user-selected hyperparameter that must be decided before model training is initiated, can be anywhere from 0 (equivalent to no dropout layer) to 1 (which would stop all information flowing through the network and make training impossible), typical dropout values lie between 0.1 and 0.5 [186]. Dropout layers are only active during model training, and when in use for inference proper are not employed and can be removed without affecting model function.

By randomly dropping out neurons during model training, it reduces the information that a model can rely on to produce its final output [186,187].. Because, in almost all cases, remembering the exact form of each training example will take a larger amount of information than remembering only general

features, the network is incentivized to learn input features rather than memorizing specific training examples.

Dropout can sometimes slow down model convergence, and it is not a complete solution to overfitting, but it finds use very commonly across a wide range of modern neural network architectures [187].

3.3.2 Batch normalisation

Another layer type that can be added to a network to act as regularisation as well as provide other benefits is the batch normalization layer [188]. As data moves through deep networks, a phenomenon known as internal covariate shift can take place. This describes the scenario wherein values flowing through the network can occupy a wide range of distributions that vary dramatically between layers, usually increasing in size as they move through the network.

This can be a problem as the activation functions present in a network are designed to act in specific data distributions, so large values in the network can saturate their non-linearities, and remove much of the potential for nuance, which can increase model convergence time and degrade model performance.

Batch normalization layers offer a solution to this problem by normalizing the mean and standard deviation of a layer's output distribution to certain values, normally a mean of zero and a variance of one. To ensure that this normalisation does not reduce the information content of the layer output, the layer has two tunable weight parameters per input neuron, one to scale the neuron's output after normalisation, and the other to shift it after normalisation. Finally, batch normalisation ensures that the gradients stay within a reasonable range, which also increases model convergence.

Like dropout, batch normalisation is applied differently during training and when in use in production in the inference phase of the model [188]. During training the normalisation is based on the mean and variance of the current training batch, whereas during inference the normalisation uses the moving average and moving variance computed during the training phase, primarily to ensure that the model's output is deterministic, which is often a desired characteristic.

Batch normalisation serves many purposes within the network, increasing convergence and allowing for faster training times, but it also can help to prevent overfitting because it dramatically reduces the range of possible states that can occur in inference and training.

3.3.3 Early Stopping

One simple way to prevent overfitting that is often employed is to halt the training procedure before overfitting can occur [189]. Generally, if it is possible for a given model to overfit to a given training distribution, then it will overfit more the more often it has seen that training dataset, i.e. the number of epochs that have been used in the training procedure. Shuffling the dataset each epoch will reduce this problem slightly by generating unique batch combinations and altering the order that gradient descent takes through the parameter space, but at each iteration the model is still adjusting its parameters based on the training examples, potentially closing in on a fit that is too close.

This can be alleviated by halting the training early based on model post-epoch performance when validated on your validation dataset, generated as independently as possible from your training dataset. If your model begins to overfit your training dataset, then, almost by definition, validation performance will begin to degrade or at least saturate. The model training procedure can be configured to automatically detect if this is the case, relying on a user-defined hyperparameter known as patience, which determines the number of epochs with no improvement in test dataset performance to wait before halting the training.

Stopping model training early, and restoring the model parameters that achieved the best performance on the test dataset can be an effective method to stop the model from converging on a fit that is too closely tailored to the training dataset.

3.4 Infrastructure Layers

Most GPU vector libraries, including TensorFlow [65], have strict requirements about the shapes of vectors that flow through them. Within artificial neural network models, there is often a need to change the shape and/or dimensionality of the vectors as they flow through the network – for example if we are moving from a 2D image to a 1D vector, as we saw when feeding 2D MNIST images into the 1D perceptron architecture we must employ a **flattening layer** which takes whatever dimensionality the input vector has and reduces it to a 1D vector. We can also use reshape layers to perform more complex reshapings between vector shapes as long as the requested resultant vector contains the same number of elements as the input vector; see Figure 3.13.

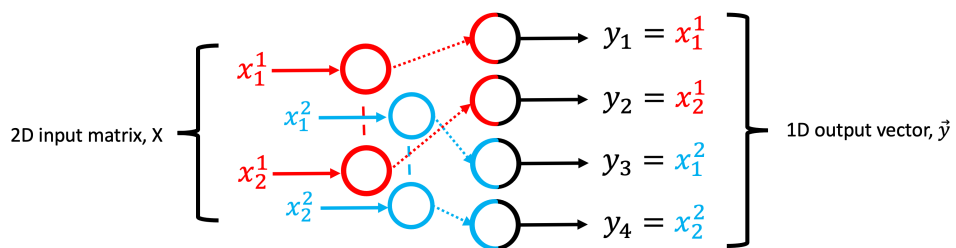


Figure 3.13 | A flattening layer. This layer takes a 2D input matrix $X = \begin{pmatrix} x_1^1 & x_2^1 \\ x_1^2 & x_2^2 \end{pmatrix}$ and converts it into a 1D vector, $\vec{y} = [y_1, y_2, y_3, y_4]$, without using any learned parameters or altering the values of the data. It simply rearranges the indexes and removes all but one dimension. Reshaping layers are a more general version of a flattening layer, where an input vector or matrix can be transformed into any equivalently sized output vector or matrix.

These kinds of “infrastructure” layers will typically not be discussed nor included in network diagrams if their existence is implied by the network construction. They do not have any trainable parameters and perform no transformation on the passing data other than to change the data layout. They are only noted when newly introduced or of special interest.

4 The Application of Machine Learning to Gravitational-Wave Data Analysis

We have demonstrated that simple artificial neural networks can be used to classify input data drawn from a restricted distribution into a number of classes, N , with a high ($> 99.9\%$) degree of accuracy. We didn't design the network with any particular consideration for the dataset (besides the dimensionality of its elements), therefore, we can infer that artificial neural networks should be general enough to classify data drawn from other distributions that contain discrete differentiable classes. It is not clear, however, which other distributions can be classified and what network complexity is required to achieve a similar degree of accuracy. It is easy to imagine distributions that are considerably simpler than the MNIST dataset [12] and, conversely, ones that are much more complex. There may be a mathematical approach to determine the link between the distribution and required model complexity.

One possible metric that touches upon this relation is the Rademacher complexity, $\hat{\mathcal{R}}_M$, given by

$$\hat{\mathcal{R}}_M(H) = \mathbb{E}_{\vec{\varepsilon}} \left[\frac{1}{M} \sum_{i=1}^M \varepsilon_i h[\vec{x}_i] \right], \quad 4.1$$

where M is the number of data points in a dataset, $X = [\vec{x}_1, \dots, \vec{x}_i, \dots, \vec{x}_M]$ where each point is a vector, \vec{x} , in our case the input vectors of our training dataset, and $\vec{\varepsilon} = [\vec{\varepsilon}_1, \dots, \vec{\varepsilon}_i, \dots, \vec{\varepsilon}_M]$ are vectors of equal length to our input vectors with data uniformly distributed in $\{-1, +1\}^M$. H represents the hypothesis space, $H = \{h_1, h_2, \dots\}$, the set of all possible functions, $\{h_i\}$, that our neural network architecture can learn. In simpler terms, H includes every pattern or rule the neural network might use to make predictions based on the input data. The diversity and complexity of functions in H are directly influenced by the network's architecture – more layers and neurons mean a larger hypothesis space. $\vec{\varepsilon}$ is a set of random variables that take on values of either -1 or $+1$, with each $\vec{\varepsilon}_i$ associated with a corresponding data point, \vec{x}_i , in the dataset. These random values are used to inject randomness into the calculation of Rademacher complexity, essentially testing how well the hypothesis space, H can fit or adapt to completely random outcomes.

The Rademacher complexity is a measure of how well functions in H can fit random noise in the data. A higher Rademacher complexity indicates that the function class can fit the noise better, which implies a higher capacity to overfit to the data. So, one approach to optimising the model would be to attempt to minimise Rademacher complexity value whilst maximising model performance. More details about this metric and its use in defining the relationship between data samples and model complexity can be found at [190]. Despite the existence of this metric, however, it would appear that there has not been substantial research into the link between dataset complexity and required model size [191], though it is possible that such a paper has been missed.

One method that we can use to explore this question is to find out the answer empirically. As we move from the MNIST dataset [12] to distributions within gravitational-wave data science, the natural starting point is to repeat the previous experiments with gravitational-wave data, both as a comparison and as a baseline as we move forward. The following subsection will explore the possible areas for detection applications, describe the example datasets and their construction, and explore the results of repeating the previous experiments on gravitational-wave data, comparing our results to similar attempts from the literature. By the end of this chapter, we will have accumulated a large number of possible network, training, and data configurations. These form the set of hyperparameters that we must, though some approach, narrow down; we will explore how we can do this in Section 5.

4.1 Gravitational-Wave Classifiers

The scope of gravitational-wave data problems to which we can apply artificial neural network models is large [192]. However, we shall limit our investigation to perhaps the simplest type of problem — classification, the same type of problem that we have previously demonstrated with our classification of the MNIST dataset [12] into discrete classes. Though classification is arguably the most straightforward problem available to us, it remains one of the most crucial — before any other type of transient signal analysis can be performed, transients must first be identified.

There are several problems in gravitational-wave data analysis which can be approached through the use of classification methods. These can broadly be separated into two classes — detection and differentiation. **Detection** problems are self-explanatory; these kinds of problems require the identification of the presence of features within a noisy background. Examples include Compact Binary Coalescence (CBC) [53,50], burst [22,28], and glitch detection [104,193]; see Figure 4.1 for a representation of the different features present in gravitational-wave data. **Differentiation** problems, usually known simply as classification problems, involve the separation of detected features into multiple classes, although this is often done in tandem with detection. An example of this kind of problem is glitch classification, in which glitches are classified into classes of known glitch types, and the classifier must separate input data into these classes [104].

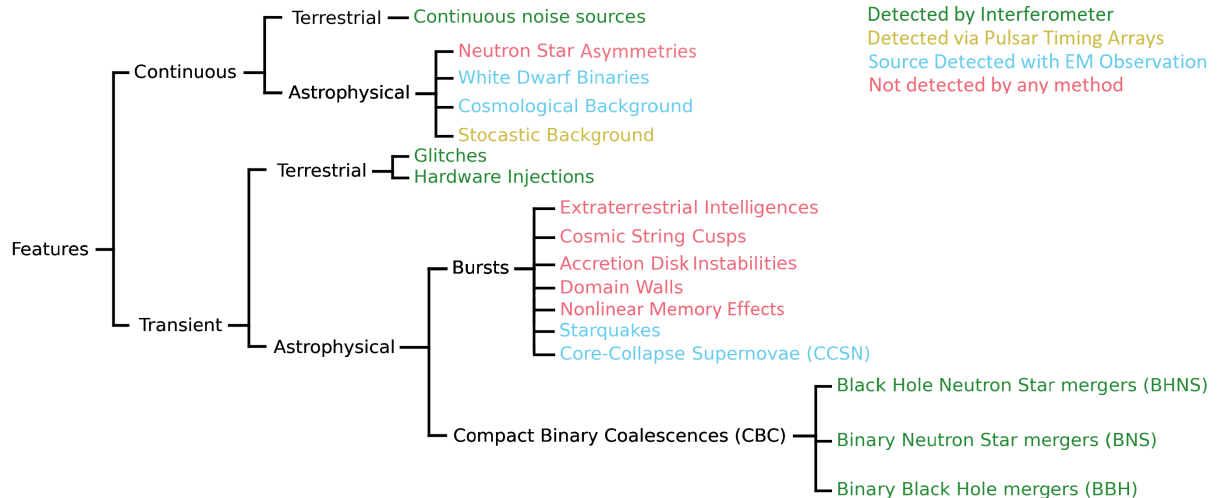


Figure 4.1 | A non-exhaustive hierarchical depiction of some of the features, and proposed features, of gravitational-wave interferometer data. The first fork splits the features into two branches, representing the duration of the features. Here, **continuous** features are defined as features for which it is extremely unlikely for us to witness their start or end within the lifespan of the current gravitational-wave interferometer network and probably the current scientific community [14]. These features have durations anywhere from thousands to billions of years. **Transient** features have comparatively short durations [15], from fractions of seconds in the case of stellar-mass Binary Black Hole (BBH) mergers [15] to years in the case of supermassive BBH mergers [16]. It should be noted that the detectable period of supermassive binaries could be much longer; although the mergers themselves are transient events, there is no hard cut-off between the long inspiral and the merger event. Nevertheless, the mergers are probably frequent enough that some will end within the lifetime of the proposed LISA space constellation, so in some cases, they can be considered transients [16]. The next fork splits features by origin. Features of **astrophysical** origin originate from beyond Earth. This distinction is practically synonymous with the distinction between gravitational waves and signals from other sources since no other astrophysical phenomena are known to have a similar effect in interferometers [15]. Features of **terrestrial** origin, unsurprisingly, originate from Earth. These primarily consist of detector glitches caused by seismic activity or experimental artifacts [17]. Astrophysical transients have a further prac-

tical division into CBCs and bursts. The category of **bursts** contains all astrophysical transients that are not CBCs [18]. The primary reason for this distinction is that CBCs have been detected and have confirmed waveform morphologies [15,19]. As of the writing of this thesis, no gravitational-wave burst events have been detected [18,20,21]. Bursts often require different detection techniques [22,23]; of the proposed sources, many are theorised to have waveforms with a much larger number of free parameters than CBCs, as well as being harder to simulate as the physics are less well-understood [24,25]. These two facts compound to make generating large template banks for such signals extremely difficult. This means that coherence detection techniques that look for coherent patterns across multiple detectors are often used over matched filtering [23,26,22,27,28]. The astrophysical leaves of the diagram represent possible and detected gravitational-wave sources; the text's colourings represent their current status. Green items have been detected using gravitational-wave interferometers, namely the merger of pairs of Binary Black Holes (BBHs) [15], Binary Neutron Stars (BNSs) [19], or one of each (BHNSs) [29]; see [30–32] for full catalogues of detections. Yellow items have been detected via gravitational waves but using Pulsar Timing Arrays (PTAs) rather than interferometers [33]. Blue items represent objects and systems that are theorised to generate gravitational waves and have been detected by electromagnetic observatories but not yet with any form of gravitational wave detection. This includes white dwarf binaries [34,35], the cosmological background [36,37], starquakes [38,39], and core-collapse supernovae CCSN [40,41]. This is because they are too weak and/or too uncommon for our current gravitational-wave detector network to have had a chance to detect them. Finally, red items are possible, theorised sources of gravitational waves that have not yet been detected by any means. These are, evidently, the most contentious items presented, and it is very possible that none of these items will ever be detected or exist at all. It should be noted that the number of proposed sources in this final category is extensive, and this is far from an exhaustive list. The presented proposed continuous sources are neutron star asymmetries [42], and the presented transient sources are extraterrestrial intelligence [43], cosmic string kinks and cusps [44], accretion disk instabilities [45], domain walls [46], and nonlinear memory effects [47].

Figure 4.1 shows that several possible transients with terrestrial and astrophysical origins could be targeted for detection. For our baseline experiments and throughout this thesis, we will select two targets.

Firstly, **Binary Black Holes (BBHs)**. We have the most numerous detections of BBH signals [30–32], and whilst this might make them seem both less interesting and as a solved problem, they have several benefits. As test cases to compare different machine learning techniques against traditional methods, they have the most material for comparison because of their frequency; they would also see the greatest benefits from any computational and speed efficiency savings that may be wrought by the improvement of their detection methods [194]. These factors may become especially relevant when the 3rd generation detectors, such as the Einstein Telescope [73] and Cosmic Explorer [74], come online. During their observing periods, they expect detection rates on the order of between 10^4 and 10^5 detections per year [195], which would stretch computing power and cost if current methods remain the only options. In the shorter term, if detection speeds can be improved, faster alerts could be issued to the greater astronomical community, allowing increased opportunity for multimessenger analysis [196]. Only one multimessenger event has thus far been detected – a Binary Neutron Star (BNS) event [19], but it is probable, due to the relative similarity in their morphologies, that methods to detect BBHs could be adapted for BNS detection.

Secondly, we will investigate the detection of unmodeled **burst** signals using a machine learning-based coherent detection technique. Bursts are exciting sources whose detection could herald immense opportunities for scientific gain [21]. Possible burst sources include core-collapse supernovae [41], starquakes [39], accretion disk instabilities [45], nonlinear memory effects [47], domain walls [46], and

cosmic string cusps [44], as well as a plethora of other proposed sources. It should be noted that whilst many bursts have unknown waveform morphologies, some, such as cosmic string cusps, are relatively easy to model and are grouped with bursts primarily due to their as-yet undetected status [44].

Our current models of the physics of supernovae are limited both by a lack of understanding and computational intractability; detecting the gravitational-wave signal of a supernova could lead to new insights into the supranuclear matter density equation of state as well other macrophysical phenomena present in such events such as neutron transport and hydrodynamics [197] `neutron_star_equation_of_state_2` [198]. We may also detect proposed events, such as accretion disk instabilities [45], which may be missed by standard searches. We can search for the gravitational-wave signals of electromagnetic events that currently have unknown sources, such as fast radio bursts [199], magnetar flares [200], soft gamma-ray repeaters [201], and long gamma-ray bursts [201]. Although it's possible that some of these events produce simple, modelable waveforms, it is not currently known, and a general search may one day help to reveal their existence. Some of the more hypothetical proposed sources could fundamentally alter our understanding of the universe, such as evidence for dark matter [202] and/or cosmic strings [44], or if we fail to find them, it could also help to draw limits on theory search space.

It is unknown whether current burst search methods have sufficient detection capability to detect all theoretically detectable sources, nor whether current methods are maximally efficient at gaining information on sources that they do detect. Currently, the LIGO-Virgo-KAGRA collaboration has a number of active burst detection pipelines, X-Pipeline [23], oLIB [26], Coherent Wave Burst (cWB) [22] and BayesWave [27]. These include both offline and online searches, including targeted searches wherein a known electromagnetic event is used to limit the search space [199–201]. It could be that the current detection software is adequate and, indeed, the search is hardware rather than software-limited. Even if this is the case, there are probably computational improvements that are possible. It seems unlikely that we have reached the limit of coherent search efficiency.

Traditional coherence techniques require the different detector channels to be aligned for successful detection; therefore, because we don't know *a priori* the direction of the gravitational-wave sources (unless we are performing a targeted offline search), coherent search pipelines such as X-Pipeline [23] and cWB [22] must search over a grid covering all possible incidence directions. In the case of all-sky searches, this grid will necessarily cover the entire celestial sphere. In targeted searches, the grid can be significantly smaller and cover only the uncertainty region of the source that has already been localised by an EM detection [201,199]. Higher resolution grids will result in a superior search sensitivity; however, they will simultaneously increase computing time. Covering the entire sky with a grid fine enough to achieve the desired sensitivity can be computationally expensive. It is possible to circumnavigate the need to search over a grid using artificial neural networks, shifting much of the computational expense to the training procedure. This has been demonstrated by the MLy pipeline [28] – the only fully machine-learning-based pipeline currently in review for hopeful deployment before the end of the fourth observing run (O4). Improvements in the models used for this task could be used to improve the effectiveness of the MLy pipeline. Indeed, some of the work discussed in this thesis was used at an early stage in the pipeline's development to help design the architecture of the models; see Section 5.6. It is hoped that in the future, more aspects of the work shown here can find use in the pipeline's development.

We will focus on the binary detection problem rather than multi-class classification, as there is only one discrete class of BBH (unless you want to draw borders within the BBH parameter space or attempt to discern certain interesting features, such as eccentricity), and in the unmodeled burst case, coherent detection techniques are not usually tuned to particular waveforms, which, in any case, are not widely

available for many types of burst. In the next subsection, we will discuss how we can create example datasets to train artificial neural networks for this task.

4.2 Dataset Design and Preparation

In the case of CBCs, we have only a very limited number (< 200) of example interferometer detections [30–32], and in the burst case, we have no confirmed examples [18,20,21]. This means that to successfully train artificial neural network models, which typically require datasets with thousands to millions of examples [203], we must generate a large number of artificial examples.

In order to facilitate the real-time generation of training datasets, a custom Python package named GWFlow was created [60]. GWFlow handles the generation of fake noise and waveforms (with the use of the custom cuPhenom GPU waveform generator [48]), as well as the acquisition and processing of real interferometer data, and the injection, projection, and scaling of waveforms. It packages this functionality into a configurable TensorFlow dataset. Since the majority of the processing, except the acquisition of real noise, is performed on the GPU, the dataset can be adjusted and training can commence without the need to pre-generate the entire dataset. This allows for much quicker iteration through dataset hyperparameters.

The following subsections describe how GWFlow handles the creation of these examples, including the acquisition of noise, the generation and scaling of simulated waveforms, and data conditioning.

4.2.1 The Power Spectral Density (PSD)

The Power Spectral Density (PSD) is an important statistical property that is used by several elements of dataset design [204]. Since a custom function was written for this thesis in order to speed up the calculation of the PSD, and since it is helpful to have an understanding of the PSD in order to understand many of the processes described in subsequent sections, a brief explanation is presented.

The PSD is a time-averaged description of the distribution of a time series's power across the frequency spectrum [204]. Unlike a Fourier transform, which provides a one-time snapshot, the PSD conveys an averaged view, accounting for both persistent and transient features; see Equation 4.4 for a mathematical description. The PSD is used during data conditioning in the whitening transform, wherein the raw interferometer data is processed so that the noise has roughly equal power across the frequency domain, see Section 4.2.7. For some types of artificial noise generation, the PSD can be used to colour white noise in order to generate more physically active artificial noise; see Section 4.2.2. The PSD is also used to calculate the optimal Signal to Noise ratio, which acts as a metric that can be used to measure the detectability of an obfuscated feature and thus can be used to scale the amplitude of the waveform to a desired detection difficulty.

Imagine a time series composed of a stationary 20 Hz sine wave. In the PSD, this would materialise as a distinct peak at 20 Hz, effectively capturing the concentrated power at this specific frequency: the frequency is constant, and the energy is localised. If at some time, t , we remove the original wave and introduce a new wave at a different frequency, 40 Hz, the original peak at 20 Hz would attenuate but not vanish, as its power is averaged over the entire time-series duration. Concurrently, a new peak at 40 Hz would appear. The power contained in each of the waves, and hence the heights of their respective peaks in the PSD, is determined by the integrated amplitude of their respective oscillations; see Figure 4.2 for a depiction of this example. When applied to a more complicated time series, like interferometer noise, this can be used to generate an easy-to-visualise mapping of the distribution of a time series's power across frequency space.

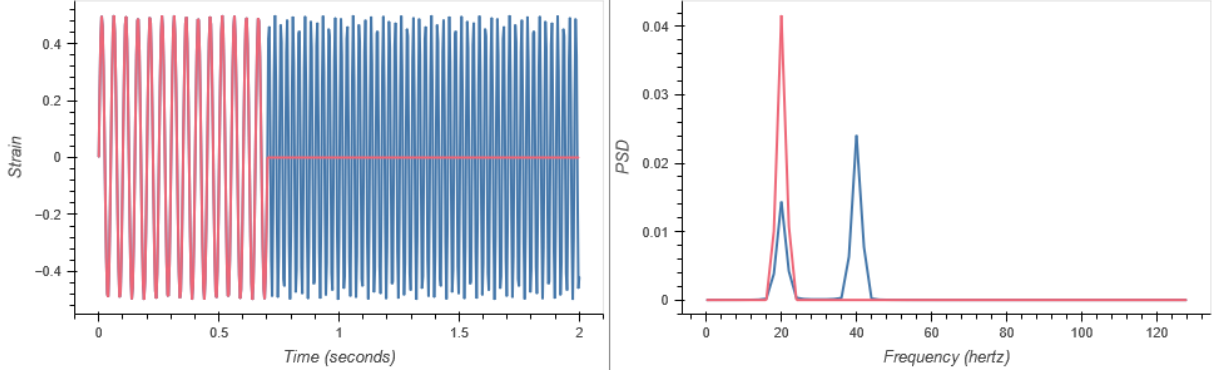


Figure 4.2 | Examples of Power Spectral Density (PSD) transforms. *Left:* Two time domain series. The red series is a 20 Hz wave with a duration of 0.7 s, and the blue series is this same time series concatenated with a 40 Hz wave from $t = 0.7$ s onwards. *Right:* The two PSDs of the time series are displayed in the left panel. The red PSD was performed across only the 0.7 s of the red wave’s duration, whereas the blue PSD was taken over the full 2.0 s duration. As can be seen, the blue PSD has two peaks, representing the two frequencies of the two waves combined to make the blue time series — each peak is lower than the red peak, as they are averaged across the full duration, and their respective heights are proportional to their durations as both waves have the same amplitude and vary only in duration.

The PSD can be calculated using Welch’s method, which uses a periodogram to calculate the average power in each frequency bin over time [205]. More specifically, the following steps are enacted:

1. First, the time series is split up into K segments of length L samples, with some number of overlapping samples D ; if $D = 0$, this method is equivalent to Bartlett’s method.
2. Each segment is then windowed with a user-chosen window function, $w(n)$. This is done in order to avoid spectral leakage, avoid discontinuities in the data, smoothly transition between segments, and control several other factors about the method, which allow for fine-tuning to specific requirements.
3. For each windowed segment, i , we then estimate the power of the segment, $I_i(f_k)$, at each frequency, f_k , by computing the periodogram with

$$I_i(f_k) = \frac{1}{L} |X_i(k)|^2 \quad 4.2$$

where $I_i(f_k)$ is the result of the periodogram, $X_i(k)$ is the FFT of the windowed segment, and f_k is the frequency corresponding to the k^{th} FFT sample.

4. Finally, we average the periodograms from each segment to get the time-average PSD:

$$S(f_k) = \frac{1}{K} \sum_{i=1}^K I_i(f_k) \quad 4.3$$

where where $S(f_k)$ is the PSD. Combining Equation 4.2 and Equation 4.3 gives

$$S(f_k) = \frac{1}{K} \sum_{i=1}^K \frac{1}{L} |X_i(k)|^2 \quad 4.4$$

To compute the PSD with enough computational speed to perform rapid whitening and SNR, ρ_{opt} , calculation during model training and inference, an existing Welch method from the SciPy scientific Python library [206] was adapted and added to the GWFlow pipeline [60], converting its use of the

NumPy vectorised CPU library [64] to the TensorFlow GPU library [65]; this converted code is seen in Listing 4.8.

```
@tf.function
def calculate_psd(
    signal : tf.Tensor,
    nperseg : int,
    noverlap : int = None,
    sample_rate_hertz : float = 1.0,
    mode : str ="mean"
) -> (tf.Tensor, tf.Tensor):

    if noverlap is None:
        noverlap = nperseg // 2

    signal = detrend(signal, axis=-1, type='constant')

    # Step 1: Split the signal into overlapping segments
    signal_shape = tf.shape(signal)
    step = nperseg - noverlap
    frames = tf.signal.frame(signal, frame_length=nperseg, frame_step=step)

    # Step 2: Apply a window function to each segment
    # Hanning window is used here, but other windows can be applied as well
    window = tf.signal.hann_window(nperseg, dtype = tf.float32)
    windowed_frames = frames * window

    # Step 3: Compute the periodogram (scaled, absolute value of FFT) for each
    # segment
    periodograms = \
        tf.abs(tf.signal.rfft(windowed_frames))**2 / tf.reduce_sum(window**2)

    # Step 4: Compute the median or mean of the periodograms based on the
    # median_mode
    if mode == "median":
        pxx = tfp.stats.percentile(periodograms, 50.0, axis=-2)
    elif mode == "mean":
        pxx = tf.reduce_mean(periodograms, axis=-2)
    else:
        raise "Mode not supported"

    # Step 5: Compute the frequencies corresponding to the power spectrum values
    freqs = fftfreq(nperseg, d=1.0/sample_rate_hertz)

    #Create mask to multiply all but the 0 and nyquist frequency by 2
    X = pxx.shape[-1]
    mask = \
        tf.concat(
            [
                tf.constant([1.]),
                tf.ones([X-2], dtype=tf.float32) * 2.0,
                tf.constant([1.])
            ],
            axis=0
        )
```

```
return freqs, (mask*pxx / sample_rate_hertz)
```

Listing 4.8 | Python [63]. TensorFlow [65] graph function used by GWFlow [60] to calculate the PSD of a signal. `signal` is the input time series as a TensorFlow tensor, `nperseg` is the number of samples per segment, L , and `noverlap` is the number of overlapping samples, D . TensorFlow has been used in order to utilise GPU parallelisation, which offers a significant performance boost over a similar function written in NumPy [64].

A closely related property, the Amplitude Spectral Density (ASD), is given by the element-wise square root of the Power Spectral Density (PSD)

$$A(f_k) = S(f_k)^{\circ\frac{1}{2}}. \quad 4.5$$

4.2.2 Noise Generation and Acquisition

There are two possible avenues for acquiring background noise to obfuscate our injections. We can either create artificial noise or use real segments extracted from previous observing runs. As was discussed in Section 2.3.3, real interferometer noise is neither Gaussian nor stationary, and many of the noise sources which compose this background are not accounted for or modelled [17]. This means that any artificial noise will only be an approximation of the real noise — it is not clear, intuitively, how well this approximation will be suited to training an artificial neural network.

One perspective argues that using more approximate noise could enhance the network’s generalisation capabilities because it prevents overfitting to the specific characteristics of any given noise distribution; this is the approach adopted by the MLy pipeline [28]. Conversely, another perspective suggests that in order to properly deal with the multitude of complex features present in real noise, we should make our training examples simulate real noise as closely as possible [207–209], even suggesting that models should be periodically retrained within the same observing run in order to deal with variations in the noise distribution. These are not discrete philosophies, and the optimal training method could lie somewhere between these two paradigms.

Evidently, in either case, we will want our validation and testing datasets to approximate the desired domain of operation as closely as possible; if they do not, we would have no evidence, other than assumption, that the model would have any practical use in real data analysis [209]. The following subsection will outline the possible types of noise that could be used to create artificial training examples. Throughout the thesis, for all validation purposes, we have used real noise at GPS times, which are not used at any point during the training of models, even when the training has been done on real noise.

White Gaussian: The most simplistic and general approach, and therefore probably the most unlike real noise, is to use a white Gaussian background. This is as simplistic as it sounds; we generate N random variables, where N is the number of samples in our noise segment. Each sample is drawn from a normal distribution with a mean of zero and some variance according to the input scaling; often, in the case of machine learning input vectors, this would be unity; see the two uppermost plots in Figure 4.3.

Coloured Gaussian: This noise approximation increases the authenticity of the noise distribution by colouring it with a noise spectrum; typically, we use an ASD drawn from the interferometer we are trying to imitate in order to do this; see Section 4.2.1. By multiplying the frequency domain transform

of Gaussian white noise by a given PSD, we can colour that noise with that PSD. The procedure to do this is as follows:

1. Generate white Gaussian noise.
2. Transform the Gaussian noise into the frequency domain using a Real Fast Fourier Transform (RFFT).
3. Multiply the noise frequency spectrum by the selected ASD in order to colour it.
4. Return the newly coloured noise to the time domain by performing an Inverse RFFT (IRFFT).

There are at least two choices of PSD we could use for this process. We could use the PSD of the detector design specification. It represents the optimal PSD given perfect conditions, no unexpected noise sources, and ideal experimental function. This would give a more general, idealistic shape of the PSD across a given observing run. Alternatively, we could use the PSD of a real segment of the background recorded during an observing run; this would contain more anomalies and be a closer approximation to the specific noise during the period for which the PSD was taken. Since the PSD is time-averaged, longer segments will result in more general noise. The MLy pipeline [28] refers to this latter kind of noise as **pseudo-real** noise; see examples of these noise realisations in the four middle plots of Figure 4.3.

Real: Finally, the most authentic type of noise that can be gathered is real interferometer noise. This is noise that has been sampled directly from a detector. Even assuming that you have already decided on which detector you are simulating, which is required for all but white noise generation, there are some extra parameters, shared with the pseudo-real case, that need to be decided. The detector data information, the time period from which you are sampling, and whether to veto any features that may be present in the segment – e.g. segments that contain events, candidate events, and known glitches.

To acquire the real data, we utilise the GWPY Python Library’s [210] data acquisition functionality – since there are multiple formats in which we could retrieve the data, we must specify some parameters, namely, the frame, the channel, and the state flag. Interferometer output data is stored in a custom file format called a frame file [211]; thus, the choice of frame determines the file to be read. Within each frame file lies multiple channels – each of which contains data from a single output stream. These output streams can be raw data, e.g. raw data from the interferometer photodetector itself; various raw auxiliary data streams, such as from a seismometer; conditioned data, e.g., the primary interferometer output with lines removed; or the state flag channel, which contains information about the status of the detector at every time increment – the state flag will indicate whether the detector is currently in observing mode or otherwise, so it is important to filter the data for the desired detector state. For the real noise used in this thesis, we use the frame, channel, and state flag, shown in Table 4.1. We have excluded all events and candidate events listed in the LIGO-Virgo-Kagra (LVK) collaboration event catalogues [30–32] but included detector glitches unless otherwise stated.

Detector	Frame	Channel	State Flag
LIGO Hanford (H1)	HOFT_C01	H1:DCS-CALIB_S-TRAIN_CLEAN_C01	DCS-ANALY-SIS_READY_C0- 1:1
LIGO Livingston (L1)	HOFT_C01	L1:DCS-CALIB_S-TRAIN_CLEAN_C01	DCS-ANALY-SIS_READY_C0- 1:1
VIRGO (V1)	V1Online	V1:Hrec_hoft_16384Hz	ITF_SCIENCE:1

Table 4.1 | The frame, channel, and state flags used when obtaining data from the respective detectors during the 3rd observing run (O3). This data was used as obfuscating noise when generating artificial examples to train and validate artificial neural network models throughout this thesis. It should be noted that although the clean channels were produced offline in previous observing runs, the current observing run, O4, produces cleaned channels in its online run, so using the cleaned channels during model development ensures that the training, testing, and validation data is closer to what would be the normal operating mode for future detection methods.

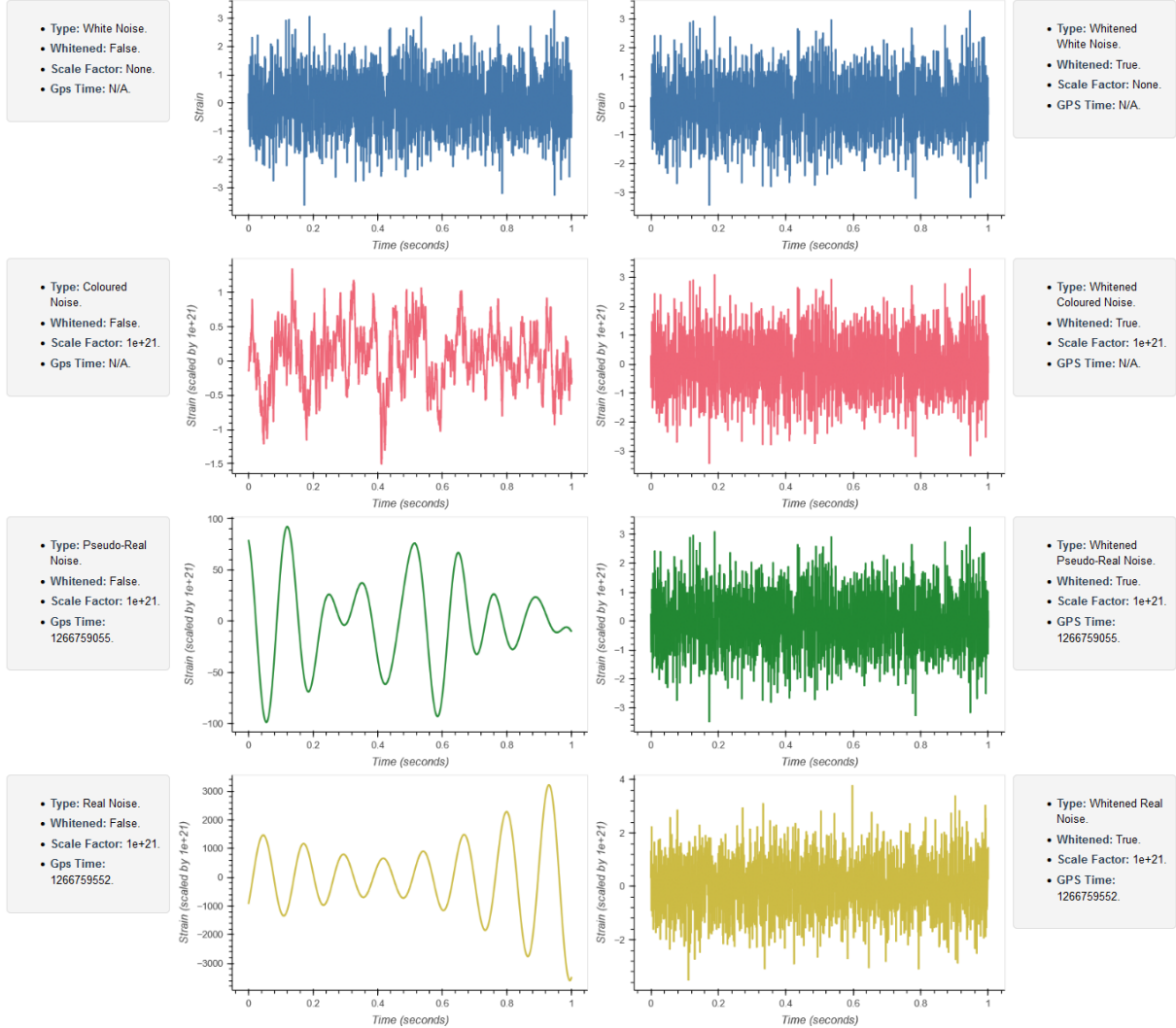


Figure 4.3 | One-second examples of the four possible types of simulated and real noise considered by this thesis. Where real noise is used, it is taken from the LIGO Livingston detector during the third observing run at the GPS times listed. In order, from top to bottom, these are examples of white Gaussian noise, coloured Gaussian noise, pseudo-real noise, and real noise. A description of these noise types and their generation can be found in Section 4.2.2. The left column shows the unaltered values of the noise. Note that the noise has been scaled in all cases except for the pure white noise, which is generated at the correct scale initially. This scaling is used to reduce precision errors and integrate more effectively with the machine learning pipeline, as most loss and activation functions are designed around signal values near unity; see Section 3.1.6 and Section 3.1.5. The right column shows the same noise realisations after they have been run through a whitening filter. In each case, the PSD of a 16.0 s off-source noise segment not displayed is used to generate a Finite Impulse Response (FIR) filter, which is then convolved with the on-source data; see Section 4.2.7. For the simulated and pseudo-real noise cases, the

off-source data is generated using the same method as the on-source data but with a longer duration. In the real noise case, the off-source data consists of real interferometer data drawn from 16.5 s before the start of the on-source segment to 0.5 s before the start of the on-source segment. This 0.5s gap is introduced because 0.5 s must be cropped from the data following the whitening procedure in order to remove edge effects induced via windowing, as well as acting as a buffer to reduce contamination of the off-source data with any features present in the on-source data. Note that the whitened noise plots look very similar for the three simulated noise cases — a close examination of the data reveals that there is some small variation between the exact values. This similarity occurs because the off-source and on-source noise segments for these examples are generated with identical random seeds and thus have identical underlying noise realisations (which can be seen exactly in the unwhitened white noise plot). Since the PSDs of the on-source and off-source data are nearly identical for the simulated cases, the whitening procedure is almost perfect and reverts it nearly perfectly to its white state. If anything, this similarity boosts confidence that our custom whitening procedure is operating as expected.

For our baseline training dataset used in this section, we will employ a real-noise background. An argument can be made that it is an obvious choice — because it is real noise, it contains the full spectrum of noise features that might be present in a real observing run, even if it does not contain the particular peculiarities of any given future observing run in which we may wish to deploy developed models.

In each case, we will acquire two seconds of data at a sample rate of 2048.0 Hz, which includes 0.5 s of data on either side of the time series, which will be cropped after whitening. The whitening is performed similarly in all cases in order to ensure symmetry when comparing obfuscation methods. A power-of-two value is used as it simplifies many of the mathematical operations that need to be performed during signal and injection processing, which may, in some cases, improve performance, as well as help to avoid edge cases that may arise from odd numbers. This frequency was selected as its Nyquist frequency of 1024.0 Hz will encompass nearly the entirety of the frequency content of BBH signals; it also covers a large portion of the search space of proposed transient burst sources. The duration of 1.0 s is a relatively arbitrary choice; however, it is one that is often the choice for similar examples found in the literature [53,52], which makes comparison easier. It also encompasses the majority of the signal power of BBH waves [15], as well as the theoretically detectable length of many burst sources [18]. For each on-source noise example gathered or generated, 16.0 s of off-source background noise is also acquired to use for the whitening procedure; see Section 4.2.7.

In the case where multiple detectors are being used simultaneously during training or inference, such as coherence detection, noise is generated independently for each interferometer using the same methods, with the restriction that noise acquired from real interferometer data is sampled from each detector within a common time window of 2048.0 s so that the noise all originates from a consistent time and date. This is done as there are periodic non-stationary noise features that repeat in daily, weekly, and yearly cycles due to weather, environmental conditions, and human activity [17]. When validating methods, we want to make our validation data as close as possible to reality whilst maintaining the ability to generate large datasets. As we are only ever training our method to operate in real noise conditions (which our validation data attempts to mimic), there is no need to deviate from this method of acquiring noise for our training datasets.

4.2.3 Waveform Generation

Once the background noise has been acquired or generated, the next step is to introduce some differentiation between our two classes, i.e. we need to add a transient signal into some of our noise examples so that our model can find purpose in its existence. When we add a transient into background noise that was not there naturally, we call this an **injection**, since we are artificially injecting a signal into the noise. This injection can be a transient of any type.

Typically, this injection is artificially simulated both due to the limited [30–32] (or non-existent [18,20,21]) number of real examples in many cases and because we will only be able to obtain the real signal through the lens of an interferometer, meaning it will be masked by existing real detector noise. If we were to inject a real injection into some other noise realisation, we would either have to perform a denoising operation (which, even when possible, would add distortion to the true signal) or inject the injection plus existing real noise into the new noise, effectively doubling the present noise and making injection scaling a difficult task. Using artificial examples also allows us granular control of the parameters of each waveform, which can be useful when designing training datasets and when evaluating our model in different areas of parameter space. Thus, we will be using simulated injections to generate our training, testing, and validation datasets. This is not unprecedented, most other gravitational-wave detection and parameter estimation methods rely on simulated signals for their operation, including matched filtering [50].

Luckily, there is a well-developed field of research into modelling gravitational-wave waveforms. These models are known as “approximants”, so named because they only approximate real gravitational-wave signals [51]. As well as providing valuable insights into general relativity and the behaviour of CBCs in and of themselves [212], approximants are used in both detection and parameter estimation pipelines [50]. In our case, approximants can be injected into simulated or real noise to generate artificial examples of interferometer data that contain gravitational-wave signals. Depending on the complexity and accuracies of the chosen approximant and the source parameter range you are investigating, there will be some level of mismatch between any approximant and the real waveform it is attempting to simulate, even when using state-of-the-art approximants [213].

To simulate BBH waveforms, we will be using a version of the IMRPhenomD approximant [51], which has been adapted from LAL Simualtion’s [214] implementation to run on GPUs using NVIDIA’s CUDA GPU library. We name this adapted waveform library cuPhenom [48] for consistency with other CUDA libraries such as cuFFT [215]. IMRPhenomD has adjustable parameters that can be altered to generate BBHs across a considerable parameter space, although it should be noted that it does not simulate eccentricity, non-aligned spins, or higher modes. IMRPhenomD was calibrated for systems up to a mass ratio of 1:18 and spins up to $\frac{a}{m} \sim 0.85$, so we must be careful not to leave this parameter space when generating examples for our training dataset. Although IMRPhenomD was first published in 2015 [51], and newer approximants now exist, it remains accurate enough for most detection and parameter estimation tasks and will only suffer from significant mismatch at the edges of its parameter space or potentially if encountering systems that have any of the aforementioned features that IMRPhenomD does not attempt to model. This is still an ongoing area of research and the exact effect of these features on detection and parameter estimation pipelines is still being investigated [216–218]. Since we have yet to detect any of these effects with a high degree of certainty, it is thought they are either rare and/or minimal enough not to affect most current searches given contemporary detector sensitivity. That being said, the search for the presence of these features is an exciting area of research that could, in time, reveal promising incites both into the sources themselves and the astrophysical conditions that lead to their creation.

The IMRPhenomD [51] approximant generates a waveform by simulating the Inspiral, Merger, and Ringdown regions of the waveform, hence the IMR in the approximant name. The waveform is generated in the frequency domain since we are working in the time domain, we must transform the signal into the time domain before we inject it into our noise segments. The inspiral is generated using post-Newtonian expressions, and the merger ringdown is generated with a phenomenological ansatz; both parts of the model were empirically tuned using a small bank of numerical relativity waveforms. Detailed investigation of approximant generation was out of the scope of this thesis and will not be covered. See Figure 4.4 for examples of waveforms generated using cuPhenom [48]

The increased performance of cuPhenom is significant and speeds up the training and iteration process of models considerably [48]. Because of cuPhenom’s ability to generate injections on the fly during the training process without significant slowdown, it allows for very quick alteration of dataset parameters for training adjustments. It was felt that this advantage outweighed any gains that would be achieved by using newer waveform models that had not yet been adapted to the GPU, as it seems unlikely, especially in the detection case, that the newer waveform models would make for a significantly harder problem for the model to solve. This statement is, however, only an assumption, and it would be recommended that an investigation is carried out to compare the differences between approximants before any of the methods are used in a real application. A final retraining with these more accurate models would be recommended, in any case.

In the case of unmodelled burst detection, the accuracy of the signal shape is not as fundamental, as the ground truth shapes are not known and, for some proposed events, cover a very large shape space [219]. In order to cover the entire search space, GWFlow uses artificially generated White Noise Bursts (WNBs) generated on the GPU via a simple custom Python [63] function utilising TensorFlow [65]. The procedure for generating WNBs with randomised duration and frequency content is as follows.

1. A maximum waveform duration is decided; typically, this would be less or equal to the duration of the example noise that you are injecting the waveform into, with some room for cropping.
2. Arrays of durations, minimum frequencies, and maximum frequencies are generated, each with a number of elements, N , equal to the number of waveforms that we wish to generate. These arrays can be pulled from any distribution as long as they follow the following rules. Duration cannot be larger than our maximum requested duration or less than zero. The frequency bounds cannot be less than zero or greater than the Nyquist frequency.
3. It is enforced that the maximum frequency is greater than the minimum frequency for any waveform by swapping values where this is not the case.
4. Gaussian white noise is generated with as many samples, which, given the selected sample rate, will produce a time series with the same duration as our requested max waveform duration.
5. A number of samples at the end of each waveform are zeroed so that each waveform has a number of samples equivalent to the randomised duration assigned to that signal.
6. Each waveform is transformed into the frequency domain by a RFFT.
7. Samples are zeroed at each end of each frequency-domain signal in order to perform a bandpass and limit the waveform between the assigned frequency constraints for each waveform.
8. The remaining signal is windowed using a Hann window to reduce the effects of the discontinuities generated by the bandpass operation.
9. The frequency domain signal is then returned to the time domain via a IRFFT.
10. Finally, the time-domain waveform is enveloped by a sigmoid window.
11. Assuming the plus polarisation component of the waveform strain was generated first, repeat with the same parameters but different initial noise distributions for the cross polarisation component.

Because we have used random noise across a range of frequency spaces, our distribution will, in theory, cover all possible signals within the specified parameter range. These WNBs can generate waveforms that look qualitatively similar to many proposed burst sources, including current supernovae simulations; see Figure 4.5. See Figure 4.4 for examples of our WNBs and Listing 4.9 for the code used to generate these waveforms.

```
@tf.function
def generate_white_noise_burst(
    num_waveforms: int,
    sample_rate_hertz: float,
```

```

max_duration_seconds: float,
duration_seconds: tf.Tensor,
min_frequency_hertz: tf.Tensor,
max_frequency_hertz: tf.Tensor
) -> tf.Tensor:

    # Casting
    min_frequency_hertz = tf.cast(min_frequency_hertz, tf.float32)
    max_frequency_hertz = tf.cast(max_frequency_hertz, tf.float32)

    # Convert duration to number of samples
    num_samples_array = tf.cast(sample_rate_hertz * duration_seconds, tf.int32)
    max_num_samples = tf.cast(max_duration_seconds * sample_rate_hertz, tf.int32)

    # Generate Gaussian noise
    gaussian_noise = tf.random.normal([num_waveforms, 2, max_num_samples])

    # Create time mask for valid duration
    mask = tf.sequence_mask(num_samples_array, max_num_samples, dtype=tf.float32)
    mask = tf.reverse(mask, axis=[-1])
    mask = tf.expand_dims(mask, axis=1)

    # Mask the noise
    white_noise_burst = gaussian_noise * mask

    # Window function
    window = tf.signal.hann_window(max_num_samples)
    windowed_noise = white_noise_burst * window

    # Fourier transform
    noise_freq_domain = tf.signal.rfft(windowed_noise)

    # Frequency index limits
    max_num_samples_f = tf.cast(max_num_samples, tf.float32)
    num_bins = max_num_samples_f // 2 + 1
    nyquist_freq = sample_rate_hertz / 2.0

    min_freq_idx = tf.cast(
        tf.round(min_frequency_hertz * num_bins / nyquist_freq), tf.int32)
    max_freq_idx = tf.cast(
        tf.round(max_frequency_hertz * num_bins / nyquist_freq), tf.int32)

    # Create frequency masks using vectorized operations
    total_freq_bins = max_num_samples // 2 + 1
    freq_indices = tf.range(total_freq_bins, dtype=tf.int32)
    freq_indices = tf.expand_dims(freq_indices, 0)
    min_freq_idx = tf.expand_dims(min_freq_idx, -1)
    max_freq_idx = tf.expand_dims(max_freq_idx, -1)
    lower_mask = freq_indices >= min_freq_idx
    upper_mask = freq_indices <= max_freq_idx
    combined_mask = tf.cast(lower_mask & upper_mask, dtype=tf.complex64)
    combined_mask = tf.expand_dims(combined_mask, axis=1)

    # Filter out undesired frequencies
    filtered_noise_freq = noise_freq_domain * combined_mask

```

```

# Inverse Fourier transform
filtered_noise = tf.signal.irfft(filtered_noise_freq)

envelopes = generate_envelopes(num_samples_array, max_num_samples)
envelopes = tf.expand_dims(envelopes, axis=1)

filtered_noise = filtered_noise * envelopes

return filtered_noise

```

Listing 4.9 | Python [63]. TensorFlow [65] graph function to generate the plus and cross polarisations of WNB waveforms; see Section 4.2.3 for a description of the generation method. `num_waveforms` takes an integer value of the number of WNBs we wish to generate. `sample_rate_hertz` defines the sample rate of the data we are working with. `max_duration_seconds` defines the maximum possible duration of any signals within our output data. `duration_seconds`, `min_frequency_hertz`, and `max_frequency_hertz` all accept arrays or in this case TensorFlow tensors, of values with a number of elements equal to `num_waveforms`, each duration. Both polarisations of the WNB are generated with parameters determined by the value of these three arrays at the equivalent index. This method is implemented by the GWFlow pipeline [60].

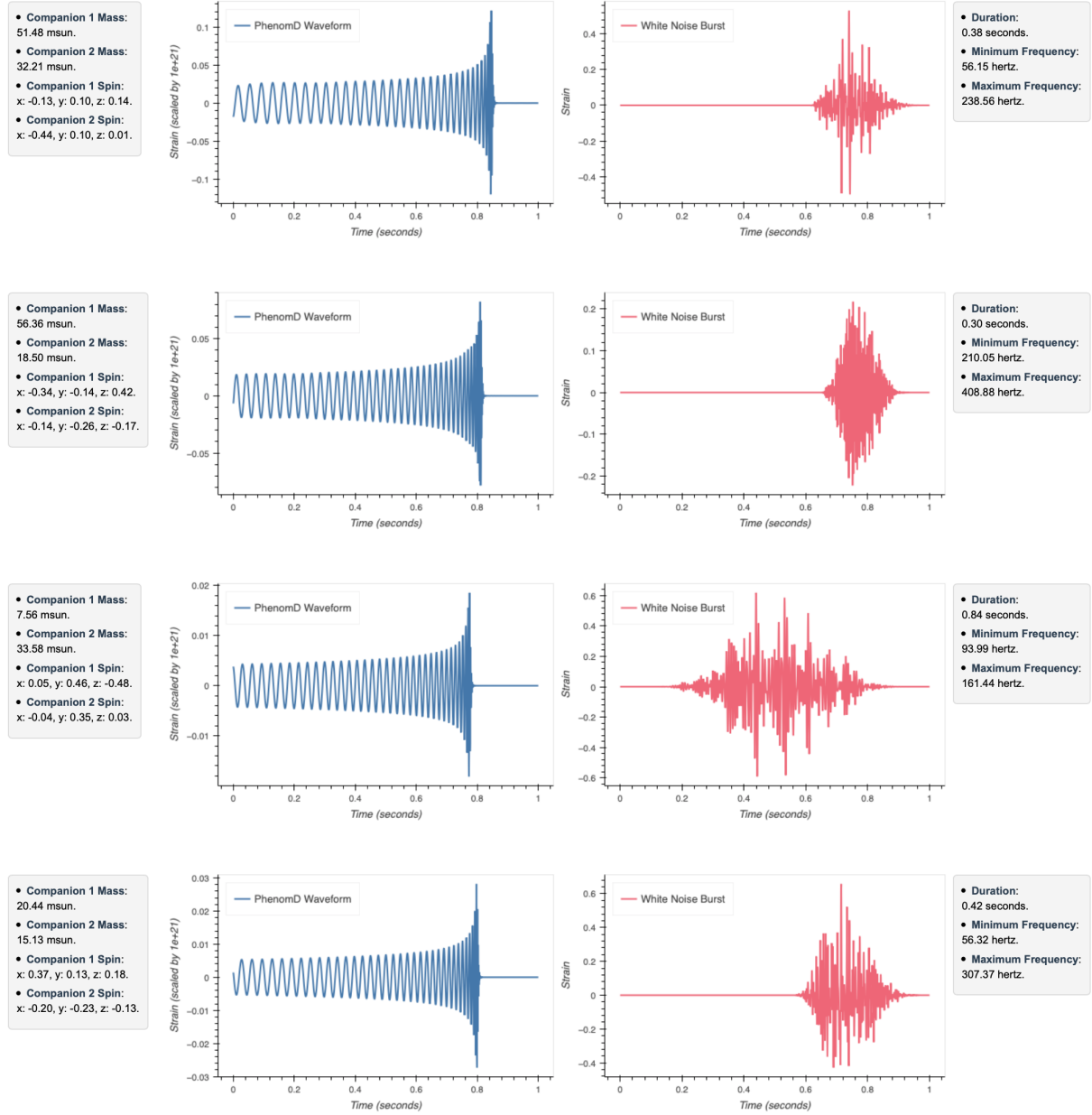


Figure 4.4 | Eight simulated waveforms that could be used for injection into noise to form an obfuscated training, testing, or validation example for an artificial neural network. Note that only the plus polarisation component of the strain, h_+ , has been plotted in order to increase visual clarity. The leftmost four injections are IMRPhenomD waveforms generated using cuPhenom [48], with parameters (shown in the adjacent grey information boxes) drawn from uniform distributions between $5.0 M_\odot$ and $95.0 M_\odot$ for the mass of both companions and between -0.5 and 0.5 for the dimensionless spin component. Note that during injection generation, the two companions are always reordered so that the mass of companion one is greater and that the IMRPhenomD waveform ignores the x and y spin components. They are included just for code completion. The rightmost four injections consist of WNB waveforms generated via the method described in Section 4.2.3. Their parameters are again drawn from uniform distributions and are shown in the grey box to their right. The durations are limited between 0.1 s and 1.0 s, and the frequencies are limited to between 20.0 Hz and 500.0 Hz, with the minimum and maximum frequencies automatically swapped.

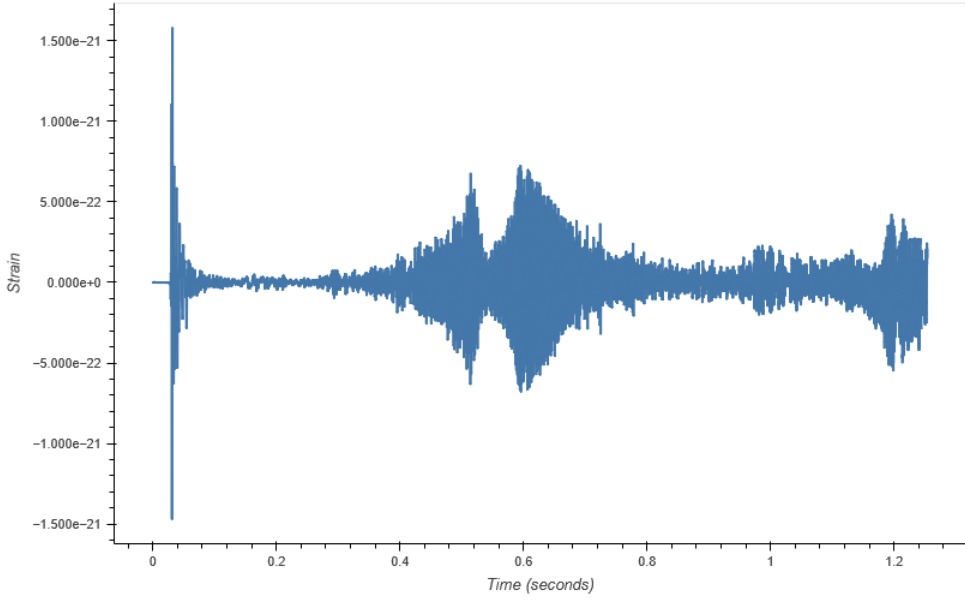


Figure 4.5 | The plus polarisation component of the gravitational-wave strain of a simulated core-collapse supernova at a distance of 10 kpc, this data was taken from [49]. Although some structures can clearly be observed, it is possible to imagine that a method trained to detect WNB signals, such as those presented in Figure 4.4, might be able to detect the presence of such a signal.

4.2.4 Waveform Projection

As has been discussed, gravitational waves have two polarisation states plus, +, and cross, \times , which each have their own associated strain values h_+ and h_\times [220,221]. Since these strain polarisation states can have different morphologies and since the polarisation angle of an incoming signal paired with a given interferometer's response will alter the proportion of each polarisation that is perceptible by the detector, our approximant signals are also generated with two polarisation components. Before being injected into any data, the waveforms must be projected onto each detector in our network in order to simulate what that signal would look like when observed with that detector. This projection will account for the full antenna response of each detector [221]. Since a given interferometer has different sensitivities depending on both the direction of the source and the polarisation angle of the incoming wave, some waves will be entirely undetectable in a given detector.

If we want accurate data when simulating multi-interferometer examples, we must account for both the polarisation angle and direction of the source so that the relative strain amplitudes and morphologies in each detector are physically realistic [221].

Since the detectors have a spatial separation, there will usually, depending on source direction, also be a difference in the arrival time of the waves at the different detectors [221] — this discrepancy is especially important for localising sources, as it provides the possibility for source triangulation, which, along with the antenna responses of each detector, can be used to generate a probability map displaying the probability that a wave originated from a given region of the sky. In coherence detection methods, it also allows for the exclusion of multi-interferometer detections if the detections arise with an arrival time difference greater than that which is physically possible based on the spatial separation of the detectors.

None of this is essential when dealing with single detector examples — in those cases, we could choose to forgo projection entirely and inject one of the strain polarisation components directly into the obfuscating noise as there are no time separations to model accurately and signal proportionality between detectors is also irrelevant.

The projection from both the antenna response parameters and the arrival time delay are dependent on the source direction [221]. The plane of the wavefront and the direction of travel of the wave are dependent on the direction of the source. Since the sources are all extremely distant, the wavefront is considered a flat plane. Waves have some time duration, so both the time delay and antenna response parameters will change over the course of the incoming wave's duration as the Earth and the detectors move in space. As we are dealing with relatively short transients (< 1.0 s), the change in these factors will be considered negligible and is not included in projection calculations.

Assuming that we ignore the Earth's motion, the final waveform present in a detector is given by

$$h(t) = F_+ h_+(t + \Delta t) + F_\times h_\times(t + \Delta t) \quad 4.6$$

where $h(t)$ is the resultant waveform present in the detector output at time t ; F_+ and F_\times are the detector antenna response parameters in the plus and cross polarisations for a given source direction, polarisation angle, and detector; h_+ and h_\times are the plus and cross polarisations of the gravitational-wave strain of simulated or real gravitational waves; and Δt is the arrival time delay taken from a common reference point, often another detector or the Earth's centre.

We can also calculate the relative times that the signals will arrive at a given detector,

$$\Delta t = \frac{(\vec{x}_0 - \vec{x}_d)}{c} \cdot \vec{m} \quad 4.7$$

where Δt is the time difference between the wave's arrival at location \vec{x}_d and \vec{x}_0 , c is the speed of light, \vec{x}_0 is some reference location, often taken as the Earth's centre, \vec{x}_d is the location for which you are calculating the time delay, in our case, one of our interferometers, and \vec{m} is the direction of the gravitational-wave source. If we work in Earth-centred coordinates and take the Earth's centre as the reference position so that $x_0 = [0.0, 0.0, 0.0]$ we can simplify Equation 4.7 to

$$\Delta t = -\frac{\vec{x}}{c} \cdot \vec{m}. \quad 4.8$$

Finally, combining Equation 4.6 and Equation 4.8, we arrive at

$$h(t) = F_+ h_+ \left(t - \frac{\vec{x}}{c} \cdot \vec{m} \right) + F_\times h_\times \left(t - \frac{\vec{x}}{c} \cdot \vec{m} \right). \quad 4.9$$

In practice, for our case of discretely sampled data, we first calculate the effect of the antenna response in each detector and then perform a heterodyne shift to each projection to account for the arrival time differences. When multiple detector outputs are required for training, testing, or validation examples, GWFlow performs these calculations using a GPU-converted version of the PyCBC [50] project_wave function; see Figure 4.6 for example projections.

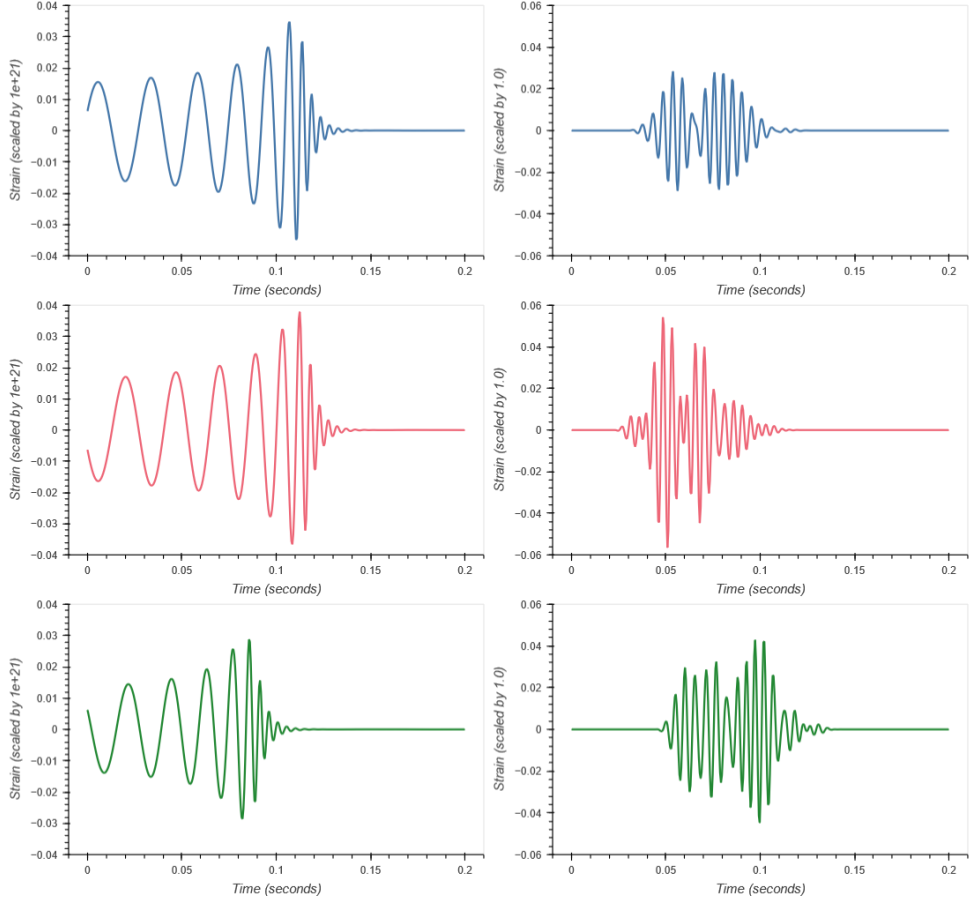


Figure 4.6 | Example projection of two artificial gravitational-wave waveforms. The blue waveforms have been projected into the LIGO Livingston interferometer, the red waveforms have been projected into the Ligo Hanford interferometer, and the green waveforms have been projected into the VIRGO interferometer. The left column displays different projections of an IMRPhenomD waveform generated with the cuPhenom GPU library [48]. The right column displays different projections of a WNB waveform generated with the method described in Section 4.2.3. The projections are performed using a GPU adaptation of the PyCBC Python library’s [50] `project_wave` function. Both waveforms are projected from different source locations; the projection and time displacement are different in each case.

4.2.5 Waveform Scaling

Once waveforms have been projected to the correct proportionality, we must have some method to inject them into obfuscating noise with a useful scaling. If using physically scaled approximants, such as the IMRPhenomD waveform, we could forgo scale by calculating the resultant waveform that would be generated by a CBC at a specified distance from Earth, then injecting this into correctly scaled noise (or simply raw real noise). However, since we are also using non-physical waveforms such as WNBs, and because we would like a more convenient method of adjusting the detectability of our waveforms, we will use a method to scale the waveforms to a desired proportionality with the noise.

Evidently, if we injected waveforms that have been scaled to values near unity into real unscaled interferometer noise (which is typically on the order of 10^{-21}), even a very simple model would not have much of a problem identifying the presence of a feature. Equally, if the reverse were true, no model could see any difference between interferometer data with or without an injection. Thus, we must acquire a method to scale our injections so that their amplitudes have a proportionality with the background noise that is similar to what might be expected from real interferometer data.

Real data holds a distribution of feature amplitudes, with quieter events appearing in the noise more commonly than louder ones [222,96] — this is because gravitational-wave amplitude scales inversely with distance [96,5], whereas the volume of searchable space, and thus matter and, generally, the number of systems which can produce gravitational waves, scale cubically with distance from Earth.

Features with quieter amplitudes will, in general, be harder for a given detection method to identify than features with louder amplitudes. We must design a training dataset that contains a curriculum that maximises model efficacy across our desired regime, with examples that are difficult but never impossible to classify and perhaps some easier cases that can carve channels through the model parameters, which can be used to direct the training of more difficult examples.

In any given noise distribution, there will, for any desired false alarm rate, be a minimum detectable amplitude below which it becomes statistically impossible to make any meaningful detections [223]. This minimum amplitude occurs because even white Gaussian noise will occasionally produce data that looks indistinguishable from a certain amplitude of waveform.

We can use matched filtering statistics to prove this point, as we know that given an exactly known waveform morphology and perfect Gaussian noise, matched filtering is the optimal detection statistic [223]. The probability that a matched filtering search of one template produces a false alarm is dependent only on the rate at which you are willing to miss true positives. We can use the \mathcal{F} -statistic, \mathcal{F}_0 , for our probability metric to adjust this rate. Assuming that the noise is purely Gaussian, and we are only searching for one specific template, the probability of false detections of this exact waveform, i.e. $P(\mathcal{F} > \mathcal{F}_0)$, can be expressed as

$$P_F(\mathcal{F}_0) = \int_{\mathcal{F}_0}^{\infty} p_0(\mathcal{F}) d\mathcal{F} = \exp(-\mathcal{F}_0) \sum_{k=0}^{\frac{n}{2}-1} \frac{\mathcal{F}_0^k}{k!} \quad 4.10$$

where n is the number of degrees of freedom of χ^2 distributions. We can see from Equation 4.10 that the False Alarm Rate (FAR) in this simple matched filtering search is only dependent on the arbitrary choice of \mathcal{F}_0 . However, in practice, the choice of \mathcal{F}_0 will be determined by the minimum amplitude waveform you wish to detect because the probability of detection, P_d given the presence of a waveform, is dependent on the optimal SNR, ρ_{opt} of that waveform, ρ , which has a loose relationship to the amplitude of the waveform. The probability of detection is given by

$$P_D(\rho, \mathcal{F}_0) = \int_{\mathcal{F}_0}^{\infty} \frac{(2\mathcal{F})^{\frac{n}{2}-1}}{\rho^{\frac{n}{2}-1}} I_{\frac{n}{2}-1}(\rho\sqrt{2\mathcal{F}}) \exp\left(-\mathcal{F} - \frac{1}{2}\rho^2\right) d\mathcal{F} \quad 4.11$$

where $I_{\frac{n}{2}-1}$ is the modified Bessel function of the first kind and order $\frac{n}{2} - 1$. For more information on this, please refer to [223].

More complex types of noise, however, like real LIGO interferometer noise, could potentially produce waveform simulacra more often than artificially generated white noise [17].

Louder false alarms are less likely than quieter ones, and at a certain amplitude, a given detection method will start producing a greater number of false alarms than the desired false alarm rate. If our training dataset includes waveforms with an amplitude that would trigger detections with a false alarm rate near or less than our desired rate, this could significantly reduce the performance of our network [224], so we must select a minimum amplitude that maximises our detection efficiency at a given false alarm rate.

Our minimum possible detection amplitude is limited by the combination of the noise and the false alarm rate we desire. There is not a maximum possible signal amplitude, other than some very un-

useful upper bound on the closest possible gravitational-wave-producing systems to Earth (a nearby supernova or CBC, for example), but these kinds of upper limit events are so astronomically rare as not to be worth considering. Events will, however, follow a distribution of amplitudes [96,222]. As is often the case, we can try to generate our training data using a distribution that is as close as possible to the observed data, with the exception of a lower amplitude cutoff [209], or we can instead use a non-realistic distribution, uniformly or perhaps Gaussianly distributed across some amplitude regime which contains the majority of real signals — making the assumption that any detection methods we train using this dataset will generalise to higher amplitudes, or failing that, that the missed signals will be so loud that they would not benefit greatly from improved detection methods.

Thus far in this subsection, we have been talking rather nebulously about waveform “amplitude”, as if that is an easy thing to define in a signal composed of many continuous frequency components. There are at least three properties we might desire from this metric. Firstly, magnitude, some measure of the energy contained by the gravitational wave as it passes through Earth — this measure contains a lot of physical information about the gravitational wave source. Secondly, significance, given the circumstances surrounding the signal, we may want to measure how likely the signal is to have been astrophysical rather than terrestrial, and finally, closely related to the significance and perhaps most importantly when designing a dataset for artificial neural network training, the detectability, given a chosen detection method this would act as a measure of how easy it is for that method to detect the signal.

Naively, one might assume that simply using the maximum amplitude of the strain, h_{peak} , would be a good measure, and indeed, this would act as a very approximate measure of the ease of detection — but it is not a complete one. Consider, for a moment, a sine-Gaussian with an extremely short duration on the order of tens of milliseconds but a maximum amplitude that is only slightly louder than a multi-second long BNS signal [19]. You can imagine from this example that the BNS would be considerably easier to detect, but if you were going by h_{peak} alone, then you would have no idea.

Within gravitational-wave data science, there are nominally two methods for measuring the detectability of a signal — the Root-Sum-Squared strain amplitude [221,225], h_{rss} , and the optimal matched filter Signal Noise Ratio, ρ_{opt} [226,221]. What follows is a brief description of these metrics.

4.2.5.1 The Root-Sum-Squared strain amplitude, h_{rss}

The Root-Sum-Squared strain amplitude, h_{rss} , is a fairly simple measure of detectability [225]. Unlike ρ_{opt} , it is exclusive to gravitational-wave science. It accounts for the power contained across the whole signal by integrating the square of the strain across its duration, essentially finding the area contained by the waveform. It is given by

$$h_{\text{rss}} = \sqrt{\int (h_+(t)^2 + h_\times(t)^2) dt} \quad 4.12$$

or written in its discrete form, which is more relevant for digital data analysis

$$h_{\text{rss}} = \sqrt{\sum_{i=1}^N (h_+[t_i]^2 + h_\times[t_i]^2)} \quad 4.13$$

when h_{rss} is the root-sum-squared strain amplitude, $h_+(t)$ and $h_\times(t)$ are the plus and cross polarisations of the continuous strain, $h_+(t_i)$ and $h_\times(t_i)$ are the plus and cross polarisations of the discrete strain at the i^{th} data sample, and N is the number of samples in the waveform.

It should be noted that with any measure that utilises the strain, such as h_{peak} and h_{rss} , there is some ambiguity concerning where exactly to measure strain. You could, for example, measure the raw strains

h_+ and h_\times before they have been transformed by the appropriate detector antenna response functions, or you could take the strain h after it has been projected onto a given detector. The advantage of the former is that you can fairly compare the magnitude of different gravitational waves independent of information about the interferometer in which it was detected. This is the commonly accepted definition of the h_{rss} .

The h_{rss} is most often used during burst analysis as a measure of the detectability, magnitude, and significance of burst transients. Within CBC detection SNR, ρ_{opt} , is often preferred. Whilst h_{rss} is a simple and convenient measure, it ignores noise, so it cannot by itself tell us if a signal is detectable.

4.2.5.2 Optimal Signal-to-Noise Ratio (SNR) (ρ_{opt})

The optimal Signal-to-Noise Ratio (SNR), ρ_{opt} , solves both of these issues by acting as a measure of detectability, magnitude, and significance in comparison to the background noise. Consequently, because it is relative to the noise, the magnitude of a given waveform can only be compared to the optimal SNR of a waveform that was obfuscated by a similar noise distribution. If a real gravitational-wave signal were detected in a single LIGO detector, say, LIGO Hanford, for example, then its optimal SNR would be significantly larger than the same signal detected only in VIRGO, even if the signal was aligned in each case to the original from the optimally detectable sky location. This is because the sensitivity of the VIRGO detector is substantially lower than the two LIGO detectors [227], so the noise is proportionally louder compared to the waveforms.

It is, however, possibly a good measure of detectability, as detection methods do not much care about the actual magnitude of the signal when they are attempting to analyse one; the only relevant factors, in that case, are the raw data output, consisting of the portion of the gravitational-wave strain perceptible given the detector's antenna response function, see Equation 4.9, and the interferometer noise at that time.

The SNR can also sometimes be an ambiguous measurement, as there are multiple different metrics that are sometimes referred to by this name, most prominently, a ratio between the expected value of the signal and the expected value of the noise, or sometimes the ratio between the root mean square of the signal and noise. Within gravitational-wave data science, though there is sometimes confusion over the matter, the commonly used definition for SNR is the matched filter SNR, ρ_{opt} [226]. Since matched filtering is the optimal method for detecting a known signal in stationary Gaussian noise [226], we can use the result of a matched filter of our known signal with that signal plus noise as a measure of the detectability of the signal in a given noise distribution.

The optimal SNR, ρ_{opt} , is given by

$$\rho_{\text{opt}} = \sqrt{4 \int_0^\infty \frac{|\tilde{h}(f)|^2}{S(f)} df} \quad 4.14$$

where ρ_{opt} is the optimal SNR, $S(f)$ is the one sided PSD, and

$$\tilde{h}(f) = \int_{-\infty}^{\infty} h(x) e^{-i2\pi f t} dt \quad 4.15$$

is the Fourier transform of $h(f)$. The coefficient of 4 is applied since, in order to use only the one-sided transform, we assume that $S(f) = S(-f)$, which is valid because the input time series is entirely real. This applies a factor of two to the output, and since we are only integrating between 0 and ∞ rather than $-\infty$ to ∞ , we apply a further factor of 2.

Because, again, for data analysis purposes, the discrete calculation is more useful, the ρ_{opt} of discrete data is given by

$$\rho_{\text{opt}} = \sqrt{4 \sum_{k=1}^{N-1} \frac{|\tilde{h}[f_k]|^2}{S(f_k)}} \quad 4.16$$

where N is the number of samples, and, in this case, the discrete Fourier transform $\tilde{h}[f]$ is given by

$$\tilde{h}[f_k] = \sum_{i=1}^{N-1} h[t_i] e^{-\frac{2\pi}{N} k i} \quad 4.17$$

For the work during this thesis, we have added a TensorFlow [65] implementation for calculating the ρ_{opt} to GWFlow [60]. This implementation is shown in Listing 4.10.

```
@tf.function
def calculate_snr(
    injection: tf.Tensor,
    background: tf.Tensor,
    sample_rate_hertz: float,
    fft_duration_seconds: float = 4.0,
    overlap_duration_seconds: float = 2.0,
    lower_frequency_cutoff: float = 20.0,
) -> tf.Tensor:

    injection_num_samples      = injection.shape[-1]
    injection_duration_seconds = injection_num_samples / sample_rate_hertz

    # Check if input is 1D or 2D
    is_1d = len(injection.shape) == 1
    if is_1d:
        # If 1D, add an extra dimension
        injection = tf.expand_dims(injection, axis=0)
        background = tf.expand_dims(background, axis=0)

    overlap_num_samples = int(sample_rate_hertz * overlap_duration_seconds)
    fft_num_samples     = int(sample_rate_hertz * fft_duration_seconds)

    # Set the frequency integration limits
    upper_frequency_cutoff = int(sample_rate_hertz / 2.0)

    # Calculate and normalize the Fourier transform of the signal
    inj_fft = tf.signal.rfft(injection) / sample_rate_hertz
    df = 1.0 / injection_duration_seconds
    fsamples = \
        tf.range(0, (injection_num_samples // 2 + 1), dtype=tf.float32) * df

    # Get rid of DC
    inj_fft_no_dc  = inj_fft[:, 1:]
    fsamples_no_dc = fsamples[1:]

    # Calculate PSD of the background noise
    freqs, psd = \
        calculate_psd(
            background,
            sample_rate_hertz = sample_rate_hertz,
            nperseg           = fft_num_samples,
            noverlap          = overlap_num_samples,
```

```

        mode="mean"
    )

# Interpolate ASD to match the length of the original signal
freqs = tf.cast(freqs, tf.float32)
psd_interp = \
    tfp.math.interp_regular_1d_grid(
        fsamples_no_dc, freqs[0], freqs[-1], psd, axis=-1
    )

# Compute the frequency window for SNR calculation
start_freq_num_samples = \
    find_closest(fsamples_no_dc, lower_frequency_cutoff)
end_freq_num_samples = \
    find_closest(fsamples_no_dc, upper_frequency_cutoff)

# Compute the SNR numerator in the frequency window
inj_fft_squared = tf.abs(inj_fft_no_dc*tf.math.conj(inj_fft_no_dc))

snr_numerator = \
    inj_fft_squared[:,start_freq_num_samples:end_freq_num_samples]

if len(injection.shape) == 2:
    # Use the interpolated ASD in the frequency window for SNR calculation
    snr_denominator = psd_interp[:,start_freq_num_samples:end_freq_num_samples]
elif len(injection.shape) == 3:
    snr_denominator = psd_interp[:, :, start_freq_num_samples:end_freq_num_samples]

# Calculate the SNR
SNR = tf.math.sqrt(
    (4.0 / injection_duration_seconds)
    * tf.reduce_sum(snr_numerator / snr_denominator, axis = -1)
)

SNR = tf.where(tf.math.is_inf(SNR), 0.0, SNR)

# If input was 1D, return 1D
if is_1d:
    SNR = SNR[0]

return SNR

```

Listing 4.10 | Python [63]. The GWFlow TensorFlow [65] graph function to calculate the optimal SNR, ρ_{opt} , of a signal. `injection` is the input signal as a TensorFlow tensor, `background` is the noise into which the waveform is being injected, `sample_rate_hertz` is the sample rate of both the signal and the background, `fft_duration_seconds` is the duration of the FFT window used in the PSD calculation, `overlap_duration_seconds` is the duration of the overlap of the FFT window in the PSD calculation, and `lower_frequency_cutoff` is the frequency of the lowpass filter, below which the frequency elements are silenced.

Once the optimal SNR or h_{rss} of an injection has been calculated, it is trivial to scale that injection to any desired optimal SNR or h_{rss} value. Since both metrics scale linearly when the same coefficient scales each sample in the injection,

$$h_{\text{scaled}} = h_{\text{unscaled}} \frac{M_{\text{desired}}}{M_{\text{current}}} \quad 4.18$$

where h_{scaled} is the injection strain after scaling, h_{unscaled} is the injection strain before scaling, M_{desired} is the desired metric value, e.g. h_{rss} , or ρ_{opt} , and M_{current} is the current metric value, again either h_{rss} , or ρ_{opt} . Note that since h_{rss} and ρ_{opt} are calculated using different representations of the strain, h_{rss} before projection into a detector, and ρ_{opt} after, the order of operations will be different depending on the scaling metric of choice, ie. for h_{rss} : scale \rightarrow project, and for ρ_{opt} : project \rightarrow scale.

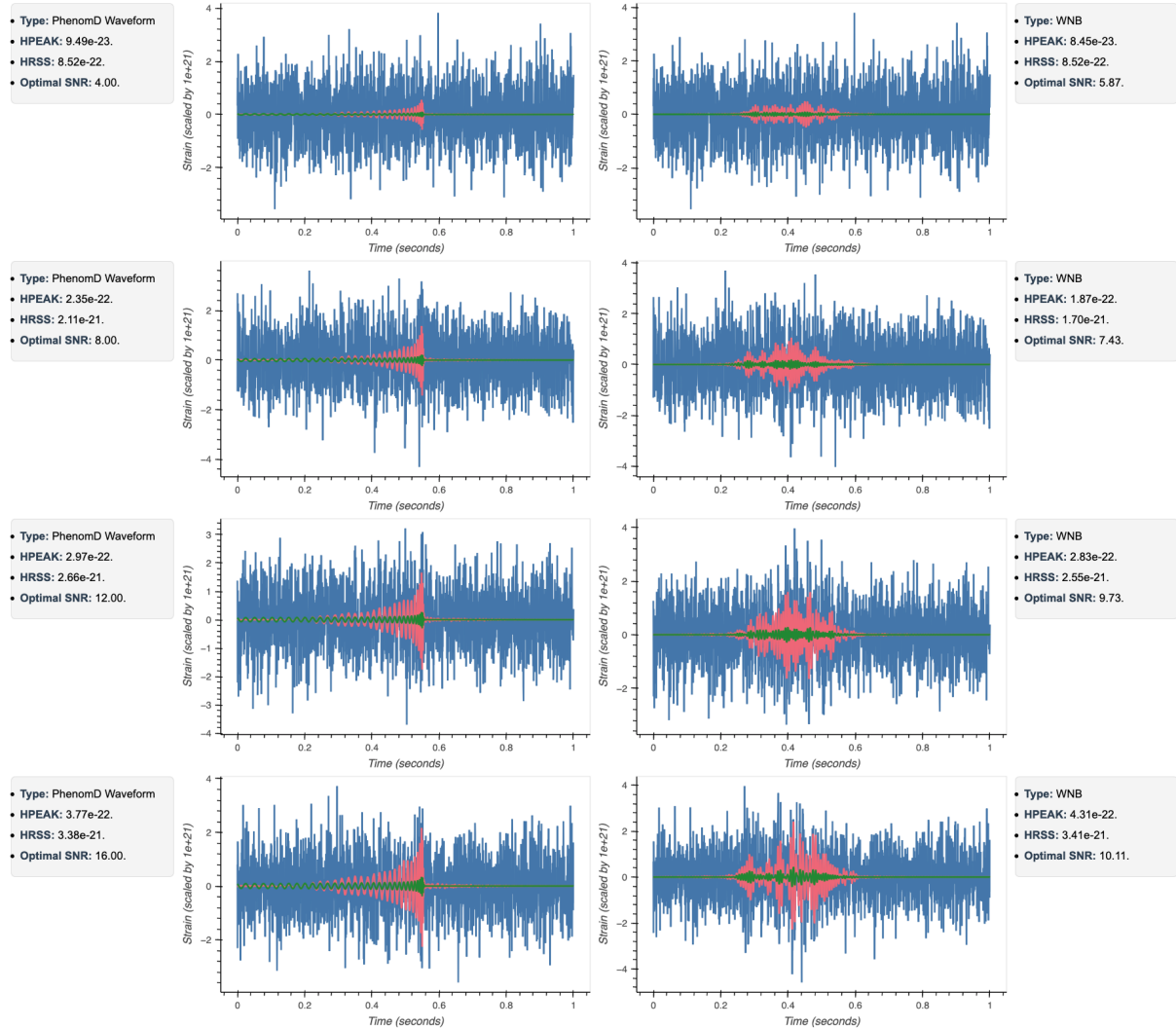


Figure 4.7 | Eight examples of artificial injections scaled to a particular scaling metric and added to a real noise background to show variance between different scaling methods. The blue line demonstrates the whitened background noise plus injection; the red line represents the injection after being run through the same whitening transform as the noise plus injection, and the green line represents the injection after scaling to the desired metric. The leftmost column contains an IMRPhenomD waveform, generated using [48], injected into a selection of various background noise segments and scaled using SNR; see Section 4.2.5.2. From upper to lower, the SNR values are 4, 8, 12, and 16, respectively. The rightmost column displays a WNB injected into various noise distributions, this time scaled using h_{rss} ;

see Section 4.2.5.1. From upper to lower, the h_{rss} values are as follows: 8.52×10^{-22} , 1.70×10^{-21} , 2.55×10^{-21} , and 3.41×10^{-21} . As can be seen, though both sequences are increasing in linear steps with a uniform spacing of their respective metrics, they do not keep in step with each other, meaning that if we double the optimal SNR of a signal, the h_{rss} does not necessarily also double.

For the experiments performed later in this section, we will use SNR as our scaling metric drawn from a uniform distribution with a lower cutoff of 8 and an upper cutoff of 20. These values are rough estimates of a desirable distribution given the SNR values of previous CBC detections.

If we wish to utilise multiple detectors simultaneously as our model input, we can scale the injections using either the network SNR or the h_{rss} before projection into the detectors. In the case of h_{rss} , the scaling method is identical, performed before detection and injection. Network SNR is computed by summing individual detector SNRs in quadrature [96], as shown by

$$\rho_{\text{network}} = \sqrt{\sum_{i=1}^N \rho_i^2} \quad 4.19$$

where ρ_{network} is the network SNR, N is the total number of detectors included in the input, and ρ_i is the detector SNR of the i^{th} detector given in each case by Equation 4.16. To scale to the network, SNR Equation 4.18 can still be used, with the network SNR of Equation 4.19 as the scaling metric, by multiplying the resultant projected injection in each detector by the scaling coefficient.

4.2.6 Data Dimensionality and Layout

Interferometer output data is reasonably different from the example MNIST data [12] we have been using to train models thus far, the primary difference being that it is one-dimensional rather than two, being more similar to audio than image data. In fact, most of the features we are looking for within the data have a frequency that, when converted to sound, would be audible to the human ear [228], so it is often useful to think of the problem in terms of audio classification. In many ways, this reduced dimensionality is a simplification of the image case. In pure dense networks, for example, we no longer have to flatten the data before feeding it into the model; see Section 3.4.

There are, however, multiple interferometers across the world. During an observing run, at any given time, there are anywhere between zero to five operational detectors online: LIGO Livingston (L1), LIGO Hanford (H1), Virgo (V1), Kagra (K1), and GEO600 (G1) [8] (although as of this thesis, there has yet been a time when all five detectors were online). GEO600 is not considered sensitive enough to detect any signals other than ones that would have to be so local as to be rare enough to dismiss the probability, so it is usually not considered for such analysis [229]. It should also be noted that during O4, both Virgo and Kagra are currently operating with a sensitivity and up-time frequency that makes it unlikely they will be of much assistance for detection [230]. It is hoped that the situation at these detectors will improve for future observing runs. Even with just the two LIGO interferometers, it is possible to include multiple detectors within our model input, and in fact, such a thing is necessary for coherence detection to be possible [23,22].

This multiplicity brings some complications in the construction of the input examples. Currently, we have only seen models that ignore the input dimensionality; however, with other network architectures, such as Convolutional Neural Networks (CNNs), this is not always the case [10]. Therefore, we must consider the data layout. In the simplest cases, where we are not modifying the shape of the data before injection, we can imagine three ways to arrange the arrays; see Figure 4.8 for a visual representation.

- **Lengthwise:** wherein the multiple detectors are concatenated end to end, increasing the length of the input array by a factor equal to the number of detectors. This would evidently still be a 1D problem, just an extended one. While perhaps this is the simplest treatment, we can imagine that this might perhaps be the hardest to interpret by the model, as we are mostly discarding the dimensionality, although no information is technically lost.
- **Depthwise:** Here, the detectors are stacked in the depth dimension, an extra dimension that is not counted toward the dimensionality of the problem, as it is a required axis for the implementation of CNNs, in which each slice represents a different feature map; see Section 4.4. Often, this is how colour images are injected by CNNs, with the red, green, and blue channels each taking up a feature map. This would seem an appropriate arrangement for the detectors. However, there is one significant difference between the case of the three-colour image and the stacked detectors, that being the difference in signal arrival time between detectors; this means that the signal will be offset in each channel. It is not intuitively clear how this will affect model performance, so this will have to be empirically compared to the other two layouts.
- **Heightwise:** The last possible data layout that could be envisioned is to increase the problem from a 1D problem to a 2D one. By concatenating the arrays along their height dimension, the 1D array can be increased to a 2D array.

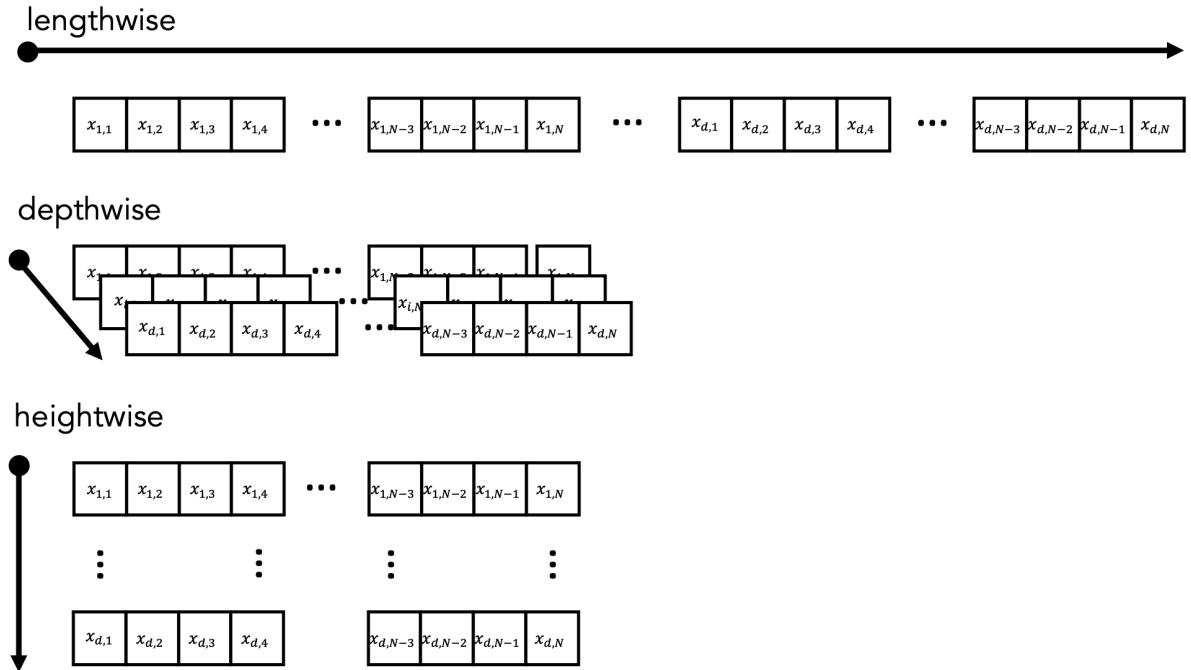


Figure 4.8 | Possible data layouts for multi-detector examples. Here, d is the number of included detectors, and N is the number of input elements per time series. There are three possible ways to align interferometer time-series data from multiple detectors. These layouts are discussed in more detail in Section 4.2.6.

For pattern-matching methods, like that which is possible in the CBC case, there are also advantages to treating each detector independently. If we do this, we can use the results from each model as independent statistics, which can then be combined to create a result with a far superior False Alarm Rate (FAR) [231]. We could combine the score from both models and calculate a false alarm rate empirically using this combined score, or use each detector as a boolean output indicating the presence of a detector or not, and combine the FARs using Equation 4.21.

For the first case treating the two models as one, the combined score is calculated by

$$S_{\text{comb}} = \prod_{i=1}^N S_i \quad 4.20$$

where S_{comb} is the combined classification score, which can be treated approximately as a probability if the output layer uses a softmax, or single sigmoid, activation function, see Section 3.1.5.4, S_i is the output score of the i^{th} classifier input with the data from the i^{th} detector, and N is the number of included detectors. Note that one could employ a uniquely trained and/or designed model for each detector or use the same model for each detector.

In the second case, treating each model as an independent boolean statistic and assuming that the output of the detectors is entirely independent except for any potential signal, the equation for combining FARs is

$$\text{FAR}_{\text{comb}} = (w - o) \prod_{i=1}^N \text{FAR}_i \quad 4.21$$

where FAR_{comb} is the combined FAR, N is the number of included detectors, w is the duration of the input vector, and o is the overlap between windows [231]. This equation works in the case when a detection method tells you a feature has been detected within a certain time window, w , but not the specific time during that window, meaning that $t_{\text{central}} > w_{\text{start}} \wedge t_{\text{central}} < w_{\text{end}}$, where t_{central} is the signal central time, w_{start} is the input vector start time and w_{end} is the input vector end time.

If a detection method can be used to ascertain a more constrained time for a feature ($w_{\text{duration}} < \text{light_travel_time}$), then you can use the light travel time between the two detectors to calculate a FAR [231]. For two detectors, combining the FAR in this way can be achieved by

$$\text{FAR}_{1,2} = 2 \text{FAR}_1 \text{FAR}_2 w_{1,2} \quad 4.22$$

where FAR_{comb} is the combined FAR, and $w_{1,2}$ is the light travel time between detectors 1 and 2, as this is the largest physically possible signal arrival time separation between detectors; gravitational waves travel at the speed of light, and detector arrival time difference is maximised if the direction of travel of the wave is parallel to the straight-line path between the two detectors.

In the case where we are using t_{central} and coincidence times to calculate our combined FAR, if we use overlapping data segments to feed our model, we must first group detections that appear in multiple inferences and find one central time for the detection. We can use an empirical method to determine how best to perform this grouping and identify if and how model sensitivity varies across the input window.

4.2.7 Feature Engineering and Data Conditioning

Invariably, there are data transforms that could be performed prior to ingestion by the model. If there are operations that we imagine might make the task at hand easier for the model, we can perform these transforms to improve network performance. Because we are attempting to present the data to the model in a form that makes the features easier to extract, this method of prior data conditioning is known as **feature engineering** [232]. It should be noted that feature engineering does not necessarily add any extra information to the data. In fact, in many cases, it can reduce the overall information content whilst simultaneously simplifying the function that the model is required to approximate in order to operate as intended [232], see for example the whitening procedure described in Section 4.2.7.2. As we have said before, although the dense neural network with a CAP above two, is, at its limit, a universal function approximator [151], there are practical limitations to finding the right architecture and parameters for a given function, so sometimes simplifying the task can be beneficial. This can

reduce the model size and training time, as well as improve achievable model performance when the time available for model and training optimisation is limited [233].

4.2.7.1 Raw Data

When designing the package of information that will be presented to the network at each inference, the simplest approach would be to feed the raw interferometer data directly into the model. There are certainly some methodologies that consider it optimal to present a model with as much unaltered information as possible [10]. By performing little to no data conditioning, you are allowing the network to find the optimal path to its solution; if all the information is present and an adequate model architecture is instantiated, then a model should be able to approximate the majority of possible conditioning transforms during model training, not only this, but it may be able to find more optimal solutions that you have not thought of, perhaps ones customised to the specific problem at hand, rather than the more general solutions that a human architect is likely to employ. This methodology, however, assumes that you can find this adequate model architecture and have an adequate training procedure and dataset to reach the same endpoint that could be achieved by conditioning the data. This could be a more difficult task than achieving a result that is almost as good with the use of feature engineering.

4.2.7.2 Whitened Data

One type of data conditioning that we will employ is time-series whitening [234]. As we have seen in Section 2.3.3, as well as containing transient glitches, the interferometer background is composed of many different continuous quasi-stationary sources of noise, the frequency distributions of which compose a background that are unevenly distributed across our frequency search space [17]. This leaves us with 1D time series that have noise frequency components with much greater power than any interesting features hidden within the data. This could potentially make detections using most methods, including artificial neural networks, much more difficult, especially when working in the time domain; see Figure 4.9 for an example of the PSD of unwhitened noise.

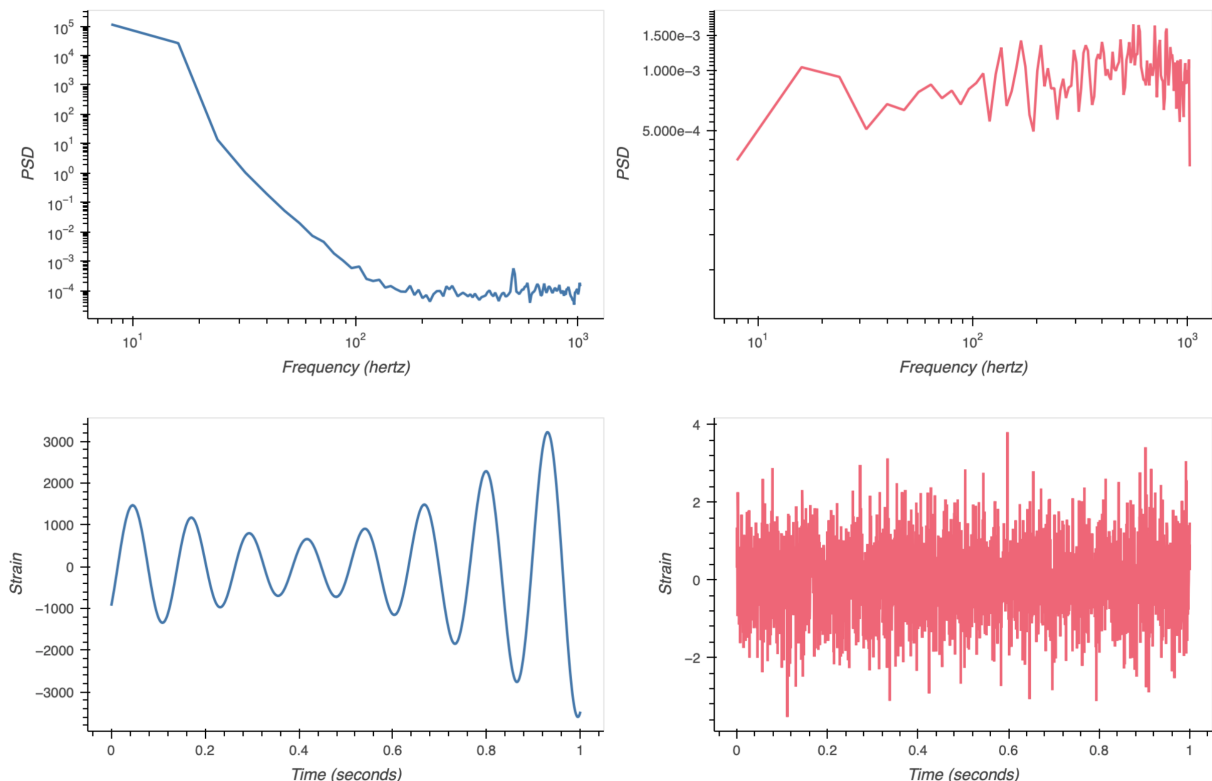


Figure 4.9 | An example of a segment of interferometer data before and after whitening. The two left-most plots in blue show the PSD, *upper*, and raw data, *lower*, output from the LIGO Hanford detector

before any whitening procedure was performed. The two rightmost plots show the same data after the whitening procedure described in Section 4.2.7.2 has been implemented. The data was whitened using the ASD of a 16.0 s off-source window from 16.5 s before the start of the on-source window to 0.5 s before. The 0.5 s gap is introduced as some data must be cropped after whitening due to edge effects caused by windowing. This also acts to ensure that it is less likely that any features in the on-source data contaminate the off-source data, which helps reduce the chance that we inadvertently whiten any interesting features out of the data.

Fortunately, there exists a method to flatten the noise spectrum of a given time series whilst minimising the loss of any transient features that don't exist in the noise spectrum [234]. This requires an estimate of the noise spectrum of the time series in question, which does not contain the hidden feature. In this case, this noise spectrum will take the form of an ASD; see Equation 4.5.

Since the noise spectrum of the interferometer varies with time, a period of noise close to but not overlapping with the section of detector data selected for analysis must be chosen — we call this time series the **off-source** period. The period being analysed, the **on-source** period, is not included in the off-source period so that any potential hidden features that are being searched for, e.g. a CBC signal, do not contribute significant frequency components to the ASD, which may otherwise end up dampening the signal along with the noise during the whitening procedure. It should be noted, then, that whitening via this process uses additional information from the off-source period that is not present in the on-source data. During this thesis, we have elected to use an off-source window duration of 16.0 s, as this was found to be an optimal duration by experiments performed as part of previous work during the development of MLy [28], although it should be noted that we have taken the on-source and crop regions after the off-source as opposed to the initial MLy experiments wherein it was taken at the centre of the off-source window. See Figure 4.10 for a depiction of the relative locations of the on-source and off-source segments.

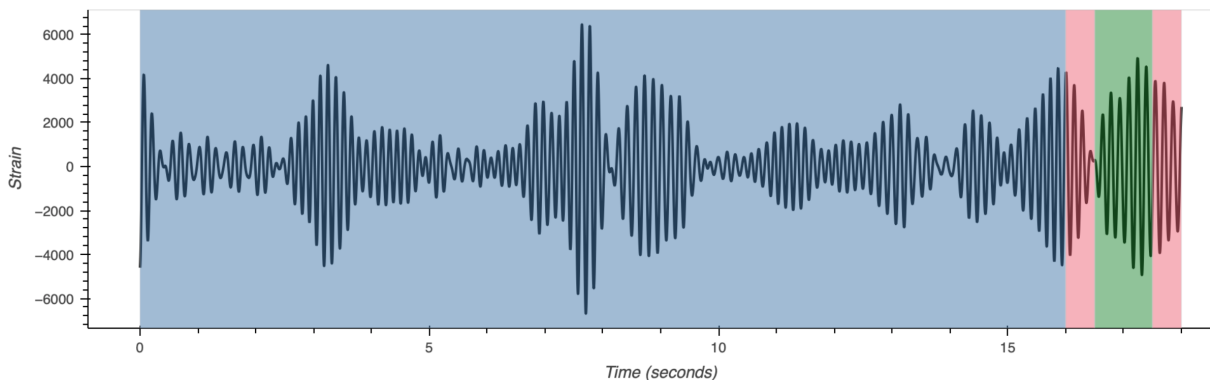


Figure 4.10 | Demonstration of the on-source and off-source regions used to calculate the ASD used during the whitening operations throughout this thesis wherever real noise is utilised. Where artificial noise is used, the off-source and on-source segments are generated independently but with durations equivalent to what is displayed above. The blue region shows the 16.0 s off-source period, the green region shows the 1.0 s on-source period, and the two red regions represent the 0.5 s crop periods, which are removed after whitening. During an online search, the on-source region would advance in second-long steps, or if some overlap was implemented, less than second-long steps, meaning all data would eventually be searched. The leading 0.5 s crop region will introduce an extra 0.5 s of latency to any search pipeline. It may be possible to avoid this latency with alternate whitening methods, but that has not been discussed here.

We can whiten the data by convolving it with a suitably designed Finite Impulse Response (FIR) filter. This procedure is described by the following steps:

1. Calculate the ASD using Equation 4.5, this will act as the transfer function, $G(f)$, for generating the FIR filter. This transfer function is a measure of the frequency response of the noise in our system, and during the whitening process, we will essentially try to normalise the on-source by this off-source noise in order to flatten its PSD. We generate a filter with a 1 s duration.
2. Next, we zero out the low and high-frequency edges of the transfer function with

$$G_{\text{trunc}}(f) = \begin{cases} 0 & \text{if } f \leq f_{\text{corner}} \\ G(f) & \text{if } f_{\text{corner}} < f < f_{\text{Nyquist}} - f_{\text{corner}} \\ 0 & \text{if } f \geq f_{\text{Nyquist}} - f_{\text{corner}} \end{cases}. \quad 4.23$$

This stage discards frequency components which we no longer care about both because these frequencies are outside of the band we are most interested in and because discarding them can improve function stability and performance whilst reducing artifacting.

3. Optionally, we can apply a Planc-taper window to smooth the discontinuities generated by step 2; we will apply this window in all cases. The Planc-taper window has a flat centre with smoothly tapering edges, thus the windowing is only applied as such to remove discontinuities whilst affecting the central region as little as possible.

$$G_{\text{smoothed}}(f) = G_{\text{trunc}}(f) \cdot W(f). \quad 4.24$$

4. Next we compute the inverse Fourier transform of $G_{\text{smoothed}}(f)$ to get the FIR filter, $g(t)$, with

$$g(t) = \frac{1}{2\pi} \int_{-\infty}^{\infty} G_{\text{smoothed}}(f) e^{jft} df. \quad 4.25$$

This creates a time-domain representation of our noise characteristics, which can then be used as a filter to remove similar noise from another time-domain signal. In practice, we utilise an RFFT function to perform this operation on discrete data. As opposed to an FFT, this transform utilises symmetries inherent when transforming from complex to real data in order to halve the computational and memory requirements.

5. Finally, we convolve our FIR filter, $g(t)$, with the data we wish to whiten, $x(t)$,

$$x_{\text{whitened}}(t) = x(t) * g(t) \quad 4.26$$

where $x_{\text{whitened}}(t)$ is the resultant whitened time-series, $x(t)$ is the original unwhitened data, and $g(t)$ is the FIR filter generated from the off-source ASD. This convolution effectively divides the power of the noise at each frequency by the corresponding value in $G(f)$. This flattens the PSD, making the noise uniform across frequencies; see Figure 4.9 for an example of this transform being applied to real interferometer data.

This method was adapted from the GWPy Python library [210] and converted from using NumPy functions [64] to TensorFlow GPU operations [65] in order to work in tandem with the rest of the GWFlow [60] pipeline and allow for rapid whitening during the training process.

4.2.7.3 Pearson Correlation

A method of feature engineering that is employed prominently by the MLy pipeline [28] involves extracting cross-detector correlation using the Pearson correlation [235]. The Pearson correlation is given by

$$r = \frac{N(\sum_{i=0}^N x_i y_i) - (\sum_{i=0}^N x_i)(\sum_{i=0}^N y_i)}{\sqrt{[N \sum_{i=0}^N x_i^2 - (\sum_{i=0}^N x_i)^2] \times [N \sum_{i=0}^N y_i^2 - (\sum_{i=0}^N y_i)^2]}} \quad 4.27$$

where r is the Pearson correlation coefficient, N is the number of data points in each input array, and x_i and y_i are the i^{th} elements of the \vec{x} and \vec{y} arrays respectively [235].

Nominally, this produces one scalar output value given two input vectors, \vec{x} and \vec{y} , of equal length, N . A value of $r = 1$ indicates perfect correlation between the two vectors, whereas a value of $r = -1$ indicates perfect anti-correlation. Finally, a value of $r = 0$ indicates no correlation between the vectors. Note that if one of the vectors is entirely uniform, then the result is undefined.

This calculation assumes that the two vectors are aligned such that the value in x_i corresponds to the value in y_i . If this is not the case, as would happen for interferometer data if there is an arrival time difference (which there will be for most sky locations), then this will be an imperfect measure of correlation, even discarding the obfuscation of the noise. Because, as was discussed previously in Section 4.2.4, we do not know the direction of the source a priori, MLy [28] calculates the correlation for all possible arrival times given the light travel time between the two detectors in question. It uses minimum increments of the sample duration so that no heterodyning is necessary. This is done with the assumption that any difference in arrival time less than the sample duration will have a negligible effect on the correlation. It should be noted that this method is still hampered by the different polarisation projections dependent on the source polarization and by the obfuscating noise. See Figure 4.11 for examples of the rolling Pearson correlation calculated for LIGO Hanford and LIGO Livingston interferometer data.

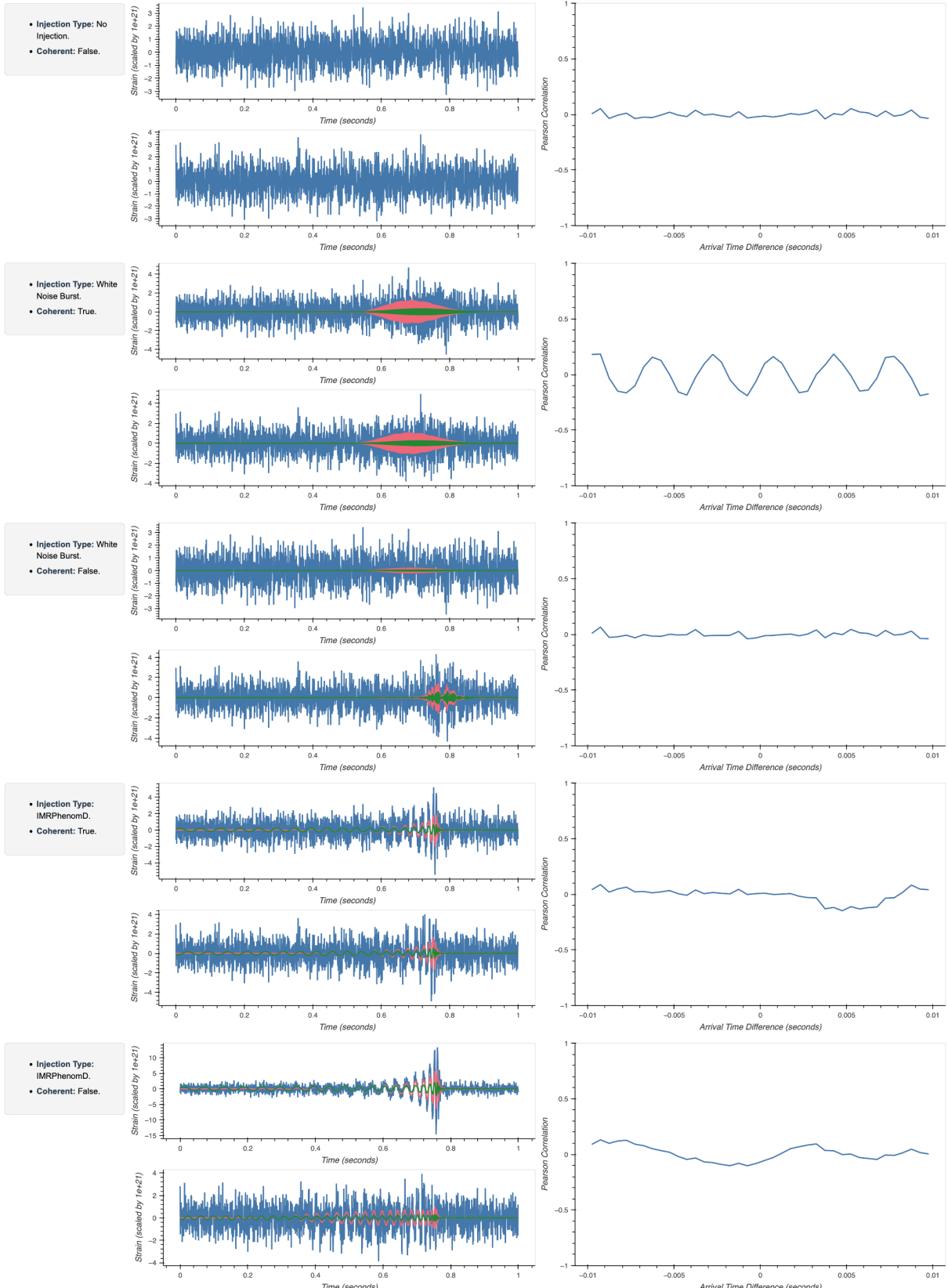


Figure 4.11 | Example whitened on-source and correlation plots of real interferometer noise from a pair of detectors, in this case, LIGO Livingston and LIGO Hanford, with either coherent, incoherent, or no injections added. The leftmost plots adjacent to the info panels are grouped into pairs. In each case, LIGO Livingston is at the top, and LIGO Hanford is underneath. Identical on-source and off-source noise segments are used for each example of the same detector, and noise for each detector

was gathered with a time difference of no more than 2048.0 s. In the leftmost plots, the green series is the unwhitened but projected waveform to be injected into the real noise from that detector. The red series is that same injection but subject to the same whitening procedure that will also be applied to the on-source plus injections, and the blue series is the whitened on-source plus injections. The rightmost plots each correspond to a pair of detectors and display the rolling Pearson correlation values between those two whitened on-source plus injection series. Since there is approximately a max arrival time difference of 0.01 s between LIGO Livingston and LIGO Hanford, the number of correlation calculations performed corresponds to the rounded number of samples required to represent 0.02 s of data at 2048.0 Hz. This number is two times the maximum arrival time difference because the difference could be positive or negative. In this case, that difference comes to 40 samples. All injections have been scaled to an optimal network SNR of 30 using the method described in Section 4.2.5.2. The upper pair of detectors has no injection. As would be expected, the correlation is low regardless of the assumed arrival time difference. The second pair from the top has been injected with a coherent white noise burst (WNB), see Section 4.2.3, which has been projected onto the two detectors using a physically realistic mechanism previously described in Section 4.2.4. Here, the correlation is much stronger. We can see it rise and fall as the waveforms come in and out of coherence. The third from the top, the central plot, shows an injection of two incoherent WNBs. They are processed identically to the coherent case, but the initial waveforms are generated independently, including their durations. The Pearson correlation looks very similar to the pure noise case in the uppermost plot, as might be expected. The second from the lowest pair has been injected with a coherent IMRPhenomD waveform, which again has been correctly projected. We can observe that a small correlation is observed at an arrival time difference of around 0.005 s, suggesting that the two waveforms arrived at the detectors 0.005 s apart. Finally, the lowest plot depicts two incoherent IMRPhenomD waveforms projected into the noise. Though these are generated with different parameters, the shared similarities in morphology between all CBC waveforms cause correlation to be registered. By maximum amplitude alone, it may even appear as though there is more correlation happening here than in the correlated case. This highlights one potential weakness of using the Pearson correlation, which can sometimes show some degree of correlation even if the two waveforms are not produced using the same physically simulated mechanism.

As with most mathematical functions, we have created a new GPU-based function for the calculation of the Pearson correlation in Python [63], using the TensorFlow GPU library [65] for computational speed and easy integration with the rest of the GWFlow pipeline [60].

4.2.7.4 Fourier Transform

So far, we have looked at data conditioning, which produces results in the time domain. As we know, and as has been demonstrated by the previous discussion, many aspects of time series processing are performed in the frequency domain. Often, features that are hard to distinguish in the time domain are relatively easy to spot in the frequency domain, even with the human eye. Many have characteristic morphologies, such as distinct lines due to powerline harmonics and violin modes. If we make the assumption that if it is easier for a human, it might also be easier for a machine learning method, we should certainly examine feature engineering methods that take us into the frequency domain. The most obvious way to do this would be to use a simple Fourier transform [236], which takes us directly from a time-domain series to a frequency-domain one. The discrete form of the Fourier transform is given above in Equation 4.17.

4.2.7.5 Power Spectral Density (PSD) and Amplitude Spectral Density (ASD)

As discussed in Section 4.2.1 [204], the PSD is used in many calculations and transforms in gravitational wave data analysis, so it makes sense that along with the closely related property, the ASD, it

may also be useful information to provide to a model. Since the PSD has already been discussed in detail in Section 4.2.1, we will not linger on it here.

4.2.7.6 Spectrograms

The final feature engineering method that we will discuss allows us to represent data in both the time and frequency domains simultaneously. Spectrograms are visualisations of the Short-Time Fourier Transform (STFT) of a time series [237]. The STFT is computed by dividing a time series into many smaller periods, much like in the calculation of a PSD; however, instead of being averaged, you can simply use this 2D output as an image in its own right, which displays how the frequency components of a time series fluctuate over its duration. This retains some information from the time domain. The 2D STFT of a continuous time series, $x(t)$, is given by

$$\text{STFT}(x)(t, f) = \int_{-\infty}^{\infty} x(\tau)w(t - \tau)e^{-i2\pi f\tau}d\tau \quad 4.28$$

where $\text{STFT}(x)(f, t)$ is the value of the STFT of $x(t)$ at a given time, t , and frequency, f , $w(t)$ is a configurable window function that helps to minimize the boundary effects, and τ is a dummy integration variable used to navigate through the time domain at the expense of losing some information from the frequency domain, making the spectrogram, like whitening, a lossy transform. In its discrete form, this becomes

$$\text{STFT}(x)[n, k] = \sum_{m=0}^{N-1} x[m]w[n - m]e^{-i2\pi km/N} \quad 4.29$$

where $\text{STFT}(x)[n, k]$ is the value of the discrete STFT of a discrete time series, $x[m]$ at a given time index, n , and frequency index, k , $w[t]$ is a discrete window function, and N is the number of samples in our discrete time series. It should be noted that there are two time indices present, n and m , because a reduction in dimensionality along the time axis usually occurs since the step between adjacent FFT segments is commonly greater than one.

When creating a spectrogram, the values are typically squared,

$$S[k, n] = (\text{STFT}(x)[n, k])^2 \quad 4.30$$

to represent the power of the frequency components, similar to the process of calculating the PSD. Alternatively, the magnitude can be taken with

$$S[k, n] = |\text{STFT}(x)[n, k]|. \quad 4.31$$

Before plotting, the data is often converted into decibels to better visualize the dynamic range,

$$\text{DATA} = 10 \times \log(S[k, n]). \quad 4.32$$

We have created a custom Python TensorFlow function [65] to perform these calculations on the GPU; see Figure 4.12 for illustrations of this in use on real noise with injected waveform approximants. As is the case with multiple 1D time series, the question also remains of how to combine multiple spectrograms in the case of multiple detector outputs, see Section 4.2.6.

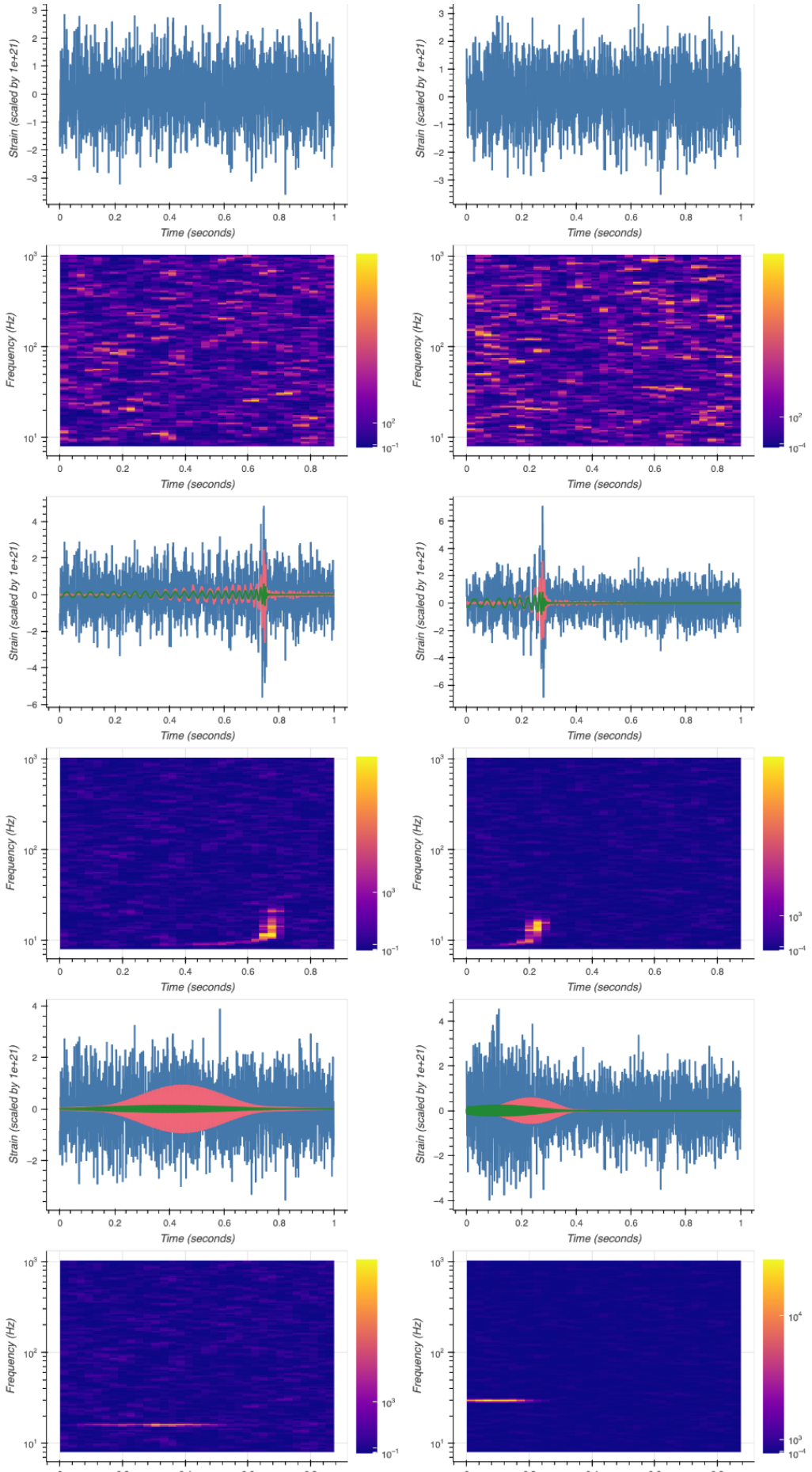


Figure 4.12 | Six example noise segments and their corresponding spectrograms. In all cases, the noise is real interferometer data acquired from the LIGO Hanford detector during the 3rd observing run. It is whitened using the procedure described in Section 4.2.7.2. For the time series plots, the green series represents the original, unwhitened waveform before injection, the red series is the waveform with the same whitening transform applied to it as was applied to the on-source background plus injection, and the blue series is the whitened on-source background plus injection, except for the first two time series plots which contain no injection. The spectrograms are generated using the STFT described by Equation 4.29, converted into power with Equation 4.30, and finally transformed into a decibel logarithmic scale for plotting using Equation 4.32. The two uppermost plots and their respective spectrograms have no injections. The two middle plots and their respective spectrograms, have IMRPhenomD [51] approximants created with cuPhenom injected into the noise [48], and the two lower plots and their respective spectrograms, have White Noise Burst (WNB) waveforms generated using the method described in Section 4.2.3, injected into the noise. In all cases, the injections are scaled to an optimal SNR randomly selected between 15 and 30; these are quite high values chosen to emphasize the features in the spectrograms. As can be seen, the whitened noise that contains injected features has spectrograms with highlighted frequency bins that have a magnitude much larger than the surrounding background noise; the different signal morphologies also create very different shapes in the spectrograms. This allows us to see the frequency components of the signal more easily, observe the presence of interesting features, and differentiate between the WNB and the CBC case.

4.2.7.7 Summary

There are multiple different possibilities for how to condition the data before it is fed into any potential machine learning model; see Table 4.2, and we have only covered some of the possibilities. Most methods come at the cost of removing at least some information from the original data. It remains to be seen, however, if this cost is worthwhile to ensure adequate model performance and feasible training durations.

Possible Model Inputs	Dimensionality of Output	Output Domain
Raw Onsource + Injection	1	Time
Whitened Onsource + Injection	1	Time
Pearsons Correlation	1	Time
Fourier Transform (PSD)	1	Frequency
Power Spectral Density (PSD)	1	Frequency
Spectrogram	2	Time and Frequency

Table 4.2 | A non-exhaustive table of possible data conditioning modes. Feature engineering is often used in order to simplify a problem before it is presented to a machine learning model. There are many ways we could do this with gravitational-wave data. Presented are some of the most common. Each is described in more detail in Section 4.2.7.

4.2.8 Transient Glitch Simulation

As has previously been noted, as well as a quasi-stationary coloured Gaussian background, interferometer noise also contains transient detector glitches caused by a plethora of sources, both known and unknown. These glitches have a prominent effect on the upper-sensitivity bound of most types of search, so it may be important to represent features of this type in our training pipeline. Previous experiments performed during the development of the MLy pipeline [28] had shown that networks can often have greatly increased FARs when performing inference on data segments that contain transient glitches, even when those glitches were only present in the off-source segment used to generate the PSD used for data whitening. As such, a method to add glitches to the training distribution should be considered so that methods to deal with features of this type can hopefully be incorporated into the model's learned parameters during training.

There have been multiple attempts to classify and document the many transient glitches found in real interferometer data [238,239,104], both through automated and manual means [240]. During operation within a standard observing run, there are both intensive manual procedures [54] to characterise the detector state and automated pipelines such as the iDQ pipeline [193]. There is also a large amount of work done offline to characterise the noise in a non-live environment [54]. These methods utilize correlation with auxiliary channels, frequency of triggers, and other information about the detector state to ascertain the likelihood that a given feature is a glitch or of astrophysical origin.

One of the most prominent attempts to classify transient glitches is the Gravity Spy project [104], which combines machine learning and citizen science to try and classify the many morphologies of transient glitches into distinct classes. Successful methods to classify glitches are highly useful since if a similar morphology appears again in the data it can be discounted as a probable glitch. Gravity Spy differentiates glitches into 19 classes plus one extra “no_glitch” class for noise segments that are proposed that do not contain a glitch. The other 19 classes are as follows: air_compressor, blip, chirp, extremely_loud, helix, koi_fish, light_modulation, low_frequency_burst, low_frequency_lines, none_of_the_above, paired_doves, power_line, repeating_blips, scattered_light, scratchy, tomte, violin_mode, wandering_line, and whistle. Some types, such as blips, are much more common than others.

There are two options we could use as example data in our dataset in order to familiarise the model with glitch cases. We could either use real glitches extracted from the interferometer data using the timestamps provided by the Gravity Spy catalog [104] or simulated glitches we generate ourselves. The forms of each would vary depending on whether it was a multi, or single-detector example and whether we are attempting to detect CBCs or bursts.

Real Glitches: The addition of real glitches to the training dataset is a fairly intuitive process, though there are still some parameters that have to be decided upon. By using timestamps from the Gravity Spy catalog [104], we can extract time segments of equal length to our example segments, which contain instances of different classes of glitches. We should process these identically to our regular examples with the same whitening procedure and off-source segments. Real glitches have the distinct advantage that any model will be able to use commonalities in their morphology to exclude future instances; this is also, however, their disadvantage. If you train a model on specific morphologies, then the introduction of new glitch types in future observing runs, which may well be possible given the constant upgrades and changes to detector technology, then it may be less capable of rejecting previously unseen glitch types [104]. However, it is still possible that these glitches will help the model to reject anything other than the true type of feature it has been trained to recognise by weaning it off simple excess power detection.

Simulated Glitches: The other option is to use simulated glitches. The form of these glitches depends highly on the nature of the search, primarily because you wish to avoid confusion between the mor-

phology of the feature you want the method to identify and simulated glitches. For example, in a CBC search, you could use WNBs as simulated glitches, as their morphologies are entirely distinct, and there is no possibility of confusion. However, if we are using coherent WNBs across multiple detectors to train a model to look for coherence, then we must be careful that our glitch cases do not look indistinguishable from true positive cases, as this would poison the training pool by essentially mislabeling some examples. We could, in this case, use incoherent WNBs as simulated glitches as, ideally, we want our coherent search to disregard incoherent coincidences. This is the approach taken by the MLy pipeline [28], as a method to train the models to reject counterexamples of coherent features.

Other than the question of whether to use simulated or real glitches or maybe even both, a few questions remain: what is the ideal ratio between examples of glitches and non-glitched noise examples? Should the glitched background also be injected with waveforms at some rate? A real search would occasionally see glitches overlapping real signals, though this would occur in a relatively low number of cases, and including these types of signal-glitch overlaps could perhaps interfere with the training process whilst not adding a great deal of improvement to the true positive rate. Should glitches form their own class so that the model instead has to classify between signal, noise, or glitch rather than just signal or noise? These questions must be answered empirically.

For the multi-detector case, and thus also the burst detection case, we must decide how to align glitches across detectors. It seems safe to assume that adding coherent glitches across multiple detectors would be a bad idea in a purely coherence-based search pipeline — although perhaps if the model can learn to disregard certain morphologies based on prior experience, this would be a nice extension. For some simple glitch types, coincident and fairly coherent instances across detectors are not extremely unlikely. For example in the case of the most common glitch class identified by GravitySpy [104], blips, we often see coincident glitches in multiple detectors with a physically plausible arrival time difference, and because they are only glitches, their morphologies can often be similar.

We could also include cases of incoherent glitches across detectors but of the same class, incoherent glitches across detectors but of different classes, and any combination of glitches found in less than the full complement of detectors. Perhaps it would be the case that a good mix of all of these cases would better inoculate our model against glitches.

4.3 Perceptron Results

Now that we have finally assembled all the pieces required to generate training, testing, and validation datasets that can acquire training examples using and/or real data, we can finally repeat the experiments we performed on the MNIST data in Section 3.1.3, with both single and multi-layer perceptrons. The model architectures are similar, though the input vectors are now the size of our simulated interferometer output examples: `(NUM_EXAMPLES_PER_BATCH, NUM_SAMPLES)` in the case of the single detector CBC search and `(NUM_EXAMPLES_PER_BATCH, NUM_DETECTORS, NUM_SAMPLES)` in the multi-detector coherent burst search. We will use 32 training examples per batch, `NUM_EXAMPLES_PER_BATCH = 32`, as this is a standard power-of-two value used commonly across artificial neural network literature, and, in the multi-detector case, we will use only LIGO Hanford and LIGO Livingston, for now, excluding the Virgo detector, `NUM_DETECTORS = 2`. We have chosen to use only the two LIGO detectors as in many ways, this is the simplest possible multi-detector network case; signals projected onto these two detectors will have a greater similarity than signals projected onto either of these two detectors and the Virgo detector, both due to sensitivity and orientation and position differences. We have chosen to use a sample rate of 2048.0 Hz and an on-source duration of 1.0 s, allowing an additional crop region 0.5 s either side of the onsource segment to remove edge effects created when whitening with 16.0 s of off-source background. The reasoning for these choices has been described previously in this chapter. This means we will have 2048 samples per detector, `NUM_SAMPLES = 2048`, after it has been passed through the whitening layer. A flattening layer, see

Section 3.4, will only be required in the multi-detector case; in the single-detector case, the input is already one-dimensional. The batch dimensions are not a dimension of the input data and simply allow for parallel processing and gradient descent; see Section 3.2.

The obfuscating noise consists of real data taken from LIGO Hanford and LIGO Livingston [8] for each respective detector. Locations of confirmed and candidate events are excluded from the data, but known glitch times have been included in the training, testing, and validation datasets.

For the single CBC case, cuPhenom [48] waveforms with masses drawn from uniform distributions between $5.0 M_{\odot}$ and $95.0 M_{\odot}$ for the mass of both companions and between -0.5 and 0.5 for the dimensionless aligned-spin component are injected into the noise and scaled with optimal SNR values taken from a uniform distribution of between 8.0 and 15.0 unless explicitly stated.

For the multi-detector Burst case, coherent WNBs are injected with durations between 0.1 s and 1.0 s, and the frequencies are limited to between 20.0 Hz and 500.0 Hz. The injected bursts are projected correctly onto the detectors using a physically realistic projection. The bursts are injected using the same scaling type and distribution as the CBC case, although notably, the network SNR was used rather than a single detector SNR.

During network training, the gradients are modified by batches consisting of 32 examples at a time, chosen as an industry standard batch size, and with a learning rate of 1.0×10^{-4} , and using the Adam optimiser [183], which again is a common standard across the industry [241]. During training epochs, 10^5 examples are used before the model is evaluated against 10^4 examples of the previously unseen test data. It should be noted that due to the nature of the generators used for the training, unlike in standard model training practices, no training examples are repeated across epochs, but the test dataset is kept the same for each epoch. After each epoch, if the validation loss for that epoch is the lowest yet recorded, the model is saved, replacing the existing lowest model. If no improvement in validation loss is seen in ten epochs (patience), the training is halted, and the best model is saved for further validation tests. Table 4.3 shows a large number of the training and dataset hyperparameters.

Hyperparameter	Value
Batch Size	32
Learning Rate	10^{-4}
Optimiser	Adam
Scaling Method	SNR
Minimum SNR	8.0
Maximum SNR	15.0
SNR Distribution	Uniform
Data Acquisition Batch Duration	2048.0 s
Sample Rate	2048.0 Hz
On-source Duration	1.0 s

Off-source Duration	16.0 s
Scale Factor	10^{21}

Table 4.3 | The common training and dataset hyperparameters shared by the CBC and Burst perceptron experiments. Note that the scale factor here refers to the factor used during the upscaling of the CBC waveforms and real interferometer noise from their extremely small natural dimensions to make them artificial neuron-friendly. This is done both to ensure that the input values work well with the network activation functions and learning rates, which are tuned around values near one, and to reduce precision errors in areas of the code that use 32-bit precision, employed to reduce memory overhead, computational cost and duration. Data acquisition batch duration is a parameter of the GWFlow data acquisition module [60]. For speed, the GWFlow data acquisition system downloads data in larger segments than is required for each training batch, then randomly samples examples from this larger segment to assemble each training batch. The data acquisition batch duration determines how long this larger batch is. Smaller values will result in a more evenly mixed training data set and a lower overall GPU memory overhead but will be more time-consuming during the training process.

4.3.1.1 Architectures

We used architectures with four different layer counts: zero, one, two, and three hidden layers; see Figure 4.13. All models have a custom-implemented whitening layer, which takes in two vectors, the on-source and off-source segments, and performs a whitening operation as described in Section 4.2.7.2. They also all have a capping dense layer with a single output value that represents either the presence of a feature or the absence of one. The capping layer uses the Sigmoid activation function; see Equation 3.12, and the other hidden layers use ReLU activation functions, see Equation 3.9.

Layers are built with a number of neurons selected from this list [64, 128, 256, 512], though fewer combinations are tested in architectures with a greater number of model layers. Models tested have these 14 configurations of neuron numbers per layer, specified as [num_hidden_layers:num_neurons_in_layer_1 ... num_layers_in_layer_n]: ([0], [1:64], [1:128], [1:256], [1:512], [2:64,64], [2:128,64], [2:128,128], [2:256,64], [2:256,128], [2:256,256], [3:64,64,64], [3:128,128,128], [3:256,256,256]). These combinations were chosen to give a reasonable coverage of this section of the parameter space, though it is notably not an exhaustive hyperparameter search. From the performances demonstrated in this search compared to other network architectures, it was not deemed worthwhile to investigate further.

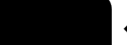
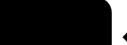
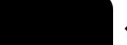
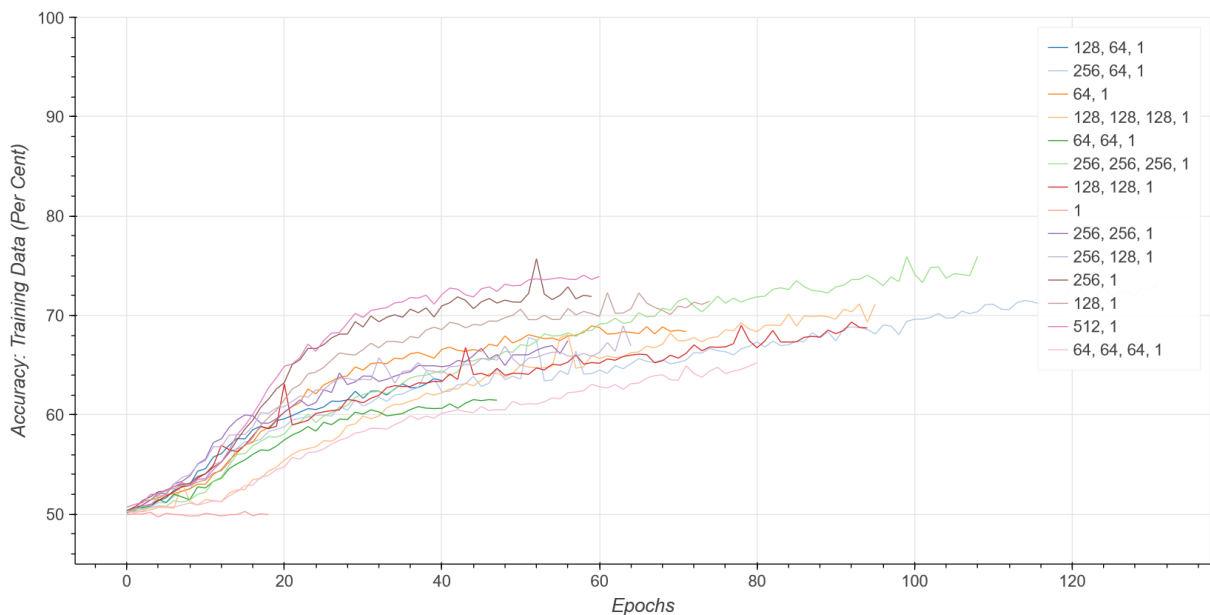
Type	Num Filters / Neurons	Filter / Pool Size	Stride	Activation Function	Dropout	off-source	on-source
Whitening	-	-	-	-	-		
Dense	1	-	-	SoftMax	-		
Binary Classification							
Type	Num Filters / Neurons	Filter / Pool Size	Stride	Activation Function	Dropout	off-source	on-source
Whitening	-	-	-	-	-		
Dense	64/128/ 256/512	-	-	ReLU	-		
Dense	1	-	-	SoftMax	-		
Binary Classification							
Type	Num Filters / Neurons	Filter / Pool Size	Stride	Activation Function	Dropout	off-source	on-source
Whitening	-	-	-	-	-		
Dense	64/128/ 256	-	-	ReLU	-		
Dense	64/128/ 256	-	-	ReLU	-		
Dense	1	-	-	SoftMax	-		
Binary Classification							
Type	Num Filters / Neurons	Filter / Pool Size	Stride	Activation Function	Dropout	off-source	on-source
Whitening	-	-	-	-	-		
Dense	64/128/ 256	-	-	ReLU	-		
Dense	64/128/ 256	-	-	ReLU	-		
Dense	64/128/ 256	-	-	ReLU	-		
Dense	1	-	-	SoftMax	-		
Binary Classification							

Figure 4.13 | Perceptron diagrams. The four different architectures used to test the use of purely dense models for both the single-detector CBC detection case and the multi-detector burst detection problem. The only differences are that the input vector sizes are different between the cases: `(NUM_EXAMPLES_PER_BATCH, NUM_SAMPLES)` in the case of the single detector CBC search and `(NUM_EXAMPLES_PER_BATCH, NUM_DETECTORS, NUM_SAMPLES)` in the multi-detector coherent burst search. All models take in two input vectors into a custom-designed GWFlow whitening layer, the off-source and the on-source vectors; see Section 4.2.7.2 for more information about the whitening procedure, and all models are capped with a dense layer with a single output neuron that is used to feed the binary loss function, with a sigmoid activation function. Each hidden layer has been tested with 64, 128, and 256 neurons, and one hidden layer was tested with 512 as a sample with higher neuron counts: *Top*: Zero-hidden layer model. *Second to top*: Two-hidden layer model. *Second to bottom*: Three-hidden layer model. *Bottom*: One hidden layer model.

4.3.2 CBC Detection Dense Results

4.3.2.1 Training

First, we can examine the results of applying dense-layer perceptrons to the CBC single-detector morphology detection problem. Even during the training process, it is clear that, at least amongst the selected hyperparameters, these models will not be useful; see Figure 4.14 and Figure 4.15. None reach an accuracy of above 75% with a training patience of ten epochs. Setting a training patience of ten ensures that if no improvement in the validation loss is seen within ten epochs, the training process is halted. Examining the plots; see Figure 4.14 and Figure 4.15, it seems possible that some of the perceptrons are on a very slow training trajectory and could have seen some marginal improvement if the training patience had been increased. It is also possible that other larger perceptron architectures may achieve greater success, as this was far from an exhaustive or even guided search of the perceptron hyperparameter space. However, as can be seen in Figure 4.14, the models take a significant number of epochs to reach the values they do, which is what we would expect from entirely dense models. As will be seen in later sections, see Section 4.5, other architectures can achieve much better results in fewer epochs. These results are here to act as an example of the difficulties of training dense networks for complex recognition tasks. For comparison with other methods, a more sophisticated analysis will be shown after the training history plots; see Section 4.3.2.2.



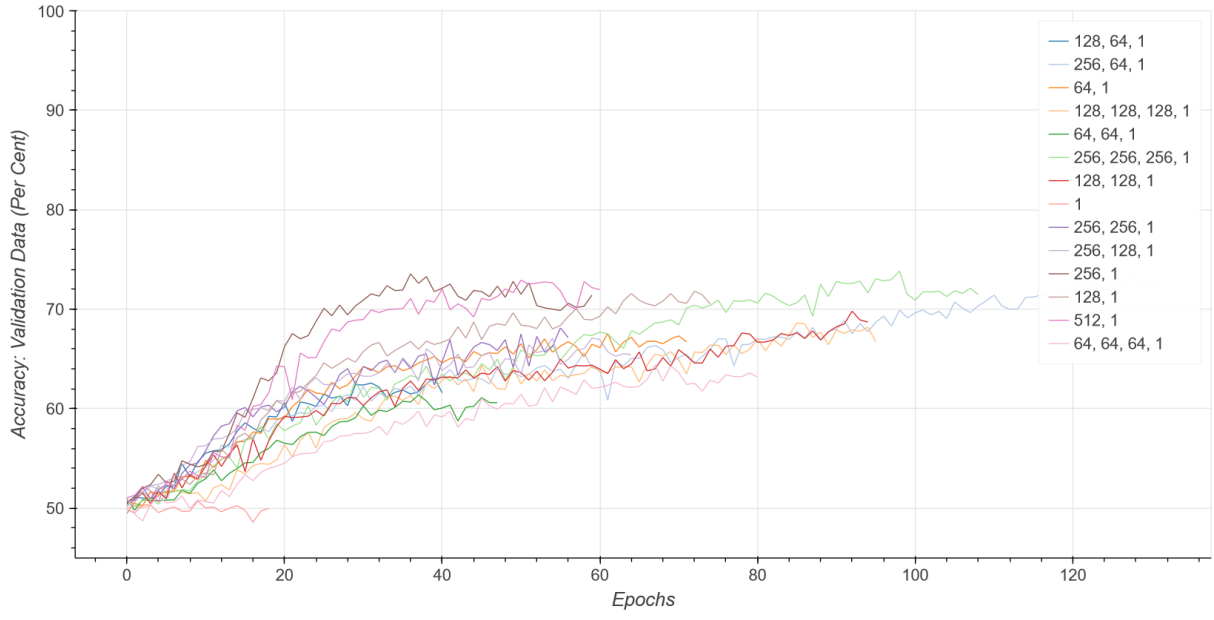


Figure 4.14 | The accuracy history of perceptron models training to detect IMRPhenomD waveforms generated using cuPhenom [48] that have been obfuscated by real interferometer noise sampled from the LIGO Livingston detector during the 3rd observing run. Visit <https://tinyurl.com/ypu3d97m> for interactive plots, whilst they’re still working. The optimal SNR of waveforms injected into the training and validation sets was uniformly distributed between 8 and 15. Input was from a single detector only. A rough search was performed over a relatively arbitrary selection of model architectures, which varied the number of layers and the number of perceptrons in each layer. The architectures of each model can be seen in the figure legends as a list of numbers where each digit is the number of artificial neurons in that layer. All are trained with the same training hyperparameters, details of which can be found in Table 4.3. Each epoch consisted of 10^5 training examples, and it should be noted that, unlike the regular training pipelines, each training epoch consisted of newly generated waveforms injected into unseen noise segments, though the validation examples are consistent. Training of each model was halted after ten consecutive epochs with no improvement to validation loss, the values of which are shown in Figure 4.15. Validation noise was drawn from a separate pool of data segments inaccessible to the training data loader. We can see that the maximum accuracy achieved by any perceptron model only approaches 75%. Although these validations are performed with a pool containing mixed waveform SNRs and at an unrestrained False Alarm Rate (FAR) (this accuracy uses a score threshold of 0.5 regardless of FAR), it is clear that this is insufficient to be useful. *Upper:* Plot of model accuracies when measured with training data (10^5 epoch-unique examples). *Lower:* Plot of model accuracies when measured with validation data (10^4 epoch-consistent examples).

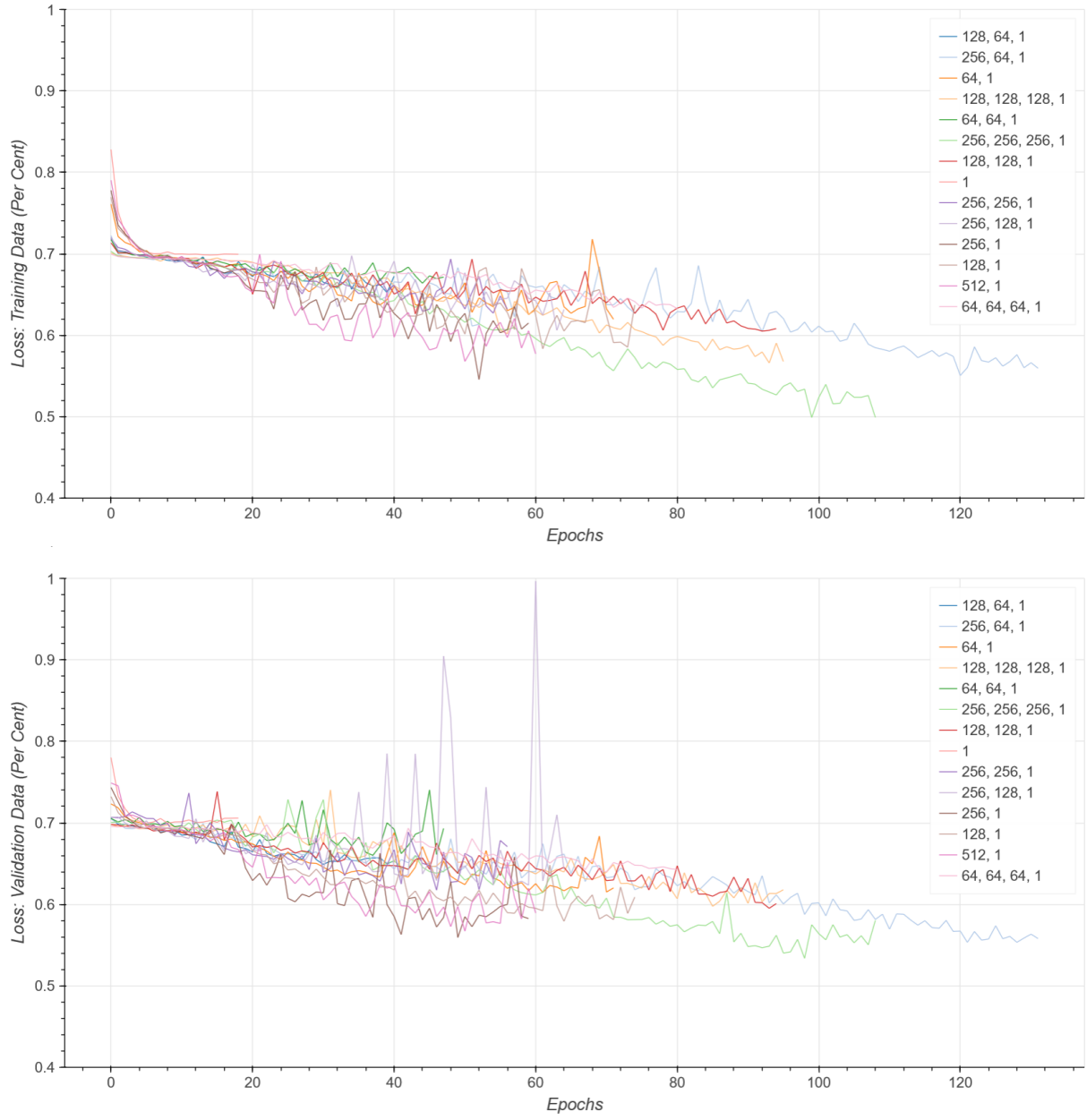


Figure 4.15 | Training loss history of perceptron models training to detect IMRPhenomD waveforms generated using cuPhenom [48], obfuscated by real interferometer noise from the LIGO Livingston detector from the 3rd observing run. The loss is computed using binary cross entropy loss function and is used by the gradient descent algorithm, in this case, the Adam optimizer, as a minimization target. It also acts as the monitor by which the pipeline knows to stop the training process early. If the pipeline detects that the validation model loss has not decreased in more than 10 epochs, training is halted. Visit <https://tinyurl.com/ypu3d97m> for interactive plots. See Figure 4.14 for a more detailed description of the training data. *Upper:* Plot of model loss when measured with training data (10^5 epoch-unique examples). *Lower:* Plot of model loss when measured with validation data (10^4 epoch-consistent examples).

4.3.2.2 Validation

Although the perceptron training performance was low, and probably sufficient to tell us that at least these configurations of perceptrons are not capable enough for CBC detection, a more complete validation was nonetheless performed on the trained models using the third as-yet-unseen validation

dataset. This was both for comparison with later methods and to ensure that our initial assessment of the results was correct. Although it is easy to draw quick conclusions from the training results, it is not an accurate profile of the model performance, as the training validation results draw from a mixed pool of SNR values, do not consider the classes independently, and in the case of the accuracy result, use an uncalibrated detection threshold of 0.5. This means that if a model outputs a score over 0.5 it is considered a detection, and a score lower than 0.5 is considered noise. By tuning this threshold, we can arrive at the desired False Alarm Rate (FAR), though this will have an inverse effect on the sensitivity, (the true positive rate) of the model.

Before we can apply this tuning we must evaluate our model's performance on a dataset consisting exclusively of noise examples. The perfect classifier would output zero for all examples in such a dataset. We are not dealing with perfect classifiers, so the model will output a score value for each pure noise example. If our classifier has good performance most of these scores will be low, preferably near zero, but some will inevitably rise above whatever detection threshold we set, dependant of course on the size of our validation dataset, the larger the dataset the larger the expected value of our largest noise score. The size of the dataset required for threshold calibration will depend on the value of FAR that is desired, with smaller FARs requiring larger datasets. We will require a dataset in which the combined example durations sum to at least the duration of time wherein, given our desired FAR, we would expect one detection. However, since this is a statistical result, having only the exact duration required for our FAR would result in a great deal of error on that value. The larger the validation dataset, the more confident we can be in our calculation of the required FAR threshold. We will attempt to use a validation dataset around ten times larger than the minimum required, so we would, on average, expect ten false alarms total from running the model on the dataset with the given threshold.

Of course, there is only so far we can tune the threshold value within the precision available to us with 32-bit floats, and if the model gives scores to pure noise examples of exactly one, there is no way to differentiate them from true positive classifications. This means any model will have a maximum possible threshold, and therefore minimum FAR, beyond which it cannot distinguish positive results from negative ones.

In order to determine the score threshold of a model for a given FAR, we can run that model over a sufficiently large pure noise dataset, sort these scores from smallest to highest, and then assign each score an equivalent FAR. For example, if we sorted the scores from lowest to highest, and the first score was above the score threshold, then the FAR would be $\frac{1.0}{d_{\text{example}}}$ Hz, where d_{example} is the length of the input example in our case 1 s. If we set the threshold to be smaller than the smallest score this would mean that almost every noise example would score above the threshold, therefore the model would produce a false alarm nearly every time it ran. If the second sorted score was above the threshold but not the first, then all but one of the examples would be a false alarm, therefore we can estimate the FAR to be $\frac{d_{\text{total}} - d_{\text{example}}}{d_{\text{total}}} \times \frac{1.0}{d_{\text{example}}}$ Hz, d_{total} is the total duration of examples in the validation set. This gives a general formula for the y-axis,

$$y = \frac{d_{\text{total}} - i \times d_{\text{example}}}{d_{\text{total}}} \times \frac{1.0}{d_{\text{example}}} \text{ Hz}, \quad 4.33$$

where i is the x-axis index. The FAR is plotted against the required model threshold to achieve that FAR in Figure 4.16.

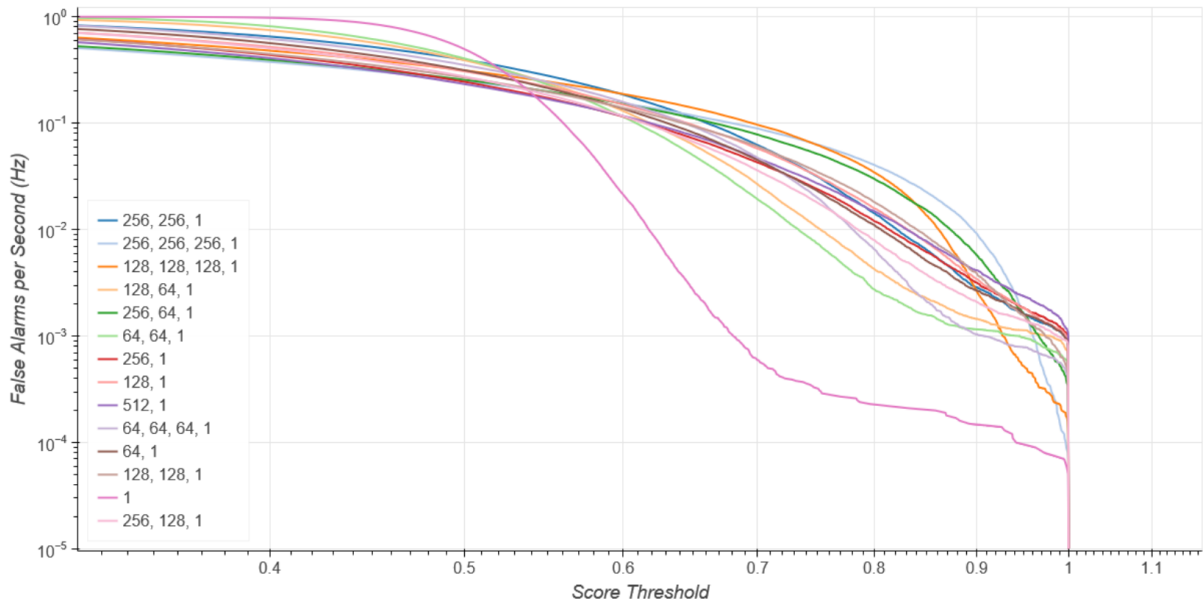


Figure 4.16 | Perceptron False Alarm Rate (FAR) curves. This plot was created by running each of our 14 models over a pure noise validation dataset of 10^5 noise examples. A relatively small number of noise examples are used due to the observed inaccuracy of the models during training which suggested that they would not be able to reach low FAR scores and thus would not necessitate a larger validation dataset. The output scores of the model from each inference over the pure noise validation dataset are sorted and plotted on this graph. The x-axis is the output score of the model inference on that example of noise. The y-axis is calculated by using Equation 4.33 and provides the estimated number of false alarms that the model would output per second of pure noise data given the threshold score displayed on the x-axis. We can use this graph to calculate positive result thresholds for our classifier, at different false alarm rates. Once again, the models are listed with the number of artificial neurons in each hidden layer. Visit <https://tinyurl.com/2wkaarkh> to view an interactive plot.

Using Figure 4.16, we can select the score index that is closest to our desired FAR, and find the threshold that will generate a FAR of approximately this value. With a method to calculate threshold values in hand, we can create efficiency curves at specific FARs. Efficiency curves allow us to examine the sensitivity of the model to detect signals at different optimal SNR values. This time we can utilize datasets containing true results at set SNR values. We can run the models over these datasets and extract model scores for each true example. From those scores, we can calculate the sensitivity at different FARs. The sensitivity is given by

$$\text{sensitivity} = \frac{\| \text{scores} > \text{score_threshold} \|}{\| \text{scores} \|} \quad 4.34$$

where $\| \text{scores} > \text{score_threshold} \|$ is the number of scores above the score threshold, and $\| \text{scores} \|$ is the total number of examples tested. In Figure 4.17, we present the efficiency curves at three different values of FAR, 0.1 Hz, 0.01 Hz, and 0.001 Hz, which are not particularly low FARs, but as can be seen from the plots, below these values we would encounter only negligible accuracies in the SNR ranges considered. As can be seen from the curves, the models do not perform well even with very generous FAR constraints.

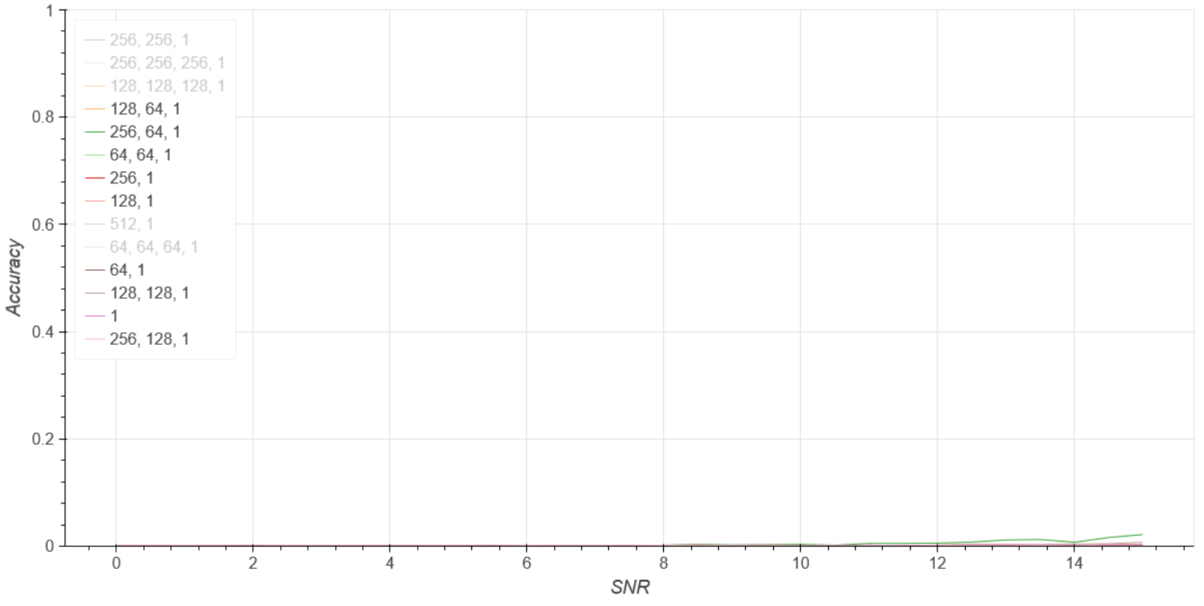
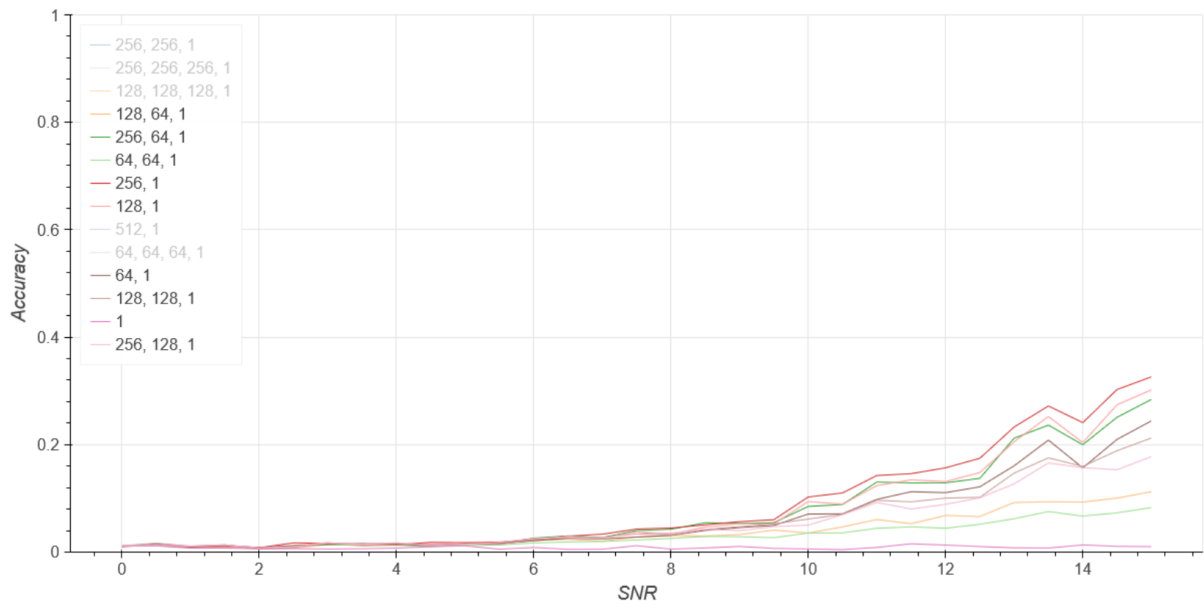
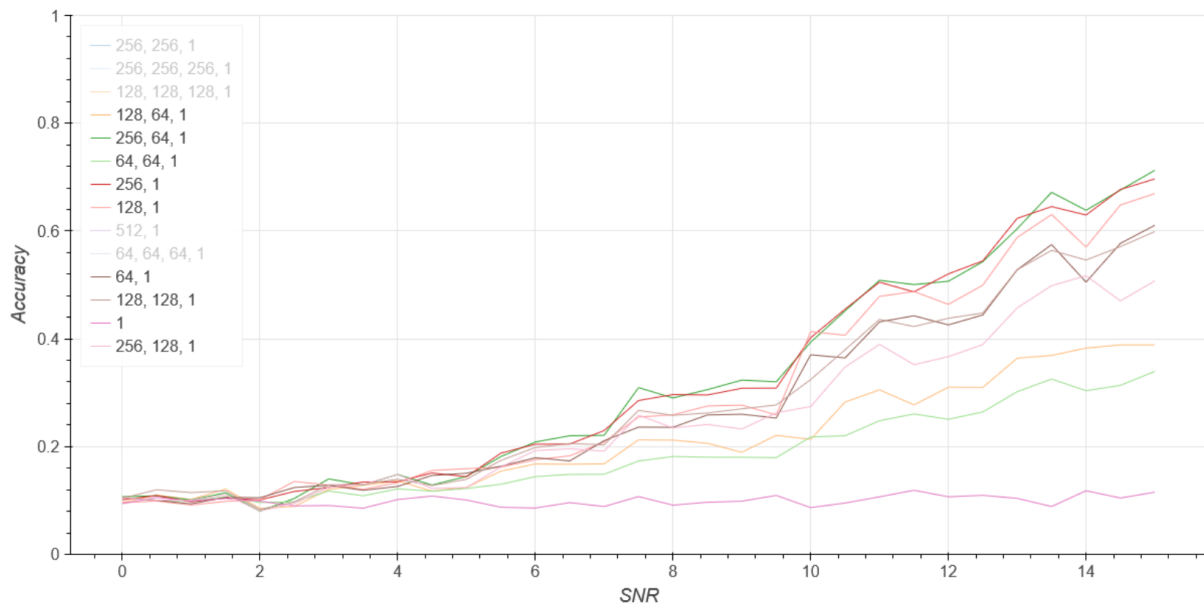


Figure 4.17 | Perceptron efficiency curves. For each of the 14 perceptron models trained, 31 efficiency tests are performed at evenly spaced optimal SNR values between 0 and 15. For each test, 8192 examples with signals of the relevant SNR are examined by the model, and the percentage of those that scored above the threshold was plotted, see Equation 4.34, for three different False Alarm Rate (FAR) thresholds: 0.1 Hz, 0.01 Hz, and 0.001 Hz. The efficiency curve for each FAR threshold is presented on a unique plot. Some models have been excluded, they are shaded grey on the legends, because they are incapable of performing any classification at the chosen FAR thresholds. Visit <https://tinyurl.com/2wkaarkh> to view an interactive plot. . *Upper*: Efficiency curves at a FAR of 0.1 Hz. *Middle*: Efficiency curves at a FAR of 0.01 Hz. *Lower*: Efficiency curves at a FAR of 0.001 Hz.

Finally, we can examine the model performance from a different perspective by freezing the SNR of the validation dataset and plotting the True Positive Rate (TPR), i.e. the sensitivity, against the False Alarm Rate (FAR). This will give us a Reciever Operator Curve (ROC), see Figure 4.18. We can compare the area under the curve for each model to make a comparison of its relative performance; although in this case, all the models perform very similarly at the chosen optimal SNR of eight. Eight was chosen as this is often considered a good detectability threshold for CBCs, in the catalog of events from the first half of the third joint observing run, all confident detections had an SNR above nine, and candidate signals had SNRs above eight [31].

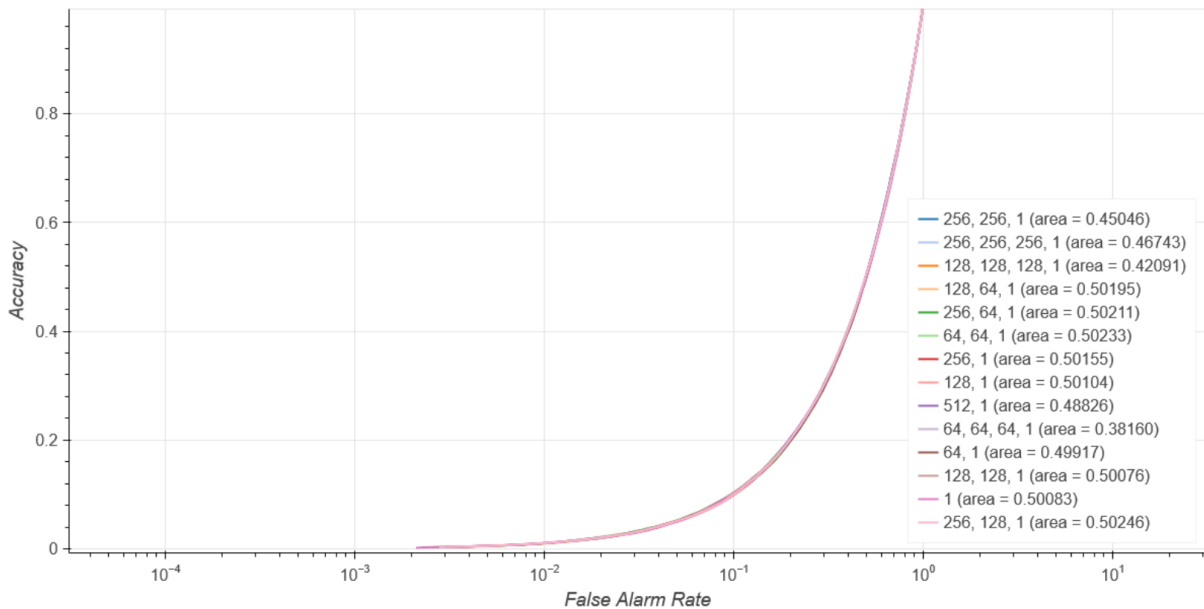


Figure 4.18 | Reciever Operator Curve (ROC) Curve at $\rho_{\text{opt}} = 8$. To create this plot a validation dataset containing waveforms all of an SNR of eight was generated. The ability of the model to detect these waveforms was then measured at different FARs. All models show very similar, poor performance. Visit <https://tinyurl.com/2wkaarkh> to view an interactive plot.

From these results, we can summarise that things are as anticipated from the results of the training. None of these models would have any useful application in gravitational-wave data science, as they all fall well below the performance of matched filtering, and they are unable to perform at acceptable FARs. In order to offer a competitive approach, we must turn to other network architectures.

4.3.3 Burst Detection Dense Results

4.3.3.1 Training

Although it may seem unlikely that we will have better results with what is arguably a more complex problem, we present the application of dense neural networks to multi-detector arbitrary waveform detection. Note that there are no incoherent or single detector counter-examples added to either the training or validation data, so in order to function a model would only have to identify the presence of excess power. The training and validation SNR ranges were also increased from 8 to 15 to 12 to 30 since initial testing at the SNR range used for CBC detection provided small accuracies across all FARs. From the training results it was clear that this was going to be a more complex problem than CBC detection; see Figure 4.19. Again there is the possibility that less constrained training or larger models could lead to better performance, but even if a solution was found outside the considered hyperparameter range, training time and computational requirements would soon become prohibitive. If other, less general networks can offer far superior results, they will be preferred.

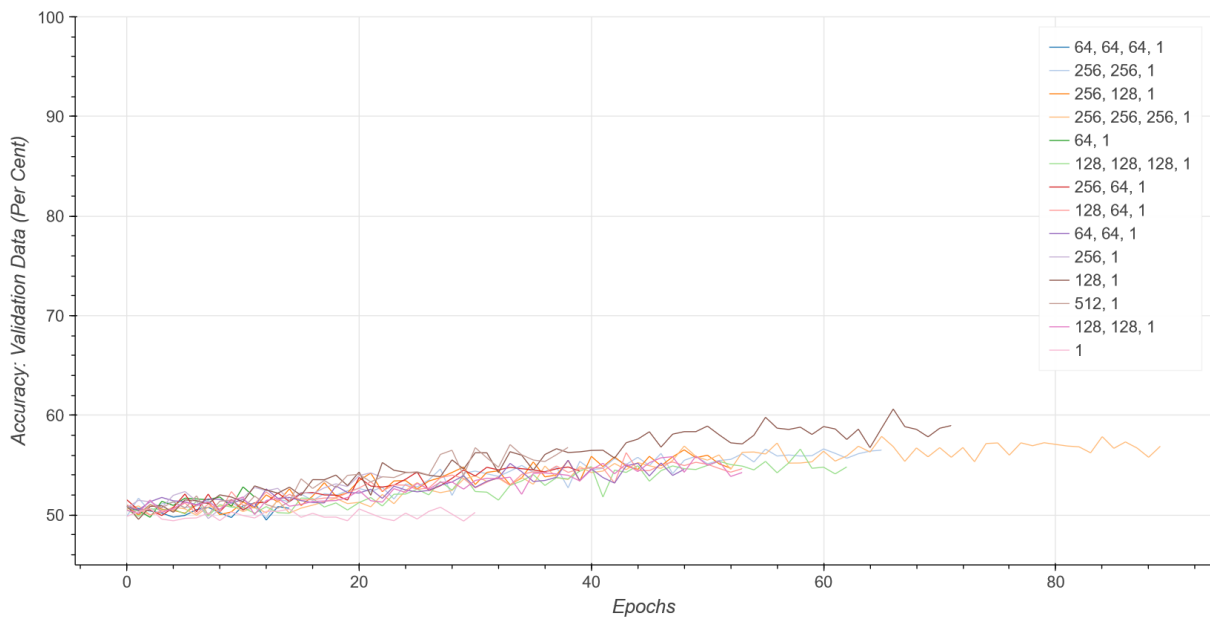
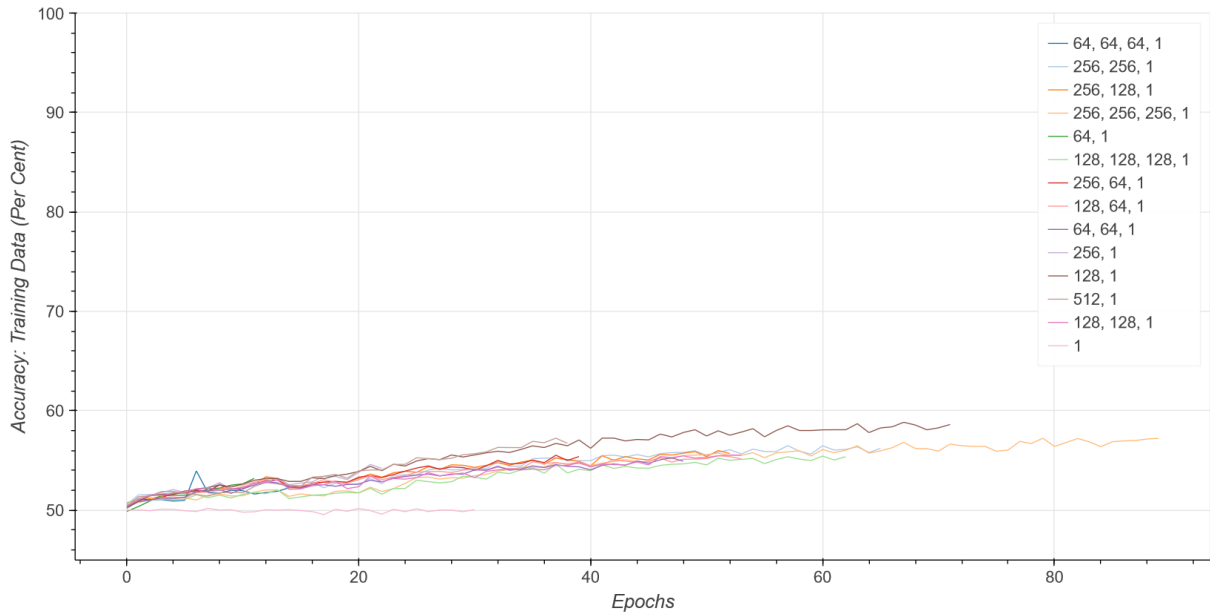


Figure 4.19 | The accuracy history of perceptron models training to detect multi-detector WNBs generated using GWFlow and obfuscated by real interferometer noise sampled from the LIGO Livingston and LIGO Hanford detectors during the 3rd observing run. Visit ADD_LINK for interactive plots. The optimal SNR of waveforms injected into the training and validation sets was uniformly distributed between 12 and 30. The input was generated using real noise from LIGO Hanford and LIGO Livingston. The training procedure was identical to the single detector case, except for the SNR range increase and the multiple detector data supply. We can see in these training plots, that despite the increased SNR range, training and validation accuracy barely creep above 50% (which can be achieved by random selection). This indicates that dense networks are even less suited for the more complex coherence detection problem. Further validation will be performed for completion. Visit <https://tinyurl.com/4jj3t5fj> to view an interactive plot. *Upper:* Plot of model accuracies when measured with training data (10^5 epoch-unique examples). *Lower:* Plot of model accuracies when tested with validation data (10^4 epoch-consistent examples).

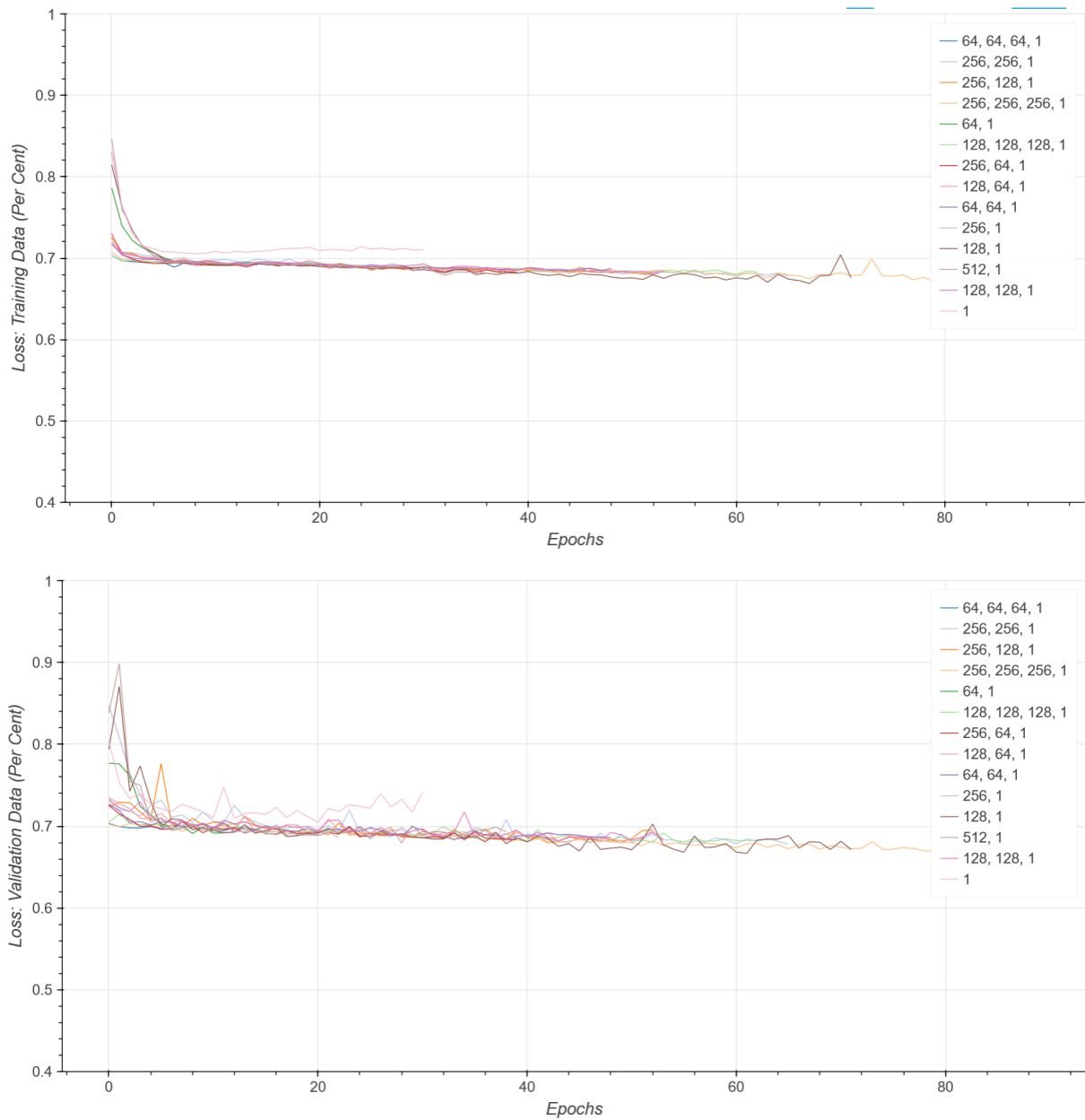


Figure 4.20 | The loss history of perceptron models training to detect multi-detector WNBs generated using GWFlow and obfuscated by real interferometer noise sampled from the LIGO Livingston and LIGO Hanford detectors during the 3rd observing run. Visit ADD_LINK for interactive plots. The optimal SNR of waveforms injected into the training and validation sets was uniformly distributed between 12 and 30. The input was generated using real noise from LIGO Hanford and LIGO Livingston. The losses show a similar picture to the accuracy plots, and although we see a gradual decline it is very shallow and triggers the patience early stopping before it has had any chance to gain significant performance, assuming that is even possible. Patience could be increased, but as we will see in later architectures, this is not competitive. *Upper*: Plot of model losses when measured with training data (10^5 epoch-unique examples). *Lower*: Plot of model losses when tested with validation data (10^4 epoch-consistent examples). Visit <https://tinyurl.com/4jj3t5fj> to view an interactive plot.

4.3.3.2 Validation

As with the CBC case, we first present the FAR curve that will be used to determine model FAR thresholds in Figure 4.21. Then we show the efficiency curves at two FARs, 0.1 Hz, and 0.01 Hz see Figure 4.22. Only two FAR thresholds are presented here as lower FARs resulted in negligible accuracies. Finally, we show the ROC curves for these models, which are unsurprisingly also poor; see Figure 4.23.

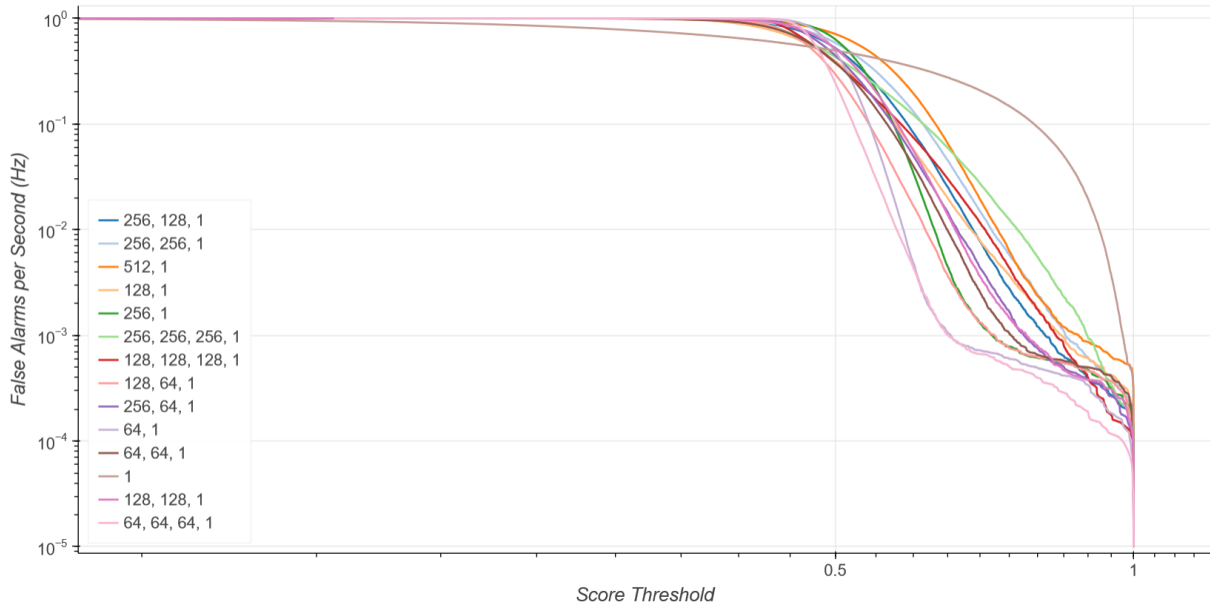


Figure 4.21 | Perceptron False Alarm Rate (FAR) curves. This plot was created by running each of our 14 models over a pure noise validation dataset of 10^5 noise examples. Performance is low across the board demonstrating that dense layer perceptrons are unsuitable for this kind of WNB detection, at least within the hyperparameter range tested. Visit <https://tinyurl.com/bdz9axpf> to view an interactive plot.

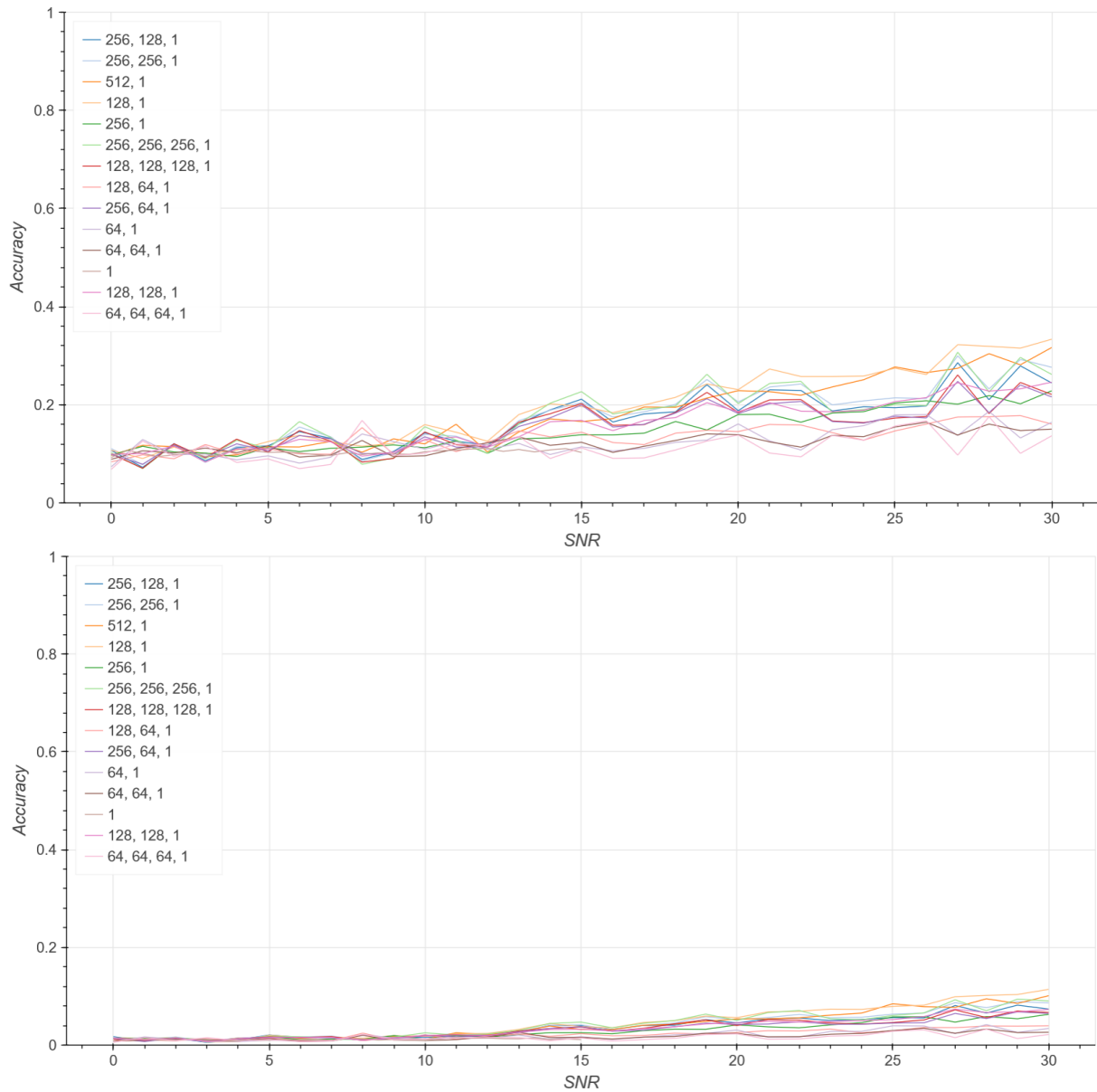


Figure 4.22 | Perceptron efficiency curves for the multi-detector WNB detection model. For each of the 14 perceptron models trained, 31 efficiency tests are performed at evenly spaced optimal SNR values between 0 and 30. For each test, 8192 examples with signals of the relevant SNR are examined by the model. The percentage of those that scored above the threshold is plotted, see Equation 4.34, for two different False Alarm Rate (FAR) thresholds: 0.1 Hz and 0.01 Hz, lower FARs are excluded due to small accuracies. *Upper:* Efficiency curves at a FAR of 0.1 Hz. *Lower:* Efficiency curves at a FAR of 0.01 Hz. Visit <https://tinyurl.com/bdz9axpf> to view an interactive plot.

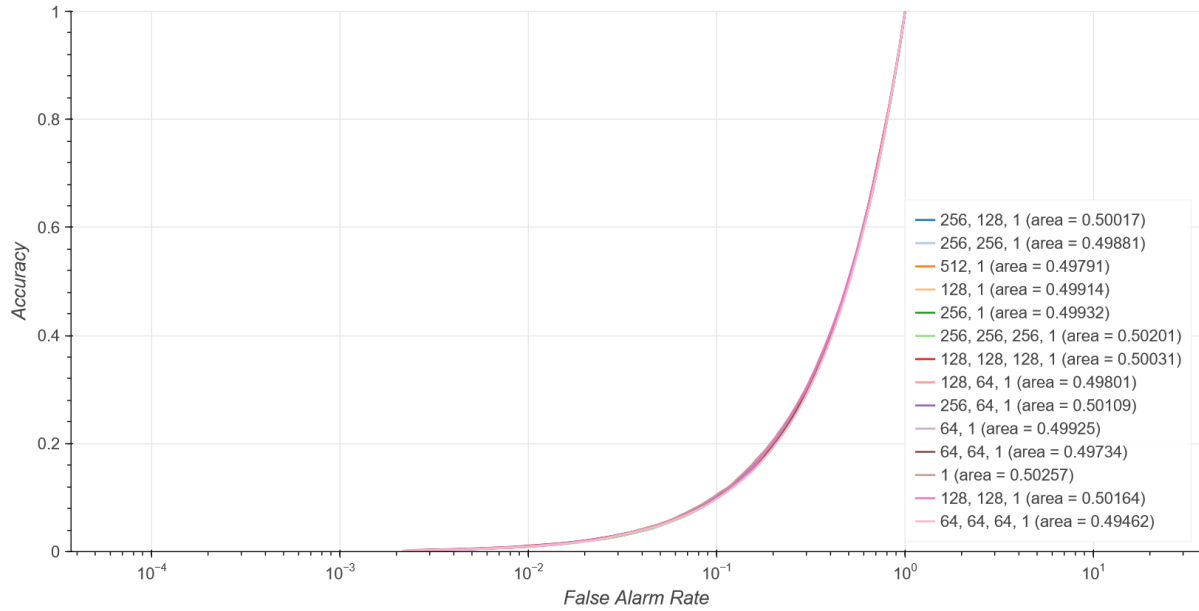


Figure 4.23 | Reciever Operator Curve (ROC) Curve at an optimal SNR of eight. To create this plot a validation dataset containing waveforms all of an SNR of eight was generated. The ability of the model to detect these waveforms was then measured at different FARs. Again, all models show very similar, poor performance. Visit <https://tinyurl.com/bdz9axpf> to view an interactive plot.

From these validation results, we can determine that dense layer networks alone are unsuitable for the task of coherence detection. Once again these results are not surprising and presented as a reference. In the next section, we will describe another deep-learning architecture that has seen much more promising results in the literature.

4.4 Introducing Convolutional Neural Networks (CNNs)

As we have seen, simple dense-layer perceptrons can not adequately perform detection tasks on gravitational-wave data. This was anticipated, given the complexity of the distribution. Perceptrons have not been at the forefront of artificial neural network science for some time. We must turn toward other architectures. Although, in some ways, specialising the network will limit the capacity of our model to act as a universal function approximator [151], in practice, this is not a concern, as we have at least some idea of the process that will be involved in completing the task at hand, in this case, image, or more correctly time-series recognition.

The Convolutional Neural Network (CNN) is currently one of the most commonly used model archetypes [10,242]. In many ways, the development of this architecture was what kickstarted the current era of artificial neural network development. On 30th December 2012, the AlexNet CNN [128] achieved performance in the ImageNet multi-class image recognition competition, far superior to any of its competitors. This success showed the world the enormous potential of artificial neural networks for achieving success in previously difficult domains.

CNNs are named for their similarity in operation to the mathematical convolution [10,242], although it is more closely analogous to a discrete cross-correlation wherein two series are compared to each other by taking the dot product at different displacements. Unless you are intuitively familiar with mathematical correlations, it is not a useful point of reference for understanding CNNs. So, we will not continue to refer to convolutions in the mathematical sense.

CNNs are primarily employed for the task of image and time-series recognition [10,242]. Their fundamental structure is similar to dense-layer networks on a small scale [243]. They are comprised of artificial neurons that take in several inputs and output a singular output value after processing their inputs in conjunction with that neuron's learned parameters; see Section 3.1.1. Typical CNNs ingest an input vector, have a single output layer that returns the network results, and contain a variable number of hidden layers. However, the structure and inter-neural connections inside and between the layers of a CNN are fundamentally different.

Unlike perceptrons, layers inside CNNs are, by definition, not all dense, fully-connected layers [10,242]. CNNs introduce the concept of different types of sparsely-connected computational layers. The classical CNN comprises a variable number, C , of convolutional layers stacked upon the input vector, followed by a tail of D dense layers, which output the result of the network. This gives a total of $N = C + D$ layers, omitting any infrastructure layers that may also be present, such as a flattening layer (which is often employed between the last convolutional layer and the first dense layer; convolutional layers inherently have multidimensional outputs and dense layers do not). Purely convolutional networks, which consist only of convolutional layers, are possible [97], but these are a more unusual configuration, especially for classification tasks. Purely convolutional networks appear more often as autoencoders [244] and in situations where you want to lessen the black-box effects of dense layers. Convolutional layers are often more interpretable than pure dense layers as they produce feature maps that retain the input vector's dimensionality [245].

Convolutional layers can and often do appear as layers in more complex model architectures, which are not necessarily always feed-forward models [10,242]. They can appear in autoencoders [244], Generative Adversarial Networks (GANs) [246], Recurrent Neural Networks (RNNs) [247], and as part of attention-based architectures such as transformers [248] and generative diffusion models [249]. We will, for now, consider only the classical design: several convolutional layers capped by several dense ones.

As discussed, CNNs have a more specialised architecture than dense layers [10,242]. This architecture is designed to help the network perform in a specific domain of tasks by adding *a priori* information defining information flow inside the network. This can help reduce overfitting in some cases, as it means a smaller network with fewer parameters can achieve the same task as a more extensive dense network. Fewer parameters mean less total information can be stored in the network, so it is less likely that a model can memorise specific information about the noise present in training examples. A CNN encodes information about the dimensionality of the input image; the location of features within the input image is conserved as it moves through layers. It also utilises the fact that within some forms of data, the same feature is likely to appear at different locations within the input vector; therefore, parameters trained to recognise features can be reused across neurons. For example, if detecting images of cats, cats' ears are not always going to be in the same location within the image. However, the same pattern of parameters would be equally helpful for detecting ears wherever it is in the network.

The following subsections describe different aspects of CNNs, including a description of pooling layers, which are companion layers often employed within convolutional networks.

4.4.1 Convolutional Layers

CNNs take inspiration from the biological visual cortex [250]. In animal vision systems, each cortical neuron is not connected to every photoreceptor in the eye; instead, they are connected to a subset of receptors clustered near each other on the 2D surface of the retina [251]. This connection area is known as the **receptive field**, a piece of terminology often borrowed when discussing CNNs [250].

Convolutional Layers behave similarly. Instead of each neuron in every layer being connected to every neuron in the previous layer, they are only connected to a subset, and the parameters of each

neuron are repeated across the image, significantly reducing the number of model parameters and allowing for translation equivariant feature detection [10,242]. It is a common misnomer that convolutional layers are translation invariant [252]; this is untrue, as features can and usually do move by values that are not whole pixel widths, meaning that even if the filters are the same, the pixel values can be different and give different results. One common problem with CNNs is that very small changes in input pixel values can lead to wildly different results, so this effect should be mitigated if possible. If they do not involve subsampling, however, CNNs are sometimes equivariant. This means that independent of starting location, ignoring edge effects, if you shift the feature by the same value, the output map will be the same – this can be true for some configurations of CNN but is also broken by most common architectures.

This input element subset is nominally clustered spacially, usually into squares of input pixels [10,242]. This means that unlike with dense input layers, wherein 2D and greater images must first be flattened before being ingested, the dimensionality of the input is inherently present in the layer output. In a dense layer, each input is equally important to each neuron. There is no distinguishing between inputs far away from that neuron and inputs closer to that neuron (other than distinctions that the network may learn during the training process). This is not the case inside convolutional layers, as a neuron on a subsequent layer only sees inputs inside its receptive field.

As the proximity of inputs to a neuron can be described in multiple dimensions equal to that of the input dimensionality, the network, therefore, has inherent dimensionality baked into its architecture – which is one example of how the CNN is specialised for image recognition [10,242]. In the case of a 2D image classification problem, we now treat the input vector as 2D, with the receptive field of each neuron occupying some shape, most simply a square or other rectangle, on the 2D vector’s surface.

The term receptive field is usually reserved to describe how much of the input image can influence the output of a particular neuron in the network [10,242]. The set of tunable parameters that define the computation of a neuron in a convolutional layer when fed with a subset of neuron outputs or input vector values from the previous layer is called a **kernel**. Each kernel looks at a subset of the previous layers’ output and produces an output value dependent on the learned kernel parameters. A kernel with parameters tuned by model training is sometimes called a **filter**, as, in theory, it filters the input for a specific translation-invariant feature (although, as we have said, this is only partially true). The filter produces a strong output if it detects that feature and a weak output in its absence. Identical copies of this kernel will be tiled across the previous layer to create a new image with the same dimensionality as the input vector, i.e. kernels in a time-series classifier will each produce their own 1D time-series feature map, and kernels fed a 2D image will each produce a 2D image feature map. In this way, each kernel produces its own feature map where highly scoring pixels indicate the presence of whatever feature they have been trained to identify, and low-scoring ones indicate a lack thereof. Because the network only needs to learn parameters for this single kernel, which can be much smaller than the whole image and only the size of the feature it recognises, the number of trainable parameters required can be significantly reduced, decreasing training time, memory consumption, and overfitting risk. For a single kernel with no stride or dilation, see Section 4.4.2, applied to an input vector with no depth dimension, the number of trainable parameters is given by

$$\text{len}(\theta_{\text{kernel}}) = \left(\prod_i^N S_i \right) + 1 \quad 4.35$$

where $\text{len}(\theta_{\text{kernel}})$ is the number of trainable parameters in the kernel, N is the number of dimensions in the input vector, and S_i is the configurable hyperparameter, kernel size in the i^{th} dimension. The extra plus one results from the bias of the convolutional kernel.

For example, a 1D kernel of size 3, would have $3 + 1 = 4$ total parameters, independent of the size of the input vector, and a 2D kernel of size 3×3 would have $3 \times 3 + 1 = 10$ total parameters, again independent of the size of the 2D input vector in either dimension. See Figure 4.24 for an illustration of the structure of a convolutional kernel.

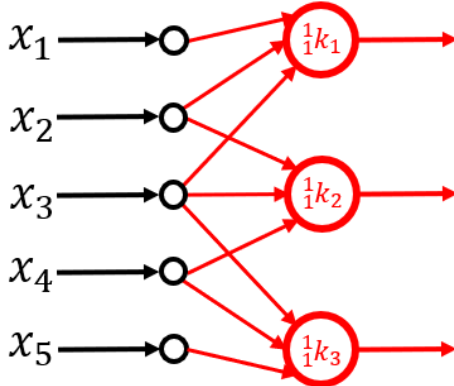


Figure 4.24 | Diagram of a single kernel, $\frac{1}{1}k$, in a single convolutional layer. In this example, a 1D vector is being input; therefore, the single kernel's output is also 1D. This kernel has a kernel size of three, meaning that each neuron receives three input values from the layer's input vector, \vec{x} , which in this case is length five. This means there is room for three repeats of the kernel. Its parameters are identical for each iteration of $\frac{1}{1}k$ at a different position. This means that if a pattern of inputs recognised by the kernel at position 1, $\frac{1}{1}k_1$ is translated two elements down the input vector, it will be recognised similarly by the kernel at $\frac{1}{1}k_3$. Although this translational invariance is only strict if the translation is a whole pixel multiple and no subsampling (pooling, stride, or dilation) is used in the network, this pseudo-translational invariance can be useful, as often, in images and time series data, similar features can appear at different spatial or temporal locations within the data. For example, in a speech classification model, a word said at the start of the time series can be recognised just as easily by the same pattern of parameters if that word is said at the end of the time series (supposing it lies on the sample pixel multiple). Thus, the same kernel parameters and the same filter can be repeated across the time series, reducing the number of parameters needed to train the model. This particular kernel would have $3 + 1 = 4$ total parameters, as it applied to a 1D input vector, and has a kernel size of three, with an additional parameter for the neuron bias. With only a single kernel, only one feature can be learned, which would not be useful in all but the most simple cases. Thus, multiple kernels are often used, each of which can learn its own filter.

When first reading about convolutional layers, it can be confusing to understand how they each “choose” which features to recognise. What should be understood is that this is not a manual process; there is no user input on which kernels filter which features; instead, this is all tuned by the chosen optimiser during the training process [10,242]. Even the idea that each kernel will cleanly learn one feature type is an idealised simplification of what can happen during training. Gradient descent has no elegant ideas of how it should and should not use the architectures presented to it and will invariably follow the path of least resistance, which can sometimes result in strange and unorthodox uses of neural structures. The more complex and non-linear the recognition task, the more often this will occur.

Although we do not specify exactly which features each kernel should learn, there are several hyperparameters that we must fix for each convolutional layer before the start of training [10,242]. We must set a kernel (or filter) size for each dimension of the input vector. For a 1D input vector, we will set one kernel size per kernel; for a 2D input vector, we must set two, and so on. These kernel dimensions

d dictate the number of input values read by each kernel in the layer and are nominally consistent across all kernels in that layer; see Figure 4.25 for an illustration of how different kernel sizes tile across a 2D input.

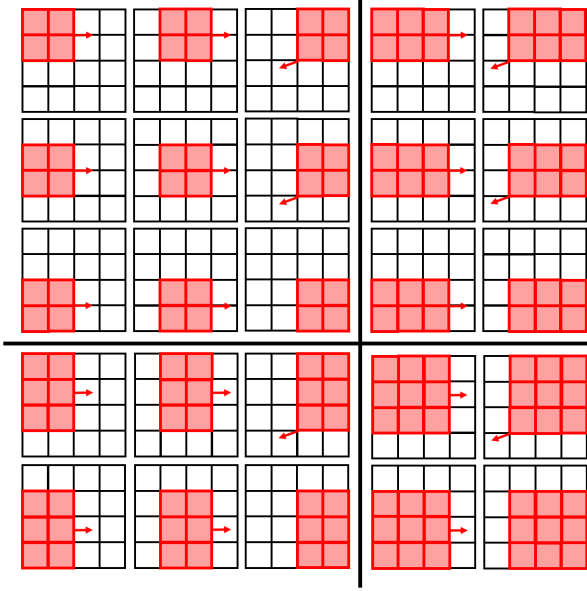


Figure 4.25 | Illustration of how different values of kernel size would be laid out on a 4×4 input image. In each case, unused input image values are shown as empty black squares on the grid, and input values read by the kernel are filled in red. The grids show the input combinations that a single kernel would ingest if it has a given size, assuming a stride value of one and zero dilation. The kernel sizes are as follows: *Upper left*: 2×2 . *Upper right*: 3×2 . *Lower left*: 2×3 . *Lower right*: 3×3 . One pixel in the output map is produced for each kernel position. As can be seen, the size of the output map produced by the kernel depends both on the input size and the kernel size; smaller kernels produce a larger output vector.

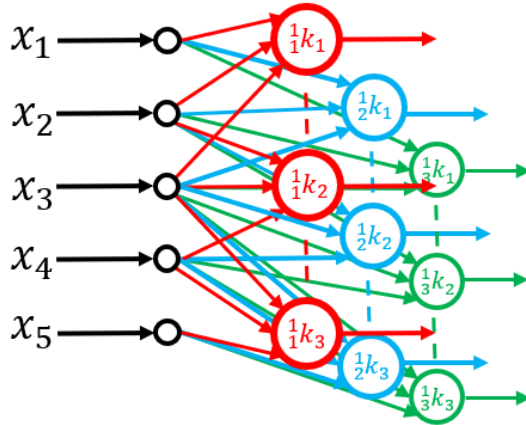
The other hyperparameters that must be set are the number of different kernels and the choice of activation function used by the kernel's neurons [10,242]. These hyperparameters can sometimes be manually tuned using information about the dataset, i.e. the average size of the features for kernel size and the number of features for the number of kernels, but these can also be optimised by hyperparameter optimisation methods, which might be preferable as it is often difficult to gauge which values will work optimally for a particular problem [253].

Multiple kernels can exist up to an arbitrary amount inside a single convolutional layer [10,242]. The intuition behind this multitude is simply that input data can contain multiple different types of features, which can each need a different filter to recognise; each kernel produces its own feature map as it is tiled across its input, and these feature maps are concatenated along an extra **depth** dimension on top of the dimensionality of the input vector. A 1D input vector will have 2D convolutional layer outputs, and a 2D input vector will result in 3D convolutional outputs. The original dimensions of the input vector remain intact, whilst the extra discrete depth dimension represents different features of the image; see Figure 4.26.

In the case of a colour picture, this depth dimension could be the red, green, and blue channels, meaning this dimension is already present in the input vector. The number of trainable parameters of a single convolutional layer is given by

$$\text{len}(\theta_{\text{conv_layer}}) = K \times \left(\left(D \times \prod_i^N S_i \right) + 1 \right) \quad 4.36$$

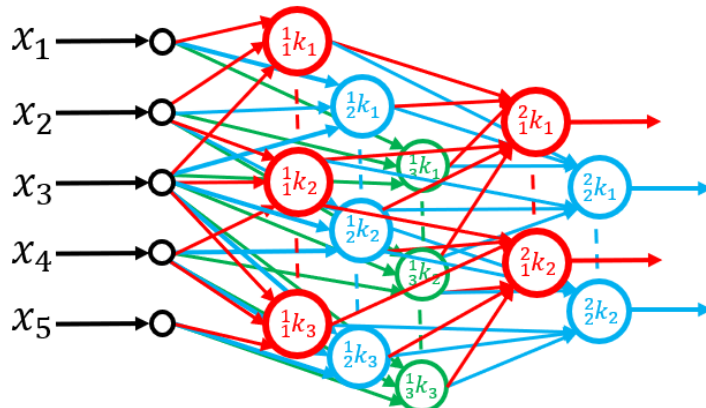
where $\text{len}(\theta_{\text{conv_layer}})$ is the total number of parameters in a convolutional layer, K is the number of convolutional kernels in that layer, a tunable hyperparameter, and D is the additional feature depth dimension of the layer input vector, which is determined either by the number of pre-existing feature channels in the input vector, i.e. the colour channels in a full-colour image or, if the layer input is a previous convolutional layer, the number of feature maps output by that previous layer, which is equivalent to the number of kernels in the previous layer. For example, a 1D convolutional layer with three kernels, each with size three, ingesting a 1D input with only a singleton depth dimension would have $3 \times ((1 \times (3)) + 1) = 12$ total trainable parameters, whereas a 2D convolutional layer with three kernels of size 3×3 looking at a colour RGB input image would have $3 \times (3 \times (3 \times 3) + 1) = 84$ total trainable parameters.



Type	Num Filters / Neurons	Filter / Pool Size	Stride	Activation Function	Dropout	1D input vector
Convolutional	3	3	1	ReLU	-	other layers

Figure 4.26 | Upper: Diagram of three convolutional kernels, $[1/1k, 1/2k, 1/3k]$, in a single convolutional layer. Each kernel is coloured differently, in red, green, and blue. Artificial neurons of the same colour will share the same learned parameters. Again, a 1D vector is being input; therefore, the output of each of the kernels is 1D, and the output of the kernels stack to form a 2D output vector, with one spatial dimension retained from the input vector and an extra discrete depth dimension representing the different features learned by each of the kernels. Again, each kernel has a kernel size of three. Multiple kernels allow the layer to learn multiple features, each of which can be translated across the input vector, as with the single kernel. Using Equation 4.36, this layer would have $3 \times ((1 \times 3) + 1) = 12$ trainable parameters. It should be noted that this is a very small example simplified for visual clarity; real convolutional networks can have inputs many hundreds or thousands of elements long and thus will have many more iterations of each kernel, as well as many more kernels sometimes of a much larger size. **Lower:** Abstracted diagram of the same layer with included hyperparameter information.

As with dense layers, multiple convolutional layers can be stacked to increase the possible range of computation available [10,242]; see Figure 4.27. The first convolutional layer in a network will ingest the input vector, but subsequent layers can ingest the output of previous convolutional layers, with kernels slicing through and ingesting the entirety of the depth dimension. In theory, this stacking allows the convolutional layers to combine multiple more straightforward features in order to recognise more complex, higher-level features of the input data — although, as usual, things are not always quite so straightforward in practice. When calculating the number of trainable parameters in multiple convolutional layers, we can use Equation 4.36 for each layer and sum the result.



Type	Num Filters / Neurons	Filter / Pool Size	Stride	Activation Function	Dropout
Convolutional	3	3	1	ReLU	-
Convolutional	2	2	1	ReLU	-

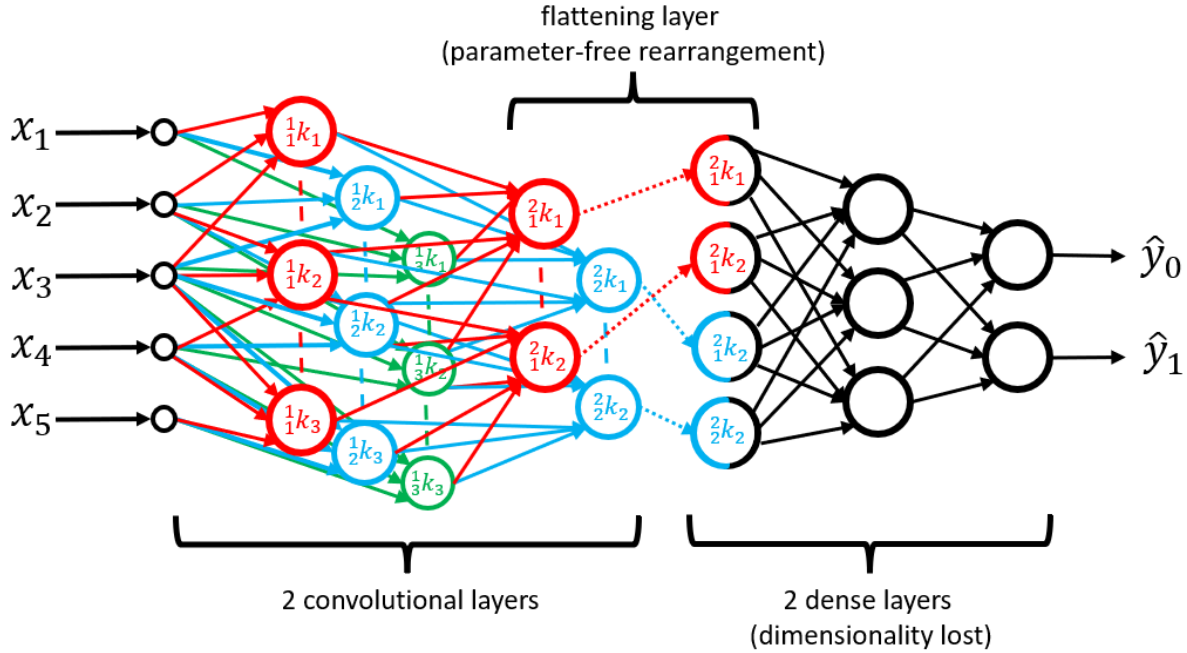
1D input vector

other layers

Figure 4.27 | Upper: Diagram of two convolutional layers, each with independent kernels. The first layer has three kernels, each with a size of three. The second layer has two kernels, both with a size of two. Again, this is a much-simplified example that would probably not have much practical use. Different kernels are coloured differently, in red, green, and blue. Although it should be noted that similar colours across layers should not be taken as any relationship between kernels in different layers, they are each tuned independently and subject to the whims of the gradient descent process. This example shows how the kernels in the second layer take inputs across the entire depth of the first layer but behave similarly along the original dimension of the input vector. In theory, the deeper layer can learn to recognise composite features made from combinations of features previously recognised by the layers below and visible in the output feature maps of the different kernels. This multi-layer network slice would have $(3 \times ((1 \times 3) + 1)) + (2 \times ((3 \times 2) + 1)) = 26$ total trainable parameters. This was calculated by applying Equation 4.36 to each layer. **Lower:** Abstracted diagram of the same layers with included hyperparameter information.

The result of using one or more convolutional layers on an input vector is an output vector with an extra discrete depth dimension, with each layer in the stack representing feature maps [10,242]. Whilst often considerably more interpretable than maps of the parameters in dense layers, these maps are

often not very useful alone [245]. However, a flattened version of this vector is now, hopefully, much easier for dense layers to classify than the original image; see Section 3.4. As such, CNNs used for classification are almost always capped by one or more dense layers in order to produce the final classification result; see Figure 4.28 for a toy example of a CNN used for binary classification.



Type	Num Filters / Neurons	Filter / Pool Size	Stride	Activation Function	Dropout	1D input vector
Convolutional	3	3	1	ReLU	-	
Convolutional	2	2	1	ReLU	-	
Dense	3	-	-	ReLU	-	
Dense	2	-	-	SoftMax	-	

binary classification vector

Figure 4.28 | Upper: Diagram of a very simple convolutional neural network binary classifier consisting of four layers with tunable parameters plus one infrastructure layer without parameters. Two consecutive convolutional layers ingest the five-element input vector, \vec{x} . The 2D output of the latter of the two layers is flattened into a 1D vector by a flattening layer. This flattened vector is then ingested by two dense layers, the latter of which outputs the final classification score. The first convolutional layer has three convolutional kernels, each with a size of three, and the second convolutional layer has two kernels, both with a size of two. The first dense layer has three artificial neurons, and the final output dense layer has a number of neurons dictated by the required size of the output vector. In the case of binary classification, this is either one or two. Different kernels within a layer are differentiated by colour, in this case, red, green, or blue, but a similar colour between layers does not

indicate any relationship. Dimensionless neurons are shown in black; it should be noted that after flattening, dimensional information is no longer necessarily maintained by the network structure. Of course, no information is necessarily lost either, as the neuron index itself contains information about where it originated, so, during training, this information can still be used by the dense layers; it is just not necessarily maintained as it is in convolutional layers. This network will have in total $26 + (3 \times 4 + 4) + (2 \times 3 + 2) = 50$ trainable parameters. This network is very simple and would probably not have much practical use in real-world problems other than straightforward tasks that would probably not necessitate using neural networks. *Lower:* Abstracted diagram of the same model with included hyperparameter information.

4.4.2 Stride, Dilation, and Padding

Stride is a user-defined hyperparameter of convolutional layers that must be defined before training [10,242,253]. Like kernel size, it is a multidimensional parameter with a value for each input vector dimension. A convolutional layer's stride describes the distance the kernel moves between instances. A stride of one is the most commonly used choice. For example, if the stride is one, then a kernel is tiled with a separation of one input value from its last location. Stride, S , is always greater than zero, $S > 0$. The kernels will overlap in the i^{th} dimension if $S_i < k_i$. If $S_i = k_i$, there will be no overlap and no missed input vector values. If $S_i > k_i$, some input vector values will be skipped; this is not usually used. Along with kernel size, stride determines the output size of the layer. A larger stride will result in fewer kernels and, thus, a smaller output size; see Figure 4.29 below for an illustration of different kernels strides.

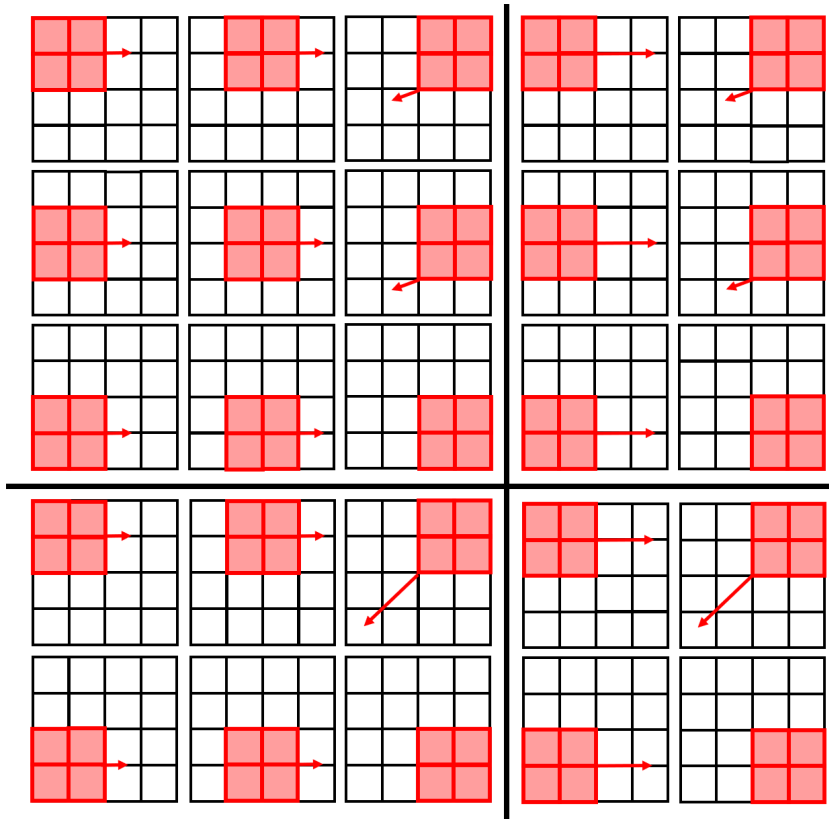


Figure 4.29 | Illustration of how different values of kernel stride would be laid out on a 4×4 input image. In each case, unused input image values are shown as empty black squares on the grid, and input values read by the kernel are filled in red. Similar to kernel size, different values of stride result

in a different output vector size. The strides shown are as follows: *Upper left*: 1, 1. *Upper right*: 2, 1. *Lower left*: 1, 2. *Lower right*: 2, 2.

Introducing kernel stride primarily serves to reduce the overall size of the network by reducing the output vector without adding additional parameters; in fact, the number of parameters is independent of stride [10,242]. Reducing the size of the network might be a desirable outcome as it can help reduce computational time and memory overhead. It can also help to increase the receptive field of neurons in subsequent layers as it condenses the distance between spatially separated points, so when adjusting the resolution of feature maps in a model to balance the identification of smaller and larger scale features, it could potentially be a useful dial to tune. In most cases, however, it's left at its default value of one, with the job of reducing the network size falling to pooling layers; see Section 4.4.3.

One interesting and potentially unwanted effect of introducing stride into our network is that it removes the complete translation equivariance of the layer by subsampling; instead, translations are only equivariant if they match the stride size, i.e. if a kernel has a stride of two features are invariant if they move exactly two pixels, which is not a common occurrence.

Dilation is a further hyperparameter that can be adjusted prior to network training [10,242,253]. Dilation introduces a spacing inside the kernel so that each input value examined by the kernel is no longer directly adjacent to another kernel input value, but instead, there is a gap wherein the kernel ignores that element; see Figure 4.30. By default, this value would be set to zero, and no dilation would be present. This directly increases the receptive field of that kernel without introducing additional parameters, which can be used to help the filters take more global features into account. It can also be used in the network to try and combat scale differences in features; if multiple kernels with different dilations are used in parallel on different model branches, the model can learn to recognise features at the same scale but with different dilations.

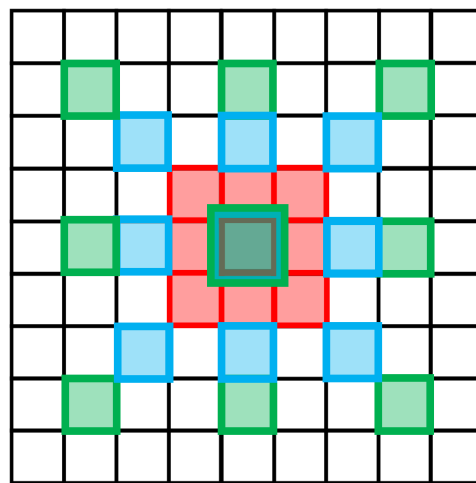


Figure 4.30 | Diagram illustrating how different values of kernel dilation affect the arrangement of the kernel input pixels. In this example, the receptive field of a single 3×3 kernel at three different dilation levels is displayed; differing colours represent the input elements at each dilation level. The shaded red kernel illustrates dilation level zero; the shaded blue region is a kernel with dilation of one, and the green kernel has a kernel dilation of two.

Particular stride, dilation, and size combinations will sometimes produce kernel positions that push them off the edge of the boundaries of the input vector. These kernel positions can be ignored, or the input vector can be padded with zeros or repeats of the nearest input value; see Figure 4.31.

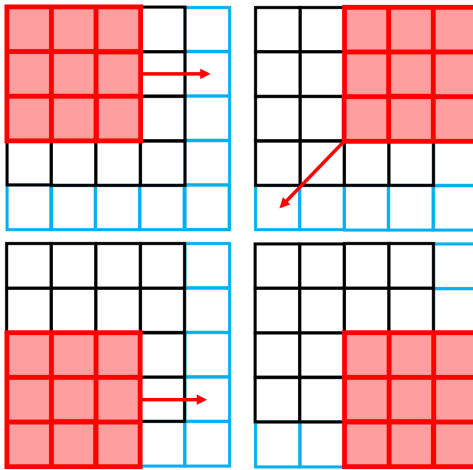


Figure 4.31 | Diagram illustrating how padding can be added to the edge of an input vector in order to allow for otherwise impossible combinations of kernel, stride, size, and dilation. In each case, unused input image values are shown as empty black squares on the grid, input values read by the kernel are shaded red, and empty blue squares are unused values added to the original input vector, containing either zeros or repeats of the closest data values. In this example, the kernel size is 3×3 , and the kernel stride is 2, 2.

4.4.3 Pooling

Pooling layers, or simply pooling, is a method used to restrict the number of data channels flowing through the network [10,242]. They see widespread application across the literature and have multiple valuable properties. They can reduce the size of the network and thus the computation and memory overhead, and they can also make the network more robust to small translational, scale, and rotational differences in your input features. Convolutional layers record the position of the feature they recognise but can sometimes be overly sensitive to tiny shifts in the values of input pixels. Small changes in a feature's scale, rotation, or position within the input can lead to a very different output, which is evidently not often desirable behaviour.

Pooling layers do not have any trainable parameters, and their operation is dictated entirely by the user-selected hyperparameters chosen before the commencement of model training. Instead, they act to group pixels via subsampling throwing away excess information by combining their values into a single output. In this way, they are similar to convolutional kernels, however, instead of operating with trained parameters, they use simple operations. The two most common types of pooling layers are **max pooling** and **average pooling**; max pooling keeps only the maximum value within each of its input bins, discarding the other values; intuitively, we can think of this as finding the strongest evidence for the presence of the feature within the pooling bin and discarding the rest. Average pooling averages the value across the elements inside each pooling bin, which has the advantage that it uses some information from all the elements.

As can be imagined, the size of CNNs can increase rapidly as more layers and large numbers of kernels are used, with each kernel producing a feature map nearly as large as its input vector. Although the number of parameters is minimised, the number of operations increases with increasing input size. Pooling layers are helpful to reduce redundant information and drastically reduce network size whilst also making the network more robust to small changes in the input values.

Along with the choice of operational mode, i.e. average or maximum, pooling layers have some of the same hyperparameters as convolutional kernels, size, and stride. Unlike convolutional layers, the pooling stride is usually set to the same value as the pooling size. Meaning that there will be no overlap

between pooling bins but also no gaps. This is due to the purpose of pooling layers, which attempt to reduce redundant information; if stride were set to smaller values, there would be little reduction and little point to the layer.

Because pooling with stride is a form of subsampling, it does not maintain strict translational equivariance unless the pool stride is one, which, as stated, is uncommon. Thus, as most CNN models use pooling, most CNNs are neither strictly translationally invariant nor equivariant [252].

4.5 Results from the Literature

Both gravitational-wave astrophysics and deep learning methods have been through rapid advancement in the previous decade, so it is perhaps unsurprising that there has also developed a significant intersection between the two fields [254]. Multiple artificial network architectures, CNNs [53,52], autoencoders [255], generative adversarial networks [256], recurrent neural networks [257], and attention-based networks like transformers [258] have been applied to numerous gravitational-wave data analysis problems. This review will focus on efforts to apply CNN classifiers to detect features hidden within interferometer data. First, we will look at attempts to detect Compact Binary Coalescences (CBCs), followed by a look at unmodeled Bursts detection attempts. More complex network architectures will be reviewed later when we examine attention layers in closer detail; see Section 6. This is not intended to be an exhaustive catalogue, although efforts have been made to be as complete as possible.

4.5.1 Convolutional Neural Networks (CNNs) for the detection of Compact Binary Coalescences (CBCs)

The earliest attempts at CBC classification using artificial neural networks were a pair of papers by George *et al.* [52] which was followed up by Gabbard *et al.* [53]. George *et al.* [52] applied CNNs to the binary classification problem and basic parameter estimation. They used CNNs with two outputs to extract parameter estimates for the two companion masses of the binary system. They used the whitened outputs of single interferometers as inputs and utilized CNNs of a standard form consisting of convolutional, dense, and pooling layers; see Figure 4.33 and Figure 4.32. They evaluated two models, one smaller and one larger. In their first paper, they used only simulated noise, but they produced a follow-up paper showing the result of the model’s application to real interferometer noise [259]. Gabbard *et al.* [53] used an alternate CNN design with a different combination of layers. They only used a single network architecture, and no attempt at parameter estimation was made. A differentiating feature of their paper was the training of individual network instances to recognize different SNRs. Both George *et al.* [52] and Gabbard *et al.* [53] achieved efficiency curves that closely resembled that of matched filtering; of note, however, both were validated at a considerably higher FAR ($\sim 10^3$ Hz) than is useful for a gravitational-wave search, this will be a consistent theme throughout the literature and is one of the greatest blockers to using CNNs in gravitational-wave transient detection.

There have been many papers that follow up on these two initial attempts. Several papers with mixed results are difficult to compare due to a variety of different conventions used to characterise signal amplitude and assess model performance. Luo *et al.* [260] attempted to improve the model described by Gabbard *et al.* They have presented their results using a non-standard “Gaussian noise amplitude parameter”. Whilst within their own comparisons, they seem to have improved network operation over the original design, at least at higher FARs, it is difficult to make a comparison against other papers because of the unorthodox presentation. Schmitt *et al.* [261] attempted to compare the performance of one of the models presented in George *et al.* [52] with three different model architectures, Temporal Convolutional Networks (TCNs), Gated Recurrent Units (GRUs), and Long Short-Term Memory (LSTMs). They seem to show that the other model architectures can achieve higher performance than CNNs, but they have used an unfamiliar waveform scaling method, so it is hard to compare to other results.

A more interesting follow-up by Fan *et al.* [262] took the smaller of the two models introduced in George *et al.* [52] and extended it to use multiple detectors as inputs rather than the previously mentioned studies, which looked at only single detectors. They do this for both detection and parameter estimation and appear to show improved accuracy results over the original paper [52], although they do not address the confounding factor of having to deal with real noise. Krastev *et al.* tested the use of the other larger model introduced by George *et al.* [52]. They tested its use on Binary Neutron Star (BNS) signals, as well as reaffirming its ability to detect BBH signals. They used significantly longer input windows to account for the longer detectable duration of BNS signals. They found BNS detection to be possible, although it proved a significantly harder problem.

Using a different style of architecture, Gebhard *et al.* [97] argued that convolution-only structures are more robust and less prone to error, as they remove much of the black-box effect produced by dense layers and allow for multiple independently operating (though with overlapping input regions) networks, creating an ensemble which generates a predictive score for the presence of a signal at multiple time positions. This results in a time-series output rather than a single value, which allows the model to be agnostic to signal length. Their determination of the presence of a signal can thus rely on the overall output time series rather than just a single classification score. Similarly to Fan *et al.* [262], they used multiple detector inputs.

There have been at least two papers that utilise ensemble approaches to the problem. Ensembles consist of multiple independently trained models in the hopes that the strengths of one will counteract the weaknesses of another under the assumption that it is less likely for them both to be weak in the same area. A joint decision is then taken through some mechanism that takes the result of all models into consideration, often waiting for certain models' votes under certain criteria. Huerta *et al.* [263] used an approach consisting of four independently trained models, each of which has two separate CNN branches for the LIGO Hanford and LIGO Livingston detectors, which are then merged by two further CNN layers. Still, they have efficiency results down to a lower FAR than any paper reviewed so far, at 1×10^{-5} , which is impressive, although the efficiency scores at these FARs are low ($< 1\%$). Overall, the paper is more focused on the software infrastructure for deploying neural network models. Ma *et al.* [264] used an ensemble network that employ one of the architectures described by Gabbard *et al.* [53]. They utilise two “subensembles” in an arrangement in which each detector has its own ensemble composed of networks that vote on a false/positive determination; the results of both of the two subensembles are then combined for a final output score. They do not give efficiency scores at set SNRs, so again, it is difficult to compare against other results.

There have also been some interesting studies that use feature engineering to extract features from the input data before those features are fed into the CNN models, see Section 4.2.7. Wang *et al.* [265] use a sparse matched filter search, where template banks of only tens of features, rather than the usual hundreds of thousands or millions, were used. The output of this sparse matched filter was then ingested by a small CNN, which attempted to classify the inputs. Notably, they use real noise from the 1st LIGO observing run [30] and multi-detector inputs. Though an interesting method, their results appear uncompetitive with other approaches. Reza [266] *et al.* used a similar approach but split the input into patches before applying the matched filter. However, results are not presented in an easily comparable fashion. Bresten *et al.* [267] adapts one of the architectures from George *et al.* [52] but applies a feature extraction step that uses a topological method known as persistent homology before the data is ingested by the network. It is an interesting approach, but their results are unconvincing. They limited their validation data to 1500 waveforms at only 100 specific SNR values in what they term their “hardest case”. They showed poor results compared to other methods, suggesting their method is undeveloped and heavily SNR-tailored.

There have been at least three spectrogram-based attempts to solve the CBC detection problem. Yu *et al.* [268] used single detector spectrograms, which are first analysed in strips using multiple 1D CNNs before being fed into a 2D CNN for final classification; they achieve middle-of-the-range efficiency results. Aveiro *et al.* [269] focused on BNS detection and used an out-of-the-box object detection network to try and detect patterns in spectrograms. They do not state efficiencies for SNRs less than ten. Finally, there was also a search paper [270], which searched through the second observing run using spectrograms-based CNNs; they detected nothing of significance.

There has also been an attempt to use wavelet decomposition for the problem. Lin *et al.* [271] focused on the detection of BNS signals by wavelet decomposition with some very promising results shown to outperform matched filtering; a subsequent follow-up paper [272] showed that the same method could be applied to BBH signals with equal promise. They achieve an efficiency of 94% when detecting waveforms with an SNR of 2 at a FAR of 1×10^{-3} , which undercuts the competition by considerable margins. Their method is certainly worth investigation but was unfortunately missed until this thesis was in the latter stages of construction, so no wavelet decomposition methods have been attempted.

There have also been a number of papers utilising CNNs for specialised detection cases, such as mass asymmetric CBCs [273] by Andrés-Carcasona *et al.*, who employ spectrogram-based CNNs to run a search over O3, and eccentric CBCs by Wei *et al.* [274], the latter of which also focuses on early detection along with a few other papers [275–277] which attempt to find CBC inspirals before they are detectable by standard methods. There have also been a number of papers that discuss the use of CNNs for the analysis of data from future space-based detectors [278,279]. For brevity, and as they are less relevant to our problems, these special cases will not be discussed here.

As can be seen, it is very difficult to compare the performance of many of the architectures and methods presented in the literature. The results are presented at wildly different FARs and SNR ranges, often using different incomparable metrics and with varying levels of rigour. There is a tendency to apply new tools and ideas to the problem without careful thought about how the results can be standardised. Table 4.4 displays results from some of the papers that were found to have at least somewhat comparable metrics.

Name	Model	Real Noise?	Detectors	Target	Feature	SNR Tailored	FAR	Acc 8	Acc 6	Acc 4
George <i>et al.</i> [52]	Smaller Novel CNN	No	Single	BBH	No	No	5×10^{-2}	0.98	0.70	0.16
-	Larger Novel CNN	-	-	-	-	-	-	0.99	0.80	0.21
George <i>et al.</i> [259]	-	Yes	-	-	-	-	-	0.98	0.77	0.18
Gabbard <i>et al.</i> [53]	Novel CNN	No	Single	BBH	No	Yes	1×10^{-1}	1.0	0.88	0.44
-	-	-	-	-	-	-	1×10^{-2}	0.99	0.69	0.10
-	-	-	-	-	-	-	1×10^{-3}	0.98	0.49	0.02
Fan <i>et al.</i> [262]	Based on George <i>et al.</i> Small	No	Three	BBH	No	No	4×10^{-2}	0.99	0.84	0.32
Krastev <i>et al.</i> [280]	Based on George <i>et al.</i> Large	No	Single	BNS	No	No	1×10^{-1}	0.71	0.42	0.20
-	-	-	-	-	-	-	1×10^{-2}	0.32	0.10	0.02
-	-	-	-	-	-	-	1×10^{-3}	0.11	0.00	0.00
Gebhard <i>et al.</i> [97]	Novel Conv-Only Model	Yes	Two	BBH	No	No	1.25×10^{-3}	0.83	0.35	Not Given

Wang <i>et al.</i> [265]	-	Yes	Two	BBH	Matched Filter	No	1×10^{-1}	0.60	0.24	0.12
-	-	-	-	-	-	-	1×10^{-2}	0.30	0.05	0.00
-	-	-	-	-	-	-	1×10^{-3}	0.08	0.00	0.00
Huerta <i>et al.</i> [263]	Novel Ensemble	Yes	Two	BBH	No	No	5×10^{-4}	0.20	0.15	Not Given
-	-	-	-	-	-	-	5×10^{-5}	0.01	0.001	Not Given
Yu <i>et al.</i> [268]	Novel Multi-Branched CNN	Yes	Single	BBH	Spectrogram	No	6×10^{-2}	0.89	0.67	0.20

Table 4.4 | A comparison of results from the literature, red values indicate the significant feature of the study. Note: Some accuracy values are extracted from plots by eye, so substantive error will have been introduced. Some results were not included as they did not state comparable performance metrics.

4.5.2 Convolutional Neural Networks (CNNs) for the detection of Gravitational-Wave Bursts

The literature surrounding burst detections with CNNs is considerably more limited than for CBCs. In all of the previously mentioned deep-learning studies, the training of the network has relied on accurate models of CBC waveforms. As has been noted, the availability of reliable waveforms for other potential gravitational-wave sources, i.e. bursts, is considerably narrower due to unknown physical processes, large numbers of free parameters, and computational intractability, making it nearly impossible to have a sufficiently sampled template bank.

Despite this, there have been some attempts, most notably using simulated supernovae waveforms, as these are the most likely candidates for initial burst detection. There have been at least five attempts to classify supernovae with this method. Iess *et al.* [100] used a CNN mode with two separate inputs; a 1D time series and a 2D spectrogram were fed into different input branches of the model. They used supernova signals taken from simulation catalogues along with a simple phenomenological model for two transient glitches classes in order to train the CNN to distinguish between the glitches and supernovae in the hopes that if a supernova signal were to appear in future interferometer data, it could be identified as such, rather than being ruled out as a glitch. Perhaps unsurprisingly, due to the complexity of the signal compared to CBCs, they require a significantly higher SNR in order to achieve similar accuracy results as the CBC case, although they still achieve some efficiency at lower SNRs. Chan *et al.* [101] trained a CNN using simulated core-collapse supernovae signals drawn from several catalogues covering both magnetorotational-driven and neutrino-driven supernovae. They measured the ability to detect the signal and correctly classify which of the two types it fell into. They used moderately deep CNNs and emphasised the importance of multi-detector inputs for the task. They found it possible to detect magnetorotational-driven events at considerably greater distances than neutrino-driven supernovae.

Lopez *et al.* [281,282] forgoes the use of simulated template backs in their training for a phenomenological approach in an attempt to try and avoid the problem of small template banks. They used an intricate model architecture comprised of mini-inception-resnets to detect supernova signals in time-frequency images of LIGO-Virgo data. Mini-inception resnets consist of multiple network branches of different lengths, which run in parallel before combining to produce a final classification score. Having some paths through the network that are shorter than others can be beneficial to avoid the vanishing gradient problem, wherein gradients fall off to zero within the network; having shortcuts allows the network to maintain a clearer view of the inputs even when other paths have become deep [158]. Blocks of layers within networks that have **skip connections** periodically like this are known as residual blocks [159], and allow much deeper architectures than would otherwise be possible. Networks that employ skip connections are known as **residual networks** or **resnets** [159]. Inception designs have multiple different network branches, all consisting of residual blocks, so there are many paths through the network from input vector to output.

Sasaoka *et al.* [283,284] use gradient-weighted feature maps to train CNNs to recognise supernovae spectrograms. They utilised core-collapse supernovae waveforms from a number of catalogues. However, they only achieved good classification performances at 1 kpc. They attributed some of their difficulties to features lost to the lower resolution of their time-frequency maps and recommended trying a different algorithm for their generation.

There have also been a few attempts to apply CNNs to the problem of unmodelled signal detection, looking for generic signals using methods that do not require a precisely tailored training set. As has been discussed, we do not yet know how well our simulations will align with real supernovae' gravitational emissions, and it is hard to tell whether the differences between our training datasets and the real signals will significantly hinder our model's ability to detect real signals. Such difficulty could certainly be a possibility; often, deep learning modules can be very sensitive to changes in their dis-

tribution and can lose significant efficacy when applied to out-of-distribution examples. If a sensitive enough generic model could be trained, this would alleviate this problem.

Marianer *et al.* [102] attempt a generic detection method via anomaly recognition. This is not a novel idea in the field of machine learning. However, its application to a generic burst search is intriguing. They apply their model to spectrograms of known transient noise glitches and use a mini-inception resnet to classify the input spectrograms into glitch classes. While examining the feature space of the classifier as it examines data, i.e. the feature maps of the neurons in internal convolutional layers, they utilise two anomaly detection methods to identify when a particular feature space does not look like it belongs to any of the known classes. This means they do not rely directly on the model to output a “novel” class. The latter poses a difficult problem as it is unclear how to ensure the training set is well sampled over every possible counterexample.

The other and most relevant work to this thesis on unmodeled glitch detection is MLy [28]. MLy is a deep learning pipeline that relies on CNN models, which are trained to directly identify coherence between multiple detectors rather than using any pattern recognition or anomaly rejection techniques. This makes it somewhat unique amongst the methods presented. Rather than using a dataset consisting of particular morphologies of signal, MLy utilises distributions of generic white noise burst signals that, in their entirety, will cover all possible burst morphologies with a certain frequency range and duration. One would note that these distributions would also cover all possible glitch morphologies within that parameter space. Therefore, MLy is trained not only to notice the presence of a signal but also the coherence of that signal across detectors. In that sense, it is similar to the operation of many of the preexisting burst pipelines, though it is the only purely machine-learning pipeline to attempt to do this.

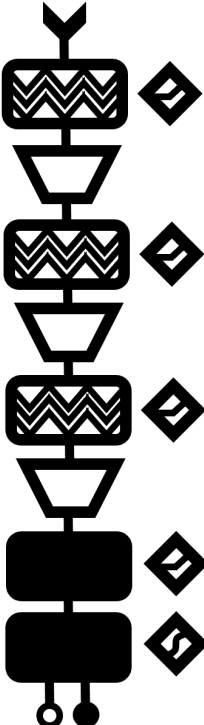
MLy achieves this goal by utilising two independent CNN models, one of which looks simply for excess power in both detectors, the coincidence model, and one of which attempts to determine coherence between detections; the second model is fed feature-engineered data in the form of the rolling Pearson correlation between detectors with a number of factor-of-sample-interval timeshifts equivalent to the maximum arrival time difference between the two detectors in question. It does this for the two LIGO detectors and the Virgo detector. It is trained on four types of example: pure noise, noise with a simulated transient (WNB) in one detector only, noise with a simulated transient in all three detectors but with enforced incoherence, and coherent WNBs projected into the three detectors in a physically realistic manner. Using this method, the coherence network can learn to differentiate between coincident glitches and coherent signals.

As baseline models to compare with the results of our improvement attempts, in the next section, we will train five model architectures using the GWFlow data acquisition and training pipeline [60]. Since they are the basis of many of the subsequent attempts at CBC detection, we will train both the models presented in George *et al.* [52] along with the model presented in Gabbard *et al.* [53] and for the coherence case, the two models of the MLy pipeline [28].

4.5.3 CBC Detection Recreation

We present an attempt to recreate the model and training procedure presented in George *et al.* [52] and Gabbard *et al.*, see Figure 4.32 and Figure 4.33 respectively. The model architectures themselves were recreated as closely as possible to how they are presented in the literature, except for the addition of GWFlow whitening layers as their first layer in order to replicate the data conditioning performed in both studies. These models will act as performance baselines as we move forward and try to improve their operation. Rather than trying to recreate the exact training procedure and training distribution from the literature, however, which could end up being a difficult task, we have standardized the train-

ing procedure to achieve parity with the previously conducted perceptron experiments. See Table 4.3 for details of the parameters used in the training procedure.

Type	Num Filters / Neurons	Filter / Pool Size	Stride	Dilation	Activation Function	Dropout	
Convolutional	16	16	1	0	ReLU	-	
MaxPooling	-	4	4	0	-	-	
Convolutional	32	8	1	4	ReLU	-	
MaxPooling	-	4	4	0	-	-	
Convolutional	64	8	1	4	ReLU	-	
MaxPooling	-	4	4	0	-	-	
Dense	64	-	-	-	ReLU	-	
Dense	2	-	-	-	SoftMax	-	

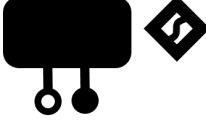
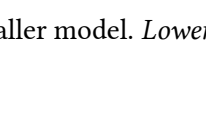
Type	Num Filters / Neurons	Filter / Pool Size	Stride	Dilation	Activation Function	Dropout	
Convolutional	64	16	1	1	ReLU	-	
MaxPooling	-	4	4	0	-	-	
Convolutional	128	16	1	2	ReLU	-	
MaxPooling	-	4	4	0	-	-	
Convolutional	256	16	1	2	ReLU	-	
MaxPooling	-	4	4	0	-	-	
Convolutional	512	32	1	2	ReLU	-	
MaxPooling	-	4	4	0	-	-	
Dense	128	-	-	-	ReLU	-	
Dense	64	-	-	-	ReLU	-	
Dense	2	-	-	-	SoftMax	-	

Figure 4.32 | The two CNN architectures presented in George *et al.* [52]. *Upper*: Smaller model. *Lower*: Larger model.

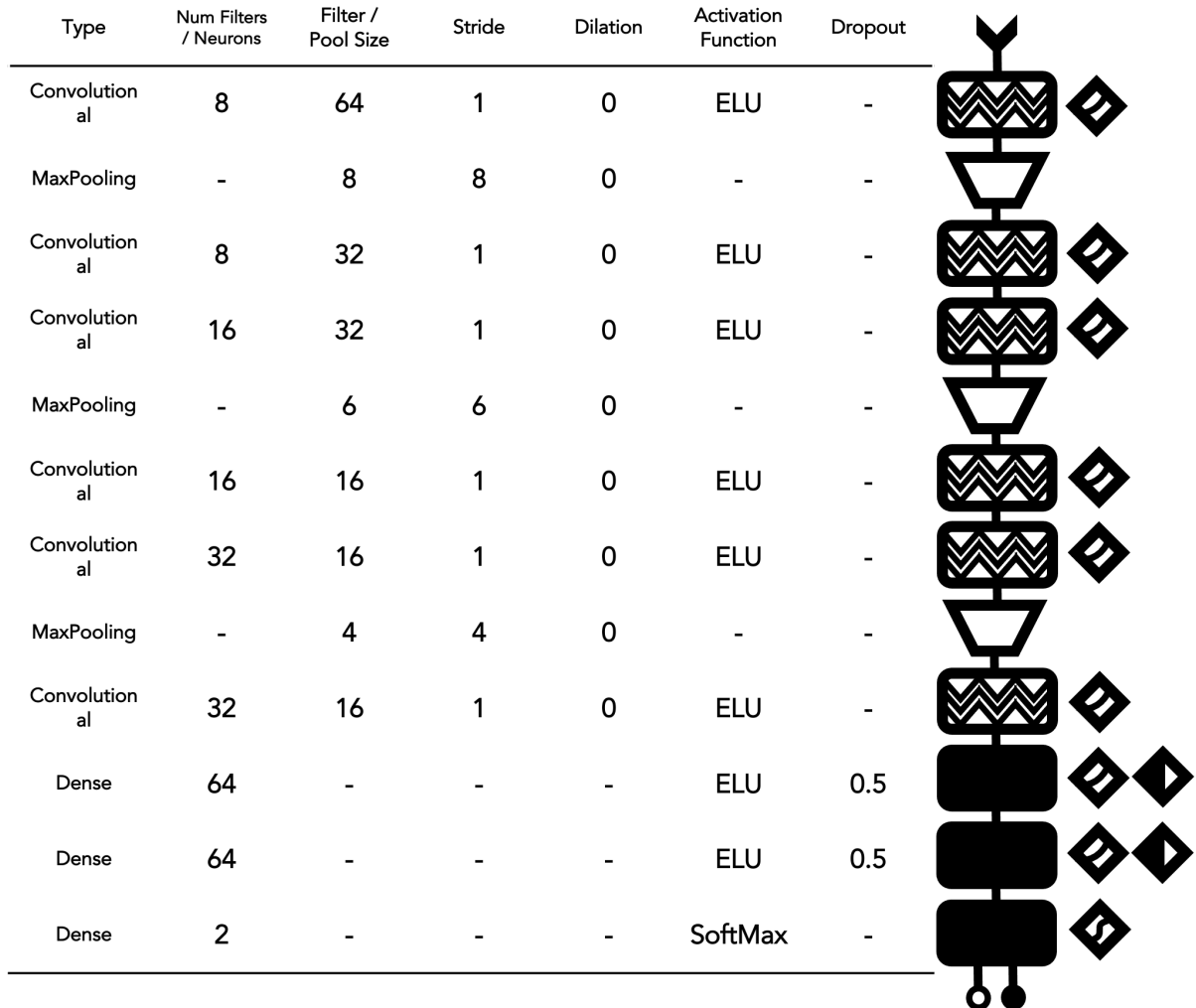


Figure 4.33 | CNN architecture from Gabbard *et al.* [53].

4.5.3.1 Training

Looking at the training plots, shown in Figure 4.34, it is quickly obvious that these models drastically outperform any of the perceptrons. This is perhaps unsurprising, as the CNN architecture was specifically designed for pattern recognition both in images and time series. The training parameters are identical to those used for the single detector perceptron, see Table 4.3. The models also train more rapidly, saturating their validation loss in fewer epochs than was required for the perceptrons, which only reached a lower accuracy even with a longer training time, see Figure 4.35. This is also as expected; more of the function that the networks are attempting to approximate has been predefined in the CNNs architecture. Convolutional kernels can learn from features wherever they appear in the image. If dense layers used a similar technique they would have to learn equivalent “kernels” individually for every possible feature location and they would have to do so with far fewer examples for each of these unique positions. In CNNs, a kernel learning to recognize a feature can train on instances of that feature wherever they appear in the image if a similar kernel-like structure were to develop in a dense layer, each instance of that kernel-like structure would have to learn to recognize a feature from its appearance at a single location, which would presumably occur much less often than the feature as a whole. Similar to the perceptron experiments, further validation results are presented in Section 4.5.3.2.

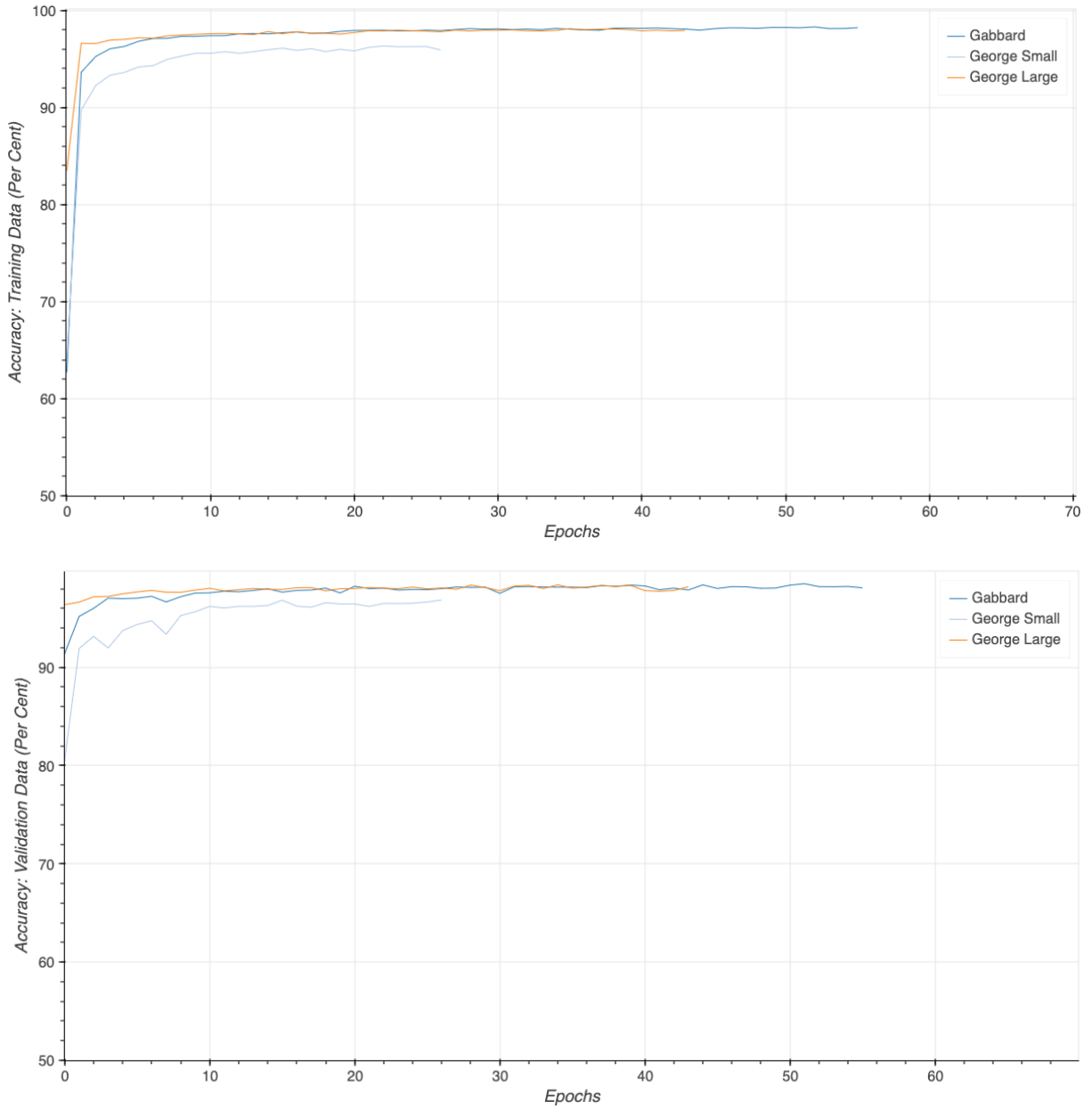
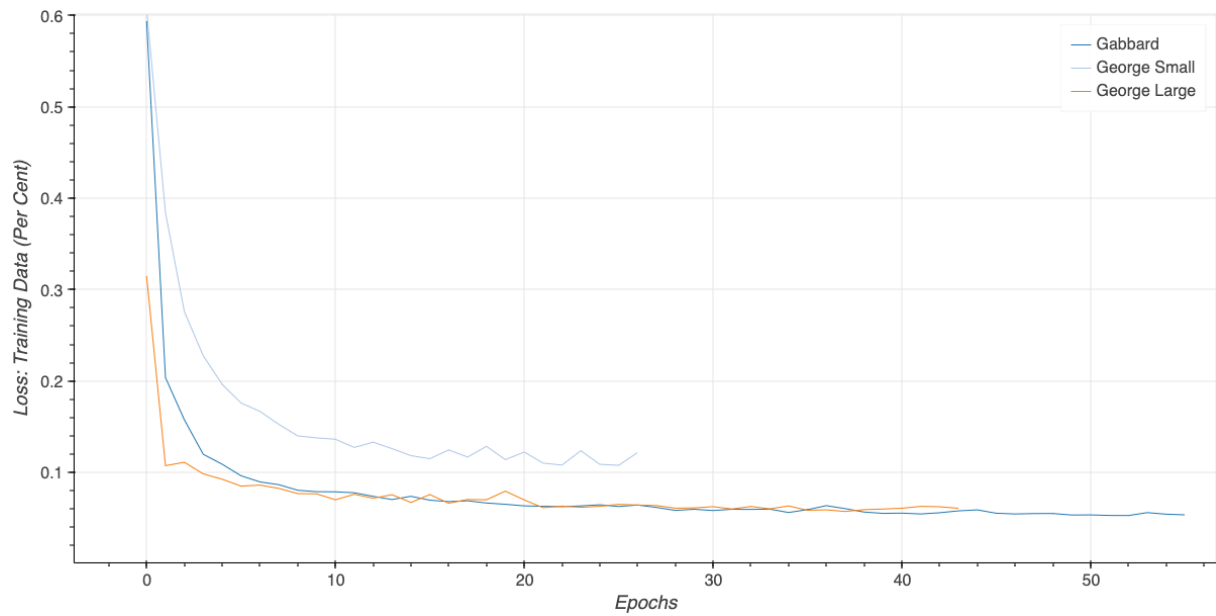


Figure 4.34 | The accuracy history of attempts to retrain Convolutional Neural Networks (CNNs) with architectures adapted from the literature using the GWFlow pipeline. A custom GWFlow whitening layer has been added to the start of each model in order to reproduce the whitening data conditioning step applied in the original studies. The structure of the models is otherwise identical. Differences in the training and validation procedures, however, may lead to slightly different results than in the original studies. Rather than exactly attempting to mimic the datasets and training process used in each of these studies, it has been kept consistent with the other results throughout the thesis, in order to facilitate comparison. The models presented are the two models from George *et al.* [52], labeled “George Small”, and “George Large”, to differentiate them in terms of parameter count, and the single model from Gabbard *et al.* [53]. The network structure of these models can be seen in Figure 4.32 and Figure 4.33, respectively. The training and validation datasets were maintained from the perceptron single-detector training experiment. The dataset contains IMRPhenomD waveforms generated using cuPhenom [48] injected into real interferometer noise sampled from the LIGO Livingston detector during the 3rd joint observing run [54]. The optimal SNR of waveforms injected into the training and validation sets was uniformly distributed between 8 and 15. Input was from a single detector only.

Each epoch consisted of 10^5 training examples, and it should be noted that, unlike regular training pipelines, each training epoch consisted of newly generated waveforms injected into unseen noise segments, though the validation examples are consistent. Training of each model was halted after ten consecutive epochs with no improvement to validation loss, the values of which are shown in Figure 4.35. Validation noise was drawn from a separate pool of data segments inaccessible to the training data loader. It is immediately clear that this is a huge improvement over the perceptron models, and it makes it evident why we abandon the idea of perceptrons so quickly. Both the training and validation accuracies jump to above 90% almost immediately, and in the case of the model from Gabbard *et al.*, and the largest of the models from George *et al.*, they plateau at approximately 98% accuracy, with only marginal improvements from there. The smaller model from George *et al.* plateaus closer to 96% accuracy. Considering approximants from both the training and validation datasets are generated with CBCs drawn uniformly between an optimal SNR of 8 and 15, this demonstrates good performance. Because two of the models plateau at statistically similar accuracies with quite different architectures, it suggests that they are approaching the detectability limit in both cases. An interesting examination will be to compare their performance with FAR-calibrated detection thresholds. *Upper:* Plot of model accuracies when measured with training data (10^5 epoch-unique examples). Visit <https://tinyurl.com/mwxvp33> for interactive plots. *Lower:* Plot of model accuracies when measured with validation data (10^4 epoch-consistent examples).



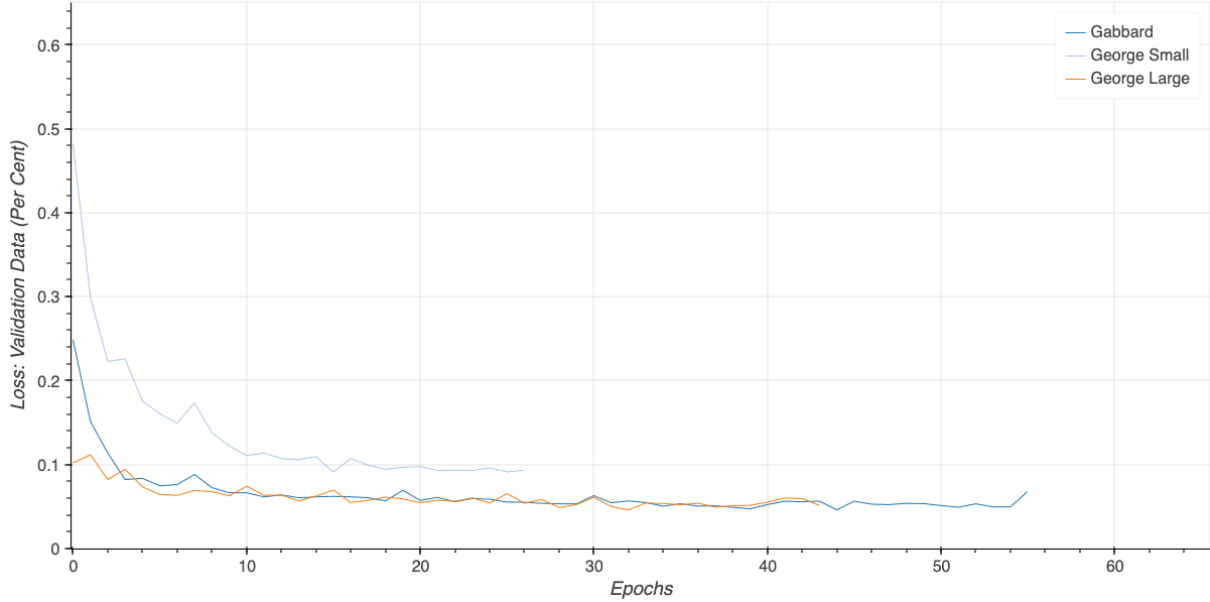


Figure 4.35 | The loss history of attempts to retrain Convolutional Neural Networks (CNNs) from the literature using the GWFlow pipeline. These loss values correspond to the accuracies displayed in Figure 4.34. The models presented are the two models from George *et al.* [52], labeled “George Small”, and “George Large”, to differentiate them in terms of parameter count, and the single model from Gabbard *et al.* [53]. The network structure of these models can be seen in Figure 4.32 and Figure 4.33, respectively. The training and validation datasets were maintained from the perceptron single-detector training experiment. The dataset contains IMRPhenomD waveforms generated using cuPhenom [48] and real interferometer noise sampled from the LIGO Livingston detector during the 3rd joint observing run [54]. The optimal SNR of waveforms injected into the training and validation sets was uniformly distributed between 8 and 15. Input was from a single detector only. Each epoch consisted of 10^5 training examples, and it should be noted that, unlike regular training pipelines, each training epoch consisted of newly generated waveforms injected into unseen noise segments, though the validation examples are consistent. The loss is the metric used to determine when training is halted; this is done after ten epochs have passed with no improvement. Again we can see that this is a vast improvement over the perceptron case, see Figure 4.15, at least in the time frame that is monitored, with loss values quickly falling to a region with a much smaller reduction gradient and then gradually improving from there with diminishing returns. It is these diminishing returns that can have a great impact on the ability of the model to sustain high accuracies with low FAR thresholds. Visit <https://tinyurl.com/mwxvp33> for interactive plots. *Upper:* Plot of model losses when measured with training data (10^5 epoch-unique examples). *Lower:* Plot of model accuracies when measured with validation data (10^4 epoch-consistent examples).

4.5.3.2 Validation

The validation results portray a similar picture – vastly improved performance over the perceptron results. We can see in the False Alarm Rates (FAR) curves, Figure 4.36, that we can utilize significantly lower FARs without dramatically increasing the required score threshold. In most cases, we expect this to allow higher efficiencies at lower FARs if the model has gained adequate detection ability. The benefit of this is displayed in the efficiency plots, Figure 4.37, and the ROC plots, Figure 4.38. We can very clearly see, that these models are dramatically improved over the perceptron case, whose efficiency curves can be seen in Figure 4.17, and ROC curves can be seen in Figure 4.18.

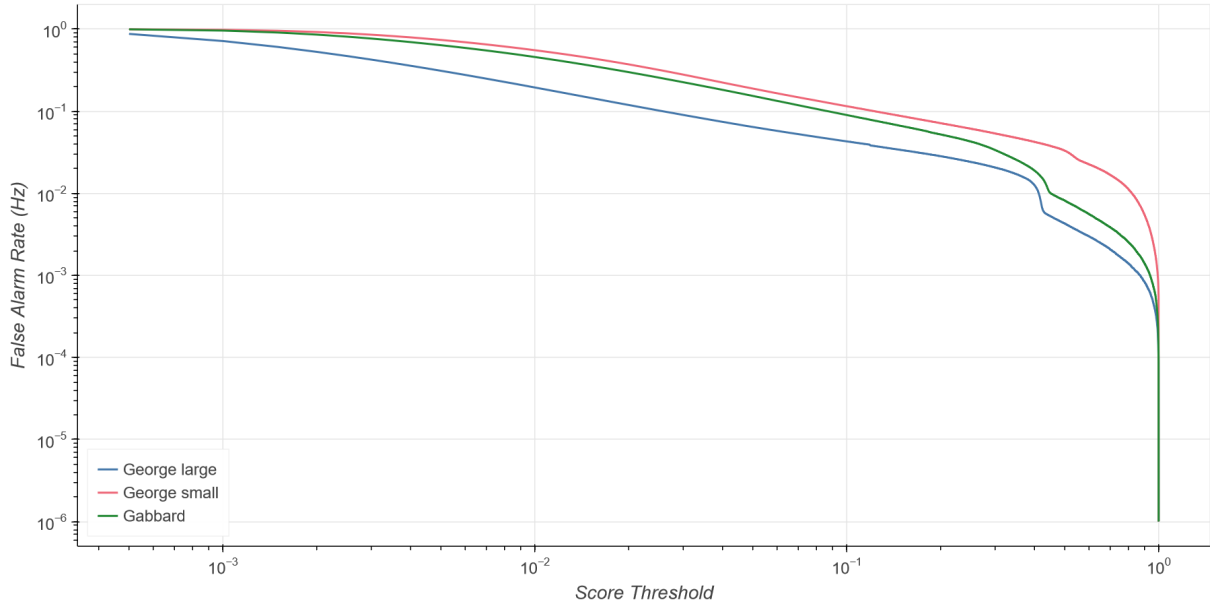
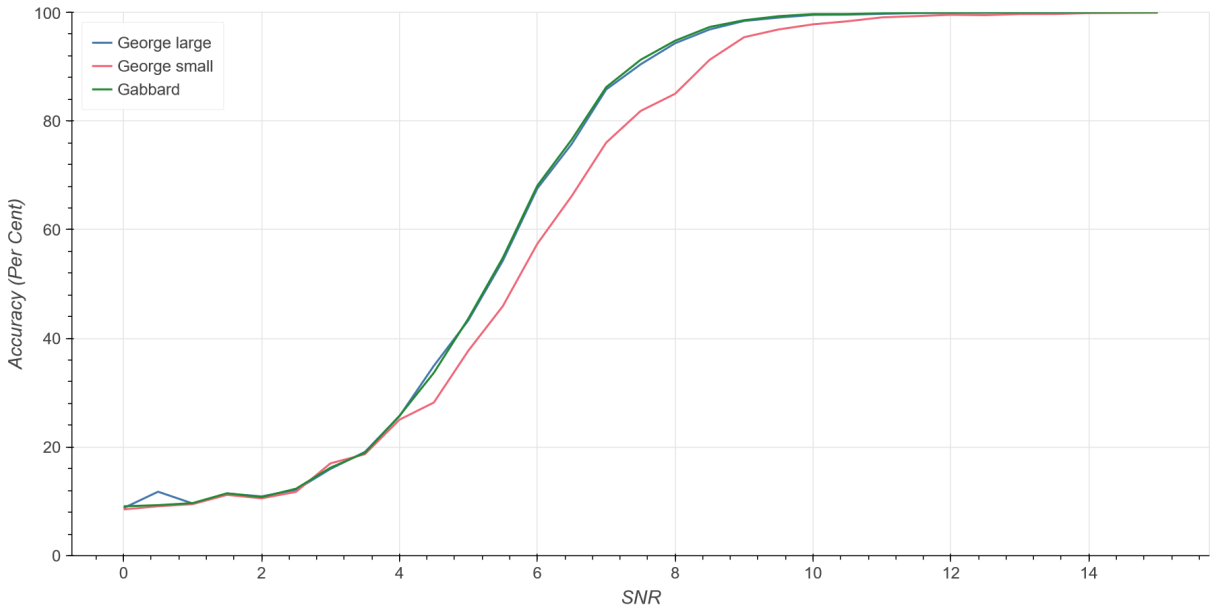


Figure 4.36 | False Alarm Rate (FAR) plotted against the score threshold required to achieve that FAR, for three recreations of models from the literature. Two models are adapted from George *et al.* [52], labeled “George Small”, and “George Large”, to differentiate them in terms of model parameter count, and the single model from Gabbard *et al.* was also adapted. The network structure of these models can be seen in Figure 4.32 and Figure 4.33, respectively. The presented FAR curves are significantly lower than those achieved by the perceptrons in the single detector case, see Figure 4.16. This means that we will be able to achieve lower FARs with lower score thresholds, which typically, though not necessarily, leads to higher efficiencies at those FARs. We explore the efficiency results in Figure 4.37. Visit <https://tinyurl.com/2s3dtd8a> for interactive plots.



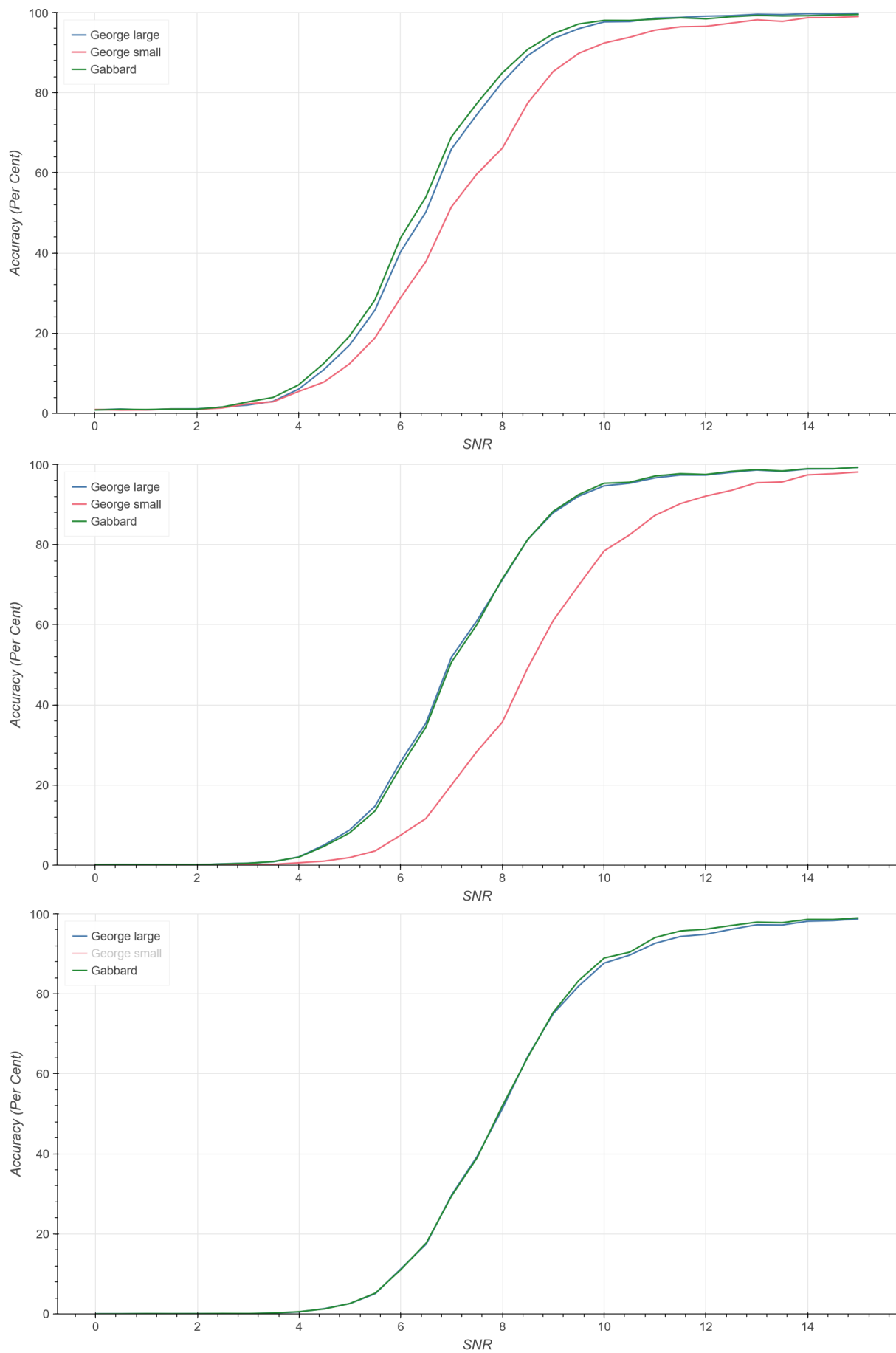


Figure 4.37 | Model efficiency curves for three models adapted from the literature. Two models are adapted from George *et al.* [52], labelled “George Small”, and “George Large”, to differentiate them in terms of model parameter count, and the single model from Gabbard *et al.* [53] was also adapted. The network structure of these models can be seen in Figure 4.32 and Figure 4.33, respectively. These models verify that CNNs can achieve much higher accuracies within the training regime utilized, even when using threshold scores that are calibrated to specific False Alarm Rates (FARs). The perceptron efficiency curves for the single detector CBC detection case can be seen in Figure 4.17. They achieve higher accuracies almost across the board at the highest FARs depicted, 0.1 Hz and 0.01 Hz, except at SNRs where detection becomes virtually impossible (< 2) in which case they perform similarly. They are also able to achieve results at lower FARs 0.001 Hz and 0.0001 Hz at these FARs, the perceptron models had negligible performance and were not depicted, so this is a significant improvement. Visit <https://tinyurl.com/2s3dtd8a> for interactive plots. *First:* Efficiency curves at a FAR of 0.1 Hz. *Second:* Efficiency curves at a FAR of 0.01 Hz. *Third:* Efficiency curves at a FAR of 0.001 Hz. *Fourth:* Efficiency curves at a FAR of 0.0001 Hz.

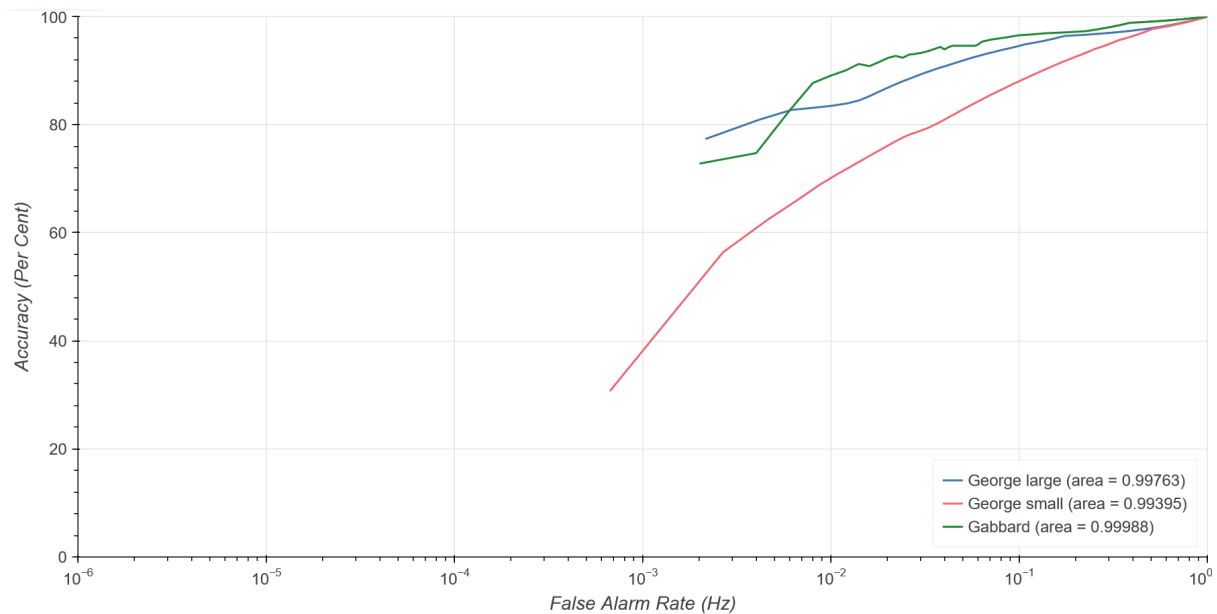


Figure 4.38 | Reciever Operator Characteristic (ROC) curves, for three models adapted from the literature. Two models are adapted from George *et al.* [52], labelled “George Small”, and “George Large”, to differentiate them in terms of model parameter count, and the single model from Gabbard *et al.* [53] was also adapted. The network structure of these models can be seen in Figure 4.32 and Figure 4.33, respectively. In comparison with the ROC curves achieved by the perception models, see Figure 4.18, which at an optimal SNR of 8 looks to be almost randomly guessing, this is a significant improvement. The curves shown illustrate the model operating on a pool of injected signals at an optimal SNR of 8. Visit <https://tinyurl.com/2s3dtd8a> for interactive plots.

It would appear from our investigation that CNNs offer a far superior solution to the single-detector CBC detection problem than perceptrons do. Several questions remain, however. Are we nearing the limit of the CNN’s capacity to solve this problem, or could further hyperparameter tuning, squeeze additional performance out of the architecture, especially at low False Alarm Rates? There have been many attempts to improve on these models throughout the literature [268,280], but there lacks a systematic algorithm to search across all possible solutions, (or at least a large number of possible solutions), to find the optimal detection architecture and training procedure. We investigate this in Sec-

tion 5, where we attempt to use genetic algorithms to search the large hyperparameter space presented for more optimal solutions. There are also several more recently developed architectures, including attention-based models [56], which offer alternate and possibly superior alternatives to convolutional layers, we explore the use of attention layers for CBC classification in Section 6. Finally, there are other, potentially more challenging problems facing gravitational-wave data science, including parameter estimation. In Section 7 we tackle a special case wherein two overlapping signals are present in our input data and examine if we can separate the case of single and overlapping signals. We then test if we can extract parameters from each signal, both in aid of alternate parameter estimation methods, and potentially as a precursor to a full machine learning-based parameter estimator.

5 Dragonn: Exploring Deep Gravitational-Wave Classifier Hyperparameter Space with Genetic Algorithms

5.1 The Problem with Parameters

An applicable machine-learning approach can be found for almost every problem in gravitational-wave data science [254]. That does not mean that machine learning should be applied to every problem in gravitational-wave data science. We must be careful with a liberal application of machine learning approaches and always keep the goal in mind: what exactly are we trying to achieve by applying this particular method? As described in the “No free lunch theorem” [285], for every possible algorithm, there are advantages and disadvantages, and there is no algorithm that completely supersedes another in all cases. This means a rigorous and systematic method for comparing different techniques is required. This problem is confounded with deep learning techniques, as the number of free parameters when designing and optimising your neural network is vast — technically infinite in the non-real case where network size is not a constraint.

There are a huge number of adaptations that can be applied to a network [286,10,242,56], and the number of developed layer types and model architectures is considerable and increasing in an almost exponential fashion year on year [287]. Even ignoring the number of different types of network modifications, most modifications have multiple associated parameters, including parameters specifying the design of individual network layers [243,56,186,188]. We label any parameter to do with the model design or any parameter that is not optimized during the model training process as a **hyperparameter** [288,253].

Hyperparameters include values to do with the greater structure of the network, such as the type and number of layers in a network, the configuration of the layers themselves, such as the number of neurons in a dense layer, or the number of filters in the convolutional layer; the training of the network, such as the learning rate, the number of epochs, and the optimiser; as well as all the parameters associated with the training dataset [288,253]. Essentially, hyperparameters encompass all parameters that must be determined before the initiation of model training.

This chapter will first give a brief overview of available hyperparameter optimisation methods, then discuss why evolutionary population-based methods were chosen as the hyperparameter optimisation technique of choice, followed by a demonstration of the effectiveness of hyperparameter optimisation to improve model performance on various gravitational-wave data analysis problems. We will conclude by discussing how this work has been pivotal in developing MLy [28], a machine learning pipeline currently preparing for live deployment in the latter half of the fourth joint observing run.

The goal of any given hyperparameter optimisation process is to maximise the model’s performance given a specific **objective function** [288,253]. This objective function could be as simple as minimising the model loss, but other performance metrics might also be important to us, such as model inference time or memory usage — or, as is the case for gravitational wave transient detection, minimising values that it would not necessarily make sense to have as part of the loss function, like the False Alarm Rate (FAR) [231]. If we naively gave models a loss function that only allows a once-in-one-hundred-year FAR, they might never produce a positive result at all [231]. It would be hard to balance such a low FAR requirement with other terms in the loss function, and balancing loss function terms is always a difficult challenge that can lead to training instability.

If one is to compare two different sets of architectures, for example, comparing fully connected networks [145] to networks with some convolutional layers [10,242], a method must be used to determine all of these hyperparameters. Many, if not most, of these hyperparameters, will have some effect,

somewhere between significant and small, on the model's overall performance [289]. Thus, just like the tunable parameters of the model itself, the vector space defined by these hyperparameters comprises regions of different model performances, and indeed model performance can be measured in multiple ways. Presumably, given the task at hand, there will be some region within this parameter space that maximises desired performance goals. In the optimal scenario, the comparison of two sets of architectures will occur between these regions. Thus, a method must find approximate values for these optimal hyperparameters.

We might now see the recursion that has started. We are applying an optimisation method to an optimisation that will introduce its own set of hyperparameters. Such hyperparameters will, in turn, need to be at least selected if not optimised. However, it can be shown that the selection of network hyperparameters can make a profound impact [289] on the performance of the model. It is hoped that with each optimisation layer, the effects are considerably diminished, meaning that roughly tuned hyperparameters for the hyperparameter optimiser are sufficient to find comparably optimised solutions.

We can use a similar example parameter space to the one that we generated in Section 3.2, except this time it is being used to represent the hyperparameter space against the model objective function, rather than parameter space against the model loss. See Figure 5.1.

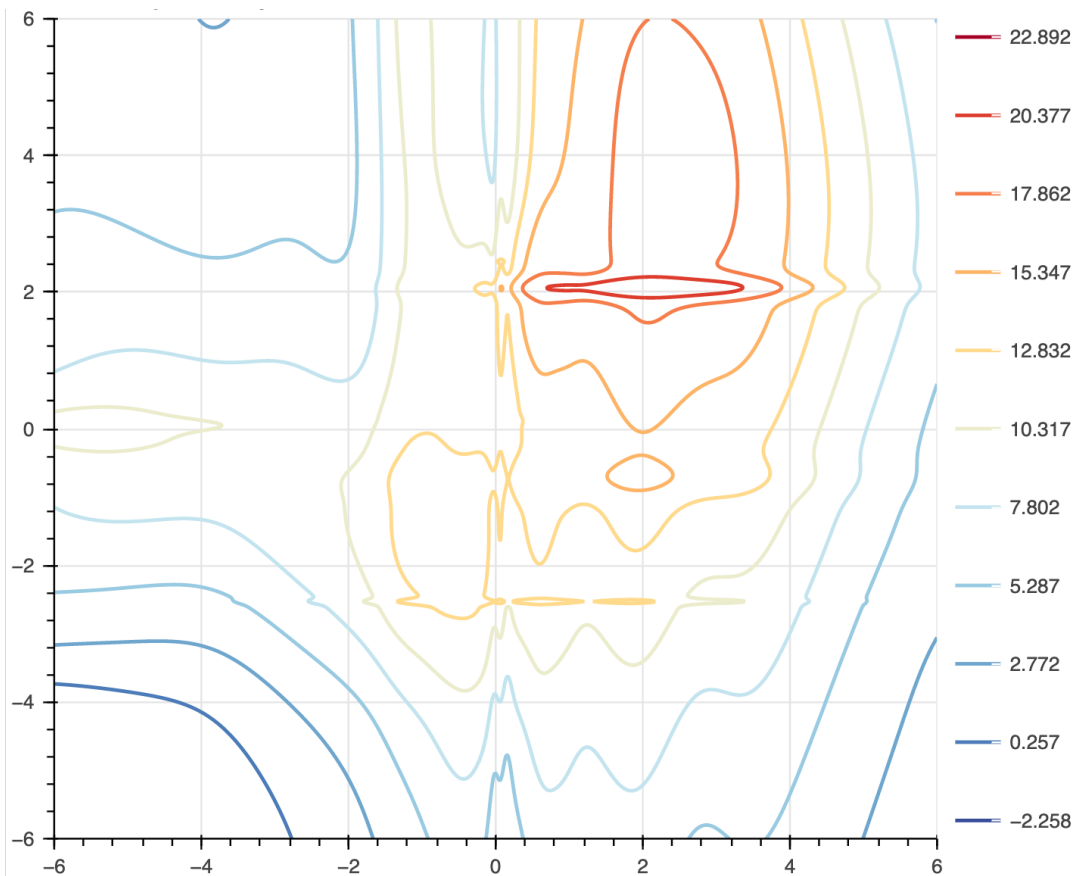


Figure 5.1 | An example arbitrary hyperparameter space generated from a random mixture of Gaussians. The space presented here is 2D. In actuality, the space is likely to have a much larger dimensionality. Unlike in gradient descent where we are trying to minimize our loss, here we are trying to maximize our objective function, whatever we have determined that to be.

Perhaps unsurprisingly, hyperparameter optimisation is an area of considerable investigation and research in machine learning [288]. However, similar to the rest of the field, it would be incorrect to call it well-understood. Whilst there are several effective methods for hyperparameter optimisation, there

is no universally accepted set of criteria for which method to use for which problems. What follows is a brief non-comprehensive review of currently available hyperparameter optimisation techniques.

5.1.1 Human-guided trial and error

The most straightforward and obvious method to find effective model hyperparameters relies on human-guided trial and error. This method, as might be expected, involves a human using their prior assumptions about the nature of the problem, the dataset, and the model structure, to roughly guide them towards an acceptable solution, using multiple trials to rule out ineffective combinations and compare the results to the human's hypothesised intuitions. Evidently, whilst this technique is simple to implement and can be time efficient, it suffers from several deficiencies. The results of this method can vary in effectiveness depending on the previous experience of the guiding human; if they have a lot of experience with prior optimisation tasks, they are likely to have more effectively tuned priors. It is also possible that an experienced optimiser might have overly tuned priors, and this bias might cause them to miss possible new solutions that were either previously overlooked or are only relevant to the particular problem being analysed. The results of this method also suffer from a lack of consistency; even the most experienced human optimiser is unlikely to perform precisely the same optimisation technique across multiple problems. Despite these weaknesses, this method is commonly used throughout gravitational wave machine-learning papers [53,52] and can still be an effective solution for isolated optimisation.

5.1.2 Grid Search

A more methodical approach is to perform a grid search across the entirety or a specified subsection of the available parameter space [288]. In this method, a grid of evenly spaced points is distributed across the selected parameter space. A trial is performed at each grid point, and the performance results of those trials are then evaluated. Depending on the computing power and time available, this process can be recursed between high-performing points. This method has the advantage of performing a much more rigorous search over the entirety of the parameter space. However, it can be highly computationally expensive if your parameter space has large dimensionality, which is often the case. A grid search can also be ineffective at finding an optimal solution if the objective function is non-linear and highly variable with minor changes, or evidently, if its solution lies outside of the range of initial boundaries. See Figure 5.2 for an example grid search.

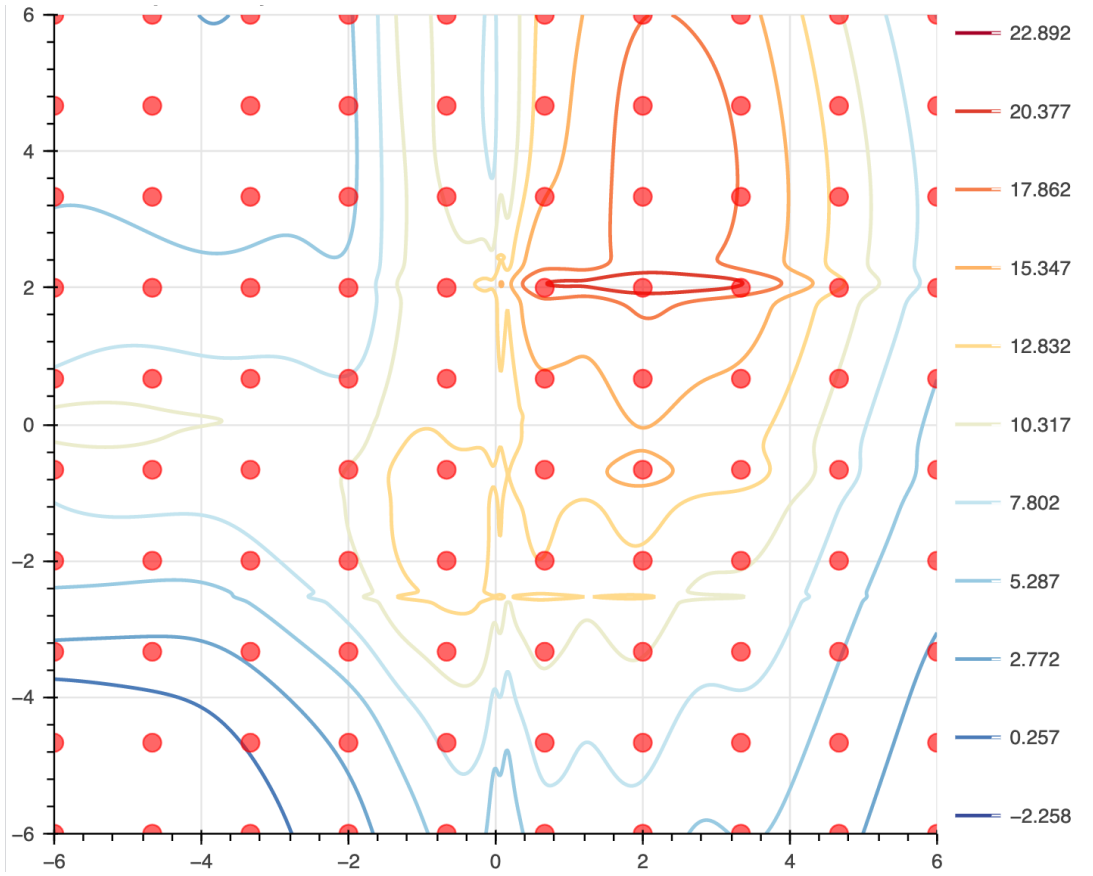


Figure 5.2 | An example of the samples a grid search might use to find an optimal hyperparameter solution.

5.1.3 Random Search

Random search is very similar to a grid search; however, instead of selecting grid points evenly spaced across the parameter space, it randomly selects points from the entirety of the space [288]. It has similar advantages and disadvantages to grid search, and with infinite computing resources, both would converge on the ground truth value for the objective function. However, random search has some benefits over grid search that allow it to more efficiently search the parameter space with fewer evaluations. When performing a grid search, the separation of grid points is a user-defined parameter, which both introduces a free parameter and creates possible dimensional bias. A grid search will also search the same value for any given hyperparameter many times, as along the grid axis, it will appear many times, whereas a random search should rarely repeat samples on any hyperparameter. It should also be noted that some statistical uncertainty will be introduced, which would not be present in the case of a grid search and might limit the comparability of different approaches. Both the random and grid search techniques have the disadvantage that all samples are independently drawn, and unless the processes are recursed, no information from the performance results can influence the selection of new points. See Figure 5.3.

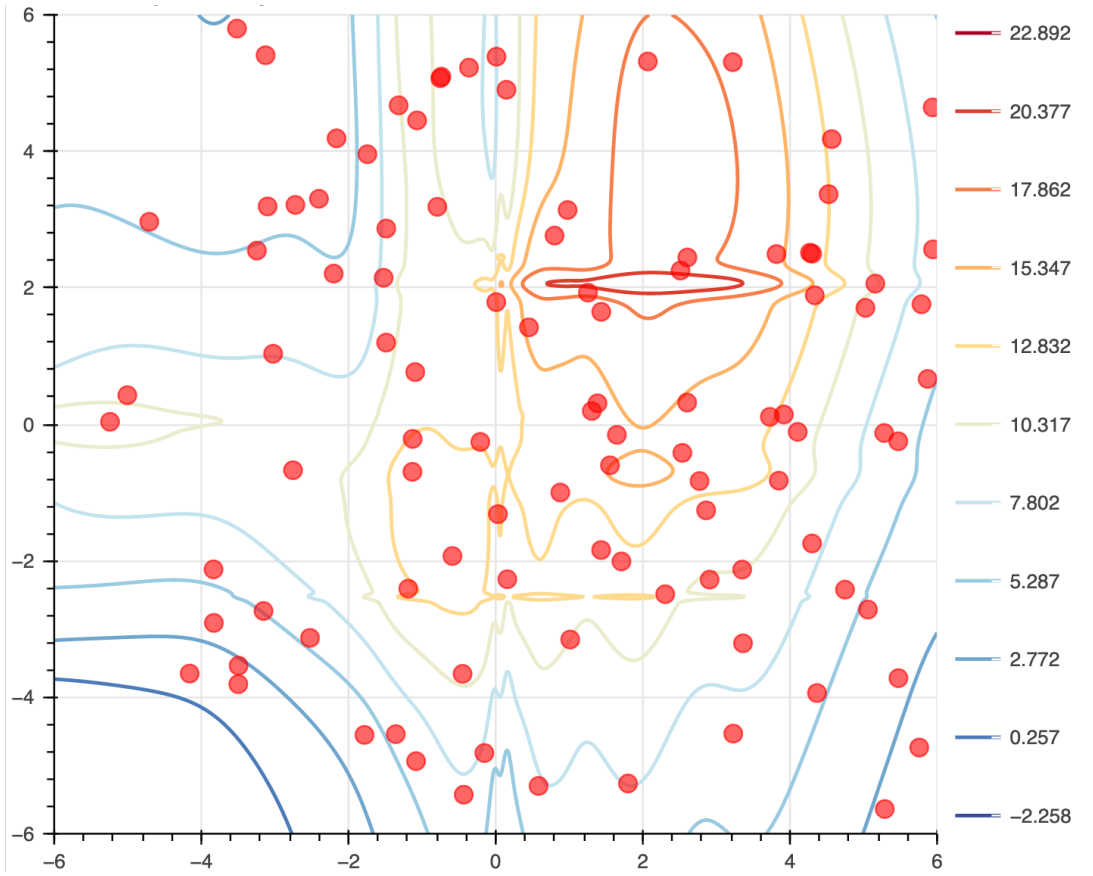


Figure 5.3 | An example of the samples a random search might use to find an optimal hyperparameter solution.

5.1.4 Bayesian Optimisation

A Bayesian optimisation approach makes use of our initial beliefs, our priors, about the structure of the objective function [288]. For example, you might expect the objective function to be continuous and that closer points in the parameter space might have similar performance. The objective function is estimated probabilistically across the parameter space. It is updated as more information is gathered by new samples, which can be tested either in batches or one at a time. The information obtained by these new samples is incorporated into the estimated objective function in an effort to move it closer to the ground truth objective function.

The placement of samples is determined by a combination of the updated belief and a defined acquisition function, which determines the trade-off between exploration and exploitation. The acquisition function assigns each point in the parameter space a score based on its expected contribution to the optimisation goal, effectively directing the search process. A standard method for modeling the objective function in Bayesian optimisation is Gaussian Processes, but other techniques are available, such as Random Forests and Bayesian Neural Networks, among others. This optimisation technique is often employed when evaluating the objective function is expensive or time-consuming, as it aims to find the optimal solution with as few evaluations as possible. See Figure 5.4.

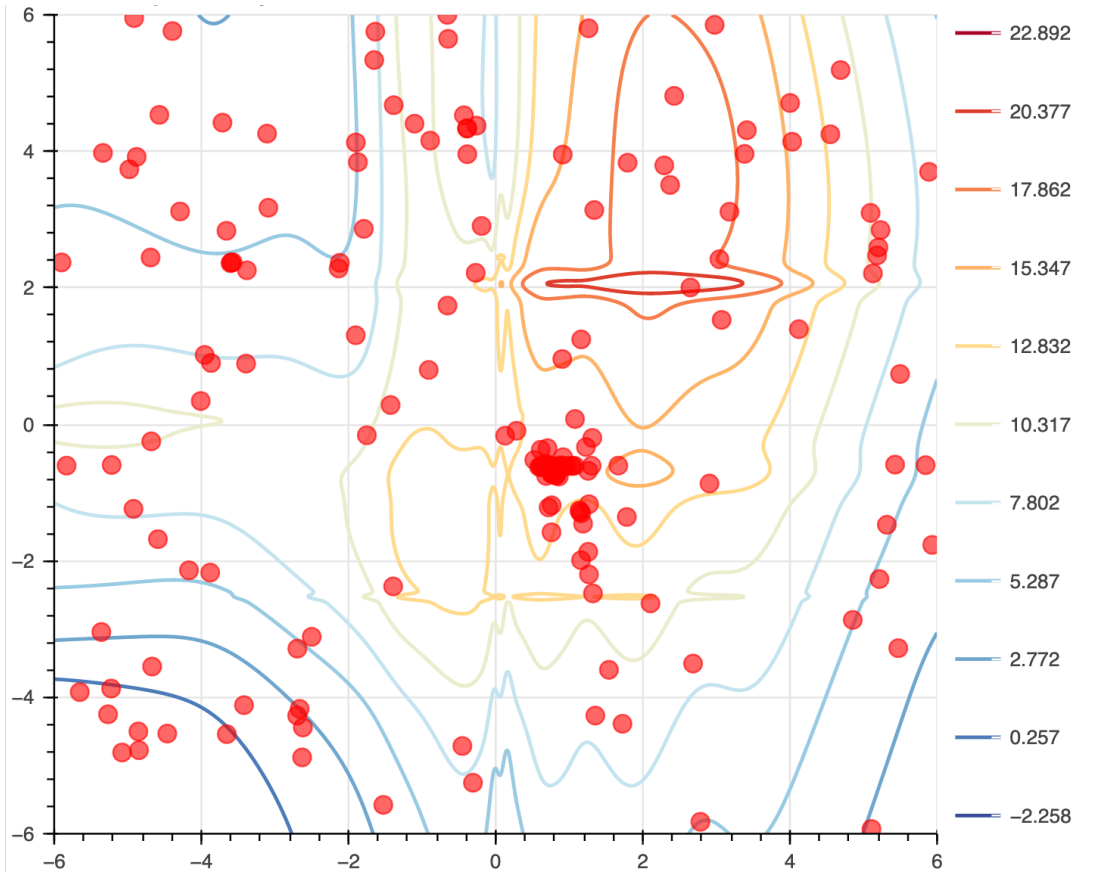


Figure 5.4 | An example of the samples a Bayesian optimization might use to find an optimal hyperparameter solution. The descent method shown here has used a Gaussian Process to attempt to find the objective function maximum but has not done so particularly successfully. The method was not tuned to try and increase performance, as it was just for illustratory purposes.

5.1.5 Gradient-Based Optimisation

In some rare cases, it is possible to find optimal model hyperparameters using a similar method to the one we used to determine model parameters during model training [288]. We can treat the hyperparameter space as a surface and perform gradient-descent (or in this case ascent, which follows the same principles but in reverse). Since gradient descent was already discussed in some detail in Section 3.2 we will not repeat ourselves here. The advantage of gradient-based optimisation is that it can utilize extremely powerful gradient descent mechanisms that we have seen are potent optimisers. The major disadvantage, however, is that for most hyperparameters, it is not possible to calculate the gradient. There are workarounds in some specific scenarios and much research has gone into making gradients available, but such work is still in early development and not applicable in many scenarios, thus we limit our discussion to this paragraph.

5.1.6 Population-Based Methods

The final category of hyperparameter optimization methods that we will discuss, and the one that we have chosen to employ in our search for more optimal classifiers, are population-based methods [290]. These come in a variety of different subtypes, most prominent of which perhaps are evolution-based methods, such as genetic algorithms. Population-based methods are any methods that trial several solutions before iterating, or iterate several solutions in parallel, as opposed to trialing one solution, and then iterating the next solution on the results of the previous. Technically, since they trial a number of solutions before iteration, both random and grid searches could be considered population-based

methods with only one step, although they are not usually included. Since we have chosen to adopt a method from this group, will will review some of the subtypes.

5.1.6.1 Genetic Algorithms

For our hyperparameter search, we have chosen to implement genetic algorithms, a population-based evolutionary method [291,288,290]. Genetic algorithms are inspired by the principle of survival of the fittest found in nature within Darwinian evolution [291]. They require the ability to list and freely manipulate the parameters we wish to optimize (in our case our hyperparameters). Continuing with the biological analogy these parameters are a given solution's genes, g_i the full set of which is a solution genome G_i . We must also be able to test any genome and how well a solution generated with that genome satisfies our objective function. We must be able to condense these measurements into a single performance metric – the fitness of that solution. Any optimization problem that fits these wide criteria can be attempted with genetic algorithms, meaning they are a flexible optimization solution. Our problem, the hyperparameter optimization of deep learning model, fits both criteria, thus, genetic algorithms are an applicable for the task.

Initially, a number of genomes, N , are randomly generated within predefined parameter space limits [291]. All possible gene combinations must produce a viable genome or a mechanism must be in place to return a fitness function of zero if a solution is attempted with an invalid genome. A solution (in our case, a model) is generated for each of the N genomes. This set of solutions forms your population. Every member of the population is trialed (in our case, the model is trained) either sequentially or in parallel depending on your computational resources and the scope of the problem. In the basic genetic algorithm case, each trial within a generation is independent and cannot affect another member of the population until the next generation, and is validated (the model is validated) in order to produce a fitness function. This process of generating a set of genomes that defines a population of solutions, and then testing each member of the population to measure its effectiveness is known as a generation. Multiple generations will be iterated through, but each generation after the first is based on the fitnesses and the genomes of the previous generation rather than just being randomly generated as in the first generation. Genes and gene combinations that are found in highly-scoring members of the population are more likely to be selected for use in the next generation. After the algorithm has run for a number of generations, possibly determined by some cut-off metric, in theory, you should have produced a very highly-scoring population. You can then select the best-performing model from the entirety of your evolutionary history.

It is the selection process between generations that gives the genetic algorithm its optimising power [291], rather than grid or random methods, each generation uses information from the previous generation to guide the current generation's trials. There are multiple slightly different variations, we use one of the most common techniques, which is described in more detail in Section 5.2.

As mentioned genetic algorithms are very flexible, they can be applied to a wide variety of optimization problems [291]. They can handle almost any objective function and operate in any kind of parameter space, including discrete, continuous, or mixed search spaces [291]. They are also quite robust, unlike many optimization solutions which, sometimes rapidly, single out a small area of the parameter space for searching, genetic algorithms perform a more global search over the parameter space. Despite these advantages, they have the large disadvantage of requiring a large number of trials before converging on a high-performing solution, for this reason, they are less often used for hyperparameter optimization as each trial requires model training and validation [290].

5.1.6.2 Particle Swarm Optimisation

For completion, we will also discuss several other population-based optimization techniques. One of which is particle swarm optimization, which is inspired by the emergent behavior found in swarms

of insects, flocks of birds, and schools of fish [290]. Seemingly without coordination or central intelligence, large numbers of individually acting agents can arrive at a solution to a problem using information from their nearest neighbours [292].

In particle swarm optimisation, akin to genetic algorithms, an initial population is randomly generated and trialed. In this case, each member of the population is called a particle, forming the elements of a swarm. Rather than waiting for the end of each generation in order to update the parameters of each solution, each solution is given a parameter-space velocity which is periodically, or continuously updated by the performance of the other members of the population. Some variations aim to imitate real animal swarms more closely by limiting each particle's knowledge to certain regions, or to improve convergence rates by weighting some particles more highly than others [290].

Particle swarms can have much quicker convergence than genetic algorithms, due to the continual updates to their trajectory in parameter space. However, effective employment of particle swarms requires that your solutions can adjust their parameters quickly, which is not the case for many deep learning hyperparameters, most prominently structural hyperparameters which would often require retraining the model from scratch after only small changes.

5.1.6.3 Differential Evolution

Like genetic algorithms, differential evolution methods are a form of evolutionary algorithm, but rather than generating a new population based on a selection of genes from the previous generation, differential evolution instead generates new parameters based on differentials between current solutions [290,293]. This means that genes in the current generation are not necessarily anything like genes in the previous generation – parameters are treated in a vector-like manner rather than discreetly.

Differential evolution can work well for continuous parameter spaces, and shares many of the advantages of genetic algorithms as well as sometimes converging more quickly, however, it deals less well with discrete parameters than genetic algorithms and is less well studied, so understanding of their operation is not as well developed [293].

5.2 Dragon Method

As our attempt to apply genetic algorithms to the problem of deep learning model optimisation in gravitational waves, we introduce Dragonn (Dynamic Ranking And Genetic Optimisation of Neural Networks). Originally a standalone software library developed in C, Dragonn was rewritten in Python utilizing other recent advances made in the GWFlow pipeline. A previous version which was used to optimise the core MLy models was existent, but data from those early experiments was lost, so a decision was made to remake the experiments with the updated Dragonn tools. In the following subsection, we will justify our selection of genetic algorithms as the hyperparameter optimisation method of choice, explain in detail the operation of genetic algorithms, and discuss the choice of optimiser parameters selected for tests of Dragonn's optimization ability.

5.2.1 Why Genetic Algorithms?

Genetic algorithms are an unusual choice for artificial neural network hyperparameter optimization and have fallen somewhat out of fashion in recent years, with Bayesian methods taking the limelight. Genetic algorithms typically require many trials before they converge on an acceptable solution, and although they are extremely flexible and adaptable methods, which are easy to implement and fairly straightforward to understand, the computational expense of individual trials of neural network architectures can often be prohibitively expensive to the application of genetic algorithms. Many of the hyperparameters of artificial neural networks are immutable without completely restarting training. While it is possible to adjust the training dataset and training hyperparameters such as the learning rate during model training, there are many hyperparameters related to the network architecture for

which training would have to be completely restarted should they be altered, typically reinitializing the model’s tunable parameters in the process. This means that for each trial during our optimization campaign, we will have to train a model from scratch, which can be a computationally expensive endeavour especially if the models are large. More computationally hungry layers, such as the attention-based layers that are discussed in future chapters, would require even more time and resources per trial, making genetic algorithms even more costly.

Unfortunately, most of this was not known at the initiation of the project. It should be noted, that at that time, hyperparameter optimization methods were less developed. As the project developed, however, there were new ideas for how genetic algorithms could be better adapted for their task. We can imagine some methods to alter model architectural hyperparameters without entirely resetting the tunable weights of the model in the process. For example, we could add an extra convolutional filter to a convolutional layer, randomly initializing only the new parameters, and keeping existing parameters the same, similarly, we could remove a convolutional kernel. It might also be possible to add and deduct entire layers from the model without completely resetting the tunable parameters every time. A method to reuse existing trained parameters was envisioned. Unfortunately, performing such surgery on models compiled using one of the major machine-learning libraries, in our case TensorFlow, is fairly difficult. So although many alternative methods were conceived, none progressed to the point where they were ready for testing.

With all that said, population-based methods are far from dead, and there are still some significant advantages over other methods. For extremely complex spaces, with many parameters to optimize, genetic algorithms can be the best solutions possible, though as noted they can take many trials to reach this optimum solution. It should also be noted, that although hyperparameter optimization can be very highly dimensional, it is usual, in artificial neural network design, for the number of dimensions that are important to model performance to be quite low, meaning that the search space is considerably lessened. There are big players in AI who use population-based methods similar to genetic algorithms for model optimization, including Google DeepMind [294], so it is hoped that further development of this method could result in a highly adaptable population-based method for the optimization of neural networks for use in gravitational-wave research. Much of the software has already been developed, and although it would be a complex task, it would be a rewarding one.

We have some things in our favour: our input data is not particularly highly dimensional, and the models we are attempting to train, are simple Convolutional Neural Networks (CNNs) that are not especially memory or resource intensive, meaning that it should be possible for us to run a relatively large number of trials. The method and software developed for this research have also seen use in a gravitational wave detection pipeline, MLy [28], so it has already been useful to the scientific community. The developed genetic algorithm software included as part of GWFlow makes it very easy to add new hyperparameters to the optimisation task, those parameters can be continuous, discrete, or boolean. The range of hyperparameters set up for optimisation with Dragonn is already extensive, as is demonstrated in Section 5.2.2.

There has been at least one attempt to use genetic algorithms for hyperparameter optimisation within gravitational wave data science in the past [295]. Deighan *et al.* share an interest in developing a consistent method for generating hyperparameter solutions, and they use a similar approach to the method described here. They demonstrate that genetic algorithms can indeed generate models with high performance. The work of Deighan *et al.* optimizes a reasonable, but limited number of hyperparameters, predefining several structural elements of the network. We have allowed our optimiser considerably more freedom, although we note that this could also lead to an increased convergence time.

5.2.2 Selection of Mutable Hyperparameters

Genetic Algorithms are optimisation methods that can be used to find a set of input parameters that maximise a given fitness function. Often, this fitness function measures the performance of a certain process. In our case the process being measured is the training and testing of a given set of hyperparameters – the hyperparameters then, form the parameters that are optimization method will adjust to find a performant solution. The GWFlow optimisation model allows us to optimize a wide range of hyperparameters, and whilst it was wished to perform a large optimisation run over all possible hyperparameters, we elected to use only a subset in order to improve convergence speeds due to time constraints.

Model hyperparameters can be split into three categories, with the last category divisible into two subcategories: **Dataset Hyperparameters**, **Training Hyperparameters**, and **Structural Hyperparameters**.

- **Dataset hyperparameters** control the structure and composition of the training dataset, including its size, the number of each class of example within the dataset, and the properties of each example. In our case, the properties of the noise, the signals injected into that noise, and any additional obfuscations we wish to add to the data like the injection of simulated glitches. It's important that our method cannot also adjust the properties of the validation and testing dataset. It would be very easy for the genetic algorithm to find a solution wherein it makes the difference between classes in the validation set as easy as possible to identify, or make the validation dataset incredibly short, or perhaps remove all but one class of example. If we restrict our optimisation to the training dataset, however, this can be a good way to find optimal hyperparameters. The composition of the training dataset can often be a crucial part of optimising model performance. Unfortunately, we did not run the genetic algorithm on any dataset parameters, since we attempted to optimise for time. The set of possible genes for dataset hyperparameters is shown in Table 5.1.

Hyperparameters Name (gene)	Type	Optimised	Range
Sample Rate (Hz)	Integer	No	-
Onsource Duration (s)	Integer	No	-
Offsource Duration (s) ⁺	Integer	No	-
Total Num Examples	Integer	No	-
Percent Signal	Float	No	-
Percent Noise	Float	No	-
Percent Glitch	Float	No	-
Noise Type	Discrete	No	-
Whiten Noise? (+)	Boolean	No	-
<i>For each feature type</i>			
SNR Min*	Float	No	-
SNR Max*	Float	No	-
SNR Mean*	Float	No	-
SNR Median*	Float	No	-
SNR Distribution (*)	Discrete	No	-

Table 5.1 | Possible Dataset Hyperparameters. These are parameters that alter the structure and composition of the dataset used to train or model. None of these parameters were selected for inclusion in our hyperparameter optimization test, in order to decrease convergence time. Parameters with a su-

perscript symbol become active or inactive depending on the value of another parameter in which that symbol is contained within brackets. Range entries are left black for Hyperparameters not included in optimisation, as no ranges were selected for these values.

- **Training hyperparameters** are parameters used by the gradient descent algorithm, which dictate the training procedure of the neural network. These include things like the learning rate, batch size, and optimization choice. As with the dataset hyperparameters, these are fairly easy to alter after training has begun without first resetting all of the model's tunable parameters, so could easily be incorporated into a more complex population-based method. None of these parameters were selected for optimization. The set of possible genes for dataset hyperparameters is shown in Table 5.2.

Hyperparameters Name (gene)	Type	Optimised	Range
Batch Size	Integer	No	-
Learning Rate	Float	No	-
Choice of Optimiser(*)	Discrete	No	-
Various Optimiser Parameters*	Discrete	No	-
Num Training Epochs	Float	No	-
Patience	Discrete	No	-
Choice of Loss function	Discrete	No	

Table 5.2 | Possible Training hyperparameters. These are parameters that alter the training procedure of the model. None of these parameters were selected for inclusion in our hyperparameter optimization test, in order to decrease convergence time. Parameters with a superscript symbol become active or inactive depending on the value of another parameter in which that symbol is contained within brackets. There are different optimiser parameters that could also be optimized depending on your choice of optimiser, for example, values for momentum and decay. It is not typical to optimise your choice of loss function for most tasks, but some are possible with a range of loss functions, such as regression, which could benefit from optimisation of this parameter. Range entries are left black for Hyperparameters not included in optimisation, as no ranges were selected for these values.

- **Architecture hyperparameters** are parameters that control the number and type of layers in a network. This is by far the most extensive category of hyperparameters since many of the layers that themselves are controlled by hyperparameters contain hyperparameters. For example, a layer in a network could be any of several types, dense, convolutional, or pooling. If convolutional were selected by the optimizer as the layer type of choice, then the optimizer must also select how many filters to give that layer, the size of those filters, and whether any dilation or stride is used. Each layer also comes with a selection of possible activation functions. This increases the number of hyperparameters considerably. In order to allow the optimizer maximal freedom, no restrictions on the order of layers in the network were imposed, any layer in a generated solution could be any of the possible layer types. Another independent hyperparameter selected how many of those layers would be used in the generation of the network in order to allow for various network depths. The output layer was fixed as a dense layer with fixed output size, to ensure compatibility with label dimensions. The set of possible genes for dataset hyperparameters is shown in Table 5.3

Hyperparameters Name (gene)	Type	Optimised	Range
Number of Hidden Layers	Integer	Yes	0 to 10
<i>One each for each active layer</i>			

Layer Type	Discrete	Yes	Dense(*, +), Convolutional(*, \times), Pooling(\diamond), Dropout(\square)
Activation Function*	Discrete	Yes	ReLU, ELU, Sigmoid, TanH, SeLU, GeLU, Swish, SoftMax
Num Dense Neurons $^+$	Integerr	Yes	1 to 128 (all values)
Num Filters \times	Integer	Yes	1 to 128 (all values)
Kernel Size \times	Integer	Yes	1 to 128 (all values)
Kernel Stride \times	Integer	Yes	1 to 128 (all values)
Kernel Dilation \times	Integer	Yes	0 to 64 (all values)
Pool Size \diamond	Integer	Yes	1 to 32 (all values)
Pool Stride \diamond	Integer	Yes	1 to 32 (all values)
Dropout Value \square	Float	Yes	0 to 1 (all values)

Table 5.3 | Possible architecture hyperparameters. These are parameters that alter the architectural structure of the model, or the internal structure of a given layer. All these parameters were selected for optimisation. Parameters with a superscript symbol become active or inactive depending on the value of another parameter in which that symbol is contained within brackets. For each of the N layers, where N is the value of the number of hidden layers genome, a layer type gene determines the type of that layer, and other hyperparameters determine the internal structure of that layer.

These parameters are called genes (g), and each set of genes is called a genome **genomes** (G). $G = [g_1, g_i \dots g_{\{x\}}]$, where x is the number of input parameters. Each genome should map to a single fitness score (F) via the fitness function.

5.2.3 Genetic Algorithms in Detail

Genetic algorithms operate under the following steps, note that this describes the procedure as performed in this paper, slight variations on the method are common:

1. **Generation:** First, an initial population of genomes, P is generated. $P = [G_1, G_i, \dots G_N]$, where N is the number of genomes in the population. Each genome is randomised, with each gene limited within a search space defined by $g_{i\min}$ and $g_{i\max}$.
2. **Evaluation:** Next, each genome is evaluated by the fitness function to produce an initial fitness score. In our case, this means that each genome is used to construct a CNN model which is trained and tested. The result of each test is used to generate a fitness score for that genome.
3. **Selection:** These fitness scores are used to select which genomes will continue to the next generation. There are a few methods for doing this, however, since we do not expect to need any special functionality in this area we have used the most common selection function - “the Roulette Wheel” method. In this method, the fitness scores are normalised so that the sum of the scores is unity. Then the fitness scores are stacked into bins with each bin width determined by that genome’s fitness score. N random numbers between 0 and 1 are generated, and each genome is selected by the number of random numbers that fall into its bin. Any given genome can be selected multiple or zero times.
4. **Crossover and Mutation:** The genomes that have been selected are then acted upon by two genetic operators, crossover and mutation. Firstly, genomes are randomly paired into groups of two, then two new genomes are created by randomly selecting genes from each parent. A “mutation

"is then performed on each of the new genomes with a certain mutation probability M . Mutation and Crossover create genomes that share elements of both parents but with enough differences to continue exploring the domain space.

5. **Termination:** If the desired number of generations has been reached the process ends and the highest-performing solution is returned. Else-wise the process loops back to step 2 and the newly created genomes are evaluated.

5.2.3.1 Choice of Fitness Function

There are multiple possible variants on the standard genetic algorithm model but for the most part, we have kept to the generic instantiation. It is a common choice to use the model loss as the fitness metric for optimisation, this makes sense in many ways, as the goal of training a model is to reduce its loss function, a better loss indicates a better model. However, the model loss function often fails to map exactly for our requirements to the model. The form of the loss function affects the model's training dramatically, so we cannot just use any function we wish as the loss function, and some things we are trying to optimise for might be too expensive to compute during every training iteration, or impossible to compute directly in this manner. We have chosen to use the area under a FAR-calibrated efficiency curve. Only values above an SNR of 8 were included in the sum, and the FAR chosen was 0.01 Hz, with the assumption that performance at this FAR would translate to performance at a lower FAR. A lower FAR was not directly used because it would be computationally expensive to compute for every trial. This objective function was chosen as it is representative of the results we look for to determine whether our model is performant or not. If those are the results we will be examining, we may as well attempt to optimise them directly.

5.2.3.2 Choice of Crossover Method

There are several potential choices for crossover methods, one-point crossover, k-point crossover, or uniform crossover. In one-point crossover we treat our two genomes, one from each parent, as long arrays, like two DNA strands, the crossover mechanism randomly cuts both strands in two and selects half from one strand, and the second half from the other genome, generating a new genome by splicing the old, this the simplest approach which in some cases can lead to faster convergence, but it can reduce the possibility for mixing genomes in interesting ways, reducing the total search space. K-point crossover is similar, but selects multiple places to cut, and splices the gene in a more complex manner, this can increase mixing possibilities but can decrease convergence, as the new genome is more likely to gain combinations of genes that perform poorly. The final possibility is uniform mixing, which effectively equates to cutting before and after every genome. Each genome in the new genome is randomly selected between parent a and parent b, this maximizes mixing but can increase convergence time. We selected to use uniform crossover in order to maximise the possible search space, although we were concerned about increasing convergence times, we wanted to ensure that we explored a wide area of the parameter space effectively.

5.2.4 Choice of Mutation Method

As well as crossover, mutation was also performed at the inception of every new genome. Mutation ensures that the population keeps exploring new areas of parameter space even as certain traits dominate the population, by introducing a small chance that a gene can randomly change value. Our method for performing mutation is dependent on whether the value of that gene is an integer, continuous, discrete, or boolean. For all cases, there is a 5% chance for mutation to occur in any given gene after crossover has taken place. For continuous and integer values, the value of the gene is mutated either negatively or positively by an amount drawn from a Gaussian distribution, in the case of integer parameters this is then rounded to the nearest parameter. For discrete and boolean values, a new value is drawn from the possible selection, with all values being equally likely – this is different from the integer case as choices in the discrete category are not ordered.

5.2.5 Datasets

The GWFlow data [60] and training pipeline were used to generate the datasets used in each of the trial solutions. We are attempting to detect BBH IMRPhenomD signals generated with cuPhenom [48] and obfuscated by real LIGO interferometer noise drawn from the LIGO Livingston detector. Although GWFlow lends itself well for use in hyperparameter optimization methods due to its rapid generation of datasets and lack of requirement for pre-generated datasets, we elected not to optimize dataset parameters in an attempt to decrease the time till model convergence. Instead, we used identical dataset parameters to those used for the perceptron experiments, but we decreased the training patience to a single epoch, meaning if any epoch has a validation loss higher than the epoch previous, training halts. This was done in order to reduce the time taken for each trial. The parameters used for the training and dataset can be seen in Table 5.3.

5.3 Dragonn Results

The genetic algorithm work presented in this chapter has been in development for a long time, but this particular iteration only reached its full capabilities in recent months. What this has meant is that time pressure did not allow for a large number of generations to be run. Optimization was performed over four generations, which is very low for a genetic algorithm optimization run. Nonetheless, we can explore the results, and we have made some intriguing discoveries, even if they were somewhat accidental.

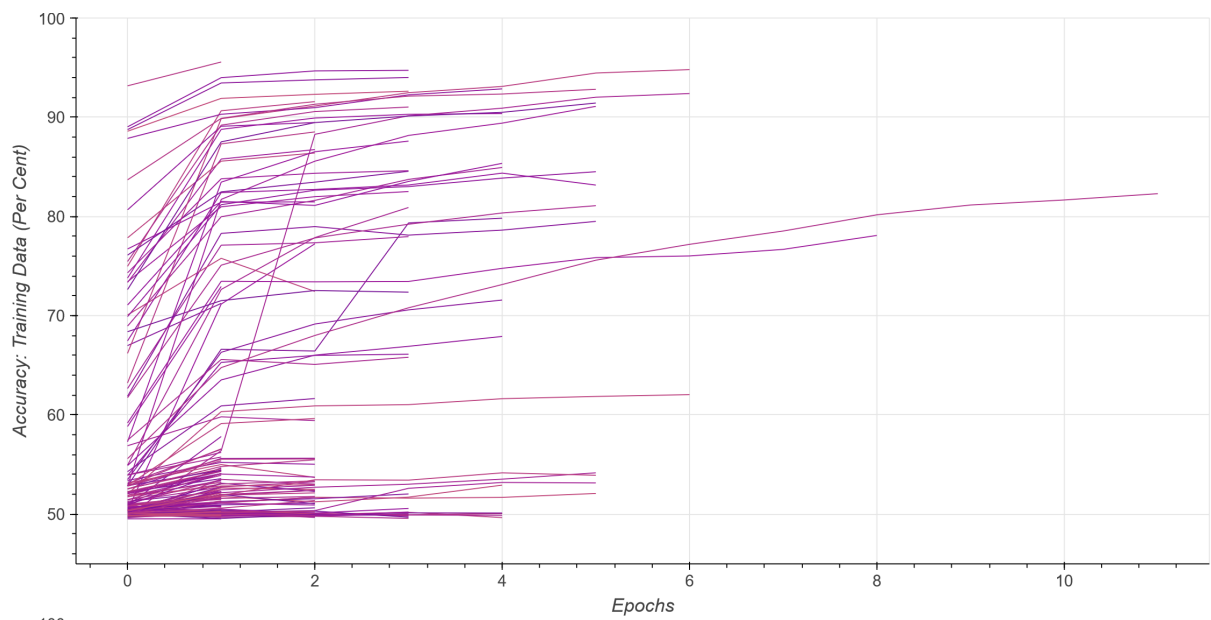
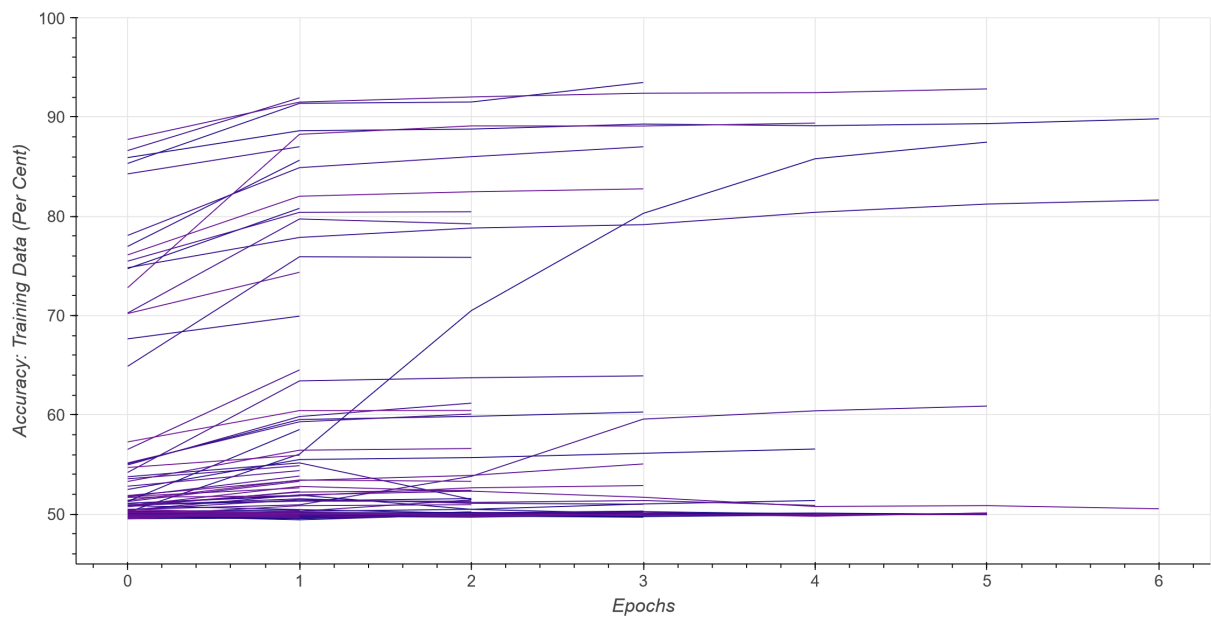
5.4 Dragonn Training

First, we can examine the training histories of our models, and note the difference in performance between generations. Figure 5.5 displays the training results, demonstrating that most of the networks fail to achieve any classification ability. This is expected. As we have allowed complete genetic freedom for layer order and parameters, many nonsensical arrangements of layers are possible which will inhibit any possibility of classification performance.

With disappointment, we note that even in the later generations no models reach accuracies above around 95%, this could, in part, be a result of our reduced training patience halting training early before extra performance can be extracted, although we note that even in cases where more epochs were reached, the accuracy seems to flatline. Setting the value of patience to one has other consequences, a great number of the somewhat models across the generations were stopped as they reached epoch two where their model loss dropped below the loss for epoch one. It is unknown exactly why this is the case since all models were trained on exactly the same training dataset generated with the same random seed, it could be that the training data in that epoch is particularly unhelpful to the model in some way though a statistical fluke. The validation datasets are consistent across epochs, so there could not be a variation in validation difficulty causing this hurdle.

Even with the chaotic diagrams, it is easy to see that the number of performant models increases with each generation, so we have verified that our optimiser works – we will examine average metrics later for verification of this. However this is not a particularly interesting result, it is known that genetic algorithms work. We do however have an interesting result that demonstrates the importance of a future, wide hyperparameter search.

performances close to gabbard small.



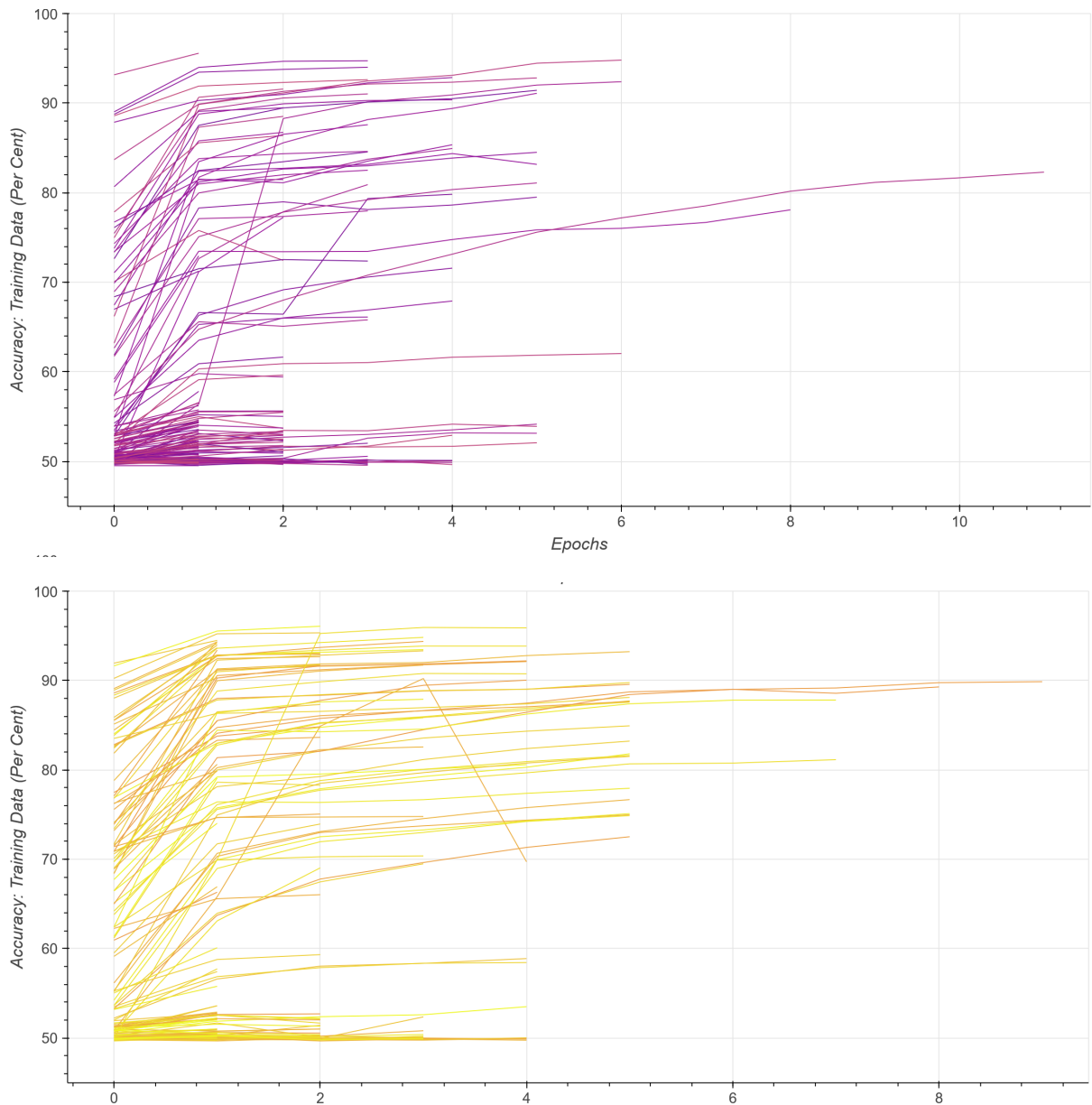


Figure 5.5 | Dragonn model training histories from each of the four generations. All models were trained with identical training datasets and validated with epoch-consistent validation data. After each epoch, a new population was generated by applying the genetic algorithms mechanism to select performant genes in previous generations. In all generations many models lack any classification ability, this is anticipated because, because of the scope of the hyperparameter search, many of the models generated will be nonsensical, with extremely small data channels or near complete dropout layers. However, we also see that our population size was enough for a considerable number of performance models. With increasing generations, we see increasing numbers of performant models, demonstrating that our genetic optimiser is operating as intended.

Next, we can examine the average metrics from each epoch. In Figure 5.6 we examine four metrics of interest; the average maximum model accuracy, that is, the average of all the highest accuracies models archived across their training run; the average lowest model validation loss, the average number of epochs a training run lasted for, and finally the average model fitness. The model fitness is the percentage of correctly classified validation examples with an optimal SNR greater than 8 when using a detection threshold calibrated to a far of 0.01. The metrics show us what we anticipated, increasing

average performance in all metrics across generations. The average number of epochs increases as the number of performant models increases since performant models are more likely to reduce their validation loss over the previous epoch.

As expected an increase in model fitness correlates with an increase in accuracy and a decrease in model loss, suggesting that better-performing models when measured with uncalibrated FAR thresholds and loss functions, in general act as better-performing methods in low FAR regimes, although this is not always the case, as we will explore when we examine the best performing models of the generation.

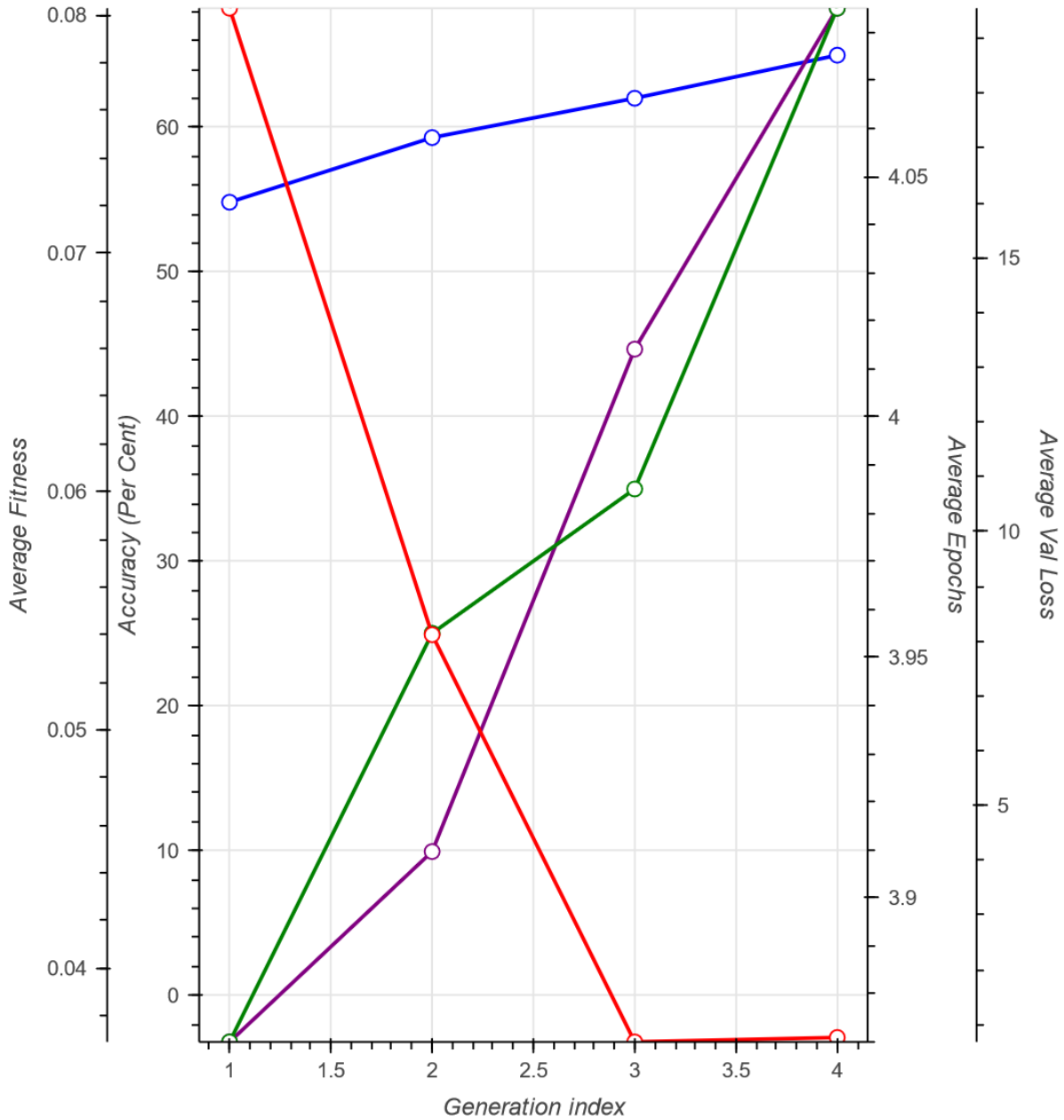


Figure 5.6 | Dragonn average metrics from each of the four generations. The blue line is the average best model accuracy across its training run, The red line is the average model loss, the purple line is the average number of epochs in a model's training history, and the green line is the average model fitness. These results are mostly as all average metrics improve with increasing generation count, the drop in loss is particularly impressive, but this probably corresponds to the shedding of extremely poorly designed models after the first epoch. Accuracy is slowly improving, as the number of performant

models increases, and with it the average number of epochs in a model's training history. Within increasing numbers of performant models comes increasing numbers of models that can perform better than their last epoch after further training.

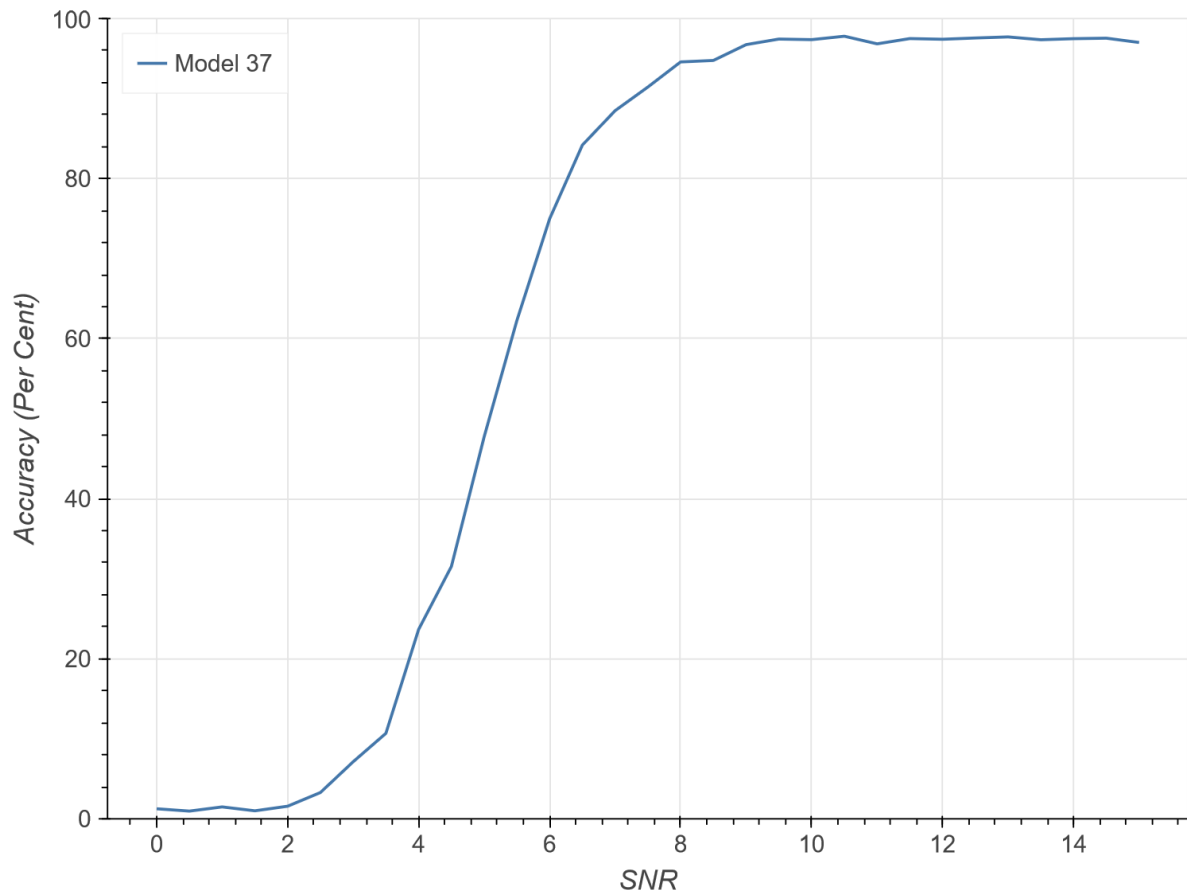
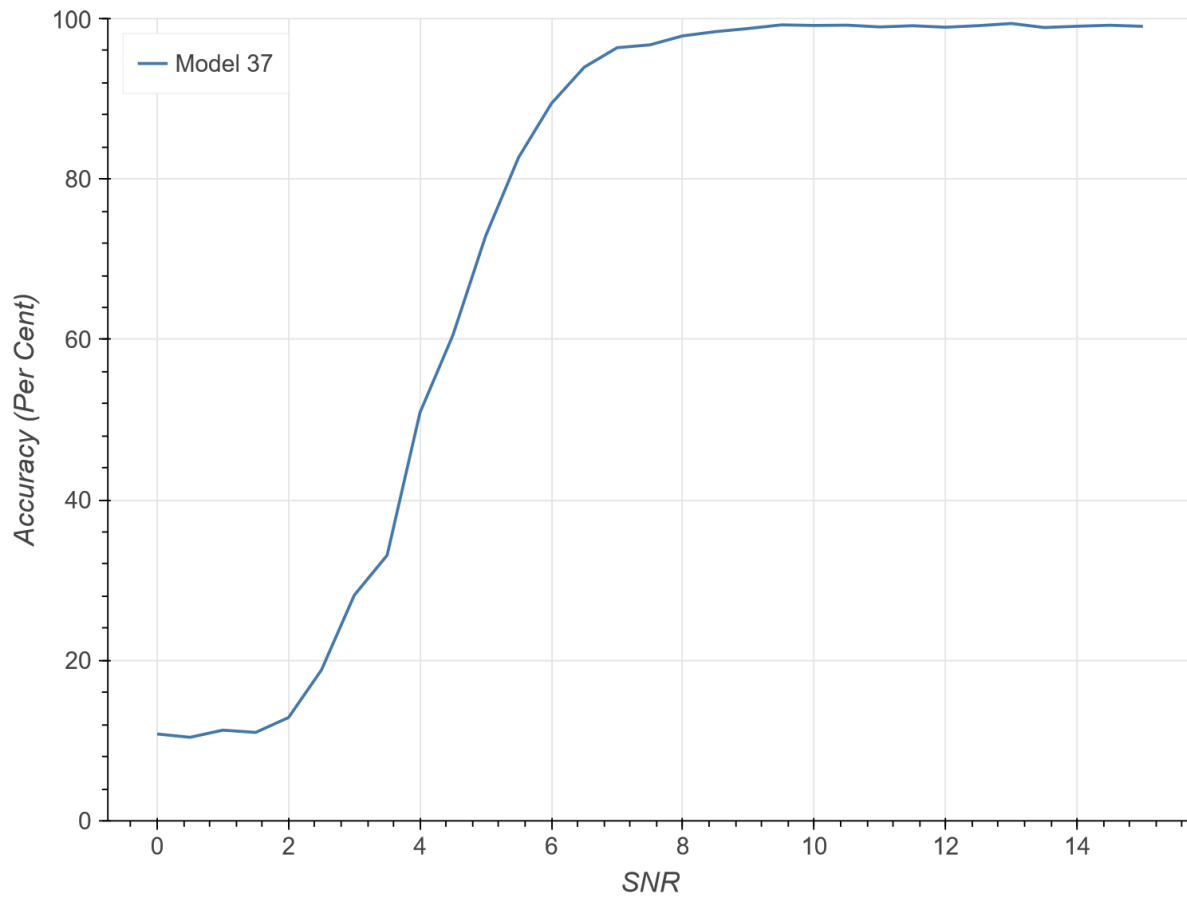
The result of an optimization algorithm is only as good as the highest-performing model. So we shall examine the population and extract the most performant models for inspection. Luckily our choice of objective function – the percentage of validation examples over an optimal SNR of 8 that are correctly classified when calibrated to a FAR of 0.02 Hz, encapsulates most of what we desire out of our models, so we can use this to guide our search to the best models.

We have extracted the top ten scoring models in Table 5.4. Interestingly, and perhaps worryingly for the effectiveness of our optimization method, the top three models are all in the first generation. This tells us that although the average fitness was increasing along with other metrics of interest, that does not necessarily equate to generating more highly scoring models, which seems counterintuitive. However, examining the validation results of the top-scoring model more closely can lead us toward a reason for this discrepancy, and perhaps an interesting area of further investigation.

Rank	Generation	Fitness
1	1	0.9423
2	1	0.9337
3	1	0.9215
4	4	0.888
5	3	0.887
6	2	0.870
7	2	0.868
8	4	0.860
9	1	0.841
10	4	0.841

Table 5.4 | The top ten models in any of the populations throughout the genetic optimisation process, out of a total of 800 trial solutions, 200 at each epoch. Unexpectedly, the three top-scoring models when ranked by fitness, the very metric our optimization method is attempting to optimise are in the first generation. The first generation of a genetic optimisation search will alone act as a random search, so it is perhaps not unsurprising that it has some ability to find good solutions, however, we would expect better solutions to arise out of on average better-performing populations. This could perhaps be a result of our very low epoch count, or a statistical fluke. If it were the latter, however, it would seem very unlikely that the top three spots were taken by a first-generation model. The other option is that there was some asymmetry between the generations.

In Figure 5.7 we examine the efficiency plot used to generate the fitness scores for the highest-scoring model, a model from the first generation. These efficiency plots show extremely strong performance in the lower FAR regimes at medium SNRs, but this appears to come at the cost of some of the performance at the higher SNRs, which do not perform as well as the CNN models from the literature.



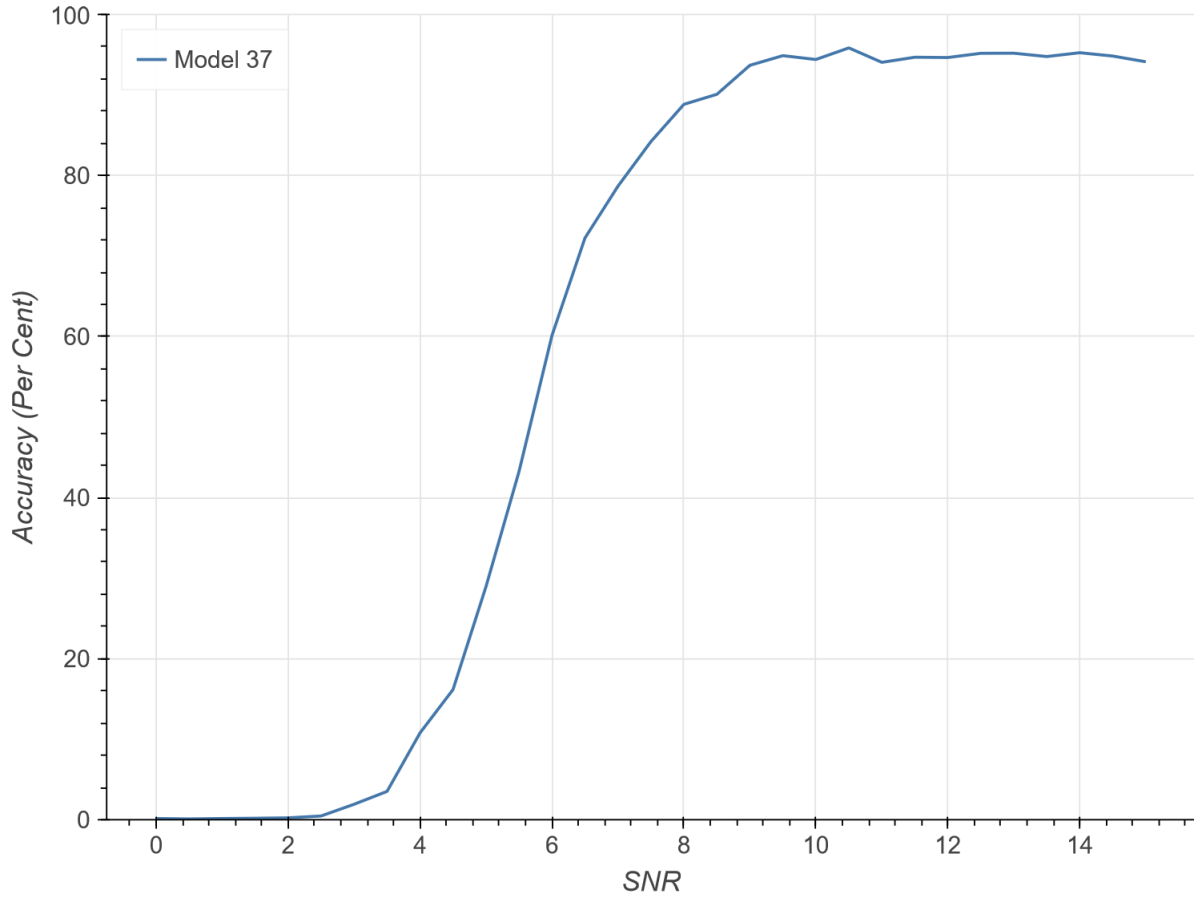


Figure 5.7 | Efficiency curves of the top performing model from the population of Dragonn trials. The curves maintain high accuracy at low FARs, though their performance at high SNRs above 10 is worse, never reaching a 100% accuracy, their performance at an SNR of 6 is considerably greater. It is hypothesized that this is due to an inoculation effect generated by the erroneous injection of WNB glitches into the dataset during the first generation. *Top*: Efficiency curve using a threshold calibrated to a FAR of 0.1 Hz. *Middle*: Efficiency curve generated using a threshold calibrated to a FAR of 0.01 Hz. *Bottom*: Efficiency curve generated using a threshold calibrated to a FAR of 0.001 Hz.

We hypothesize that this effect arises from a mistake made during the first generation. Initially, the plan had been to optimize the dataset parameters at the same time as the model parameters, and Dragonn was set up to allow the optimiser to adjust the percentage of training examples that contained CBC signals, this defaulted to 50%. However, it was also envisioned that the network could add its own synthetic glitches to the dataset, in order to act as counterexamples, this was also set to inject simulated WNBs into 50% of injections by default, including ones that also contained a CBC. It was not realised that this had been left in this state until partway through the first generation, where it was rectified, however, due to time pressure, the first trials were not repeated. Considering the three most performant results were all in the first 50 values, this oversight likely seems the cause.

The initial idea behind allowing the optimiser to inject simulated glitches was to allow it to act as an inoculant against particularly structured background noise, it would force the network to use the signal morphology because excess power could also come from glitches which would not correlate to a signal class. Due to the way the software was set up, these WNBs were also erroneously injected into the validation examples. In situations where a very high WNB is injected over the top of a signal it

could obfuscate it even if that signal had quite a high SNR, this effect could be causing the reduction in ability at the higher SNRs.

5.5 Discussion

Our attempt to expand the range of the hyperparameter search was admirable but overambitious. The time taken to perform such an expansive search was underestimated, and time pressure led to mistakes in the final optimisation run, and an insufficient number of generations to gain any real insight into the optimisation power of genetic algorithms with this degree of optimisation freedom.

Our mistakes did, however, lead us to an interesting discovery that could certainly warrant further investigation. There do not seem to be any existent investigations within the literature into such a method of using fake glitches to inoculate CBC detection models from structured background noise. The closest to such a method is perhaps the training procedure used to train the models used in the MLy pipeline [28]. MLy is a coherence detection pipeline so relies on the machine learning models being able to detect coherence between different detectors rather than specific signal morphologies. In order to train the model to distinguish between glitches and real signals, it is trained with counterexamples consisting both of coincident and incoherent glitches across multiple detectors and single detector glitches.

Without a deeper investigation, it is difficult to know whether these glitches were indeed the source of improved performance. If this does turn out to be the case it is very exciting. We can perhaps remove the degradation at high SNRs by only injecting glitches into noise examples, it is unclear whether this would maintain the impressive performance at low SNRs and FARs, but it seems reasonable to think that it might. If this investigation has unveiled anything, it is that a wide search of the parameter space of both models and datasets could reveal unpredicted and useful results.

5.6 Deployment in MLy

Whilst this attempt to demonstrate genetic algorithms for optimizing CBC detection models has fallen short, they were used to generate models for the MLy pipeline, which consists of two models. One that is designed to detect coincidence Figure 5.8, and a second model that is trained to detect coherence Figure 5.9. Since these were both relatively unknown problems compared to the CBC search, not much was known about the ideal structure of artificial neural networks for these problems.

Optimizing models by hand can be time-consuming and generates many opportunities to miss interesting areas of the parameter search space. A previous version of the Dragonn optimiser was used to develop the models that are today in use by MLy [28].

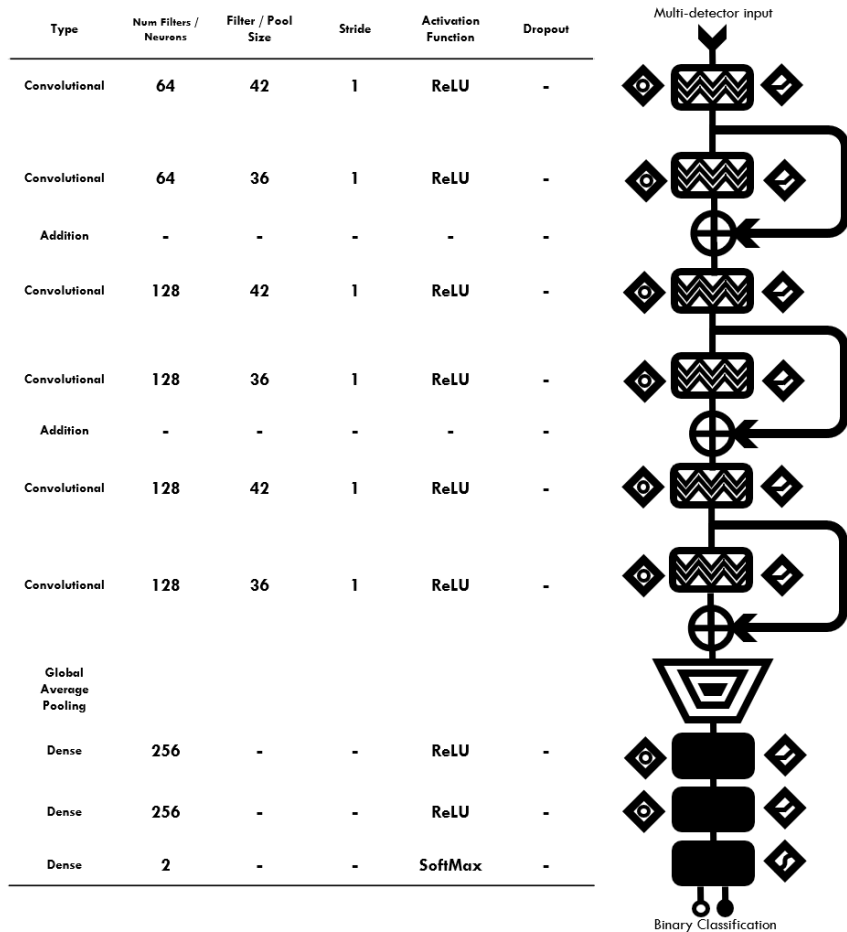


Figure 5.8 | MLy Coincidence Model developed with Dragonnn [28].

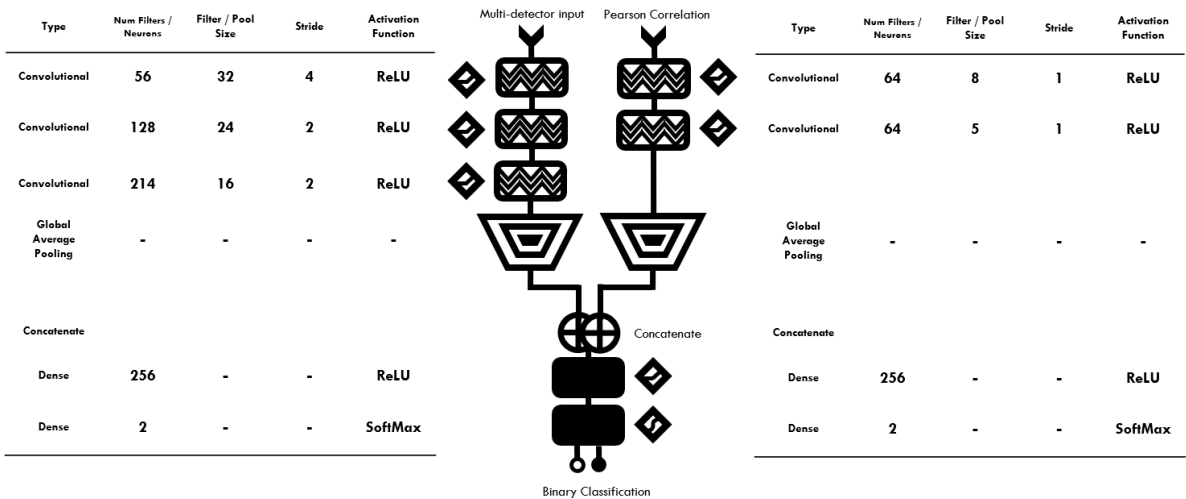


Figure 5.9 | MLy Coherence Model developed with Dragonnn [28].

6 Skywarp: An Attention-Based model for the Detection of Gravitational-Wave Compact Binary Coalescences

Convolutional Neural Networks (CNNs), though effective, have not been the stars of the machine-learning world for a few years now [286]. Just as AlexNet [128] paved the way for the era of CNNs, and the surge to prominence of artificial neural networks as problem-solving solutions in the image domain, a similar step change occurred when the confluence of several different technologies led to the development of Large Language Models (LLMs) [296], most notably of which in recent years has been the Generative Pretrained Transformer (GPT) [296,56] of ChatGPT fame [68], though it should be noted that this was far from the first LLM [296].

Although CNNs were extremely successful at solving previously intractable problems in the image and audio domain [243,10], there were still many challenges remaining within Natural Language Processing (NLP), the area of study relating to the analysis of the text domain [296]. Text sequences differ from audio time series, in that rather than vectors of continuous numerical values, they consist of sequences of discrete tokens that encode externally defined values. There had been some work to attempt these problems with CNNs [130] and Recurrent Neural Networks (RNNs) [297], but it was only through the application of multiple different insights including positional encoding [56], attention mechanisms [298], and skip connections [158], that the start of the avalanche of progress we have since seen in this area, began. The groundbreaking paper by Vaswani *et al.*, [56] first introduced the transformer architecture to the world.

Following the success of transformers in NLP, there has been much research into the application of attention-based models to other domains, including image and audio processing. Notably, AlphaFold [144], a project by Google Deepmind, successfully solved the protein folding problem. Transformers have proven effective, scalable solutions due to their highly parallelizable nature [296,299], and new attention-based architectures such as generative diffusion models have seen great success in text-to-image generation problems [300], as is seen in products such as Stable Diffusion [301], Midjourney [302], and Dall-E [303]. Gravitational-wave astronomy has also seen the application of a large number of machine-learning approaches [254]; however, there exists a considerable delay between the advent of new techniques and their application to gravitational wave data. Since this research was originally carried out, the gap has narrowed, nonetheless, it remains a relatively unexplored area that may prove fruitful in the future. In this chapter, we introduce Skywarp, an attention-based model for the detection of gravitational waves produced by Compact Binary Coalescences (CBCs).

The distinguishing feature of the transformer architecture is the use of attention [56]. Attention is a technique that can determine the information value of data elements in a series, crucially including the relative information derived contextually from the value of all other data elements within that series [304]. As opposed to convolutional layers, which learn feature-extracting filters that are convolved with the input data [242], attention layers learn a weighting for each data element, identifying the information interactions between elements. One key advantage of this method is that attention is computed globally, whereas convolutional layers only use a local context dictated by their receptive field. This makes attention an ideal candidate for analyzing time-series data, wherein important contextual information can be located at a significant temporal distance from any given datum. RNNs share many of these properties [163,160]; however, they make use of an internal state, which means they are much harder to parallelize and therefore scale, and their knowledge of data outside of their receptive field is sometimes uni-directional, as opposed to transformers, which are bi-directional (although it should be noted that bi-directional LSTMs do exist [257]). In addition, it should be noted that self-attention layers are more general than convolutional layers, as it is proven that a self-attention layer can generalize any convolution [305]. This is not to say that more generality is necessarily good. As we have

demonstrated in Section 4.3, we are unable to train dense networks, the most general of all, to identify gravitational-wave signals at a useful false alarm rate.

This section is organized into the following structure. First, we will give a brief technical overview of the concepts and structure of the transformer architecture in Section 6.1, including a discussion of tokenization, embedding, and attention, and how these elements are assembled into transformers proper. Then we will review the small amount of relevant literature that has not already been discussed in Section 6.2. Next, we will provide details on the models and training procedures we used to train Skywarp in Section 6.3. We will show the validation results from our trained models in Section 6.4, before finally in Section 6.5, we discuss the importance of these results and investigate how the method employed by the transformer models differs from that used by CNNs by comparing their respective attention and convolution maps.

6.1 Attend Closely

The transformer is a deep learning model first described in Vaswani *et al.* [56]. This paper was an NLP paper, demonstrating a deep learning sequence-to-sequence model that could ingest text data and predict the token that was most likely to appear next in the sequence. By recursing inferences of the model, new sentences could be generated based on previous inputs. In some sense, our time series data is already closer to the required input of a deep learning model, however, it is easiest to explain attention by using NLP as an example. Therefore whilst describing attention we will use the text domain as example data before replacing the relevant vectors with gravitational-wave equivalents.

6.1.1 Tokenisation and Embedding

There are several steps required in order to condition text data for consumption by deep learning models. Artificial neural networks work solely with numerical data therefore text must somehow be converted into numbers before it is ingested by the model. The most obvious way to do this would be to use a preexisting character format such as ASCII [306] or Unicode [307]. However, if we were to do this, the numbers would relate very little even to the characters they represented, let alone the words. This would make these inputs very difficult for the model to analyze. Therefore, in order to make the task easier, we can use a method to embed the words into a numerically defined N-dimensional space in a manner that maintains some of their meaning in their new vectorised representation. Typically this is achieved in two or three steps [55], tokenization [308], vectorisation, and embedding [309]; see Figure 6.1.

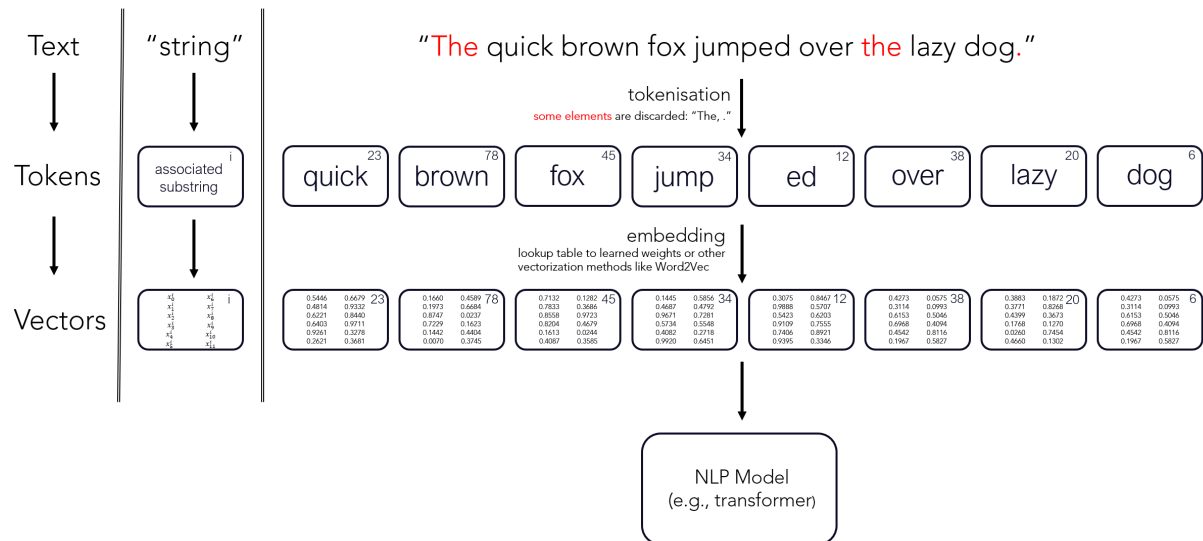


Figure 6.1 | The process of conditioning text data for input into a deep learning model. Text data is not intrinsically digestible by artificial neural network models, as artificial neurons can only process numerical inputs. Therefore, in order to apply deep learning models to text data, we must have some method of converting the data into a numerical format [55]. Transformers expect a sequence of same-length vectors forming an input matrix, X . This diagram shows the process of converting text data into an input matrix. Typically, this conversion is completed in three steps, tokenization, vectorisation, and embedding. However, often, and in the case of the first described transformer model, vectorisation and embedding occur simultaneously and are often labelled simply embedding [56]. This is the method depicted in the diagram. In the example, we see the sentence “The quick brown fox jumped over the lazy dog.” as it is prepared for ingestion by an NLP model. **Tokenisation** is the process of splitting one contiguous sequence of characters into a number of unique discrete tokens, N . This can be done at multiple levels but is usually done at the scale of words. Sometimes, especially with longer words, words can be split into multiple tokens, as is seen in this example where the word “jumped” is split into “jump” and “ed” [55]. There are numerous algorithms to achieve this, which will not be discussed in detail. Every word, or word subset, within the training dataset, should have a unique token ID. Before running inference on new text data, that data must be tokenized, and each word in the new data will be mapped onto an existing token ID that was generated during the initial tokenisation process. Often some information-low words, known as “stop words”, and punctuation are removed during the tokenisation process [55]. In the example shown, the words “The”, and full stops are removed from the input string. During **vectorisation**, each token is assigned a numerical vector, and **embedding** ensures that this vector is transformed into a meaningful vector space to allow for easier interpretation by the model. There are a number of methods to achieve both of these steps, some of which are simultaneous. In the example shown, each token ID is associated with a vector of tunable weights, as was the case in the first transformer paper. These vectors are randomised at the start of training, but as the process continues, they become tuned to values that represent the information contained by the tokens. In this manner, the vectorisation and embedding steps occur at the same time.

First, the input sequence must be tokenized [55]. Tokenization involves splitting the input text into N unique discrete tokens. Often the text is processed first, sometimes removing low information elements known as stop-words and punctuation. Then, using one of a variety of algorithms that will not be discussed here [310], the text is consolidated into N tokens, often these could be whole words, but sometimes, depending on the tokenization algorithm and the size of the training data, word fragments could also be tokens. One will note that often words can have multiple meanings, which is a problem when trying to describe each token in a way that somehow presents the value it represents in a sentence. This can be a problem, and methods have been developed that can split identical sequences of characters into multiple tokens contextually. The very existence of this problem is an example of the contextual information that is provided by surrounding tokens in the sentence, this is the information that attention layers attempt to extract and distil.

After tokenization, we must convert each token into a unique vector. This can also be done through a variety of methods. In Vaswani *et al.* [56] each token has an associated vector in a look-up table, initially these vectors are randomly generated; however, the values in each of these vectors act as tunable parameters inside the model, so that whenever a certain token is present in a particular training example, the weights of its vector are tuned through the usual gradient-descent methods. In this way, as the training progresses, the vectors become, at least to the model, meaningful numerical representations of the value contained within their associated tokens.

Gravitational-wave data is intrinsically vectorized so the embedding layer should not be much of a problem, however, it is not intrinsically discretised. Since transformers are sequence-to-sequence mod-

els, they ingest a series of N vectors forming an input matrix [56,299], whereas gravitational-wave time series data is a single vector, at least when dealing with one detector. It is unclear how best to split the gravitational wave data into smaller vectors. We could simply cut along equally separated lines, “chunking” our data into smaller timesteps, or we could embed the data using some learned weights, for example with one or more dense or convolutional layers, in the latter case, feeding the transformer with feature slices at different timesteps; see Figure 6.2. Using different detectors as this extra dimension will only give us two to four features per timestep, which would be very small vectors for the transformer to work with.

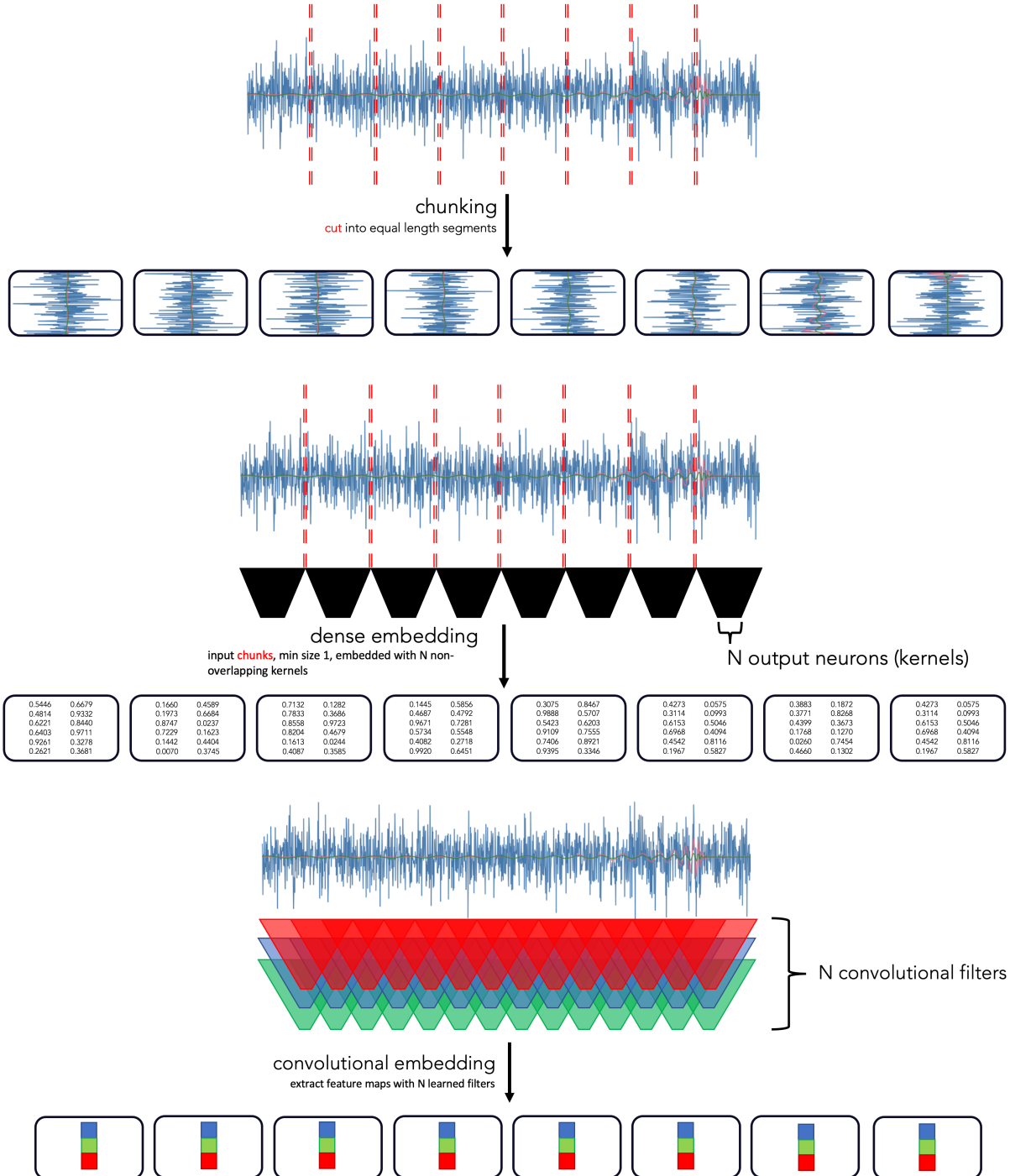


Figure 6.2 | Different embedding possibilities to discretise and embed gravitational-wave time-series data. *Upper*: “Chunking” method of discretisation, where the input time-series is split into N equal-

length segments which can be fed into an attention-based model. This method would seem to have the disadvantage that it could split the waveform at any point, leading to chunks with very different waveform content depending on the waveform offset; it also assumes that the innate interferometer output vector is a good embedding for the attention mechanism, which is not necessarily true. *Middle*: Embedding with dense layers, this setup is similar to the chunking method, but it applies one or more dense layers to each chunk so that the model can learn an embedding that will be better adapted to the attention mechanism in subsequent layers. Since the parameters of the dense layers are repeated for each chunk, this method is equivalent to a convolutional layer with N filters and no overlap, where N is the size of your embedded vector output. *Lower*: Embedding with convolutional layers. This type of embedding involves creating feature maps of the input vector using a combination of convolutional and/or pooling layers. It is the equivalent of attaching a CNN head at the front of your model. The output of a 1D CNN would be a 2D matrix where one dimension, the depth, is different features, and the other is time. This can then be split into discrete vectors by splitting it along the time dimension to create vectors of features with length equivalent to the number of features.

We have managed to transform our input text from a list of symbols into discrete tokens and finally into vectors that contain some aspect of the value represented by that token, and we have some ideas about how we might do the same with gravitational-wave data. However, unlike convolutional layers, attention layers treat each input element equally and intrinsically have no information about the location of the word in the sentence. We must use feature engineering to add to each vector, some information about the position of the token in the input sequence.

6.1.2 Positional Encoding

Much information is embedded in the relative and absolute positions of tokens within text data [299]. The same can be said to be true of gravitational-wave data — we would always expect the merger to come after the inspiral, for example. Whilst there is some possibility within the dense layers of a traditional CNN for the model to use this ordinal information in its classification, it might be a challenging process. We can use attention layers to look at the global information in a sequence, but since, unlike CNNs [242], there is no structure inherent to the architecture that maintains information about the position of the inputs, if we feed in the word sequence as-is, we end up with a “bag of words” [311]; see Figure 6.3. Whilst some models can do quite well with just a bag of words approach, able to infer context simply from the numbers of each word present [311], it is clear that some information is lost when discarding order.

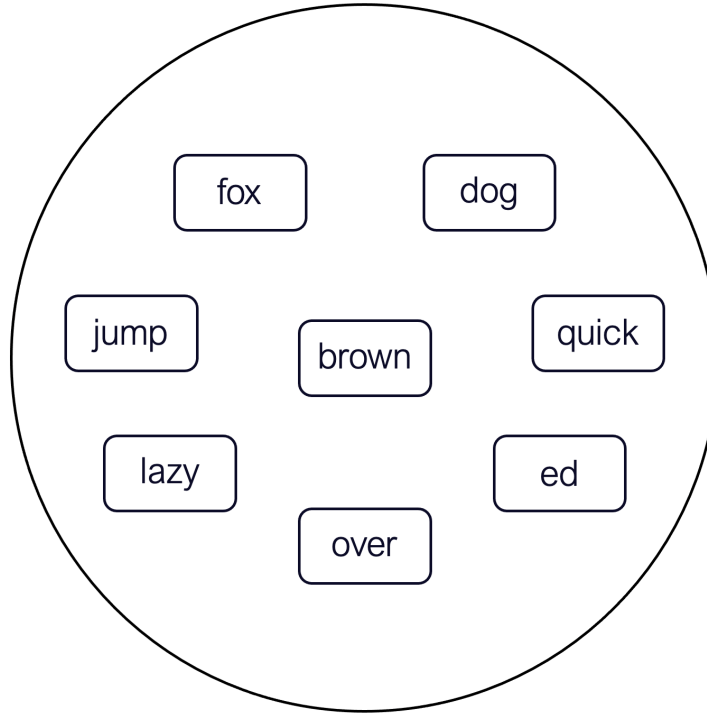


Figure 6.3 | A “Bag of words”. Without ordinality, the meaning represented by this sentence becomes significantly harder, if not impossible, to parse. If we had not already seen this sentence then we would not know if the fox was lazy or quick, or rather if it were the dog that was lazy or quick, and just who is jumping over whom? There are NLP models that are designed to use a bag of words as inputs, but it is easy to see that much information is lost when word order is discarded, thus we can infer that the order and position of the words contain a significant amount of information. The same can be true for time series, a CBC signal that contains a merger, an inspiral, and a ringdown, in that order, can probably be discounted as a glitch, but if we feed it in as a bag of words model, there could be no distinction between this and the expected arrangement.

We solve this problem by adding extra information to our input embeddings with positional encoding [56,312]. To do this, we create a matrix that is the same size as our attention input matrix: [num_time_steps, num_feature_channels]. Each column in our matrix must have certain properties: it must be unique so that no two feature embeddings are given the same encoding, and it must convey information about the absolute and relative position of a given feature vector in the input sequence. We create this matrix using

$$\text{PE}(t, i) = \begin{cases} \sin\left(\frac{t}{\log(10000)^{\frac{i}{d_{\text{model}}}}}\right) & \text{if } i \text{ is even} \\ \cos\left(\frac{t}{\log(10000)^{\frac{i}{d_{\text{model}}}}}\right) & \text{if } i \text{ is odd} \end{cases} \quad 6.1$$

where $\text{PE}(t, i)$ is the positional encoding matrix, t is the time index, i is the feature index, and d_{model} is the dimension of our model, the relevance of which will become clear later. The periodicity of sine and cosine functions enables a unique identifier for each vector whilst maintaining a consistent pattern that evolves across the time dimension [56]. This uniqueness ensures that absolute position is encoded; all feature vectors get a unique encoding, which will be the same independent of the vector’s contents so the model can learn which encodings map to which positions. The logarithmic term, $\log(10000)$

ensures that the variation in frequency between steps is large enough to be detectable by the model, whereas the scaling by d_{model} ensures that the positional encoding values do not become too large and overshadow the feature vectors, or become so small they are undetectable. The relative position between any two vectors in the sequence can be estimated due to the linear superposition property of the sin and cos functions; the sum of the positional encodings will approximate $t_1 + t_2$, and the difference will approximate the difference, $t_1 - t_2$. Therefore, when the model adds or subtracts positional encodings (as it might do implicitly during training), the resulting encoding still carries meaningful positional information. This matrix is added to our sequence of input vectors by simple element-wise addition, therefore inherently encoding positional information into each feature vector.

Fortunately, this embedding process is just as appropriate to use on gravitational wave data as it is on text data. In early testing, we found that including positional encoding improved model performance significantly.

By adding positional encoding to our input vectors, we have ensured that even if we (or a model) look at the vector in isolation we will still be able to know where in the vector it originated [56,312]. So we have stored extra information within the vector, however, if we look at this new vector in isolation, there is still much contextual information provided by the rest of the sequence that we cannot access alone. If we look at the word “dog” in isolation for example, even if we knew it was the ninth word in the sequence, we would have no idea that it was lazy, or that a fox was jumping over it. To embed this kind of information, we must turn to attention layers.

6.1.3 Attention!

The global information provided by an individual element within a sequence is often greater than the local information contained within the isolated element [298,57,56,304]. This extra information is stored contextually within the relationship between the given element and the other elements in the sequence, both within the information stored locally by the other elements and by the relative and absolute positions of the other elements.

The set of possible combinations of elements is large, even within relatively small sequences. Therefore, in order to enable a machine learning model to extract contextual information efficiently, a method must be implemented to determine which elements contribute the most contextual information to each element. This method is attention [298,57,56,304], a type of differentiable memory in which a global context vector is learned over an input sequence, $X = [\vec{x}_1 \dots \vec{x}_i \dots \vec{x}_n]$. The attention mechanism aims to embed global context locally; in order to do this, a comparison must be made between each element of the sequence and (in the case of self-attention) each other element of the same sequence. It is trivial to see that not every element in every sequence will be equally relevant and that this contextual dependence will depend on the information being extracted. In this way, one learns intra-sequence relations; long-term dependencies are captured because the entire input sequence is used to compute a single element of the output sequence. Ideally, this process makes the output elements, now with contextual information embedded locally, easier for other machine-learning methods to interpret.

A transformer model is a machine learning algorithm that implements this method to localize global information using attention [56,299]. The output of a transformer block has the same dimensionality as the block’s input, as it retains the same number of elements. Ideally, each element has been transformed to contain a proportion of the relevant global information stored within the input sequence.

The question becomes, how can we calculate the attention? We can use an analogous problem to demonstrate the principle. In search and retrieval tasks, such as a search engine query, the user, in this case, a human, must generate a **query** phrase that can be used to find relevant information. This query phrase will not contain the entire information content of whatever document we are attempting to discover, if it did then we would not need to perform the search. Instead, it is generated using

words and phrases that are associated with the information we are searching for. The search engine then has the unenviable task of searching through its entire library to find documents that might have information relevant to the query.

The first instinct might be to look through every document and check to see if there are words and phrases in that document that match the content of the query. Immediately, we can tell that this will quickly become infeasible if the library is large, and/or contains large documents — the process of searching would rapidly become very expensive. Instead, the search engine could have preprocessed these files, and in a similar manner to how the query was generated, it could pick out the key information content of each document in a distilled form that contains the information that it is most likely to match with a query. It generates a **key** or keys for that document, which can be checked against queries much more efficiently than searching the entire content.

Finally, the **value** of the information that the end user extracts from whatever document is returned, will not necessarily equate to the entire information content of the document. Depending on what information the user was originally searching for, and hence what query they entered into the search bar, they might only read a particular chapter of a book, or, even more specifically than that, they might only retain certain parts of information from that chapter that are relevant to their needs. During a search session, a user might enter a single query that matches well with multiple keys that return documents which the user then reads and summarises parts of the information in each document to gain new knowledge on whatever the original subject of their query was.

This analogy introduces the three key information concepts of the query, key, and value. We can use these concepts to build a deep learning layer that can, for every element of our input sequence, search through each element in the sequence and extract relevant contextual information that can then be embedded into that element, in a similar manner to how we can embed information about the elements position using positional encoding. In attention layers, query, \vec{q}_i , key, \vec{k}_i , and value \vec{v}_i vectors are generated for each sequence element \vec{x}_i , forming three matrices for the sequence as a whole: Q , K , and V . We create these matrices by multiplying three projection matrices with the input matrix, X , the query, W_q , key, W_k , and value, W_v , matrices. Q , K , and V are generated with

$$Q = W_q X, \quad 6.2$$

$$K = W_k X, \quad 6.3$$

and

$$V = W_v X. \quad 6.4$$

The elements inside these weights matrices are the only tunable parameters that are learned during the model training process [298,57]. During model training, the weights will adapt so that they can generate effective query, key, and value vectors that allow for proficient model function. Since this is a neural network and these are learned weights, multiplication by these weights matrices is equivalent to the application of a dense layer with no bias values.

The nature of attention layers makes it more difficult to draw artificial neuron connection diagrams as we have previously with perceptrons and CNNs, since the information flow is more complex. However, we can attempt to visualize the interaction between the various vectors as interacting functional elements, like machines in a factory, organelles in a cell, or gears in a clock; see Figure 6.4.

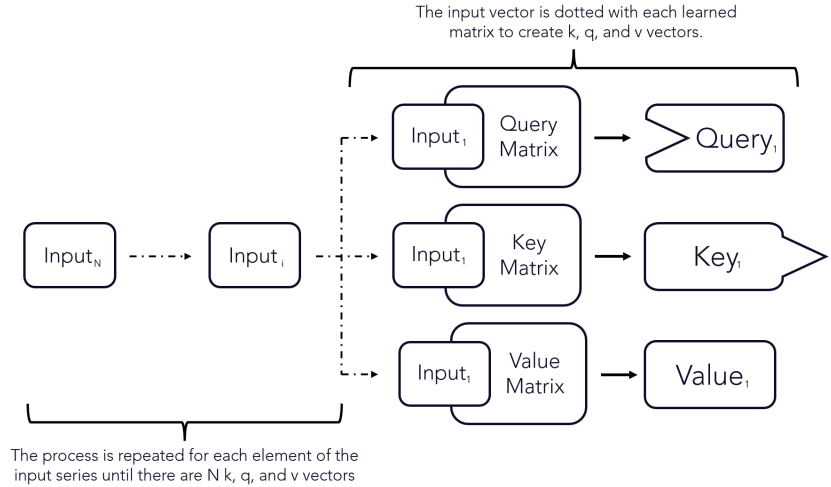


Figure 6.4 | Generation of query, key, and value vectors for each element in the input sequence of length, N . Before attention scores are calculated, each input vector, \vec{x}_i is dotted with the learned query, W_q , key, W_k , and value, W_v , weights projection matrices to produce a query, \vec{q}_i , key, \vec{k}_i , and value \vec{v}_i vector for the input element, \vec{x}_i . This operation is equivalent to the multiplication of the projection matrices and the input matrix, X , to produce the query, Q , key K , and value V matrices. The key takeaway is that the only tunable parameters are contained in the weights matrices, which act as projection functions to convert the input vector into functional vectors.

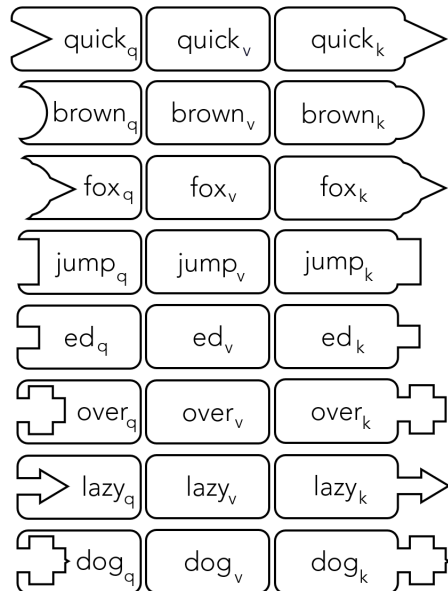


Figure 6.5 | Illustration of example query, key, and value vectors generated for the sentence “The quick brown fox jumped over the lazy dog.”. After tokenisation and embedding, each vector in the embedded input sequence generates its own query, key, and value vector. Which together form query, key, and value matrices.

The query, key, and value matrices are used to calculate attention; see Figure 6.5 for an illustrative example of the projection matrices applied to the example sentence. The attention method aims to collect relevant information about a given sequence element within that element, extracting the information content from the position and meaning of the surrounding elements. Understandably, language does not have words for every possible concept, instead, it relies on combinations of words to provide many

more concepts than single words could alone [313]. For example, language could have developed a single word for “lazy-dog” and “quick-fox”; but you would soon end up with an extraordinarily large vocabulary (assuming that new words were invented rather than just cheating and compounding words with a hyphen). If we wanted to include more complex concepts like “quick-brown-fox-that-jumped-over-the-lazy-dog” and “lazy-dog-that-has-had-quick-brown-fox-jump-over-it”, the number of potential concepts becomes vast. Within the vector space, however, we are not limited by discretized tokens, and such concepts can all exist in a highly multi-dimensional space, since, in effect, we can add vectors together to sum their meanings. Attention layers essentially attempt to assemble these complex words [299].

In order to assemble these new vectors with embedded contextual meaning, we must work out the magnitude to which each other element affects the meaning of that element. This score is the “attention” for which the process is named [298,57,304]. In the example sentence, “The quick brown fox jumped over the lazy dog,” we can see that almost all of the concepts are somehow interacting with each other in a significant manner. If we were to extend the string however say to, “The quick brown fox jumped over the lazy dog. Incy wincy spider climbed up the water spout.”, we can see that tokens in the second sentence have very little effect on the concepts in the first sentence, so we might expect the attention scores between tokens in different sentences to be much lower than in the same sentence. Now in very advanced LLMs, there could be some cross-sentence attention as the model tries to determine why those two sentences in particular are next to each other, a question which could certainly hold some information, but this would be at a much higher level of abstraction than the simpler cases we have been discussing.

The query value for each sequence element is matched against the key value of each other element [298,57,304]; see Figure 6.6. The alignment of the key and query determines a weighting for the value vector, a distilled representation of the relevant information contained within that element; see Figure 6.7. The weighted value vectors are then summed to produce the new, contextually embedded, element. The two most common attention methods are dot-product [57] and additive attention [298], our models utilise the former and so we restrict our discussion to the work of Luong *et al.* and extensions. In either case, the function α maps a set of query q , key k , and value v vectors to a weighted sum of the values. This is given by

$$\alpha(q_i, K, V) = \sum_{j=1}^N a(q_i, k_j) v_j \quad 6.5$$

where $a(., .)$ is called the alignment function and measures the similarity between the queries and keys. In the case of dot-product attention

$$a(q, k) = \sigma\left(\frac{q^T k}{\sqrt{d_k}}\right) \quad 6.6$$

where σ is the Softmax function; see Section 3.1.5.4, and d_k is the number of elements in the key vector, used to scale the value so that differences remain large when d_k is large. This scaling was not a part of the original dot-product attention approach [57] and was added by Vaswani *et al.* [56], it has since become a common feature in attention layers.

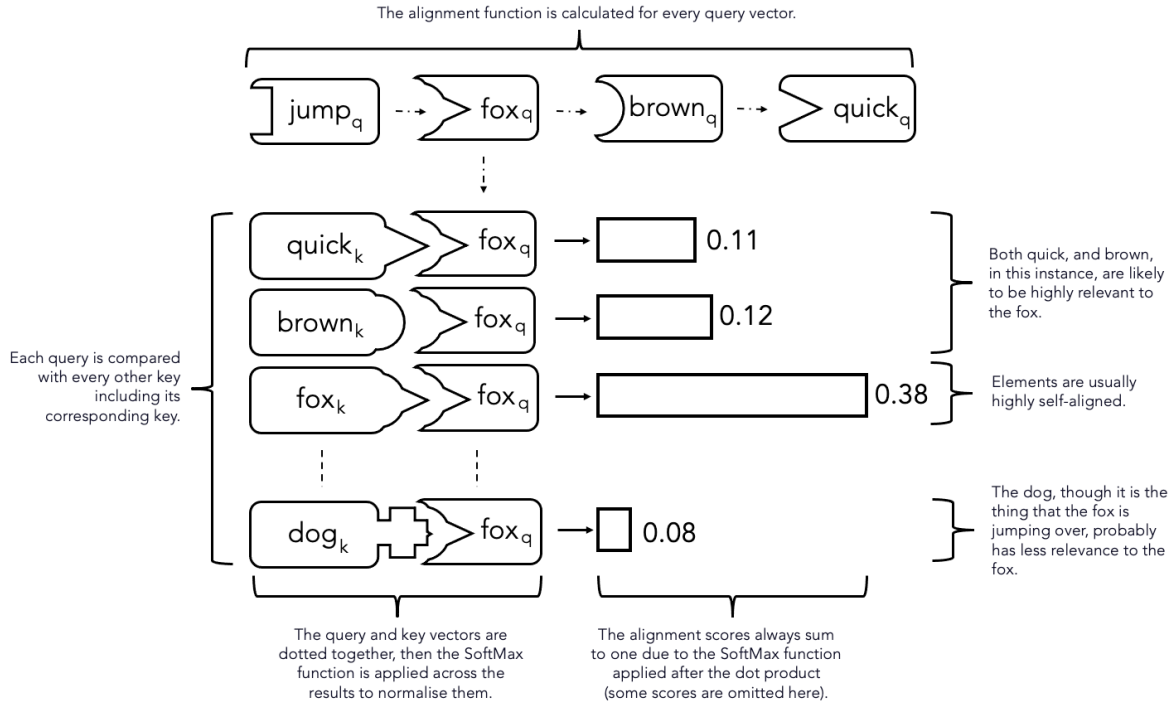


Figure 6.6 | Illustration of the operation of how the alignment function utilizes the query and key vectors to produce alignment scores for each sequence element. In dot-product attention [57], this is achieved using Equation 6.6. Note that the numbers used here are for illustratory purposes only and not extracted from a real model.

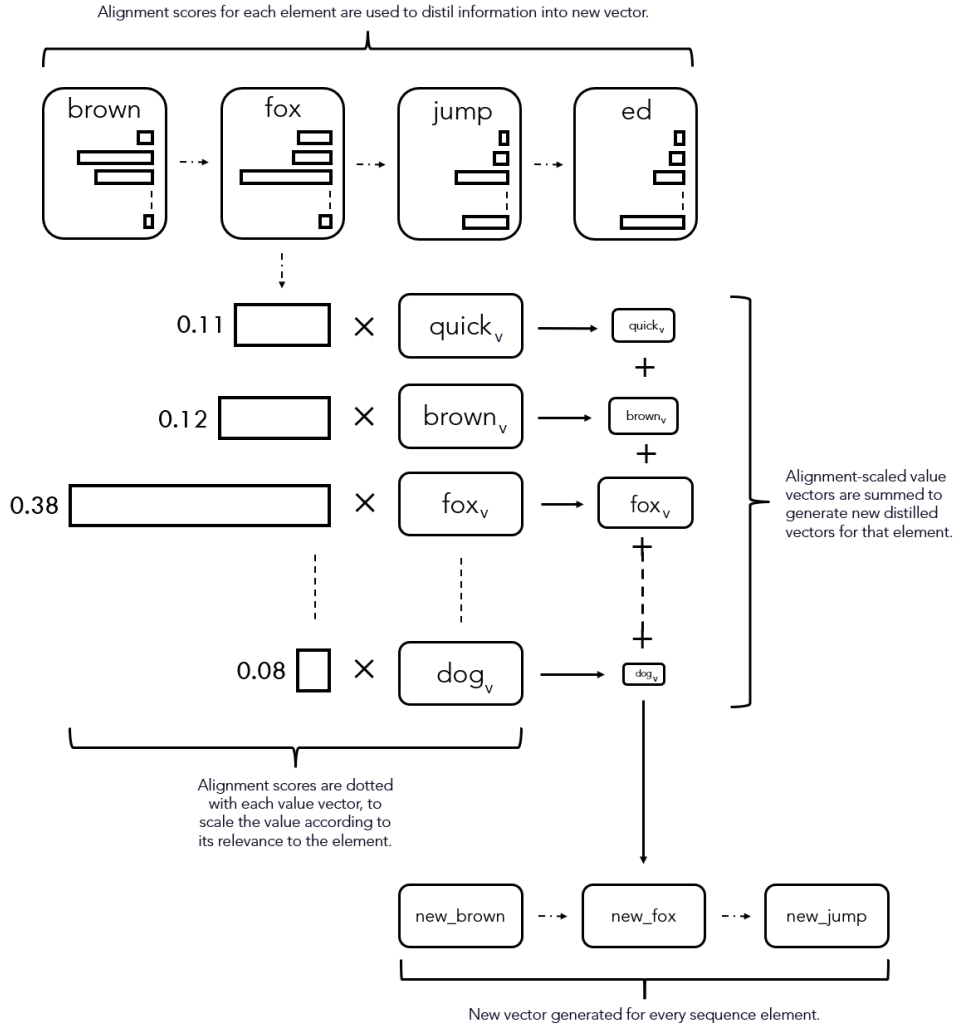


Figure 6.7 | Illustration of how the alignment scores are used to scale the respective value vectors for each sequence element, and are then summed to produce a new vector that contains global information embedded contextually. Each value vector is multiplied by the respective score, and then these scaled elements are summed together to produce the new vector.

This calculation is performed on each element of the sequence to produce a new sequence of equal length, hopefully with some contextual context embedded [56,304]. Generalizing Equation 6.5 for the entire input matrix, X , we get

$$\alpha(Q, K, V) = \sigma\left(\frac{QK^T}{\sqrt{d_{\text{model}}}}\right)V. \quad 6.7$$

Where again, σ is the Softmax function [13]. Combining Equation 6.7 with Equation 6.2, Equation 6.3, and Equation 6.4 gives a mapping between the attention input matrix, X , and the attention output matrix, Y .

$$Y = \sigma\left(\frac{(XW_q)(XW_k)^T}{\sqrt{d_k}}\right)(XW_v). \quad 6.8$$

The convenience that this complex procedure can be performed with a few matrix multiplications is one of the reasons for its great success. See Figure 6.8 and Figure 6.9 for illustrative diagrams.

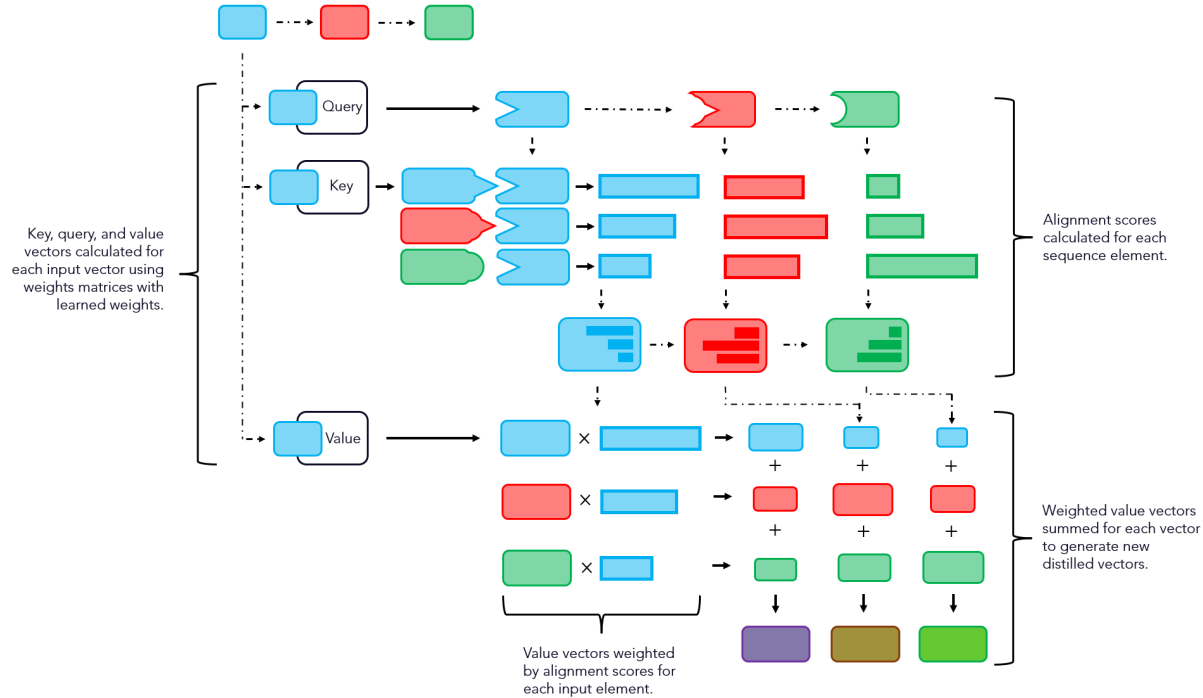


Figure 6.8 | Illustration of the operation of a single attention head. Here a very small three-element sequence is examined. Each element of the original input sequence is coloured differently, in red, green, and blue. All vectors and scalars associated with an input element are coloured similarly. The output sequence vectors are coloured with a mix of the input colours to show their new information content which consists of distilled global information. More detailed descriptions of the processes shown can be found in Figure 6.4, Figure 6.6, and Figure 6.7.

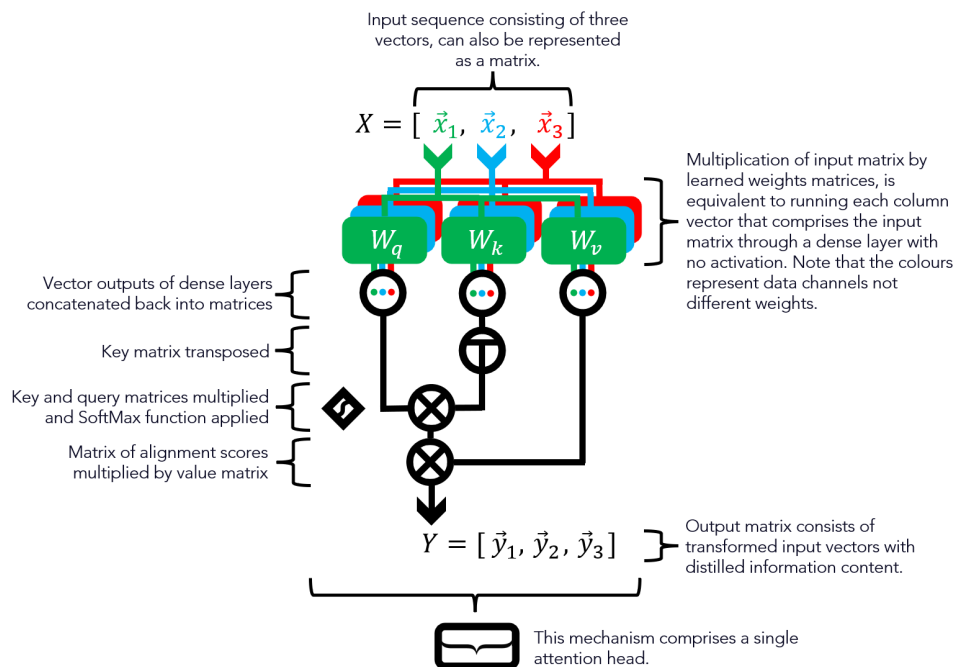


Figure 6.9 | *Upper:* Alternate method of visualizing attention mechanism as a network diagram. Although this is more similar to how networks have been displayed elsewhere in the thesis, it might obfuscate some aspects of the reasoning behind the attention layer operation. As in the Figure 6.8, this illustrates the operation of the attention mechanism on a sequence of length three, with each input

vector coloured differently, in red, green, and blue. In this representation, the projection matrices, W_q , W_k , and W_v , are represented as dense layers, which are applied to each of the column vectors that comprise the input matrix in turn. It should be noted that although the dense layers are coloured differently as they are applied to each input element, this is just to show the different data flows, the weights are maintained by each application of each dense layer. The key, query, and value-dense layers, however, have different weights, and notably, no activation function, as they are just supplying a linear mapping rather than any more complex behaviour. *Lower:* Abstraction of a single attention head layer, that will be used in future diagrams of models which contain attention layers, in order to limit diagram complexity.

6.1.4 Multi-Head Attention

Thus far, the process we have described is the operation performed in a single attention head. We have worked under the assumption that all contextual information can be embedded locally with one pass from one head. In reality, this is not true, except for trivially simple sequences it would not be possible to embed all global information in one pass. In a similar manner to convolutional filters, wherein each filter looks at a particular feature of the input data, an attention layer typically has multiple heads each of which focuses on a particular information feature. One could look at colour for example, whilst another focuses on punctuation (if not removed in tokenisation), or sentence structure.

In multi-head attention layers, the number of heads is a user-specified hyperparameter, N , just like the number of filters in a convolutional layer [56,304]. Each head has independent weights for the query, W_q , key, W_k , and value, W_v , projection matrices, which are each tuned to find specific features in the data. After these heads have been applied the output is concatenated along the feature dimension, and then multiplied by a further weights matrix, used to mix the outputs of different heads and to reshape the output vector to a desired size, which does not necessarily have to be the same size as the input vector, though this is a common choice; see Figure 6.10 for a representation of a multi-attention head.

It should be noted that in practice, all of the query, key, and value matrices for each head are calculated simultaneously with the same large weights matrices comprising the individual weights matrices from each head combined into large matrices. After multiplication with the input sequence, the large output matrices are split into separate matrices for each of the individual heads for the alignment scores calculation and vector summation. This is done to reduce the number of matrix multiplications required for the layer as a whole.

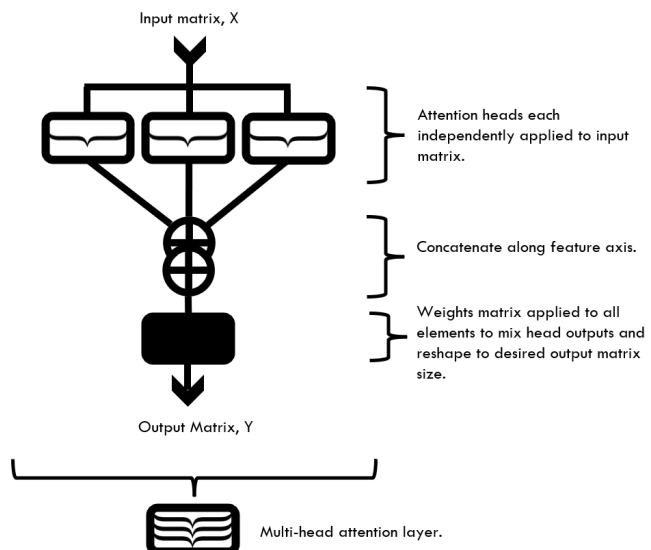


Figure 6.10 | Upper: Network diagram of multi-attention head. Similar to how multiple convolutional kernels work in tandem in convolutional layers, multiple attention heads work together in multi-attention heads to focus on different information aspects of the input vector. These are then concatenated along the feature axis before finally being multiplied by a further weights matrix, here shown as a dense layer, which serves to mix the output of the different heads and to reshape the output to a desired size. **Lower:** Abstraction of a multi-head attention layer, that will be used in future diagrams of models which contain attention layers.

6.1.5 Attention Blocks

Within transformers and other similar architectures, multi-head attention layers are often paired with a number of complementary layers within a residual block [56,304,299]. The input and output matrices of this block usually have identical shapes so that the block can be repeated, N times without having any intermediate reshaping layers. Attention blocks typically feature a number of dense layers with activation functions in order to perform non-linear computation, regularisation methods such as dropout and batch normalisation, and a residual skip connection wherein the block input is added to the block output, in order to reduce the vanishing gradient problem that can occur in very deep networks; see Figure 6.11.

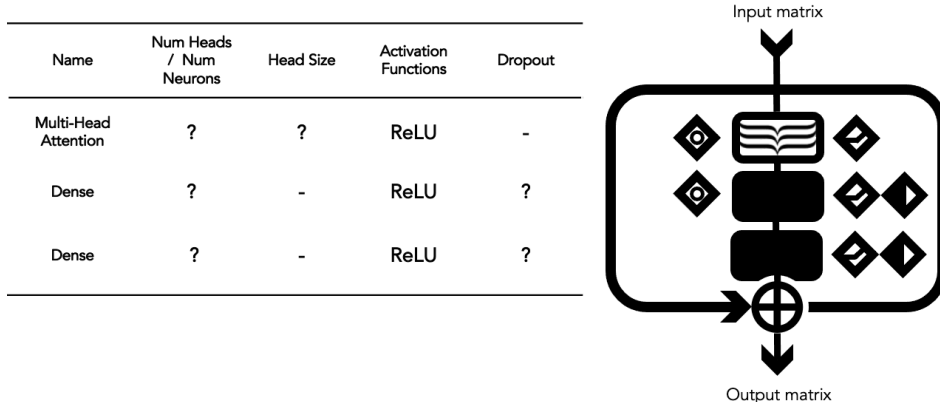


Figure 6.11 | Typical attention block comprising multiple layers. Residual attention blocks vary in design between architectures but usually maintain the consistent elements shown. The skip connection is here represented by the encircling arrow, which shows that the input of the block is fed to the output before it is returned. There are also several regularisation methods present, batch normalisation, and dropout which help to reduce overfitting and ensure that values within the network remain bounded. Finally, the addition of dense layers and activation functions ensures that non-linear computation can be performed. Sometimes, if a reduction in total model parameter count and inference time is required, convolutional layers can be used in place of dense layers. The question marks indicate user-selectable hyperparameters.

6.1.6 Transformers

Since their introduction, attention mechanisms have been utilized in a number of different neural network architectures, including transformers [56,299] and generative diffusion models [300]. Transformers were first proposed by Vaswani *et al.* [56] to solve natural-language processing tasks, showing a significant improvement over previous recurrent and convolutional architectures. For these reasons, we decided to investigate a fully attention-based model, inspired by a Transformer encoder.

The transformer proposed by Vaswani *et al.* [56] consists of two branches each comprised of stacks of transformer blocks - the encoder and the decoder. See Figure 6.12. Since the model is designed for sentence generation, its architecture is a little different from what we will use in Skywarp. The encoder model takes the input sequence, your input prompt adds positional encoding, and then runs that sequence through six encoder blocks, each consisting of a multi-attention head and two dense layers, both the multi-attention head and the two dense layers are surrounded by a residual skip connection and the outputs are normalized. The encoder converts an input sequence into a discrete latent space, which is then fed to the decoder, which similarly consists of a multi-attention head and two dense layers. In addition, the decoder has a cross-attention layer that receives the output of the encoder and converts that output into key-value pairs, matching them against the queries generated by the decoder sequence. Cross-attention allows attention maps to be generated between elements in different sequences, in opposition to self-attention where attention is only calculated within the sequence.

The design of this encoder-decoder serves the next token prediction capabilities of the transformer [56,299]. The purpose of the encoder is to encode the full training input sequence and provide a comparison for the decoder output. The decoder output then, gets a shifted input sequence, on the token to the right, with an additional start token. During the first attention layer in the encoder, a masking is added, so that no element can see any elements ahead of it in time. This is because whenever a token is at the end of a sequence it cannot see any future tokens. The outputs this process generates are then compared against the encoder output, which can see the whole input sequence, therefore the decoder learns to guess what the next tokens might be. That is a slight simplification but is an approximate description of the function of a standard transformer model. See Figure 6.12.

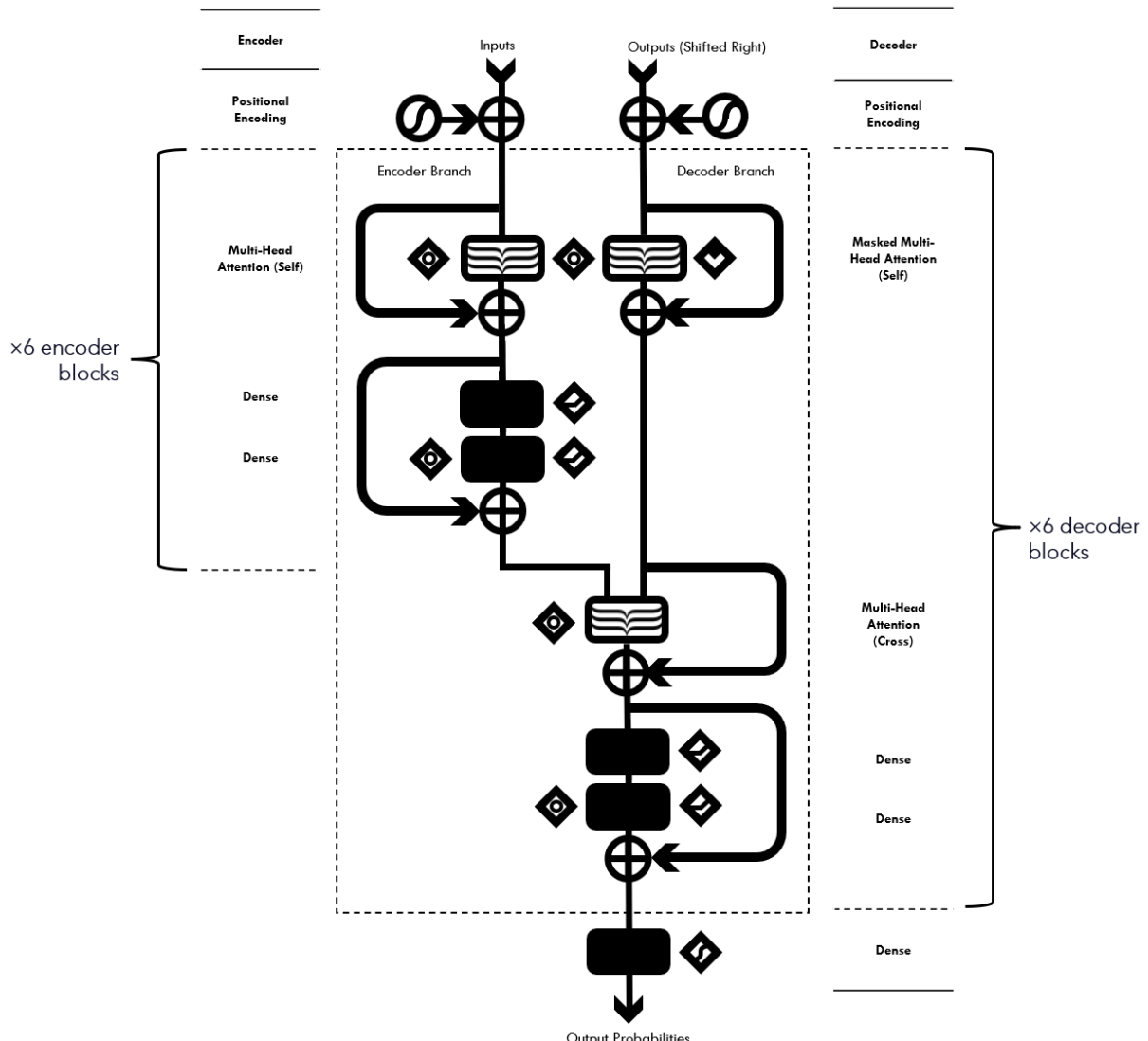


Figure 6.12 | The transformer model described by Vaswani *et al.* [56]. This encoder-decoder architecture can be used to generate predictions of the next token in a sequence. In the case of [56], this sequence was natural language.

Since we are attempting to perform classification rather than next-element prediction, we will use only the encoder part of the transformer architecture, and adapt it to use gravitational-wave data.

6.2 Transient Detection beyond CNNs

When expanding our literature search to include models outside of CNNs we encounter a large body of work that has expanded greatly in recent years, even since this work was carried out [254]. The volume presented makes it difficult to perform a complete review as it would be beyond the scope of this document. A review article [254] is suggested for a more extensive overview.

An architecture commonly applied to time series problems is the Recurrent Neural Network [163]. Recurrent neural networks have an internal state determined by previous inferences, and thus, they can retain some information about previous data. In many ways, RNNs were the predecessor to Transformer models, largely because they are able, in some way, to make inferences from global information rather than being limited by the receptive fields of convolutional filters [243]. There have been many studies on the application of RNNs to the transient detection problem.

One of the most widely applied RNN subtypes is the Long Short Term Memory (LSTM) network [314,315], which utilizes network controllable gates, which, based on learned computation, can control what data is preserved between inferences. Though this is not a permanent memory solution, as LSTMs will eventually lose recall ability from temporally distant inferences, it has the potential to store information across many thousands of inferences, hence the name Long Short-Term Memory. Bidirectional LSTMs, which are used almost exclusively throughout the literature, operate on sequences in both directions, allowing the model to see information both after and before the segment currently being analyzed.

There have been several attempts to apply LSTMs to CBC detection. Schmitt *et al.* [316] performed a comparison of multiple network architectures including bidirectional LSTMs and found that Temporal Convolutional Networks, which utilize a combination of convolutional and recurrent layers outperformed both the CNN employed by George *et al.* [52] and traditional matched filtering approaches. Nigam *et al.* [317] perform a comparison of many different machine learning methods not limited to artificial neural networks or deep learning; whilst the results presented are limited and difficult to compare, they found CNNs and RNNs similarly effective. Chatterjee *et al.* [257] present a model consisting of multiple convolutional and recurrent layers. They also present their model as a method for denoising signals for further analysis. They lack a robust discussion of False Alarm Rates. Lin *et al.* [318] present an interesting method that utilizes Bayesian networks along with LSTMs to incorporate uncertainty into the network. This allows the model to present its result along with variable confidence, though it demonstrates comparable predictive power it has a high false alarm rate, and they suggest that a larger training dataset is required to improve results.

Beveridge *et al.* [319] present a model that is imagined as a post-processing step that consumes the output of a matched filtering search, perhaps unsurprisingly considering their model input, they achieve impressive accuracy scores down to very low FARs, although their method loses many of the benefits typically provided by deep learning searches: computational speed and cost, and is imagined as a way to improve current matched-filtering detection pipelines rather than replace them.

Utilizing a different RNN architecture, Zhang *et al.* [320] demonstrated a Bidirectional Gated Recurrence Unit (GRU) model, in comparison to a CNN and a Fourier Convolutional Neural Network (FCNN). They found the GRU to be the best-performing model and achieved an impressive performance of 89.6% accuracy at a False Alarm Rate (FAR) of 4.88×10^{-4} Hz on a pool of injections with SNRs between 5 and 20.

RNNs can be computationally expensive to train and run compared to other methods like CNNs [286], there have been several papers focused on performance improvements [321,322].

There have also been attempts to apply LSTMs to burst detection problems, including a pattern-matching supernovae search [323], and an unmodeled search using anomaly detection autoencoders [255]. The supernovae detection model by Iess *et al.* [323] demonstrates detection ability across several supernovae template banks but lacks false alarm rate discussion. Moreno *et al.* [255] use recurrent autoencoders for anomaly detection, autoencoders attempt to learn a function to project elements drawn from an input distribution into a dimensionally reduced latent space and then reconstruct the original input element from this reduced latent space. Because the encoder and decoder are trained on a specific distribution, if they are fed an element from outside the distribution, there will be a larger difference between model input and output, indicating an anomaly. In the case of burst detection, there would be no burst events in the training distribution, so if a burst event did come through the model, it would be out of distribution. They found the LSTM performed better than CNN and GRU autoencoders with accuracies of 30.4% for BBH signals, and 11.4% for BNS signals at a FAR of 0.01 Hz.

As a newer architecture, and one that is slightly less obvious to apply to time series data, since it is primarily used in NLP [299], there has been less attention on the application of transformers and attention-based models to transient detection problems. Yan *et al.* [324] use attention layers in a coherence-based detection model. Zhao *et al.* [325] focus on the problem of space-based detection. Jiang *et al.* [258], is the most relevant work, which was published around the time this investigation was being performed. They used a similar model architecture to that which is proposed by Skywarp, combining convolutional and attention layers and achieving results that are superior to purely convolutional models. During hyperparameter tuning, they found that the best performance was achieved by applying a single transformer layer after the convolutional head. One weakness of the paper is that their validation results are calculated using pools of mixed SNR, using the area under the ROC curve as their primary performance metric, this makes efficiency comparisons difficult.

6.3 Skywarp Method

6.3.1 Skywarp Architectures

We have investigated a number of attention-based models and compared their performance to a CNN. We have investigated a fully attention-based model utilizing a dense embedding Figure 6.13, as well as a combined convolutional-attention model utilizing convolutional embedding, Figure 6.14. In response to Jiang *et al.* [258] who found the best performance with a single attention block, a final model, with only one transformer block was created. For the pure CNN model, we adapted the model from Gabbard *et al.* [53], with architecture as illustrated in Figure 6.33. We used this model as a reference CNN model to compare performance, this particular model was chosen as it is used often throughout the literature as a baseline CNN.

When transformers are utilised for Natural Language Processing (NLP) tasks, the input strings of natural language are first tokenised into discrete tokens before those tokens are fed into an embedding layer to convert the discrete tokens into continuous vectors that the network can ingest [310,56]. When adapting the architecture for use on time series data, there are some design decisions that must be taken. Tokenization, although still possible, is no longer required as the input data is initially in a continuous form. However, when deciding how to feed the series into the transformer, there are several options. Although it is possible to feed an attention block with the length of one vector from the input time series, it was found that this naive approach eliminated much of the transformer's potential for element-wise comparison. To resolve this, the method used by the vision transformer can be used; the input data can be segmented into N segments, and then fed into the network. In addition or in place of such a segmentation, an embedding layer can also be employed to increase the dimensionality of the segments.

In the pure attention model, we reshaped the input time series (1.0 s at 8192.0 Hz) into 512 segments each consisting of 16 samples, these segments were then encoded into larger vectors with 128 elements by a single convolutional layer with a filter size of 1. This embedding was performed to allow sufficient size for the positional encoding to be added to each vector. This solution was found after trialling several variations. See Figure 6.13, for more detailed information on the network.

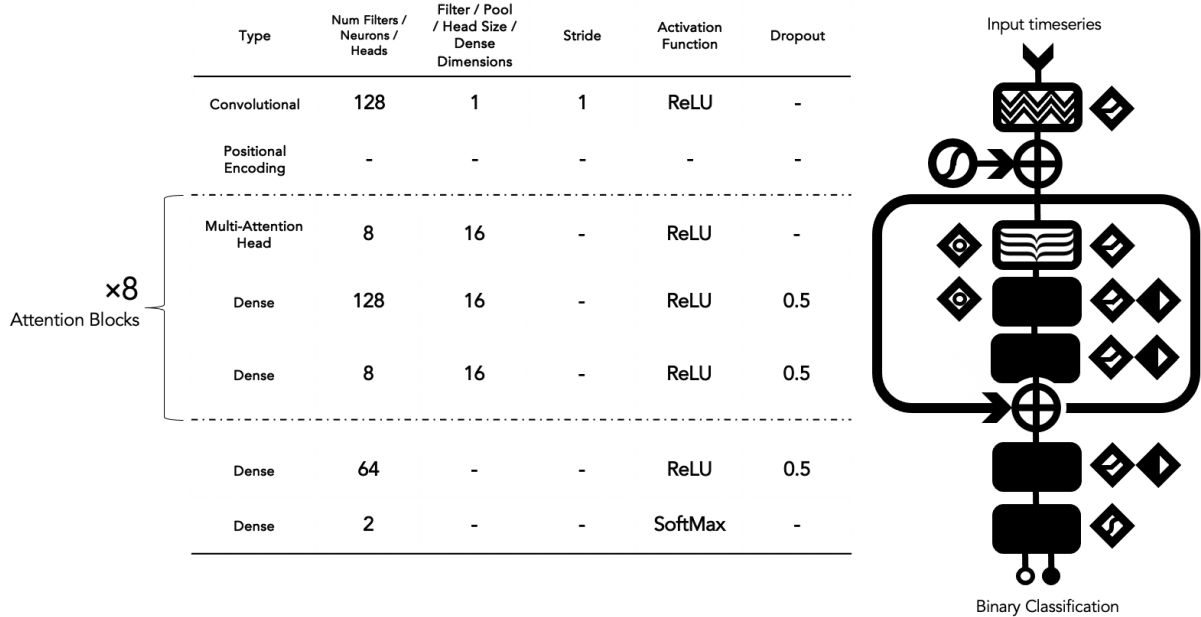


Figure 6.13 | Skywarp pure attention model with dense embedding. This model architecture was used to test the purest application of attention layers to the detection problem by removing any convolutional layers within the model. The single convolutional layer was employed to increase the input dimensionality of the sequence elements from 16 to 128; this was necessary in order to add positional encoding of the appropriate size. Without positional encoding, models were almost impossible to train. The other hyperparameters were obtained using a rough trial-and-error search of the parameter space. Using a more sophisticated hyperparameters search, though a desired goal, proved difficult due to the increased computational requirements of attention-based models over CNNs. (Attention layer's memory usage scales approximately quadratically with input dimensionality, N : $O(N^2)$ [58] similar to dense layers, as opposed to CNNs, which scale linearly with input dimensionality, N , and the number of filters, F , in the layers: $O(N \times F)$ [59], so we encountered so difficulty fitting attention models in memory compared to CNNs.)

During testing, we found that the pure attention model did not perform as well as the CNN model. It was found that the transformer model could much more easily overfit the training data, even with large training datasets. In order to combat this — a combination convolutional-attention model was introduced. This model, described in Figure 6.14, feeds the output of the convolutional layers from the CNN described by Figure 6.33 into the attention blocks described in Figure 6.13, in attempts to gain the benefits of both methods. The single-layer model shares the same architecture as Figure 6.14 but with only a single attention block.

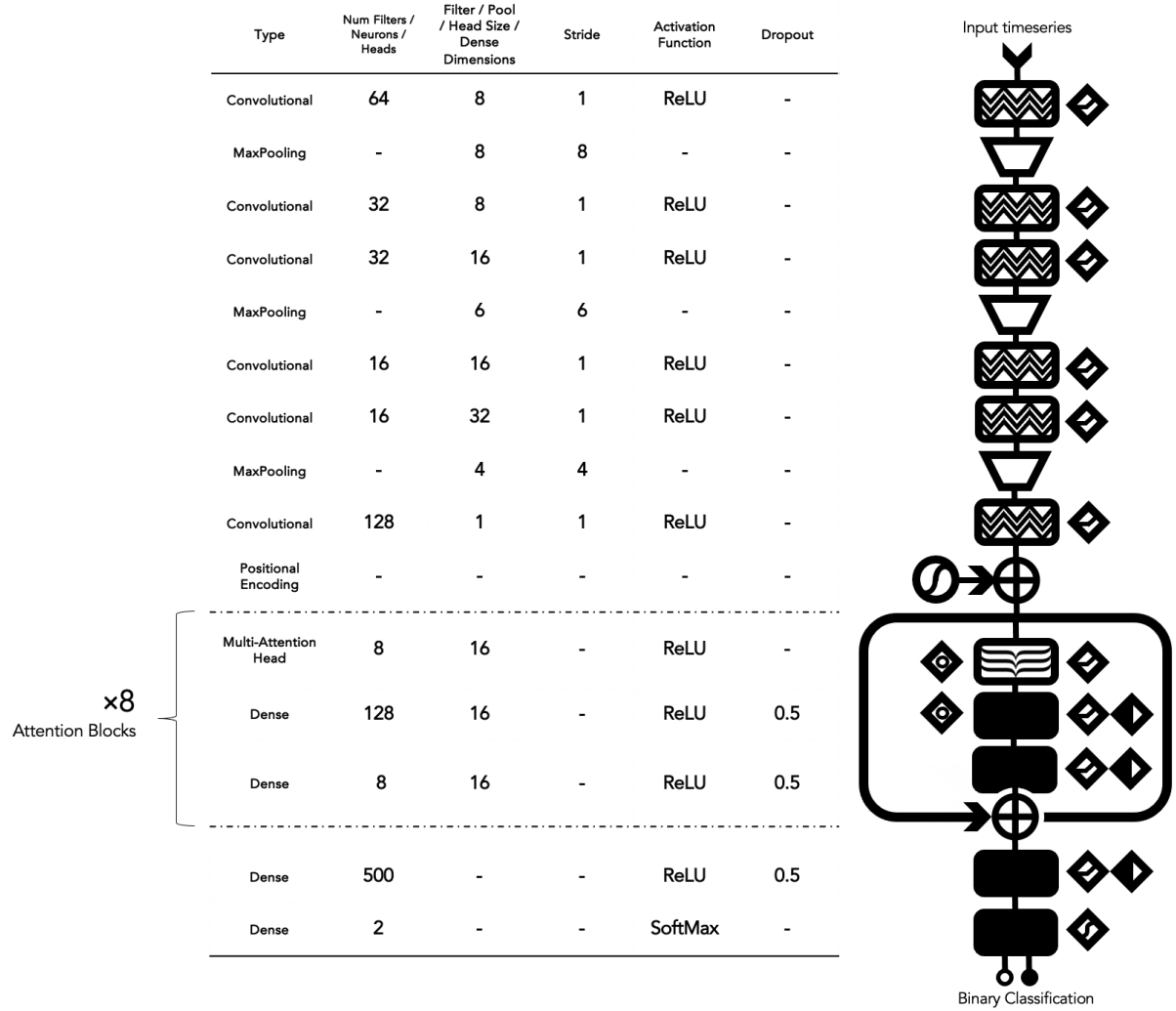


Figure 6.14 | Skywarp convolutional attention with convolutional embedding. This model architecture was employed to test if a convolutional embedding scheme, using the proven CNN architecture of Gabbard *et al.* [53] embeds the input into feature maps which could then be input into attention layers. We have the greatest success with this model variety, again hyperparameters were manually tuned, so it is expected that with a more thorough hyperparameter investigation, a superior model could be found.

6.3.2 Skywarp Training, Testing, and Validation Data

The training dataset was very similar to the datasets used in previous sections. IMRPhenomD waveforms [51] were generated using cuPhenom [48] and injected into real background noise taken from the LIGO Livingston detector from the 3rd LIGO-Virgo joint observing run using GWFlow [60]. The waveforms were generated with masses drawn from a uniform distribution between $5.0 M_{\odot}$ and $95.0 M_{\odot}$ for both companions and between -0.5 and 0.5 for the dimensionless spin component. A difference to note is that these waveforms were scaled with optimal SNRs drawn uniformly between 8.0 and 20.0, rather than between 8.0 and 15.0. There is no specific reason for this difference and were this experiment to be repeated these values would be standardised. Also, note that these experiments were performed with an earlier version of the GWFlow data pipeline [60], so there may be some small inconsistencies, although both cuPhenom and the data acquisition functionality should operate very similarly to more contemporary versions. Another arbitrary difference is that real noise data was collected in batches

of length 3600.0 s rather than 2048.0 s, this was changed after this work due to some stability improvements when working with power-of-two length data.

Hyperparameter	Value
Batch Size	32
Learning Rate	10^{-4}
Optimiser	Adam
Scaling Method	SNR
Minimum SNR	8.0
Maximum SNR	20.0
SNR Distribution	Uniform
Data Acquisition Batch Duration	3600.0 s
Sample Rate	2048.0 Hz
On-source Duration	1.0 s
Off-source Duration	16.0 s
Scale Factor	10^{21}

Table 6.1 | The training and dataset hyperparameters used in Skywarp experiments. This is very similar to the data used for the burst and perceptron experiments seen in Section 4.3. Note that the scale factor here refers to the factor used during the upscaling of the CBC waveforms and real interferometer noise from their extremely small natural dimensions to make them artificial neuron-friendly. This is done both to ensure that the input values work well with the network activation functions and learning rates, which are tuned around values near one, and to reduce precision errors in areas of the code that use 32-bit precision, employed to reduce memory overhead, computational cost, and duration. Data acquisition batch duration is a parameter of the GWFlow data acquisition module. For speed, the GWFlow [60] data acquisition system downloads data in larger segments than is required for each training batch, then randomly samples examples from this larger segment to assemble each training batch. The data acquisition batch duration determines how long this larger batch is. Smaller values will result in a more evenly mixed training data set and a lower overall GPU memory overhead but will be more time-consuming during the training process.

6.3.3 Training Procedure

The training procedure is also very similar to previous experiments, using a learning rate of 10^{-4} , a batch size of 32, and the Adam optimizer as well used industry standards, though it is possible that some of these hyperparameter decisions could be optimized with tuning. The training was performed in epochs with 10^6 rather than 10^5 examples, though the training validation pool remained at 10^4 .

6.4 Skywarp Results

To profile the performance of Skywarp we compare it against a Convolutional Neural Network (CNN) with architecture taken from this early paper by Gabbard *et al.* [53] at different false alarm rates. As is the usual procedure, we first calculate the required model score thresholds to achieve various False Alarm Rates, see Figure 6.15.

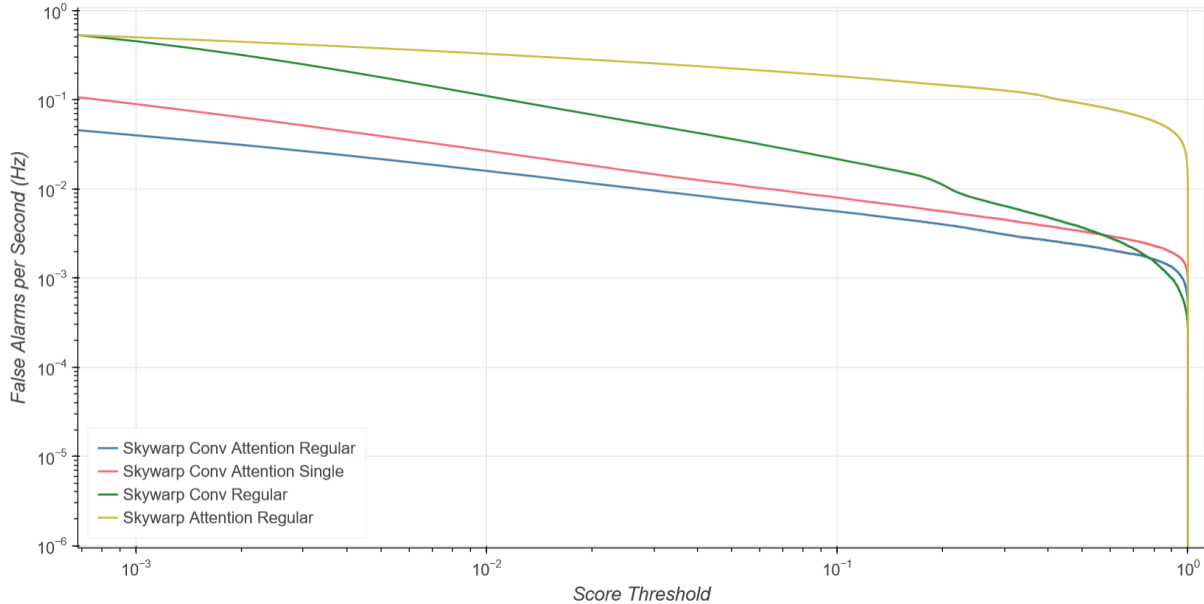


Figure 6.15 | Model False Alarm Rate (FAR) vs score threshold required to achieve that false alarm rate for the three Skywarp models and the recreated CNN model from Gabbard *et al.* [53]. The four models display notably different FAR curve profiles, though it is important to note that a lower curve on this plot will not necessarily translate to model performance as it says nothing about the True Positive Rate, a classifier that labels everything as noise, for example, would be entirely flat on this plot, but would remain useless. Still, there is a notable difference between the curves, the pure attention model, consistently requires a much higher score threshold than the other three models, which will be seen in its poor efficiency performance.

When we examine model efficiency curves in Figure 6.16, with key results extracted into Table 6.2 for easier reading of the small differences, the most evident takeaway is that the pure attention model utilizing dense embedding has by far the weakest performance, we can easily discount this method as ineffectual. It is not clear, however, whether this poor performance is due to the choice of embedding, or because attention layers alone are not adequate for gravitational-wave classification. We suggest that it is the former since there have been very successful image [326] and audio attention [327] models in other domains that do not utilize a convolutional head, and because, in theory, an attention layer is general enough to mimic any convolution. It is theorized that either the dense layer dimensionality increase that is performed to upscale the chunks enough to add positional encoding, is not adequate to convert the segments into a digestible feature space, or that the chunking is ineffectual because it splits the data without knowledge of the signal offset, creating sequence vectors which do not have consistent signal elements.

The other three models perform much more consistently. There is no clear advantage at a FAR of 0.1 Hz, or 0.01 Hz, although the attention-convolution hybrids consistently score higher, with the larger eight-layer model's advantage increasing with lower FARs. In many cases, this advantage is small however ranging from one to five percent. At 0.001 Hz, the lowest power-of-ten FAR where all models still have classification ability, it appears that the combined convolutional attention network has a more notable

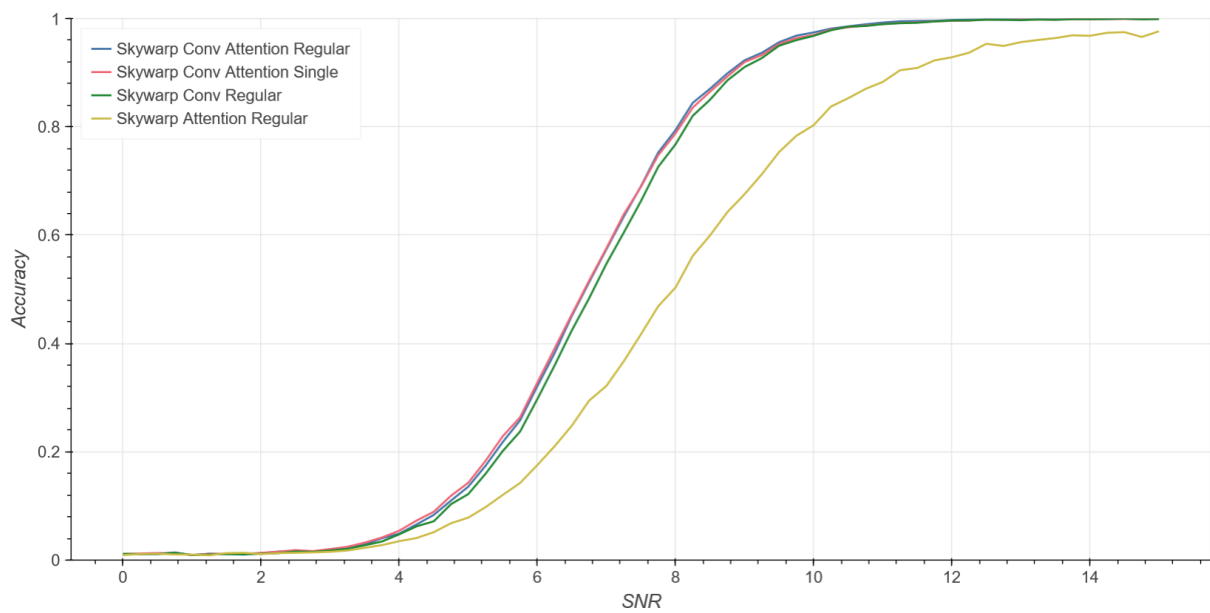
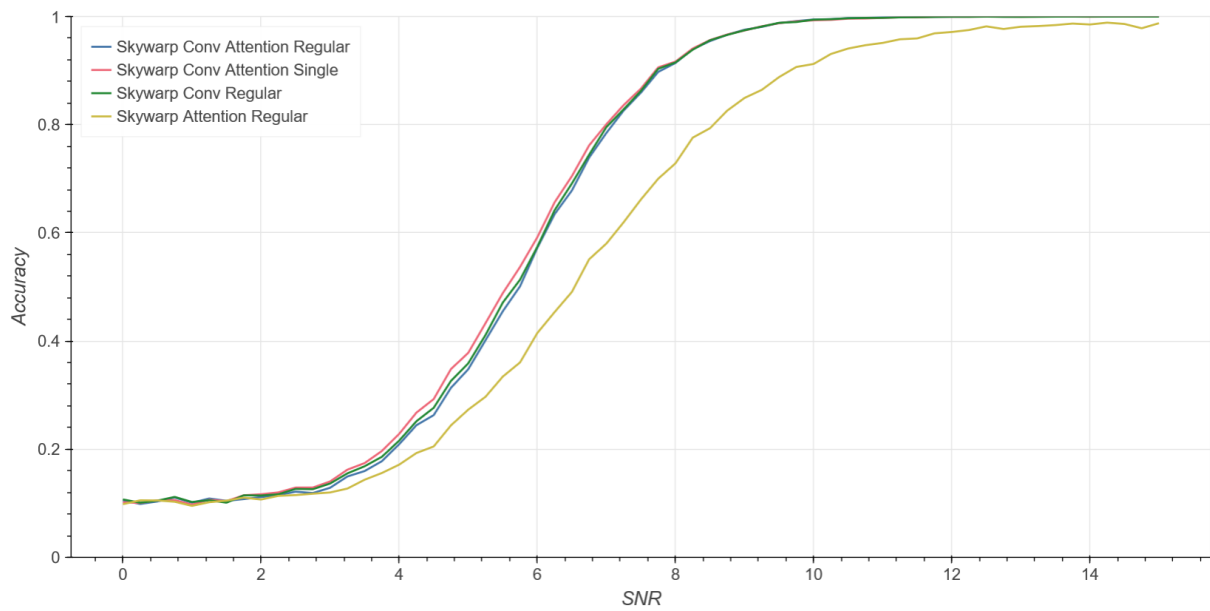
advantage over the other two competitive networks. However, this gap remains small enough to be somewhat unconvincing, and perhaps down to statistical variances in model training, which is not a perfect method and can fluctuate depending on the dataset order and parameter initialization. What can be said is that the advantage seen by the single attention layer over the larger eight-layer model that was suggested by Jiang *et al.* [258], was presumably down to their use of the area under ROC curves as performance metrics, since this metric benefits from higher efficiencies at lower FARs. At the lowest FAR presented 0.0001 Hz, both the pure attention network and the single layer attention model ceased to have any classification ability, since their score thresholds have reached one. At this FAR the combined convolutional-attention model appears to greatly outperform the CNN. However, this is operating very close to the 32-bit precision limit, (threshold > 0.999), which would probably be uncomfortable for use in a transient search, as small statistical variations could have a large effect on model performance. The efficiencies are also quite low at this threshold, perhaps lower than one would wish to be to remain competitive with other detection methods.

Model	FAR (Hz)	Accuracy 6	Accuracy 8	Accuracy 10
Gabbard <i>et al.</i>	10^{-1}	57.4	91.5	99.4
Skywarp Pure Attention	10^{-1}	41.5	72.9	91.2
Skywarp Conv Attention Single	10^{-1}	59.2	91.7	99.3
Skywarp Conv Attention	10^{-1}	57.2	91.4	99.4
Gabbard <i>et al.</i>	10^{-2}	29.6	76.6	96.8
Skywarp Pure Attention	10^{-2}	17.3	50.0	80.2
Skywarp Conv Attention Single	10^{-2}	32.5	78.6	96.9
Skywarp Conv Attention	10^{-2}	31.9	79.2	97.4
Gabbard <i>et al.</i>	10^{-3}	13.5	57.6	91.2
Skywarp Pure Attention	10^{-3}	4.4	22.0	51.8
Skywarp Conv Attention Single	10^{-3}	13.3	56.7	90.2
Skywarp Conv Attention	10^{-3}	16.9	63.3	93.0
Gabbard <i>et al.</i>	10^{-4}	0.4	8.7	46.0
Skywarp Pure Attention	10^{-4}	-	-	-
Skywarp Conv Attention Single	10^{-4}	-	-	-

Skywarp Conv Attention	10^{-4}	5.4	38.4	81.2
------------------------	-----------	-----	------	------

Table 6.2 | Accuracy results at different optimal SNRs from the four models tested at different FAR thresholds. Scores in red are the highest results for that SNR threshold at that FAR, in the one case where there is a tie, both scores are highlighted. With a very marginal lead, the single-layer attention-convolution hybrid appears to be the best model at a FAR of 10^{-1} Hz, only losing out to the CNN and deeper hybrid model by 0.1 percentage points at the highest SNR of 10. This is not a particularly useful FAR range, however, and as we decrease the FAR, the deeper attention layer seems to be victorious, but again the lead is quite small. This appears to show that the convolutional-attention model may have a slight advantage at lower FARs. At the lowest FAR presented, 10^{-4} Hz, the required score threshold for both convolutional-attention hybrid with the single attention layer, and the pure attention model, have reached one, and therefore lack any classification ability. For the remaining models, the required model score threshold is greater than 0.999, and although at this FAR the deep attention hybrid appears to be the clear winner, it is unclear whether victory at such a high score threshold is meaningful, or simply due to statistical variance in model training and the validation dataset. Although it should be noted that the lead is similar in all SNR bins, which were created independently, so if it is statistical variance, it is suggested that it probably originates in the training procedure.

It should be reiterated that these are single-detector results, in a real search pipeline. The FAR would have a significant advantage. Assuming a detection pipeline with no overlap, 1.0 s duration, and two detectors, the network FAR is given by $\text{FAR}_1 \times \text{FAR}_2 \times t$, we assume that $\text{FAR}_1 = \text{FAR}_2$ and our $t = 1.0\text{s}$ and since we have two detectors they can overlap in either direction, adding a factor of 2, therefore our network FAR is given by 2.0 times $\text{FAR}^2 \times 1\text{s}$ which turns the presented FARs from 10^{-1} Hz, 10^{-2} Hz, 10^{-3} Hz, and 10^{-4} Hz, into 2×10^{-2} Hz, 2×10^{-4} Hz, 2×10^{-6} Hz, and 2×10^{-8} Hz respectively. The latter two of which begin to approach the regime of other detection pipelines; the threshold for significant burst detections used by the LVK collaboration is 3.9×10^{-9} Hz (once per month) for CBCs and 3.2×10^{-8} Hz (once per year) for bursts [328]. However, in practice, it is expected that some overlap would be employed to reduce the change of a signal falling at a boundary. As well as efficiency curves, ROCs are also presented for comparison with other results, Figure 6.17. Due to the nature of the current calculation of the ROC curves, their maximum FAR resolution is considerably lower than what is presented in Figure 6.16, due to lower numbers of validation examples, so these plots cannot be as effectively used to compare performance at different FARs, but can give a general impression of model performance at higher FARs.



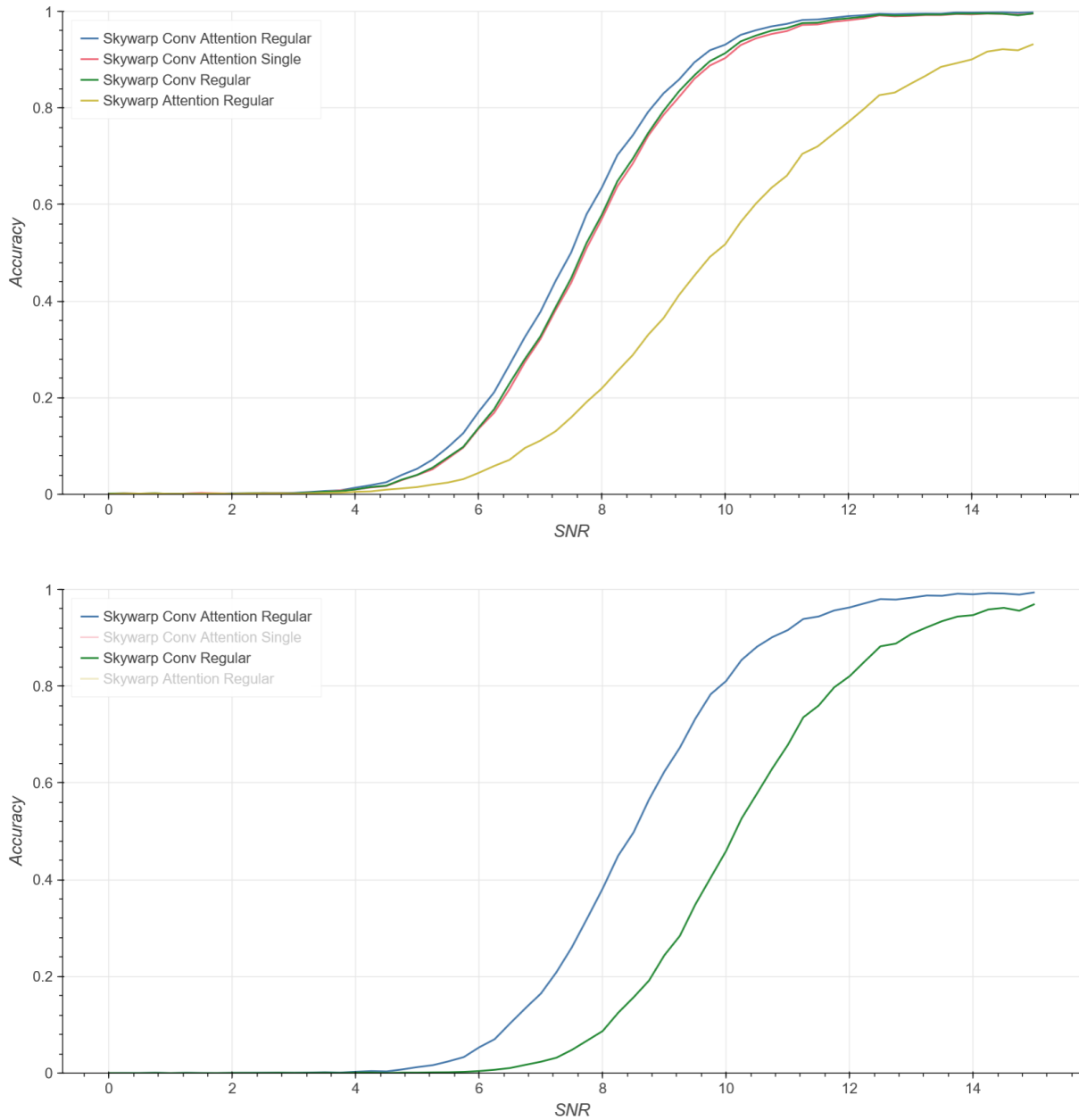
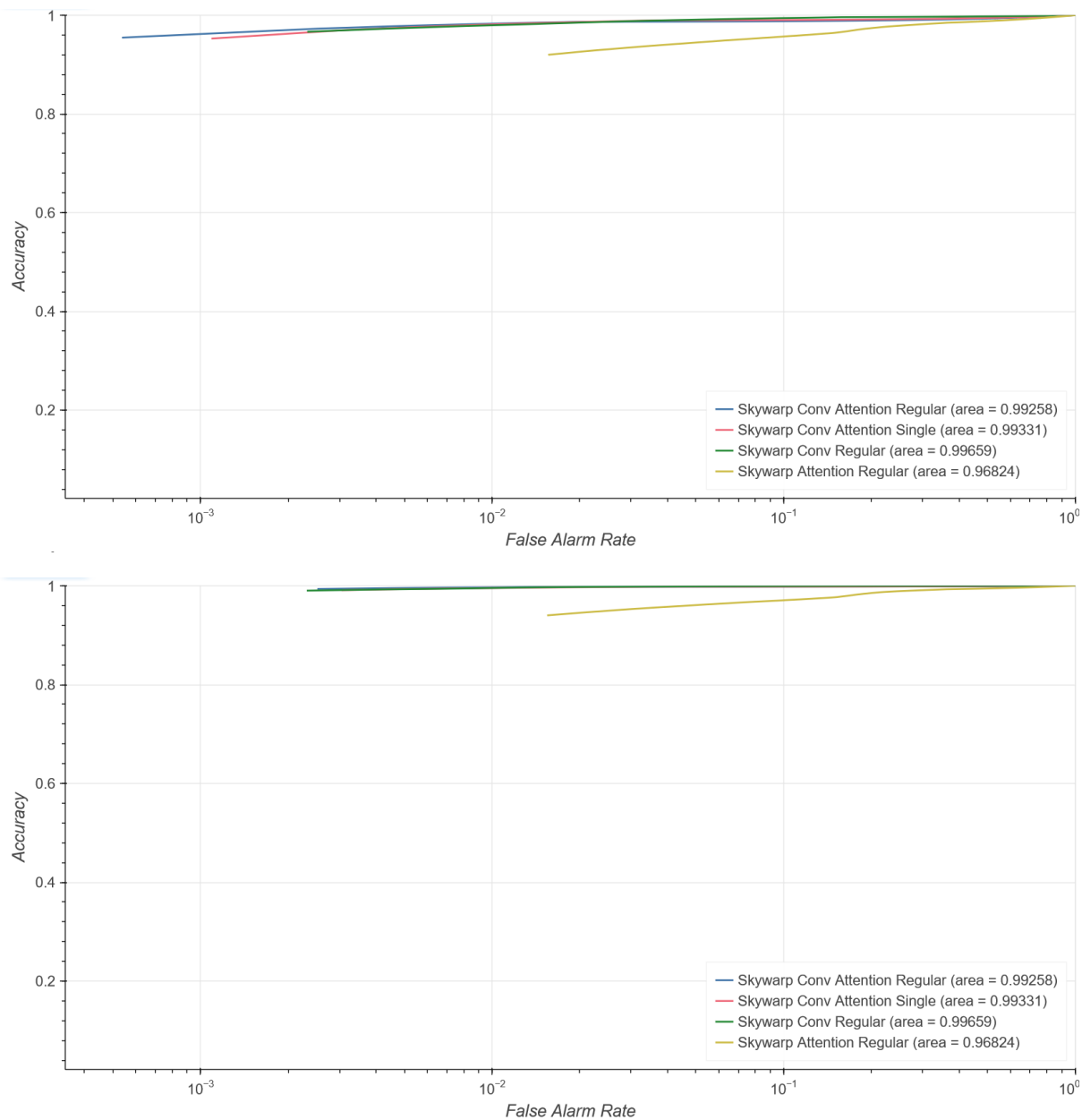
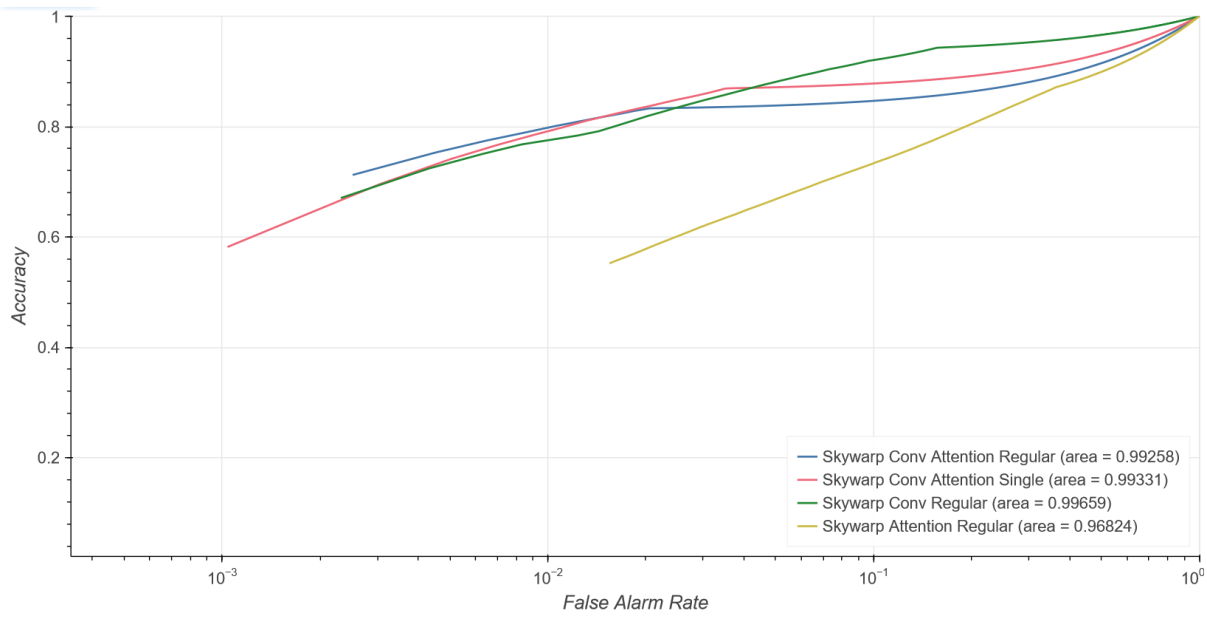
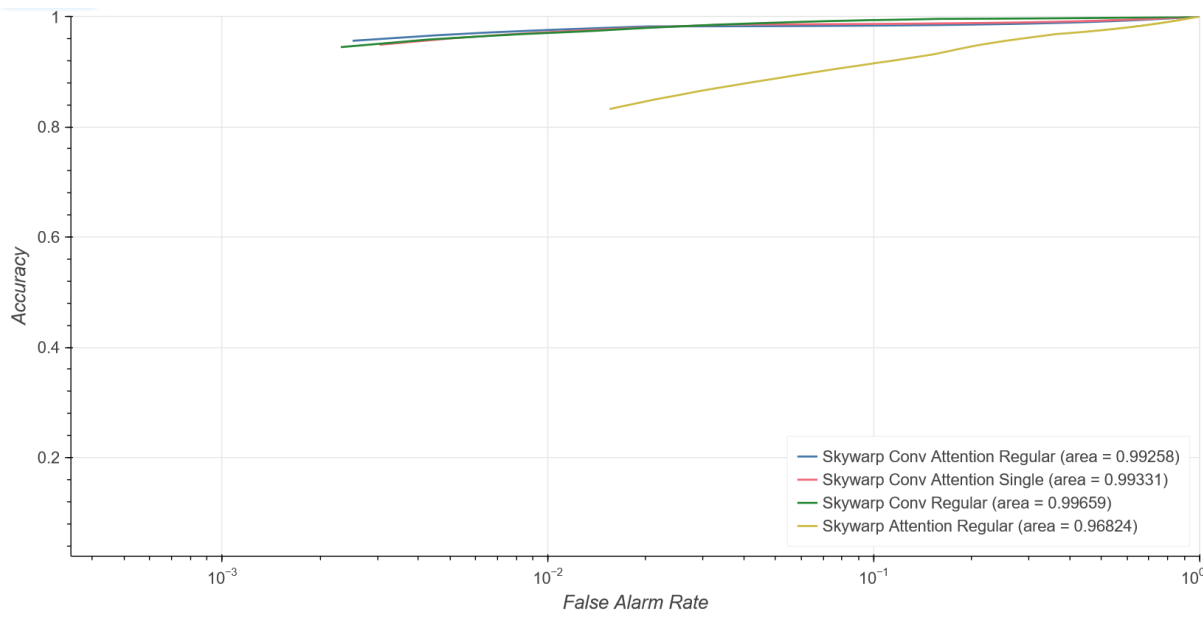


Figure 6.16 | Efficiency curves of the Skywarp models and the recreated model from Gabbard *et al.* at different False Alarm Rates. For each of the 4 models trained, 61 efficiency tests are performed at evenly spaced optimal SNR values between 0 and 15. For each test, 16384 examples with signals of the relevant SNR are examined by the model. The most evident distinction is between the pure attention model utilizing dense embedding, and the other models, which are either purely convolutional or have a convolutional head. There is considerably less distinction between the other three models, which appear statistically indistinguishable at FARs of 10^{-1} Hz and 10^{-2} Hz. A slight advantage may arise between the combined attention-convolution model and the other two competitive models at the 10^{-3} Hz, which is perhaps the strongest evidence of an advantage, but this small difference is still too small to draw any definite conclusions of improved efficacy. At 10^{-4} Hz, the difference is much more apparent, but we are approaching 32-bit precision limits, so it is unclear exactly how seriously we should view these results. The efficiencies at this low FAR are also considerably reduced, reducing the appeal of the use of these models at this FAR. *First:* Efficiency curves at a FAR of 10^{-1} Hz. *Second:* Efficiency curves at a FAR of 10^{-2} Hz. *Third:* Efficiency curves at a FAR of 10^{-3} Hz. *Fourth:* Efficiency curves at a FAR of 10^{-4} Hz.





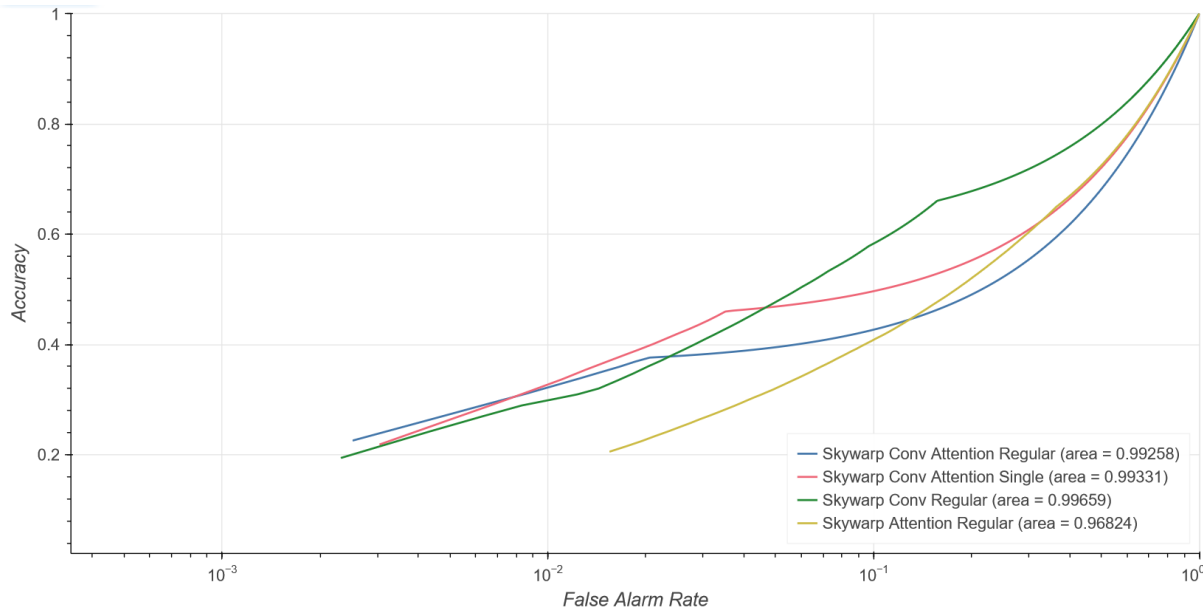


Figure 6.17 | Receiver Operator Curves (ROCs) generated for each of the four Skywarp models for a variety of different SNR pools. The story demonstrated by these plots is very similar to what is shown by the efficiency curves, Figure 6.16, albeit with less granularity. The pure attention model performs considerably worse than the other three models, which are nearly indistinguishable. The pure convolution model has a slightly higher area under the ROC curve, primarily boosted by higher efficiencies at higher false alarm rates and the combined convolutional-attention network achieves higher accuracies at the lower FAR ranges, with the single-layer convolutional-attention network somewhere between the two. *First:* ROC generated with a pool of signals with optimal SNRs drawn uniformly between 8 to 20. *Second:* ROC generated with a pool of signals with optimal SNRs of 12. *Third:* ROC generated with a pool of signals with optimal SNRs of 10. *Fourth:* ROC generated with a pool of signals with optimal SNRs of 8. *Fifth:* ROC generated with a pool of signals optimal SNRs of 6.

6.5 Discussion

The use of attention layers in CBC detection models shows promise. Although these results fail to prove a decisive advantage, they demonstrate that even with rudimentary parameter optimization, a model can be generated to beat a CNN from the literature that is often used as a standard. One firm conclusion that can be drawn is that the use of a pure attention model, with the dense embedding presented, performs significantly worse than the other methods presented.

Although it does not seem like there is a very significant advantage to using the Skywarp transformer architecture presented over the more traditional CNN model, it does appear that attention layers are better adapted for work in low FAR regimes. A more complete hyperparameter optimization procedure, and a more thorough investigation of signal embedding methods, as well as experiments in multi-detector inputs utilizing inter-detector cross attention, may yield more significant performance benefits.

7 CrossWave: Cross-detector Attention for the Detection and Parameterisation of Overlapping Gravitational-Wave Compact Binary Coalescences

Thus far, we have focused our attention on perhaps one of the simpler problems in gravitational-wave data analysis, transient detection; the fact remains, that many, more complex, tasks are yet to be satisfactorily solved. One of the largest and most intriguing of these is Parameter Estimation (PE) [329]. Whilst detection merely identifies the presence of a signal, and, in a modeled search, tells us the type of signal we have detected, there is invariably other scientifically valuable information that can be extracted from a signal. During PE, we attempt to predict, with error margins, several parameters about a gravitational-wave-producing system. Typically this is a CBC system, although PE could also be performed on burst events if they were to be detected [330]. Fortunately, CBCs can be described quite well in as few as 14 parameters that contain information both about the internal state of a CBC system, known as intrinsic parameters, and its relation to us as observers, known as extrinsic parameters [331]. Care should be taken to distinguish between the parameters being extracted by PE, and the parameters of a neural network model, as they are unrelated.

Without further analysis, detection alone is useful for little more than rudimentary population analysis; PE, therefore, is a crucial part of gravitation-wave data science [332]. Extrinsic parameters, like the source distance and sky location, aid in population studies and multimessenger analysis [333], and intrinsic parameters such as the companion mass and spin properties can help unveil information about the underlying physics of sources themselves [25,197,334], as well as their formation channels [222].

This section does not focus on a general PE method for either CBC or burst signals. Those have both been well investigated and although there is arguably a greater room for improvement and a larger need for innovation on these fronts than in detection alone it was not within the scope of this work. In this section, we present an analysis of a much smaller subproblem within PE; the detection and isolation, of overlapping signals contained within a single stretch of interferometer data. Because of the somewhat limited nature of the problem, it has not been studied as thoroughly as any of the other problems we have yet examined, which, in some ways, gives us more space for exploration, and an increased potential for novel scientific output.

7.1 Frequency of Overlapping Compact Binary Coalescences (CBCs)

Significant improvements to our gravitational wave detection capability are anticipated within the next few decades, with improvements to existing detectors such as LIGO-Voyager [335], as well as future 3rd and 4th generation space and ground-based detectors such as the Einstein Telescope (ET) [73], Cosmic Explorer (CE) [74], and the space-based Laser Interferometer Space Antenna (LISA) [75]. Whilst the current detection rate ($1\sim 2 \text{ week}^{-1}$ [BBHs]) and average detectable duration ($\sim 7\text{s}$ [BBHs]) of Compact Binary Coalescences (CBCs) is too low for any real concern about the possibility of overlapping detections [336], estimated detection rates ($50\sim 300 \text{ week}^{-1}$ [BBHs]) and durations ($40\sim 20000\text{s}$ [BBHs]) for future networks will render such events a significant percentage of detections [336]. See Table 7.1 for a more detailed breakdown of overlapping event estimates. Contemporary detection and PE pipelines do not currently have any capabilities to deal with overlapping signals — and although, in many cases, detection would still be achieved [336,62], PE would likely be at least somewhat compromised by the presence of the overlap, especially if more detailed information about higher modes and spins [336] are science goals.

Config- uration	Range (Mpc)	Cut Off (Hz)	Mean Visible	P(Overlap) (year ⁻¹)	N_{events} (year ⁻¹)	N_{overlaps} (year ⁻¹)

			Dura-tion (s)			
aLIGO: O3	611.0	20	6.735	$3.9_{-1.3}^{+1.9} \times 10^{-6}$	$42.0_{-13.0}^{+21.0}$	$0.0_{-0.0}^{+0.0}$
aLIGO: O4	842.5	20	6.735	$1.0_{-0.3}^{+0.5} \times 10^{-5}$	$100.0_{-29.0}^{+56.0}$	$0.0_{-0.0}^{+0.0}$
aLIGO: Design	882.9	20	6.735	$1.2_{-0.4}^{+0.6} \times 10^{-5}$	$120.0_{-38.0}^{+60.0}$	$0.0_{-0.0}^{+0.0}$
LIGO-Voyager	2684.0	10	43.11	$2.3_{-0.8}^{+1.2} \times 10^{-3}$	$2700.0_{-38.0}^{+60.0}$	$6.3_{-3.4}^{+7.7}$
Einstein Tele-scope	4961.0	1	19830.0	$1.0_{-0.0}^{+0.0}$	$15000.0_{-5000.0}^{+7100.0}$	$15000.0_{-5000.0}^{+7100.0}$

Table 7.1 | Estimated overlap rates of BBH signals in current and future detectors, sourced from Relton [61] and Relton and Raymond [62]. Presented error values are 90% credible intervals. Note that these results, including past observing runs are estimates rather than real values, and are meant only as an illustration of the probable difference in overlap rates between current and future detector configurations. The number of overlapping signals, N_{overlap} , anticipated within one year is determined by the number of detections, N_{events} , and the visible duration of those detections, which are, in turn, affected by the detection range and lower frequency cut off the detector configuration in question. We can see that although with the current and previous detector configurations an overlapping event is extremely unlikely, it will increase with LIGO-Voyager to the point where we would expect $6.3_{-3.4}^{+7.7}$ overlapping signals per year of observing time, and further increase with the Einstein Telescope to the point where we would not expect any event to be detected without components of other signals also present in the detector. Similar overlaps are expected for LISA and Cosmic Explorer.

7.2 Detection and Parameter Estimation (PE) of Overlapping Compact Binary Coalescences (CBCs)

Two studies examined the rate at which overlaps were likely to occur in different detector configurations along with the effect of overlapping signals on PE. Samajdar *et al.* [336], determined that during an observing period of the future Einstein Telescope, the typical BNS signal will have tens of overlapping BBH signals and that there will be tens of thousands of signals per year that have merger times within a few seconds of each other. They found that for the most part, this had little effect on parameter recovery except in cases where a short BBH or quiet BNS overlapped with a louder BNS signal. Relton and Raymond [62] performed a similar study and produced the overlap estimates seen in Table 7.1. They found that PE bias was minimal for the larger of the two signals when the merger time separation was greater than 0.1 s and when the SNR of the louder signal was more than three times that of the quieter signal. This bias was also smaller when the two signals occupied different frequency regions, and when the louder of the two signals appeared first in the detector stream. Despite this, they found evidence of PE bias even when the smaller signal was below the detectable SNR threshold. They found that overlapping signals can mimic the effects of procession; it will be important to be able to distinguish the two when detailed procession analysis becomes possible.

Much of the work in this area focuses on performing PE with overlapping signals, and there has not been as much attention to simply distinguishing pairs of mergers from single mergers. Relton *et al.* [195] measured the detection performance of both a modelled (PyCBC) [50] and unmodeled (coherent WaveBurst [cWB]) [22] search pipeline when searching for overlapping signals. They determined that both pipelines were able to recover signals with minimal efficiency losses (< 1%) although they noted that the clustering algorithm used in both pipelines was inadequate to separate the two events. They concluded that adjustments to clustering could be made to both pipelines in order to return both events given a sufficient merger time separation. Using these altered pipelines it would then be possible to separate the data into two regions, which could be used for independent PE.

Once an overlapping single has been identified, the next step is to deal with PE. Although in many cases, existing PE techniques may provide results with little bias [336,62], there are some situations in which this may not be the case. If the PE method can be improved in order to reduce that bias, it is useful so long as it does not result in a reduction of PE accuracy that is greater than the bias introduced by the overlapping signal.

There are four types of methods we can apply to alleviate the issues with PE [61].

1. **Global-fit** methods attempt to fit both signals simultaneously. There have been several studies investigating this method by Antonelli *et al.* [337], which attempts to apply it to both Einstein Telescope and LISA data, [338] which compares this method to hierarchical subtraction, and several studies focusing solely on LISA data [339–341]. This has the advantage of being somewhat a natural extension of existing methods, with no special implementation other than an increased parameter count, but that can also be its greatest disadvantage. The total number of parameters can quickly become large when an overlap is considered, especially if multiple overlaps are present which will be expected to occur in ET and LISA data.
2. **Local-fit** methods attempt to fit each signal independently and correct for the differences. The original proposal by Antonelli *et al.* [337] suggests using local fits to supplement a global-fit approach. This will reduce the number of parameters that you require your method to fit, but its efficacy is highly dependent on the proficiency of your correction method.
3. **Hierarchical Subtraction** methods suggest first fitting to the most evident signal, then subtracting the signal inferred from your original fit and repeating this process for all anticipated signals [342,338]. This method would be effective at subtracting multiple sets of parameters for overlapping signals, assuming that the overlap does not cause bias in the initial fit, which the previously mentioned studies have shown is not always a correct assumption [336,62].
4. Finally, and most relevantly, **machine learning** methods can be employed as a global fit technique to try and extract parameters from overlapping signals. They come with all the usual advantages, (inference speed, flexibility, computational backloading) and disadvantages (lack of interpretability, unpredictable failure modes). Langendorff *et al.* [343] attempt to use normalizing flows to output estimations for parameters.

Most of the aforementioned methods benefit from having prior knowledge about each of the pairs of signals, especially the merger times of each signal. As well as acting as a method to distinguish between overlapping and lone signals, CrossWave was envisioned as a method to extract the merger times of each of the binaries in order to assist further PE techniques. Crosswave was able to achieve this and also demonstrated some more general, but limited PE abilities.

7.3 CrossWave Method

We introduce Overlapnet and CrossWave, two neural network models for the identification and PE of overlapping CBC signals. This section describes two complementary models, Overlapnet for the

separation of the overlapping case from the non-overlapping case and CrossWave as a PE follow-up to extract the merger times of the overlapping signals in order to allow other PE methods to be performed. Overlapnet can differentiate between overlapping signals and lone signals with efficiencies matching that of more conventional matched filtering techniques but with considerably lower inference times and computational costs. CrossWave can extract the merger times of the two overlapping CBCs with an average error of less than 0.1 s. We suggest these two models or similar architectures may be used to augment existing CBC detection and PE infrastructure, either as a complementary confirmation of the presence of overlap or to extract the merger times of each signal in order to use other PE techniques on the separated parts of the signals.

Since the CrossWave project was an exploratory investigation rather than an attempt to improve the results of a preexisting machine learning method, it has a different structure to the Skywarp project. Initially, we applied architecture from the literature, again taking Gabbard *et al.* [53], with architecture illustrated here Figure 7.33. This worked effectively for the differentiation of overlapping and lone signals. We named this simpler model OverlapNet. However, when attempting to extract the signal merger times from the data, we found this model to be inadequate, therefore, we utilized the attention methods described in Section 6, along with insights gained throughout other projects to construct a more complex deep network for the task, seen in Figure 7.9. We name this network CrossWave, as it utilises cross attention between a pair of detectors. It is hoped that this architecture can go on to be used in other problems, as nothing in its architecture, other than its output features, have been purpose-designed for the overlapping waveform case.

7.3.1 Crosswave Training, Testing, and Validation Data

The dataset utilized in this section differs from previous sections, in that it was not generated using the GWFlow data pipeline. Since this was part of a PE investigation, the exact morphology of the waveforms injected into the signal is crucial to validating performance. The cuPhenom IMRPhenomD waveform generator that was developed for rapid waveform generation on the GPU has a relatively high degree of mismatch (5%) with IMRPhenomD signals [51] generated with LALSimulation [214] in some areas of parameter space. This is primarily thought to be caused by cuPhenom's [48] reduced precision (32-bit in most areas rather than 64-bit) and the lack of implementation of several post-Fourier conditioning steps. Whilst this mismatch was deemed to be mostly adequate for detection searches, especially for comparison of methods, we considered it inadequate for PE tasks. IMRPhenomD is also an older approximant, which does not take into consideration the latest improvements to waveform approximation including several physical phenomena, such as higher modes. Whilst there is currently no one approximant that can generate waveforms that include all physical effects, we opted to use IMRPhenomTPHM [213], which is a Time-Domain approximant that includes the physics of precession, which allows for studies of Higher Modes.

A static dataset was created using BBH waveforms generated using LALSimulation [214] and injected into Gaussian noise coloured by the LIGO Hanford and LIGO Livingston aLIGO design specifications [344] using the technique described in Section 4.2.2 but not with the GWFlow [60] pipeline. No BNS signals were considered. We used a 16 s on-source duration, to allow more space for different signal start times and to examine the effects of distant signal overlap on PE. We used a sample rate of 1024 Hz, as this was considered adequate to contain the vast majority of relevant frequency content for the CBCs examined.

Unlike in the detection case, wherein our training distribution consisted of some examples with obfuscated signals and some consisting of pure noise, we assume that a detection has already been made by a detection pipeline, so our examples always contain signal content of some kind. This assumption was made to simplify the task to its minimal possible case. Our generated waveform bank consisted of 2×10^5 IMRPhenomTPHM approximants. From that template bank, we constructed 2×10^5 examples

of lone signals injected into obfuscated noise and 2×10^5 examples of pairs of signals injected into obfuscated noise, totaling 4×10^5 training examples. In the latter case, each waveform was unique to a single pair, generating 10^5 pairs, but each pair was injected into two different noise realizations in order to generate identical numbers of lone and paired templates. The use of the same waveforms in both the single case and the pairs was a conscious decision that was made in order to attempt to reduce the chance of the network overfitting to any particular signal morphologies that it learned to associate specifically with lone signals or pairs of signals.

The waveforms were generated with a wide parameter range drawn uniformly from across parameter space. The primary component of each waveform was generated with masses between $10.0 M_\odot$ and $70.0 M_\odot$, this is notably inconsistent with our previous studies, but was reduced to reduce task complexity and because this still covers most of the range that is of interest to PE studies. This also ensured that their visual duration, (starting at 20.0 Hz, which is both the whitening low-pass filter and around the limit that the detector design curve starts to make detection impossible), remained well contained within the 16 s on-source duration. Also unlike in our previous detection studies, the mass ratio was constrained between 0.1 and 1. Since the approximants were generated in an alternate method utilising luminosity distance as the scaling factor rather than SNR, the SNRs are not uniformly distributed, however, the Network SNR of any signal is not less than 5 or greater than 100. For each injection, luminosity distance in MPc was drawn from a power law distribution with base two scaled by 145, with a minimum distance of 5.0 MPc, this luminosity distance range was generated by a trial and error approach to achieve the desired SNR distribution. An overview of the parameters used to train both the CrossWave and Overlapnet models is shown in Table 7.2.

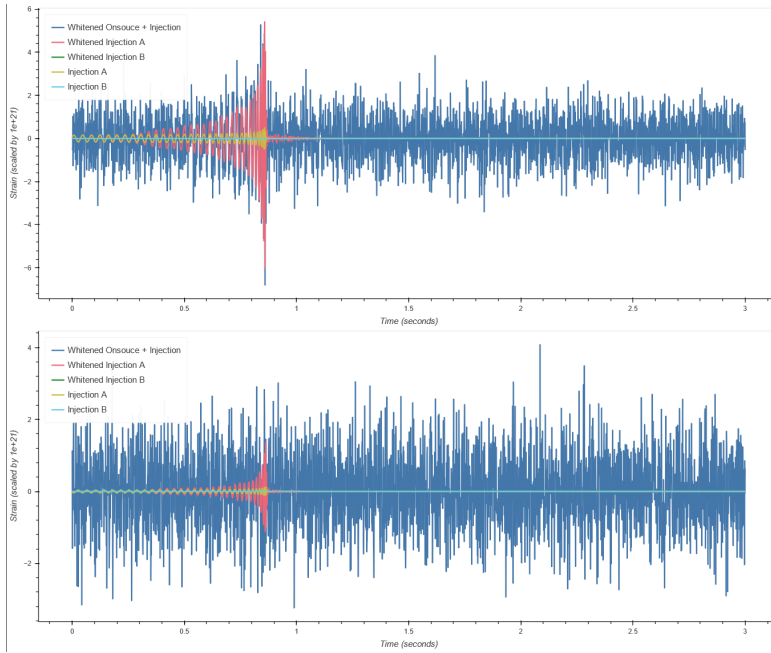
A validation dataset was also generated with independent signals and background noise, with 2×10^4 singles and 2×10^4 pairs generated similarly to the training data but with different random seeds, totalling 4×10^4 validation examples.

Hyperparameter	Value
Batch Size	32
Learning Rate	10^{-4}
Optimiser	Adam
Scaling Method	Luminosity Distance
Min Luminosity Distance	5.0
Max Luminosity Distance	N/A
Luminosity Distance Distribution	(Power-Law (base 2) \times 145) + 5 MPc
Data Acquisition Batch Duration	N/A
Sample Rate	1024.0 Hz
On-source Duration	16.0 s
Off-source Duration	N/A

Scale Factor	10^{21}
--------------	-----------

Table 7.2 | The training and dataset hyperparameters used in CrossWavea and Overlapnet experiments.

In the case of the pairs of injections, the two waveforms are injected so that their merger times never have a separation exceeding 2 s. “Signal A” is defined as the signal whose merger arrives second at the Earth’s centre, whereas “Signal B” is always defined as the signal whose merger time arrives first. This allows the model to differentiate between the two signals for the PE tasks. When only one waveform is present, that waveform is labelled “Signal A”. It is possible, if the merger arrival time separation between signal A and signal B is low enough, that the order of A and B in the Hanford and Livingston detectors may be switched, if this is the case it would only happen in very few cases since the vast majority of training and validation examples with pairs of signals have merger time separations larger than the light travel time between detectors (0.01 s).



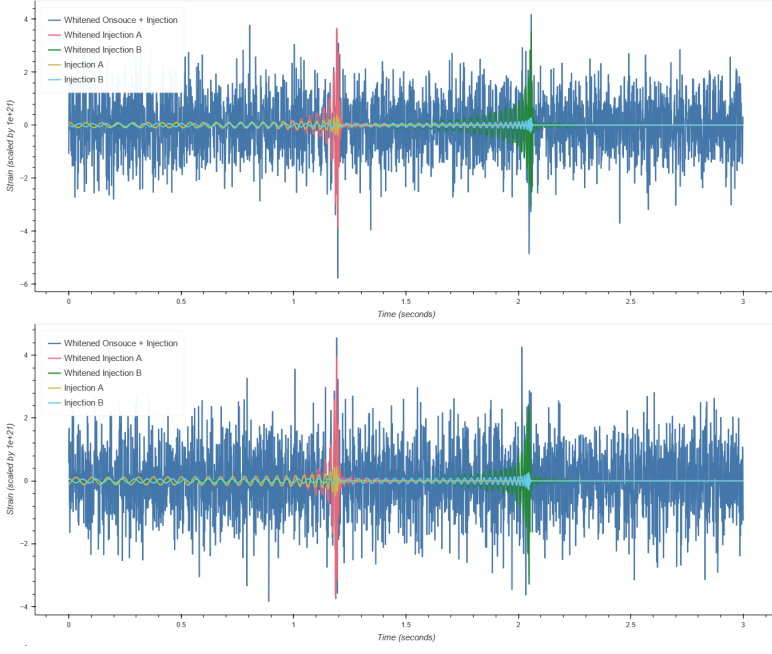


Figure 7.1 | Two illustrative examples of the example used to train CrossWave, the upper demonstrates the single signal case, the lower the multiple signal case. Since the real data used to train CrossWave was unwhitened, it is not easy to parse by eye. Thus, as an illustrative example, these two examples are shown in whitened data generated using cuPhenom and GWFlow. The example duration has also been cropped from 16 s to 5 s, since the merger times never have a separation greater than 2 s this is ample as an example. Both examples show time series from both detectors, simulating LIGO Livingstone and LIGO Hanford. *Upper:* Single waveform injected into noise drawn from the two LIGO detectors. *Lower:* A pair of waveforms injected into noise drawn from the two LIGO detectors. The waveforms are always injected with merger times less than 2 s distant.

7.3.1.1 A note on Whitening

Interestingly, since the data was generated independently from GWFlow, it was not whitened prior to model injection. Since this is not a comparison to other machine learning methods that use whitening, this is not particularly an issue, but it also can't tell us about the efficacy we have lost/gained due to the lack of whitening. Since this investigation does have positive results, this could potentially be an area for future experimentation, forgoing the whitening step before ingestion by a model would streamline a lot of the problems faced by low-latency machine learning pipelines. It should be remembered, however, that the training and validation data was generated using the unchanging PSDs of the aLIGO design specification [344] for each given detector. Attempting to train models with real or pseudo-real noise which is non-stationary, and in the former case contains non-linear glitches, may not be as viable.

The use of unwhitened noise, if possible, may have some benefits in the case of overlapping signal detection and PE. Because this work is only expected to become relevant in the regime of very long-lived signals, it may be difficult to get clean off-source data at a close enough time separation from the on-source data which is not also contaminated with other signals.

7.4 Overlapnet Results

7.4.1 Classification

The first attempt to classify input examples generated with the method described in Section 7.3.1 utilized an architecture from the literature adapted from Gabbard *et al.* [53], the model architecture of

this model can be seen at Figure 7.33. To distinguish this model from later models, this model was named Overlapnet. We trained a binary classifier to output a score near or equal to one if there were two signals present in the input data, and a score near or equal to zero if there was only one signal in the data.

Since data for this experiment was generated independently, validation was also performed alternately. Since we are assuming the presence of at least one signal, in either case, the problem is not hugely asymmetric as it is in the CBC detection case. The penalty for incorrectly classifying a single signal as a double is much less than for classifying noise as a signal. This is because a detection model must examine many more noise examples than an overlap detection model would signals since we are assuming at least one signal has already been detected by another method. If we assume that misidentifying a single signal as a double is as undesirable as misidentifying a pair of signals as a single, we can set a classification threshold of 0.5 so that neither class is favoured (unless the model intrinsically favours one class over another, which is also possible), as an equal ratio between classes is usually recommended to maximize overall model performance [345]. This means we can focus on optimizing our model to gain as high accuracy as possible, without needing performance in extremely low FAR regimes; therefore FAR plots are not particularly useful.

The trained model was run over the validation dataset consisting of 4×10^4 examples generated independently but with the same method as the training data. The parameters for each waveform were recorded and compared with the classification results.

This initial attempt at applying a preexisting model from the literature to the problem proved sufficient even in unwhitened noise. The model was able to correctly classify most pair examples where both of the optimal network SNRs are above 10, and correctly identify almost all single signals. See Figure 7.2.

For the single signal validation examples, the model can correctly identify almost all cases, (assuming a detection score threshold of 0.5). We note that although the classification error very rarely exceeds 0.5, there is still some notable error. It is thought that this may be because of deficiencies in the construction of the dataset. Since there is very little to differentiate between pairs of signals where one signal is rendered almost indetectable due to a small SNR, and single signals; and between pairs of signals where both detectors have a low SNR and a single signal with a low SNR, this adds significant confusion to the training process, which encourages the model to show less confidence when classifying signals as singles. This could be ameliorated by increasing the minimum SNR threshold of the signals to the point where no (or fewer) training examples have one undetectable signal, although this change may come to the detriment of other classification abilities.

In the pair validation examples, the model has a much wider range of detection ability determined by the optimal network SNR of each of the examples' two signals. The model shows good performance when both signals have an optimal network SNR of at least ten, with a rapid decline below these values, which is roughly consistent with the efficiency curves we see in detection cases. This is anticipated. When one of the signals has a low SNR, the example becomes very similar to a single signal; when both of the signals have a low SNR, the example becomes indistinguishable from a single signal with a low SNR. In both of these cases, the model prefers to classify examples as single signals rather than double. This makes sense, the model will try to minimize the difference between its output and the ground truth values, half the examples in the training dataset are single signals, whereas considerably less than half the signals are pairs of signals with one low SNR — if the model has to guess between the two, it is more likely that the example will be in the former category than the latter. This is also probably true for real signals, so this is possibly not a bad feature of the classifier. For the case when both signals in a pair have low SNR, it also makes sense that the classifier would want to classify these as single signals, as there are many more examples of a single signal with a low SNR in the training dataset than there are of a pair of signals both with a low SNR.

It is also speculated that the model may have learned to associate low overall excess power with single signals. Since the two classes were not normalized to contain roughly equal excess power, the average excess power found in pair examples will be double that of the average excess power found in single examples. This is certainly a feature that the classifier could have learned to recognize. This could be alleviated by normalizing the excess power between the classes, which would force the detector to rely on the signal morphologies alone rather than the excess power contained within the example. It is not clear whether this would be a useful feature or not. Certainly, in nature, overlapping signals would, in general, mean greater excess power, but this may have detrimental effects in model training.

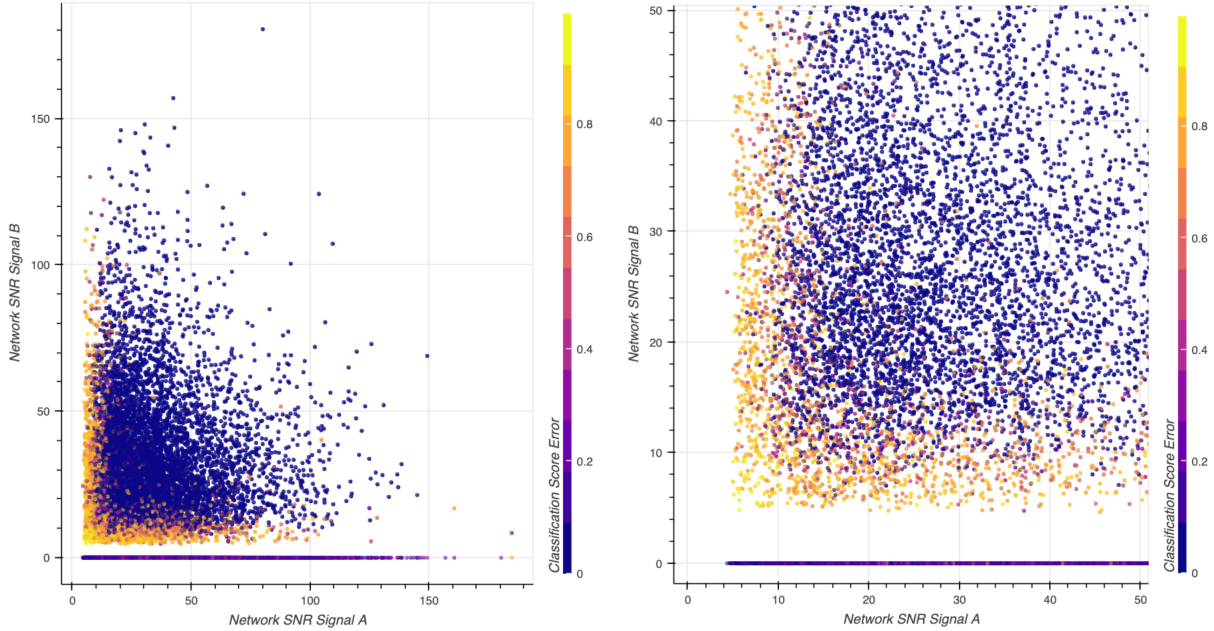


Figure 7.2 | Classification error of Overlapnet output when fed validation examples, plotted with signal A optimal network SNR and signal B optimal network SNR. A total of 4×10^4 validation examples were used to produce this plot. All examples consist of two-channel synthetic detector noise generated by colouring Gaussian white noise with the LIGO Hanford and LIGO Livingston aLIGO design specifications. Half the validation examples were injected with one each of 2×10^4 IMRPhenomTPHM waveforms with no repetitions, these are the single injection examples, which only contain Signal A. In these cases the SNR of signal B is always zero, these signals are seen arranged along the bottom of the plot. The other half of the examples consist of two each of the same 2×10^4 IMRPhenomTPHM waveforms with two repeats of the same pairs of signals injected into different noise realizations. A model score near one indicates the model has determined that the example has two hidden signals and a score near zero indicates that the model thinks the example has only one hidden signal. The classification score error shows the difference between the ground truth value and the predicted model output. Therefore an error nearer zero indicates good model performance, and an error nearer one indicates poor model performance. Assuming a classification threshold of 0.5 we can see that the model can successfully classify almost all single examples, and can successfully classify most pairs of signals when the Network SNR of both signals is above an optimal SNR of ten. We note that although classification is achieved in most cases, there is still substantial error in many cases, though mostly below the threshold required for an inaccurate classification, 0.5. It is theorised that this is because the model is trained with many examples of pairs of detectors with one low SNR that are hard to distinguish from single detectors with one signal. This confusion could add considerable uncertainty to the model predictions, and it is recommended that if this project were to be repeated the minimum SNR threshold for both of the signals should be increased. When either of the optimal network SNRs of one of the signals falls below 10, the rate of classification error increases in a curve that is consistently shaped

with the detection efficiency curves discussed in previous sections. This is anticipated — in the case that one of the SNRs becomes low, the signal will appear to look like a single signal as the other signal becomes hard to distinguish. In the case where both signals have a low SNR, both signals are hard to distinguish and it becomes difficult to differentiate between a single hard to identify signal and multiple hard to identify signals. In this latter case, where both signals have a low SNR, the model appears to favour classification as a single signal rather than double. It is hypothesized that this may be because the pairs and single examples were not normalized to have consistent excess power, meaning that the total excess power contained in the set of all two signal examples will be double that of the total excess power in all single signal examples. This might bias the network to associate low excess power with single signal examples. *Left:* Full validation results. *Right:* Zoomed result for increased detail below optimal network SNRs of 50.

We also plot several pseudo-efficiency curves for easier comparison to other results in Figure 7.3. Since there are now two network SNR values for each pair example and one network SNR value for each single example, we present the result in five distinct efficiency curves, four curves for the pair examples, and one curve for the single example. The four curves for the pair examples are generated by sorting the dataset by the maximum network SNR of the pairs, minimum network SNR of the pairs, and the SNR of signals A and B, then by generating a rolling average of the model scores. The single signal SNR is generated by sorting by the lone SNR value and calculating a rolling average. Note that unlike previous efficiency curves, which displayed the percentage of results that were above a certain FAR-calibrated model threshold, these curves just plot the rolling average model predictions, which are correct at a score of one for the four pair curves, and correct at zero for the one single signal curve.

The minimum SNR signal curve reaches an average model score near one at a minimum network SNR of around 37, which is quite high. However, it still achieves relatively good scores above an optimal SNR of 16. The reason this curve appears with this different shape to the detection efficiency curves is presumably because there are factors other than the measured SNR that are relevant to the model performance. In all the pair examples, the other non-ranking SNR value will have a large effect on the model's ability to distinguish between the two cases, along with the merger time separation, and the parameter space difference between the two injections. Since the minimum network SNR is the only curve that reaches scores near one of the four curves for pair examples, we can infer that this is the bottleneck for detection ability. The other curves never reach one no matter how high the network SNR suggesting that a percentage of the other SNRs in the pairs are low and decrease detection ability.

The maximum SNR line, as expected shows, considerably lower performance at lower SNRs. In each of the examples on this line, the lower SNR signal, which we know is the limiting factor, is equal to or lower than the SNR metric. This also explains why the line starts at a higher SNR — because the line is a rolling average of the examples sorted by SNR metric, the first average SNR value for the maximum signals will naturally be higher than the first average of the minimum signals. Interestingly, the maximum SNR curve reaches approximate parity with the lines plotting efficiencies when sorted by the SNR of signals A and B. This is presumably because there is a large range of SNRs less than the maximum, so the lower SNR is likely to still be detectable, with the difference between this maximum efficiency and one due to the undetectable percentage of SNRs under this maximum value.

Curves were also plotted by sorting the pair validation results when sorted by signal A SNR and signal B SNR. These were plotted to see if the model had any bias between the signals. Signal B is defined as the signal that arrives first in the detection, so it might in theory be possible for the classifier to develop bias toward one signal or another. However, the results show very little difference between the two curves, suggesting that the model does not have a preference between which signal has the higher SNR. Again the model does not reach an average model score of one, but this is because the

other SNR in the pair is unconstrained, so a certain percentage of examples at each average calculation will have a pairing with an SNR that is undetectable.

Finally, an efficiency curve was plotted for the single signal examples. Only one curve was plotted for this example, as a single network SNR value can capture the entire SNR information content of the example. Note that in this case, a model prediction of zero rather than one is correct, so lower scores indicate a more accurate prediction. We see that the model performs best at SNR values less than 20, before plateauing and slowly increasing beyond that. This shape is created because the training data contained many pair examples with one low SNR value which would look very similar to single signal examples, creating confusion in the training process and leading the model to predict single signals with some uncertainty. The higher performance at low SNRs is presumably due to the excess power bias because there are considerably more single signal examples on the lower excess power end, the model can more confidently predict a single signal if the total excess power is low. For the same reason, model performance degrades at higher single signal SNRs as it is more likely there is higher excess power in double signal examples, although in double signal examples with high excess power the double morphologies are more likely to be visible, so this bias is considerably less than the low power bias demonstrated.

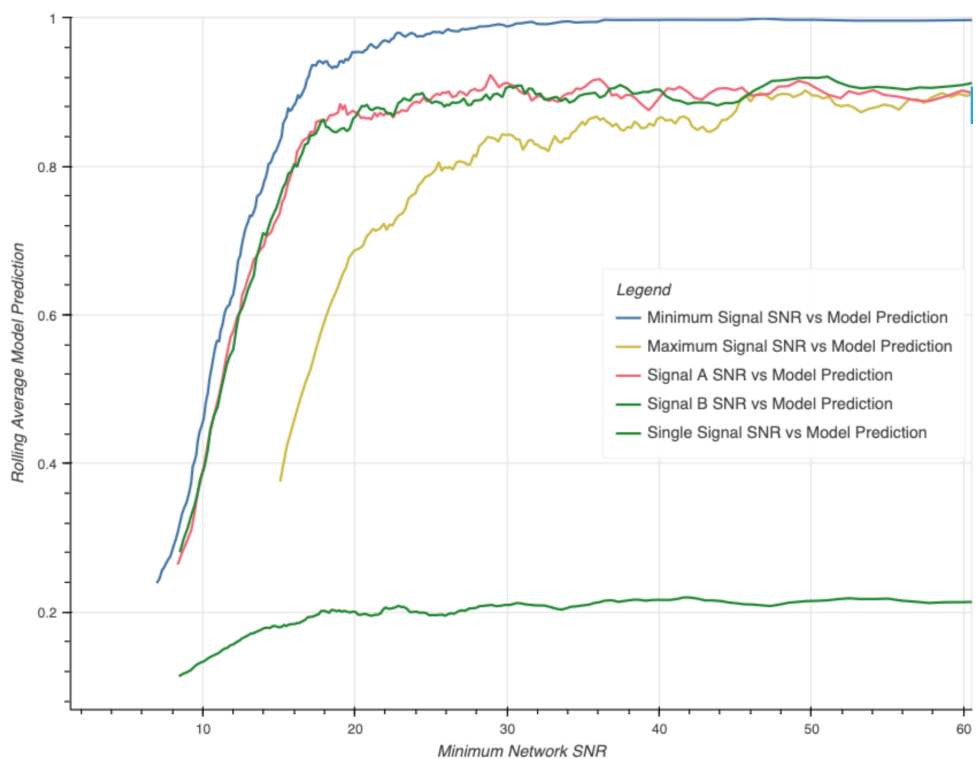


Figure 7.3 | Overlapnet pair efficiency plots created from the combined overlapnet validation data pool using rolling averages with a window of 1000 and plotting every 100th average value. This plot gives an approximate comparison to the efficiency plots generated in the detection cases; although generation was done with a rolling average over a pool of logarithmically distributed SNRs rather than with pools of discrete SNRs at specific test SNR values that have been used previously in the detection cases. Also note that this plots the model output score, rather than the percentage of cases which fall above a calibrated SNR threshold. These efficiency plots show the relationship between the SNR values of one of the signals and the model prediction. One of the five lines gives the rolling average model score when the validation results pool is sorted by minimum SNR value. This is perhaps the most useful of the four lines as it is the bottleneck in classification ability. It reaches a classification score of 1.0 at a minimum optimal network SNR of around 37. It remains above 0.9 for SNRs above

19 and increases slowly until 37. This separates it from the detection case and is presumably because there are extra factors not accounted for on this plot, primarily the SNR of the second signal, but also things like the parameter space difference of the two waveforms and the merger time separation of the two waveforms, which could both add increased difficulty without being visible on the efficiency plot. Two of the lines plot the rolling average model score when plotted with the SNR of one of the two signals, signal A and signal B. Signal B always arrives before signal A. The similarity between these lines shows that it is unlikely there is any bias between whether signal A has the lower SNR or signal B. The maximum scores achieved by these lines are less than the minimum, as there are always low SNR signals in the average used to calculate this. The last of the four pair example lines shows the moving average when the validation pool is sorted by the maximum SNR of the two injected signals. This is the lowest still, as it is more likely that the uncounted-for signals have low SNR. Lastly, we show the single signal SNR scores. Unlike the other signals, a lower score is better in this case, as a model prediction of zero indicates the lack of a second signal. We see that at low SNRs this score is lowest; this is expected as there are considerably more low SNR single signals in the dataset than pairs of signals, and this supports our hypothesis that the network is using excess power as a differentiation method. Above an optimal network SNR of 18 the classification score plateaus at an average of 0.2, as stated previously it is believed this is induced through confusing examples in the training dataset where it is almost impossible for the network to determine between a pair of signals where one signal has a low SNR and a single signal, teaching the network to guess with some uncertainty in all apparent single signal cases. We also see a slight decrease in prediction accuracy as SNR increases, again this probably results from the excess power bias. From this plot we can conclude that as expected the lowest SNR signal in the pair is the largest factor in model efficiency, but that other factors are probably also relevant.

We create additional plots to explore how classification performance varies with other areas of parameter space. First, we examine how the time difference between the merger arrival of signal B and signal A at the earth center (assumed to be very close to the arrival at any of the detectors. Only in a very small number of cases will the order of arrival at the Earth's center be different from the arrival time at any detector when using this range of time separations), which affects the classification performance. Figure 7.4 shows that there is little correlation between model performance and the arrival time difference, except when the time separation is very small. There appears to be some degradation of performance below 0.8 s, but this only becomes very significant below 0.2 s. Since the average model performance values are calculated using a rolling average, when we examine the distribution of individual example performance by eye this first bin also seems to be heavily weighted by examples whose separation is very close to zero. As the time separation moves toward zero, the model has less opportunity to use distinct merger peaks to aid in its classification and must begin to rely on morphology alone. Since the model maintains performance, though at a reduced efficiency, at separations down to zero seconds, we can determine that the model can use morphologies as well as distinct peaks, in order to distinguish between the two cases. Further analysis of a validation set consisting only of zero separated signals would be useful to examine this further. However, since signals arriving with such small separations are very unlikely even when detection rates are massively increased, this is not considered a priority.

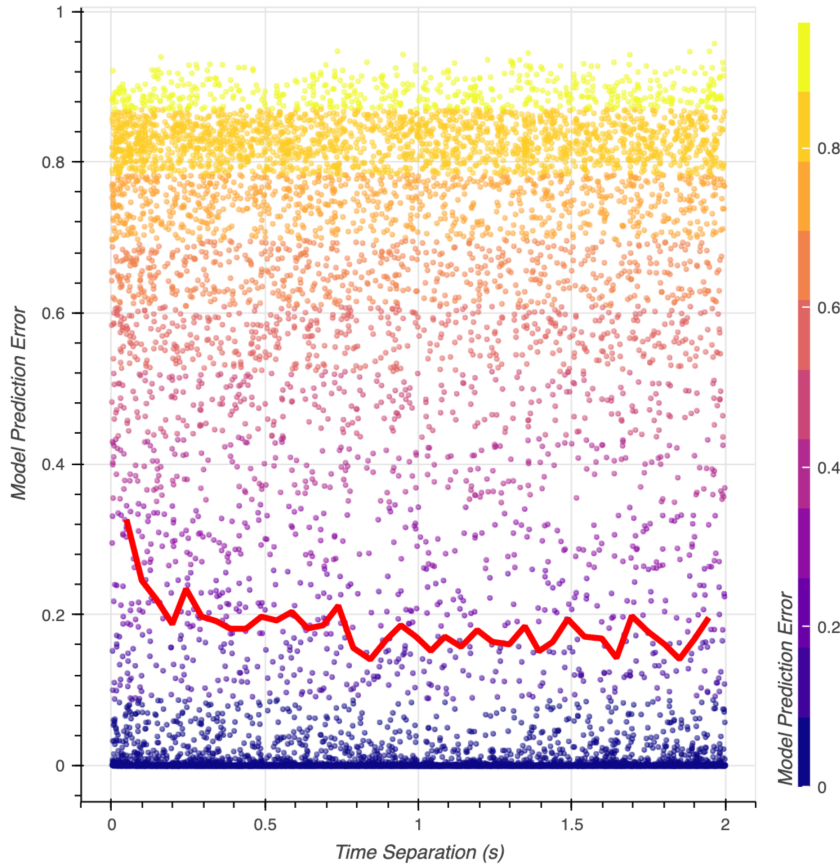


Figure 7.4 | Overlapnet classification results plotted against the time elapsed in seconds between the arrival of the merger of signal B and signal A. The coloured circles represent individual validation classification results colour-coded for visual clarity. The red line is the moving average model prediction error at the stated time separation with a window of 500 validation examples. Only pairs are plotted, as single examples have no time separation. We see that for time differences above 0.8 s the separation has little effect on the average prediction error. Between 0.2 s and 0.8 s there is a slight but notable increase in error, and below a merger time difference of 0.2 s there is a more notable uptick in error. It appears that this uptick at lower time separations is mostly caused by signals that have very low separation (< 0.1 s) – this seems to be the only significant predictor of model performance, other than this, and the small decrease in performance below 0.8 s the classifier seems to work with equal efficiency across time separations. This is perhaps less of a correlation than might be expected, but it demonstrates that only very close signals are problematic if at detectable SNRs. This is a good sign for the chances of developing a useful classifier.

For our final analysis of the classification results, we explore the parameter space of the waveform by examining model performance at different values of chirp mass and mass ratio; see Figure 7.5. These plots are less illuminatory, the only visible correlation exists between a lower chirp mass in one or both signals and poor performance. This is likely caused because sources will have a lower h_{rss} and therefore SNR (assuming identical detector noise conditions, sky localization, and polarization) if they are at the same luminosity distance as another signal with a higher chirp mass. This is also corroborated by the decrease in single signal classification performance at higher chirp masses, which is seen with higher SNRs. However, if luminosity distance is variable, which it is in the dataset, chirp mass alone does not correspond directly to SNR. Thus we don't see as strong of a correlation as we see in Figure 7.2.

Since there is no visible correlation along the line where the two parameters are equal to each other, we can conclude that both waveforms having similar mass parameters have relatively little effect on the ability of the model to correctly classify the signal. This is slightly surprising, as we would expect signals with similar frequency contents to be more difficult for the model to separate. However, in most cases within the validation dataset, the arrival time separation was large enough that the model could use the distinct merger peaks as evidence for mergers rather than relying on the morphologies alone. Which may explain this seeming lack of dependence on waveform parameters.

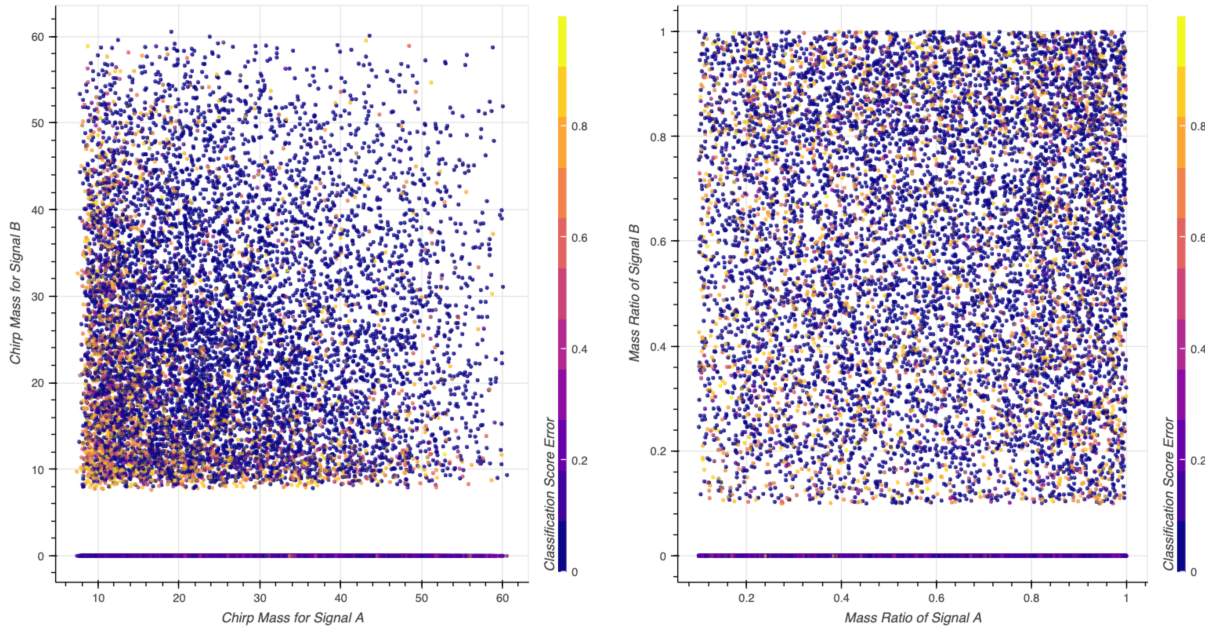


Figure 7.5 | Overlapnet classification results compared with the mass parameters of the constituent waveforms. *Left:* Overlapnet classification scores plotted with source chirp masses for signal A and signal B. There appears to be some correlation between lower chirp masses and poor model performance, however, because there are highly performing examples even in cases where both chirp masses are low we can conclude that this does not explain the entire picture. It is hypothesized, that this correlation is primarily caused by the fact that lower chirp masses are more likely to produce a low SNR signal. If two sources were at the same luminosity distance but one had a higher chirp mass, the higher chirp mass would have a louder SNR (assuming identical detector noise conditions, sky localization, and signal polarisation). This hypothesis is supported by the lower model performance of single signals at higher chirp masses, as we have seen that single signal classification is slightly worse at higher SNRs. *Right:* Overlapnet classification scores plotted with source mass ratio for signal A and signal B. This plot shows that there is very little, if any correlation between the mass ratio of the two signals, and model performance. This continues to show that signal morphology does not make a decisive difference in classification ability, which is primarily determined by the minimum SNR of a signal in the pairs, and secondarily weakened if the signals have a very small time separation.

We conclude that Overlapnet is capable enough to differentiate between single and overlapping signals in the majority of cases, and with some adjustment to the training dataset, performance could probably be improved by removing the ambiguity generated by impossible-to-distinguish examples.

7.4.2 Regression

Following the relative success of Overlapnet in differentiating between examples with one CBC signal present and two overlapping CBC signals present, we attempted to use the same model, with an adjusted activation function on the last layer, (linear rather than softmax), to attempt a regression prob-

lem on pairs of overlapping signals, in an attempt to extract useful information that could be used in a parameter estimation pipeline. The most useful parameters that can be extracted from an overlapping signal, are the merger times of the two signals A and B. Using the same training dataset and procedure, we changed only the activation function applied to the model output to allow for regression rather than classification, the model loss function used, again to allow for regression, and the labels that the model was trained to output. Rather than output a score between zero and one, we trained the model to output a merger time for signal A, and a merger time for signal B.

Due to an error in the data labelling procedure, which was not spotted until later experiments. Regression test results were extremely poor. Initially, it was thought that this was down to using an insufficient model for the task, therefore a much more complex and experimental network was constructed, utilizing much of the insight gained from previous experiments, as well as denoising autoencoder heads, and cross-attention layers between detectors. These concepts are explained in Section 7.5. We name this more complex network structure CrossWave. It should be noted that it is not proven that such a complex network is necessary for successfully overlapping parameter estimation of overlapping CBC signal with machine learning.

7.5 Aditonal Structural Elements

7.5.1 Cross-Attention

The multi-head attention layers we have explored thus far in Section 6 have all consisted of self-attention heads, which is the most natural application of attention [56,304]. However, attention layers can also be used to compare two different sequences; this is a principle component of the archetypical transformer design [56,299], wherein cross-attention layers compare the model-predicted vectors to the ground truth vectors of the training data. See Section 6.1.6. Since we were not concerned with next-token prediction in Section 6 we opted not to use cross-attention layers and instead focus entirely on self-attention.

However, there is a scenario in gravitational-wave data science for which a natural application of cross attention can be applied – between the detector outputs of the multiple interferometers of a gravitational-wave detection network. There are two ways in which we could deal with this scenario, we could apply the appropriate temporal encoding and add an encoding element informing the model which detector each sequence element originated from, or we could simply use cross attention between the multiple detectors. See Figure 7.6> for an illustration of the cross-attention mechanism.

In cross-attention, query, key, and value vectors are still generated, but for two sequences instead of one [56,299]. The query vectors from one sequence are then compared with the key vectors of the other sequence, and the value vectors of that sequence are summed together similarly as in self-attention. What this does is it allows the attention layer to accumulate information from the other sequence that is relevant to vectors in the first sequence. Because the choice of which sequence will provide the query and which the key and value, matters, cross-attention is not commutative. After calculating the cross-attention between detectors, you can then add this result to the self-attention result, allowing you to accumulate relevant information both from other temporal locations in one detector and from information provided by other detectors.

Overlapnet used both LIGO detectors as input since there was no need to try and optimise for low FAR. When attempting to improve on this network operation with attention layers, it is a natural choice to apply cross-attention.

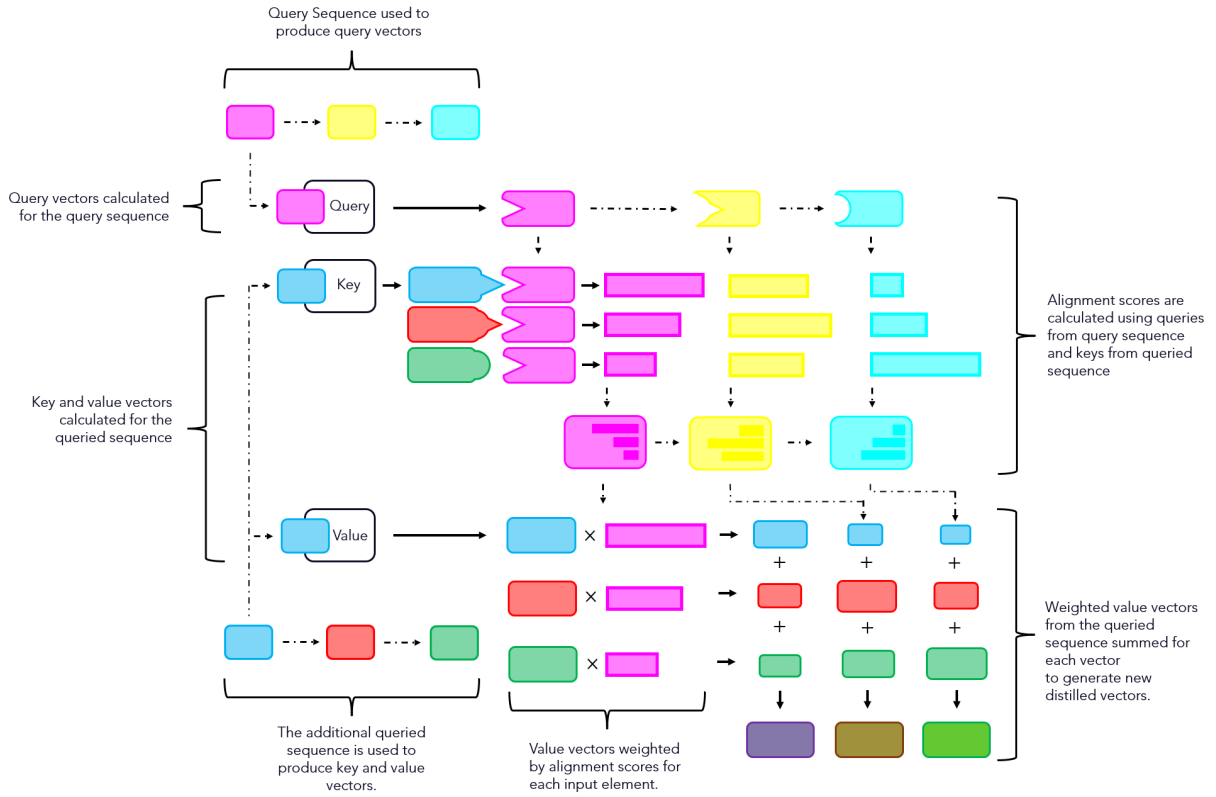


Figure 7.6 | Illustration of the action of a single cross-attention head. In contrast to a self-attention head, a cross-attention head takes two sequences as input: a querier sequence, and a queried sequence. The querier sequence is converted into query vectors with a learned weights matrix, and the queried sequence is converted into key and value vectors. The rest of the attention mechanism functions identically to self-attention but uses query, key, and value vectors that originate from different sources. For more details on the self-attention mechanism see the description in Section 6.1.3.

7.5.2 Autoencoders and Denoising

Autoencoders are a family of artificial neural network architectures [244]. They can utilise many different layer types including pure dense layers, convolutional layers, and attention-layers, but they are defined fundamentally by their inputs and outputs and the shape of the data as it moves through the network. The vanilla autoencoder can be described as a form of unsupervised learning since the model input is the same as the model output, and therefore, although it has in some sense a model label – its input, the data does not need to be labeled, as it is its own label.

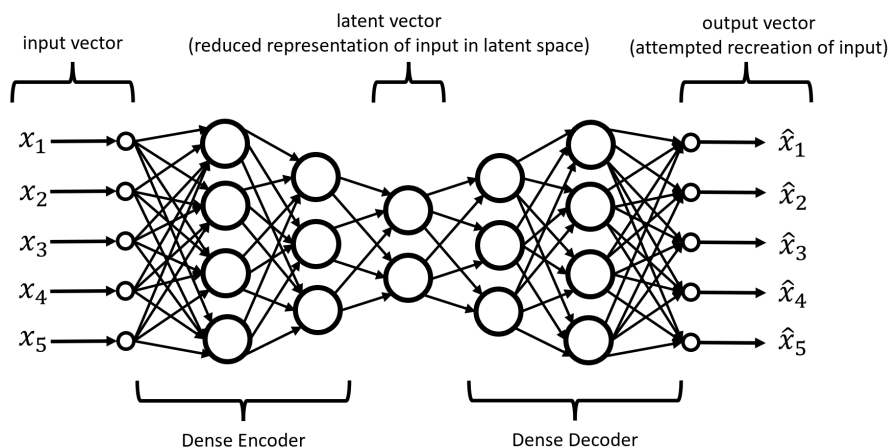
A vanilla autoencoder attempts to compress the information content of its input into a latent vector that is typically significantly smaller than the input vector, then regenerate the original input vector from that reduced latent vector with as little loss as possible [244]. This has useful applications as a compression algorithm, but also sometimes in encryption and many other applications. Having access to a lower dimensional latent space that can represent elements of a unique distribution has many uses in generative models and classifiers. Many different subtypes of autoencoder try to regularise the latent space into a more useful format, the most common of which is the Variational AutoEncoder (VAE) [346].

Autoencoders can also be used for anomaly rejection [244] which has application in gravitational-wave analysis in both glitch [347] and burst detection [255]. Because an autoencoder is trained to reconstruct data from a given distribution, if it is fed a result that lies outside that distribution this will likely result in a high reconstruction loss. The value of this loss then can be used to determine if the

autoencoder has encountered something from outside its training distribution. In the case of gravitational-wave glitches, we can train a model on known glitch types or a single known glitch type. We can then reject glitches that the autoencoder can successfully reconstruct as specimens of known detector glitches. For anomaly detection, we can instead train the model to reconstruct a standard interferometer background, if the autoencoder fails to reconstruct a section of the background well, it could be an indication of the presence of an anomaly, which in some cases could be a gravitational wave burst. When detected in conjunction with coherent anomalies from multiple detectors, this could lead to a confirmed burst detection once glitches have been ruled out.

An autoencoder has three parts, an encoder, a decoder, and a latent vector [244]. See Figure 7.7. The encoder attempts to reduce the input vector into a smaller latent space vector. Performing a kind of dimensional reduction which hopefully preserves most of the information content of the input vector by representing it in a more efficient data format. In most distributions that are interesting, there is a significant structure that can be learned and used to compress the data. Similar to compression algorithms, if the input data is random and has no structure, there will not be a way to represent that data in a much more efficient way. The encoder commonly has an identical structure to the convolutional layers in a CNN. A function to compress the input data down into smaller feature maps is identical to what we require from our encoder. Encoders can also be built with dense or attention layers, and share most of the benefits and drawbacks of these previously discussed. The decoder is similar but acts in reverse to reconstruct the original input data from the reduced representation generated by the encoder. Often the decoder is a mirror image of the encoder and uses inverted layers such as transpose convolutional layers.

As well as acting as unsupervised models, it is possible to use pseudo-autoencoders which have the same structure as autoencoders but are not autoencoders in the truest definition, to produce an output that is not the same as its input, but instead an altered version of the input. This can be used to transform the input in some way, for example adding a filter to an image or audio input, or it can be used to try and remove noise from the original image. This latter type is known as a **denoising autoencoder** [348], and it is what we will be using as part of our expanded CrossWave architecture. Denoising autoencoders are no longer considered unsupervised models, as the labels must be denoised versions of the input vectors. During training, the denoising autoencoder learns to extract important features from the input image but ignores the noise, as it is not present in the output label and would be unnecessary information to propagate through the model. There have been some attempts to apply denoising autoencoders to gravitational-wave data in order to remove interferometer noise and reveal hidden gravitational-wave signals.



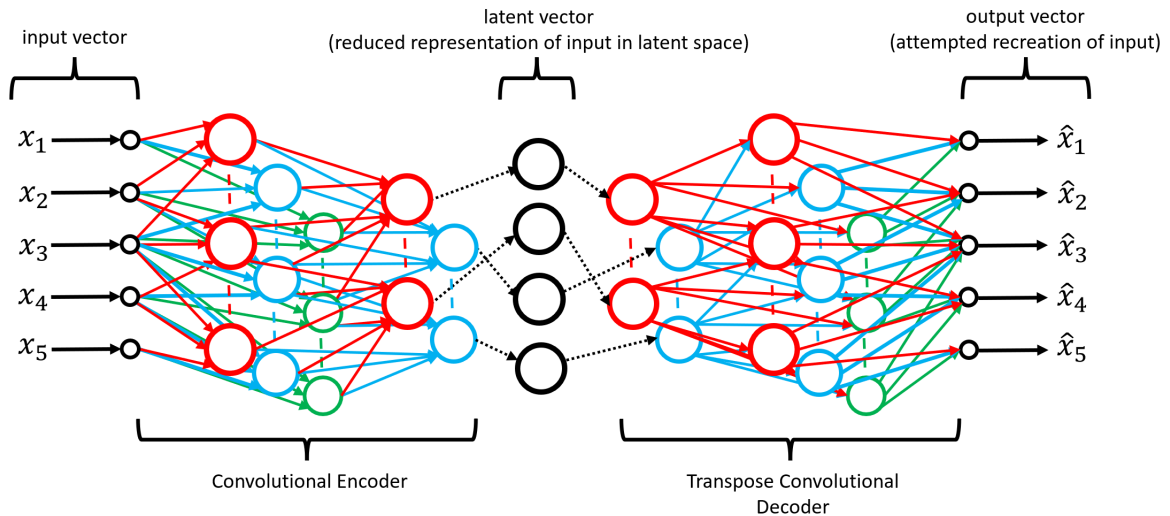


Figure 7.7 | Illustration of two trivial autoencoder architectures, one using only dense layers, the other using convolutional layers. Both networks have very few neurons and would likely not see use in any real practical application but are presented for illustration only. Autoencoders consist of an encoder that performs dimensional reduction on an input vector to reduce its dimensionality to a smaller latent space and produce a latent vector, this latent vector is then processed by the decoder which attempts to perform the inverse operation and reconstruct the original input image, or a slightly altered version of the input, for example a denoised version of the original input. Often the decoder is simply an inverted version of the encoder, which introduces the concept of transposed convolutional layers which perform the inverted operation of convolutional layers. *Upper:* Illustrative dense layer autoencoder with a two-layer encoder and a two-layer decoder. The latent space of this autoencoder has two dimensions meaning the dimensionality of the input vector has been reduced from five down to two *Lower:* Illustrative convolutional autoencoder with a two-layer encoder consisting of convolutional layers and a two-layer decoder consisting of transposed convolutional layers. The latent vector of this autoencoder has four elements, which means there has only been a reduction of one element between the input vector and the latent space.

7.6 CrossWave Architecture

The CrossWave architecture is the most ambitious model architecture presented in this thesis. It attempts to combine many intuitions gained throughout the research, with contemporary network features that are known to work well in similar domains. We utilize several new conceptual elements: denoising autoencoder heads, and cross-attention layers, which are described in more detail in Section 7.5.

The Crosswave architecture has a dual branch structure, which, rather than immediately combining both detectors into one multi-dimensional input stream, deals with input streams from both detectors in separate network branches in the first stage of the model. Each detector input is first fed into independent denoising autoencoder heads, with the idea that each autoencoder can learn to deal with the specificities of that particular detector noise, extract only the important signal features, and filter out detector glitches. These could first be trained independently to denoise signals before being used in the larger regression model, which was the original intention, however, due to time constraints, these were trained in unison with the greater model. The architecture of the autoencoder encoder is based on the model described in Gabbard *et al.* [53], with the decoder consisting of the inverse of that architecture, using transpose convolutions in place of convolutions, and upscaling in place of pooling layers. This

model was chosen as it is known to be able to effectively extract the features of a gravitational-wave signal.

In order to facilitate an effective comparison between the two detectors inside the cross-attention layers, it is desirable to have the features from both models mapped inside a shared latent space. For this reason, after the denoising heads, each branch was fed through an identical set of feature-extracting convolutional layers with shared weights. It is hoped that these shared weights will force the denoising heads to output vectors of the same form, which can then be processed by the shared feature extractor into the same latent space to allow for easier comparison by the cross-attention layers. In this manner, it is hoped that the independent denoising heads can deal with and remove differences in detector noise and configuration, whilst the shared feature-extracting layers can learn to recognize the features that are shared across detectors due to the detector-agnostic intrinsic properties of the waveforms proper. The feature-extracting layers are identical to the encoding layers inside the denoising heads, taken from Gabbard *et al.* [53].

Two models were trialed, which are illustrated in Figure 7.8, and Figure 7.9. The small model only utilizes a single cross-attention layer, which combines the output of multiple self-attention blocks applied independently to each detector output. The larger model computes both self-attention and cross-attention inside each attention block, summing the results of both layers in order to combine both global contexts from other parts of the input vector, and the other detector into a single sequence for each detector. These results are finally concatenated after repetition and a final classification is performed with two dense layers. The larger model was found to have increased performance over the smaller one, and so was used for further experimentation.

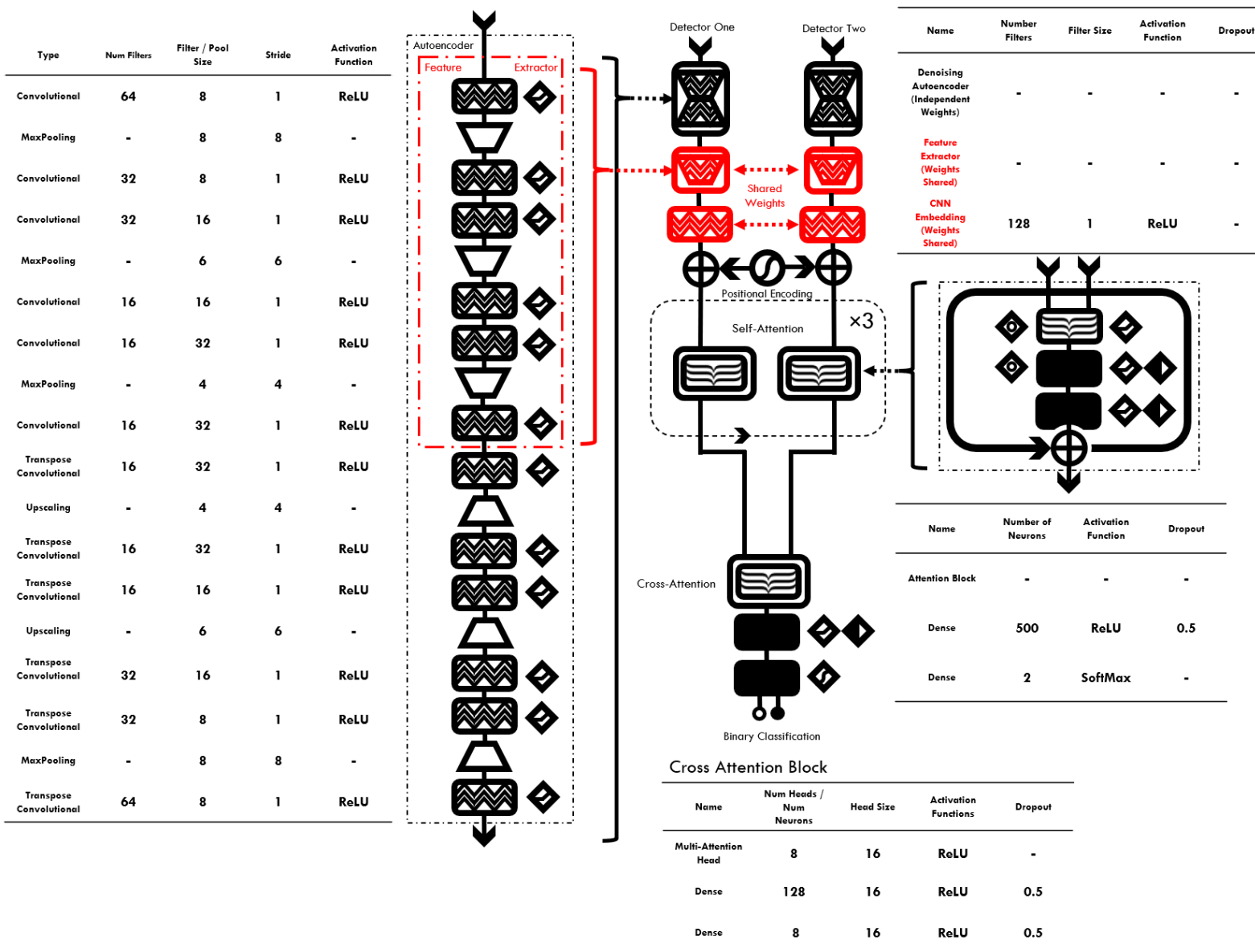
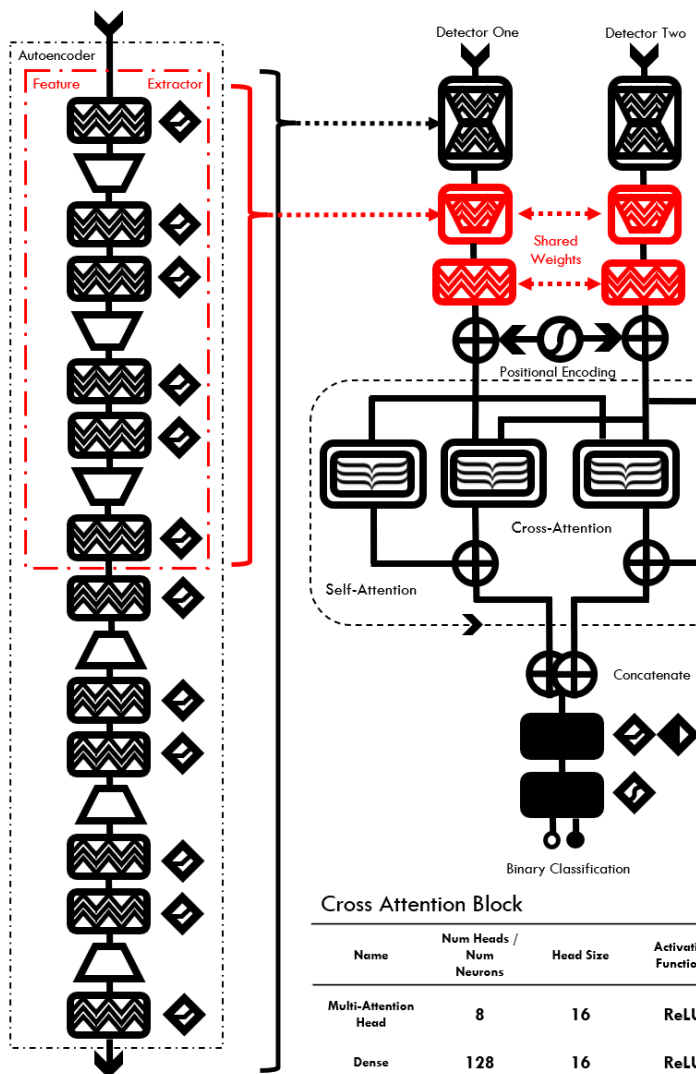


Figure 7.8 | Diagram of the network structure of the smaller of the two trialled CrossWave models. Both the CrossWave models have a novel structure with denoising heads, and feature extraction layers adapted from Gabbard *et al.* [53], as well as utilization of cross-attention layers. The denoising heads are composed of an autoencoder structure, with one for each input detector. In this case, we have used simulated inputs from the LIGO Hanford and LIGO Livingston detectors so there are two autoencoding heads. Each autoencoder has independently trained weights. It is envisioned that during network training these will adapt individually to the peculiarities of the noise in its given detector, and, due to the shared weights utilized by the feature extractor, learn to output a standardized denoised version of the input from each detector, although it is expected this will not be a perfect correlated to a denoised detector stream since the autoencoders were not independently pre-trained before training of the larger model. After the autoencoding heads, several feature-extracting layers also adapted from Gabbard *et al.* [53] are used to embed the autoencoder outputs into two sequences that can be ingested by the attention layers. It is imagined, that because these feature-extracting layers share weights between detectors, they will map the output of the denoising layers into a shared latent space that can be interpreted similarly by the attention layers, and is therefore useful for cross-attention between detectors.

The core of the small CrossWave model utilizes a repeating block of self-attention layers applied repeatedly to each detector data stream, much like in the Skywarp transformer. These blocks are repeated three times. This repeating self-attention layer should help the model understand the global context of the data within each detector. After completion, these data streams are combined in a cross-attention block, and then processed by two dense layers to give the final regression output scores. This model was trialled and was somewhat performant, but the application of the cross-attention in this method was causing a lot of information to be lost, so the model was abandoned in favour of the larger variant shown in Figure 7.9.

Type	Num Filters	Filter / Pool Size	Stride	Activation Function
Convolutional	64	8	1	ReLU
MaxPooling	-	8	8	-
Convolutional	32	8	1	ReLU
Convolutional	32	16	1	ReLU
MaxPooling	-	6	6	-
Convolutional	16	16	1	ReLU
Convolutional	16	32	1	ReLU
MaxPooling	-	4	4	-
Convolutional	16	32	1	ReLU
Transpose Convolutional	16	32	1	ReLU
Upscaling	-	4	4	-
Transpose Convolutional	16	32	1	ReLU
Transpose Convolutional	16	16	1	ReLU
Upscaling	-	6	6	-
Transpose Convolutional	32	16	1	ReLU
Transpose Convolutional	32	8	1	ReLU
MaxPooling	-	8	8	-
Transpose Convolutional	64	8	1	ReLU



Name	Number Filters	Filter Size	Activation Function	Dropout
Denoising Autoencoder (Independent Weights)	-	-	-	-
Feature Extractor (Weights Shared)	-	-	-	-
CNN Embedding (Weights Shared)	128	1	ReLU	-

Name	Number of Neurons	Activation Function	Dropout
Dense	500	ReLU	0.5
Dense	2	SoftMax	-

Cross Attention Block				
Name	Num Heads / Num Neurons	Head Size	Activation Functions	Dropout
Multi-Attention Head	8	16	ReLU	-
Dense	128	16	ReLU	0.5
Dense	8	16	ReLU	0.5

Figure 7.9 | Diagram of the network structure of the larger of the two trialled Crosswave models. Both the CrossWave models have a novel structure with denoising heads, and feature extraction layers adapted from Gabbard *et al.* [53], as well as utilization of cross-attention layers. The denoising heads are composed of an autoencoder structure, with one for each input detector. In this case, we have used simulated inputs from the LIGO Hanford and LIGO Livingston detectors so there are two autoencoding heads. Each autoencoder has independently trained weights. It is envisioned that during network training these will adapt individually to the peculiarities of the noise in its given detector, and, due to the shared weights utilized by the feature extractor, learn to output a standardized denoised version of the input from each detector, although it is expected this will not be a perfect correlated to a denoised detector stream since the autoencoders were not independently pre-trained before training of the larger model. After the autoencoding heads, several feature-extracting layers also adapted from Gabbard *et al.* [53] are used to embed the autoencoder outputs into two sequences that can be ingested by the attention layers. It is imagined, that because these feature-extracting layers share weights between detectors, they will map the output of the denoising layers into a shared latent space that can be interpreted similarly by the attention layers, and is therefore useful for cross-attention between detectors.

The core of the larger CrossWave block contains both self-attention blocks and cross-attention blocks in each iteration, this means that the model can compare data streams from both detectors multiple times, each time adding extra relevant information from the other detector into that detector's branch. Also, since the cross-attention is being performed in both directions, no information is lost as it was in the small model. Again, these blocks are repeated three times. After the repeating blocks, rather than using a cross-attention block to combine the branches, the outputs from each branch were concatenated before being fed into the dense tail, which then produced the final regression outputs.

7.7 CrossWave Dataset

We used the same independently produced dataset to provide the regression labels for the CrossWave regression models, described in Section 7.6. Fortunately, the dataset was produced with comprehensive labels of relevant parameters, including luminosity distance, signal arrival time, companion masses, and spin parameters for each of the two waveforms in the pairs.

As opposed to binary classification, there is slightly more to consider when designing the form of the output labels. Initially, we must consider if we want to perform a classification at the same time as the regression of parameters. When training a model, the model can learn information from the input vector, but also from the labels. At the onset of experimentation with CrossWave it was thought that perhaps allowing the dataset more information about the data, in the form of more detailed labels of parameters, might aid in the classification process. This has several issues, primarily, if we wish to perform classification at the same time as a regression, we must include both pairs and singles in the training dataset. Therefore we must decide what to do with the parameter regression labels for signal B, in the case where there is no signal B. The natural decision might be to set these labels to zero, however, this might cause significant problems in the network. Whenever a training example without signal B is presented, the gradient descent algorithm will attempt to move the network toward producing zero for all of signal B's parameters, but zero is not an accurate representation of an undetectable signal for many of the parameters. For example, it might be more natural to put the luminosity distance very high for an invisible signal, but for other labels, it is not quite as easy to select a null value that won't disrupt the parameter estimation in some way. Joint classification regression trials proved ineffective across several different selections of null parameters for signal B, causing parameter estimation and classification confusion in the network. A method to gate outputs by multiplication with the classification output was also trialled, but this too proved ineffective.

Due to the failure of early experiments to perform parameter estimation with datasets comprised of both pairs of signals and single singles, the decision was made to focus on the more specific task of extracting parameters from pairs of signals, without the capability to perform parameter estimation on single signals, or classify between the two cases. Therefore all single signals were removed from the validation and training datasets, shrinking the training dataset size to 2×10^5 examples, and the validation dataset to 2×10^4 examples.

The second consideration is which parameters to attempt to extract. The inclusion of additional parameters did not appear to reduce the ability of the model to correctly extract other parameters, even if those additional parameters were difficult or impossible to extract. Neither did the opposite appear to be the case; the inclusion of additional labels did not appear to improve the ability of the model to classify other parameters. The following 24 parameters were selected for extraction by the models: [**“Signal A Geocentric Arrival Time (s)”, “Signal B Geocentric Arrival Time (s)”, “Signal A H1 Arrival Time (s)”, “Signal B H1 Arrival Time (s)”, “Signal A L1 Arrival Time (s)”, “Signal B L1 Arrival Time (s)”, “Signal A Companion Mass 1 (M_{\odot})”, “Signal B Companion Mass 1 (M_{\odot})”, “Signal A Companion Mass 2 (M_{\odot})”, “Signal B Companion Mass 2 (M_{\odot})”, “Signal A Luminosity Distance (MPc)”, “Signal B Luminosity Distance (MPc)”, “Signal A Dimensionless Spin Component X Companion 1”, “Signal B Dimensionless Spin Component X Companion 1”, “Signal A Dimensionless Spin Component Y Companion 1”, “Signal B Dimensionless Spin Component Y Companion 1”, “Signal A Dimensionless Spin Component Z Companion 1”, “Signal B Dimensionless Spin Component Z Companion 1”, “Signal A Dimensionless Spin Component X Companion 2”, “Signal B Dimensionless Spin Component X Companion 2”, “Signal A Dimensionless Spin Component Y Companion 2”, “Signal B Dimensionless Spin Component Y Companion 2”, “Signal A Dimensionless Spin Component Z Companion 2”, “Signal B Dimensionless Spin Component Z Companion 2s”**].

Finally, we can consider if and how we want to normalize the values of the labels. Out of the selected parameters, many are in a different range, with the Spin Components between -1 and 1 , the masses between 10 and 70 , and the luminosity distance between 500 and 700 . This is not necessarily a problem, and the model would still be able to produce these outputs assuming we use the right activation functions. However, this could cause the model to take a longer time to converge on correct solutions, as it would consider some parameters, with larger values, to be much more important than the others. Ideally, we want the gradient descent mechanism to treat all parameters approximately equally. For that reason, all label values were normalized between 0 and 1 . The only exception to this was the merger times for signal B, as these were incorrectly normalized leading to some ground truth values of less than one, which the model was unable to predict due to ReLU activation functions used on the output layer, which limit neuron outputs to values of zero or greater.

7.8 CrossWave Results

7.8.1 Merger Time Parameter Estimation Results

Although a single model to predict all aforementioned parameters was produced, we shall focus on examining the merger time predictions before we look at the other results. These are the more important outputs of the model, as they fulfil the initial goal of providing more information for use in more established parameter estimation methods. The model was trained to output merger arrival time predictions for the LIGO Hanford Detector, the LIGO Livingston Detector, and the Earth's centre. Results are consistent between detectors, so for the first set of comparisons we compare only the predictions for the LIGO Hanford arrival time to the ground truth LIGO Hanford arrival time.

First, can examine the arrival time predictions compared to the individual signal SNRs – unlike in the classification case where only a single result is output, (albeit from two output neurons normalized by a SoftMax layer), the model is now tasked to output two regression values (along with the other parameters): a merger time for signal A and a merger time for signal B. Therefore, we have generated two plots, one for each signal; see Figure 7.10.

Examining the results, we observe that there are a few outliers with high errors above 0.25 s, but the majority of merger times were predicted with errors under this margin. On average, errors were notably worse for signal B than for signal A, but their magnitudes do not seem to be correlated to the signals' network SNR so it is unclear whether this increased error in signal B lies in the method or is a result of systematic training degradation introduced by the normalisation error. Another possibility is that this increased error arises from the asymmetry caused because signal B always arrives in the detector before signal A (except in very rare edge cases previously discussed); because of this, the entirety of signal B is always contaminated with the inspiral of signal A, whereas signal often has at least some clear signal after signal B has merged and the ringdown has petered out. Some errors could originate from the misidentification of signals A and B. However, if this were to be the case, we would expect to see this error correlated with SNR, but we do not, at least on first inspection.

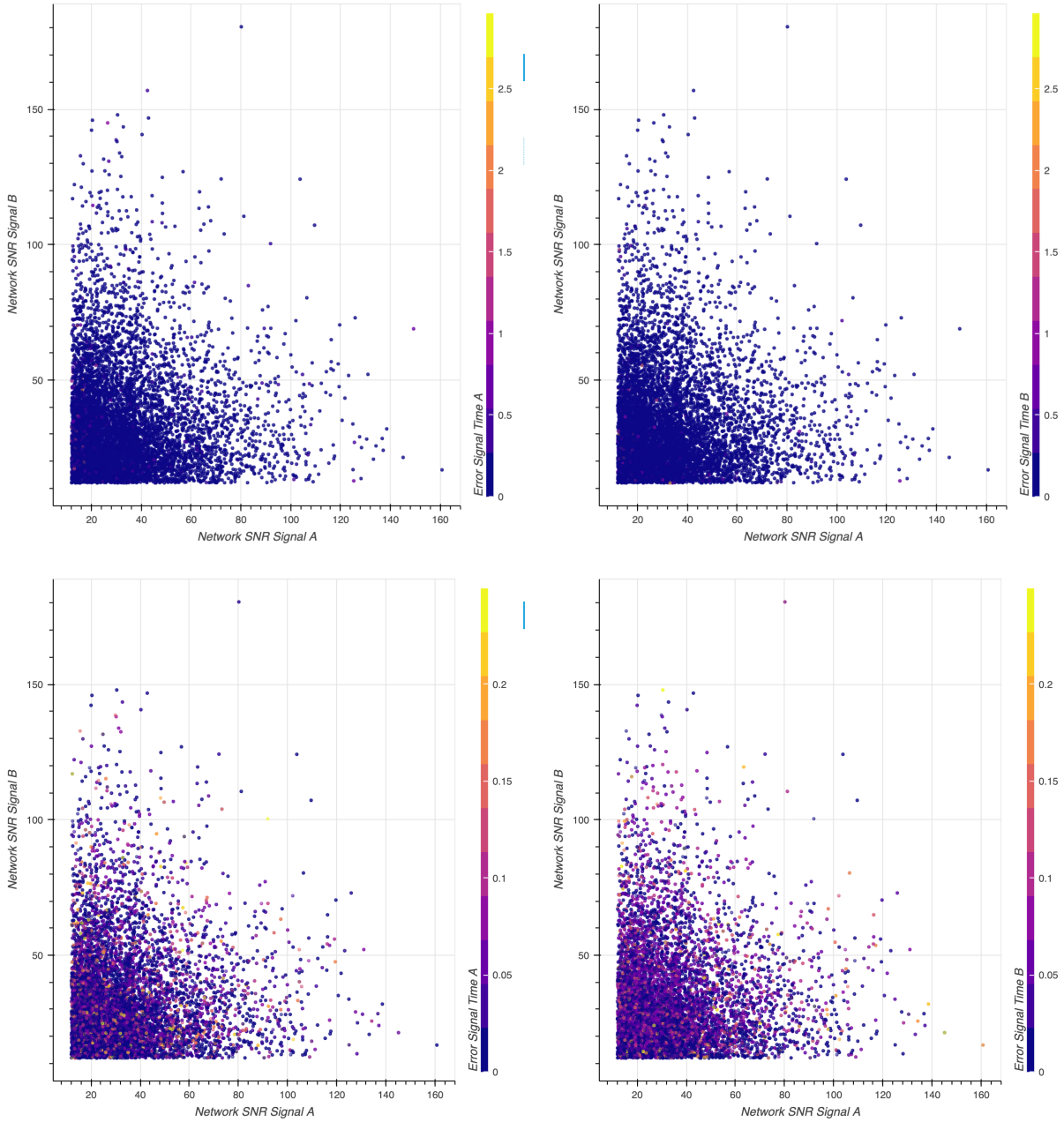


Figure 7.10 | CrossWave merger time prediction error of Signal A, *upper left*, and Signal B, *upper right*. Compared to the classification results, the merger time errors look more consistent. This is primarily because the model output is not restricted between one and zero like it is in classification, so a few outliers with very high errors saturate the colour map. Given this, we have also plotted the same results with all examples that have errors greater than 0.25 s removed, for a more granular view of the bulk of the regression prediction errors. These are the lower two plots. In these focused plots, we can see that a significant number of results have a regression error of less than 0.1 s, which could be helpful to aid a secondary parameter estimation method. On these lower plots, there is also a notable difference between the average error on signal A merger time predictions, and the average error on signal B merger time predictions, with a higher average error on signal B. It is unclear exactly why this is the case, but we speculate that this is because signal B arrives first in the detector, meaning that the inspiral of signal A can interfere significantly with signal B, whereas the opposite is only the case when the merger separation is very small. It is also possible that sometimes, signal A can be misclassified as signal B. We would expect this latter confusion to have some correlation to SNR, but this does not seem to be the case. It could also be due to the aforementioned normalisation error reducing model

training efficacy for signal B merger time predictions. Interestingly, the relationship between signal SNR and regression error appears low. This suggests that the substantive cause of regression error lies elsewhere, we plot additional comparisons to further investigate.

Next, we can plot the rolling average prediction error as it changes with SNR; see Figure 7.11. The picture is mostly as anticipated, with the determining factor for high merger time error at low SNRs (< 20) being the SNR of the signal whose merger time is being predicted. This suggests that the expected SNR relationship is present in Figure 7.10, but is hidden under variance created by other factors. At optimal Network SNRs between 20 and 60, the results are roughly consistent between signal A prediction error and signal B prediction error. With a high SNR in the opposing signal leading to higher error. Above an optimal network SNR of 60, the pictures change, with the signal A prediction error average roughly equal whether ranked by signal A SNR, signal B SNR, or maximum SNR. This suggests estimation of signal A merger time is independent of signal B. For signal B however, high signal A SNR increases error on signal B, suggesting that as theorized, the inspiral of signal A can interfere with the parameter estimation of signal B.

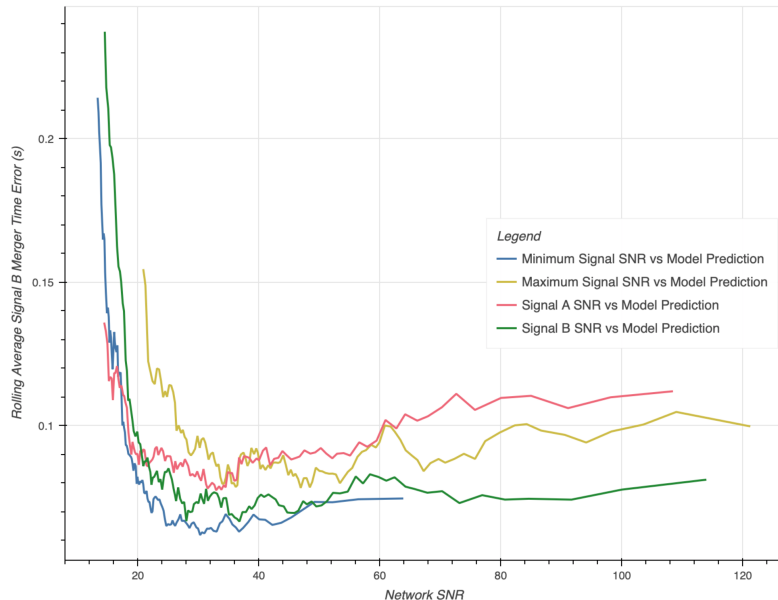
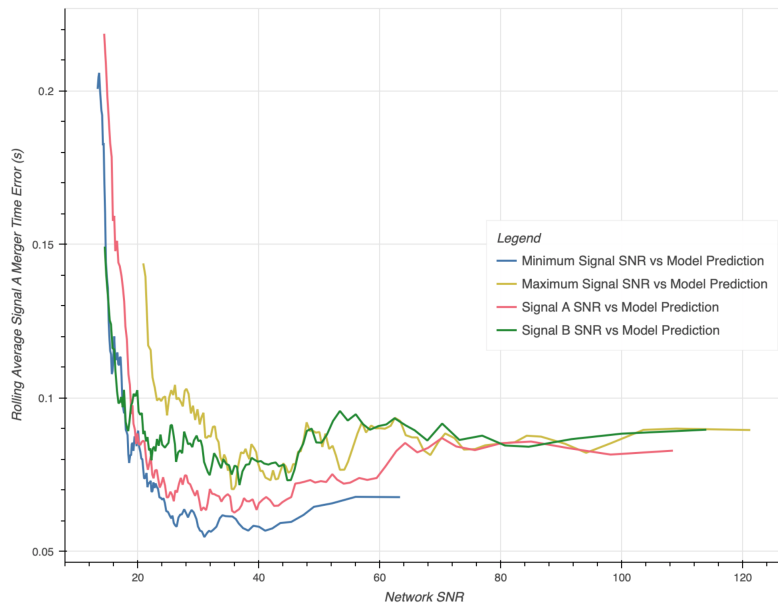


Figure 7.11 | CrossWave rolling average merger time prediction error plotted when ranked by different SNR combinations. Since the model now has two outputs, one for each merger time in the input example, a plot was generated for each merger time prediction. A plot showing signal A merger time prediction on the left, and a plot showing signal B merger time prediction on the right. At low SNR, the error is dominated by the SNR in the given signal, which is anticipated — a low SNR in a given signal would, evidently, make it difficult for the model to detect, and hence, estimate the merger time, of that signal. We can also see the notable difference in average prediction error between the upper signal A plot and the lower signal B plot. Interestingly, we see that the error on the signal B merger time increases when the SNR of signal A is higher. This seems to be the case regardless of the SNR of signal B. Since signal B always arrives first in the detector, this could be because a loud signal A inspiral obfuscates the presence of signal B, rendering the signal B merger time hard to identify.

As was the case with classification, we might expect the difference in merger times to affect merger time estimation ability. Thus we have created similar plots to determine the effect of the difference in merger arrival time between the two signals on model prediction ability; see Figure 7.12. In both cases, there is a sharp peak in the magnitude of the prediction error when the merger time separation nears zero. As would be expected, if it gets difficult to determine if there are one or two signals at a particular spot, with perhaps another smaller SNR signal hiding elsewhere, the model becomes confused when trying to predict the merger time. In the case of signal A, defined as the second signal to arrive in the detector, when incorrect, the model tends to predict the signal will arrive later than it does, and vice versa in the case of signal B. We also note that in both cases, though more distinctly in the signal B case, a cluster of errors falls along the line where error equals the merger time separation, we can label these events as misidentifications, where signal A has been misidentified as signal B or vice versa. In both cases, there seems to be a very slight uptick in error at high separations, this could be due to a smaller number of examples present in these areas of parameter space, leading the model to think these are unlikely parameters.

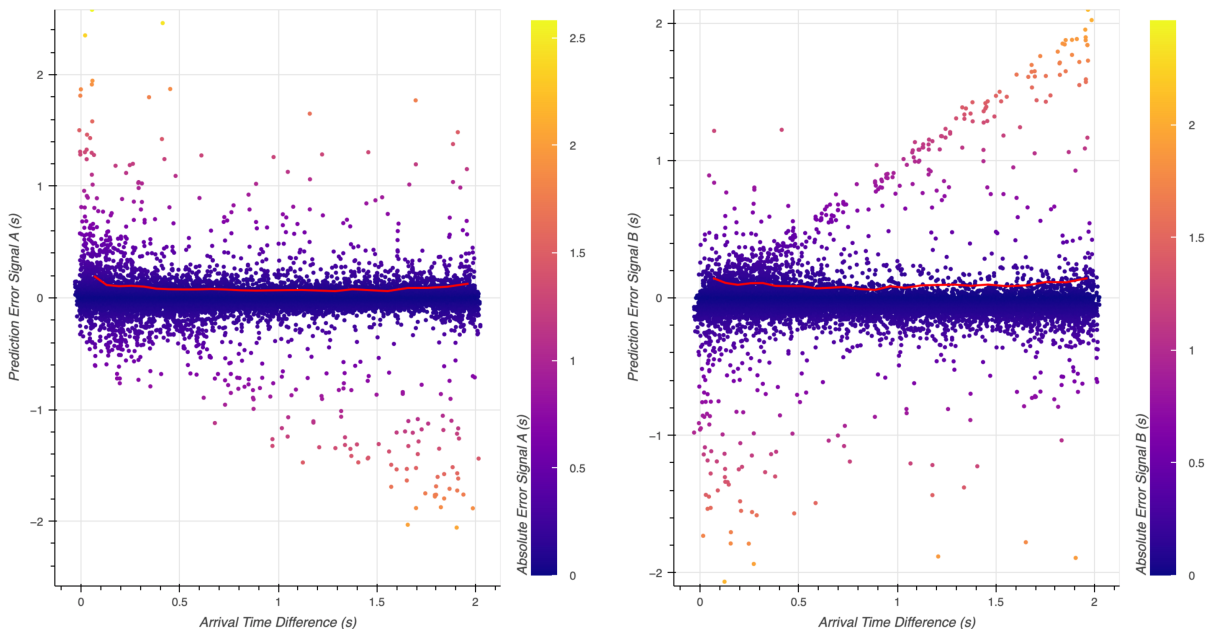
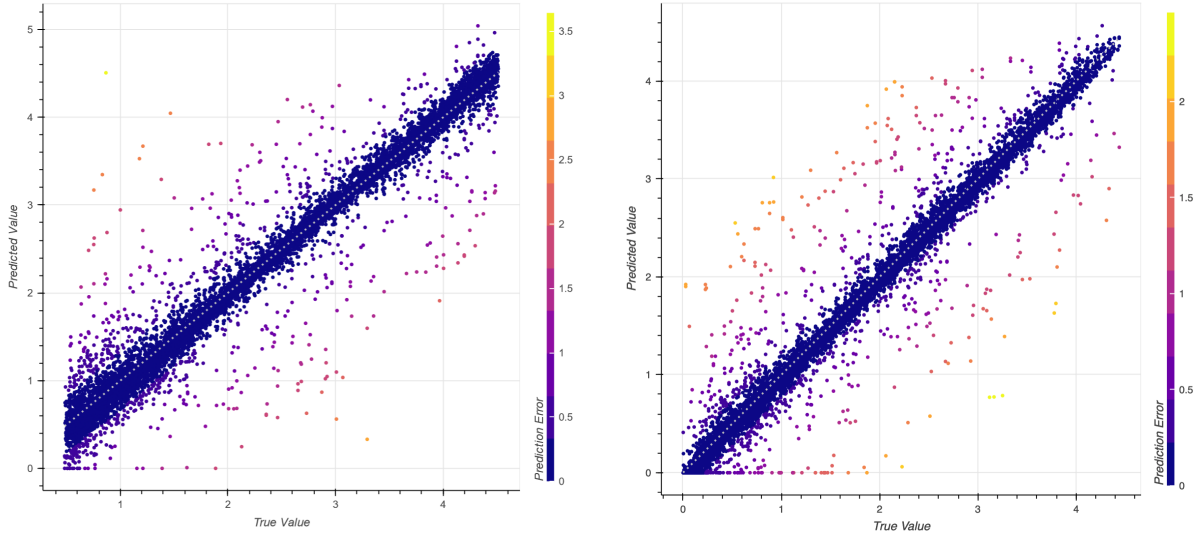


Figure 7.12 | CrossWave merger arrival time prediction errors compared with the time separation between signal A and signal B merger arrival times in the LIGO Hanford detector. *Left:* Error on signal A merger time prediction compared with the time separation between the two mergers. *Right:* Error on signal B merger time prediction compared with the time separation between the two mergers. The colour of the plotted examples depicts the absolute error between the model prediction and the ground

truth value, and the red line shows the rolling average absolute prediction error. For both merger times, we can see a spike in erroneous merger time predictions when the time separation is near zero. This is similar behaviour to what is seen in the classification examples. It is also expected here, since if the mergers are hard to distinguish from each other it will be difficult to determine the specific merger times. An asymmetry arises in which way the model will incorrectly predict the merger, in signal A, defined as the second to arrive in the detector, the model often predicts the signal will arrive later than it does, and for signal B, the model often thinks it will arrive earlier than it does. Since B always arrives first, these are logical assumptions for the model to make in both cases. In both cases, we also see lines of erroneous predictions where the model error equals the time separation. These are believed to be cases where the model believes signal A to be signal B and vice versa. This line is more pronounced for signal B errors, suggesting that signal B's are more commonly mistaken for signal A's than the other way around.

We have decided not to plot the merger times against the mass parameters as we did in the classification case, as these did not seem to have much of an effect on classification ability.

Finally, we finish with a direct comparison of the model prediction to the ground truth value; see Figure 7.13. This is plotted to align with the further presentation of parameter estimation results in Section 7.8.2. We have plotted the predicted merger time in the LIGO Hanford detector compared to the ground truth, as well as the predicted merger time in the LIGO Livingston detector compared to the ground truth. The results for Earth centre merger arrival times are omitted, as these were not considered particularly relevant to this analysis. A full table of parameter estimation results is given by Table 7.3.



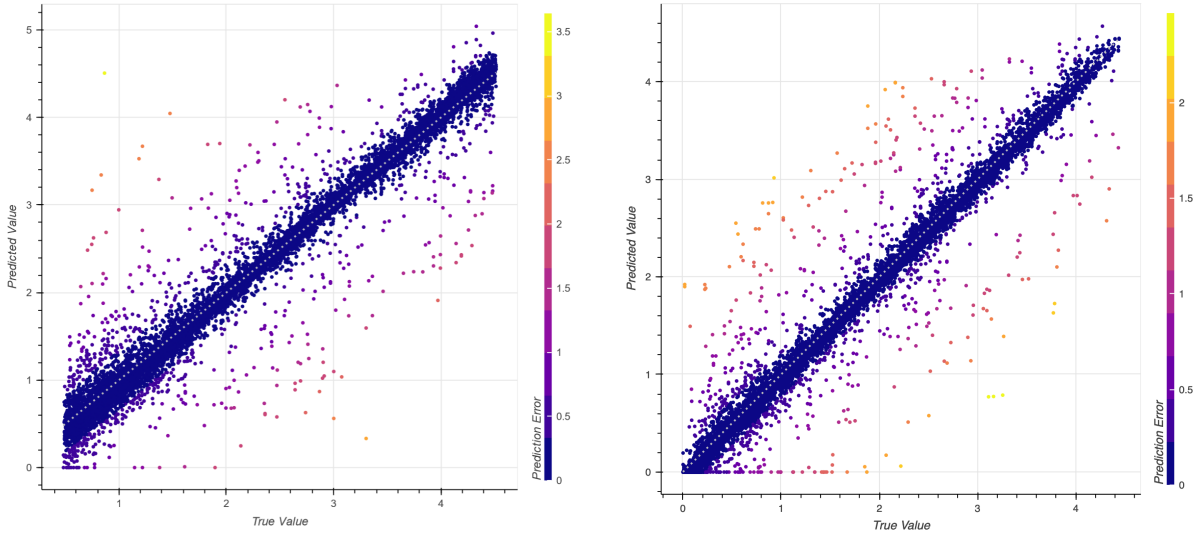


Figure 7.13 | CrossWave signal merger time parameter estimation results. Each pair of plots shows the merger time estimate of signal A (*left*) and signal B (*right*). For each validation example, the ground truth value is represented on the x-axis, and the model prediction is on the y-axis. Each represents the signal merger time in seconds. The colour of each circle depicts the absolute difference between the ground truth value and the model prediction, which will be zero if the point falls on the line of $x = y$, which is also shown on the plot as a dashed grey line. Due to an error in label normalisation, some ground truth values for signal B were less than zero. Unfortunately, due to the choice of loss function used for the regression (ReLU), the model could not output predictions below zero, this meant that it was unable to predict these values correctly. This error may have interfered slightly with the rest of the training process, however other than its inability to classify these examples, there does not seem to be a significant reduction in the performance of classification of signal B merger times. Validation examples with round truth values below zero, and their associated predictions have been omitted from signal B plots for visual clarity. If training were to be repeated this error could be easily rectified, either by correcting the normalization or by altering the choice of activation function. *Upper Left:* Predicted against actual signal A merger time in the simulated LIGO Hanford output. *Upper Right:* Predicted against actual signal B merger time in the simulated LIGO Hanford output. *Lower Left:* Predicted against actual signal A merger time in the simulated LIGO Livingston output. *Lower Right:* Predicted against actual signal B merger time in the simulated LIGO Livingston output.

7.8.2 Other Parameter Estimation Results

As well as attempting to predict the merger arrival times for both signal A and signal B, the model was also tasked to output several other parameters. This was initially done to attempt to increase the model's knowledge about the task at hand but was found to have no significant positive or negative effect on the estimation of the merger time parameters. Thus, it was kept as a feature of the final model as a potential feature of interest for future development into a more advanced fully machine learning-based parameter estimation model for overlapping signals.

A full table of the results of the CrossWave parameter estimation model when run on the 2×10^5 pair validation examples and compared to the ground truth labels can be seen in Table 7.3. For each parameter, an R^2 score is plotted as well as a Mean Absolute Error (MAE). The R^2 score or the “coefficient of determination” is a measure of the goodness of fit of a model. It provides an indication of how well the independent variables in a regression model explain the variability of the dependent variable. An R^2 score of one indicates a perfect predictor, whereas a R^2 score of zero indicates the model is doing no better than outputting the mean value, and a negative value indicates that the model

is performing worse than outputting the mean and so possibly indicates an error in training. The MAE simply indicates the average magnitude of the difference between the model prediction and the ground truth value.

Parameter	R^2 score A	Mean Absolute Error A	R^2 score B	Mean Absolute Error B
H1 Time	0.968	0.100 s	0.963	0.0967 s
L1 Time	0.963	0.0915 s	0.963	0.0965 s
Geocent Time	0.963	0.0923 s	0.963	0.0974 s
Luminosity Distance	-0.834	23.2 Mpc	-0.791	22.7 Mpc
Mass 1	0.613	$7.95 M_\odot$	0.623	$7.79 M_\odot$
Mass 2	0.718	$5.59 M_\odot$	0.715	$5.47 M_\odot$
Spin 1x	-0.00897	0.162	-0.0119	0.165
Spin 1y	-0.0780	0.174	-0.0749	0.178
Spin 1z	0.268	0.273	0.234	0.280
Spin 2x	-0.0117	0.161	-0.0114	0.163
Spin 2y	-0.0709	0.179	-0.0705	0.179
Spin 2z	0.0699	0.311	0.0620	0.316

Table 7.3 | Results of the CrossWave parameter estimation model. For each of the model’s outputted parameters, a Mean Absolute Error (MAE) along with an R^2 score is presented. The MAE indicates the average magnitude of the errors between the model’s predictions on the validation dataset and the corresponding ground truth values. It is a measure of average prediction accuracy, though it doesn’t distinguish between overestimation and underestimation. The R^2 score quantifies how well the model’s predictions explain the variance of the ground truth values in the validation dataset. An R^2 score of one signifies perfect prediction accuracy in the validation examples used. In contrast, a score of zero suggests the model’s predictive capability is no better than simply using the mean value of the validation examples. Negative R^2 values indicate that the model performs worse than a model that would always predict the mean, possibly signalling errors in the training process or model selection.

Out of the parameters that the model was trained to predict, the most accurate are the merger times, with R^2 scores between 0.96 and 0.97, and MAEs between 0.1 s and 0.09 s. As we have seen from previous analyses of these results, this average is driven up by outliers. There does not seem to be a particular detector that performs worse than any other, however, the Hanford signal A MAE is notably higher than the other predictions, whether this is driven up by statistical variance or some other factor is unknown. These results are discussed in more detail previously in Section 7.8.1.

The parameters that the model was next most proficient at extracting, were the mass parameters of each of the two component masses in each of the two binaries, generating four mass values in total: signal A mass 1, signal B mass 1, signal a mass 2, and signal B mass 2. The R^2 scores are lower and the MAE values are higher for mass 1 than for mass 2. This is probably because during parameter generation mass 1 is always forced, by convention, to be the higher mass, meaning that, in general, mass 1 has a larger range of possible values than mass 2. Because the model can use its prediction of mass 1 to constrain mass 2, it can reduce its error. This constraint also allows for a better guess at the average mass for mass 2, since its values have a smaller distribution than mass 2 values. These results can be seen in Figure 7.14. The error margins may be low enough for these results to have some limited usefulness, however, since they lack any form of uncertainty it is unclear exactly what that would be. Perhaps they could be used to inform the priors of another parameter estimation search.

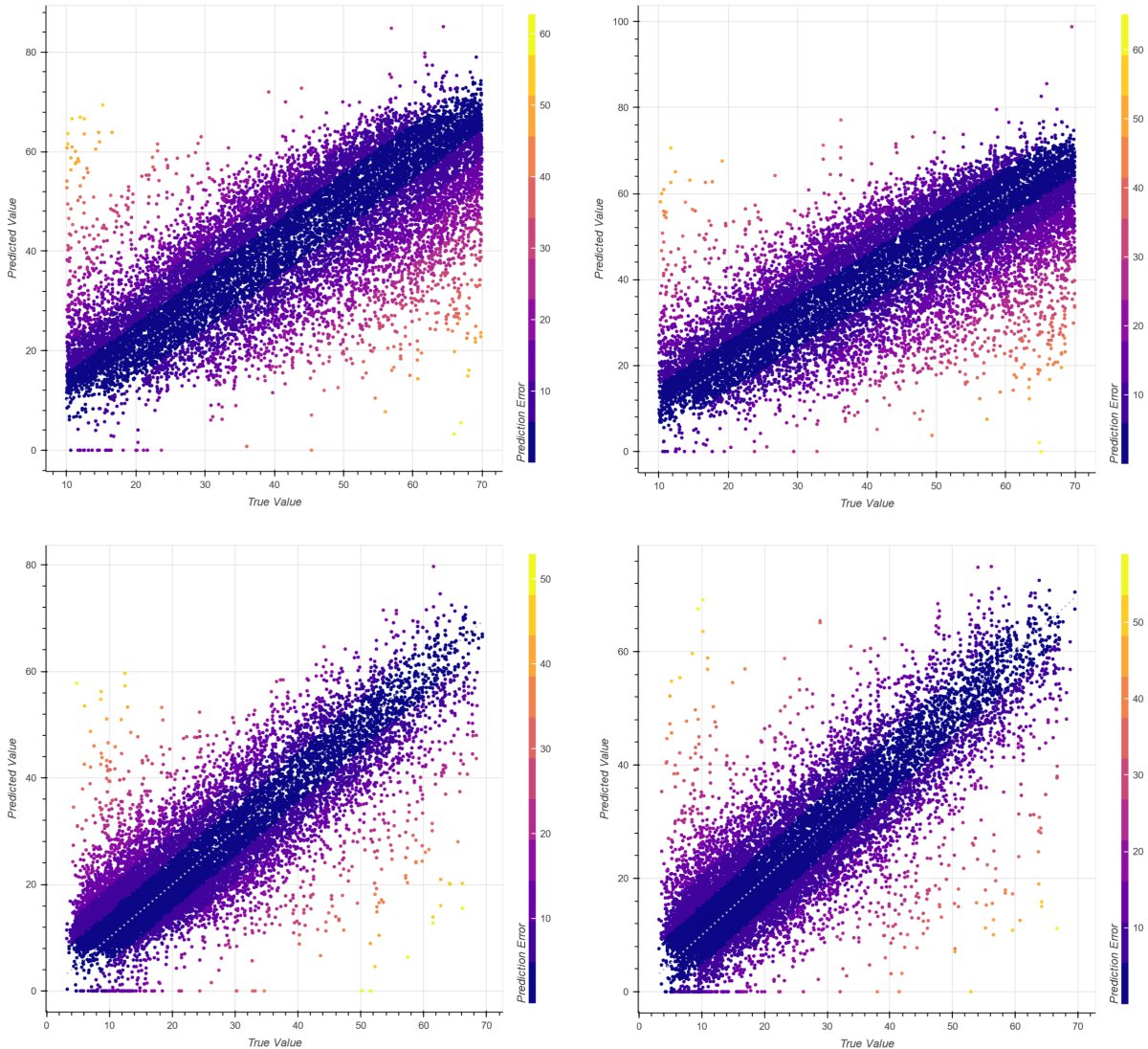
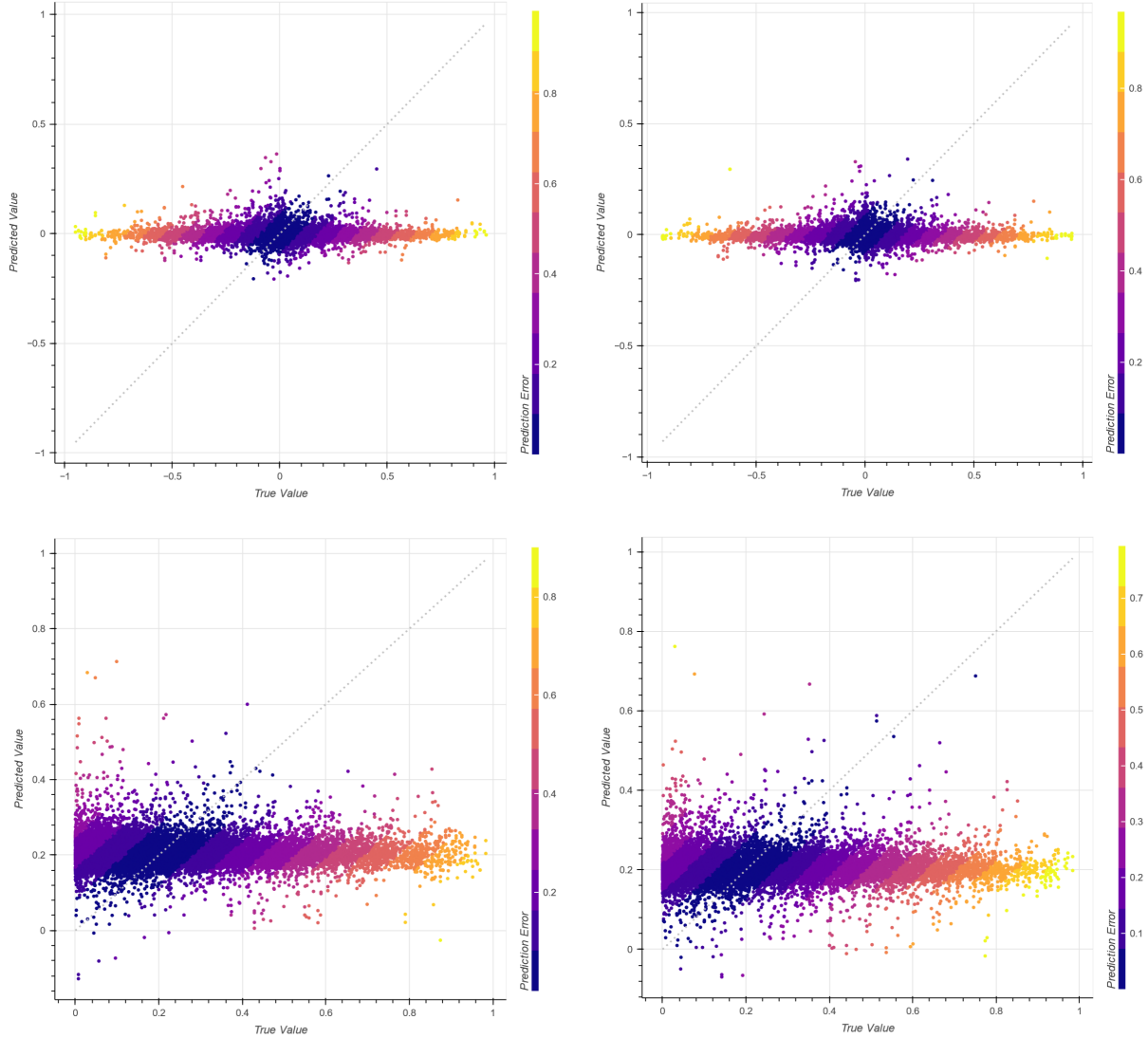
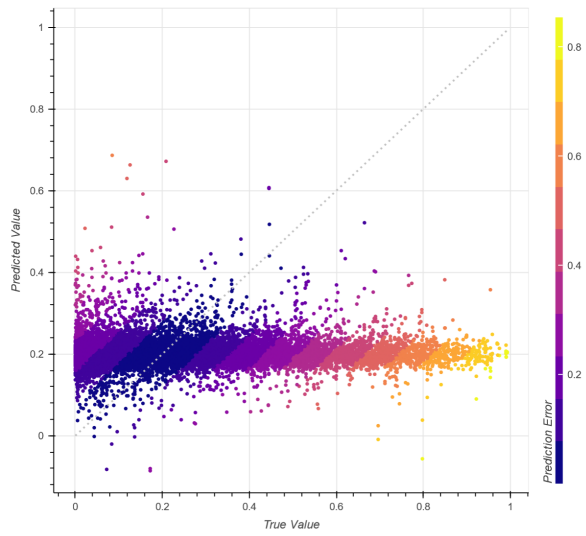
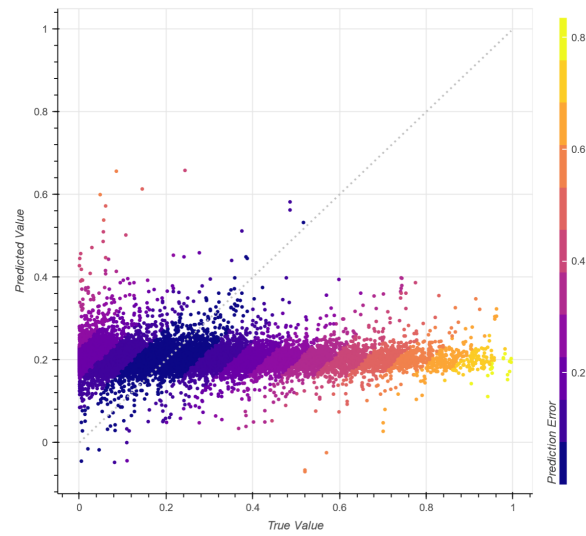
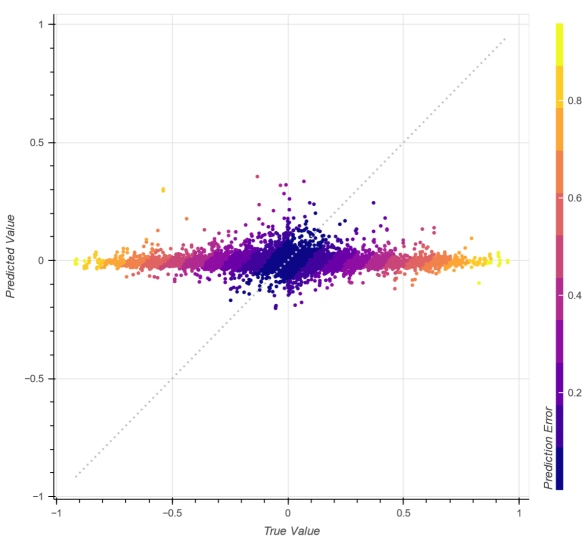
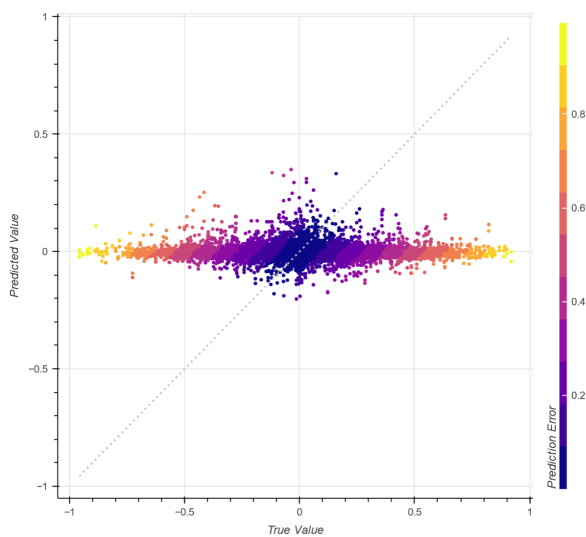
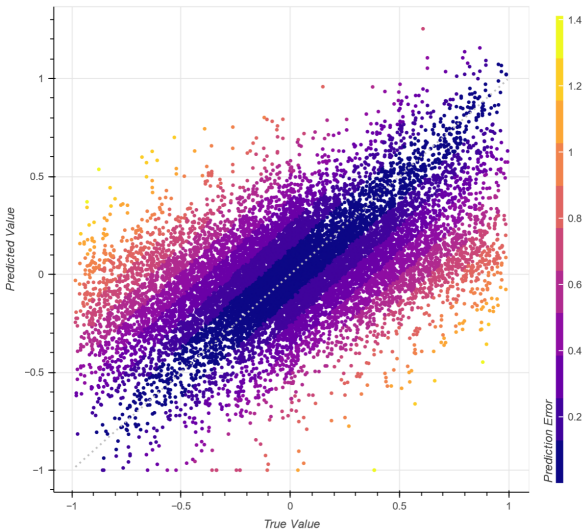
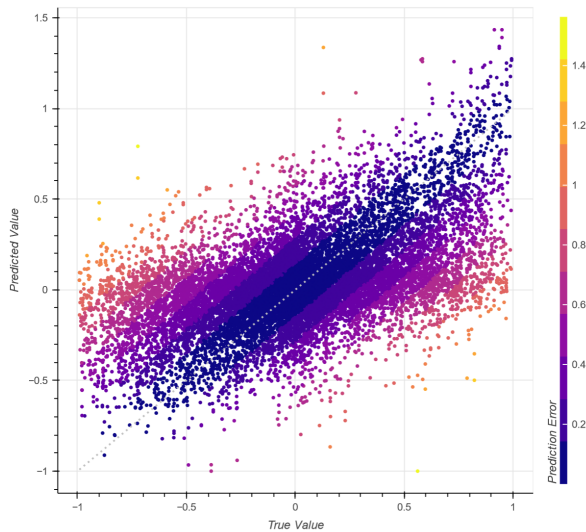


Figure 7.14 | CrossWave companion mass parameter estimation results. Each pair of plots shows the companion mass estimates of signal A (left) and signal B (right). For each validation example, the ground truth value is represented on the x-axis, and the model prediction is on the y-axis. Each represents the companion mass in solar masses. The colour of each circle depicts the difference between the ground truth value and the model prediction, which will be zero if the point falls on the line of $x = y$, which is also shown on the plot as a dashed grey line. After the merger time predictions, the mass plots show the greatest promise, able to predict component masses with a moderate degree of accuracy. Without a comparison to another parameter estimation method, it is unclear exactly how

much use these results can be. *Upper Left*: Predicted against actual signal A companion 1 mass. *Upper Right*: Predicted against actual signal B companion 1 mass. *Lower Left*: Predicted against actual signal A companion 2 mass. *Lower Right*: Predicted against actual signal B companion 2 mass.

Beyond the companion mass parameter estimation results, CrossWave's parameter estimation ability is very limited and is explored here as a demonstration of its lack of proficiency, rather than as a suggestion of usefulness. Of the attempted extraction of the companion spins, only the Z components show any signs of successful estimation. In particular, the Z component of the larger companion shows partial predictive power, although the usefulness of this extraction is questionable. These results are shown in Figure 7.15.





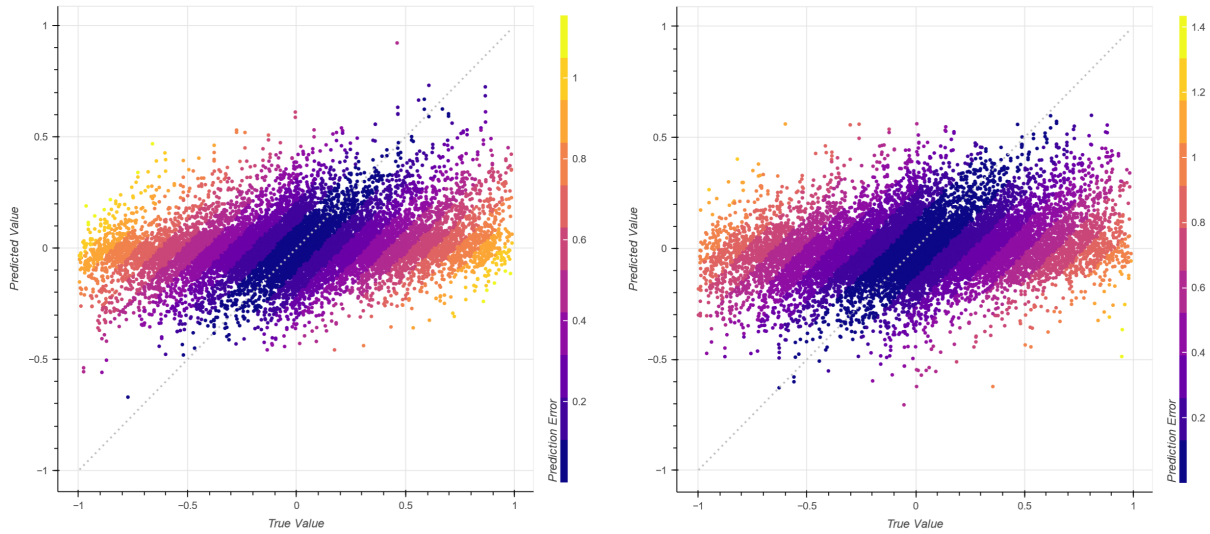


Figure 7.15 | CrossWave regression results for the dimensionless spin components of the two companions in each binary merger, A and B. The left plots show the parameter extracted from merger A, whereas the right results show the same parameter extracted by CrossWave from merger B. The plots show the ground truth value of the dimensionless spin component plotted against the predicted value of the dimensionless spin component. The colour of each validation example indicates the difference between the ground truth and the predicted value, in this case, equivalent to the distance the point is from the line of $x = y$. The results are in the following order from upper to lower:

1. Mass 1 Spin Component X [Left: Signal A, Right: Signal B]
2. Mass 1 Spin Component Y [Left: Signal A, Right: Signal B]
3. Mass 1 Spin Component Z [Left: Signal A, Right: Signal B]
4. Mass 2 Spin Component X [Left: Signal A, Right: Signal B]
5. Mass 2 Spin Component Y [Left: Signal A, Right: Signal B]
6. Mass 2 Spin Component Z [Left: Signal A, Right: Signal B]

There appears to be little difference in classification ability between signal A and signal B. The X and Y components show no classification ability, with the model finding an approximate output value to omit for all validation examples. It was known that extracting the spin parameters from the injected signals would be a challenging task, so this is anticipated. The model appears to show limited classification ability for the Z components, with the Z component for the more massive companion extracted with a stronger correlation than the lower mass companion, for which CrossWave shows only very slight predictive ability.

Finally, CrossWave attempted to extract the luminosity distance of the source. This extraction has failed in an unusual manner. Not only did the model fail to correctly predict the luminosity distance to any degree, but also the results produced a R^2 score, which indicates the model did not even find a good mean value. Why this is the case is unknown. The luminosity distance could be difficult to extract due to its degeneracy with the source inclination angle, a parameter for which prediction was not attempted. The negative R^2 score could be due to another normalisation error which further investigation may reveal. These results can be seen in Figure 7.16.

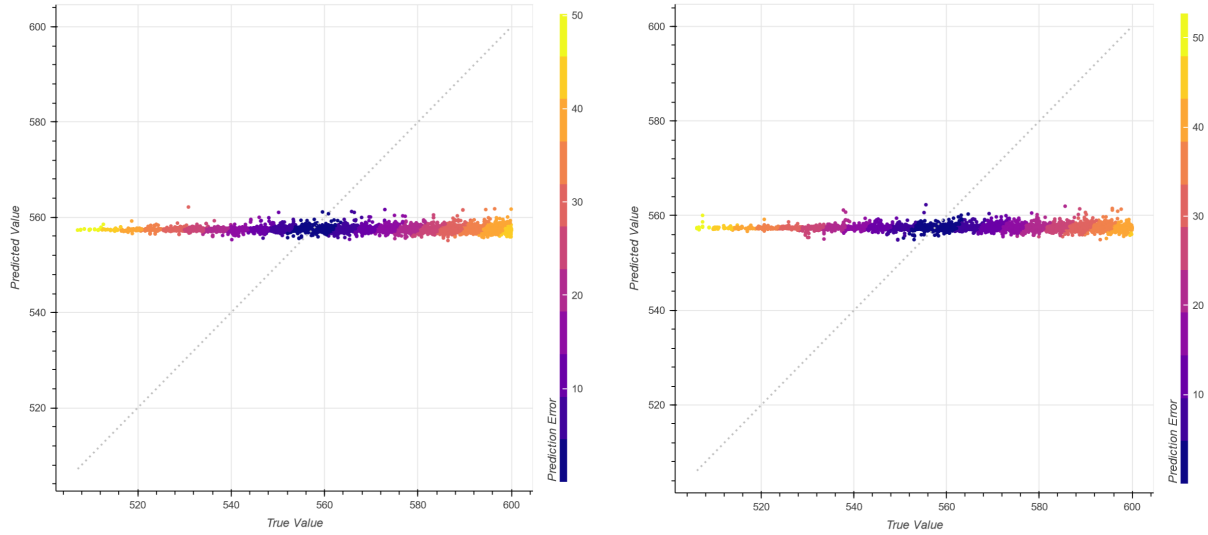


Figure 7.16 | CrossWave model predicted luminosity distance vs ground truth luminosity distance of simulated BBH waveforms. *Left:* Predicted signal A luminosity distance. *Right:* Predicted signal B luminosity distance. The colour of each example point indicates the difference between the predicted and the ground truth value for that example. These plots indicate that there is almost no correlation between the predicted luminosity distance and the ground truth value. The model outputs a very similar value independent of luminosity distance, it is unclear whether this inability arises from a problem with model training and/or data processing, or whether luminosity distance is too difficult for the model to determine because of degeneracy with other parameters such as inclination.

7.9 Discussion and Limitations

Overlapnet shows us that a machine learning model can be trained to distinguish between a single signal and a pair of signals separated by time separations of less than 2.0 s and greater than 0.1 s if the minimum SNR of the signal was sufficient for differentiation. With greater hyperparameter tuning and adjustments to the training dataset, substantive improvements in differentiation ability could be made. This suggests that a machine learning method such as Overlapnet may be a good addition to a future CBC pipeline which has to contend with the possibility of overlapping signals. It could act alone or as one of a suite of methods to switch between alternate parameter estimation methods designed to deal specifically with overlapping signals.

CrossWave has shown that machine learning methods can be used to extract the merger times of two overlapping signals with moderate success. Again, CrossWave or an improved model could be used as part of a larger parameter estimation pipeline, to provide priors to a more established parameter estimation method, once a pair of overlapping signals has been identified in the data.

CrossWave has also demonstrated limited parameter estimation ability of its own, across a few other parameters. It most successfully extracted predictions for the masses of the companions of signals A and B with some accuracy. It also showed limited potential to extract predictions of the Z dimensionless spin component. This method of directly extracting parameters using CrossWave has limited application, as it cannot deal with uncertainty or multi-modal probability spaces, which are needed for a robust and modern parameter search. It is possible that a machine learning method could be created with these features, through the use of Bayesian Neural Networks (notably distinct from Bayesian networks), or a multimodal latent space perhaps within an autoencoder framework, similar to the function of the VITAMIN parameter estimation method [99].

The large model developed for CrossWave has performed well, and warrants further investigation, and comparison against other detection methods in the single signal detection problem are recommended and were desired but abandoned due to time constraints.

Bibliography

- [1] Sir Issac Newton, *Newton's Principia: The Mathematical Principles of Natural Philosophy* (1846)
- [2] E. J. Khamara, *Space, Time, And Theology in the Leibniz-Newton Controversy*, Vol. 6 (Walter de Gruyter, 2013)
- [3] N. David Mermin, *Space and Time in Special Relativity* (McGraw-Hill, 1968)
- [4] A. P. French, *Special Relativity* (CRC Press, 2017)
- [5] K. S. Thorne, J. A. Wheeler, and C. W. Misner, *Gravitation* (Freeman San Francisco, CA, 2000)
- [6] S. Dodelson, *Gravitational Lensing*. (Cambridge University Press, 2017)
- [7] D. Park, C. Kim, H. M. Lee, Y.-B. Bae, and K. Belczynski, *Black Hole Binaries Dynamically Formed in Globular Clusters*, Monthly Notices of the Royal Astronomical Society **469**, 4665 (2017), URL: <https://doi.org/10.1093/mnras/stx1015>
- [8] R. Abbott et al., *Open Data from the Third Observing Run of LIGO, Virgo, KAGRA and GEO*, The Astrophysical Journal Supplement Series **267**, (2023), URL: <https://doi.org/10.3847/1538-4365/acdc9f>
- [9] A. Buikema et al., *Sensitivity and Performance of the Advanced LIGO Detectors in the Third Observing Run*, Physical Review D **102**, (2020), URL: <https://doi.org/10.1103/PhysRevD.102.062003>
- [10] L. Alzubaidi, J. Zhang, A. J. Humaidi, A. Al-Dujaili, Y. Duan, O. Al-Shamma, J. Santamaría, M. A. Fadhel, M. Al-Amidie, and L. Farhan, *Review of Deep Learning: Concepts, CNN Architectures, Challenges, Applications, Future Directions*, Journal of Big Data **8**, (2021), URL: <https://doi.org/10.1186/s40537-021-00444-8>
- [11] Dmitry Ivanov, Aleksandr Chezhegov, Mikhail Kiselev, Andrey Grunin, and Denis Larionov, *Neuromorphic Artificial Intelligence Systems*, Frontiers in Neuroscince (n.d.), URL: <https://doi.org/10.3389/fnins.2022.959626>
- [12] L. Deng, *The Mnist Database of Handwritten Digit Images for Machine Learning Research*, IEEE Signal Processing Magazine **29**, (2012), URL: <https://doi.org/10.1109/MSP.2012.2211477>
- [13] John S. Bridle, *Probabilistic Interpretation of Feedforward Classification Network Outputs, With Relationships to Statistical Pattern Recognition.*, Neurocomputing: Algorithms, Architectures and Applications
- [14] B. Haskell and M. Bejger, *Astrophysics with Continuous Gravitational Waves*, Nature Astronomy (2023), URL: <https://doi.org/10.1038/s41550-023-02059-w>
- [15] B. P. Abbott, R. Abbott, T. D. Abbott, M. R. Abernathy, F. Acernese, K. Ackley, C. Adams, T. Adams, and T. Adams, *Observation of Gravitational Waves from a Binary Black Hole Merger*, Physical Review Letters **116**, (2016), URL: <https://doi.org/10.1103/PhysRevLett.116.061102>
- [16] N. J. Cornish and K. Shuman, *Black Hole Hunting with LISA*, Physical Review D **101**, (n.d.), URL: <https://doi.org/10.1103/PhysRevD.101.124008>
- [17] D Davis et al., *LIGO Detector Characterization in the Second and Third Observing Runs*, Classical and Quantum Gravity **38**, (2021), URL: <https://doi.org/10.1088/1361-6382/abfd85>
- [18] B. P. Abbott, R. Abbott, T. D. Abbott, S. Abraham, F. Acernese, K. Ackley, C. Adams, and et al, *All-Sky Search for Short Gravitational-Wave Bursts in the First Advanced LIGO Run*, Physical Review D **95**, (2016), URL: <https://doi.org/10.1103/PhysRevD.95.042003>

- [19] B. P. Abbott et al., *Multi-Messenger Observations of a Binary Neutron Star Merger**, The Astrophysical Journal Letters **848**, (2017), URL: <https://doi.org/10.3847/2041-8213/aa91c9>
- [20] B. P. Abbott et al., *All-Sky Search for Short Gravitational-Wave Bursts in the Second Advanced LIGO and Advanced Virgo Run*, Physical Review D **100**, (2019), URL: <https://doi.org/10.1103/PhysRevD.100.024017>
- [21] R. Abbott et al., *All-Sky Search for Short Gravitational-Wave Bursts in the Third Advanced LIGO and Advanced Virgo Run*, Physical Review D **104**, (2021), URL: <https://doi.org/10.1103/PhysRevD.104.122004>
- [22] Marco Drago et al., *Coherent Waveburst, A Pipeline for Unmodeled Gravitational-Wave Data Analysis*, Softwarex **14**, (2021), URL: <https://doi.org/10.1016/j.softx.2021.100678>
- [23] Patrick J Sutton et al., *X-Pipeline: An Analysis Package for Autonomous Gravitational-Wave Burst Searches*, New Periodical of Physics **12**, (2010), URL: <https://doi.org/10.1088/1367-2630/12/5/053034>
- [24] David Radice, Viktoriya Morozova, Adam Burrows, David Vartanyan, and Hiroki Nagakura, *Characterizing the Gravitational Wave Signal from Core-Collapse Supernovae*, The Astrophysical Periodical Letters **876**, (2019), URL: <https://doi.org/10.3847/2041-8213/ab191a>
- [25] Antonis Mytidis, Michael Coughlin, and Benrand Whiting, *Constraining the R-Mode Saturation Amplitude from a Hypothetical Detection of R-Mode Gravitational Waves from a Newborn Neutron Star*, The Astrophysical Periodical **810**, (2015), URL: <https://doi.org/10.1088/0004-637X/810/1/27>
- [26] R. Lynch, S. Vitale, R. Essick, E. Katsavounidis, and F. Robinet, *Information-Theoretic Approach to the Gravitational-Wave Burst Detection Problem*, Physical Review D **95**, (2017), URL: <https://doi.org/10.1103/PhysRevD.95.104046>
- [27] Neil J Cornish and Tyson B Littenberg, *Bayeswave: Bayesian Inference for Gravitational Wave Bursts and Instrument Glitches*, Classical and Quantum Gravity **32**, (2015), URL: <https://doi.org/10.1088/0264-9381/32/13/135012>
- [28] Vasileios Skliris, Michael R. K. Norman, and Patrick J. Sutton, *Real-Time Detection of Unmodelled Gravitational-Wave Transients Using Convolutional Neural Networks*, Arxiv, URL: <https://doi.org/10.48550/arXiv.2009.14611>
- [29] R. Abbott et al., *Observation of Gravitational Waves from Two Neutron Star–Black Hole Coalescences*, The Astrophysical Journal Letters **915**, (2021), URL: <https://doi.org/10.3847/2041-8213/ac082e>
- [30] B. P. Abbott et al., *GWTC-1: A Gravitational-Wave Transient Catalog of Compact Binary Mergers Observed by LIGO and Virgo during the First and Second Observing Runs*, Physical Review X **9**, (2019), URL: <https://doi.org/10.1103/PhysRevX.9.031040>
- [31] R. Abbott et al., *GWTC-2: Compact Binary Coalescences Observed by LIGO and Virgo during the First Half of the Third Observing Run*, Physical Review X **11**, (2021), URL: <https://doi.org/10.1103/PhysRevX.11.021053>
- [32] R. Abbott et al., *GWTC-3: Compact Binary Coalescences Observed by LIGO and Virgo during the Second Part of the Third Observing Run*, Arxiv, URL: <https://doi.org/10.48550/arXiv.2111.03606>
- [33] J. Antoniadis et al., *The Second Data Release from the European Pulsar Timing Array - III. Search for Gravitational Wave Signals EPTA Collaboration and Inpta Collaboration*, Astronomy & Astrophysics **678**, (2023), URL: <https://doi.org/10.1051/0004-6361/202346844>

- [34] Warren R. Brown, Mukremin Kilic, Carlos Allende Prieto, A. Gianninas, and Scott J. Kenyon, *The ELM Survey. V. Merging Massive White Dwarf Binaries*, The Astrophysical Journal **769**, (2013), URL: <https://doi.org/10.1088/0004-637X/769/1/66>
- [35] A. Lamberts, S. Blunt, T. B. Littenberg, S. Garrison-Kimmel, T. Kupfer, and R. E. Sanderson, *Predicting the LISA White Dwarf Binary Population in the Milky Way with Cosmological Simulations*, JF Monthly Notices of the Royal Astronomical Society **450**, (2019), URL: <https://doi.org/10.1093/mnras/stz2834>
- [36] P. A. R. Ade et al., *Planck 2015 Results: XIII. Cosmological Parameters*, Astronomy & Astrophysics **594**, (2016), URL: <https://doi.org/10.1051/0004-6361/201525830>
- [37] Chiara Caprini and Daniel G Figueroa, *Cosmological Backgrounds of Gravitational Waves*, Classical and Quantum Gravity **35**, (2018), URL: <https://doi.org/10.1088/1361-6382/aac608>
- [38] B. Link, L. M. Franco, and R. I. Epstein, *Starquake-Induced Magnetic Field and Torque Evolution in Neutron Stars*, Astrophysical Journal **508**, (1998), URL: <https://doi.org/10.1086/306457>
- [39] E. Giliberti and G. Cambiotti, *Starquakes in Millisecond Pulsars and Gravitational Waves Emission*, Monthly Notices of the Royal Astronomical Society **511**, (2022), URL: <https://doi.org/10.1093/mnras/stac245>
- [40] M. Modjaz, C. P. Gutiérrez, and I. Arcavi, *New Regimes in the Observation of Core-Collapse Supernovae*, Nature Astronomy **3**, 717 (2019), URL: <https://doi.org/10.1038/s41550-019-0856-2>
- [41] S. E. Gossan, P. Sutton, A. Stuver, M. Zanolin, K. Gill, and C. D. Ott, *Observing Gravitational Waves from Core-Collapse Supernovae in the Advanced Detector Era*, Physical Review D **93**, (2016), URL: <https://doi.org/10.1103/PhysRevD.93.042002>
- [42] N. Andersson, V. Ferrari, D. I. Jones, K. D. Kokkotas, B. Krishnan, J. S. Read, L. Rezzolla, and B. Zink, *Gravitational Waves from Neutron Stars: Promises and Challenges*, General Relativity and Gravitation **43**, 409 (2011), URL: <https://doi.org/10.1007/s10714-010-1059-4>
- [43] M. Abramowicz, M. Bejger, É. Gourgoulhon, and O. Straub, *A Galactic Centre Gravitational-Wave Messenger*, Scientific Reports **10**, (2020), URL: <https://doi.org/10.1038/s41598-020-63206-1>
- [44] S. Olmez, V. Mandic, and X. Siemens, *Gravitational-Wave Stochastic Background from Kinks and Cusps on Cosmic Strings*, Physical Review D **81**, (2010), URL: <https://doi.org/10.1103/PhysRevD.81.104028>
- [45] M. H. P. M. van Putten, *Proposed Source of Gravitational Radiation from a Torus around a Black Hole*, Physical Review Letters **87**, (2001), URL: <https://doi.org/10.1103/PhysRevLett.87.091101>
- [46] Takashi Hiramatsu, Masahiro Kawasaki, and Ken'ichi Saikawa, *On the Estimation of Gravitational Wave Spectrum from Cosmic Domain Walls*, Journal of Cosmology and Astroparticle Physics **2014**, (2014), URL: <https://doi.org/10.1088/1475-7516/2014/02/031>
- [47] Marc Favata, *The Gravitational-Wave Memory Effect*, Classical and Quantum Gravity **27**, (2010), URL: <https://doi.org/10.1088/0264-9381/27/8/084036>
- [48] Michael R. K. Norman, *Cuphenom*, (2023), URL: <https://github.com/mrknorman/cuphenom>
- [49] Christian D. Ott, Adam Burrows, Luc Dessart, and Eli Livne, *Characterizing the Gravitational Wave Signal from Core-Collapse Supernovae*, Physical Review Letters (2006), URL: <https://doi.org/10.1103/PhysRevLett.96.201102>
- [50] C. M. Biwer, Collin D. Capano, Soumi De, Miriam Cabero, Duncan A. Brown, Alexander H. Nitz, and V. Raymond, *Pycbc Inference: A Python-Based Parameter Estimation Toolkit for Compact Bi-*

- nary Coalescence Signals*, Publications of the Astronomical Society of the Pacific **131**, (2019), URL: <https://doi.org/10.1088/1538-3873/aaef0b>
- [51] M. Purrer, S. Khan, F. Ohme, O. Birnholtz, and L. London, *Imrphenomd: Phenomenological Waveform Model*, URL: <https://ui.adsabs.harvard.edu/abs/2023ascl.soft07019P/abstract>
- [52] Daniel George and E. A. Huerta, *Deep Neural Networks to Enable Real-Time Multimessenger Astrophysics*, Physical Review D **97**, (2018), URL: <https://doi.org/10.1103%2Fphysrevd.97.044039>
- [53] H. Gabbard, M. Williams, F. Hayes, and C. Messenger, *Matching Matched Filtering with Deep Networks for Gravitational-Wave Astronomy*, Physical Review Letters **120**, (2018), URL: <https://doi.org/10.1103/PhysRevLett.120.141103>
- [54] D Davis et al., *LIGO Detector Characterization in the Second and Third Observing Runs*, Classical and Quantum Gravity **38**, (2021), URL: <https://doi.org/10.1088/1361-6382/abfd85>
- [55] P. Singh, *Natural Language Processing*, in *Machine Learning with Pyspark: with Natural Language Processing and Recommender Systems* (2019), pp. 191–218, URL: https://doi.org/10.1007/978-1-4842-4131-8_9
- [56] Ashish Vaswani, Noam Shazeer, Niki Parmar, Jakob Uszkoreit, Llion Jones, Aidan N. Gomez, Łukasz Kaiser, and Illia Polosukhin, *Attention Is All You Need*, in *Advances in Neural Information Processing Systems*, Vol. 30 (Curran Associates, Inc., 2017), URL: <https://doi.org/10.5555/3295222.3295349>
- [57] T. Luong, H. Pham, and C. D. Manning, *Effective Approaches to Attention-Based Neural Machine Translation*, in *Proceedings of the 2015 Conference on Empirical Methods in Natural Language Processing* (Association for Computational Linguistics, 2015), pp. 1412–1421, URL: <https://doi.org/10.18653/v1/D15-1166>
- [58] Y. Yan, J. Chen, W. Qi, N. Bhendawade, Y. Gong, N. Duan, and R. Zhang, *EL-Attention: Memory Efficient Lossless Attention for Generation*, in *Proceedings of the 38th International Conference on Machine Learning* (2021), pp. 11648–11658, URL: <https://proceedings.mlr.press/v139/yan21a.html>
- [59] C. Li, Y. Yang, M. Feng, S. Chakradhar, and H. Zhou, *Optimizing Memory Efficiency for Deep Convolutional Neural Networks on Gpus*, in *SC '16: Proceedings of the International Conference for High Performance Computing, Networking, Storage and Analysis* (2016), pp. 633–644, URL: <https://doi.org/10.1109/SC.2016.53>
- [60] Michael R. K. Norman, *Gwflow*, (2023), URL: <https://github.com/mrknorman/gravyflow>
- [61] P. Relton, Accurate Identification of the Nature of Signals in Ground-Based Gravitational-Wave Interferometer Data, 2023, URL: <https://orca.cardiff.ac.uk/id/eprint/160395>
- [62] P. Relton and V. Raymond, *Parameter Estimation Bias from Overlapping Binary Black Hole Events in Second Generation Interferometers*, Physical Review D **104**, (2021), URL: <https://doi.org/10.1103/PhysRevD.104.084039>
- [63] Python Software Foundation, *Python Programming Language*, URL: <https://www.python.org/>
- [64] Charles R. Harris et al., *Array Programming with Numpy*, Nature **585**, 357 (2020), URL: <https://doi.org/10.1038/s41586-020-2649-2>
- [65] Martin Abadi et al., *Large-Scale Machine Learning on Heterogeneous Systems*, URL: <https://doi.org/10.5281/zenodo.4724125>

- [66] Bokeh Development Team, *Bokeh: Python Library for Interactive Visualization*, in (2018), URL: <https://bokeh.pydata.org/en/latest/>
- [67] J. T. Hancock and T. M. Khoshgoftaar, *Survey on Categorical Data for Neural Networks*, Journal of Big Data **7**, (2020), URL: <https://doi.org/10.1186/s40537-020-00305-w>
- [68] S. K. Singh, S. Kumar, and P. S. Mehra, *Chat GPT & Google Bard AI: A Review*, in *2023 International Conference on IoT, Communication and Automation Technology (ICICAT)* (2023), pp. 1–6, URL: <https://doi.org/10.1109/ICICAT57735.2023.10263706>
- [69] M. Anand, *Analyzing Moon Rocks*, Science **344**, 365 (2014), URL: <https://doi.org/10.1126/science.1253266>
- [70] D. A. Gurnett and W. S. Kurth, *Plasma Densities near and Beyond the Heliopause from the Voyager 1 and 2 Plasma Wave Instruments*, Nature Astronomy **3**, 1024 (2019), URL: <https://doi.org/10.1038/s41550-019-0918-5>
- [71] C. L. Cowan, F. Reines, F. B. Harrison, H. W. Kruse, and A. D. McGuire, *Detection of the Free Neutrino: A Confirmation*, Science **124**, 103 (1956), URL: <https://doi.org/10.1126/science.124.3212.103>
- [72] J. O'Callaghan, *The Oh-My-God Particle*, New Scientist **258**, 46 (2023), URL: [https://doi.org/10.1016/S0262-4079\(23\)01010-2](https://doi.org/10.1016/S0262-4079(23)01010-2)
- [73] M. Punturo et al., *The Einstein Telescope: A Third-Generation Gravitational Wave Observatory*, Classical and Quantum Gravity **27**, (2010), URL: <https://doi.org/10.1088/0264-9381/27/19/194002>
- [74] David Reitze et al., *Cosmic Explorer: The U.S. Contribution to Gravitational-Wave Astronomy Beyond LIGO*, arXiv, URL: <https://doi.org/10.48550/arXiv.1907.04833>
- [75] Karsten Danzmann and Albrecht Rüdiger, *LISA Technology—Concept, Status, Prospects*, Classical and Quantum Gravity **20**, (2003), URL: <https://doi.org/10.1088/0264-9381/20/10/301>
- [76] S. Braibant, G. Giacomelli, and M. Spurio, *Particles and Fundamental Interactions: An Introduction to Particle Physics* (Springer Netherlands, 2011)
- [77] M. K. Gaillard, P. D. Grannis, and F. J. Sciulli, *The Standard Model of Particle Physics*, Reveiws of Modern Physics **71**, (1999), URL: <https://doi.org/10.1103/RevModPhys.71.S96>
- [78] M. Ishak, *Testing General Relativity in Cosmology*, Living Reviews in Relativity **22**, (2018), URL: <https://doi.org/10.1007/s41114-018-0017-4>
- [79] A. Cappi, *The Concept of Gravity Before Newton*, Culture and Cosmos **16**, 207 (2012), URL: <https://doi.org/10.46472/CC.01216.0233>
- [80] *2018 CODATA Value: Newtonian Constant of Gravitation*, The NIST Reference on Constants, Units, And Uncertainty. (n.d.), URL: <https://physics.nist.gov/cgi-bin/cuu/Value?bg>
- [81] G. Musser, *What Is Spacetime?*, Scientific American **318**, (2018), URL: <https://www.jstor.org/stable/27173507>
- [82] *This Month in Physics History*, (n.d.), URL: <https://www.aps.org/publications/apsnews/202008/history.cfm>
- [83] N. I. Amel'kin, *Precession of the Orbit of Mercury*, Doklady Physics **64**, 470 (2019), URL: <https://doi.org/10.1134/S1028335819120073>
- [84] R. S. Shankland, *Michelson-Morley Experiment*, American Journal of Physics **32**, 16 (1964)
- [85] A. Michaud, *From Classical to Relativistic Mechanics via Maxwell*, International Journal of Engineering Research and Development (2013)

- [86] H. A. Lorentz, *Electromagnetic Phenomena in a System Moving with Any Velocity Smaller Than That of Light*, **6**, 809 (1904), URL: https://en.wikisource.org/wiki/Electromagnetic_phenomena
- [87] D C Champeney, G R Isaak, and A M Khan, *A Time Dilatation Experiment Based on the Mössbauer Effect*, Proceedings of the Physical Society **85**, (n.d.), URL: <https://doi.org/10.1088/0370-1328/85/3/317>
- [88] Bernard Schutz, *Gravity from the Ground up* (Cambridge University Press, 2003)
- [89] A. Einstein and N. Rosen, *On Gravitational Waves*, Journal of the Franklin Institute **223**, 43 (1937), URL: [https://doi.org/10.1016/S0016-0032\(37\)90583-0](https://doi.org/10.1016/S0016-0032(37)90583-0)
- [90] S. Du, *On the Measurement of the Speed of Gravitational Waves*, The European Physical Journal Plus **136**, (2021), URL: <https://doi.org/10.1140/epjp/s13360-021-01362-7>
- [91] M. Pitkin, S. Reid, S. Rowan, and J. Hough, *Gravitational Wave Detection by Interferometry (Ground and Space)*, Living Reviews in Relativity **15**, (2011), URL: <https://doi.org/10.12942/lrr-2011-5>
- [92] B. P. Abbott et al., *Gw150914: The Advanced LIGO Detectors in the Era of First Discoveries*, URL: <https://doi.org/10.1103/PhysRevLett.116.131103>
- [93] C. Bond, D. Brown, A. Freise, and K. A. Strain, *Interferometer Techniques for Gravitational-Wave Detection*, Living Reviews in Relativity **19**, (2017), URL: <https://doi.org/10.1007/s41114-016-0002-8>
- [94] B. F. Schutz and M. Tinto, *Antenna Patterns of Interferometric Detectors of Gravitational Waves – I. Linearly Polarized Waves*
- [95] M. Saleem et al., *The Science Case for LIGO-India*, URL: <https://doi.org/10.1088/1361-6382/ac3b99>
- [96] B. F. Schutz, *Networks of Gravitational Wave Detectors and Three Figures of Merit*, Classical and Quantum Gravity **28**, (2011), URL: <https://doi.org/10.1088/0264-9381/28/12/125023>
- [97] T. D. Gebhard, N. Kilbertus, I. Harry, and B. Scholkopf, *Convolutional Neural Networks: A Magic Bullet for Gravitational-Wave Detection?*, Physical Review D **100**, (n.d.), URL: <https://doi.org/10.1103/PhysRevD.100.063015>
- [98] J. D. Álvares, J. A. Font, F. F. Freitas, O. G. Freitas, A. P. Morais, S. Nunes, A. Onofre, and A. Torres-Forné, *Exploring Gravitational-Wave Detection and Parameter Inference Using Deep Learning Methods*, Classical and Quantum Gravity **38**, (2021), URL: <https://doi.org/10.1088/1361-6382/ac0455>
- [99] H. Gabbard, C. Messenger, I. S. Heng, F. Tonolini, and R. Murray-Smith, *Bayesian Parameter Estimation Using Conditional Variational Autoencoders for Gravitational-Wave Astronomy*, Nature Physics **18**, (2022), URL: <https://doi.org/10.1038/s41567-021-01425-7>
- [100] Alberto Iess, Elena Cuoco, Filip Morawski, and Jade Powell, *Core-Collapse Supernova Gravitational-Wave Search and Deep Learning Classification*, Machine Learning: Science and Technology **1**, (2020), URL: <https://doi.org/10.1088/2632-2153/ab7d31>
- [101] M. L. Chan, I. S. Heng, and C. Messenger, *Detection and Classification of Supernova Gravitational Wave Signals: A Deep Learning Approach*, Physical Review D **102**, (2020), URL: <https://doi.org/10.1103/PhysRevD.102.043022>
- [102] T. Marianer, D. Poznanski, and J. X. Prochaska, *A Semisupervised Machine Learning Search for Never-Seen Gravitational-Wave Sources*, Monthly Notices of the Royal Astronomical Society **500**, (2021), URL: <https://doi.org/10.1093/mnras/staa3550>

- [103] R. Biswas et al., *Application of Machine Learning Algorithms to the Study of Noise Artifacts in Gravitational-Wave Data*, Physical Review D **88**, (2013), URL: <https://doi.org/10.1103/PhysRevD.88.062003>
- [104] S. Bahaaadini, V. Noroozi, N. Rohani, S. Coughlin, M. Zevin, J.R. Smith, V. Kalogera, and A. Katsaggelos, *Machine Learning for Gravity Spy: Glitch Classification and Dataset*, Information Sciences **444**, 172 (2018), URL: <https://doi.org/10.1016/j.ins.2018.02.068>
- [105] C. Dreissigacker, R. Sharma, C. Messenger, R. Zhao, and R. Prix, *Deep-Learning Continuous Gravitational Waves*, Physical Review D **100**, (2019), URL: <https://doi.org/10.1103/PhysRevD.100.044009>
- [106] C. Dreissigacker and R. Prix, *Deep-Learning Continuous Gravitational Waves: Multiple Detectors and Realistic Noise*, Physical Review D **102**, (2020), URL: <https://doi.org/10.1103/PhysRevD.102.022005>
- [107] J. Bayley, C. Messenger, and G. Woan, *Robust Machine Learning Algorithm to Search for Continuous Gravitational Waves*, Physical Review D **102**, (2020), URL: <https://doi.org/10.1103/PhysRevD.102.083024>
- [108] B. Beheshtipour and M. A. Papa, *Deep Learning for Clustering of Continuous Gravitational Wave Candidates*, Physical Review D **101**, (2020), URL: <https://doi.org/10.1103/PhysRevD.101.064009>
- [109] A. Utina, F. Marangio, F. Morawski, A. Iess, T. Regimbau, G. Fiameni, and E. Cuoco, *Deep Learning Searches for Gravitational Wave Stochastic Backgrounds*, in *2021 International Conference on Content-Based Multimedia Indexing (CBMI)* (2021), URL: <https://doi.org/10.1109/CBMI50038.2021.9461904>
- [110] G. Vajente, Y. Huang, M. Isi, J. C. Driggers, J. S. Kissel, M. J. Szczepanficzky, and S. Vitale, *Machine-Learning Nonstationary Noise Out of Gravitational-Wave Detectors*, Physical Review D **101**, (2020), URL: <https://doi.org/10.1103/PhysRevD.101.042003>
- [111] R. Ormiston, T. Nguyen, M. Coughlin, R. X. Adhikari, and E. Katsavounidis, *Noise Reduction in Gravitational-Wave Data via Deep Learning*, Physical Review Research **2**, (2020), URL: <https://doi.org/10.1103/PhysRevResearch.2.033066>
- [112] N. Mukund et al., *Neural Sensing and Control in a Kilometer-Scale Gravitational-Wave Observatory*, URL: <https://doi.org/10.1103/PhysRevApplied.20.064041>
- [113] F. Badaracco et al., *Machine Learning for Gravitational-Wave Detection: Surrogate Wiener Filtering for the Prediction and Optimized Cancellation of Newtonian Noise at Virgo*, Classical and Quantum Gravity **37**, (2020), URL: <https://doi.org/10.1088/1361-6382/abab64>
- [114] S. Khan and R. Green, *Gravitational-Wave Surrogate Models Powered by Artificial Neural Networks*, Physical Review D **103**, (2021), URL: <https://doi.org/10.1103/PhysRevD.103.064015>
- [115] Stuart J. Russell and Peter Norvig, *Artificial Intelligence: A Modern Approach*, 4th ed. (Pearson, 2021)
- [116] Murray Campbell, A. Joseph Hoane, and Feng-hsiung Hsu, *Deep Blue*, Artificial Intelligence **13**, 57 (2002), URL: [https://doi.org/10.1016/S0004-3702\(01\)00129-1](https://doi.org/10.1016/S0004-3702(01)00129-1)
- [117] Edward Moore Geist, *It's Already Too Late to Stop the AI Arms Race—We Must Manage It Instead*, Bulletin of the Atomic Scientists **72**, 318 (2016), URL: <https://doi.org/10.1080/00963402.2016.1216672>

- [118] Brady D. Lund, Ting Wang, Nishith Reddy Mannuru, Bing Nie, Somipam Shimray, and Ziang Wang, *Chatgpt and a New Academic Reality: Artificial Intelligence-Written Research Papers and the Ethics of the Large Language Models in Scholarly Publishing*, Periodical of the Association for Information Science and Technology **74**, 570 (2023), URL: <https://doi.org/10.1002/asi.24750>
- [119] Pat Langley, *The Changing Science of Machine Learning*, Machine Learning **82**, 275 (2011), URL: <https://doi.org/10.1007/s10994-011-5242-y>
- [120] A. L. Samuel, *Some Studies in Machine Learning Using the Game of Checkers*, IBM Periodical of Research and Development **3**, 210 (1959), URL: <https://doi.org/10.1147/rd.33.0210>
- [121] Christopher M. Bishop, *Pattern Recognition and Machine Learning* (Springer New York, NY, 2006)
- [122] A. Sagheer and M. Kotb, *Unsupervised Pre-Training of a Deep LSTM-Based Stacked Autoencoder for Multivariate Time Series Forecasting Problems*, Scientific Reports **9**, (2019), URL: <https://doi.org/10.1038/s41598-019-55320-6>
- [123] M. Nadif and F. Role, *Unsupervised and Self-Supervised Deep Learning Approaches for Biomedical Text Mining*, Briefings in Bioinformatics **22**, (2021), URL: <https://doi.org/10.1093/bib/bbab016>
- [124] M. Hady, A. Faeouk, and F. Schwenker, *Semi-Supervised Learning*, in *Handbook on Neural Information Processing* (Springer Berlin Heidelberg, 2013), pp. 215–239, URL: https://doi.org/10.1007/978-3-642-36657-4_7
- [125] J. Morimoto, G. Cheng, C. Atkeson, and G. Zeglin, *A Simple Reinforcement Learning Algorithm for Biped Walking*, in *IEEE International Conference on Robotics and Automation, 2004.*, Vol. 3 (2004), pp. 3030–3035, URL: <https://doi.org/10.1109/ROBOT.2004.1307522>
- [126] J. Koutník, C. Giuseppe, S. Jürgen, and G. Faustino, *Evolving Large-Scale Neural Networks for Vision-Based Reinforcement Learning*, in *The 15th Annual Conference on Genetic and Evolutionary Computation*. (2013), pp. 1061–1068, URL: <https://doi.org/10.1145/2463372.2463509>
- [127] M. Zahangir Alom, T. M. Taha, C. Yakopcic, S. Westberg, P. Sidike, M. Shamima Nasrinn, M. Hasan, B. C. Van Esen, A. A. S. Awwal, and V. K. Asari, *A State-of-the-Art Survey on Deep Learning Theory and Architectures*, Electronics **8**, (2019), URL: <https://doi.org/10.3390/electronics8030292>
- [128] A. Krizhevsky, I. Sutskever, and G. E. Hinton, *Imagenet Classification with Deep Convolutional Neural Networks*, in *Communications of the ACM*, Vol. 60 (2017), pp. 84–90, URL: <https://doi.org/10.1145/3065386>
- [129] K. J. Piczak, *Environmental Sound Classification with Convolutional Neural Networks*, in *2015 IEEE 25th International Workshop on Machine Learning for Signal Processing (MLSP)* (2015), pp. 1–6, URL: <https://doi.org/10.1109/MLSP.2015.7324337>
- [130] Y. Kim, *Convolutional Neural Networks for Sentence Classification*, in *The 2014 Conference on Empirical Methods in Natural Language Processing (EMNLP)* (Association for Computational Linguistics, 2014), pp. 1746–1751, URL: <https://doi.org/10.3115/v1/D14-1181>
- [131] O. Vinyals, A. Toshev, S. Bengio, and D. Erhan, *Show and Tell: A Neural Image Caption Generator*, in *Proceedings of the IEEE Conference on Computer Vision and Pattern Recognition (CVPR)* (2015), URL: <https://doi.org/10.1109/CVPR.2015.7298935>
- [132] S. Ikawa and K. Kashino, *Neural Audio Captioning Based on Conditional Sequence-to-Sequence Model*, in *Proceedings of the Detection and Classification of Acoustic Scenes and Events 2019 Workshop (Dcase2019)* (2019), pp. 99–103, URL: <https://doi.org/10.33682/7bay-bj41>

- [133] Alexander M. Rush, Sumit Chopra, and Jason Weston, *A Neural Attention Model for Abstractive Sentence Summarization*, in *Proceedings of the 2015 Conference on Empirical Methods in Natural Language Processing* (2015), pp. 379–389, URL: <https://doi.org/10.18653/v1/D15-1044>
- [134] I. Goodfellow, J. Pouget-Abadie, M. Mirza, B. Xu, D. Warde-Farley, S. Ozair, A. Courville, and Y. Bengio, *Generative Adversarial Nets*, in *Proceedings of the 27th International Conference on Neural Information Processing Systems*, Vol. 2 (Curran Associates, Inc., 2014), pp. 2672–2680, URL: <https://doi.org/10.5555/2969033.2969125>
- [135] Aäron van den Oord, Sander Dieleman, Heiga Zen, Karen Simonyan, Oriol Vinyals, Alexander Graves, Nal Kalchbrenner, Andrew Senior, and Koray Kavukcuoglu, *Wavenet: A Generative Model for Raw Audio*, URL: <https://www.deeplearning.com/blog/wavenet-a-generative-model-for-raw-audio>
- [136] I. Sutskever, James Martens, and Geoffrey E. Hinton, *Generating Text with Recurrent Neural Networks*, in *The 28th International Conference on Machine Learning (ICML-11)* (2011), pp. 1017–1024
- [137] David Silver et al., *Mastering the Game of Go with Deep Neural Networks and Tree Search*, *Nature* **529**, 484 (2016), URL: <https://doi.org/10.1038/nature16961>
- [138] David Silver et al., *A General Reinforcement Learning Algorithm That Masters Chess, Shogi, And Go Through Self-Play*, *Science* **362**, 1140 (2018), URL: <https://doi.org/10.1126/science.aar6404>
- [139] Oriol Vinyals et al., *Grandmaster Level in Starcraft II Using Multi-Agent Reinforcement Learning*, *Nature* **575**, 350 (2019), URL: <https://doi.org/10.1038/s41586-019-1724-z>
- [140] A. Lohokare, A. Shah, and M. Zyda, *Deep Learning Bot for League of Legends*, in *The AAAI Conference on Artificial Intelligence and Interactive Digital Entertainment*, Vol. 16 (2020), pp. 322–324, URL: <https://doi.org/10.1609/aiide.v16i1.7449>
- [141] M.N.Q. Macedo, J.J.M. Galo, L.A.L. de Almeida, and A.C. de C. Lima, *Demand Side Management Using Artificial Neural Networks in a Smart Grid Environment*, *Renewable and Sustainable Energy Reviews* **41**, 128 (2015), URL: <https://doi.org/10.1016/j.rser.2014.08.035>
- [142] S. T. A. Niaki and M. Davoodi, *Designing a Multivariate–Multistage Quality Control System Using Artificial Neural Networks*, *International Periodical of Production Research* **47**, (2009), URL: <https://doi.org/10.1080/00207540701504348>
- [143] Claudine Badue et al., *Self-Driving Cars: A Survey*, *Expert Systems with Applications* **165**, (2021), URL: <https://doi.org/10.1016/j.eswa.2020.113816>
- [144] J. Jumper et al., *Highly Accurate Protein Structure Prediction with AlphaFold*, 583 (2021), URL: <https://doi.org/10.1038/s41586-021-03819-2>
- [145] A. V. Joshi, *Perceptron and Neural Networks*, in *Machine Learning and Artificial Intelligence* (Springer International Publishing, 2023), URL: https://doi.org/10.1007/978-3-031-12282-8_6
- [146] S. C. Kleene, *Representation of Events in Nerve Nets and Finite Automata*, in *Automata Studies. (AM-34)*, Vol. 34 (1956), pp. 3–42, URL: <https://doi.org/10.1515/9781400882618-002>
- [147] F. Pulvermüller, R. Tomasello, M. R. Henningsen-Schomers, and T. Wennekers, *Biological Constraints on Neural Network Models of Cognitive Function*, *Nature Reviews Neuroscience* **22**, (2021), URL: <https://doi.org/10.1038/s41583-021-00473-5>
- [148] A. Zador et al., *Catalyzing Next-Generation Artificial Intelligence Through Neuroai*, *Nature Communications* **14**, (2023), URL: <https://doi.org/10.1038/s41467-023-37180-x>

- [149] J. Schmidhuber, *Deep Learning in Neural Networks: An Overview*, Neural Networks **61**, (2015), URL: <https://doi.org/10.1016/j.neunet.2014.09.003>
- [150] Y. LeCun, Y. Bengio, and G. Hinton, *Deep Learning*, Nature **521**, (2015), URL: <https://doi.org/10.1038/nature14539>
- [151] Kurt Hornik, Maxwell Stinchcombe, and Halbert White, *Multilayer Feedforward Networks Are Universal Approximators*, Neural Networks **2**, 359 (1989), URL: https://cognitivemedium.com/magic_paper/assets/Hornik.pdf
- [152] Frank Rosenblatt, *The Perceptron: A Probabilistic Model for Information Storage and Organization in the Brain*, Psychological Review 386 (1958), URL: <https://doi.org/10.1037/h0042519>
- [153] R. Parhi and R. D. Nowak, *The Role of Neural Network Activation Functions*, IEEE Signal Processing Letters **27**, (2020), URL: <https://doi.org/10.1109/LSP.2020.3027517>
- [154] Y. Zhou and Y. Wu, *Analyses on Influence of Training Data Set to Neural Network Supervised Learning Performance*, Advances in Computer Science, Intelligent System and Environment (2011), URL: https://doi.org/10.1007/978-3-642-23753-9_4
- [155] M. V. Narkhede, P. P. Bartakke, and M. S. Sutaone, *A Review on Weight Initialization Strategies for Neural Networks*, Artificial Intelligence Review **55**, (2022), URL: <https://doi.org/10.1007/s10462-021-10033-z>
- [156] Terence Parr and Jeremy Howard, *The Matrix Calculus You Need for Deep Learning*, ArXiv, URL: <https://doi.org/10.48550/arXiv.1802.01528>
- [157] Neil Savage, *Breaking into the Black Box of Artificial Intelligence*, Nature Outlooks (2022), URL: <https://doi.org/10.1038/d41586-022-00858-1>
- [158] Y. Furusho and K. Ikeda, *Theoretical Analysis of Skip Connections and Batch Normalization from Generalization and Optimization Perspectives*, APSIPA Transactions on Signal and Information Processing, URL: <https://doi.org/10.1017/ATSIP.2020.7>
- [159] K. He, X. Zhang, S. Ren, and J. Sun, *Deep Residual Learning for Image Recognition*, in *2016 IEEE Conference on Computer Vision and Pattern Recognition (CVPR)* (2016), URL: <https://doi.org/10.1109/CVPR.2016.90>
- [160] Y. Yu, X. Si, C. Hu, and J. Zhang, *A Review of Recurrent Neural Networks: LSTM Cells and Network Architectures*, Neural Computation **31**, 1235 (2019), URL: https://doi.org/10.1162/neco_a_01199
- [161] D. H. Ackley, G. E. Hinton, and T. J. Sejnowski, *A Learning Algorithm for Boltzmann Machines*, Cognitive Science **9**, (1985), URL: [https://doi.org/10.1016/S0364-0213\(85\)80012-4](https://doi.org/10.1016/S0364-0213(85)80012-4)
- [162] Sepp Hochreiter, *The Vanishing Gradient Problem during Learning Recurrent Neural Nets and Problem Solutions*, World Scientific **6**, 107 (1997), URL: <https://doi.org/10.1142/S0218488598000094>
- [163] L. R. Medsker and L. Jain, *Recurrent Neural Networks, Design and Applications* **5**, (2001)
- [164] M. Unser, *Ridges, Neural Networks, And the Radon Transform*, Journal of Machine Learning Research **34**, 1 (2023)
- [165] K. Fukushima, *Cognitron: A Self-Organizing Multilayered Neural Network*, Biological Cybernetics **20**, (1975), URL: <https://doi.org/10.1007/BF00342633>
- [166] A. G. Bors and I. Pitas, *Median Radial Basis Function Neural Network*, IEEE Transactions on Neural Networks **7**, (1996), URL: <https://doi.org/10.1109/72.548164>

- [167] Xavier Glorot, Antoine Bordes, and Yoshua Bengio, *Deep Sparse Rectifier Neural Networks*, in *Proceedings of Machine Learning Research*, Vol. 15 (2011), URL: <https://proceedings.mlr.press/v15/glorot11a.html>
- [168] Z. Jiang, Y. Wang, C.-T. Li, P. Angelov, and R. Jiang, *Delve into Neural Activations: Toward Understanding Dying Neurons*, *IEEE Transactions on Artificial Intelligence* **4**, 959 (2023), URL: <https://doi.org/10.1109/TAI.2022.3180272>
- [169] A. L. Maas, A. Y. Hannun, and A. Y. Ng, *Rectifier Nonlinearities Improve Neural Network Acoustic Models*, *Proc. Imcl* **30**, (2013)
- [170] S. Fujii and H. Hayashi, *Comparison of Performance by Activation Functions on Deep Image Prior*, in *2019 International Conference on Artificial Intelligence in Information and Communication (ICAICC)* (2019), URL: <https://doi.org/10.1109/ICAICC.2019.8669063>
- [171] L. B. Godfrey, *An Evaluation of Parametric Activation Functions for Deep Learning*, in *2019 IEEE International Conference on Systems, Man and Cybernetics (SMC)* (2019), URL: <https://doi.org/10.1109/SMC.2019.8913972>
- [172] U. Ruby and V. Yendapalli, *Binary Cross Entropy with Deep Learning Technique for Image Classification*, *Int. J. Adv. Trends Comput. Sci. Eng* **9**, (2020)
- [173] D. S. K. Karunasingha, *Root Mean Square Error or Mean Absolute Error? Use Their Ratio as Well*, *Information Sciences* **585**, (2022), URL: <https://doi.org/10.1016/j.ins.2021.11.036>
- [174] S. Huang and Q. Wu, *Robust Pairwise Learning with Huber Loss*, *Journal of Complexity* **66**, (2021), URL: <https://doi.org/10.1016/j.jco.2021.101570>
- [175] Leon Bottou, *Large-Scale Machine Learning with Stochastic Gradient Descent*, in *Proceedings of Compstat'2010* (2010), pp. 177–186, URL: https://doi.org/10.1007/978-3-7908-2604-3_16
- [176] S. Khirirat, H. R. Feyzmahdavian, and M. Johansson, *Mini-Batch Gradient Descent: Faster Convergence under Data Sparsity*, *2017 IEEE 56th Annual Conference on Decision and Control (CDC)* (2017), URL: <https://doi.org/10.1109/CDC.2017.8264077>
- [177] D. Wilson and T. R. Martinez, *The General Inefficiency of Batch Training for Gradient Descent Learning*, *Neural Networks* **16**, (2003), URL: [https://doi.org/10.1016/S0893-6080\(03\)00138-2](https://doi.org/10.1016/S0893-6080(03)00138-2)
- [178] Ning Qian, *On the Momentum Term in Gradient Descent Learning Algorithms*, *Neural Networks* **12**, 145 (1999), URL: [https://doi.org/10.1016/S0893-6080\(98\)00116-6](https://doi.org/10.1016/S0893-6080(98)00116-6)
- [179] E. YAZAN and M. F. Talu, *Comparison of the Stochastic Gradient Descent Based Optimization Techniques*, in *2017 International Artificial Intelligence and Data Processing Symposium (IDAP)* (2017), URL: <https://doi.org/10.1109/IDAP.2017.8090299>
- [180] E. M. Dogo, O. J. Afolabi, N. I. Nwulu, B. Twala, and C. O. Aigbavboa, *A Comparative Analysis of Gradient Descent-Based Optimization Algorithms on Convolutional Neural Networks*, in *2018 International Conference on Computational Techniques, Electronics and Mechanical Systems (CTEMS)* (2018), URL: <https://doi.org/10.1109/CTEMS.2018.8769211>
- [181] R. Ward, X. Wu, and L. Bottou, *Adagrad Stepsizes: Sharp Convergence over Nonconvex Landscapes*, **21**, (2020), URL: <https://doi.org/10.5555/3455716.3455935>
- [182] D. Xu, S. Zhang, H. Zhang, and D. P. Mandic, *Convergence of the Rmsprop Deep Learning Method with Penalty for Nonconvex Optimization*, *Neural Networks* **139**, (2021), URL: <https://doi.org/10.1016/j.neunet.2021.02.011>

- [183] Diederik P. Kingma and Jimmy Ba, *Adam: A Method for Stochastic Optimization*, arXiv, URL: <https://doi.org/10.48550/arXiv.1412.6980>
- [184] D. E. Rumelhart, G. E. Hinton, and R. J. Williams, *Learning Representations by Back-Propagating Errors*, Nature **323**, (1986), URL: <https://doi.org/10.1038/323533a0>
- [185] X. Ying, *An Overview of Overfitting and Its Solutions*, Journal of Physics: Conference Series (2019), URL: <https://doi.org/10.1088/1742-6596/1168/2/022022>
- [186] Nitish Srivastava, Geoffrey Hinton, Alex Krizhevsky, Ilya Sutskever, and Ruslan Salakhutdinov, *Dropout: A Simple Way to Prevent Neural Networks from Overfitting*, Journal of Machine Learning Research **15**, 1929 (2014), URL: <https://doi.org/10.5555/2627435.2670313>
- [187] I. Salehin and D.-K. Kang, *A Review on Dropout Regularization Approaches for Deep Neural Networks within the Scholarly Domain*, Electronics **23**, (2023), URL: <https://doi.org/10.3390/electronics12143106>
- [188] Sergey Ioffe and Christian Szegedy, *Batch Normalization: Accelerating Deep Network Training by Reducing Internal Covariate Shift*, arXiv, URL: <https://doi.org/10.48550/arXiv.1502.03167>
- [189] Katsuyuki Hagiwara, *Regularization Learning, Early Stopping and Biased Estimator*, Neurocomputing **48**, 937 (2002), URL: [https://doi.org/10.1016/S0925-2312\(01\)00681-6](https://doi.org/10.1016/S0925-2312(01)00681-6)
- [190] Noah Golowich, Alexander Rakhlin, and S. Ohad, *Size-Independent Sample Complexity of Neural Networks*, in *The 31st Conference on Learning Theory*, Vol. 75 (2018), pp. 297–299, URL: <https://proceedings.mlr.press/v75/golowich18a.html>
- [191] Xia Hu, Jian Pei, Lingyang Chu, Weiqing Liu, and Jiang Bian, *Model Complexity of Deep Learning: A Survey*, Knowledge and Information Systems (2021), URL: <https://doi.org/10.1007/s10115-021-01605-0>
- [192] V. Benedetto, F. Gissi, G. Ciaparrone, and L. Troiano, *AI in Gravitational Wave Analysis, An Overview*, Applied Sciences **13**, (2023), URL: <https://doi.org/10.3390/app13179886>
- [193] Reed Essick, Patrick Godwin, Chad Hanna, Lindy Blackburn, and Erik Katsavounidis, *Idq: Statistical Inference of Non-Gaussian Noise with Auxiliary Degrees of Freedom in Gravitational-Wave Detectors*, Machine Learning: Science and Technology **2**, (2020), URL: <https://doi.org/10.1088/2632-2153/abab5f>
- [194] K. Soni, B. U. Gadre, S. Mitra, and S. Dhurandhar, *Hierarchical Search for Compact Binary Coalescences in the Advanced Ligo's First Two Observing Runs*, Physical Review D **105**, (2022), URL: <https://doi.org/10.1103/PhysRevD.105.064005>
- [195] P. Relton, A. Virtuoso, S. Bini, V. Raymond, I. Harry, M. Drago, C. Lazzaro, A. Miani, and S. Tiwari, *Addressing the Challenges of Detecting Time-Overlapping Compact Binary Coalescences*, Physical Review D **106**, (2022), URL: <https://doi.org/10.1103/PhysRevD.106.104045>
- [196] M. Branchesi, *Multi-Messenger Astronomy: Gravitational Waves, Neutrinos, Photons, And Cosmic Rays*, Journal of Physics: Conference Series **718**, (2016), URL: <https://doi.org/10.1088/1742-6596/718/2/022004>
- [197] C. A. Raithel, *Constraints on the Neutron Star Equation of State from Gw170817*, The European Physical Journal a **55**, (2019), URL: <http://doi.org/10.1140/epja/i2019-12759-5>
- [198] D. Radice, A. Perego, F. Zappa, and S. Bernuzzi, *Gw170817: Joint Constraint on the Neutron Star Equation of State from Multimessenger Observations*, The Astrophysical Journal **852**, (2018), URL: <http://doi.org/10.3847/2041-8213/aaa402>

- [199] R. Abbott et al., *Search for Gravitational Waves Associated with Fast Radio Bursts Detected by CHIME/FRB during the LIGO–Virgo Observing Run O3a*, ArXiv, URL: <https://doi.org/10.48550/arXiv.2203.12038>
- [200] A. Macquet, M. A. Bizouard, E. Burns, N. Christensen, M. Coughlin, Z. Wadiasingh, and G. Younes, *Search for Long-Duration Gravitational-Wave Signals Associated with Magnetar Giant Flares*, The Astrophysical Journal **918**, (2021), URL: <https://doi.org/10.3847/1538-4357/ac0efd>
- [201] R. Abbott et al., *Search for Gravitational Waves Associated with Gamma-Ray Bursts Detected by Fermi and Swift during the LIGO–Virgo Run O3b*, The Astrophysical Journal **928**, (2022), URL: <https://doi.org/10.3847/1538-4357/ac532b>
- [202] H. Grote and Y. V. Stadnik, *Novel Signatures of Dark Matter in Laser-Interferometric Gravitational-Wave Detectors*, Physical Review Research **1**, (2019), URL: <https://doi.org/10.1103/PhysRevResarch.1.033187>
- [203] P. Wang, E. Fan, and P. Wang, *Comparative Analysis of Image Classification Algorithms Based on Traditional Machine Learning and Deep Learning*, Pattern Recognition Letters **141**, (2021), URL: <https://doi.org/10.1016/j.patrec.2020.07.042>
- [204] Richard N. Youngworth, Benjamin B. Gallagher, and Brian L. Stamper, *An Overview of Power Spectral Density (PSD) Calculations*, Proc.spie **5869**, (2005), URL: <https://doi.org/10.1117/12.618478>
- [205] O. M. Solomon Jr, *PSD Computations Using Welch's Method. [Power Spectral Density (PSD)]*, URL: <https://doi.org/10.2172/5688766>
- [206] P. Virtanen et al., *Scipy 1.0: Fundamental Algorithms for Scientific Computing in Python*, Nature Methods **17**, 261 (2020), URL: <https://doi.org/10.1038/s41592-019-0686-2>
- [207] Mo Z and Siepel A, *Domain-Adaptive Neural Networks Improve Supervised Machine Learning Based on Simulated Population Genetic Data*, Plos Genetics (2023), URL: <https://doi.org/10.1371/journal.pgen.1011032>
- [208] Roady R, Hayes TL, Kemker R, Gonzales A, and Kanan C, *Are Open Set Classification Methods Effective on Large-Scale Datasets?*, Plos ONE **15**, (2020), URL: <https://doi.org/10.1371/journal.pone.0238302>
- [209] Schat E, van de Schoot R, V. D. Kouw WM, and Mendrik AM, *The Data Representativeness Criterion: Predicting the Performance of Supervised Classification Based on Data Set Similarity.*, Plos ONE (2020), URL: <https://doi.org/10.1371/journal.pone.0237009>
- [210] D. Macleod, J. Areeda, S. Coughlin, T. Massinger, and A. Urban, *Gwpy: A Python Package for Gravitational-Wave Astrophysics*, Softwarex **13**, (n.d.), URL: <https://doi.org/10.1016/j.softx.2021.100657>
- [211] Kent Blackburn, Benoit Mours, Stuart Anderson, Albert Lazzarini, John Zweizig, and Ed Maros, *Specification of a Common Data Frame Format for Interferometric Gravitational Wave Detectors (IGWD)*, URL: <https://dcc.ligo.org/LIGO-T970130-v3/public>
- [212] M. Hannam, *Modelling Gravitational Waves from Precessing Black-Hole Binaries: Progress, Challenges and Prospects*, General Relativity and Gravitation **46**, (2014), URL: <https://doi.org/10.1007/s10714-014-1767-2>
- [213] M. Colleoni, M. Mateu-Lucena, H. Estelles, C. Garcia-Quiros, D. Keitel, G. Pratten, A. Ramos-Buades, and S. Husa, *Towards the Routine Use of Subdominant Harmonics in Gravitational-Wave*

Inference: Reanalysis of Gw190412 with Generation X Waveform Models, URL: <https://10.0.4.79/PhysRevD.103.024029>

- [214] Karl Wette, *SWIGLAL: Python and Octave Interfaces to the Lalsuite Gravitational-Wave Data Analysis Libraries*, Softwarex **12**, (2020), URL: <https://doi.org/10.1016/j.softx.2020.100634>
- [215] *Cufft*, (n.d.), URL: <https://docs.nvidia.com/cuda/cufft/index.html#notices>
- [216] E. Payne, C. Talbot, and E. Thrane, *Higher Order Gravitational-Wave Modes with Likelihood Reweighting*, Physical Review D **100**, (n.d.), URL: <https://doi.org/10.3847/2041-8213/ac3138>
- [217] Isobel Romero-Shaw, Paul D. Lasky, and Eric Thrane, *Signs of Eccentricity in Two Gravitational-Wave Signals May Indicate a Subpopulation of Dynamically Assembled Binary Black Holes*, The American Astronomical Society **921**, (2021), URL: <https://doi.org/10.3847/2041-8213/ac3138>
- [218] R. Green, C. Hoy, S. Fairhurst, M. Hannam, F. Pannarale, and C. Thomas, *Identifying When Precession Can Be Measured in Gravitational Waveforms*
- [219] Christian D Ott, *The Gravitational-Wave Signature of Core-Collapse Supernovae*, Classical and Quantum Gravity **26**, (2009), URL: <https://doi.org/10.1088/0264-9381/26/6/063001>
- [220] Kip S. Thorne, *Gravitational Waves*, ArXiv, URL: <https://doi.org/10.48550/arXiv.gr-qc/9506086>
- [221] Dr. Jolien D. E. Creighton and Dr. Warren G. Anderson, *Gravitational-wave Physics and Astronomy* (2011)
- [222] S. Mastrogiovanni, C. Leyde K. and Karathanasis, E. Chassande-Mottin, J. Steer D. A. and Gair, A. Ghosh, R. Gray, S. Mukherjee, and S. Rinaldi, *On the Importance of Source Population Models for Gravitational-Wave Cosmology*, Physical Review D **104**, (2021), URL: <https://doi.org/10.1103/PhysRevD.104.062009>
- [223] Piotr Jaranowski and Andrzej Kr'olak, *A. Gravitational-Wave Data Analysis. Formalism and Sample Applications: The Gaussian Case.*, Living Reveiw in Relativity **8**, (2005), URL: <https://doi.org/10.12942/lrr-2005-3>
- [224] A. Shanthini, G. Vinodhini, R. M. Chandrasekaran, and P. Supraja, *A Taxonomy on Impact of Label Noise and Feature Noise Using Machine Learning Techniques*, Soft Computing **23**, 8597 (2019), URL: <https://doi.org/10.1007/s00500-019-03968-7>
- [225] J. Markowitz, M. Zanolin, L. Cadonati, and E. Katsavounidis, *Gravitational Wave Burst Source Direction Estimation Using Time and Amplitude Information*, Physical Review D **78**, (2008), URL: <https://doi.org/10.1103/PhysRevD.78.122003>
- [226] B. Allen, W. G. Anderson, P. R. Brady, D. A. Brown, and J. D. E. Creighton, *FINDCHIRP: An Algorithm for Detection of Gravitational Waves from Inspiring Compact Binaries*, Physical Review D **85**, (2012), URL: <https://doi.org/10.1103/PhysRevD.85.122006>
- [227] A. Buikema et al., *Sensitivity and Performance of the Advanced LIGO Detectors in the Third Observing Run*, Physical Review D **102**, (2020), URL: <https://doi.org/10.1103/PhysRevD.102.062003>
- [228] T. E. Bell, *Hearing the Heavens: The Cosmos Is Thought to Be Awash with Gravitational Waves to Which Humanity Is, As yet, Deaf.*, Nature **18** (2008)
- [229] D. Sigg, *The Advanced LIGO Detectors in the Era of First Discoveries*, Interferometry XVIII **9960**, 72 (2016)
- [230] *Gwistat*, (n.d.), URL: <https://online.igwn.org/grafana/public-dashboards/1a0efabe65384a7287abfcc1996e4c4d?orgId=1&refresh=5s&from=now-2d&to=now>

- [231] M. Wąs, P. Kalmus, J. R. Leong, T. Adams, N. Leroy, D. M. Macleod, C. Pankow, and F. Robinet, *A Fixed False Alarm Probability Figure of Merit for Gravitational Wave Detectors*, Classical and Quantum Gravity **32**, (2014), URL: <https://doi.org/10.1088/0264-9381/31/8/085004>
- [232] G. Dong and H. Liu, *Feature Engineering for Machine Learning and Data Analytics* (CRC press, 2018)
- [233] S. Khalid, T. Khalil, and S. Nasreen, *A Survey of Feature Selection and Feature Extraction Techniques in Machine Learning*, in *2014 Science and Information Conference* (2014), pp. 372–378, URL: <https://doi.org/10.1109/SAI.2014.6918213>
- [234] *Whitening of Non-Stationary Noise from Gravitational Wave Detectors*, Classical and Quantum Gravity **21**, (2004), URL: <https://doi.org/10.1088/0264-9381/21/5/061>
- [235] J. Adler and I. Parmryd, *Quantifying Colocalization by Correlation: The Pearson Correlation Coefficient Is Superior to the Mander's Overlap Coefficient*, Cytometry Part a **77**, 733 (2010)
- [236] H. J. Nussbaumer, *The Fast Fourier Transform* (springer, 1982)
- [237] T. Arias-Vergara, P. Klumpp, J. C. Vasquez-Correa, E. Nöth, J. R. Orozco-Arroyave, and M. Schuster, *Multi-Channel Spectrograms for Speech Processing Applications Using Deep Learning Methods*, Pattern Analysis and Applications **24**, (2021), URL: <https://doi.org/10.1007/s10044-020-00921-5>
- [238] E. Cuoco, A. Iess, F. Morawski, and M. Razzano, *Machine Learning for the Characterization of Gravitational Wave Data*, in *Handbook of Gravitational Wave Astronomy* (Springer Singapore, 2020), pp. 1–23
- [239] Miquel Llorens-Monteagudo, Alejandro Torres-Forné, and Antonio Marquina, *Classification of Gravitational-Wave Glitches via Dictionary Learning*, Classical and Quantum Gravity **36**, (2019), URL: <https://doi.org/10.1088/1361-6382/ab0657>
- [240] Jade Powell, Alejandro Torres-Forné, Ryan Lynch, Daniele Trifirò, Elena Cuoco, Marco Cavaglià, Ik Siong Heng, and José A Font, *Classification Methods for Noise Transients in Advanced Gravitational-Wave Detectors II: Performance Tests on Advanced LIGO Data*, Classical and Quantum Gravity **34**, (2017), URL: <https://doi.org/10.1088/1361-6382/34/3/034002>
- [241] Zijun Zhang, *Improved Adam Optimizer for Deep Neural Networks*, 2018 IEEE/ACM 26th International Symposium on Quality of Service (Iwqos) 1 (2018), URL: <https://api.semanticscholar.org/CorpusID:52062957>
- [242] Z. Li, F. Liu, W. Yang, S. Peng, and J. Zhou, *A Survey of Convolutional Neural Networks: Analysis, Applications, And Prospects*, IEEE Transactions on Neural Networks and Learning Systems **33**, 6999 (2022), URL: <https://doi.org/10.1109/TNNLS.2021.3084827>
- [243] *A Survey of the Recent Architectures of Deep Convolutional Neural Networks*, Artificial Intelligence Review **53**, (2020), URL: <https://doi.org/10.1007/s10462-020-09825-6>
- [244] D. Bank, N. Koenigstein, R. Giryes, L. Rokach, O. Maimon, and E. Shmueli, *Autoencoders*, in *Machine Learning for Data Science Handbook: Data Mining and Knowledge Discovery Handbook* (Springer International Publishing, 2023), pp. 343–374, URL: https://doi.org/10.1007/978-3-031-24628-9_16
- [245] Q.-s. Zhang and S.-c. Zhu, *Visual Interpretability for Deep Learning: A Survey*, Frontiers of Information Technology & Electronic Engineering **19**, (2018), URL: <https://doi.org/10.1631/FITEE.1700808>

- [246] D. Bank, N. Koenigstein, R. Giryes, L. Rokach, O. Maimon, and E. Shmueli, *Generative Adversarial Networks*, in *Machine Learning for Data Science Handbook: Data Mining and Knowledge Discovery Handbook* (Springer International Publishing, 2023), pp. 375–400, URL: https://doi.org/10.1007/978-3-031-24628-9_17
- [247] K. Choi, G. Fazekas, M. Sandler, and K. Cho, *Convolutional Recurrent Neural Networks for Music Classification*, in *2017 IEEE International Conference on Acoustics, Speech and Signal Processing (ICASSP)* (2017), pp. 2392–2396, URL: <https://doi.org/10.1109/ICASSP.2017.7952585>
- [248] Y. Liu, G. Sun, Y. Qiu, L. Zhang, A. Chhatkuli, and L. Van Gool, *Transformer in Convolutional Neural Networks*
- [249] H. Chefer, Y. Alaluf, Y. Vinker, L. Wolf, and D. Cohen-Or, *Attend-and-Excite: Attention-Based Semantic Guidance for Text-to-Image Diffusion Models*, ACM Transactions on Graphics (TOG) **42**, 1 (2023)
- [250] G. W. Lindsay, *Convolutional Neural Networks as a Model of the Visual System: Past, Present, And Future*, URL: https://doi.org/10.1162/jocn_a_01544
- [251] D. H. Hubel, T. N. Wiesel, and 1962-01-01, *Receptive Fields, Binocular Interaction and Functional Architecture in the Cat's Visual Cortex*, URL: <https://doi.org/10.1113/jphysiol.1962.sp006837>
- [252] C. Mouton, J. C. Myburgh, M. H. Davel, and A. Gerber, *Stride and Translation Invariance in Cnns*, Artificial Intelligence Research 267 (2020), URL: https://doi.org/10.1113/10.1007/978-3-030-66151-9_17
- [253] E. Tuba, N. Baćanin, I. Strumberger, M. Tuba, and E. Pap, *Convolutional Neural Networks Hyperparameters Tuning*, in *Artificial Intelligence: Theory and Applications* (Springer International Publishing, 2021), pp. 65–84, URL: https://doi.org/10.1007/978-3-030-72711-6_4
- [254] V. Benedetto, F. Gissi, G. Ciaparrone, and L. Troiano, *AI in Gravitational Wave Analysis, An Overview*, Applied Sciences **13**, (2023), URL: <https://doi.org/10.3390/app13179886>
- [255] Eric A Moreno, Bartłomiej Borzyszkowski, Maurizio Pierini, Jean-Roch Vlimant, and Maria Spiropulu, *Source-Agnostic Gravitational-Wave Detection with Recurrent Autoencoders*, Machine Learning: Science and Technology **3**, (2022), URL: <https://doi.org/10.1088/2632-2153/ac5435>
- [256] J. McGinn, C. Messenger, M. J. Williams, and I. S. Heng, *Generalised Gravitational Wave Burst Generation with Generative Adversarial Networks*, Classical and Quantum Gravity **38**, (2021), URL: <https://doi.org/10.1088/1361-6382/ac09cc>
- [257] C. Chatterjee, L. Wen, F. Diakogiannis, and K. Vinsen, *Extraction of Binary Black Hole Gravitational Wave Signals from Detector Data Using Deep Learning*, Physical Review D **104**, (2023), URL: <https://doi.org/10.1103/PhysRevD.104.064046>
- [258] L. Jiang and Y. Luo, *Convolutional Transformer for Fast and Accurate Gravitational Wave Detection*, in *2022 26th International Conference on Pattern Recognition (ICPR)* (2022), URL: <https://doi.org/10.1109/ICPR56361.2022.9956104>
- [259] Daniel George and E.A. Huerta, *Deep Learning for Real-Time Gravitational Wave Detection and Parameter Estimation: Results with Advanced LIGO Data*, Physics Letters B **778**, 64 (2018), URL: <https://doi.org/10.1016/j.physletb.2017.12.053>
- [260] H.-M. Luo, W. Lin, Z.-C. Chen, and Q.-G. Huang, *Extraction of Gravitational Wave Signals with Optimized Convolutional Neural Network*, Frontiers of Physics **15**, (2019), URL: <https://doi.org/10.1007/s11467-019-0936-x>

- [261] A. Schmitt, K. Fu, S. Fan, and Y. Luo, *Investigating Deep Neural Networks for Gravitational Wave Detection in Advanced LIGO Data*, in (Association for Computing Machinery, 2019), pp. 73–78, URL: <https://doi.org/10.1145/3339363.3339377>
- [262] X. Fan, J. Li, X. Li, Y. Zhong, and J. Cao, **62**, (2019), URL: <https://doi.org/10.1007/s11433-018-9321-7>
- [263] E. A. Huerta et al., *Accelerated, Scalable and Reproducible AI-Driven Gravitational Wave Detection*, Nature Astronomy **5**, (2021), URL: <https://doi.org/10.1038/s41550-021-01405-0>
- [264] C. Ma, W. Wang, H. Wang, and Z. Cao, *Ensemble of Deep Convolutional Neural Networks for Real-Time Gravitational Wave Signal Recognition*, Physical Review D **105**, (2022), URL: <https://doi.org/10.1103/PhysRevD.105.083013>
- [265] H. Wang, S. Wu, Z. Cao, X. Liu, and J.-Y. Zhu, *Gravitational-Wave Signal Recognition of LIGO Data by Deep Learning*, Physical Review D **101**, (2020), URL: <https://doi.org/10.1103/PhysRevD.101.104003>
- [266] Chetan Verma, Amit Reza, Dilip Krishnaswamy, Sarah Caudill, and Gurudatt Gaur, *Employing Deep Learning for Detection of Gravitational Waves from Compact Binary Coalescences*, ArXiv, URL: <https://doi.org/10.48550/arXiv.2110.01883>
- [267] Christopher Bresten and Jae-Hun Jung, *Detection of Gravitational Waves Using Topological Data Analysis and Convolutional Neural Network: An Improved Approach*, ArXiv, URL: <https://doi.org/10.48550/arXiv.1910.08245>
- [268] S. Fan, Y. Wang, Y. Luo, A. Schmitt, and S. Yu, *Improving Gravitational Wave Detection with 2d Convolutional Neural Networks*, in *2020 25th International Conference on Pattern Recognition (ICPR)* (2021), pp. 7103–7110, URL: <https://doi.org/10.1109/ICPR48806.2021.9412180>
- [269] J. Aveiro, F. F. Freitas, M. Ferreira, A. Onofre, C. Providencia, G. Goncalves, and J. A. Font, *Identification of Binary Neutron Star Mergers in Gravitational-Wave Data Using Object-Detection Machine Learning Models*, Physical Review D **106**, (2022), URL: <https://doi.org/10.1103/PhysRevD.106.084059>
- [270] A. Menendez-Vazquez, M. Kolstein, M. Martinez, and L. M. Mir, *Searches for Compact Binary Coalescence Events Using Neural Networks in the Ligo/virgo Second Observation Period Author*, Physical Review D **103**, (2021), URL: <https://doi.org/10.1103/PhysRevD.103.062004>
- [271] B.-J. Lin, X.-R. Li, and W.-L. Yu, *Binary Neutron Stars Gravitational Wave Detection Based on Wavelet Packet Analysis and Convolutional Neural Networks*, Frontiers of Physics **15**, (2019), URL: <https://doi.org/10.1007/s11467-019-0935-y>
- [272] X.-R. Li, W.-L. Yu, X.-L. Fan, and G. J. Babu, *Some Optimizations on Detecting Gravitational Wave Using Convolutional Neural Network*, Frontiers of Physics **15**, (2020), URL: <https://doi.org/10.1007/s11467-020-0966-4>
- [273] M. Andres-Carcasona, A. Menendez-Vazquez, M. Martinez, and L. M. Mir, *Searches for Mass-Asymmetric Compact Binary Coalescence Events Using Neural Networks in the Ligo/virgo Third Observation Period*, Physical Review D **107**, (2023), URL: <https://doi.org/10.1103/PhysRevD.107.082003>
- [274] Wei Wei, E. A. Huerta, Mengshen Yun, Nicholas Loutrel, Md Arif Shaikh, Prayush Kumar, Roland Haas, and Volodymyr Kindratenko, *Deep Learning with Quantized Neural Networks for Gravitational-Wave Forecasting of Eccentric Compact Binary Coalescence*, The Astrophysical Journal **919**, (2021), URL: <https://doi.org/10.3847/1538-4357/ac1121>

- [275] G. Baltus, J. Janquart, M. Lopez, A. Reza, S. Caudill, and J. R. Cudell, *Convolutional Neural Networks for the Detection of the Early Inspiral of a Gravitational-Wave Signal*, Physical Review D **103**, (2021), URL: <https://doi.org/10.1103/PhysRevD.103.102003>
- [276] G. Baltus, J. Janquart, M. Lopez, H. Narola, and J.-R. Cudell, *Convolutional Neural Network for Gravitational-Wave Early Alert: Going down in Frequency*, Physical Review D **106**, (2022), URL: <https://doi.org/10.1103/PhysRevD.106.042002>
- [277] G. Baltus, J.-R. Cudell, J. Janquart, M. Lopez, S. Caudill, and A. Reza, *Detecting the Early Inspiral of a Gravitational-Wave Signal with Convolutional Neural Networks*, in *2021 International Conference on Content-Based Multimedia Indexing (CBMI)* (2021), URL: <https://doi.org/10.1103/10.1109/CBMI50038.2021.9461919>
- [278] X. Fan, J. Li, X. Li, Y. Zhong, and J. Cao, *Applying Deep Neural Networks to the Detection and Space Parameter Estimation of Compact Binary Coalescence with a Network of Gravitational Wave Detectors*, Science China Physics, Mechanics & Astronomy **62**, (2019), URL: <https://doi.org/10.1007/s11433-018-9321-7>
- [279] W.-H. Ruan, H. Wang, C. Liu, and Z.-K. Guo, *Rapid Search for Massive Black Hole Binary Coalescences Using Deep Learning*, Physics Letters B **841**, (2023), URL: <https://doi.org/10.1016/j.physletb.2023.137904>
- [280] P. G. Krastev, *Real-Time Detection of Gravitational Waves from Binary Neutron Stars Using Artificial Neural Networks*, Physics Letters B **803**, (2020), URL: <https://doi.org/10.1016/j.physletb.2020.135330>
- [281] M. López, M. Drago, I. Di Palma, F. Ricci, and P. Cerdá-Durán, *Deep Learning Algorithms for Gravitational Waves Core-Collapse Supernova Detection*, in *2021 International Conference on Content-Based Multimedia Indexing (CBMI)* (2021), pp. 1–6, URL: <https://doi.org/10.1109/CBMI50038.2021.9461885>
- [282] M. Lopez, I. Di Palma, M. Drago, P. Cerda-Duran, and F. Ricci, *Deep Learning for Core-Collapse Supernova Detection*, Physical Review D **103**, (2021), URL: <https://doi.org/10.1103/PhysRevD.103.063011>
- [283] Seiya Sasaoka, Yilun Hou, Diego Sebastian Dominguez, Suyog Garg, Naoki Koyama, Yuto Omae, Kentaro Somiya, and Hirotaka Takahashi, *Deep Learning Application for Detecting Gravitational Waves from Core-Collapse Supernovae*, in *Proceedings of 38th International Cosmic Ray Conference — Pos(Icrc2023)* (2023), URL: <https://doi.org/10.1103/10.22323/1.444.1499>
- [284] S. Sasaoka, Y. Hou, D. S. Dominguez, S. Garg, N. Koyama, Y. Omae, K. Somiya, and H. Takahashi, *Deep Learning for Detecting Gravitational Waves from Compact Binary Coalescences and Its Visualization by Grad-CAM*, in *Proceedings of Science* (2023), URL: <https://doi.org/10.22323/1.444.1498>
- [285] D. Wolpert and W. Macready, *No Free Lunch Theorems for Optimization*, IEEE Transactions on Evolutionary Computation **1**, 67 (1997), URL: <https://doi.org/10.1109/4235.585893>
- [286] A. Shrestha and A. Mahmood, *Review of Deep Learning Algorithms and Architectures*, IEEE Access **7**, 53040 (2019), URL: <https://doi.org/10.1109/ACCESS.2019.2912200>
- [287] M. Krenn et al., *Predicting the Future of AI with AI: High-Quality Link Prediction in an Exponentially Growing Knowledge Network* (2022)

- [288] *Hyperparameter Optimization: Foundations, Algorithms, Best Practices, And Open Challenges*, Wires Data Mining and Knowledge Discovery **13**, (2023), URL: <https://doi.org/10.1002/widm.1484>
- [289] L. Liao, H. Li, W. Shang, and L. Ma, *An Empirical Study of the Impact of Hyperparameter Tuning and Model Optimization on the Performance Properties of Deep Neural Networks*, URL: <https://doi.org/10.1145/3506695>
- [290] A. Morales-Hernández, I. Van Nieuwenhuysse, and S. Rojas Gonzalez, *A Survey on Multi-Objective Hyperparameter Optimization Algorithms for Machine Learning*, Artificial Intelligence Review **56**, 8043 (2023), URL: <https://doi.org/10.1007/s10462-022-10359-2>
- [291] M. Gen and L. Lin, *Genetic Algorithms and Their Applications*, in *Springer Handbook of Engineering Statistics* (Springer London, 2023), pp. 635–674, URL: https://doi.org/10.1007/978-1-4471-7503-2_33
- [292] M. Berrondo and M. Sandoval, *Defining Emergence: Learning from Flock Behavior*, Complexity **21**, 69 (2016), URL: <https://doi.org/10.1002/cplx.21711>
- [293] Bilal, M. Pant, H. Zaheer, L. Garcia-Hernandez, and A. Abraham, *Differential Evolution: A Review of More Than Two Decades of Research*, Engineering Applications of Artificial Intelligence **90**, (2020), URL: <https://doi.org/10.1016/j.engappai.2020.103479>
- [294] Max Jaderberg, *Population Based Training of Neural Networks*, URL: <https://deepmind.google/discover/blog/population-based-training-of-neural-networks/>
- [295] D. S. Deighan, S. E. Field, C. D. Capano, and G. Khanna, *Genetic-Algorithm-Optimized Neural Networks for Gravitational Wave Classification*, Neural Computing and Applications **33**, 13859 (2021), URL: <https://doi.org/10.1007/s00521-021-06024-4>
- [296] B. Min, H. Ross, E. Sulem, A. P. B. Veyseh, T. H. Nguyen, O. Sainz, E. Agirre, I. Heintz, and D. Roth, *Recent Advances in Natural Language Processing via Large Pre-Trained Language Models: A Survey*, **56**, (2023), URL: <https://doi.org/10.1145/3605943>
- [297] Y. Zhang, Z. Gan, K. Fan, Z. Chen, R. Henao, D. Shen, and L. Carin, *Adversarial Feature Matching for Text Generation*, in *International Conference on Machine Learning* (2017), pp. 4006–4015
- [298] Dzmitry Bahdanau, K. H. Cho, and Yoshua Bengio, *Neural Machine Translation by Jointly Learning to Align and Translate*, in *3rd International Conference on Learning Representations, ICLR 2015* (2015)
- [299] T. Lin, Y. Wang, X. Liu, and X. Qiu, *A Survey of Transformers*, AI Open **3**, 111 (2022), URL: <https://doi.org/10.1016/j.aiopen.2022.10.001>
- [300] F. -A. Croitoru, V. Hondru, R. T. Ionescu, and M. Shah, *Diffusion Models in Vision: A Survey*, in *IEEE Transactions on Pattern Analysis and Machine Intelligence*, Vol. 45 (2023), pp. 10850–10869, URL: <https://doi.org/10.1109/TPAMI.2023.3261988>
- [301] *Stable Diffusion Public Release*, (n.d.), URL: <https://stability.ai/news/stable-diffusion-public-release>
- [302] *Midjourney*, (n.d.), URL: <https://www.midjourney.com/home>
- [303] J. Betker et al., *Improving Image Generation with Better Captions*, URL: <https://cdn.openai.com/papers/dall-e-3.pdf>
- [304] *A Review on the Attention Mechanism of Deep Learning*, Neurocomputing **452**, 48 (2021), URL: <https://doi.org/10.1016/j.neucom.2021.03.091>

- [305] J.-B. Cordonnier, A. Loukas, and M. Jaggi, *On the Relationship between Self-Attention and Convolutional Layers*, arXiv preprint arXiv:1911.03584, URL: <https://doi.org/10.48550/arXiv.1911.03584>
- [306] V. G. Cerf, *ASCII Format for Network Interchange*, (1969), URL: <https://www.rfc-editor.org/rfc/rfc20.html>
- [307] M. Needleman, *The Unicode Standard*, Serials Review **26**, 51 (2000), URL: <https://doi.org/10.1080/00987913.2000.10764582>
- [308] J. J. Webster and C. Kit, *Tokenization as the Initial Phase in NLP*, in *COLING 1992 Volume 4: The 14th International Conference on Computational Linguistics* (1992), URL: <https://aclanthology.org/C92-4173.pdf>
- [309] L. Ma and Y. Zhang, *Using Word2vec to Process Big Text Data*, 2015 IEEE International Conference on Big Data (Big Data) 2895 (2015), URL: <https://doi.org/10.1109/BigData.2015.7364114>
- [310] A. Kathuria, A. Gupta, R. K. Singla, V. Singh, V. K. Asari, S. Kumar, and R. B. Patel, *A Review of Tools and Techniques for Preprocessing of Textual Data*, in *Computational Methods and Data Engineering* (2021), pp. 407–422, URL: https://doi.org/10.1007/978-981-15-6876-3_31
- [311] Y. Zhang, R. Jin, and Z.-H. Zhou, *Understanding Bag-of-Words Model: A Statistical Framework*, International Journal of Machine Learning and Cybernetics **1**, 43 (2010), URL: <https://doi.org/10.1007/s13042-010-0001-0>
- [312] A. Liutkus, O. Cifka, S.-L. Wu, U. Simsekli, Y.-H. Yang, and G. Richard, *Relative Positional Encoding for Transformers with Linear Complexity*, in *Proceedings of the 38th International Conference on Machine Learning*, Vol. 139 (2021), pp. 7067–7079, URL: <https://proceedings.mlr.press/v139/liutkus21a.html>
- [313] P. Juola, *Measuring Linguistic Complexity: The Morphological Tier*, Journal of Quantitative Linguistics **5**, 206 (1998), URL: <https://doi.org/10.1080/09296179808590128>
- [314] S. Hochreiter and J. Schmidhuber, *Long Short-Term Memory*, Neural Computation **9**, 1735 (1997), URL: <https://doi.org/neco.1997.9.8.1735>
- [315] A. Graves, *Long Short-Term Memory*, in *Supervised Sequence Labelling with Recurrent Neural Networks* (Springer Berlin Heidelberg, 2012), pp. 37–45, URL: https://doi.org/10.1007/978-3-642-24797-2_4
- [316] A. Schmitt, K. Fu, S. Fan, and Y. Luo, *Investigating Deep Neural Networks for Gravitational Wave Detection in Advanced LIGO Data*, in *Proceedings of the 2nd International Conference on Computer Science and Software Engineering* (Association for Computing Machinery, 2019), URL: <https://doi.org/10.1145/3339363.3339377>
- [317] R. Nigam, A. Mishra, and P. Reddy, *Transient Classification in Low SNR Gravitational Wave Data Using Deep Learning*, ArXiv, URL: <https://doi.org/10.48550/arXiv.2009.12168>
- [318] Y.-C. Lin and J.-H. P. Wu, *Detection of Gravitational Waves Using Bayesian Neural Networks*, Physical Review D **103**, (2021), URL: <https://doi.org/10.1103/PhysRevD.103.063034>
- [319] Damon Beveridge, Linqing Wen, and Andreas Wicenec, *Detection of Binary Black Hole Mergers from the Signal-to-Noise Ratio Time Series Using Deep Learning*, URL: <https://api.semanticscholar.org/CorpusID:260926510>
- [320] Y. Zhang, H. Xu, M. Liu, C. Liu, Y. Zhao, and J. Zhu, *Deep Learning Model Based on a Bidirectional Gated Recurrent Unit for the Detection of Gravitational Wave Signals*, Physical Review D **106**, (2022), URL: <https://doi.org/10.1103/PhysRevD.106.122002>

- [321] Z. Que et al., *Accelerating Recurrent Neural Networks for Gravitational Wave Experiments*, in *2021 IEEE 32nd International Conference on Application-Specific Systems, Architectures and Processors (ASAP)* (2021), pp. 117–124, URL: <https://doi.org/10.1109/ASAP52443.2021.00025>
- [322] A. A. S. Shaikh, A. Ghosh, A. C. Joshi, C. S. Akhilesh, and S. K. Savitha, *Optimizing Large Gravitational-Wave Classifier Through a Custom Cross-System Mirrored Strategy Approach*, in *2022 IEEE International Conference on Data Science and Information System (ICDSIS)* (2022), pp. 1–7, URL: <https://doi.org/10.1109/ICDSIS55133.2022.9915926>
- [323] A. Iess, E. Cuoco, F. Morawski, C. Nicolaou, and O. Lahav, *LSTM and CNN Application for Core-Collapse Supernova Search in Gravitational Wave Real Data*, *Astronomy & Astrophysics* **669**, (n.d.), URL: <https://doi.org/10.1051/0004-6361/202142525>
- [324] Rui-Qing Yan, Wei Liu, Zong-Yao Yin, Rong Ma, Si-Ying Chen, Dan Hu, Dan Wu, and Xian-Chuan Yu, *Gravitational Wave Detection Based on Squeeze-and-Excitation Shrinkage Networks and Multiple Detector Coherent SNR*, *Research in Astronomy and Astrophysics* **22**, (2022), URL: <https://doi.org/10.1088/1674-4527/ac846c>
- [325] T. Zhao, R. Lyu, H. Wang, Z. Cao, and Z. Ren, *Space-Based Gravitational Wave Signal Detection and Extraction with Deep Neural Network*, *Communications Physics* **6**, (2023), URL: <https://doi.org/10.1038/s42005-023-01334-6>
- [326] K. Han et al., *A Survey on Vision Transformer*, *IEEE Transactions on Pattern Analysis and Machine Intelligence* **45**, 87 (2023), URL: <https://doi.org/10.1109/TPAMI.2022.3152247>
- [327] Prateek Verma and Jonathan Berger, *Audio Transformers:Transformer Architectures For Large Scale Audio Understanding. Adieu Convolutions*, ArXiv, URL: <https://doi.org/10.48550/arXiv.2105.00335>
- [328] (n.d.), URL: <https://emfollow.docs.ligo.org/userguide/analysis/index.html>
- [329] N. Christensen and R. Meyer, *Parameter Estimation with Gravitational Waves*, *Reveiws Modern Physics* **94**, (2022), URL: <https://doi.org/10.1103/RevModPhys.94.025001>
- [330] B. Bécsy, P. Raffai, N. J. Cornish, R. Essick, J. Kanner, E. Katsavounidis, T. B. Littenberg, M. Millhouse, and S. Vitale, *Parameter Estimation for Gravitational-Wave Bursts with the Bayeswave Pipeline*, *The Astrophysical Journal* **839**, (2017), URL: <https://doi.org/10.3847/1538-4357/aa63ef>
- [331] C. Pankow, L. Sampson, L. Perri, E. Chase, S. Coughlin, M. Zevin, and V. Kalogera, *ASTROPHYSICAL PRIOR INFORMATION AND GRAVITATIONAL-WAVE PARAMETER ESTIMATION*, *The Astrophysical Journal* **834**, (2017), URL: <https://doi.org/10.3847/1538-4357/834/2/154>
- [332] M. Bailes et al., *Gravitational-Wave Physics and Astronomy in the 2020s and 2030s*, *Nature Reviews Physics* **3**, 344 (2021), URL: <https://doi.org/10.1038/s42254-021-00303-8>
- [333] M. Branchesi, *Multi-Messenger Astronomy: Gravitational Waves, Neutrinos, Photons, And Cosmic Rays*, (2016), URL: <https://doi.org/10.1088/1742-6596/718/2/022004>
- [334] L. Rezzolla, E. R. Most, and L. R. Weih, *Using Gravitational-Wave Observations and Quasi-Universal Relations to Constrain the Maximum Mass of Neutron Stars*, *The Astrophysical Journal Letters* **852**, (2018), URL: <https://doi.org/10.3847/2041-8213/aaa401>
- [335] R. Robie, A. Brooks, C. Wipf, K. Arai, and R. Adhikari, *LIGO Voyager: A Cryogenic Silicon Interferometer for Gravitational-Wave Detection*, *Bulletin of the American Physical Society* **65**, (n.d.), URL: <https://meetings.aps.org/Meeting/APR20/Session/D05.5>

- [336] A. Samajdar, J. Janquart, C. Van Den Broeck, and T. Dietrich, *Biases in Parameter Estimation from Overlapping Gravitational-Wave Signals in the Third-Generation Detector Era*, **104**, (2021), URL: <https://doi.org/10.1103/PhysRevD.104.044003>
- [337] A. Antonelli, O. Burke, and J. R. Gair, *Noisy Neighbours: Inference Biases from Overlapping Gravitational-Wave Signals*, Monthly Notices of the Royal Astronomical Society **507**, 5069 (2021), URL: <https://doi.org/10.1093/mnras/stab2358>
- [338] Justin Janquart, Tomasz Baka, Anuradha Samajdar, Tim Dietrich, and Chris Van Den Broeck, *Parameter Estimation Methods for Analyzing Overlapping Gravitational Wave Signals in the Third-Generation Detector Era*, arXiv, URL: <https://doi.org/10.48550/arXiv.2211.01304>
- [339] T. Robson and N. Cornish, *Impact of Galactic Foreground Characterization on a Global Analysis for the LISA Gravitational Wave Observatory*, Classical and Quantum Gravity **34**, (2017), URL: <https://doi.org/10.1088/1361-6382/aa9601>
- [340] T. B. Littenberg, N. J. Cornish, K. Lackeos, and T. Robson, *Global Analysis of the Gravitational Wave Signal from Galactic Binaries*, Physical Review D **101**, (2020), URL: <https://doi.org/10.1103/PhysRevD.101.123021>
- [341] N. Karnesis, S. Babak, M. Pieroni, N. Cornish, and T. Littenberg, *Characterization of the Stochastic Signal Originating from Compact Binary Populations as Measured by LISA*, Physical Review D **104**, (2021), URL: <https://doi.org/10.1103/PhysRevD.104.043019>
- [342] J. Janquart, T. Baka, A. Samajdar, T. Dietrich, and C. Van Den Broeck, *Analyses of Overlapping Gravitational Wave Signals Using Hierarchical Subtraction and Joint Parameter Estimation*, Monthly Notices of the Royal Astronomical Society **523**, (2023), URL: <https://doi.org/10.1093/mnras/stad1542>
- [343] J. Langendorff, A. Kolmus, J. Janquart, and C. Van Den Broeck, *Normalizing Flows as an Avenue to Studying Overlapping Gravitational Wave Signals*, Physical Review Letters **130**, (n.d.), URL: <https://doi.org/10.1103/PhysRevLett.130.171402>
- [344] L. Barsotti, L. McCuller, M. Evans, and P. Fritschel, *The A+ Design Curve*, URL: <https://dcc-lho.ligo.org/public/0149/T1800042/005/T1800042-v5.pdf>
- [345] F. Thabtah, S. Hammoud, F. Kamalov, and A. Gonsalves, *Data Imbalance in Classification: Experimental Evaluation*, Information Sciences **513**, 429 (2020), URL: <https://doi.org/10.1016/j.ins.2019.11.004>
- [346] T. Cemgil, S. Ghaisas, K. Dvijotham, S. Gowal, and P. Kohli, *The Autoencoding Variational Autoencoder*, in *Advances in Neural Information Processing Systems*, Vol. 33 (2020), pp. 15077–1508, URL: https://proceedings.neurips.cc/paper_files/paper/2020/file/ac10ff1941c540cd87c107330996f4f6-Paper.pdf
- [347] S. Bini, G. Vedovato, M. Drago, F. Salemi, and G. A. Prodi, *An Autoencoder Neural Network Integrated into Gravitational-Wave Burst Searches to Improve the Rejection of Noise Transients*, Classical and Quantum Gravity **40**, (2023), URL: <https://doi.org/10.1088/1361-6382/acd981>
- [348] K. Bajaj, D. K. Singh, and M. A. Ansari, *Autoencoders Based Deep Learner for Image Denoising*, in *Third International Conference on Computing and Network Communications (Coconet'19)*, Vol. 171 (2020), pp. 1535–1541, URL: <https://doi.org/10.1016/j.procs.2020.04.164>